# SCIENTIFIC RESULTS OF THE NASA-SPONSORED STUDY PROJECT ON MARS: EVOLUTION OF VOLCANISM, TECTONICS, AND VOLATILES

MEVTV



LPI Technical Report Number 90-06
LUNAR AND PLANETARY INSTITUTE 3303 NASA ROAD 1 HOUSTON, TEXAS 77058-4399

# SCIENTIFIC RESULTS OF THE NASA-SPONSORED STUDY PROJECT ON MARS: EVOLUTION OF VOLCANISM, TECTONICS, AND VOLATILES

Sean C. Solomon
Department of Earth, Atmospheric, and Planetary Sciences
Massachusetts Institute of Technology
Cambridge MA 02139

Virgil L. Sharpton
Lunar and Planetary Institute
3303 NASA Road 1
Houston TX 77058-4399

James R. Zimbelman
Center for Earth and Planetary Studies
National Air and Space Museum
Smithsonian Institution
Washington DC 20560

Lunar and Planetary Institute 3303 NASA Road 1 Houston TX 77058-4399

LPI Technical Report Number 90-06

Compiled in 1990 by the
LUNAR AND PLANETARY INSTITUTE

The Institute is operated by Universities Space Research Association under Contract NASW-4066 with the National Aeronautics and Space Administration.



This report may be cited as:
Solomon S. C., Sharpton V. L., and Zimbelman J. R., eds. (1990) *Scientific Results of the NASA-Sponsored Study Project on Mars: Evolution of Volcanism, Tectonics, and Volatiles*. LPI Tech. Rpt. 90-06, Lunar and Planetary Institute, Houston. 322 pp.

Papers in this report may be cited as:
Author A. A. (1990) Title of paper (abstract). In *Scientific Results of the NASA-Sponsored Study Project on Mars: Evolution of Volcanism, Tectonics, and Volatiles* (S. C. Solomon, V. L. Sharpton, and J. R. Zimbelman, eds.), pp. xx–yy. LPI Tech. Rpt. 90-06, Lunar and Planetary Institute, Houston.

This report is distributed by:

ORDER DEPARTMENT
Lunar and Planetary Institute
3303 NASA Road 1
Houston TX 77058-4399

*Mail order requestors will be invoiced for the cost of shipping and handling.*

# Contents

# Project Summary

Among the principal accomplishments of the MEVTV project are several important and widely accepted scientific findings about Mars. The global and regional volcanic flux has been established from systematic geological mapping using Viking images, providing a relative volcanic chronology for most of martian history. Petrologic and chemical analyses of SNC meteorites, inferred to have been derived from Mars, have revealed an abundance of volatile materials, including hydrous minerals (amphiboles), oxidized sulfur, possible carbonates, and various salts; these results provide direct evidence that Mars is likely to be volatile-rich. Geological mapping and temporal groupings of major fault systems have provided strong new constraints on the sequence and timing of martian tectonic events, particularly in the vicinity of the Tharsis region.

Although many fundamental aspects of martian evolution remain to be resolved, substantial progress was forthcoming on several fronts during the MEVTV program. The origin of the crustal dichotomy on Mars was the subject of intensive investigations, and two classes of hypotheses have emerged: One relates the northern lowlands to the effects of large impact(s); the other calls for tectonic foundering subsequent to subcrustal erosion by mantle convection. The kinematics and mode of formation of wrinkle ridges are the subjects of continuing research. While it is clear that these features represent compressional deformation, whether they are predominantly the expression of buckling or faulting remains problematic, as does the cause and implications of their remarkably straight trends and periodic spacing in some locales. Isotopic and petrologic analyses have revealed significant variations within the group of SNC meteorites that, if these objects come from Mars, suggests heterogeneous sources for the parental martian magmas.

Several intriguing new ideas have resulted from project-sponsored research and workshop discussions. A number of tectonic features have been identified as probable transcurrent faults documenting horizontal offsets of a least several tens of kilometers. Such faulting, along with the large extensional strains required to form Valles Marineris, could indicate an early episode of significant horizontal motions of lithospheric blocks. One speculative hypothesis is that such motions were accommodated in a very early episode of plate tectonics on Mars, during which the original lithosphere of the northern lowlands was subducted beneath the Tharsis region and new lithosphere with thinner crust was generated at a now extinct spreading center. This hypothesis, which remains to be tested rigorously, links the formation of the crustal dichotomy to the formation of Tharsis.

# Science Report

## INTRODUCTION

Mars has been the target of a number of ambitious spacecraft missions, including the American Viking orbiters and landers in the late 1970s and, more recently, the Soviet Phobos spacecraft in 1989. Soon after the Viking mission it became clear that data from that mission would constitute a long-term source of important information about the nature and evolution of Mars. In recognition of this potential, NASA established the Mars Data Analysis Program (MDAP) in 1979 to coordinate the funding and the direction of Mars research. The first of several major thematic investigations supported by MDAP was a focused three-year study project entitled "Mars: Evolution of its Climate and Atmosphere" (MECA), initiated in 1984 under the direction of the Lunar and Planetary Institute in Houston, Texas. The success of the MECA project (*Clifford et al.*, 1988a,b) led to a follow-on three-year study project entitled "Mars: Evolution of Volcanism, Tectonics, and Volatiles" (MEVTV), initiated by NASA in 1987, also under the direction of the Lunar and Planetary Institute.

The organization of the MEVTV project was styled after that of the successful MECA project. It combined elements of a project approach and targeted research by independent investigators. Specific goals and objectives were defined from the project perspective, but investigators were funded individually and operated independently within the context of the study. The first meeting of the MEVTV project was held in the spring of 1987, where a science steering committee was chosen and general guidelines for the project were defined. Participation in MEVTV was open to all investigators with research interests encompassed by the goals of the project, regardless of funding source, to ensure broad-based involvement (see Appendix 1). A program of workshops was organized to provide cohesion to the project and to ensure that the project's objectives would be addressed (Table 1). The MEVTV project provided a rich environment for collaborative efforts between investigators from very diverse fields of investigation, often resulting in new approaches to difficult problems related to the study of Mars.

This report reviews the research highlights of the MEVTV study project and discusses some of the important scientific issues that remain unresolved. Several of the questions brought to the attention of the community through the MEVTV project are now the focus of a new three-year study project entitled "Martian Surface and Atmosphere Through Time" (MSATT), which was initiated by NASA in the spring of 1990. A bibliography of published abstracts and papers written by project participants is given in Appendix 2, and abstracts of papers given at the final meeting of the project are included as Appendix 3.

TABLE 1. MEVTV workshops.

| Name Of Workshop | Date |
|---|---|
| Nature and Composition of Surface Units on Mars | December 1987 |
| Volcanism on Mars | June 1988 |
| Early Tectonic and Volcanic Evolution of Mars | October 1988 |
| Tectonic Features on Mars | April 1989 |
| Tharsis | October 1989 |
| Evolution of Magma Bodies on Mars | January 1990 |
| Special Sessions on Martian Tectonic, Volcanic, Magmatic, and Surface Evolution at LPSC XXI | March 1990 |

## OBJECTIVES OF THE MEVTV PROJECT

The objectives of the MEVTV project were to outline the volcanic and tectonic history of Mars, to determine the influence of volatiles on martian volcanic and tectonic processes, and to attempt to determine the compositional, thermal, and volatile history of Mars from its volcanic and tectonic evolution.

The scientific rationale for the project was based on the recognition that Mars is the only planet other than the Earth that has had a long volcanic and deformational history that could be studied in detail. The Moon and Mercury became inactive relatively early in their history, and there was then insufficient information to make appropriate comparisons with Venus. Earth's deformational and volcanic history is dominated by plate tectonics, which has tended to obscure and destroy much of its early record. In contrast, plate tectonics was not thought to have occurred during Mars' decipherable history. Volcanic and deformational features on Mars were held to be well-preserved products of the chemistry and long-term dynamics of the relatively deep mantle rather than the result of thin-skinned tectonics. Furthermore, surficial erosional processes have been relatively modest, causing many ancient structures to display only minor degradation. For these reasons Mars was regarded as providing an environment in which volcanic and deformational processes could be studied in a relatively simple tectonic framework in contrast to Earth, where most geologic features are the result of the complex and destructive interaction of many processes.

At the outset of the project, the nature, type, and distribution of martian volcanic and tectonic features had been broadly established. Much work had also been done on the nature of the volcanic activity on the planet. For

example, the styles of volcanic activity and possible rheological properties of the erupted lavas had been inferred from studies of the morphology and dimensions of volcanic features. Similarly, the global patterns of deformation were reasonably well understood. The development of the hypothesis that Mars may be the parent body of the SNC meteorites (shergottites, nakhlites, and Chassigny) had been recently developed. Enough was then known about the SNC meteorites to begin to influence our way of thinking about many aspects of Mars, including its bulk composition, oxidation state, differentiation history, thermal history, magma generation capability, volatile inventory (including degassing history), volcanism, weathering, and cratering. What was lacking at the start of the MEVTV project was detailed information on how the volcanic and tectonic activity changed with time (requiring careful analysis of age relations by crater counts and geometric relations); systematic integration of information from the SNC meteorites into studies of martian magmatism and global evolution; and a full understanding of the implications of the volcanic, tectonic, and volatile histories for the evolution of the martian crust and interior.

Following are scientific tasks that were identified prior to the MEVTV project as important and achievable with existing data. It was recognized that some progress had already been made on most of these tasks, but most of the effort to that time had involved data reduction more than analysis or synthesis. The general approach adopted was to use available datasets (e.g., photogeology, topography, gravity) to test general models of the volcanic and tectonic history of Mars. The specific tasks were to:

1. Determine the locations and relative ages of volcanic features and trace the history of emplacement of volcanic materials on the surface.
2. Determine changes in the pattern of faulting with time by such means as crosscutting structural relations and crater density statistics.
3. Define and test models of the current state of stress in the martian lithosphere using gravity and topography data.
4. Use fault patterns to infer past states of stress in the lithosphere and how the stresses may have changed with time.
5. Use the stress history within the lithosphere and the volcanic history to place limits on the thermal history of the interior and internal dynamics.
6. Examine the nature and possible causes of the global dichotomy on Mars, with particular emphasis on modeling the topography and gravity.
7. Relate the stress history to the volcanic history and infer how the thickness and other properties of the lithosphere have evolved with time.
8. Assess reasons for the contrasting styles of martian and terrestrial volcanism, particularly the apparent longevity and large size of martian volcanos and the possible role played by volatiles in the eruption process.
9. Compare the vertical deformation and faulting of broad crustal regions of Mars with broad structural uplifts and basins in the interior of lithospheric plates on Earth.
10. Determine to the extent possible the composition of magmas related to volcanic materials, the source reservoirs, and the processes responsible for magma migration to those reservoirs.
11. Investigate the relationship between atmosphere-surface interactions and volcanism during the period of time when surface morphology suggests a substantially different volatile regime.
12. Determine the effect of quasiperiodic (e.g., axial changes) and episodic processes (e.g., volcanism) on the near-surface thermal regime, and on the exchange of volatiles among the atmosphere, regolith, and polar caps.

## SCIENTIFIC OVERVIEW OF THE MEVTV PROJECT

### The Global Volcanic and Tectonic Evolution of Mars

Important progress was made during the MEVTV project on documenting the geological evidence for the volcanic and tectonic history of Mars. Also advanced during the course of the project were the formulation and testing of models for mantle dynamics, magmatism, and interior evolution consistent with this geological history. While a number of hypotheses for martian evolution have been considerably sharpened as a result of these efforts, it is perhaps not surprising that many fundamental questions remain at best incompletely answered.

***The crustal dichotomy.*** The approximately hemispherical division of the martian surface between the topographically lower and stratigraphically younger northern plains and the heavily cratered southern uplands is often termed the crustal dichotomy. The difference in elevations of the two hemispheres appears to be isostatically supported by differences in average crustal thickness (*Janle*, 1983). The 2.1-km offset of the center-of-figure from the center-of-mass on Mars can be explained by the contributions of a nearly compensated Tharsis rise and an isostatically compensated crustal dichotomy. The direction of this offset, toward 58°S, 94°W (*Kobrick et al.*, 1981), is approximately midway between the centers of the southern highlands and the Tharsis rise (*Roth et al.*, 1981). The ancient age of the southern uplands suggests that the dichotomy was largely established very early in martian geological history,

although erosion may have modified the dichotomy boundary over a considerable period of time (*Maxwell and McGill*, 1988).

Two classes of hypotheses have been offered for the origin of the dichotomy. In one class, the northern lowlands are held to occupy one or more large impact basins. In the first discussion of this idea (*Wilhelms and Squyres*, 1984), the largest expanse of lowlands was proposed to result from the formation of a single large impact basin 7700 km in diameter, the "Borealis Basin." This hypothesis was held to account for the approximately circular planform and scarp-like morphology of much of the dichotomy boundary, the concentric massifs and narrow tracts of highlands not related to other basins, the thinned lowland crust, and the heat required for lowlands plains volcanism. A modification of the single-impact hypothesis is that the northern lowlands occupy several large impact basins, on the grounds that the proposed Borealis Basin is much larger than the few next-largest recognized basins (*Frey and Schultz*, 1988) and that high-standing cratered terrain as ancient as the cratered uplands can be found within the proposed basin interior (*Frey et al.*, 1988). Buried topography in the Utopia Planitia region of the northern lowlands suggests the presence of a 3300-km-diameter buried basin (Fig. 1), which is less than half the size of the proposed Borealis

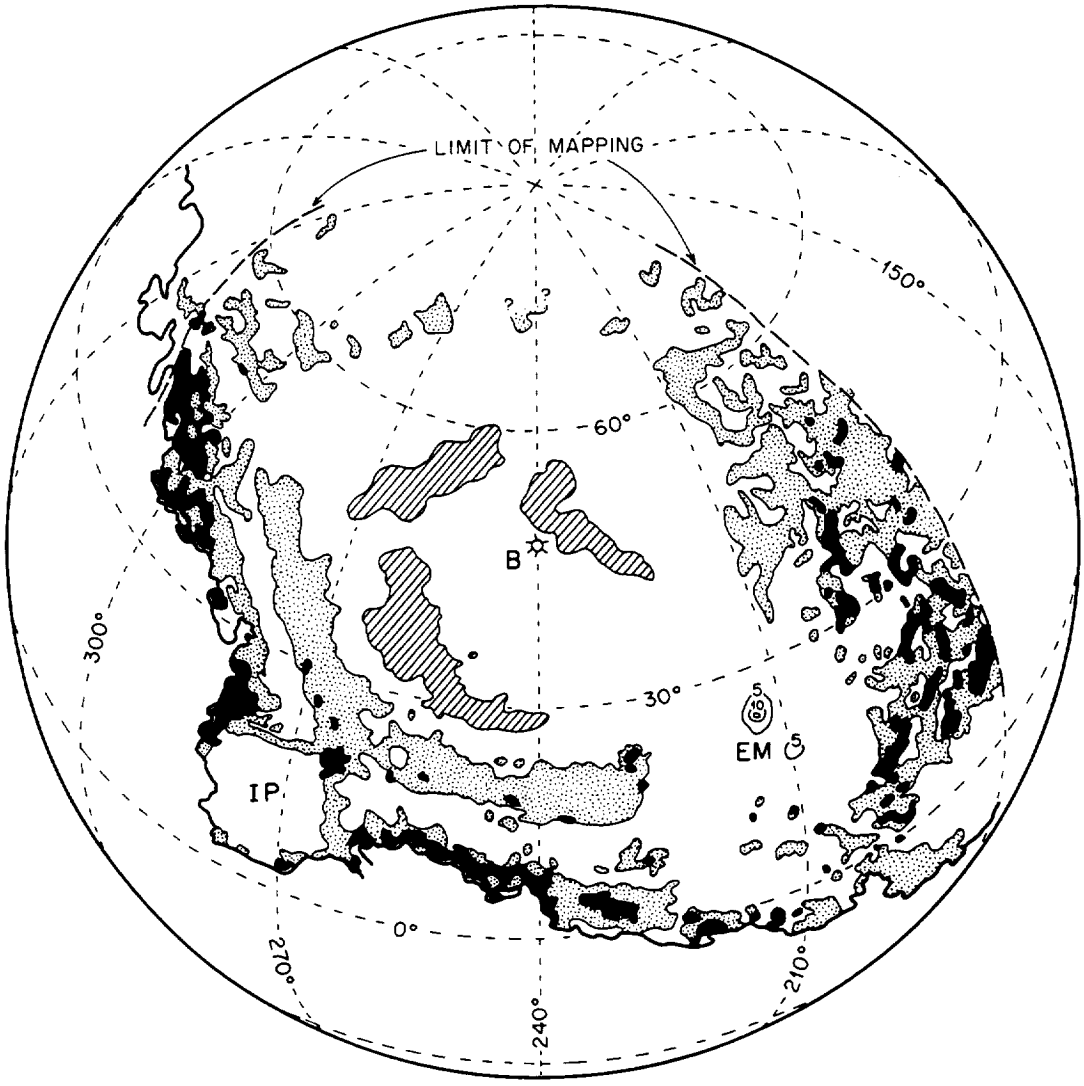


**Fig. 1.** Distribution of knobs suggesting the presence of a buried impact basin in Utopia Planitia (from McGill, 1989b). Solid shading, abundant knobs and mesas; stippled shading, scattered knobs; diagonal shading, polygonal terrain. IP, Isidis Planitia; EM, Elysium Mons; B, estimated center of Utopia Basin. The heavy solid line is the boundary between the southern cratered highlands and the northern lowlands. (Figure reproduced with permission of American Geophysical Union.)

Basin (*McGill*, 1989b). The large impact hypothesis, whether single or multiple impacts were involved, has been criticized as inconsistent with the absence of evidence for crust substantially thicker than average beneath the rim and inner ejecta blankets of the postulated large basins, with an early Hesperian peak in global volcanic activity (i.e., substantially after the time of basin formation; *Tanaka et al.*, 1988), and with the fact that stratigraphic units partially filling the lowlands and embaying highland units include nothing older than early Hesperian (*McGill*, 1989a).

In the second class of hypotheses the crustal dichotomy is the product of tectonic processes. According to the first specific scenario suggested (*Wise et al.*, 1979b), the northern regions foundered isostatically after subcrustal "erosion" by a first-degree mantle convection pattern that prevailed prior to core formation. Planetary accretion considerations (*Wetherill*, 1985) and Pb isotope systematics in the Shergotty parent body (*Chen and Wasserburg*, 1986), presumed to be Mars (e.g., *McSween*, 1984; *Bogard et al.*, 1984) as discussed below, now indicate that core-mantle differentiation on Mars occurred very early, perhaps contemporaneously with planet formation. The suggestion has recently been made (N. H. Sleep, unpublished remarks, 1989) that the lowlands lithosphere was produced during an early episode of plate tectonics on Mars. Such a hypothesis provides an explanation for the large horizontal displacements of the lithosphere inferred from the opening of Valles Marineris and the interpretation of Gordii Dorsum and other related ridges as large-offset transcurrent faults (*Forsythe and Zimbelman*, 1988). It has been speculatively suggested that the Phlegra Montes, centrally located in the northern lowlands, may have been a spreading center that ceased activity by the Late Noachian and that the Tharsis Montes originated by arc-type volcanism at a Noachian subduction zone (N. H. Sleep, unpublished remarks, 1989; *Tanaka*, 1990b).

***Martian volcanic flux.*** The volcanic flux on Mars as a function of space and time provides a critical constraint on models of mantle dynamics, global thermal evolution, mantle melting, and crustal growth. While the relative chronology of large-scale surface units on Mars was reasonably well established on the basis of stratigraphic and crater density relationships inferred from Mariner 9 images (*Carr et al.*, 1973; *Scott and Carr*, 1978), detailed analysis of the tens of thousands of higher-resolution Viking orbiter images has led to a new global geological map of substantially improved stratigraphic resolution (*Tanaka*, 1986) and unit definition (*Scott and Tanaka*, 1986; *Greeley and Guest*, 1987; *Tanaka and Scott*, 1987). From this analysis, several noteworthy characteristics of the history of emplacement of volcanic material at the martian surface have been documented (*Tanaka et al.*, 1988; *Tanaka*, 1990b). The global rate of volcanic resurfacing generally declined from levels near 1 $km^2/yr$ in the Middle Noachian to on the order of 0.01 $km^2/yr$ in the Amazonian (Fig. 2), presumably reflecting a general cooling of the martian mantle from an initial state sufficiently hot to permit very early differentiation of core and crust. Superimposed on this gradual decline, however, was an apparent peak in volcanic resurfacing rate in the Early Hesperian, with the strength of the peak a function of the uncertain rate of production of impact craters over the past 3.5–4 b.y. and the uncertain proportion of Noachian volcanic material (Fig. 2). Most of the Early Hesperian peak consists of the areally extensive ridged plains units, thought to have formed by the voluminous eruptions of low-viscosity, mafic lavas (*Greeley and Spudis*, 1981). At the end of the Early Hesperian, the spatial pattern of volcanism changed dramatically from one of globally dispersed activity to regionally concentrated plains formation and large shield construction focused in the Tharsis and Elysium areas. Igneous and tectonic activity in these major volcanic provinces apparently led to breakouts of debris flows and catastrophic floods that carved the outflow channels in adjacent lower lying terrain, discharges that eroded extensive areas of highlands, contributed to the resurfacing of the northern plains, and redistributed a significant fraction of subsurface water on the planet (*Tanaka*, 1990b).

Accounting for this history of volcanic flux with quantitative models of martian thermal evolution and interior dynamics remains a topic of ongoing effort and

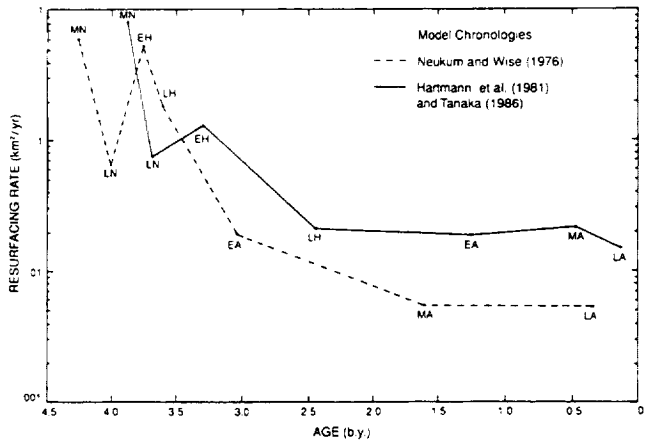


**Fig. 2.** Average resurfacing rates for volcanic plains corresponding to each martian epoch (modified from *Tanaka et al.*, 1988). Rates are based on the reconstructed areas of volcanic plains for two crater chronologies. Note the corrected resurfacing rates (reduced by a factor of 1000) from those of *Tanaka et al.* (1988). Martian epochs: MN, Middle Noachian; LN, Late Noachian; EH, Early Hesperian; LH, Late Hesperian; EA, Early Amazonian; MA, Middle Amazonian; LA, Late Amazonian.

controversy. *Stevenson and Bittker* (1990) have drawn attention to the potential for the extraction of basaltic melt from the martian mantle to stabilize convection because of the strong reduction in the density of the mantle residuum, which they argue would likely reside in an upper boundary layer. These authors suggest that such a stabilizing effect could lead to long intervals in which volcanism is modest to absent while the interior warms and distinct layers develop in the convecting mantle. Gradual merging of convecting layers would lead to an episode of widespread volcanism; extraction of significant melt from the mantle during this episode would initiate a new cycle. This viewpoint has been challenged by *Turcotte and Huang* (1990), who assert that the residuum remaining after melt extraction would be well mixed into the convecting mantle, leading to a "marble-cake" structure rather than a stably layered system. In their models and in other parameterized convection calculations (e.g., *Schubert et al.*, 1990b), global heat flow, mean mantle temperature, and the average rate of addition of magma to the crust all decrease monotonically with time. The general history of volcanism on Mars is one of a gradually decreasing flux (*Tanaka et al.*, 1988), consistent with the predictions of parameterized convection models, but the apparent peak in flux during the Early Hesperian may be an example of mantle warming of the type predicted by the *Stevenson and Bittker* (1990) scenario.

Accounting for the localization of volcanic activity on Mars to a few major volcanic provinces after the Early Hesperian remains a challenge to theoretical models. The long duration of activity and the excess heat flux implied by the thinning of the elastic lithosphere in the center of major volcanic provinces (*Solomon and Head*, 1990) indicate that the excess heat is being supplied from the underlying mantle, presumably in the form of localized regions of enhanced upwelling, or mantle plumes. Numerical calculations of three-dimensional convection in a viscous spherical shell have been recently carried out by *Schubert et al.* (1990a) to simulate possible convective planforms in a martian mantle heated both from within (by radiogenic heat) and from below (by core cooling). These calculations support the view that the most prominent form of convective upwelling in the martian mantle is the cylindrical plume, but the models yield a large number of plumes (more than 10) unless both an unreasonably large fraction of heat is supplied from the core and the core radius is considerably smaller than inferred from the present martian moment of inertia (*Bills*, 1989; *Kaula et al.*, 1989). While some aspects of these results may be consequences of the assumptions required in current three-dimensional convection codes (constant viscosity mantle, Rayleigh numbers no more than about 100 times the critical value), the concentration of sustained volcanic activity in Tharsis and Elysium may have arisen from the focusing of multiple plumes beneath each province, perhaps as a result of thinning and fracturing of the lithosphere by earlier tectonic activity in each region.

***Martian tectonic history.*** The Tharsis province of Mars, by virtue of its large scale and its complex and extended history of activity (*Carr*, 1974; *Wise et al.*, 1979a), dominates the discussion of martian tectonic evolution. Approximately 8000 km in diameter and occupying an area equal to 25% of the surface area of Mars, the Tharsis region is marked by a broad topographic rise standing as much as 10 km above the surrounding terrain. A positive gravity anomaly coincides with the long-wavelength topographic high (*Phillips and Saunders*, 1975). Swarms of extensional fractures and graben extend outward from Tharsis for thousands of kilometers in a crudely radial array (*Plescia and Saunders*, 1982). There are also important compressional features located in the ridged plains of Tharsis and oriented approximately circumferential to the center of activity (*Wise et al.*, 1979a). The duration of faulting and volcanic activity represented by the tectonic and volcanic features of Tharsis span a large fraction of martian history. The long-wavelength gravity and topography of the region are not consistent with complete isostatic compensation by a single mechanism, such as crustal thickness variations (*Phillips and Saunders*, 1975). Complete local isostasy is possible, however, if a combination of Airy (crustal thickness variations) and Pratt (mantle density variations) mechanisms act in concert, but only if the crust is relatively thin (or is pervasively intruded by high-density plutonic material) beneath the Tharsis rise and substantial density anomalies persist to several hundred kilometers depth (*Sleep and Phillips*, 1979, 1985; *Finnerty et al.*, 1988). Alternatively, a portion of the high topography of Tharsis can be supported by membrane stresses in the martian elastic lithosphere (*Banerdt et al.*, 1982; *Willemann and Turcotte*, 1982).

These compensation models can be used to predict long-wavelength lithospheric stresses for comparison with the observed distribution of tectonic features. The situation at the outset of the MEVTV project was that the isostatic model for Tharsis predicted stresses in approximate agreement with the distribution and orientation of extensional fractures in the central Tharsis region and of compressive wrinkle ridges, while the model involving lithospheric support of a topographic load predicted stresses generally consistent with the more distal extensional features (Fig. 3) in regions adjacent to the Tharsis rise (*Banerdt et al.*, 1982; *Sleep and Phillips*, 1985). An evolution in the nature of the support of Tharsis topography was suggested (*Banerdt et al.*, 1982; *Solomon and Head*, 1982), though it was recognized that a sequence of distinct support models depends upon the distal and

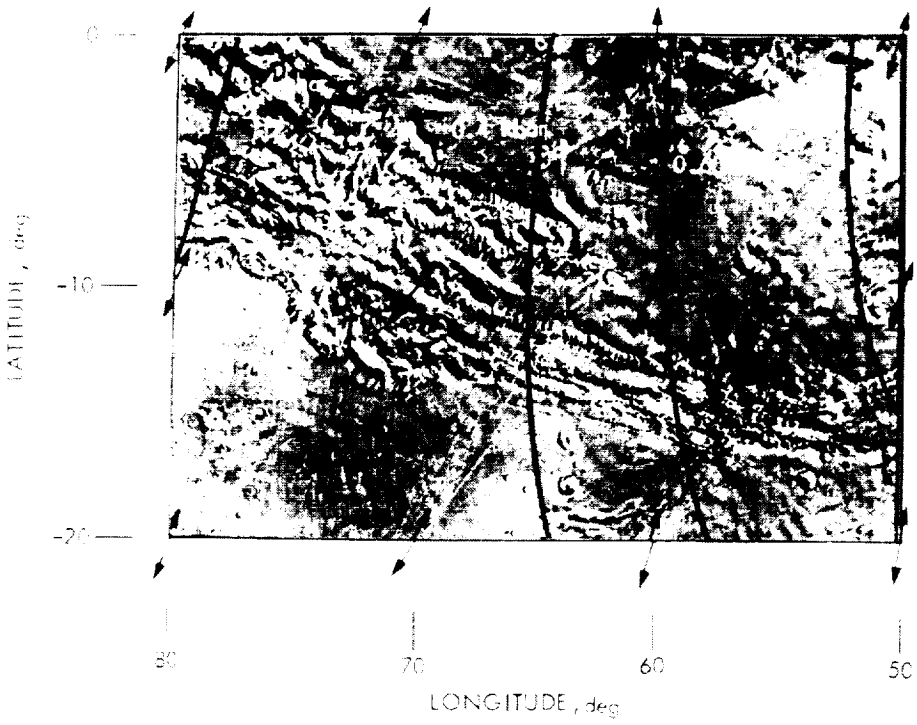


**Fig. 3.** Prediction of surface stress trajectories in the Valles Marineris region from a Tharsis flexural loading model (after *Banerdt et al.*, 1982). The greatest extensional stress is horizontal and approximately orthogonal to Valles Marineris. Contours of stress magnitude are in kilobars.

proximal tectonic features having different ages. If the distal features were older, then viscoelastic relaxation of stresses associated with an early episode of lithospheric loading might have led to an essentially isostatic state at present; if the distal features were younger, then a progression from local isostasy to lithospheric support as the Tharsis rise was constructed might have been the natural consequence of global interior cooling and lithospheric thickening (*Sleep and Phillips*, 1985).

Recent geological mapping and detailed studies, as part of the MEVTV project, of the history of faulting in the Tharsis province and surrounding areas have provided a wealth of new constraints on possible evolutionary models for the region. The earliest recognized set of faults, dating from the Early Noachian, are east-west trending normal faults and graben in the Claritas Fossae region (*Tanaka and Davis*, 1988). These faults are among the few tectonic features in the Tharsis province that are orthogonal to extensional stress directions predicted by flexural uplift models for Tharsis (*Banerdt et al.*, 1982) and support an early episode of large-scale uplift of the region (*Tanaka and Davis*, 1988; *Phillips et al.*, 1990). During the Noachian and Hesperian, major systems of extensional fractures and graben formed in patterns predominantly radial but also concentric to a series of areas within central Tharsis (*Wise et al.*, 1979a; *Plescia and Saunders*, 1982; *Tanaka and Davis*, 1988). The principal episode of formation of wrinkle ridges, oriented generally concentric to Tharsis (*Wise et al.*, 1979a), occurred shortly after ridged plains emplacement in the Early Hesperian (*Scott and Tanaka*, 1986). Because the major episodes of faulting during the Late Noachian to Hesperian involve nearly contemporaneous formation of features both distal and proximal to central Tharsis, neither the isostatic nor the lithospheric flexure models of *Banerdt et al.* (1982) provide an adequate fit to the full distribution of faulting during any single tectonic episode.

Several promising directions have been identified to improve on existing models for the tectonic evolution of Tharsis and of Mars in general. First, it is important to distinguish faulting associated with localized centers of uplift and subsidence from that associated with the long-wavelength stress distribution across Tharsis, and ongoing mapping efforts provide a basis for such a separation (*Tanaka and Davis*, 1988). Second, it is necessary to explicitly include global thermal stress. The Early Hesperian age for most major ridged plains units (*Tanaka*, 1986) and the contrast between the widespread occurrence of wrinkle ridges in the ancient cratered uplands and their spotty occurrence in volcanic plains younger than Early Hesperian (*Chicarro et al.*, 1985) suggest that ridge formation may have been concentrated in a comparatively early stage in martian evolution (*Watters and Maxwell*, 1986), perhaps dominantly in the Early Hesperian (see below). Examination of crosscutting relations between ridges and graben also supports the view

that most ridge formation in the Tharsis region was restricted to an early time period (*Watters and Maxwell*, 1983). Martian thermal histories calling for a hot initial state and rapid cooling concentrated within the period 3–4 b.y. ago (*Schubert et al.*, 1990b; *Turcotte and Huang*, 1990) are most consistent with an Early Hesperian episode of global contraction and widespread wrinkle ridge formation.

Finally, it appears that lateral variations in heat flux and crustal thickness across Tharsis have led to pronounced horizontal variations in the mechanical properties of the lithosphere (*Solomon and Head*, 1990) that can have a significant effect on stress models (*Banerdt and Golombek*, 1990). Specifically, a thicker crust and higher heat flow in the central Tharsis region may act to decouple the crust in that region from the underlying strong layer of the upper mantle. In such a situation the strong upper mantle layer will deform as part of the globally continuous elastic lithosphere shell, some 100–200 km thick (*Banerdt et al.*, 1982; *Willemann and Turcotte*, 1982; *Solomon and Head*, 1990), while the comparatively thin layer of strong upper crust in central Tharsis will deform as a spherical cap with a lubricated lower surface and a periphery fixed to the global shell. Preliminary models (*Banerdt and Golombek*, 1990) suggest that the central area will respond primarily to isostatic spreading forces and increases in radius of curvature induced by subsidence of the lower lithosphere, leading to radial extensional structures in central Tharsis, while outside of the central region of crust-mantle decoupling the faulting will generally follow the predictions of the earlier flexural models for the formation of distal radial extensional fractures (Fig. 3). Horizontal radial compression, leading to the formation of concentric wrinkle ridges, is likely to be concentrated near the boundary between the two regions (*Banerdt and Golombek*, 1990).

## Martian Magmas and Their Weathering Products

A primary goal of studying volcanic materials is to place constraints on the composition and the physical conditions of the source magmas. As noted above, a unique group of basaltic achondrites, known collectively as the SNC meteorites, may represent samples from the volcanic plains of Mars (*Wood and Ashwal*, 1981). While this hypothesis has not been conclusively proven, the evidence in support of a martian origin for these meteorites is very compelling. Analyses of the SNC meteorites provide clues to the composition of the martian mantle and the sources of volcanic activity on Mars. In particular, conclusions obtained from meteorite analysis have interesting implications for the observed characteristics of martian volcanos and the interaction of volcanic materials with volatiles in the martian environment.

***Inferences from SNC meteorites.*** Return of a documented sample from Mars will provide the first conclusive compositional information about the red planet, but until that occurs, the SNC meteorites (Fig. 4) will remain the most likely examples of martian volcanic material. None of the SNC meteorites are older than 1.3 b.y. (*Wood and Ashwal*, 1981; *McSween*, 1984, 1985), and isotopic evidence suggests that the shergottites contain an igneous component that is both quite young (<200 m.y.) and mantle-derived (*Jones*, 1989). These ages are much younger than those of all other dated meteorites (>4.4 b.y.; from *Sears*, 1978) and are difficult to reconcile with a parent body smaller than the size of Mars. The very close match between the gases trapped in the glassy portions of the SNC meteorites and atmospheric measurements made by the Viking landers on Mars strengthens the case for a Mars origin, particularly since both sets of results are distinct from any other sampled region of the solar system (*Bogard et al.*, 1984; *Becker and Pepin*, 1984; *Pepin*, 1985). If one assumes that the SNC meteorites are from Mars, then the martian mantle can be modeled using the SNC chemistry and the assumption of a chondritic bulk composition, opening the martian interior to both experimental and petrochemical techniques (*Holloway*, 1990).

Experimental and thermodynamic constraints on the bulk composition give a mineralogy for the martian mantle, at a pressure of 30 kbar, of approximately 50 wt% olivine, 25 wt% orthopyroxene, 15 wt% Ca-pyroxene, and 10 wt% garnet (although the Ca-pyroxene/garnet ratio is highly variable), a composition quite similar to that of the


**Fig. 4.** SNC meteorite EETA 79001, found in Antarctica in 1979. Gases trapped within the glassy portions of this meteorite have isotopic abundances very similar to the atmosphere of Mars, as measured by the Viking spacecraft.

Earth's upper mantle (*Bertka and Holloway*, 1989; *Holloway*, 1990). Garnet is stabilized at lower pressures in Mars than in the Earth (*Holloway*, 1990) and Mars appears to have a lower mg# [= atomic Mg/(Mg + Fe)], which could affect the partitioning of rare earth elements between the source region and the primary magmas (*Holloway*, 1990). The measured viscosity of a generalized SNC parent magma ranges from 10–200 poise over a temperature range of 1250°–1350°C at 1 bar pressure (*Spera and Stein*, 1990), only slightly higher than the 1–3 poise viscosity of the magma at 1450°C and 23 kbar pressure (*Bertka and Holloway*, 1989).

Synthesized glasses with the approximate bulk composition of various SNC meteorites have been used to determine the position of phase boundaries and crystal/liquid tie lines (*Longhi and Pan*, 1989). All these materials could have fractionated to produce the pyroxenes observed in Shergotty and Zagami (a shergottite). The calculated parent magma compositions have low aluminum contents and vary widely in the concentrations of a calcium-rich component (*Longhi and Pan*, 1989). These results require either that the source region was dominated by augite, which should be accompanied by a small negative Eu anomaly that is not observed, or that $CO_2$ fluxed the melt at pressures >25 kbar (*Longhi*, 1990). Thus the martian mantle may have interesting characteristics that distinguish it from volcanic source regions on Earth.

***Volcanic materials and volatiles.*** The volcanic products derived from SNC primary magmas have important implications for volcanic features observed on the martian surface. Primary magmas derived from a volatile-free mantle at 25 kbar would resemble an iron-rich, picritic, alkali basalt at low degrees of partial melting (*Bertka and Holloway*, 1988). With an increase in the degree of melting, the primary magmas will trend toward iron-rich komatiites (*Bertka et al.*, 1990), consistent with field observations of komatiite flows that may be analogous to long lava flows observed on Mars (*Treiman*, 1987). Flow dimensions have been used to estimate rheologic properties for martian flow features (e.g., *Hulme*, 1976) but with varying degrees of uncertainty (*Baloga*, 1988). Application of photoclinometric techniques to images of martian lava flows have led to refinements in some estimates (*Moore and Davis*, 1990), which tend toward the low viscosities that should accompany flows derived from a SNC parent magma. A new method for estimating eruption rates from considerations of the temperature distribution throughout an active flow (*Crisp and Baloga*, 1990), rather than the equivocal interpretation of levee heights, should provide an independent check on martian lava properties derived from images.

The confirmed presence and abundance of volatiles in SNC meteorites have important implications for possible explosive volcanism on Mars. The high $H_2O$ content documented for the Chassigny and Shergotty parent magmas (*Treiman*, 1985; *Johnson et al.*, 1990), coupled with the very low solubility of $CO_2$ at low pressures for SNC parent magmas (*Pan and Holloway*, 1990), indicate that some erupting lavas on Mars could include a significant explosive component. Tyrrhena Patera (Fig. 5), one of the oldest volcanos on Mars, includes deposits that have been interpreted to include a substantial ash component (*Greeley and Spudis*, 1981). Whether these ash deposits are products of phreatomagmatic volcanism is presently a matter of some debate (*Greeley and Crown*, 1990; *Robinson*, 1990). Ash deposits also have been identified on or around Hecates Tholus (*Mouginis-Mark et al.*, 1982), Alba Patera (*Mouginis-Mark et al.*, 1988), and near Elysium Mons (*Zimbelman and McBride*, 1989). Exsolution of juvenile volatiles in the erupting magmas may have driven explosive stages of eruptions of these volcanos



**Fig. 5.** Tyrrhena Patera, a low-relief volcanic feature in the cratered highlands of Mars that likely includes a significant component of ash. The volatiles involved in the pyroclastic eruption may have been from liquid or frozen groundwater, or juvenile gases that accompanied the rise of the magma, or both. Viking Orbiter frame 87A14; area shown is 280 km across.

without requiring extensive chemical fractionation, as discussed by *Francis and Wood* (1982).

Volatiles should have an important effect on both the chemistry and physical condition of volcanic materials at the martian surface. Sulfur was observed in considerable quantities at the Viking landing sites (*Clark et al.*, 1977), an observation that stimulated consideration of possible mechanisms for its emplacement at the martian surface (*Burns*, 1988) as well as the chemical and weathering effects of iron sulfides on Mars (*Burns and Fisher*, 1990). Oxidized sulfur is present in substantial quantities in several SNC meteorites (*Gooding and Muenow*, 1986; *Burgess et al.*, 1989), strengthening the probable significance of this material to martian chemistry. Other volatile substances reported in SNC meteorites include apparent carbonate carbon (*Carr et al.*, 1985; *Gooding et al.*, 1990), carbon and deuterium of apparent preterrestrial origin (*Kerridge*, 1988), and various salts (*Gooding et al.*, 1988, 1990). Recent observations by the Infrared Spectro-Imager (ISM) instrument on the Phobos spacecraft document a variation in the hydration of martian surface materials (*Bibring et al.*, 1990; *Erard et al.*, 1991), consistent with the high $H_2O$ content of some SNC meteorites (*Johnson et al.*, 1990). While the martian atmosphere contains relatively little water vapor (*Farmer et al.*, 1977), it still holds about as much water vapor as it can under present surface conditions (*Davies*, 1979). Water transported ephemerally through the atmosphere can have a pronounced weathering effect even in extremely cold and arid environments. Slow chemical alteration associated with intermittent, thin ice layers turns fine-grained, nonvesicular basalt in Antarctica into deeply pitted, irregular rocks; a similar, slow process may have played a part in forming the pitted rocks abundant at the Viking landing sites (*Allen and Conca*, 1991). Surface conditions in the past were likely very different from present conditions on Mars (e.g., *Toon et al.*, 1980), perhaps allowing liquid water to accumulate in transient northern oceans, causing planetwide climatic effects (*Baker et al.*, 1990). A variable climatic history on Mars will complicate the identification of past weathering processes from present surface materials.

## Origin and Distribution of Tectonic Features on Mars

The surface of Mars displays a spectacular array of compressional and extensional features. A long-standing objective of Mars studies is to understand the controls over the orientation, position, and spacing of these features and the constraints they impose on the rheology and state of stress of martian surface units. Considerable attention was directed toward this goal during the MEVTV project, including two MEVTV workshops, one to address questions regarding the early tectonic and volcanic evolution of Mars (*Frey*, 1989), and another to assess the current knowledge of martian tectonic features, including kinematic and mechanical models for their origin (*Watters and Golombek*, 1989). While some fundamental issues remain unresolved, it is clear that substantial progress has been made in several key areas.

***Controls over the distribution of tectonic features through time.*** The distribution and relative ages of major extensional and compressional tectonic features on Mars are now sufficiently documented through detailed mapping that the timing and relative significance of local and regional tectonic controls are well constrained (except for the Thaumasia province of southeastern Tharsis, which is currently being studied; K. L. Tanaka, personal communication, 1990). In addition to the global tectonic influence of the Tharsis rise, discussed above, eight other centers exerted regional control over faults and graben systems on Mars. Five of these centers are volcanic complexes similar to, but smaller than, the Tharsis rise. Listed in order of decreasing influence they are the Syria Planum rise (*Tanaka and Davis*, 1988), Alba Patera (*Rotto and Tanaka*, 1989; *Tanaka*, 1990a), Tharsis Montes, Elysium Mons, and Olympus Mons (*Scott and Dohm*, 1990).

All these volcanic centers are surrounded by regional systems of graben and/or ridges, and several show indications of substantial flank and summit deformation. Recent efforts to understand the tectonic evolution of these large centers have focused on the dramatic suite of surface features on Olympus Mons. *Borgia et al.* (1989) suggested that its prominent and enigmatic peripheral scarp is the surface expression of a fault-propagation fold that formed by gravitational failure and outward spreading of the volcano. Collapse and thrusting associated with magma chamber evacuation could account for the series of terraces on the slopes of Olympus Mons (*Thomas et al.*, 1989). Calculations based on the topography and radial distribution of tectonic features within the Olympus Mons caldera complex predict that this magma chamber was located at a depth of ~15 km (*Zuber and Mouginis-Mark*, 1989). It remains a task for future analyses to determine if these models are compatible with the full range of features observed both at Olympus Mons and on other large volcanos.

The extensive parallel fault systems that bracket and delineate the highlands-lowlands boundary scarp demonstrate that it is a major tectonic influence, regardless of uncertainties over the origin of the crustal dichotomy (*Maxwell and McGill*, 1988; *Scott and Dohm*, 1990). The remaining three tectonic centers are the large impact basins Hellas, Isidis, and Argyre (*Wichman and Schultz*, 1989; *Scott and Dohm*, 1990). The younger plains units flanking these basins are deformed by concentric graben.

Thus it appears that these large martian impact basins acted as centers of sustained volcanic and tectonic activity in a manner consistent with that of lunar mare basins of comparable size.

Martian wrinkle ridges, similar in many respects to those on the lunar maria (*Sharpton and Head*, 1987), are typically associated with plains-forming materials interpreted to be lava flows (Fig. 6). Ridges range in age from Middle Noachian to Early Amazonian, but the widely recognized "surge" in ridged plains emplacement occurred in Early Hesperian (*Scott and Dohm*, 1990; *Frey et al.*, 1991). Most of the extensive systems of Early Hesperian wrinkle ridges were formed concentric to the Tharsis rise more than 2000 km away from its center. Generally less pronounced but widespread wrinkle ridges and associated scarps formed during the late Noachian, and a few ridges formed during the early Amazonian (*Scott and Tanaka*, 1986; *Chicarro*, 1989).

***Wrinkle ridge formation.*** Little doubt remains that martian wrinkle ridges, like their better-studied lunar counterparts, are produced by compressional deformation. *Scott* (1990) maintains that rare examples of ridge-graben colinearity suggest an extensional ridge origin, but numerous studies have demonstrated that many properties of wrinkle ridges are difficult to reconcile with extensional deformation (*Sharpton and Head*, 1987; *Plescia and Golombek*, 1986; *Watters*, 1988; *Aubele*, 1989; *Schultz*, 1990). The subsurface structure and details of wrinkle ridge formation nonetheless remain the subjects of considerable debate. Detailed understanding in these areas is required before martian ridges can be used confidently as strain gauges (*Golombek et al.*, 1991) or in constraining the mechanical properties of the martian lithosphere (*Saunders et al.*, 1981; *Watters*, 1988; *Zuber and Aist*, 1989; *Watters and Chadwick*, 1990).

A variety of models have been proposed for martian wrinkle ridge formation, ranging from buckling of upper crustal layers (*Watters*, 1988) to deep-seated thrust faulting that leads to near-surface folding (*Plescia and Golombek*, 1986; *Zuber and Aist*, 1990), and a range of planetary analogs have been called upon in support of these models. The failure to resolve the details of wrinkle ridge formation is due in large measure to the lack of imaging and topographic data of sufficient resolution to characterize these features. Photoclinometric profiles of some martian ridges indicate a topographic offset across these structures similar to that associated with some lunar mare ridges. The presence of such an offset has been used to argue against the thin-skinned buckling model for wrinkle ridge formation and in favor of deep-seated thrust faulting (*Golombek et al.*, 1991). This argument can be inverted, however, because it is equally difficult for thrust faulting to explain those ridges that have considerable topographic development unaccompanied by noticeable offsets (*Watters*, 1988). *Sharpton and Head* (1987) have concluded that lunar ridges appear to be polygenetic landforms: The basic morphological properties that identify ridges as a single class of landform reflect their common compressional origin and rheological similarities, but each ridge system is the product of a sustained and variable deformational path that is locally influenced. Some involve buckling and thrusting and others high-angle reverse faulting as compression is accommodated along preexisting basement faults. Only by examination of high-resolution topography and imaging can the details of this process be unraveled for the Moon, and presumably the same holds true for martian ridges.

**Fig. 6.** Wrinkle ridges in the Lunae Planum region of Mars. The morphology of these ridges appears very similar to wrinkle ridges found on the Moon. Viking Orbiter frame 610A22; area shown is 150 km across.

***Valles Marineris.*** The similarities between Valles Marineris and block-faulted structures on Earth have long been recognized (*Frey*, 1979; *Lucchitta et al.*, 1989). The tremendous size of this system (hundreds of kilometers wide, thousands of kilometers long, and many kilometers deep), although undoubtedly enhanced by severe mass wasting and collapse, points to extensional deformation

involving the entire martian lithosphere and prompts comparisons with terrestrial rift valleys. Stress modeling constrained by long-wavelength gravity and topography (e.g., *Banerdt et al.*, 1982) generally predicts extensional stresses orthogonal to Valles Marineris (Fig. 3). One problem in understanding the origin of Valles Marineris is explaining the many closed depressions, such as Ganges Catena and Hebes Chasma, and their relationships to the larger open canyons. A proposed explanation is that these closed depressions are collapse structures over deep-seated fractures, in the manner of pit crater chains (*Tanaka and Golombek*, 1989). *Schultz* (1989a) argues against this mechanism for the origin of large closed depressions, maintaining that, while both features are produced by extensional processes, they are distinctly different in morphology. One problem that all such tectonic explanations face is how to account kinematically for the large amounts of lithospheric extension required to produce the chasmata. *Croft* (1989) presents a novel alternative. He suggests that individual closed features up to ~1000 $km^3$ in volume could be karst features, while larger features are primarily due to tectonic subsidence. While this mechanism may reduce the need for crustal spreading somewhat, considerable extension is still required to produce the larger features.

***Possible strike-slip faulting on Mars.*** In contrast to the attention garnered by both extensional and compressional processes on Mars, strike-slip deformation, until recently, has gone virtually uninvestigated. This is probably because occurrences of clear strike-slip indicators such as offset craters rims, valley walls, or structural trends are not obvious on Mars (*Golombek*, 1985). However, as *Schultz* (1989b) recently noted, such primary strain markers are not always observed in conjunction with major shear zones on Earth either. Near the surface, discrete offsets at depth can be distributed over a broad zone characterized by such secondary features as shear fractures, tear faults, and echelon folds. Echelon structures alone, however, do not necessarily indicate strike-slip faulting; rather they attest to fracture and fold growth through inhomogeneous stress fields (*Schultz*, 1990). Thus, while these secondary features may be more common than primary structural offsets, they are less compelling evidence of strike-slip deformation.

Recent studies of martian surface images have revealed a number of structural elements that resemble the secondary features associated with strike-slip deformation on Earth. *Schultz* (1989b) has noted evidence of limited strike-slip faulting of the ridged plains near Valles Marineris in the form of consistent *en echelon* arrangements of wrinkle ridges.

Transcurrent faulting on Mars at a much larger scale has been advanced by *Forsythe and Zimbelman* (1988, 1989). From their analysis of probable secondary shear indicators in the vicinity of the Gordii Dorsum escarpment and the similarity of this feature to a major terrestrial shear zone, the Dasht-e-Bayez (Iran), they conclude that this escarpment is the surface expression of an ancient left-lateral fault zone of lithospheric proportions (*Forsythe and Zimbelman*, 1988). The width of this shear zone suggests that offsets across this structure could be in the range of tens of kilometers. Horizontal offsets of this scale call for a dramatically different tectonic regime early in the history of Mars, one in which horizontal motion of the lithosphere played a much more significant role than in more recent times. It should be noted that the interpretation of early faulting on Gordii Dorsum requires that portions of the Medusae Fossae formation be Noachian in age, rather than the Amazonian age indicated by the paucity of impact craters (*Scott and Tanaka*, 1986). While further work is clearly required to substantiate the strike-slip origin of Gordii Dorsum and similar escarpments elsewhere, this hypothesis raises the intriguing possibility that early Mars was, at least tectonically, more similar to the Earth than previously imagined.

## A LOOK FORWARD

Research activities encompassed by the MEVTV project nave clarified many of the issues relevant to the global evolution of Mars, but the wealth of information revealed by detailed studies of regional problems has raised many new questions. Some of the answers to these questions will be provided by the further analysis of data already available, which is the approach taken in the MSATT study project that succeeds MEVTV. New data from the Mars Observer mission, scheduled for launch in 1992, will aid in evaluating both global and regional problems through a combination of long-term monitoring activities and high-resolution information from selected locations. Several of the problems addressed during the MEVTV project will require geophysical and geochemical measurements from widely dispersed locations on Mars, observations that could be made at multiple lander, rover, and penetrator sites envisioned for missions following Mars Observer. The return of documented samples to Earth will resolve many of the intriguing possibilities raised by the study of the SNC meteorites, as well as providing calibration for measurements made from orbit and from the Earth.

***Acknowledgments.*** The authors appreciate the helpful review comments of K. L. Tanaka, J. R. Holloway, and R. J. Phillips, and manuscript preparation by C. Howard. This is LPI Contribution No. 752. The Lunar and Planetary Institute is operated by Universities Space Research Association under Contract No. NASW-4066 with the National Aeronautics and Space Administration.

## REFERENCES


Allen C. A. and Conca J. L. (1991) Weathering of basaltic rocks under cold, arid conditions: Antarctica and Mars. *Proc. Lunar Planet. Sci., Vol. 21*, pp. 711–717.

Aubele J. C. (1989) Morphologic components and patterns in wrinkle ridges: Kinematic implications (abstract). In *MEVTV Workshop on Tectonic Features on Mars* (T. R. Watters and M. P. Golombek, eds.), pp. 13–15. LPI Tech. Rpt. 89-06, Lunar and Planetary Institute, Houston.

Baker V. R., Strom R. G., Croft S. K., Gulick J. S., Kargel J. S., and Komatsu G. (1990) Ancient ocean-land-atmosphere interactions on Mars: Global model and geological evidence (abstract). In *Lunar and Planetary Science XXI*, pp. 40–41. Lunar and Planetary Institute, Houston.

Baloga S. M. (1988) A review of quantitative models for lava flows on Mars (abstract). In *MEVTV Workshop on Nature and Composition of Surface Units on Mars* (J. R. Zimbelman, S. C. Solomon, and V. L. Sharpton, eds.), pp. 17–19. LPI Tech. Rpt. 88-05, Lunar and Planetary Institute, Houston.

Banerdt W. B. and Golombek M. P. (1990) The evolution of Tharsis: Implications of gravity, topography, and tectonics (abstract). In *Lunar and Planetary Science XXI*, pp. 42–43. Lunar and Planetary Institute, Houston.

Banerdt W. B., Phillips R. J., Sleep N. H., and Saunders R. S. (1982) Thick-shell tectonics on one-plate planets: Applications to Mars. *J. Geophys. Res., 87*, 9723–9733.

Becker R. H. and Pepin R. O. (1984) The case for a martian origin of the shergottites: Nitrogen and noble gases in EETA 79001. *Earth Planet. Sci. Lett., 69*, 225–242.

Bertka C. M. and Holloway J. R. (1988) Martian mantle primary melts: An experimental study of iron-rich garnet lherzolite minimum melt composition. *Proc. Lunar Planet. Sci. Conf. 18th*, pp. 723–739.

Bertka C. M. and Holloway J. R. (1989) Martian mantle primary melts. An experimental study of melt density (abstract). In *Lunar and Planetary Science XX*, pp. 69–70. Lunar and Planetary Institute, Houston.

Bertka C. M., Holloway J. R., and Pan V. (1990) Martian mantle primary melts (abstract). In *MEVTV Workshop on the Evolution of Magma Bodies on Mars* (P. Mouginis-Mark and J. Holloway, eds.), pp. 17–19. LPI Tech. Rpt. 90-04, Lunar and Planetary Institute, Houston.

Bibring J.-P., Combes M., Langevin Y., Cara C., Drossart P., Encrenaz T., Erard S., Forni O., Gondet B., Ksanfomaliti L., Lellouch E., Masson P., Moroz V., Rocard F., Rosenqvist J., Soton C., and Soufflot A. (1990) ISM Observations of Mars and Phobos: First results. *Proc. Lunar Planet. Sci. Conf. 20th*, pp. 461–471.

Bills B. G. (1989) The moments of inertia of Mars. *Geophys. Res. Lett., 16*, 385–388.

Bogard D. D., Nyquist L. E., and Johnson P. (1984) Noble gas contents of shergottites and implications for the martian origin of SNC meteorites. *Geochim. Cosmochim. Acta, 48*, 1723–1740.

Borgia A., Burr J., Montero W., Morales L. D., and Alvarado G. I. (1989) The Olympus Mons Scarp: A fault-propagation fold generated by gravity failure of the volcano? (abstract). In *MEVTV Workshop on Tectonic Features on Mars* (T. R. Watters and M. P. Golombek, eds.), pp. 16–17. LPI Tech. Rpt. 89-06, Lunar and Planetary Institute, Houston.

Burgess R., Wright I. P., and Pillinger C. T. (1989) Distribution of sulfides and oxidized sulphur components in SNC meteorites. *Earth Planet. Sci. Lett., 93*, 314–320.

Burns R. G. (1988) Gossans on Mars. *Proc. Lunar Planet. Sci. Conf. 18th*, pp. 713–721.

Burns R. G. and Fisher D. S. (1990) Chemical evolution and oxidative weathering of magmatic iron sulfides on Mars (abstract). In *Lunar and Planetary Science XXI*, pp. 145–146. Lunar and Planetary Institute, Houston.

Carr M. H. (1974) Tectonism and volcanism of the Tharsis region of Mars. *J. Geophys. Res., 79*, 3943–3949.

Carr M. H., Masursky H., and Saunders R. S. (1973) A generalized geologic map of Mars. *J. Geophys. Res., 78*, 4031–4036.

Carr R. H., Grady M. M., Wright I. P., and Pillinger C. T. (1985) Martian atmospheric carbon dioxide and weathering products in SNC meteorites. *Nature, 314*, 248–250.

Chen J. H. and Wasserburg G. J. (1986) Formation ages and evolution of Shergotty and its parent from U-Th-Pb systematics. *Geochim. Cosmochim. Acta, 50*, 955–968.

Chicarro A. F. (1989) Towards a chronology for compressive tectonics on Mars (abstract). In *MEVTV Workshop on Early Tectonic and Volcanic Evolution of Mars* (H. Frey, ed.), pp. 223–225. LPI Tech. Rpt. 89-04, Lunar and Planetary Institute, Houston.

Chicarro A. F., Schultz P. H., and Masson P. (1985) Global and regional ridge patterns on Mars. *Icarus, 63*, 153–174.

Clark B. C., Baird A. K., Rose H. J., Toulmin P., Christian R. P., Kelliher W. C., Castro A. J., Rowe C. D., Keil K., and Huss G. R. (1977) The Viking X-ray fluorescence experiment: Analytical methods and early results. *J. Geophys. Res., 82*, 4577–4594.

Clifford S. M., Greeley R., and Haberle R. M. (1988a) *Scientific Results of the NASA-Sponsored Study Project on Mars: Evolution of Its Climate and Atmosphere.* LPI Tech. Rpt. 88-09, Lunar and Planetary Institute, Houston. 33 pp.

Clifford S. M., Greeley R., and Haberle R. M. (1988b) NASA Mars project: Evolution of climate and atmosphere. *Eos Trans. AGU, 69*, 1585–1596.

Crisp J. and Baloga S. (1990) A method for estimating eruption rates of planetary lava flows. *Icarus, 85*, 512–515.

Croft S. K. (1989) Spelunking on Mars: The carbonate-tectonic hypothesis for the origin of Valles Marineris (abstract). In *MEVTV Workshop on Tectonic Features on Mars* (T. R. Watters and M. P. Golombek, eds.), pp. 21–24. LPI Tech. Rpt. 89-06, Lunar and Planetary Institute, Houston.

Davies D. W. (1979) The relative humidity of Mars' atmosphere. *J. Geophys. Res., 84*, 8335–8342.

Erard S., Bibring J.-P., Mustard J. F., Forni O., Head J. W., Hurtrez S., Langevin Y., Pieters C. M., Rosenqvist J., and Sotin C. (1991) Spatial variations in composition of the Valles Marineris and Isidis Planitia regions of Mars derived from ISM data. *Proc. Lunar Planet. Sci., Vol. 21*, pp. 437–455.

Farmer C. B., Davies D. W., Holland A. L., LaPorte D. D., and Doms P. E. (1977) Mars: Water vapor observations from the Viking Orbiters. *J. Geophys. Res., 82*, 4225–4248.

Finnerty A. A., Phillips R. J., and Banerdt W. B. (1988) Igneous processes and closed system evolution of the Tharsis region of Mars. *J. Geophys. Res., 93*, 10225–10235.

Forsythe R. D. and Zimbelman J. R. (1988) Is the Gordii Dorsum escarpment on Mars an exhumed transcurrent fault? *Nature, 336*, 143–146.

Forsythe R. D. and Zimbelman J. R. (1989) The transcurrent fault hypothesis for Mars' Gordii Dorsum escarpment (abstract). In *MEVTV Workshop on Tectonic Features on Mars* (T. R. Watters and M. P. Golombek, eds.), pp. 30–32. LPI Tech. Rpt. 89-06, Lunar and Planetary Institute, Houston.

Francis P. W. and Wood C. A. (1982) Absence of silicic volcanism on Mars: Implications for crustal composition and volatile abundance. *J. Geophys. Res., 87*, 9881–9889.

Frey H. V. (1979) Martian canyons and African rifts: Structural comparisons and implications. *Icarus, 37*, 142–155.

Frey H. V., ed. (1989) *MEVTV Workshop on Early Tectonic and Volcanic Evolution of Mars.* LPI Tech. Rpt. 89-04, Lunar and Planetary Institute, Houston. 102 pp.

Frey H. and Schultz R. A. (1988) Large impact basins and the mega-impact origin for the crustal dichotomy on Mars. *Geophys. Res. Lett., 15*, 229–232.

Frey H., Semeniuk A. M., Semeniuk J. A., and Tokarcik S. (1988) A widespread common age resurfacing event in the highland-lowland transition zone in eastern Mars. *Proc. Lunar Planet. Sci. Conf. 18th*, pp. 679–699.

Frey H. V., Doudnikoff C. E. , and Mongeon A. M. (1991) Are Noachian-age ridged plains (Nplr) actually Early Hesperian in age? *Proc. Lunar Planet. Sci., Vol. 21*, pp. 635–644.

Golombek M. P. (1985) Fault type predictions from stress distributions on planetary surfaces: Importance of fault initiation depth. *J. Geophys. Res., 90*, 3065–3074.

Golombek M. P., Plescia J. B., and Franklin B. J. (1991) Faulting and folding in the formation of planetary wrinkle ridges. *Proc. Lunar Planet. Sci., Vol. 21*, pp. 679–693.

Gooding J. L. and Muenow D. W. (1986) Martian volatiles in shergottite EETA 79001: New evidence from oxidized sulfur and sulfur-rich aluminosilicates. *Geochim. Cosmochim. Acta, 50*, 1049–1059.

Gooding J. L., Wentworth S. J., and Zolensky M. E. (1988) Calcium carbonate and sulfate of possible extraterrestrial origin in the EETA 79001 meteorite. *Geochim. Cosmochim. Acta, 52*, 909–915.

Gooding J. L., Aggrey K. E., and Muenow D. W. (1990) Volatile compounds in shergottite and nakhlite meteorites (abstract). In *Lunar and Planetary Science XXI*, pp. 423–424. Lunar and Planetary Institute, Houston.

Greeley R. and Crown D. A. (1990) Volcanic geology of Tyrrhena Patera, Mars. *J. Geophys. Res., 95*, 7133–7149.

Greeley R. and Guest J. E. (1987) Geologic map of the eastern equatorial region of Mars. *U.S. Geol. Surv. Misc. Inv. Ser. Map I-1802-B.*

Greeley R. and Spudis P. D. (1981) Volcanism on Mars. *Rev. Geophys. Space Phys., 19*, 13–41.

Holloway J. R. (1990) Martian magmas and mantle source regions: Current experimental and petrochemical constraints (abstract). In *Lunar and Planetary Science XXI*, pp. 528–529. Lunar and Planetary Institute, Houston.

Hulme G. (1976) The determination of the rheological properties and effusion rates of an Olympus Mons lava flow. *Icarus, 27*, 207–213.

Janle P. (1983) Bouguer gravity profiles across the highland-lowland escarpment on Mars. *Moon Planets, 28*, 55–67.

Johnson M. C., Rutherford M. E., and Hess P. C. (1990) Intensive parameters of SNC petrogenesis (abstract). In *MEVTV Workshop on the Evolution of Magma Bodies on Mars* (P. Mouginis-Mark and J. Holloway, eds.), pp. 33–34. LPI Tech. Rpt. 90-04, Lunar and Planetary Institute, Houston.

Jones J. H. (1989) Isotopic relationships among the Shergottites, the Nakhlites and Chassigny. *Proc. Lunar Planet. Sci. Conf. 19th*, pp. 465–474.

Kaula W. M., Sleep N. H., and Phillips R. J. (1989) More about the moment of inertia of Mars. *Geophys. Res. Lett., 16*, 1333–1336.

Kerridge J. F. (1988) Deuterium in Sherogotty and Lafayette (and on Mars?) (abstract). In *Lunar and Planetary Science XIX*, pp. 599–600. Lunar and Planetary Institute, Houston.

Kobrick M., Roth L. E., and Downs G. S. (1981) A radar redermination of the martian center of mass–center of figure offset (abstract). *Eos Trans. AGU, 62*, 942.

Longhi J. (1990) Magmatic processes on Mars: Insights from SNC meteorites (abstract). In *Lunar and Planetary Science XXI*, pp. 716–717. Lunar and Planetary Institute, Houston.

Longhi J. and Pan V. (1989) The parent magmas of the SNC meteorites. *Proc. Lunar Planet. Sci. Conf. 19th*, pp. 451–464.

Lucchitta B. K., Clow G. D., Croft S. K., Geissler P. E., McEwen A. S., Singer R. B., Squyres S. W., and Tanaka K. L. (1989) Canyon systems on Mars (abstract). In *Fourth International Conference on Mars Program and Abstracts*, pp. 36–37. Univ. of Arizona, Tucson.

Maxwell T. A. and McGill G. A. (1988) Ages of fracturing and resurfacing in the Amenthes Region, Mars. *Proc. Lunar Planet. Sci. Conf. 18th*, pp. 701–711.

McGill G. E. (1989a) Geologic evidence supporting an endogenic origin for the martain crustal dichotomy (abstract). In *Lunar and Planetary Science XX*, pp. 667–668. Lunar and Planetary Institute, Houston.

McGill G. E. (1989b) Buried topography of Utopia, Mars: Persistence of a giant impact depression. *J. Geophys. Res., 94*, 2753–2757.

McSween H. Y. Jr. (1984) SNC meteorites: Are they martian rocks? *Geology, 12*, 3–6.

McSween H. Y. (1985) SNC meteorites: Clues to Martian petrologic evolution. *Rev. Geophys., 23*, 391–416.

Moore H. J. and Davis P. A. (1990) Analysis and morphology of a lava flow, Ascraeus Mons, Mars (abstract). In *Lunar and Planetary Science XXI*, pp. 807–808. Lunar and Planetary Institute, Houston.

Mouginis-Mark P. J., Wilson L., and Head J. W. (1982) Explosive volcanism on Hecates Tholus, Mars: Investigation of eruption conditions. *J. Geophys. Res., 87*, pp. 9890–9904.

Mouginis-Mark P. J., Wilson L., and Zimbelman J. R. (1988) Polygenic eruptions of Alba Patera, Mars. *Bull. Volcanol., 50*, 361–379.

Pan V. and Holloway J. H. (1990) $CO_2$ solubility and its implications for degassing ascending magmas (abstract). In *MEVTV Workshop on the Evolution of Magma Bodies on Mars* (P. Mouginis-Mark and J. Holloway, eds.), pp. 46–47. LPI Tech. Rpt. 90-04, Lunar and Planetary Institute, Houston.

Pepin R. O. (1985) Meteorites: Evidence of martian origins. *Nature, 317*, 473–475.

Phillips R. J. and Saunders R. S. (1975) The isostatic state of martian topography. *J. Geophys. Res., 80*, 2893–2898.

Phillips R. J., Sleep N. H., and Banerdt W. B. (1990) Permanent uplift in magmatic systems with application to the Tharsis region of Mars. *J. Geophys. Res., 95*, 5089–5100.

Plescia J. B. and Golombek M. P. (1986) Origin of planetary wrinkle ridges based on the study of terrestrial analogs. *Geol. Soc. Am. Bull., 97*, 1289–1299.

Plescia J. B. and Saunders R. S. (1982) Tectonic history of the Tharsis region, Mars. *J. Geophys. Res., 87*, 9775–9791.

Robinson M. S. (1990) Precise topographic measurements of Apollinaris and Tyrrhena Paterae, Mars (abstract). In *Lunar and Planetary Science XXI*, pp. 1027–1028. Lunar and Planetary Institute, Houston.

Roth L. E., Kobrick M., Downs G. S., Saunders R. S., and Schubert G. (1981) Martian center of mass–center of figure offset (abstract). In *Reports of Planetary Geology Program—1981*, pp. 372–374. NASA TM-84211.

Rotto S. L. and Tanaka K. L. (1989) Faulting history of the Alba Patera-Ceraunius Fossae region of Mars (abstract). In *Lunar and Planetary Science XX*, pp. 926–927. Lunar and Planetary Institute, Houston.

Saunders R. S., Bills T. G., and Johansen L. (1981) The ridged plains of Mars (abstract). In *Lunar and Planetary Science XII*, pp. 924–925. Lunar and Planetary Institute, Houston.

Schubert G., Bercovici D., and Glatzmaier G. A. (1990a) Mantle dynamics in Mars and Venus: Influence of an immobile lithosphere on three-dimensional mantle convection. *J. Geophys. Res., 95*, 14105–14129.

Schubert G., Solomon S. C., Turcotte D. L., Drake M. J., and Sleep N. H. (1990b) Origin and thermal evolution of Mars. In *Mars* (H. H. Kieffer, B. M. Jakosky, C. Snyder, and M. S. Matthews, eds.). Univ. of Arizona, Tucson, in press.

Schultz R. A. (1989a) Do pit crater chains grow up to be Valles Marineris canyons? (abstract). In *MEVTV Workshop on Tectonic Features on Mars* (T. R. Watters and M. P. Golombek, eds.), pp. 47–48. LPI Tech. Rpt. 89-06, Lunar and Planetary Institute, Houston.

Schultz R. A. (1989b) Strike-slip faulting in the ridged plains of Mars (abstract). In *MEVTV Workshop on Tectonic Features on Mars* (T. R.

Watters and M. P. Golombek, eds.), pp. 49–51. LPI Tech. Rpt. 89-06, Lunar and Planetary Institute, Houston.

Schultz R. A. (1990) Origin of the echelon geometries of joints and faults on planetary surfaces (abstract). In *Lunar and Planetary Science XXI*, pp. 1105–1106. Lunar and Planetary Institute, Houston.

Scott D. H. (1990) New evidence—Old problem: Wrinkle ridge origin (abstract). In *MEVTV Workshop on Tectonic Features on Mars* (T. R. Watters and M. P. Golombek, eds.), pp. 52–54. LPI Tech. Rpt. 89-06, Lunar and Planetary Institute, Houston.

Scott D. H. and Carr M. H. (1978) Geologic map of Mars. *U.S. Geol. Surv. Misc. Inv. Ser. Map I-1083.*

Scott D. H. and Dohm J. M. (1990) Chronology and global distribution of fault and ridge systems on Mars. *Proc. Lunar Planet. Sci. Conf. 20th*, pp. 487–501.

Scott D. H. and Tanaka K. L. (1986) Geologic map of the western equatorial region of Mars. *U.S. Geol. Surv. Misc. Inv. Ser. Map I-1802-A.*

Sears D. W. (1978) *The Nature and Origin of Meteorites.* Oxford Univ., London. 187 pp.

Sharpton V. L. and Head J. W. (1987) Lunar mare ridges: Analysis of ridge-crater intersections and implications for the tectonic origin of mare ridges. *Proc. Lunar Planet. Sci. Conf. 18th*, pp. 307–317.

Sleep N. H. and Phillips R. J. (1979) An isostatic model for the Tharsis province, Mars. *Geophys. Res. Lett.*, 6, 803–806.

Sleep N. H. and Phillips R. J. (1985) Gravity and lithospheric stress on the terrestrial planets with reference to the Tharsis region of Mars. *J. Geophys. Res.*, 90, 4469–4489.

Solomon S. C. and Head J. W. (1982) Evolution of the Tharsis province of Mars: The importance of heterogeneous lithospheric thickness and volcanic construction. *J. Geophys. Res.*, 87, 9755–9774.

Solomon S. C. and Head J. W. (1990) Heterogeneities in the thickness of the elastic lithosphere of Mars: Constraints on heat flow and internal dynamics. *J. Geophys. Res.*, 95, 1073–1083.

Spera F. J. and Stein D. J. (1990) Rheological properties of Martian magmas: Experiments and inferences (abstract). In *MEVTV Workshop on the Evolution of Magma Bodies on Mars* (P. Mouginis-Mark and J. Holloway, eds.), pp. 54–55. LPI Tech. Rpt. 90-04, Lunar and Planetary Institute, Houston.

Stevenson D. J. and Bittker S. S. (1990) Why existing terrestrial planet thermal history calculations should not be believed (and what to do about it) (abstract). In *Lunar and Planetary Science XXI*, pp. 1200–1201. Lunar and Planetary Institute, Houston.

Tanaka K. L. (1986) The stratigraphy of Mars. *Proc. Lunar Planet. Sci. Conf. 17th*, in *J. Geophys. Res.*, 91, E139–E158.

Tanaka K. L. (1990a) Tectonic history of the Alba Patera-Ceraunius Fossae region of Mars. *Proc. Lunar Planet. Sci. Conf. 20th*, pp. 515–523.

Tanaka K. L. (1990b) Martian geologic "revolutions": A tale of two processes (abstract). In *Lunar and Planetary Science XXI*, pp. 1237–1238. Lunar and Planetary Institute, Houston.

Tanaka K. L. and Davis P. A. (1988) Tectonic history of the Syria Planum province of Mars. *J. Geophys. Res.*, 93, 14893–14917.

Tanaka K. L. and Golombek M. P. (1989) Martian tension fractures and the formation of grabens and collapse features at Valles Marineris. *Proc. Lunar Planet. Sci. Conf. 19th*, pp. 383–396.

Tanaka K. L. and Scott D. H. (1987) Geologic maps of the polar regions of Mars. *U.S. Geol. Surv. Misc. Inv. Ser. Map I-1802-C.*

Tanaka K. L., Isbell N. K., Scott D. H., Greeley R., and Guest J. E. (1988) The resurfacing history of Mars: A synthesis of digitized, Viking-based geology. *Proc. Lunar Planet. Sci. Conf. 18th*, pp. 665–678.

Thomas P. J., Squyres S. W., and Carr M. H. (1989) Flank tectonics of martian volcanoes (abstract). In *MEVTV Workshop on Tectonic Features on Mars* (T. R. Watters and M. P. Golombek, eds.), pp. 60–62. LPI Tech. Rpt. 89-06, Lunar and Planetary Institute, Houston.

Toon O. B., Pollack J. B., Ward W., Burns J. A., and Bilski K. (1980) The astronomical theory of climatic change on Mars. *Icarus*, 44, 552–607.

Treiman A. H. (1985) Amphibole and hercynite spinel in Shergotty and Zagami: Magmatic water, depth of crystallization, and metasomatism. *Meteoritics*, 20, 229–243.

Treiman A. H. (1987) Geology of the Nakhlite meteorites: Cumulate rocks from flows and shallow intrusions (abstract). In *Lunar and Planetary Science XVIII*, pp. 1022–1023. Lunar and Planetary Institute, Houston.

Turcotte D. L. and Huang J. (1990) Implications of crustal formation on Mars from parameterized convection calculations (abstract). In *Lunar and Planetary Science XXI*, pp. 1266–1267. Lunar and Planetary Institute, Houston.

Watters T. R. (1988) Wrinkle ridge assemblages on the terrestrial planets. *J. Geophys. Res.*, 93, 10236–10254.

Watters T. R. and Chadwick D. J. (1990) Crosscutting periodically spaced first-order ridges in the ridged plains of Hesperia Planum: Another case for a buckling model (abstract). In *MEVTV Workshop on Tectonic Features on Mars* (T. R. Watters and M. P. Golombek, eds.), pp. 68–70. LPI Tech. Rpt. 89-06, Lunar and Planetary Institute, Houston.

Watters T. R. and Golombek M. P., eds. (1989) *MEVTV Workshop on Tectonic Features on Mars.* LPI Tech. Rpt. 89-06, Lunar and Planetary Institute, Houston. 126 pp.

Watters T. R. and Maxwell T. A. (1983) Crosscutting relations and relative ages of ridges and faults in the Tharsis region of Mars. *Icarus*, 56, 278–298.

Watters T. R. and Maxwell T. A. (1986) Orientation, relative age, and extent of the Tharsis Plateau ridge system. *J. Geophys. Res.*, 91, 8113–8125.

Wetherill G. W. (1985) Occurrence of giant impacts during the growth of the terrestrial planets. *Science*, 228, 877–879.

Wichman R. W. and Schultz P. H. (1989) Sequence and mechanisms of deformation around the Hellas and Isidis impact basins on Mars. *J. Geophys. Res.*, 94, 17333–17357.

Wilhelms D. E. and Squyres S. W. (1984) The martian hemispheric dichotomy may be due to a giant impact. *Nature*, 309, 138–140.

Willemann R. J. and Turcotte D. L. (1982) The role of lithospheric stress in the support of the Tharsis rise. *J. Geophys. Res.*, 87, 9793–9801.

Wise D. U., Golombek M. P., and McGill G. E. (1979a) Tharsis province of Mars: Geologic sequence, geometry, and a deformation mechanism. *Icarus*, 38, 456–472.

Wise D. U., Golombek M. P., and McGill G. E. (1979b) Tectonic evolution of Mars. *J. Geophys. Res.*, 84, 7934–7939.

Wood C. A. and Ashwal L. D. (1981) SNC meteorites: Igneous rocks from Mars? *Proc. Lunar Planet. Sci. 12B*, pp. 1359–1375.

Zimbelman J. R. and McBride K. M. (1989) A possible pyroclastic deposit near Elysium Mons, Mars (abstract). In *Lunar and Planetary Science XX*, pp. 1241–1242. Lunar and Planetary Institute, Houston.

Zuber M. T. and Aist L. L. (1989) The shallow structure of the lithosphere in the Coprates and Lunae Planum regions of Mars from the geometries of volcanic plains ridges (abstract). In *MEVTV Workshop on Early Tectonic and Volcanic Evolution of Mars* (H. Frey, ed.), pp. 97–100. LPI Tech. Rpt. 89-04, Lunar and Planetary Institute, Houston.

Zuber M. T. and Aist L. L. (1990) The shallow structure of the martian lithosphere in the vicinity of the ridged plains. *J. Geophys. Res.*, 95, 14215–14230.

Zuber M. T. and Mouginis-Mark P. J. (1989) The depth of the Olympus Mons magma chamber as determined from the spatial distribution of tectonic features (abstract). In *MEVTV Workshop on Tectonic Features on Mars* (T. R. Watters and M. P. Golombek, eds.), pp. 74–76. LPI Tech. Rpt. 89-06, Lunar and Planetary Institute, Houston.

# Appendix 1. Participating Scientists

**TABLE A1.1. Funded investigators.**

| Name | Affiliation | Proposal Title |
|---|---|---|
| John B. Adams | University of Washington | Mars Volcanism and Weathering |
| Stephen M. Baloga | Jet Propulsion Laboratory | The Nature and Evolution of Martian Magma Chambers Inferred from Lava Flow Fields |
| G. Robert Brackenridge | Dartmouth College | Testing Crustal Heating and Climatic Change as Alternative Hypotheses for Small Valley Origins |
| Roger G. Burns | Massachusetts Institute of Technology | Chemical Pathways from Volcanic Exhalates to Dust Storm Particulates on Mars |
| Paul S. Butterworth | NASA Goddard Space Flight Center | A Census of the Small Volcanic Landforms of Mars |
| Michael H. Carr | U.S. Geological Survey, Menlo Park | Near-Surface Ground Temperatures on Early Mars and Sapping Implications |
| Philip R. Christensen | Arizona State University | Mars Surface Compositional Variations from Thermal Emissivity and Albedo Determinations |
| Fraser P. Fanale | University of Hawaii | Volatile Migration and Phase Changes on Mars |
| Herbert Frey | NASA Goddard Space Flight Center | Early Tectonic Evolution of Mars: Crustal Dichotomy to Valles Marineris |
| Matthew P. Golombek | Jet Propulsion Laboratory | Tharsis Tectonics and Deformation Mechanisms on Mars |
| Ronald Greeley | Arizona State University | Martian Volcanism: Type, Age and Distribution of Volcanic Materials on Mars |
| James W. Head | Brown University | Mars Tectonics and Volcanism |
| John R. Holloway | Arizona State University | Volatile and Primary Martian Magmas |
| George E. McGill | University of Massachusetts | The Giant Polygons of Mars |
| Henry J. Moore | U.S. Geological Survey, Menlo Park | Volatile Release from Martian Lavas |
| Peter J. Mouginis-Mark | University of Hawaii | Structural and Volcanic Evolution of Martian and Terrestrial Shield Volcanoes |
| Roger J. Phillips | Southern Methodist University | Tectonic Evolution of Mars |
| Malcolm J. Rutherford | Brown University | Role of C-O-H-S Volatiles in Mars Volcanism: Experiments on Basalts, Evolved Magmas, and the Fe-rich Shergotty Composition |
| Peter H. Schultz | Brown University | Volcanic and Tectonic History of the Martian Highlands |
| David H. Scott | U.S. Geological Survey, Flagstaff | Volcanotectonic Stratigraphic (System) Maps of Mars |
| Sean C. Solomon | Massachusetts Institute of Technology | Mars Tectonics and Volcanism |
| Frank J. Spera | University of California, Santa Barbara | Experimental Rheology of Martian Magma and Thermal Evolution of Mars |
| Edward M. Stolper | California Institute of Technology | Solubility of Noble Gases and Nitrogen in Silicate Melts to 5000 Bars |
| Kenneth L. Tanaka | U.S. Geological Survey, Flagstaff | Mars: Hydrologic Anomalies Caused by Volcanism and Tectonism |
| Donald L. Turcotte | Cornell University | Influence of Volcanism on the Tectonics and State of Stress on Mars |
| Thomas R. Watters | National Air & Space Museum | Thin and Thick-Skinned Tectonics in the Tharsis Region of Mars |

## TABLE A1.2. MEVTV Steering Committee.

| Member | Affiliation | Area |
|---|---|---|
| John B. Adams | University of Washington | Volcanism, Remote sensing |
| Ronald Greeley | Arizona State University | Volcanism |
| James W. Head | Brown University | Volcanism, Tectonics |
| Sean C. Solomon | Massachusetts Institute of Technology | Chairman, Tectonics |
| John Longhi | Columbia University | Petrology |
| Donald L. Turcotte | Cornell University | Tectonics |
| Virgil L. Sharpton | Lunar and Planetary Institute | Project Scientist (1988 to 1990) |
| James R. Zimbelman | Smithsonian Institution | Project Scientist (1988) |
| Michael H. Carr | U.S. Geological Survey | Volatiles, Volcanism |

## MEVTV Study Group

The MEVTV study group consisted of all researchers who participated in the workshops sponsored by the MEVTV project.

John B. Adams
Department of Geological Sciences
University of Washington
Seattle WA 98195

Carl Allen
Westinghouse-Hanford Co.
P.O. Box 1970
Richland WA 99352

Raymond E. Arvidson
Department of Earth and Planetary Sciences
Washington University
St. Louis MO 63130

Jayne C. Aubele
Department of Geological Sciences
Brown University
Lincoln Field Building
Providence RI 02912

Stephen M. Baloga
Mail Stop 183-501
Jet Propulsion Laboratory
4800 Oak Grove Drive
Pasadena CA 91109

W. Bruce Banerdt
Mail Stop 183-501
Jet Propulsion Laboratory
Pasadena CA 91109

Amos Banin
Department of Soil and Water Science
Seagram Center—Hebrew University
P.O. Box 12
Rehovot
Israel

Nadine G. Barlow
Mail Code SN21
NASA Johnson Space Center
Houston TX 77058

Connie M. Bertka
Arizona State University and
Geophysical Laboratory
Washington DC 20008

Jim Bell
Planetary Geosciences Division
Hawaii Institute of Geophysics
2525 Correa Road
Honolulu HI 96822

Diana Blaney
Planetary Geosciences Division
Hawaii Institute of Geophysics
2525 Correa Road
Honolulu HI 96822

Andrea Borgia
Mail Stop 183-501
Jet Propulsion Laboratory
4800 Oak Grove Drive
Pasadena CA 91106

Mark B. Boslough
Division 1131
Sandia National Laboratories
Albuquerque NM 87185

G. Robert Brakenridge
Institute of Remote Sensing
Department of Geography
Dartmouth College
Hanover NH 03755

Kevin Burke
National Academy of Sciences
HA 460
1101 Constitution Avenue N.W.
Washington DC 20418

Roger G. Burns
Department of Earth, Atmospheric, and Planetary Sciences
Massachusetts Institute of Technology
54-816
Cambridge MA 02139

Paul S. Butterworth
Code 633
NASA Goddard Space Flight Center
Greenbelt MD 20771

Michael H. Carr
U.S. Geological Survey
345 Middlefield Road
Menlo Park CA 94025

Peter Cattermole
Beaumont Building
University of Sheffield
Department of Geology
Sheffield S3 7HF
England

John Chadwick
Center for Earth and Planetary Studies
National Air and Space Museum
Smithsonian Institution
Washington DC 20560

Ben Chao
Code 621
NASA Goddard Space Flight Center
Greenbelt MD 20771

Mary Chapman
U.S. Geological Survey
2255 N. Gemini Drive
Flagstaff AZ 86001

Augustin F. Chicarro
ESTEC/Code SI
2200 Noordwijk
Postbus 299
The Netherlands

Philip Christensen
Department of Geology
Arizona State University
Tempe AZ 85287

Ben Clark
Martin Marietta Aerospace
Mail Stop 0560
P.O. Box 179
Denver CO 80201

Stephen Clifford
Lunar and Planetary Institute
3303 NASA Road 1
Houston TX 77058-4399

Lelia M. Coyne
San Jose State University
San Jose CA 95192-0102

Robert A. Craddock
Center for Earth and Planetary Studies
National Air and Space Museum, Room 3101
Smithsonian Institution
Washington DC 20560

Joy Crisp
Mail Stop 183-501
Jet Propulsion Laboratory
4800 Oak Grove Drive
Pasadena CA 91109

Steven K. Croft
Department of Planetary Sciences
Lunar and Planetary Laboratory
University of Arizona
Tucson AZ 85721

David A. Crown
Department of Geology
Arizona State University
Tempe AZ 85287

Larry S. Crumpler
Department of Geological Sciences
Brown University
Box 1846
Providence RI 02912

Rene De Hon
Department of Geoscience
Northeast Louisiana University
Monroe LA 71209

Shanaka de Silva
Lunar and Planetary Institute
3303 NASA Road 1
Houston TX 77058

Andrew Dimitriou
Department of Geology and Geography
University of Massachusetts
Amherst MA 01003

Peter A. J. Englert
Department of Chemistry
San Jose State University
One Washington Square
San Jose CA 95192-0101

Sarah A. Fagents
Lancaster University
Environmental Science Division
Lancaster LA1 4YQ
England

Karl Fecht
Westinghouse-Hanford Co.
P.O. Box 1970
Richland WA 99352

Bruce Fegley
Massachusetts Institute of Technology
Cambridge MA 02139

William C. Feldman
University of California
Los Alamos Scientific Laboratory
Los Alamos NM 87545

Randall Forsythe
Department of Geography and Earth Science
University of North Carolina
Charlotte NC 28223

Sharon Frank
Department of Geological Sciences
Brown University
Box 1846
Providence RI 02912

Peter Francis
Planetary Geosciences Division
Hawaii Institute of Geophysics
2525 Correa Road
Honolulu HI 96822

Friedman Freund
Mail Stop 239-4
NASA Ames Research Center
Moffett Field CA 94035

Herbert Frey
Code 622
NASA Goddard Space Flight Center
Greenbelt MD 20771

James Garvin
Code 622
NASA Goddard Spaceflight Center
Greenbelt MD 20771

Matthew Golombek
1053 Olive Lane
La Canada CA 91011

John Grant
Department of Geological Sciences
Brown University
Box 1846
Providence RI 02912

Ronald Greeley
Department of Geology
Arizona State University
Tempe AZ 85287

Robert Grimm
Department of Geological Sciences
Southern Methodist University
Dallas TX 75275

John Guest
University of London Observatory
Observatory Annexe
33/35 Daws Lane
London NW7 4SD
England

Edward Guinness
Department of Earth and Planetary Science
Washington University
St. Louis MO 63130

William K. Hartmann
Planetary Science Institute
2421 E. 6th St.
Tucson AZ 85719-5234

James W. Head
Department of Geological Sciences
Brown University
Providence RI 02912

Floyd Hodges
8130 W. Falls Place
Kennewick WA 99336

John R. Holloway
Chemistry and Geology Departments
Arizona State University
Tempe AZ 85287

Bruce M. Jakosky
Laboratory for Atmospheric and Space Physics
Campus Box 392
University of Colorado
Boulder CO 80309

Arvid Johnson
Department of Earth and Atmospheric Sciences
Purdue University
West Lafayette LA 47907

Krikitt Johnson
Department of Geological Sciences
Brown University
Box 1846
Providence RI 02912

Marie Johnson
Department of Geological Sciences
Brown University
Box 1846
Providence RI 02912

Susan Keddie
Department of Geological Sciences
Brown University
Box 1846
Providence RI 02912

Walter S. Kiefer
170-25 South Mudd
California Institute of Technology
Pasadena CA 91125

Elbert A. King
Department of Geology
University of Houston
Houston TX 77004

John S. King
Department of Geological Sciences
State University of New York
4240 Ridge Lea Road
Amherst NY 14226

Michael Knight
Planetary Geosciences Division
Hawaii Institute of Geophysics
2525 Correa Road
Honolulu HI 96822

Samual J. Kozak
Geology Department
Washington and Lee University
Lexington VA 24450

John Longhi
Lamont-Doherty Observatory
Columbia University
Palisades NY 10964

Rosaly Lopes
Mail Stop 183-501
Jet Propulsion Laboratory
4800 Oak Grove Drive
Pasadena CA 91109

Karen Love
Department of Geology
University of Houston
Houston TX 77004

Baerbel K. Lucchitta
Branch of Astrogeologic Studies
U.S. Geological Survey
2255 N. Gemini Drive
Flagstaff AZ 86001

Tony Mallama
ST Systems
9701-J Philadelphia Way
Lanham MD 20706

Terry Z. Martin
Mail Stop 169-237
Jet Propulsion Laboratory
4800 Oak Grove Drive
Pasadena CA 91109

Ted Maxwell
National Air and Space Museum, Room 3102
Smithsonian Institution
Washington DC 20560

Kathleen McBride
Department of Geosciences
University of Houston-Clear Lake
4753 Kinglet
Houston TX 77035

Mike McCullough
FMC Corporation
San Jose CA

Lucy-Ann McFadden
California Space Institute A-016
University of California, San Diego
2265 Sverdrup Hall
La Jolla CA 92093-0216

James J. McGee
U.S. Geological Survey
959 National Center
Reston VA 22092

Kimberly McGeehan
Department of Geology
Southern Illinois University
Carbondale IL 62901

George E. McGill
Department of Geology
University of Massachusetts
Amherst MA 01003

Patrick J. McGovern
Massachusetts Institute of Technology
54-521
Cambridge MA 02139

Albert F. Metzger
Mail Stop 183-501
Jet Propulsion Laboratory
4800 Oak Grove Drive
Pasadena CA 91109

Henry J. Moore
U.S. Geological Survey
345 Middlefield Road
Mail Stop 946
Menlo Park CA 94025

Peter J. Mouginis-Mark
Planetary Geosciences Division
Hawaii Institute of Geophysics
2525 Correa Road
Honolulu HI 96822

Scott Murchie
Department of Geological Sciences
Brown University
Box 1846
Providence RI 02912

James Orenberg
Department of Geosciences
San Francisco State University
1600 Holloway Avenue
San Francisco CA 94132

Frank Don Palluconi
Mail Stop 183-501
Jet Propulsion Laboratory
4800 Oak Grove Drive
Pasadena CA 91009

Vivian Pan
Department of Geology & Geophysics
Yale University
P.O. Box 6666
New Haven CT 06511

Tim Parker
Mail Stop 183-501
Jet Propulsion Laboratory
4800 Oak Grove Drive
Pasadena CA 91009

Bob Peterson
Westinghouse-Hanford Co.
P.O. Box 1970
Richland WA 99352

Virginia Pfaff
Department of Geology
Portland State University
Portland OR 97207-0751

Roger J. Phillips
Department of Geological Sciences
Southern Methodist University
Dallas TX 75275

Carlé Pieters
Department of Geological Sciences
Brown University
Box 1846
Providence RI 02912

Patrick Pinet
ER 234/GRGS/CNES
18 Av. E. Belin
31055 Toulouse Cédex
France

Jeffrey B. Plescia
Mail Stop 183-501
Jet Propulsion Laboratory
4800 Oak Grove Drive
Pasadena CA 91109

Sean Posin
Department of Geology
Arizona State University
Tempe AZ 85287

Susan Postawko
Planetary Geosciences Division
Hawaii Institute of Geophysics
2525 Correa Road
Honolulu HI 96822

Robert C. Reedy
Mail Stop D438
Los Alamos National Laboratory
P.O. Box 1663
Los Alamos NM 87545

Stephen Reidel
Westinghouse Hanford Co.
Mail Stop IN H4-56
P.O. Box 1970
Richland WA 99352

Don Rendquist Jr.
FMC Corporation
Santa Clara CA

Cordula Robinson
University of London Observatory
Observatory Annexe
33/35 Daws Lane
London NW7 4SD
England

Mark Robinson
Planetary Geosciences Division
Hawaii Institute of Geophysics
2525 Correa Road
Honolulu HI 96822

Ted L. Roush
Mail Stop 245-3
NASA Ames Research Center
Moffett Field CA 94035

Scott Rowland
Planetary Geosciences Division
Hawaii Institute of Geophysics
2525 Correa Road
Honolulu HI 96822

David Rubincam
Code 620
NASA Goddard Space Flight Center
Greenbelt MD 20771

S. Keith Runcorn
School of Physics
The University
Newcastle Upon Tyne NE1 7RU
England

Malcolm J. Rutherford
Department of Geological Sciences
Brown University
Providence RI 92912

. Stephen Saunders
Mail Stop 230-201 SM
Jet Propulsion Laboratory
4800 Oak Grove Drive
Pasadena CA 91109

lartha Schaefer
Code 621
NASA Goddard Space Flight Center
Greenbelt MD 20771

Dale Schneeberger
Mail Stop 183-501
Jet Propulsion Laboratory
4800 Oak Grove Drive
Pasadena CA 91109

Peter Schultz
Department of Geological Sciences
Brown University
Providence RI 02912

Richard A. Schultz
Mackay School of Mines
University of Nevada-Reno
Reno NV 89557

Deborah Schwartz
NASA Ames Research Center
Moffett Field CA 94035

David H. Scott
U.S. Geological Survey
2255 N. Gemini Drive
Flagstaff AZ 86001

Virgil L. Sharpton
Lunar and Planetary Institute
3303 NASA Road 1
Houston TX 77058

Michael Sims
NASA Ames Research Center
Moffett Field CA 94035

Robert Singer
Lunar and Planetary Laboratory
University of Arizona
Tucson AZ 85721

Norman H. Sleep
Department of Geophysics
Stanford University
Stanford CA 94305

David E. Smith
Laboratory for Terrestrial Physics
Code 621
NASA Goddard Space Flight Center
Greenbelt MD 20771

Milton O. Smith
Department of Geological Sciences
AJ-20
University of Washington
Seattle WA 98195

Sean C. Solomon
Department of Earth, Atmospheric, and Planetary Sciences
Massachusetts Institute of Technology
54-522
Cambridge MA 02139

Frank J. Spera
Department of Geological Sciences
University of California
Santa Barbara CA 93106

Edward Stolper
Division of Geological and Planetary Sciences
California Institute of Technology, 170-25
Pasadena CA 91125

John Suppe
Department of Geological and Geophysical Sciences
Princeton University
Princeton NJ 08544

Kenneth L. Tanaka
U.S. Geological Survey
2255 N. Gemini Drive
Flagstaff AZ 86001

S. Ross Taylor
Research School of Earth Sciences
Australian National University
P.O. Box 4
Canberra ACT 2600
Australia

Paul J. Thomas
Center for Radiophysics
Cornell University
Ithaca NY 86001

Thomas W. Thompson
Mail Stop 300-227
Jet Propulsion Laboratory
4800 Oak Grove Drive
Pasadena CA 91109

Terry Tolan
Portland State University
P.O. Box 751
Portland OR 97207

Allan M. Trieman
Department of Geology
Boston University
Boston MA 02215

Donald Turcotte
Department of Geological Science
Cornell University
4122 Snee Hall
Ithaca NY 14853-1504

Mike Tuttle
National Air and Space Museum
Smithsonian Institution
Washington DC 20560

James R. Underwood
Department of Geology
Kansas State University
Thompson Hall
Manhattan KS 66506

John Watkinson
Geology Department
Washington University
Pullman WA 99164

Thomas R. Watters
Center for Earth and Planetary Studies
Room 3101
National Air and Space Museum
Smithsonian Institution
Washington DC 20560

Robert Wichman
Department of Geological Sciences
Brown University
Providence RI 02912

Don E. Wilhelms
2027 Hyde St., #6
San Francisco CA 94109

Lionel Wilson
Department of Environmental Science
University of Lancaster
Lancaster LA1 4YQ
England

Alexander Woronow
Department of Geology
University of Houston
Houston TX 77004

Sherman S. C. Wu
U.S. Geological Survey
2255 N. Gemini Drive
Flagstaff AZ 86001

Aaron Zent
Planetary Geosciences Division
Hawaii Institute of Geophysics
2525 Correa Road
Honolulu HI 96822

James R. Zimbelman
Center for Earth and Planetary Studies
National Air and Space Museum
Smithsonian Institution
Washington DC 20560

Maria T. Zuber
Code 621
NASA Goddard Space Flight Center
Greenbelt MD 20771

# Appendix 2. Bibliography

What follows is a compilation of papers and abstracts authored by participants in the MEVTV program during the period 1987–1990. While every effort has been made to ensure that this bibliography is otherwise complete, a few abstracts and papers may have been inadvertently omitted. This possibility should be kept in mind when using the bibliography for research purposes.

Special thanks are due Carol Howard, who entered and revised this bibliography, and to Stephen Tellier, of the LPI's Center for Information and Research Services, who compiled and maintains the Lunar and Planetary Bibliography database from which many of these citations were originally obtained.

Adams J. B. and Smith M. O. (1990) Limits on the compositional variability of the martian surface (abstract). In *Lunar and Planetary Science XXI*, pp. 1–2. Lunar and Planetary Institute, Houston.

Adams J. B., Smith M. O., Arvidson R. E., Dale-Bannister M., Guinness E. A., and Singer R. (1988) Surface composition of Mars: A Viking multispectral view (abstract). In *MEVTV Workshop on Nature and Composition of Surface Units on Mars* (J. R. Zimbelman, S. C. Solomon, and V. L. Sharpton, eds.), pp. 13–15. LPI Tech. Rpt. 88-05, Lunar and Planetary Institute, Houston.

Agresti D. G., Wills E. L., Shelfer T. D., Iwanczyk J., Dorri N., and Morris R. V. (1990) Development of a solid-state Mössbauer spectrometer for planetary missions (abstract). In *Lunar and Planetary Science XXI*, pp. 5–6. Lunar and Planetary Institute, Houston.

Aguirre-Puente J., Costard F. M., and Posado-Cano R. (1990) Contribution to the study of thermal erosion of Mars (abstract). In *Lunar and Planetary Science XXI*, pp. 7–8. Lunar and Planetary Institute, Houston.

Allen C. C. and Conca J. L. (1991) Weathering of basaltic rocks under cold, arid conditions: Antarctica and Mars. *Proc. Lunar Planet. Sci., Vol. 21*, pp. 711–717.

Arvidson R. E., Dale-Bannister M. A., and Guinness E. A. (1988) Nature and distribution of surficial deposits in Chryse Planitia and vicinity, Mars (abstract). In *MEVTV Workshop on Nature and Composition of Surface Units on Mars* (J. R. Zimbelman, S. C. Solomon, and V. L. Sharpton, eds.), p. 16. LPI Tech. Rpt. 88-05, Lunar and Planetary Institute, Houston.

Aubele J. C. (1989) Morphologic components and patterns in wrinkle wridges: Kinematic implications (abstract). In *MEVTV-LPI Workshop on Tectonic Features on Mars* (T. R. Watters and M. P. Golombek, eds.), pp. 13–15. LPI Tech. Rpt. 89-06, Lunar and Planetary Institute, Houston.

Aubele J. C. and Crumpler L. S. (1987) The significance of block size and pit diameter in rocks at the Viking lander sites, Mars (abstract). In *Lunar and Planetary Science XVIII*, pp. 36–37. Lunar and Planetary Institute, Houston.

Aubele J. C. and Crumpler L. S. (1989) Characterization of small scale properties of basaltic lava plains: Application to Mars rover sample return missions (abstract). In *Fourth International Conference on Mars, Progr. and Abstracts*, pp. 61–62. Univ. of Arizona, Tucson.

Aubele J. C., Crumpler L. S., and Head J. W. (1987) Constraints on Mars sampling based on models of basaltic flow surfaces and interiors (abstract). In *Workshop on Mars Sample Return Science* (M. J. Drake et al., eds.), pp. 33–34. LPI Tech. Rpt. 88-07, Lunar and Planetary Institute, Houston.

Aubele J. C., Crumpler L. S., and Head J. W. (1988) Small scale surface characterization of Mars (abstract). In *Geol. Soc. Am., Abstracts with Progr., 20*, A77.

Baker V. R., Strom R. G., Croft S. K., Gulick V. C., Kargel J. S., and Komatsu G. (1990) Ancient ocean-land-atmosphere interactions on Mars: Global model and geological evidence (abstract). In *Lunar and Planetary Science XXI*, pp. 40–41. Lunar and Planetary Institute, Houston.

Baloga S. M. (1988) A review of quantitative models for lava flows on Mars (abstract). In *MEVTV Workshop on Nature and Composition of Surface Units on Mars* (J. R. Zimbelman, S. C. Solomon, and V. L. Sharpton, eds.), pp. 17–19. LPI Tech. Rpt. 88-05, Lunar and Planetary Institute, Houston.

Banerdt W. B. and Golombek M. P. (1989) A reevaluation of long-wavelength stress models for Mars. In *Reports of Planetary Geology and Geophysics Program—1988*, pp. 495–497. NASA TM-4130.

Banerdt W. B. and Golombek M. P. (1989) Long wavelength stress models for Mars: New and improved (abstract). In *Lunar and Planetary Science XX*, pp. 40–41. Lunar and Planetary Institute, Houston.

Banerdt W. B. and Golombek M. P. (1990) The evolution of Tharsis: Implications of gravity, topography, and tectonics (abstract). In *Lunar and Planetary Science XXI*, pp. 42–43. Lunar and Planetary Institute, Houston.

Banerdt W. B. and Golombek M. P. (1990) The Tharsis stress paradox: A possible solution. In *Reports of Planetary Geology and Geophysics Program—1989*. NASA TM, in press.

Banerdt W. B., Golombek M. P., and Tanaka K. E. (1990) Stress and tectonics on Mars. In *Mars* (H. Kieffer et al., eds.). Univ. of Arizona, Tucson, in press.

Barlow N. G. (1988) The history of martian volcanism determined from a revised relative chronology (abstract). In *MEVTV Workshop on Nature and Composition of Surface Units on Mars* (J. R. Zimbelman, S. C. Solomon, and V. L. Sharpton, eds.), pp. 20–21. LPI Tech. Rpt. 88-05, Lunar and Planetary Institute, Houston.

Barlow N. G. (1989) Conditions on early Mars: Constraints from the cratering record (abstract). In *MEVTV Workshop on Early Tectonic and Volcanic Evolution of Mars* (H. V. Frey, ed.), pp. 15–16. LPI Tech. Rpt. 89-04, Lunar and Planetary Institute, Houston.

Barlow N. G. (1990) Martian impact craters: Continuing analysis of lobate ejecta sinuosity (abstract). In *Lunar and Planetary Science XXI*, pp. 44–45. Lunar and Planetary Institute, Houston.

Barlow N. G. and Zimbelman J. R. (1988) Venusian coronae: Comparisons with Alba Patera, Mars (abstract). In *Lunar and Planetary Science XIX*, pp. 35–36. Lunar and Planetary Institute, Houston.

Bartels K. S. and Burns R. G. (1989) Heat-oxidized olivines: Characterization of reaction products by 4.2K Mössbauer spectroscopy. In *28th International Geological Congress, Abstracts, 1*, pp. 92–93. Washington, DC.

Bartels K. S. and Burns R. G. (1989) Oxidized olivines on Mars: Spectroscopic investigations of heat-induced aerial oxidation products (abstract). In *Lunar and Planetary Science XX*, pp. 44–45. Lunar and Planetary Institute, Houston.

Bell J. F. III and McCord T. B. (1988) Mars: Comparative spectroscopy (abstract). In *MEVTV Workshop on Nature and Composition of Surface Units on Mars* (J. R. Zimbelman, S. C. Solomon, and V. L. Sharpton, eds.), pp. 23–24. LPI Tech. Rpt. 88-05, Lunar and Planetary Institute, Houston.

Bell J. F. and McCord T. B. (1990) Can iron oxide/oxyhydroxide minerals be identified on the martian surface from ground-based VIS-NIR spectra? (abstract). In *Lunar and Planetary Science XXI*, pp. 60–61. Lunar and Planetary Institute, Houston.

Bell J. F., Lucey P. G., McCord T. B., and Ozoroski T. (1990) Groundbased imaging spectroscopy of Mars during 1988 and 1990: Instrumentation and methodologies for the future of planetary spectroscopy (abstract). In *Lunar and Planetary Science XXI*, p. 62. Lunar and Planetary Institute, Houston.

Bell J. F., Robinson M. S., McCord T. B., and Fanale F. P. (1990) Comparison of new groundbased and Phobos-2 VSK color ratio data for Mars (abstract). In *Lunar and Planetary Science XXI*, pp. 63–64. Lunar and Planetary Institute, Houston.

Ben-Shlomo T. and Banin A. (1990) Iron-enriched smectite clays as Mars soil analogs—chemical reactivity in the labeled release experiment (abstract). In *Lunar and Planetary Science XXI*, pp. 67–68. Lunar and Planetary Institute, Houston.

Bertka C. M. and Holloway J. R. (1988) Martian mantle primary melts: An experimental study of iron-rich garnet lherzolite minimum melt composition. *Proc. Lunar Planet. Sci. Conf. 18th*, pp. 723–739.

Bertka C. M. and Holloway J. R. (1989) Martian mantle primary melts. An experimental study of melt density and viscosity at 23 kb (abstract). In *Lunar and Planetary Science XX*, pp. 69–70. Lunar and Planetary Institute, Houston.

Bertka C. M. and Holloway J. R. (1990) Martian mantle primary melts (abstract). In *Lunar and Planetary Science XXI*, pp. 73–74. Lunar and Planetary Institute, Houston.

Bertka C. M., Holloway J. R., and Pan V. (1990) Martian mantle primary melts (abstract). In *MEVTV Workshop on the Evolution of Magma Bodies on Mars* (P. Mouginis-Mark and J. Holloway, eds.), pp. 17–18. LPI Tech. Rpt. 90-04, Lunar and Planetary Institute, Houston.

Bertolini L. M. and McEwen A. S. (1990) Digital mosaic and elevation model of central Valles Marineris, Mars (abstract). In *Lunar and Planetary Science XXI*, pp. 75–76. Lunar and Planetary Institute, Houston.

Betts B. H., Svitek T., Santee M. L., Murray B. C., Crisp D., Paige D. A., Naraeva M., and Selivanov A. (1990) Preliminary quantitative assessment and analyses of Phobos 88 Termoskan observations of Mars (abstract). In *Lunar and Planetary Science XXI*, pp. 77–78. Lunar and Planetary Institute, Houston.

Bibring J.-P., Langevin Y., Erard S., Forni O., Masson P., Sotin C., Moroz V., Coradini A., Formisano V., Head J., Soderblom L., Fanale F., McCord T., and Cruikshank D. (1990) The observation of the surface of Mars by the ISM instrument on board the Phobos 2 spacecraft (abstract). In *Lunar and Planetary Science XXI*, pp. 79–80. Lunar and Planetary Institute, Houston.

Bills B. G. (1990) Obliquity histories of Earth and Mars: Influence of inertial and dissipative core-mantle coupling (abstract). In *Lunar and Planetary Science XXI*, pp. 81–82. Lunar and Planetary Institute, Houston.

Blaney D. L. (1990) Implications of the low carbonate abundance in the optical surface of Mars (abstract). In *Lunar and Planetary Science XXI*, pp. 97–98. Lunar and Planetary Institute, Houston.

Blaney D. L. and McCord T. B. (1990) Earth-based telescopic observations of Mars in the 4.4 $\mu$m to 5.1 $\mu$m region (abstract). In *Lunar and Planetary Science XXI*, pp. 99–100. Lunar and Planetary Institute, Houston.

Blaney D. L., Walsh P. A., and McCord T. B. (1988) Mars: Spectral signatures seen and unseen (abstract). In *MEVTV Workshop on Nature and Composition of Surface Units on Mars* (J. R. Zimbelman, S. C. Solomon, and V. L. Sharpton, eds.), pp. 25–27. LPI Tech. Rpt. 88-05, Lunar and Planetary Institute, Houston.

Bockstein I. M., Chochia P. A., Kronrod M. A., and Gektin Yu. M. (1990) Processing of Mars surface images received from Phobos-2 space station (abstract). In *Lunar and Planetary Science XXI*, pp. 101–102. Lunar and Planetary Institute, Houston.

Borello M. C. (1987) Geometry and relative age of large patterned fractures in southern Acidalia Planitia, Mars. In *Reports of Planetary Geology and Geophysics Program—1986*, pp. 492–494. NASA TM-89810.

Borello M. C. (1987) Surficial and structural analysis of large patterned fractures in southern Acidalia Planitia, Mars (abstract). In *Lunar Planetary Science XVIII*, pp. 107–108. Lunar and Planetary Institute, Houston.

Borgia A., Burr J., Montero W., Morales L. D., and Alvarado G. I. (1989) The Olympus Mons scarp: A fault-propagation fold generated by gravity failure of the volcano? (abstract). In *MEVTV Workshop on Tectonic Features on Mars* (T. R. Watters and M. P. Golombek, eds.), pp. 16–17. LPI Tech. Rpt. 89-06, Lunar and Planetary Institute, Houston.

Boslough M. B. (1988) Selective weathering of shocked minerals and chondritic enrichment of the martian fines (abstract). In *MEVTV Workshop on Nature and Composition of Surface Units on Mars* (J. R. Zimbelman, S. C. Solomon, and V. L. Sharpton, eds.), pp. 28–30. LPI Tech. Rpt. 88-05, Lunar and Planetary Institute, Houston.

Brakenridge G. R. (1987) Small valley networks and the past and present distribution of subsurface volatiles, Aeolis Quadrangle, Mars. In *Martian Geomorphology and Its Relation to Subsurface Volatiles* (S. M. Clifford, L. Rossbacher, and J. Zimbelman, eds.), pp. 12–13. LPI Tech. Rpt. 87-02, Lunar and Planetary Institute, Houston.

Brakenridge G. R. (1988) Intercrater plains deposits and the origin of martian valleys (abstract). In *MEVTV Workshop on Nature and Composition of Surface Units on Mars* (J. R. Zimbelman, S. C. Solomon, and V. L. Sharpton, eds.), pp. 31–33. LPI Tech. Rpt. 88-05, Lunar and Planetary Institute, Houston.

Brakenridge G. R. (1989) Origin of fluvial valleys and early geological history, Aeolis Quadrangle (abstract). In *MEVTV Workshop on Early Tectonic and Volcanic Evolution of Mars* (H. V. Frey, ed.), pp. 17–19. LPI Tech. Rpt. 89-04, Lunar and Planetary Institute, Houston.

Brakenridge G. R. (1990) The origin of fluvial valleys and early geologic history, Aeolis Quadrangle, Mars. *J. Geophys. Res.*, in press.

Brakenridge G. R. and Williams D. D. (1987) Valley genesis in relation to volcanism, tectonism, and impact cratering, Aeolis Quadrangle, Mars (abstract). In *Geol. Soc. Am., Abstracts with Progr., 19*, 598.

Brückner J., Korfer M., Wänke H., Schroeder A. N. F., Filges D., Dragovitsch P., Englert P. A. J., Starr R., Trombka J. I., Taylor I., Drake D., and Shunk E. (1990) Radiation damage in germanium detectors: Implications for the gamma-ray spectrometer of the Mars Observer spacecraft (abstract). In *Lunar and Planetary Science XXI*, pp. 137–138. Lunar and Planetary Institute, Houston.

Burgess R., Wright I. P., and Pillinger C. T. (1989) Distribution of sulfides and oxidized sulphur components in SNC meteorites. *Earth Planet. Sci. Lett.*, 93, 314–320.

Burns R. G. (1987) Ferric sulfates on Mars. *Proc. Lunar Planet. Sci. Conf. 17th*, in *J. Geophys. Res.*, 92, E570–E574.

Burns R. G. (1987) Gossans on Mars. *Proc. Lunar Planet. Sci. Conf. 18th*, pp. 713–721.

Burns R. G. (1988) Mossbauer spectra of planetary materials contribution to visible—near infrared spectra of regoliths (abstract). In *Symposium on Spectroscopic Methods for Mineral and Mineral Surface Characterization*, 196th Meeting of the American Chemical Society.

Burns R. G. (1988) Sampling the oxidative weathering products and potentially acidic permafrost on Mars (abstract). In *Workshop on Mars Sample Return Science* (M. J. Drake et al., eds.), pp. 46–47. LPI Tech. Rpt. 88-07, Lunar and Planetary Institute, Houston.

Burns R. G. (1988) Sulfide mineralization: Its role in the chemical weathering of Mars (abstract). In *Workshop on Mars Sample Return Science* (M. J. Drake et al., eds.), pp. 48–50. LPI Tech. Rpt. 88-07, Lunar and Planetary Institute, Houston.

Burns R. G. (1988) Spectroscopic investigations of surface alteration products of basalts on Mars (abstract). *Eos Trans. AGU*, 69, 503.

Burns R. G. (1989) Characterization of poorly crystalline surface materials on Mars: Terrestrial analogues. In *28th International Geological Congress, Abstr., 1*, pp. 216–217. Washington, DC.

Burns R. G. (1989) Olivine alteration phases in shergottite ALHA 77005: Information from 4.2°K Mossbauer spectra (abstract). In *Lunar and Planetary Science XX*, pp. 129–130. Lunar and Planetary Institute, Houston.

Burns R. G. (1989) Spectral mineralogy of terrestrial planets: Scanning their surfaces remotely. The 19th Hallimond Lecture. *Mineral. Mag.*, 53, 135–151.

Burns R. G. (1990) Magmatic sulfides on Mars (abstract). In *MEVTV Workshop on the Evolution of Magma Bodies on Mars* (P. Mouginis-Mark and J. Holloway, eds.), pp. 20–22. LPI Tech. Rpt. 90-04, Lunar and Planetary Institute, Houston.

Burns R. G. (1990) Magmatic sulfides on Mars. *Icarus*, submitted.

Burns R. G. (1990) Structural controls on visible-region and Mossbauer spectra of mixed valency minerals. In *NATO Advanced Study Workshop on Mixed Valency Systems: Applications in Chemistry, Physics and Biology*, Crete, Greece, June 1990.

Burns R. G. and Fisher D. S. (1988) Weathering of sulfides on Mars (abstract). In *MEVTV Workshop on Nature and Composition of Surface Units on Mars* (J. R. Zimbelman, S. C. Solomon, and V. L. Sharpton, eds.), pp. 34–36. LPI Tech. Rpt. 88-05, Lunar and Planetary Institute, Houston.

Burns R. G. and Fisher D. S. (1989) Iron-sulfur mineralogy of Mars: Magmatic evolution and chemical weathering products (abstract). In *Fourth International Conference on Mars, Progr. and Abstracts*, pp. 75–76. Univ. of Arizona, Tucson.

Burns R. G. and Fisher D. S. (1989) Sulfide mineralization related to early crustal evolution of Mars (abstract). In *MEVTV Workshop on Early Tectonic and Volcanic Evolution of Mars* (H. Frey, ed.), pp. 20–22. LPI Tech. Rpt. 89-04, Lunar and Planetary Institute, Houston.

Burns R. G. and Fisher D. S. (1990) Chemical evolution and oxidative weathering of magmatic iron sulfides on Mars (abstract). In *Lunar and Planetary Science XXI*, pp. 145–146. Lunar and Planetary Institute, Houston.

Burns R. G. and Fisher D. S (1990) Mechanism of acidic oxidation of pyrrhotite. *Bull. Geol. Soc. Am.*, submitted.

Burns R. G. and Fisher D. S. (1990) Evolution of sulfide mineralization on Mars. *J. Geophys. Res.*, 95, 14169–14173.

Burns R. G. and Fisher D. S. (1990) Iron-sulfur minerology of Mars: Magmatic evolution and chemical weathering products. *J. Geophys. Res.*, 95, 14415–14421.

Burns R. G. and Martinez S. L. (1990) Mossbauer spectra of olivine-rich weathered achondrites: II. Brachina, Chassigny, ALHA 77005, and Nakhla (abstract). In *Lunar and Planetary Science XXI*, pp. 147–148. Lunar and Planetary Institute, Houston.

Burns R. G. and Solberg T. C. (1988) Mossbauer spectra of weathered stony meteorites relevant to oxidation on Mars. II.

Achondrites and SNC meteorites (abstract). In *Lunar and Planetary Science XIX*, pp. 146–147. Lunar and Planetary Institute, Houston.

Cabrol N. A. (1990) Physiographic characteristics of martian drainage basins (abstract). In *Lunar and Planetary Science XXI*, pp. 151–152. Lunar and Planetary Institute, Houston.

Calvin W. M. and King T. V. V. (1990) Analysis of Mariner 6 and 7 spectra for weak absorption features from 2 to 6 μm (abstract). In *Lunar and Planetary Science XXI*, pp. 153–154. Lunar and Planetary Institute, Houston.

Carr M. H. (1990) The effects of floods, volcanism and polar processes on the D/H ratio in the martian atmosphere (abstract). In *Lunar and Planetary Science XXI*, pp. 168–169. Lunar and Planetary Institute, Houston.

Carroll M. R. (1989) The effect of He on the solubility of Ar in silicate solids and liquids (abstract). *Eos Trans. AGU, 70*, 1402.

Carroll M. R. (1990) Ar diffusion in feldspar and rhyolite composition glasses (abstract). *Proc. Third International Symposium on Experimental Mineralogy, Petrology, and Geochemistry, Terra Abstracts, 2*, 68.

Carroll M. R. (1990) Diffusion of Ar in rhyolite, albite, and orthoclase composition glasses. *Earth Planet. Sci. Lett.*, submitted.

Carroll M. R. (1990) Simultaneous determination of inert gas solubility and diffusivity in glasses at elevated pressures and temperatures. *J. Non-Cryst. Solids*, in press.

Carroll M. R. and Rutherford M. J. (1988) Sulfur speciation in hydrous experimental glasses of varying oxidation state: Results from measured wavelength shifts of sulfur X-rays. *Am. Mineral., 73*, 845–949.

Carroll M. R. and Stolper E. M. (1987) Argon solubility and diffusion in silica glass (abstract). *Geol. Soc. Am., Abstracts with Progr., 19*, 612.

Carroll M. R. and Stolper E. M. (1988) Argon solubility and diffusion in rhyolitic and albitic glasses (abstract). *Eos Trans. AGU, 69*, 1465.

Carroll M. R. and Stolper E. M. (1989) Diffusion and solubility of molecular gas species in melts and glasses (abstract). *Terra Abstracts (EUG V), 1*, 271.

Carroll M. R. and Stolper E. M. (1990) Argon solubility and diffusion in $SiO_2$ glass: Implications for the behavior of molecular gas species. *Geochim Cosmochim. Acta*, in press.

Carroll M. R., Paris E., and Davioli I. (1990) XANES and EXAFS study of noble gases in vitreous silica (abstract). *Abstracts of Second European International Conference on Progress in X-ray Synchrotron Radiation Research*, in press.

Carroll M. R., Paris E., and Davioli I. (1990) XANES and EXAFS study of Ar and Xe bearing $SiO_2$ glasses. *Proceedings of the Second European International Conference on Progress in X-ray Synchrotron Radiation Research*, in press.

Carroll M. R., Sutton S. R., Woolum D., Lewotsky K., and Rogers P. S. Z. (1990) Kr and Xe diffusion and solubility in melts and glasses (abstract). In *Lunar and Planetary Science XX*, pp. 170–171. Lunar and Planetary Institute, Houston.

Cattermole P. (1988) Mapping of volcanic units at Alba Patera, Mars (abstract). In *MEVTV Workshop on Nature and Composition of Surface Units on Mars* (J. R. Zimbelman, S. C. Solomon, and V. L. Sharpton, eds.), pp. 37–39. LPI Tech. Rpt. 88-05, Lunar and Planetary Institute, Houston.

Cave J. A. (1990) Crater morphology variations in the Elysium region: Implications for ice distribution on Mars (abstract). In *Lunar and Planetary Science XXI*, p. 174. Lunar and Planetary Institute, Houston.

Chadwick D. J., Watters T. R., and Tuttle M. J. (1990) Crosscutting, periodically spaced wrinkle ridges of Hesperia Planum (abstract). In *Lunar and Planetary Science XXI*, pp. 175–176. Lunar and Planetary Institute, Houston.

Chang S. and Wu Z. (1988) An introduction to the historical records of China about Mars (abstract). In *MEVTV Workshop on Nature and Composition of Surface Units on Mars* (J. R. Zimbelman, S. C. Solomon, and V. L. Sharpton, eds.), pp. 40–42. LPI Tech. Rpt. 88-05, Lunar and Planetary Institute, Houston.

Chapman K. L. and Tanaka K. L. (1989) Geologic mapping of lower Mangala Valles, Mars: Evidence of flooding, sapping, debris flow, and volcanism (abstract). In *Geol. Soc. Am., Abstracts with Progr., 21*, A108.

Chapman M. G. and Tanaka K. L. (1990) Geologic mapping of lower Mangala Valles, Mars: Evidence of flooding, sapping, debris flow, and volcanism (abstract). In *Lunar and Planetary Science XXI*, p. 179. Lunar and Planetary Institute, Houston.

Chapman M. G. and Tanaka K. L. (1990) Small valleys and hydrologic history of the lower Mangala Valles region, Mars. *Proc. Lunar Planet. Sci. Conf. 20th*, pp. 531–539.

Chapman M. G., Scott D. H., and Tanaka K. L. (1990) Elysium Basin, Mars: Implications of a deep, intermittent lake system (abstract). In *Lunar and Planetary Science XXI*, pp. 180–181. Lunar and Planetary Institute, Houston.

Chicarro A. F. (1989) Towards a chronology of compressive tectonics on Mars (abstract). In *MEVTV Workshop on Early Tectonic and Volcanic Evolution of Mars* (H. Frey, ed.), pp. 23–25. LPI Tech. Rpt. 89-04, Lunar and Planetary Institute, Houston.

Chicarro A. F. (1990) Options for the scientific exploration of Mars in ESA (abstract). In *Lunar and Planetary Science XXI*, pp. 188–189. Lunar and Planetary Institute, Houston.

Clancy R. T. and Lee S. W. (1990) Derivation of Mars atmospheric dust opacities from radiative transfer analysis of Viking IRTM emission phase function sequences (abstract). In *Lunar and Planetary Science XXI*, pp. 194–195. Lunar and Planetary Institute, Houston.

Clark B. C. (1988) Elemental composition of the martian surface (abstract). In *MEVTV Workshop on Nature and Composition of Surface Units on Mars* (J. R. Zimbelman, S. C. Solomon, and V. L. Sharpton, eds.), p. 43. LPI Tech. Rpt. 88-05, Lunar and Planetary Institute, Houston.

Clifford S. M. and Duxbury E. (1988) Sub-kilometer rampart craters in the equatorial region of Mars: Possible implications for the state and distribution of regolith $H_2O$ (abstract). In *MEVTV Workshop on Nature and Composition of Surface Units on Mars* (J. R. Zimbelman, S. C. Solomon, and V. L. Sharpton, eds.), pp. 44–45. LPI Tech. Rpt. 88-05, Lunar and Planetary Institute, Houston.

Clifford S. M. and Zimbelman J. R. (1988) Softened terrain on Mars: The ground ice interpretation reconsidered (abstract). In *Lunar and Planetary Science XIX*, pp. 199–200. Lunar and Planetary Institute, Houston.

Cloutis E. A. (1990) Cold polar deserts: Weathering rates, mechanisms, and implications for remote sensing of Mars (abstract). In *Lunar and Planetary Science XXI*, pp. 205–206. Lunar and Planetary Institute, Houston.

Clow G. D. and Haberle R. M. (1990) Characteristics of the martian atmospheric surface layer (abstract). In *Lunar and Planetary Science XXI*, pp. 209. Lunar and Planetary Institute, Houston.

Clow G. D. and Haberle R. M. (1990) Free convection in the martian atmosphere (abstract). In *Lunar and Planetary Science XXI*, pp. 210–211. Lunar and Planetary Institute, Houston.

Combes M., Drossart P., Encrenaz Th., Lellouch E., Rosenqvist J., Bibring J.-P., Langevin Y., Moroz V. I., Grigoriev A. V., Sanko N. F., and Titov D. V. (1990) Scattering properties and minor constituents in the atmosphere of Mars from the ISM/Phobos experiment (abstract). In *Lunar and Planetary Science XXI*, pp. 218–219. Lunar and Planetary Institute, Houston.

Costard F. M. (1990) Thermokarstic depressions at the mouth of Elysium channels (Mars): New evidence for the presence of massive icy beds (abstract). In *Lunar and Planetary Science XXI*, pp. 232–233. Lunar and Planetary Institute, Houston.

Coyne L. M., Banin A., Orenberg J. B., Carle G. C., Chang S., and Scattergood T. W. (1988) Chemical and spectroscopic characterization of a suite of Mars soil analogs (abstract). In *MEVTV Workshop on Nature and Composition of Surface Units on Mars* (J. R. Zimbelman, S. C. Solomon, and V. L. Sharpton, eds.), pp. 46–48. LPI Tech. Rpt. 88-05, Lunar and Planetary Institute, Houston.

Craddock R. A. (1990) Rationale for a Mars rover/sample return mission to Chryse Planitia and the Viking 1 lander (abstract). In *Lunar and Planetary Science XXI*, pp. 234–235. Lunar and Planetary Institute, Houston.

Craddock R. A. and Maxwell T. A. (1990) Evidence for widespread resurfacing in the martian highlands (abstract). In *Lunar and Planetary Science XXI*, pp. 236–237. Lunar and Planetary Institute, Houston.

Craddock R. A. and Zimbelman J. R. (1989) Yorktown and Lexington as viewed by the Viking 1 Lander (abstract). In *Lunar and Planetary Science XX*, pp. 193–194. Lunar and Planetary Institute, Houston.

Craddock R. A. and Zimbelman J. R. (1990) Bedrock exposure in the Sinus Meridiani region of Mars (abstract). *Eos Trans. AGU, 71*, 547.

Craddock R. A., Greeley R., and Christensen P. R. (1989) Evidence for an ancient impact basin in Daedalia Planum, Mars (abstract). In *Lunar and Planetary Science XX*, pp. 195–196. Lunar and Planetary Institute, Houston.

Craddock R. A., Greeley R., and Christensen P. R. (1989) Origin and age of grooved features in the memnonia quadrangle (MC-16), Mars (abstract). In *MEVTV Workshop on Early Tectonic and Volcanic Evolution of Mars* (H. Frey, ed), pp. 26–28. LPI Tech. Rpt. 89-04, Lunar and Planetary Institute, Houston.

Craddock R. A., Greeley R., and Christensen P. R. (1990) Evidence for an ancient impact basin and associated volcanism in Daedalia Planum, Mars. *J. Geophys. Res.*, 95, 10729–10741.

Craddock R. A., Zimbelman J. R., and Greeley R. (1990) Geologic history of the southern reaches of Mangala Valles (abstract). In *Lunar and Planetary Science XXI*, pp. 240–241. Lunar and Planetary Institute, Houston.

Craddock R. A., Zimbelman J. R., and Watters T. R. (1989) Normal faulting associated with the Daedalia impact basin, Mars (abstract). In *MEVTV Workshop on Tectonic Features on Mars* (T. R. Watters and M. P. Golombek, eds.), pp. 18–20. LPI Tech. Rpt. 89-06, Lunar and Planetary Institute, Houston.

Croft S. K. (1989) Spelunking on Mars: The carbonate-tectonic hypothesis for the origin of Valles Marineris (abstract). In *MEVTV Workshop on Tectonic Features on Mars* (T. R. Watters and M. P. Golombek, eds.), pp. 21–24. LPI Tech. Rpt. 89-06, Lunar and Planetary Institute, Houston.

Crown D. A. and Greeley R. (1989) Origin of the martian highland pataerae: Consideration of eruptive activity of Hadriaca Patera and Tyrrhena Patera (abstract). In *Reports of Planetary Geology and Geophysics Program—1988*, pp. 384–386. NASA TM-4130.

Crown D. A. and Greeley R. (1989) The martian highland paterae: Evidence for explosive volcanism on Mars (abstract). In *MEVTV Workshop on Early Tectonic and Volcanic Evolution of Mars* (H. Frey, ed.), pp. 29–31. LPI Tech. Rpt. 89-04, Lunar and Planetary Institute, Houston.

Crown D. A. and Greeley R. (1990) Hadriaca Patera: Evidence for pyroclastic volcanism in the Hellas region of Mars (abstract). In *MEVTV Workshop on the Evolution of Magma Bodies on Mars* (P. Mouginis-Mark and J. Holloway, eds.), pp. 25–26. LPI Tech. Rpt. 90-04, Lunar and Planetary Institute, Houston.

Crown D. A. and Greeley R. (1990) Styles of volcanism, tectonic associations, and evidence for magma-water interactions in eastern Hellas, Mars (abstract). In *Lunar and Planetary Science XXI*, pp. 250–251. Lunar and Planetary Institute, Houston.

Crown D. A., Price K. H., and Greeley R. (1990) Evolution of the east rim of the Hellas Basin, Mars (abstract). In *Lunar and Planetary Science XXI*, pp. 252–253. Lunar and Planetary Institute, Houston.

Crumpler L. S. and Aubele J. C. (1989) Influence of tectonic and volcanic stresses on the flank structure of martian volcanoes (abstract). In *MEVTV Workshop on Tectonic Features on Mars* (T. R. Watters and M. P. Golombek, eds.), pp. 25–27. LPI Tech. Rpt. 89-06, Lunar and Planetary Institute, Houston.

Crumpler L. S., Aubele J. C., and Head J. W. (1990) Calderas on Mars: Implications of style and history for subsurface magmatism (abstract). In *MEVTV Workshop on the Evolution of Magma Bodies on Mars* (P. Mouginis-Mark and J. Holloway, eds.), pp. 27–28. LPI Tech. Rpt. 90-04, Lunar and Planetary Institute, Houston.

Dagge G., Dragovitsch P., Filges D., and Brückner J. (1990) Calculation of martian gamma ray spectra (abstract). In *Lunar and Planetary Science XXI*, pp. 256–257. Lunar and Planetary Institute, Houston.

Davis P. A. and Golombek M. P. (1989) Discontinuities in the shallow martian crust (abstract). In *Lunar and Planetary Science XX*, pp. 224–225. Lunar and Planetary Institute, Houston.

Davis P. A. and Golombek M. P. (1989) Discontinuities in the shallow Martian crust (abstract). In *Reports of Planetary Geology and Geophysics Program—1988*, pp. 491–492. NASA TM-4130.

Davis P. A. and Golombek M. P. (1990) Discontinuities in the shallow Martian crust at Lunae, Syria, and Sinai Plana. *J. Geophys. Res.*, 95, 14231–14248.

Davis P. A. and Tanaka K. L. (1988) Morphometric analysis of some canyons in Noctis Labyrinthus, Mars: Comparison with Hawaiian runoff and sapping channels (abstract). In *Lunar and Planetary Science XIX*, pp. 253–254. Lunar and Planetary Institute, Houston.

Davis P. A. and Tanaka K. L. (1988) Small martian volcanoes (abstract). In *MEVTV Workshop on Nature and Composition of Surface Units on Mars* (J. R. Zimbelman, S. C. Solomon, and V. L. Sharpton, eds.), pp. 49–50. LPI Tech. Rpt. 88-05, Lunar and Planetary Institute, Houston.

DeHon R. A. (1988) The martian sedimentary record (abstract). In *MEVTV Workshop on Nature and Composition of Surface Units on Mars* (J. R. Zimbelman, S. C. Solomon, and V. L. Sharpton, eds.), pp. 51–53. LPI Tech. Rpt. 88-05, Lunar and Planetary Institute, Houston.

DeHon R. A. (1988) Progress in determining the thickness and distribution of volcanic materials on Mars (abstract). In *MEVTV Workshop on Nature and Composition of Surface Units on Mars* (J. R. Zimbelman, S. C. Solomon, and V. L. Sharpton, eds.), pp. 54–56. LPI Tech. Rpt. 88-05, Lunar and Planetary Institute, Houston.

DeHon R. A. (1990) Hydraulic routing of the Maja outflow across Xanthe Terra (abstract). In *Lunar and Planetary Science XXI*, pp. 266–267. Lunar and Planetary Institute, Houston.

DeHon R. A. and Mouginis-Mark P. J. (1990) Geologic map of the Galaxias region (MTM 35217) northwest Elysium region, Mars (abstract). In *Lunar and Planetary Science XXI*, pp. 268–268. Lunar and Planetary Institute, Houston.

Dimitriou A. M. (1990) Minimum estimates for volume removal from the martian fretted terrain between 270°W and 360°W (abstract). In *Lunar and Planetary Science XXI*, pp. 291–292. Lunar and Planetary Institute, Houston.

Dimitriou A. M. (1990) Stratigraphy of the Ismenius Lacus SE subquadrangle: Clues to an upland/lowland boundary forming event? (abstract). In *Lunar and Planetary Science XXI*, pp. 293–294. Lunar and Planetary Institute, Houston.

Dollfus A., Deschamps M., and Zimbelman J. R. (1989) Granulometry of the martian surface by photopolarimetry (abstract). In *Lunar and Planetary Science XX*, pp. 250–251. Lunar and Planetary Institute, Houston.

Drake D. M., Wender S., Nelson R., Shunk E. R., Amian W., Englert P., and Drosg M. (1990) Experimental simulation of martian neutron leakage spectrum (abstract). In *Lunar and Planetary Science XXI*, p. 300. Lunar and Planetary Institute, Houston.

Economou T. and Turkevich A. (1990) A gamma ray mode of the alpha particle analytical instrument (abstract). In *Lunar and Planetary Science XXI*, pp. 307–308. Lunar and Planetary Institute, Houston.

Economou T., Iwanczyk J., and Turkevich A. (1990) The X-ray mode of the alpha particle analytical instrument (abstract). In *Lunar and Planetary Science XXI*, pp. 309–310. Lunar and Planetary Institute, Houston.

Edgett K. S. (1990) Ejecta deposits of large martian impact basins: A useful geologic tool and window to early martian history? (abstract). In *MEVTV Workshop on Early Tectonic and Volcanic Evolution of Mars* (H. Frey, ed.), pp. 32–34. LPI Tech. Rpt. 89-04, Lunar and Planetary Institute, Houston.

Edgett K. S. (1990) Possible cinder cones near the summit of Pavonis Mons, Mars (abstract). In *Lunar and Planetary Science XXI*, pp. 311–312. Lunar and Planetary Institute, Houston.

Edgett K. S. (1991) The ejecta deposit of the ancient basin Herschel: An example of a generally unrecognized martian sedimentological unit. *Proc. Lunar Planet. Sci., Vol. 21*, pp. 657–667.

Edgett K. S. and Christensen P. R. (1990) Intracrater sand on Mars: Physical properties related to regional winds, sediment supply (abstract). In *Lunar and Planetary Science XXI*, pp. 313–314. Lunar and Planetary Institute, Houston.

Edgett K. S. and Zimbelman J. R. (1990) The Arsia Mons-Oti Fossae thermal anomaly: A region with a higher thermal inertia than the rest of Tharsis (abstract). In *Lunar and Planetary Science XXI*, pp. 315–316. Lunar and Planetary Institute, Houston.

Efford N. D. (1990) Photometric techniques for lander site certification (abstract). In *Lunar and Planetary Science XXI*, pp. 317–318. Lunar and Planetary Institute, Houston.

Englert P., Reedy R. C., Drake D. M., Feldman W. C., Squyres S. W., Evans L. G., and Boynton W. V. (1988) Gamma-ray/neutron spectroscopy from the Mars Observer (abstract). In *MEVTV Workshop on Nature and Composition of Surface Units on Mars* (J. R. Zimbelman, S. C. Solomon, and V. L. Sharpton, eds.), pp. 57–59. LPI Tech. Rpt. 88-05, Lunar and Planetary Institute, Houston.

Erard S., Bibring J.-P., Langevin Y., Combes M., Hurtrez S., Sotin C., Head J. W., and Mustard J. F. (1990) Determination of spectral units in the Syrtis Major-Isidis Planitia region from Phobos/ISM observations (abstract). In *Lunar and Planetary Science XXI*, pp. 327–328. Lunar and Planetary Institute, Houston.

Erard S., Bibring J.-P., Mustard J., Forni O., Head J. W., Hurtrez S., Langevin Y., Pieters C. M., Rosenqvist J., and Sotin C. (1991) Spatial variations in composition of the Valles Marineris and Isidis Planitia regions derived from ISM data. *Proc. Lunar Planet. Sci., Vol. 21*, pp. 437–455.

Fanale F. P. (1988) The water and other volatiles of Mars. In *The NASA Mars Conference Science and Technology Series, Vol. 71*, pp. 157–176. Univelt, San Diego.

Fanale F. P. and Postawko S. E. (1990) Heat flow vs. atmospheric greenhouse on early Mars (abstract). In *Lunar and Planetary Science XXI*, pp. 343–344. Lunar and Planetary Institute, Houston.

Farrand W. H. and Singer R. B. (1990) Analysis of poorly crystalline clay mineralogy: Near infrared spectrometry versus X-ray diffraction (abstract). In *Lunar and Planetary Science XXI*, pp. 347–348. Lunar and Planetary Institute, Houston.

Feldman W. C. and Jakosky B. M. (1990) Thermal neutron leakage from martian carbonates (abstract). In *Lunar and Planetary Science XXI*, pp. 361–362. Lunar and Planetary Institute, Houston.

Fink J. H. and Zimbelman J. R. (1988) A comparison of lava flow rheology calculations for high-resolution data sets from Hawaii and Mars (abstract). In *Lunar and Planetary Science XIX*, pp. 327–328. Lunar and Planetary Institute, Houston.

Finnerty A. A., Phillips R. J., and Banerdt W. B. (1988) Igneous processes and closed system evolution of the Tharsis region of Mars. *J. Geophys. Res.*, 93, 10225–10235.

Fisher D. S. (1990) Chemical weathering of sulfide mineralization on Mars. Master's thesis, Massachusetts Institute of Technology, Cambridge. 126 pp.

Fisher D. S. and Burns R. G. (1989) Acid weathering on Mars: Spectroscopic investigations of sulfuric acid-degraded olivines and pyroxenes (abstract). In *Lunar and Planetary Science XX*, pp. 299–300. Lunar and Planetary Institute, Houston.

Fogel R. A. and Rutherford M. J. (1989) Volcanism on Mars: Experiments on $CO_2$ solubility in silicic magmas (abstract). In *Lunar and Planetary Science XX*, pp. 303–304. Lunar and Planetary Institute, Houston.

Fogel R. A. and Rutherford M. J. (1990) Solubility of C-O gases in silicate melts. Abstract presented at Goldschmidt Conference, Baltimore, Maryland, May 1990.

Fogel R. A. and Rutherford M. J. (1990) The solubility of carbon dioxide in rhyolitic melts: A quantitative F.T.I.R. study. *Am. Mineral.*, in press.

Forsythe R. D. (1989) The ubiquity and diversity of strike-slip faulting on Earth; a generality or exception for comparative planetology? (abstract). In *MEVTV Workshop on Tectonic Features on Mars* (T. R. Watters and M. P. Golombek, eds.), pp. 28–29. LPI Tech. Rpt. 89-06, Lunar and Planetary Institute, Houston.

Forsythe R. D. (1990) A case for martian salars and saline lakes during the Noachian (abstract). In *Lunar and Planetary Science XXI*, pp. 379–380. Lunar and Planetary Institute, Houston.

Forsythe R. D. (1990) Polyphase Noachian tectonism of the Memnonia/Aeolis region; evidence for greater pre-Tharsis lithospheric mobility of Mars (abstract). In *Lunar and Planetary Science XXI*, pp. 381–382. Lunar and Planetary Institute, Houston.

Forsythe R. D. and Zimbelman J. R. (1988) Is the Gordii Dorsum escarpment on Mars an exhumed transcurrent fault? *Nature*, 336, 143–146.

Forsythe R. D. and Zimbelman J. R. (1988) Transcurrent faulting on Mars: The Gordii Dorsum escarpment (abstract). In *Lunar and Planetary Science XIX*, pp. 344–345. Lunar and Planetary Institute, Houston.

Forsythe R. D. and Zimbelman J. R. (1989) The transcurrent fault hypothesis for Mars' Gordii Dorsum escarpment (abstract). In *MEVTV Workshop on Tectonic Features on Mars* (T. R. Watters and M. P. Golombek, eds.), pp. 30–32. LPI Tech. Rpt. 89-06, Lunar and Planetary Institute.

Forsythe R. D. and Zimbelman J. R. (1990) A discussion of Mars' western equatorial dichotomy boundary zone; enigmas, anomalies and controversies (abstract). In *Lunar and Planetary Science XXI*, pp. 383–384. Lunar and Planetary Institute, Houston.

Francis P. W. (1988) Variability in spectral signatures of terrestrial volcanic rocks and implications for volcanology on Mars (abstract). In *MEVTV Workshop on Nature and Composition of Surface Units on Mars* (J. R. Zimbelman, S. C. Solomon, and V. L. Sharpton, eds.), pp. 60–61. LPI Tech. Rpt. 88-05, Lunar and Planetary Institute, Houston.

Frey H. V., ed. (1989) *MEVTV Workshop on Early Tectonic and Volcanic Evolution of Mars*. LPI Tech. Rpt. 89-04, Lunar and Planetary Institute, Houston. 102 pp.

Frey H. V. and Grant T. D. (1989) Resurfacing in Coprates and thickness of the ridged plains (abstract). In *Lunar and Planetary Science XX*, pp. 313–314. Lunar and Planetary Institute, Houston.

Frey H. V. and Grant T. D. (1990) Resurfacing history of Tempe Terra and surroundings. *J. Geophys. Res.*, in press.

Frey H. V. and Schultz R. A. (1988) Large impact basins and the mega-impact origin for the crustal dichotomy on Mars. *Geophys. Res. Lett.*, *15*, 229–232.

Frey H. V. and Schultz R. A. (1989) Origin of the martian crustal dichotomy (abstract). In *MEVTV Workshop on Early Tectonic and Volcanic Evolution of Mars* (H. Frey, ed.), pp. 35–37. LPI Tech. Rpt. 89-04, Lunar and Planetary Institute, Houston.

Frey H. V. and Schultz R. A. (1989) Overlapping large impacts and the martian crustal dichotomy, Elysium and Tharsis (abstract). In *Fourth International Conference on Mars, Progr. and Abstracts*, pp. 106–107. Univ. of Arizona, Tucson.

Frey H. V. and Schultz R. A. (1990) MEVTV study: Early tectonic evolution of Mars—crustal dichotomy to Valles Marineris (abstract). In *Lunar and Planetary Science XXI*, pp. 391–392. Lunar and Planetary Institute, Houston.

Frey H. V. and Schultz R. A. (1990) Speculations on the origin and evolution of the Utopia-Elysium lowlands of Mars. *J. Geophys. Res.*, 95,14203–14213.

Frey H. V. and Semenuik J. A. (1988) Extent of buried crater terrain underlying the highland-lowland transitiion zone in eastern Mars (abstract). In *Lunar and Planetary Science XIX*, pp. 360–361. Lunar and Planetary Institute, Houston.

Frey H. V., Doudnikoff C. D., and Mongeon A. M. (1991) Are Noachian-age ridged plains (Nplr) actually Early Hesperian in age? *Proc. Lunar Planet. Sci., Vol. 21*, pp. 635–644.

Frey H., Semeniuk J., and Grant T. (1989) Early resurfacing events on Mars (abstract). In *MEVTV Workshop on Early Tectonic and Volcanic Evolution of Mars* (H. Frey, ed.), pp. 38–40. LPI Tech. Rpt. 89-04, Lunar and Planetary Institute, Houston.

Frey H. V., Semeniuk J. A., and Grant T. D. (1989) Lunae Planum age resurfacing on Mars (abstract). In *Fourth International Conference on Mars, Progr. and Abstracts*, pp. 104–105. Univ. of Arizona, Tucson.

Frey H., Semeniuk A. M., Semeniuk J. A., and Tokarcik S. (1988) A widespread common age resurfacing event in the highland-lowland transition zone in eastern Mars. *Proc. Lunar Planet. Sci. Conf. 18th*, pp. 679–699.

Gaskell R. W. (1990) Martian surface simulations (abstract). In *Lunar and Planetary Science XXI*, pp. 405–406. Lunar and Planetary Institute, Houston.

Geissler P. E., Singer R. B., and Lucchitta B. K. (1990) Dark materials in Valles Marineris: Indications of the style of volcanism and magmatism on Mars (abstract). In *Lunar and Planetary Science XXI*, pp. 413–414. Lunar and Planetary Institute, Houston.

Golombek M. (1989) A review of extensional tectonic features on Mars (abstract). In *MEVTV Workshop on Tectonic Features on Mars* (T. R. Watters and M. P. Golombek, eds.), pp. 33–35. LPI Tech. Rpt. 89-06, Lunar and Planetary Institute, Houston.

Golombek M. P. (1989) Geometry of stresses around Tharsis on Mars (abstract). In *Lunar and Planetary Science XX*, pp. 345–346. Lunar and Planetary Institute, Houston.

Golombek M. P. (1989) Geometry of stresses around Tharsis on Mars (abstract). In *Reports of Planetary Geology and Geophysics Program—1988*, pp. 520–522. NASA TM-4130.

Golombek M. P. and Plescia J. B. (1989) Subsurface structure of Martian wrinkle ridges (abstract). In *Fourth International Conference on Mars, Progr. and Abstracts*, pp. 113–114. Univ. of Arizona, Tucson.

Golombek M., Plescia J., and Franklin B. (1988) The relative importance of faulting versus folding in the formation of planetary wrinkle ridges (abstract). In *Lunar and Planetary Science XIX*, pp. 395–396. Lunar and Planetary Institute, Houston.

Golombek M. P., Plescia J. B., and Franklin B. J. (1990) Faulting and folding in the formation of planetary wrinkle ridges. *Proc. Lunar Planet. Sci., Vol. 21*, pp. 679–693.

Golombek M., Suppe J., Narr W., Plescia J., and Banerdt B. (1989) Involvement of the lithosphere in the formation of wrinkle ridges on Mars (abstract). In *Reports of Planetary Geology and Geophysics Program—1988*, pp. 498–500. NASA TM-4130.

Golombek M., Suppe J., Narr W., Plescia J., and Banerdt B. (1989) Involvement of the lithosphere in the formation of wrinkle ridges on Mars (abstract). In *MEVTV Workshop on Tectonic Features on Mars* (T. R. Watters and M. P. Golombek, eds.), pp. 36–38. LPI Tech. Rpt. 89-06, Lunar and Planetary Institute, Houston.

Golombek M., Suppe J., Narr W., Plescia J., and Banerdt B. (1990) Does wrinkle ridge formation on Mars involve most of the lithosphere? (abstract). In *Lunar and Planetary Science XXI*, pp. 421–422. Lunar and Planetary Institute, Houston.

Gooding J. L. (1988) Aqueous alteration in S-N-C meteorites and implications for weathering products on Mars (abstract). In *MEVTV Workshop on Nature and Composition of Surface Units on Mars* (J. R. Zimbelman, S. C. Solomon, and V. L. Sharpton, eds.), pp. 62–63. LPI Tech. Rpt. 88-05, Lunar and Planetary Institute, Houston.

Gooding J. L., Aggrey K. E., and Muenow D. W. (1990) Volatile compounds in shergottite and nakhlite meteorites (abstract). In *Lunar and Planetary Science XXI*, pp. 423–424. Lunar and Planetary Institute, Houston.

Gooding J. L., Wentworth S. J., and Zolensky M. E. (1988) Calcium carbonate and sulfate of possible extraterrestrial origin in the EETA 79001 meteorite. *Geochim. Cosmochim. Acta, 52*, 909–915.

Grant J. A. and Schultz P. H. (1988) Nature of the upland plains (abstract). In *MEVTV Workshop on Nature and Composition of Surface Units on Mars* (J. R. Zimbelman, S. C. Solomon, and V. L. Sharpton, eds.), pp. 65–66. LPI Tech. Rpt. 88-05, Lunar and Planetary Institute, Houston.

Greeley R. (1988) Photogeological inferences of martian surface composition (abstract). In *MEVTV Workshop on Nature and Composition of Surface Units on Mars* (J. R. Zimbelman, S. C. Solomon, and V. L. Sharpton, eds.), pp. 67–68. LPI Tech. Rpt. 88-05, Lunar and Planetary Institute, Houston.

Greeley R. (1989) Early volcanism on Mars: An overview (abstract). In *MEVTV Workshop on Early Tectonic and Volcanic Evolution of Mars* (H. Frey, ed.), pp. 41–42. LPI Tech. Rpt. 89-04, Lunar and Planetary Institute, Houston.

Greeley R. and Crown D. A. (1990) Volcanic geology of Tyrrhena Patera, Mars. *J. Geophys. Res.*, 95, 7133–7149.

Guest J. E., Hughes J. W., and Duncan A. M. (1988) Lava flow-field morphology—A case study from Mount Etna, Sicily (abstract). In *MEVTV Workshop on Nature and Composition of Surface Units on Mars* (J. R. Zimbelman, S. C. Solomon, and V. L. Sharpton, eds.), pp. 69–71. LPI Tech. Rpt. 88-05, Lunar and Planetary Institute, Houston.

Guinness E. A., Arvidson R. E., Irons J. R., and Harding D. J. (1990) Use of aircraft multispectral and multiple emission angle data to determine surface roughness and composition at the lunar lake playa in Nevada (abstract). In *Lunar and Planetary Science XXI*, pp. 441–442. Lunar and Planetary Institute, Houston.

Gulick V. C. and Baker V. R. (1990) Valley development on Mars: A global perspective (abstract). In *Lunar and Planetary Science XXI*, pp. 443–444. Lunar and Planetary Institute, Houston.

Hayashi-Smith J. and Mouginis-Mark P. (1990) Morphometry of fresh impact craters in Hesperia Planum, Mars (abstract). In *Lunar and Planetary Science XXI*, pp. 475–476. Lunar and Planetary Institute, Houston.

Henderson B. G. and Jakosky B. M. (1990) The martian south polar cap: Stability and water transport at low obliquities (abstract). In *Lunar and Planetary Science XXI*, pp. 493–494. Lunar and Planetary Institute, Houston.

Henry L. Y. and Zimbelman J. R. (1988) Physical properties of channels and aeolian features in the Oxia Palus and Margaritifer Sinus quadrangles of Mars (abstract). In *Lunar and Planetary Science XIX*, pp. 479–480. Lunar and Planetary Institute, Houston.

Herkenhoff K. E. (1990) Weathering and erosion of the polar layered deposits on Mars (abstract). In *Lunar and Planetary Science XXI*, pp. 495–496. Lunar and Planetary Institute, Houston.

Hills L. S. (1987) Origin of fractures, martian polygonal terrain. In *Reports of Planetary Geology and Geophysics Program—1986*, pp. 495–496. NASA TM-89810.

Hills L. S. (1988) Buried topography as a controlling factor in the origin of the giant polygons of Mars (abstract). In *Lunar and Planetary Science XIX*, pp. 495–496. Lunar and Planetary Institute, Houston.

Holloway J. R. (1988) Distribution of $H_2O$ between early atmospheres and magma oceans (abstract). *Eos Trans. AGU*, 69, 388.

Holloway J. R. (1988) Planetary atmospheres during accretion: The effect of C-O-H-S equilibria (abstract). In *Lunar and Planetary Science XIX*, pp. 499–500. Lunar and Planetary Institute, Houston.

Holloway J. R. (1990) Martian magmas and mantle source regions: Current experimental and petrochemical constraints (abstract). In *Lunar and Planetary Science XXI*, pp. 528–529. Lunar and Planetary Institute, Houston.

Holloway J. R. and Bertka C. M. (1989) Chemical and physical properties of primary martian magmas (abstract). In *MEVTV Workshop on Early Tectonic and Volcanic Evolution of Mars* (H. Frey, ed.), pp. 43–45. LPI Tech. Rpt. 89-04, Lunar and Planetary Institute, Houston.

Ivanov M. A., Moroz V. I., Grigoryev A. V., Nicolsky Yu, San'ko N. F., Khatuntsev I., Kiselev A. V., Bibring J.-P., Combes M., Langevin Y., and Soufflot A. (1990) Water distribution in martian soils in region southward Olympus Mons, Mars (preliminary results) (abstract). In *Lunar and Planetary Science XXI*, pp. 550–551. Lunar and Planetary Institute, Houston.

Jakosky B. M. and Haberle R. M. (1990) The thermal inertia of Mars: Re-interpretation using a better atmospheric model (abstract). In *Lunar and Planetary Science XXI*, p. 556. Lunar and Planetary Institute, Houston.

Jakosky B. M. and Scambos T. A. (1989) Volatile inventory, outgassing history, and the evolution of water on Mars (abstract). In *MEVTV Workshop on Early Tectonic and Volcanic Evolution of Mars* (H. Frey, ed.), pp. 46–47. LPI Tech. Rpt. 89-04, Lunar and Planetary Institute, Houston.

Jankowski D. G. and Squyres S. W. (1990) What's wrong with photoclinometry? (abstract). In *Lunar and Planetary Science XXI*, pp. 561–562. Lunar and Planetary Institute, Houston.

Johnson A. M. (1989) Folding in layered media (abstract). In *MEVTV Workshop on Tectonic Features on Mars* (T. R. Watters and M. P. Golombek, eds.), pp. 39–40. LPI Tech. Rpt. 89-06, Lunar and Planetary Institute, Houston.

Johnson M. C. and Rutherford M. J. (1989) Alkali basalt evolution at low pressure under anhydrous and hydrous conditions: Effects of amphibole (abstract). *Eos Trans. AGU*, 70, 1395.

Johnson M. C., Rutherford M. J., and Hess P. C. (1989) Experimental study of igneous Kaersutite stability with application to SNC petrogenesis (abstract). In *Lunar and Planetary Science XX*, pp. 472–473. Lunar and Planetary Institute, Houston.

Johnson M. C., Rutherford M. J., and Hess P. C. (1990) Chassigny petrogenesis: Melt composition, intensive parameters and water contents of Martian (?) magmas. *Geochim. Cosmochim. Acta*, submitted.

Johnson M. C., Rutherford M. E., and Hess P. C. (1990) Intensive parameters of SNC petrogenesis (abstract). In *MEVTV Workshop on the Evolution of Magma Bodies on Mars* (P. Mouginis-Mark and J. Holloway, eds.), pp. 20–21. LPI Tech. Rpt. 90-04, Lunar and Planetary Institute, Houston.

Jones J. H. (1989) Isotopic relationships among the shergottites, the nakhlites and Chassigny. *Proc. Lunar Planet. Sci. Conf. 19th*, pp. 465–474.

Jöns H.-P. (1990) Further evidences for horizontal block/plate movements or nappe tectonics within the Tanova updoming, Mars (abstract). In *Lunar and Planetary Science XXI*, pp. 585–586. Lunar and Planetary Institute, Houston.

Jöns H.-P. (1990) The planet Mars: Presentation of a global map (abstract). In *Lunar and Planetary Science XXI*, pp. 587–588. Lunar and Planetary Institute, Houston.

Justus C. G. and James B. (1990) Scientific and engineering applications of the Mars-global reference atmospheric model (Mars-GRAM) (abstract). In *Lunar and Planetary Science XXI*, pp. 595–596. Lunar and Planetary Institute, Houston.

Kargel J. S. and Strom R. G. (1990) Ancient glaciation on Mars (abstract). In *Lunar and Planetary Science XXI*, pp. 597–598. Lunar and Planetary Institute, Houston.

Kaula W. M., Sleep N. H., and Phillips R. J. (1989) More about the moment of inertia of Mars. *Geophys. Res. Lett.*, 16, 1333–1336.

Kerridge J. F. (1988) Deuterium in Shergotty and Lafayette (and on Mars?) (abstract). In *Lunar and Planetary Science XIX*, pp. 599–600. Lunar and Planetary Institute, Houston.

Kiefer W. S. and Hager B. H. (1989) Mantle convection on Mars (abstract). In *MEVTV Workshop on Early Tectonic and Volcanic Evolution of Mars* (H. Frey, ed.), pp. 49–50. LPI Tech. Rpt. 89-04, Lunar and Planetary Institute, Houston.

Kieffer H. H. (1988) How dirty is Mars' north polar cap and why isn't it black? (abstract). In *MEVTV Workshop on Nature and Composition of Surface Units on Mars* (J. R. Zimbelman, S. C. Solomon, and V. L. Sharpton, eds.), pp. 72–73. LPI Tech. Rpt. 88-05, Lunar and Planetary Institute, Houston.

King E. A. (1988) Some probable characteristics of the martian regolith (abstract). In *MEVTV Workshop on Nature and Composition of Surface Units on Mars* (J. R. Zimbelman, S. C. Solomon, and V. L. Sharpton, eds.), pp. 74–75. LPI Tech. Rpt. 88-05, Lunar and Planetary Institute, Houston.

Kochel R. C. and Miller J. R. (1990) Post-flooding modifications to Chryse Basin channels, Mars: Implications for source volumes and evolution of the channels (abstract). In *Lunar and Planetary Science XXI*, pp. 643–644. Lunar and Planetary Institute, Houston.

Komatsu G. and Strom R. G. (1990) Layered deposits with volcanic intrusions in Gangis Chasma, Mars (abstract). In *Lunar and Planetary Science XXI*, pp. 443–444. Lunar and Planetary Institute, Houston.

Kuzmin R. O., Moroz V. I., Grigoryev A. V., Nikolsky Y., San'ko N. F., Khatuntsev I. V., Kiselev A. V., Bibring J. P., Langevin Y., Soufflot A., and Combes M. (1990) Variation of the bound water contents on the martian surface from ISM-experiment data on Phobos-2: Preliminary results (abstract). In *Lunar and Planetary Science XXI*, pp. 674–675. Lunar and Planetary Institute, Houston.

Lee S. W. and Clancy R. T. (1990) The effects of atmospheric dust on observations of the surface albedo of Mars (abstract). In *Lunar and Planetary Science XXI*, pp. 688–689. Lunar and Planetary Institute, Houston.

Leshin L. A., Holloway J. R., and Bertka C. M. (1988) Atmospheric pressure experimental studies of a low-silica martian mantle composition (abstract). In *Lunar and Planetary Science XIX*, pp. 677–678. Lunar and Planetary Institute, Houston.

Lindner B. L., Ackerman T. P., Pollack J. B., Toon O. B., and Thomas G. E. (1990) Solar and IR radiation near the martian surface: A parameterization for $CO_2$ transmittance (abstract). In *Lunar and Planetary Science XXI*, pp. 696–697. Lunar and Planetary Institute, Houston.

Longhi J. (1991) Complex magmatic processes on Mars: Inferences from the SNC meteorites. *Proc. Lunar Planet. Sci., Vol. 21*, pp. 695–709.

Longhi J. and Pan V. (1988) What SNC meteorites tell us about martian magmatism (abstract). In *MEVTV Workshop on Nature and Composition of Surface Units on Mars* (J. R. Zimbelman, S. C. Solomon, and V. L. Sharpton, eds.), pp. 76–78. LPI Tech. Rpt. 88-05, Lunar and Planetary Institute, Houston.

Longhi J. and Pan V. (1989) The parent magmas of the SNC meteorites. *Proc. Lunar Planet. Sci. Conf. 19th*, pp. 451–464.

Longhi J., Knittle E., Holloway J. R., and Wänke H. (1990) The bulk composition, mineralogy, and internal structure of Mars. In *Mars* (H. Kieffer et al., eds.), Univ. of Arizona, Tucson, in press.

Lucchitta B. K. (1988) Surface units on Mars: The assemblage in the Valles Marineris (abstract). In *MEVTV Workshop on Nature and Composition of Surface Units on Mars* (J. R. Zimbelman, S. C. Solomon, and V. L. Sharpton, eds.), pp. 79–81. LPI Tech. Rpt. 88-05, Lunar and Planetary Institute, Houston.

Lucchitta B. K. and Chapman M. G. (1989) Ground ice along the northern highland scarp, Mars (abstract). In *MEVTV Workshop on Early Tectonic and Volcanic Evolution of Mars* (H. Frey, ed.), pp. 51–53. LPI Tech. Rpt. 89-04, Lunar and Planetary Institute, Houston.

Lucchitta B. K., Blaser R. A., and Bertolini L. M. (1990) Valles Marineris, Mars: Are pit chains formed by erosion and troughs by tectonism? (abstract). In *Lunar and Planetary Science XXI*, pp. 722–723. Lunar and Planetary Institute, Houston.

Lucchitta B. K., Clow G. D., Croft S. K., Geissler P. E., McEwen A. S., Singer R. B., Squyres S. W., and Tanaka K. L. (1989) Canyon systems on Mars (abstract). In *Fourth International Conference on Mars, Progr. and Abstracts* pp. 36–37. Univ. of Arizona, Tucson.

MacKinnon D. J. and Tanaka K. L. (1987) Nirgal Vallis basin: Some questions on fluvial and regolith history (abstract). In *Lunar and Planetary Science XVIII*, pp. 588–589. Lunar and Planetary Institute, Houston.

MacKinnon D. J. and Tanaka K. L. (1988) A two-layer hydrologic model for the impacted martian crust (abstract). In *Lunar and Planetary Science XIX*, pp. 707–708. Lunar and Planetary Institute, Houston.

MacKinnon D. J. and Tanaka K. L. (1989) The impacted Martian crust: Structure, hydrology, and some geologic implications. *J. Geophys. Res.*, *94*, 17359–17370.

MacKinnon D. J. and Tanaka K. L. (1990) A physical model of the impacted martian crust: Hydrologic and mechanical properties and geologic implications (abstract). In *Lunar and Planetary Science XXI*, pp. 728–729. Lunar and Planetary Institute, Houston.

MacKinnon D. J., Tanaka K. L., and Winchell P. J. (1988) Morphologic contrasts between Nirgal and Auqakuh Valles, Mars: Evidence of different crustal properties (abstract). In *MEVTV Workshop on Nature and Composition of Surface Units on Mars* (J. R. Zimbelman, S. C. Solomon, and V. L. Sharpton, eds.), pp. 82–84. LPI Tech. Rpt. 88-05, Lunar and Planetary Institute, Houston.

Martinez S. L. and Burns R. G. (1990) Mossbauer spectra of olivine-rich weathered acondrites: I. Ureilites (abstract). In *Lunar and Planetary Science XXI*, pp. 147–148. Lunar and Planetary Institute, Houston.

Masursky H., Dial A. L. Jr., Strobell M. E., and Applebee D. J. (1988) Geology of six possible martian landing sites (abstract). In *MEVTV Workshop on Nature and Composition of Surface Units on Mars* (J. R. Zimbelman, S. C. Solomon, and V. L. Sharpton, eds.), pp. 85–87. LPI Tech. Rpt. 88-05, Lunar and Planetary Institute, Houston.

Maxwell T. A. (1989) Origin of planetary wrinkle ridges—An overview (abstract). In *MEVTV Workshop on Tectonic Features on Mars* (T. R. Watters and M. P. Golombek, eds.), pp. 41–43. LPI Tech. Rpt. 89-06, Lunar and Planetary Institute, Houston.

Maxwell T. A. (1989) Structural modification along the cratered terrain boundary, eastern hemisphere, Mars (abstract). In *MEVTV Workshop on Early Tectonic and Volcanic Evolution of Mars* (H. Frey, ed.), pp. 54–55. LPI Tech. Rpt. 89-04, Lunar and Planetary Institute, Houston.

Maxwell T. A. and McGill G. A. (1988) Ages of fracturing and resurfacing in the Amenthes Region, Mars. *Proc. Lunar Planet. Sci. Conf. 18th*, pp. 701–711.

McBride K. and Barlow N. G. (1990) Martian crater counts of Elysium Mons (abstract). In *Lunar and Planetary Science XXI*, pp. 744–745. Lunar and Planetary Institute, Houston.

McBride K. and Zimbelman J. R. (1989) Evidence of pyroclastic activity near Elysium Mons, Mars (abstract). In *Lunar and Planetary Science XX*, p. 651. Lunar and Planetary Institute, Houston.

McBride K. and Zimbelman J. R. (1990) Small volcanic features in western Elysium Planitia (abstract). In *Lunar and Planetary Science XXI*, pp. 746–747. Lunar and Planetary Institute, Houston.

McBride K., Zimbelman J. R., and Clifford S. M. (1988) Potential indicators of pyroclastic activity near Elysium Mons, Mars (abstract). In *MEVTV Workshop on Early Tectonic and Volcanic Evolution of Mars* (H. Frey, ed.), pp. 56–58. LPI Tech. Rpt. 89-04, Lunar and Planetary Institute, Houston.

McDonnell J. H. (1990) Development of the southwest Elysium Canyon complex, Mars (abstract). In *Lunar and Planetary Science XXI*, pp. 753–754. Lunar and Planetary Institute, Houston.

McEwen A. S. (1990) Valles Marineris landslides: Evidence for mechanics of large rock avalanches (abstract). In *Lunar and Planetary Science XXI*, pp. 757–758. Lunar and Planetary Institute, Houston.

McFadden L. A. (1988) Spectral reflectance of SNC's (abstract). In *MEVTV Workshop on Nature and Composition of Surface Units on Mars* (J. R. Zimbelman, S. C. Solomon, and V. L. Sharpton, eds.), pp. 89–90. LPI Tech. Rpt. 88-05, Lunar and Planetary Institute, Houston.

McGill G. E. (1988) Constraints on the origin of fractured terrane, northern martian plains (abstract). In *MEVTV Workshop on Nature and Composition of Surface Units on Mars* (J. R. Zimbelman, S. C. Solomon, and V. L. Sharpton, eds.), pp. 91–93. LPI Tech. Rpt. 88-05, Lunar and Planetary Institute, Houston.

McGill G. E. (1988) Constraints on the origin of fractured terrane, northern martian plains (abstract). In *Reports of Planetary Geology and Geophysics Program—1987*, pp. 482–484. NASA TM-4041.

McGill G. E. (1988) Evidence for a very large basin beneath Utopia Planitia, Mars (abstract). In *Lunar and Planetary Science XIX*, pp. 752–753. Lunar and Planetary Institute, Houston.

McGill G. E. (1989) Buried topography of Utopia, Mars: Persistence of a giant impact depression. *J. Geophys. Res.*, *94*, 2753–2759.

McGill G. E. (1989) Geologic evidence supporting an endogenic origin for the martain crustal dichotomy (abstract). In *Lunar and Planetary Science XX*, pp. 667–668. Lunar and Planetary Institute, Houston.

McGill G. E. (1989) Terrestrial analogues for planetary extensional structures (abstract). In *MEVTV Workshop on Tectonic Features on Mars* (T. R. Watters and M. P. Golombek, eds.), pp. 44–46. LPI Tech. Rpt. 89-06, Lunar and Planetary Institute, Houston.

McGill G. E. (1989) Terrestrial analogues for planetary extensional structures (abstract). In *Reports of Planetary Geology and Geophysics Program—1988*, pp. 551–553. NASA TM-4130.

McGill G. E. (1989) The martian crustal dichotomy (abstract). In *MEVTV Workshop on Early Tectonic and Volcanic Evolution of Mars* (H. Frey, ed.), pp. 59–61. LPI Tech. Rpt. 89-04, Lunar and Planetary Institute, Houston.

McGill G. E. and Dimitriou A. M. (1990) Origin of the martian global dichotomy by crustal thinning in the late Noachian or early Hesperian. *J. Geophys. Res.*, *95*, 12595–12605.

McGill G. E. and Hills L. S. (1990) Origin of giant martian polygons. *J. Geophys. Res.*, submitted.

McGill G. E. and Hills L. S. (1990) Polygonal terrane of Mars: Stresses from drape folding (abstract). In *Lunar and Planetary Science XXI*, pp. 763–764. Lunar and Planetary Institute, Houston.

McGovern P. J. and Solomon S. C. (1990) State of stress and eruption characteristics of martian volcanoes (abstract). In *Lunar and Planetary Science XXI*, pp. 765–766. Lunar and Planetary Institute, Houston.

McGovern P. J. and Solomon S. C. (1990) State of stress and eruption characteristics of martian volcanoes (abstract). In *MEVTV Workshop on the Evolution of Magma Bodies on Mars* (P. Mouginis-Mark and J. Holloway, eds.), pp. 44–45. LPI Tech. Rpt. 90-04, Lunar and Planetary Institute, Houston.

Melendrez D. E., Zimbelman J. R., and Francis P. W. (1988) Digital photomosaic of Viking images 14A29-14A35: A preliminary look at Gangis Chasma, Mars (abstract). In *Lunar and Planetary Science XIX*, pp. 768–769. Lunar and Planetary Institute, Houston.

Moore H. J. (1989) Martian surface materials (abstract). In *Fourth International Conference on Mars, Progr. and Abstracts*, pp. 42–44. Univ. of Arizona, Tucson.

Moore H. J. and Ackerman J. A. (1989) Martian and terrestrial lava flows (abstract). In *Lunar and Planetary Science XX*, pp. 711–712. Lunar and Planetary Institute, Houston.

Moore H. J. and Davis P. A. (1990) Analyses and morphology of a lava flow, Ascraeus Mons, Mars (abstract). In *Lunar and Planetary Science XXI*, pp. 805–806. Lunar and Planetary Institute, Houston.

Moore H. J. and Jakosky B. M. (1989) Viking landing sites, remote sensing observations, and physical properties of martian surface materials. *Icarus*, *81*, 164–184.

Moore H. J. and Keller J. M. (1990) Surface-material maps of Viking landing sites on Mars (abstract). In *Lunar and Planetary Science XXI*, pp. 807–808. Lunar and Planetary Institute, Houston.

Moore H. J., Jakosky B. M., and Christensen P. R. (1988) Viking landers and remote sensing (abstract). In *MEVTV Workshop on Nature and Composition of Surface Units on Mars* (J. R. Zimbelman, S. C. Solomon, and V. L. Sharpton, eds.), pp. 94–96. LPI Tech. Rpt. 88-05, Lunar and Planetary Institute, Houston.

Morris R. V., Gooding J. L., Lauer H. V. Jr., and Singer R. B. (1990) Iron mineralogy of a Hawaiian palagonitic soil with Mars-like spectral and magnetic properties (abstract). In *Lunar and Planetary Science XXI*, pp. 811–812. Lunar and Planetary Institute, Houston.

Mouginis-Mark P. and Wilson L. (1988) Volcano evolution on Mars (abstract). In *MEVTV Workshop on Nature and Composition of Surface Units on Mars* (J. R. Zimbelman, S. C. Solomon, and V. L. Sharpton, eds.), pp. 97–99. LPI Tech. Rpt. 88-05, Lunar and Planetary Institute, Houston.

Mouginis-Mark P. J., Robinson M. S., and Zuber M. T. (1990) Evolution of the Olympus Mons caldera, Mars (abstract). In *Lunar and Planetary Science XXI*, pp. 815–816. Lunar and Planetary Institute, Houston.

Mouginis-Mark P. J., Wilson L., and Zimbelman J. R. (1988) Polygenic eruptions on Alba Patera Mars. *Bull. Volcanol., 50*, 361–379.

Musselwhite D. S. and Lunine J. I. (1990) Clathrate storage of volatiles on Mars (abstract). In *Lunar and Planetary Science XXI*, pp. 831–832. Lunar and Planetary Institute, Houston.

Mustard J. F., Bibring J.-P., Erard S., Fischer E. M., Head J. W., Hurtrez S., Langevin Y., Pieters C. M., and Sotin C. J. (1990) Interpretation of spectral units of Isidis-Syrtis major from ISM-Phobos-2 observations (abstract). In *Lunar and Planetary Science XXI*, pp. 835–836. Lunar and Planetary Institute, Houston.

Newsom H. E. and Brittelle G. E. (1990) Impact cratering on Mars and the formation of crater lakes: A possible environment for the origin of life (abstract). In *Lunar and Planetary Science XXI*, pp. 877–878. Lunar and Planetary Institute, Houston.

Oberbeck V. R., Marshall J. R., and Schwartz D. E. (1990) A model for chemical evolution of life on Mars (abstract). In *Lunar and Planetary Science XXI*, pp. 905–906. Lunar and Planetary Institute, Houston.

Oberbeck V. R, Marshall J. R., Schwartz D. E, and Mancinelli R. L. (1990) Search for life: A science rationale for a permanent base on Mars (abstract). In *Lunar and Planetary Science XXI*, pp. 907–908. Lunar and Planetary Institute, Houston.

Odezynskyj M. I. and Holloway J. R. (1989) Carbonate composition and stability in the martian mantle: Preliminary results (abstract). In *Lunar and Planetary Science XX*, pp. 806–807. Lunar and Planetary Institute, Houston.

Odezynskyj M. and Holloway J. R. (1990) Stability, composition and phase relations of martian mantle carbonates (abstract). In *Lunar and Planetary Science XXI*, pp. 911–912. Lunar and Planetary Institute, Houston.

Pan V. and Holloway J. R. (1990) $CO_2$ solubility and its implications for degassing ascending magmas (abstract). In *MEVTV Workshop on the Evolution of Magma Bodies on Mars* (P. Mouginis-Mark and J. Holloway, eds.), pp. 46–47. LPI Tech. Rpt. 90-04, Lunar and Planetary Institute, Houston.

Parker T. J. and Saunders R. S. (1988) Origin of northern lowland plains: Constraints from boundary morphology (abstract). In *MEVTV Workshop on Nature and Composition of Surface Units on Mars* (J. R. Zimbelman, S. C. Solomon, and V. L. Sharpton, eds.), pp. 100–102. LPI Tech. Rpt. 88-05, Lunar and Planetary Institute, Houston.

Petroy S. B. and Arvidson R. E. (1990) Spectral emissivity of the Silver and Lunar Lake playas—Relevance to analyses of Mars TIR data (abstract). In *Lunar and Planetary Science XXI*, pp. 952–953. Lunar and Planetary Institute, Houston.

Peulvast J. P. (1990) Erosional landforms and morphotectonic development in Valles Marineris (Mars): Melas Chasma (abstract). In *Lunar and Planetary Science XXI*, pp. 954–955. Lunar and Planetary Institute, Houston.

Phillips R. J. (1988) The geophysical signal of the Martian global dichotomy (abstract). *Eos Trans. AGU, 69*, 389.

Phillips R. J. (1990) Geophysics at Mars: Issues and answers (abstract). In *Lunar and Planetary Science XXI*, pp. 956–957. Lunar and Planetary Institute, Houston.

Phillips R. J. and Sleep N. H. (1989) Tharsis and the early evolution of Mars (abstract). In *MEVTV Workshop on Early Tectonic and Volcanic Evolution of Mars* (H. Frey, ed.), pp. 62–63. LPI Tech. Rpt. 89-04, Lunar and Planetary Institute, Houston.

Phillips R. J., Sleep N. H., and Banerdt W. B. (1990) Permanent uplift in magmatic systems with application to the Tharsis region of Mars. *J. Geophys. Res., 95*, 5089–5100.

Plescia J. B. (1990) Photoclinometric analysis of wrinkle ridges on Lunae Planum, Mars (abstract). In *Lunar and Planetary Science XXI*, pp. 967–968. Lunar and Planetary Institute, Houston.

Plescia J. B. (1990) Young flood lavas in the Elysium region, Mars (abstract). In *Lunar and Planetary Science XXI*, pp. 969–970. Lunar and Planetary Institute, Houston.

Plescia J. B. and Golombek M. P. (1989) Tectonic implications of martian wrinkle ridges (abstract). In *MEVTV Workshop on Early Tectonic and Volcanic Evolution of Mars* (H. Frey, ed.), pp. 64–65. LPI Tech. Rpt. 89-04, Lunar and Planetary Institute, Houston.

Porter T. K. and Schultz P. H. (1990) Formation of rhyolitic ridges on martian basalts (abstract). In *Lunar and Planetary Science XXI*, pp. 973–974. Lunar and Planetary Institute, Houston.

Postawko S. E., Fanale F. P., and Zent A. P. (1987) Possible effects of episodic volcanism on Martian climate (abstract). *Eos Trans. AGU, 68*, 1341.

Postawko S. E., Fanale F. P., and Zent A. P. (1988) Effects of epochal vs. episodic release of $SO_2$ by volcanoes on Mars. *Proc. Lunar Planet. Sci. Conf. 19th*, pp. 943–944.

Postawko S. E., Fanale F. P., and Zent A. P. (1988) Episodic vs. epochal release of $SO_2$ on Mars (abstract). In *MEVTV Workshop on Nature and Composition of Surface Units on Mars* (J. R. Zimbelman, S. C. Solomon, and V. L. Sharpton, eds.), pp. 103–104. LPI Tech. Rpt. 88-05, Lunar and Planetary Institute, Houston.

Postawko S. E., Fanale F. P., and Zent A. P. (1989) Episodic warming on Mars by volcanic release of $SO_2$: Implications for ice lakes (abstract). In *Fourth International Conference on Mars, Progr. and Abstracts*, pp. 164–165. Univ. of Arizona, Tucson.

Prinn R. and Fegley B. (1988) Chemical interactions between the present-day martian atmosphere and surface minerals (abstract). In *MEVTV Workshop on Nature and Composition of Surface Units on Mars* (J. R. Zimbelman, S. C. Solomon, and V. L. Sharpton, eds.), p. 105. LPI Tech. Rpt. 88-05, Lunar and Planetary Institute, Houston.

Reyes D. P. and Christensen P. R. (1990) Mid-infrared spectra of komatiite vs. basalt (abstract). In *Lunar and Planetary Science XXI*, pp. 1011–1012. Lunar and Planetary Institute, Houston.

Robinson C. (1990) The highland-lowland boundary formed on Mars between the Late Noachian and the Early Hesperian

(abstract). In *Lunar and Planetary Science XXI*, pp. 1025–1026. Lunar and Planetary Institute, Houston.

Robinson M. S. (1990) Topographic measurements of Apollinaris and Tyrrhena Patera, Mars (abstract). In *Lunar and Planetary Science XXI*, pp. 1027–1028. Lunar and Planetary Institute, Houston.

Robinson M. S. and Tanaka K. L. (1988) Stratigraphy of the Kasei Valles region, Mars (abstract). In *MEVTV Workshop on Nature and Composition of Surface Units on Mars* (J. R. Zimbelman, S. C. Solomon, and V. L. Sharpton, eds.), pp. 106–108. LPI Tech. Rpt. 88-05, Lunar and Planetary Institute, Houston.

Robinson M. S. and Tanaka K. L. (1989) Hydrology of a flow event in Kasei Valles, Mars (abstract). In *Lunar and Planetary Science XX*, pp. 912–913. Lunar and Planetary Institute, Houston.

Robinson M. S. and Tanaka K. L. (1990) Magnitude of a catastrophic flood event at Kasei Valles, Mars. *Geology*, in press.

Roth L. E. and Saunders R. S. (1988) Topography of large craters on Mars: Implications for the highlands resurfacing history (abstract). In *MEVTV Workshop on Nature and Composition of Surface Units on Mars* (J. R. Zimbelman, S. C. Solomon, and V. L. Sharpton, eds.), pp. 109–110. LPI Tech. Rpt. 88-05, Lunar and Planetary Institute, Houston.

Rotto S. L. and Tanaka K. L. (1989) Faulting history of the Alba Patera-Ceraunius Fossae region of Mars (abstract). In *Lunar and Planetary Science XX*, pp. 926–927. Lunar and Planetary Institute, Houston.

Roush T. and Singer R. B. (1990) Estimates of absolute flux and radiance factor of localized regions on Mars in the 2–4 μm wavelength region (abstract). In *Lunar and Planetary Science XXI*, pp. 1041–1042. Lunar and Planetary Institute, Houston.

Roush T. L., Roush E. A., Singer R. B., and Lucey P. G. (1988) Preliminary analysis of recent 2.2–4.2 μm telescopic observations of Elysium, Mars: Implications for crystallinity and hydration state of surface materials (abstract). In *MEVTV Workshop on Nature and Composition of Surface Units on Mars* (J. R. Zimbelman, S. C. Solomon, and V. L. Sharpton, eds.), pp. 111–113. LPI Tech. Rpt. 88-05, Lunar and Planetary Institute, Houston.

Roush T., Pollack J., and Orenberg J. (1990) Derivation of mid-infrared (5–25 μm) optical constants of some silicates and palagonite (abstract). In *Lunar and Planetary Science XXI*, pp. 1043–1044. Lunar and Planetary Institute, Houston.

Ruff S. W. and Greeley R. (1990) Sinuous ridges of the south polar region, Mars: Possible origins (abstract). In *Lunar and Planetary Science XXI*, pp. 1047–1048. Lunar and Planetary Institute, Houston.

Runcorn S. K. (1989) Solid state convection and the early evolution of Mars (abstract). In *MEVTV Workshop on Early Tectonic and Volcanic Evolution of Mars* (H. Frey, ed.), p. 66. LPI Tech. Rpt. 89-04, Lunar and Planetary Institute, Houston.

Rutherford M. J. (1990) Experimental study of dehydration and crystallization produced by decompression of dacites: Implications for magma ascent rates. Abstract presented at Goldschmidt Conference, Baltimore, Maryland, May 1990.

Rutherford M. J., Heine B., and Johnson M. (1988) Origin of SNC kaersutitic amphibole: Experimental data (abstract). In *MEVTV Workshop on Nature and Composition of Surface Units on Mars* (J. R. Zimbelman, S. C. Solomon, and V. L. Sharpton, eds.), pp. 114–116. LPI Tech. Rpt. 88-05, Lunar and Planetary Institute, Houston.

Rzhiga O. N. and Selivanov A. S. (1990) On application of SAR-method for the geological nature of Mars exploration (abstract). In *Lunar and Planetary Science XXI*, pp. 1059–1060. Lunar and Planetary Institute, Houston.

Saunders R. S. (1989) Northern plains of Mars: A sedimentary model (abstract). In *MEVTV Workshop on Early Tectonic and Volcanic Evolution of Mars* (H. Frey, ed.), pp. 67–69. LPI Tech. Rpt. 89-04, Lunar and Planetary Institute, Houston.

Schaefer M. W. (1990) Chemical evolution of the early martian hydrosphere (abstract). In *Lunar and Planetary Science XXI*, pp. 1077–1078. Lunar and Planetary Institute, Houston.

Schneid B. D. and Greeley R. (1990) Global relationships between volcanic vents and fractures radial to large impact basins on Mars (abstract). In *Lunar and Planetary Science XXI*, pp. 1091–1092. Lunar and Planetary Institute, Houston.

Schubert G., Solomon S. C., Turcotte D. L., Drake M. J., and Sleep N. H. (1990) Origin and thermal evolution of Mars. In *Mars* (H. Kieffer et al., eds.). Univ. of Arizona, Tucson, in press.

Schubert G., Turcotte D. L., Solomon S. C., and Sleep N. H. (1989) Coupled evolution of the atmosphere and interiors of planets and satellites. In *Origin and Evolution of Planetary and Satellite Atmospheres* (S. K. Atreya, J. B. Pollack, and M. S. Matthews, eds.), pp. 450–483. Univ. of Arizona, Tucson.

Schubert G., Turcotte D. L., Solomon S. C., Sleep N. H., and Drake M. J. (1989) Origin and thermal evolution of Mars (abstract). In *Fourth International Conference on Mars, Progr. and Abstracts*, pp. 50–51. Univ. of Arizona, Tucson.

Schultz P. H. (1988) Early cratering rates and the nature of the martian cratered uplands (abstract). In *MEVTV Workshop on Nature and Composition of Surface Units on Mars* (J. R. Zimbelman, S. C. Solomon, and V. L. Sharpton, eds.), pp. 117–119. LPI Tech. Rpt. 88-05, Lunar and Planetary Institute, Houston.

Schultz P. H. (1990) Evidence for atmospheric effects on martian crater shape (abstract). In *Lunar and Planetary Science XXI*, pp. 1097–1098. Lunar and Planetary Institute, Houston.

Schultz R. A. (1989) Do pit-crater chains grow up to be Valles Marineris canyons? (abstract). In *MEVTV Workshop on Tectonic Features on Mars* (T. R. Watters and M. P. Golombek, eds.), pp. 47–48. LPI Tech. Rpt. 89-06, Lunar and Planetary Institute, Houston.

Schultz R. A. (1989) Strike-slip faulting in the ridged plains of Mars (abstract). In *MEVTV Workshop on Tectonic Features on Mars* (T. R. Watters and M. P. Golombek, eds.), pp. 49–51. LPI Tech. Rpt. 89-06, Lunar and Planetary Institute, Houston.

Schultz R. A. (1990) Complex early rifting in Valles Marineris: Results from preliminary geologic mapping of the Ophir

Planum region of Mars, 1:500,000 scale (abstract). In *Lunar and Planetary Science XXI*, pp. 1103–1104. Lunar and Planetary Institute, Houston.

Schultz R. A. (1990) Echelon geometry of common martian structures and its relationship to local and regional stresses (abstract). In *Lunar and Planetary Science XXI*, pp. 1105–1106. Lunar and Planetary Institute, Houston.

Schultz R. A. (1990) Possible deficiency of large martian craters and relative cratering of the terrestrial planets (abstract). In *Lunar and Planetary Science XXI*, pp. 1107–1108. Lunar and Planetary Institute, Houston.

Schultz R. A. (1990) Strike-slip faulting, wrinkle ridges, and time variable stress states in the Coprates region of Mars (abstract). In *Lunar and Planetary Science XXI*, pp. 1109–1110. Lunar and Planetary Institute, Houston.

Schultz R. A. and Frey H. V. (1990) A new survey of multi-ring basins on Mars. *J. Geophys. Res.*, in press.

Schultz R. A. and Frey H. V. (1990) Geology, structure, and statistics of multi-ring basins on Mars (abstract). In *Lunar and Planetary Science XXI*, pp. 1111–1112. Lunar and Planetary Institute, Houston.

Scott D. H. (1989) New evidence—old problem: Wrinkle ridge origin (abstract). In *MEVTV Workshop on Tectonic Features on Mars* (T. R. Watters and M. P. Golombek, eds.), pp. 52–54. LPI Tech. Rpt. 89-06, Lunar and Planetary Institute, Houston.

Scott D. H. and Chapman M. G. (1991) Mars Elysium basin: Geologic/volumetric analyses of a young lake and exobiologic implications. *Proc. Lunar Planet. Sci., Vol. 21*, pp. 669–677.

Scott D. H. and Dohm J. M. (1988) Faulting and its relation to volcanism: Mars western equatorial region (abstract). In *NASA MEVTV Program Working Group Meeting: Volcanism on Mars*, pp. 5–8. Lunar and Planetary Institute, Houston.

Scott D. H. and Dohm J. M. (1989) Chronology and global distribution of fault and ridge systes on Mars (abstract). In *Lunar and Planetary Science XX*, pp. 976–977. Lunar and Planetary Institute, Houston.

Scott D. H. and Dohm J. M. (1989) Fault and ridge systems: Historical development in western region of Mars (abstract). In *MEVTV Workshop on Early Tectonic and Volcanic Evolution of Mars* (H. Frey, ed.), pp. 70–73. LPI Tech. Rpt. 89-04, Lunar and Planetary Institute, Houston.

Scott D. H. and Dohm J. M. (1990) Chronology and global distribution of fault and ridge systems on Mars. *Proc. Lunar Planet. Sci. Conf. 20th*, pp. 487–501.

Scott D. H. and Dohm J. M. (1990) Faults and ridges: Historical development in Tempe Terra and Ulysses Patera regions of Mars. *Proc. Lunar Planet. Sci. Conf. 20th*, pp. 503–513.

Scott D. H. and Dohm J. M. (1990) Evidence for multiple flooding episodes in Kasei Valles, Mars (abstract). In *Lunar and Planetary Science XXI*, pp. 1115–1116. Lunar and Planetary Institute, Houston.

Scott D. H. and Dohm J. M. (1990) Tectonic setting of martian volcanoes and deep-seated intrusives (abstract). In *MEVTV Workshop Evolution of Magma Bodies on Mars* (P. Mouginis-Mark and J. Holloway, eds.), pp. 52–52. LPI Tech. Rpt. 90-04, Lunar and Planetary Institute, Houston.

Scott D. H. and Tanaka K. L. (1988) Documenting volcano-tectonic episodes in Mars' stratigraphic record (abstract). In *MEVTV Workshop on Nature and Composition of Surface Units on Mars* (J. R. Zimbelman, S. C. Solomon, and V. L. Sharpton, eds.), pp. 120–121. LPI Tech. Rpt. 88-05, Lunar and Planetary Institute, Houston.

Scott D. H. and Tanaka K. L. (1988) Martian sample sites: Examples based on a global geologic perspective (abstract). In *Workshop on Mars Sample Return Science* (M. J. Drake et al., eds.), pp. 154–155. LPI Tech. Rept. 88-07, Lunar and Planetary Institute, Houston.

Scott D. H. and Underwood J. R. (1991) Mottled terrain: A continuing martian enigma. *Proc. Lunar Planet. Sci., Vol. 21*, pp. 627–634.

Selivanov A. and Naraeva M. (1990) Thermoscanning of the Mars surface (abstract). In *Lunar and Planetary Science XXI*, p. 1125. Lunar and Planetary Institute, Houston.

Shalimov I. V. (1990) The relation of the lava complexes of the Olympus Mons on Mars (abstract). In *Lunar and Planetary Science XXI*, pp. 1132–1133. Lunar and Planetary Institute, Houston.

Singer R. B. (1988) The surface composition of Mars from Earthbased observations (abstract). In *MEVTV Workshop on Nature and Composition of Surface Units on Mars* (J. R. Zimbelman, S. C. Solomon, and V. L. Sharpton, eds.), pp. 122–124. LPI Tech. Rpt. 88-05, Lunar and Planetary Institute, Houston.

Singer R. B., Miller J. S., Wells K. W., and Bus E. S. (1990) Visible and near-IR spectral imaging of Mars during the 1988 opposition (abstract). In *Lunar and Planetary Science XXI*, pp. 1164–1165. Lunar and Planetary Institute, Houston.

Sleep N. H. and Zahnle K. J. (1989) Late iron loss from the martian lithosphere: Not a likely cause of vertical tectonics (abstract). In *MEVTV Workshop on Early Tectonic and Volcanic Evolution of Mars* (H. Frey, ed.), pp. 74–75. LPI Tech. Rpt. 89-04, Lunar and Planetary Institute, Houston.

Solberg T. C. and Burns R. G. (1988) Mossbauer spectra of weathered stony meteorites relevant to oxidation on Mars. I. Chondrites (abstract). In *Lunar and Planetary Science XIX*, pp. 1103–1104. Lunar and Planetary Institute, Houston.

Solberg T. C. and Burns R. G. (1989) Iron Mossbauer spectral study of weathered Antarctic and SNC meteorites. *Proc. Lunar Planet. Sci. Conf. 19th*, pp. 513–522.

Solomon S. C. (1988) Geophysics and tectonics of Mars (abstract). *Geol. Soc. Am., Abstracts with Progr., 20*, A83.

Solomon S. C. and Head J. W. (1989) Estimating lithospheric thermal gradient on Mars from elastic lithosphere thickness: New constraints on heat flow and mantle dynamics (abstract). In *Reports of Planetary Geology and Geophysics Program—1988*, pp. 203–205. NASA TM-4130.

Solomon S. C. and Head J. W. (1989) Estimating lithospheric thermal gradient on Mars from elastic lithosphere thickness: New constraints on heat flow and mantle dynamics (abstract). In *Lunar and Planetary Science XX*, pp. 1030–1031. Lunar and Planetary Institute, Houston.

Solomon S. C. and Head J. W. (1989) Heterogeneities in the thickness of the elastic lithosphere of Mars: Constraints on

thermal gradients, crustal thickness, and internal dynamics (abstract). In *MEVTV Workshop on Early Tectonic and Volcanic Evolution of Mars* (H. Frey, ed.), pp. 76–78. LPI Tech. Rpt. 89-04, Lunar and Planetary Institute, Houston.

Solomon S. C. and Head J. W. (1990) Heterogeneities in the thickness of the elastic lithosphere of Mars: Constraints on heat flow and internal dynamics. *J. Geophys. Res.*, 95, 11073–11083.

Spencer J. R., Fanale F. P., and Tribble J. E. (1989) Karst on Mars? Origin of closed depressions in Valles Marineris by solution of carbonates in groundwater sulfuric acid (abstract). In *Fourth International Conference on Mars, Progr. and Abstracts*, pp. 193–194. Univ. of Arizona, Tucson.

Spera F. J. (1990) Properties of analog martian magmas by concentric cylinder viscometry. *J. Geophys. Res.*, submitted.

Spera F. J. (1990) Rheometry of dilute viscous emulsions and significance for planetary magmatic flows. *J. Geophys. Res.*, submitted.

Spera F. J. and Stein D. J. (1990) Rheological properties of martian magmas: Experiments and inferences (abstract). In *MEVTV Workshop on the Evolution of Magma Bodies on Mars* (P. Mouginis-Mark and J. Holloway, eds.), pp. 54–55. LPI Tech. Rpt. 90-04, Lunar and Planetary Institute, Houston.

Squyres S. W., Clifford S. M., Kuzmin R. O., Zimbelman J. R., and Costard F. M. (1990) Ice in the martian regolith. In *Mars* (H. Kieffer et al., eds.). Univ. of Arizona, Tucson, in press.

Stephens S. K. and Stevenson D. J. (1990) Dry carbonate formation on Mars: A plausible sink for an early dense $CO_2$ atmosphere? (abstract) In *Lunar and Planetary Science XXI*, pp. 1198–1199. Lunar and Planetary Institute, Houston.

Stevenson D. J. and Bittker S. S. (1990) Why existing terrestrial planet thermal history calculations should not be believed (and what to do about it) (abstract). In *Lunar and Planetary Science XXI*, pp. 1200–1201. Lunar and Planetary Institute, Houston.

Storrs A. D., Fanale F. P., Saunders R. S., and Stephens J. B. (1987) The formation of filamentary sublimate residues (FSR) (abstract). *Bull. Am. Astron. Soc.*, *19*, 894.

Storrs A. D., Fanale F. P., Saunders R. S., and Stephens J. B. (1988) The formation of filamentary sublimate residues (FSR) from mineral grains. *Icarus*, *76*, 493–512.

Straub D. W. and Burns R. G. (1990) Ferrolysis of iron-bearing martian brines: Origin of dust-storm particulates on Mars (abstract). In *Lunar and Planetary Science XXI*, pp. 1214–1215. Lunar and Planetary Institute, Houston.

Straub D. W. and Burns R. G. (1990) Oxidized pyroxenes and degradation of their visible-near infrared spectra: Implications to remote-sensing of Mars (abstract). In *Lunar and Planetary Science XXI*, pp. 1216–1217. Lunar and Planetary Institute, Houston.

Suppe J. and Narr W. (1989) Fault-related folding on the Earth with application to wrinkle ridges on Mars and the Moon (abstract). In *MEVTV Workshop on Tectonic Features on Mars* (H. Frey, ed.), pp. 55–56. LPI Tech. Rpt. 89-04, Lunar and Planetary Institute, Houston.

Tanaka K. L. (1988) Chaotic material and debris flows in the Simud-Tiu Valles outflow system of Mars (abstract). In *Lunar and Planetary Science XIX*, pp. 1175–1176. Lunar and Planetary Institute, Houston.

Tanaka K. L. (1990) Martian geologic "revolutions": A tale of two processes (abstract). In *Lunar and Planetary Science XXI*, pp. 1237–1238. Lunar and Planetary Institute, Houston.

Tanaka K. L. (1990) Tectonic history of the Alba Patera-Ceraunius Fossae region of Mars. *Proc. Lunar Planet. Sci. Conf. 20th*, pp. 515–523.

Tanaka K. L. (1990) Volcanism and planetary surfaces. In *The Reference Encyclopedia of Astronomy and Astrophysics*. Robert Ubell Associates, New York, in press.

Tanaka K. L. and Chapman M. G. (1990) The relation of catastrophic flooding of Mangala Valles, Mars, to faulting of Memnonia Fosse and Tharis volcanism. *J. Geophys. Res.*, 95, 14315–14323.

Tanaka K. L. and Davis P. A. (1987) History and morphology of faulting in the Noctis Labyrinthus-Claritas Fossae region of Mars (abstract). In *Reports of Planetary Geology and Geophysics Program—1988*, pp. 478–480. NASA TM-89810.

Tanaka K. L. and Davis P. A. (1988) Tectonic history of the Syria Planum province of Mars. *J. Geophys. Res.*, 93, 14893–14917.

Tanaka K. L. and Davis P. A. (1989) Development of grabens, tension cracks, and pits southeast of Alba Patera, Mars (abstract). In *MEVTV Workshop on Tectonic Features on Mars* (T. R. Watters and M. P. Golombek, eds.), pp. 57–59. LPI Tech. Rpt. 89-06, Lunar and Planetary Institute, Houston.

Tanaka K. L. and Dohm J. M. (1989) Volcanotectonic provinces of the Tharsis region of Mars: Identification, variations, and implications (abstract). In *MEVTV Workshop on Early Tectonic and Volcanic Evolution of Mars* (H. Frey, ed.), pp. 79–81. LPI Tech. Rpt. 89-04, Lunar and Planetary Institute, Houston.

Tanaka K. L. and Golombek M. P. (1989) Martian tension fractures and the formation of grabens and collapse features at Valles Marineris. *Proc. Lunar Planet. Sci. Conf. 19th*, pp. 383–396.

Tanaka K. L. and MacKinnon D. J. (1987) Development of the Chryse hydrologic system, Mars (abstract). In *Lunar and Planetary Science XVIII*, pp. 996–997. Lunar and Planetary Institute, Houston.

Tanaka K. L. and MacKinnon D. J. (1989) Release of Martian catastrophic floods by fracture discharge from volcanotectonic regions (abstract). In *Fourth International Conference on Mars, Progr. and Abstracts*, pp. 200–201. Univ. of Arizona, Tucson.

Tanaka K. L. and Scott D. H. (1987) Eruptive history of the Elysium volcanic province of Mars (abstract). In *Reports of Planetary Geology and Geophysics Program—1986*, pp. 333–335. NASA TM-89810.

Tanaka K. L., Chapman M. G., and Scott D. H. (1990) Geologic history of the Elysium region of Mars (abstract). In *Reports of Planetary Geology and Geophysics Program—1989*. NASA TM, in press.

Tanaka K. L., Chapman M. G., and Scott D. H. (1990) Geologic map of the Elysium region of Mars. *U.S. Geol. Surv. Misc. Inv. Series Map I-2147*, scale 1:5,000,000, in press.

Tanaka K. L., Davis P. A., and Golombek M. P. (1989) Development of grabens, tension cracks, and pits southeast

of Alba Patera, Mars (abstract). In *MEVTV Workshop on Tectonic Features on Mars* (T. R. Watters and M. P. Golombek, eds.), pp. 57–59. LPI Tech. Rpt. 89-06, Lunar and Planetary Institute, Houston.

Tanaka K. L., Isbell N. K., Scott D. H., Greeley R., and Guest J. E. (1988) The resurfacing history of Mars: A synthesis of digitized, Viking-based geology. *Proc. Lunar Planet. Sci. Conf. 18th*, pp. 665–678.

Tanaka K. L., Onstott T. C., and Shoemaker E. M. (1990) Magnetostratigraphy of the San Francisco volcanic field, Arizona. *U.S. Geol. Surv. Bull. 1929*, in press.

Tanaka K. L., Scott D. H., and Greeley R. (1989) Martian stratigraphy and geologic history (abstract). In *Fourth International Conference on Mars, Progr. and Abstracts*, pp. 54–55. Univ. of Arizona, Tucson.

Thomas P. J., Squyres S. W., Carr M. H. (1989) Flank tectonics of martian volcanoes (abstract). In *MEVTV Workshop on Tectonic Features on Mars* (T. R. Watters and M. P. Golombek, eds.), pp. 60–62. LPI Tech. Rpt. 89-06, Lunar and Planetary Institute, Houston.

Thompson T. W. (1988) Mars Earth-based radar: 1986 results and 1988–1990 opportunities (abstract). In *MEVTV Workshop on Nature and Composition of Surface Units on Mars* (J. R. Zimbelman, S. C. Solomon, and V. L. Sharpton, eds.), pp. 125–126. LPI Tech. Rpt. 88-05, Lunar and Planetary Institute, Houston.

Thompson T. W. and Moore H. J. (1990) A radar-echo model for Mars (abstract). In *Lunar and Planetary Science XXI*, pp. 1252–1253. Lunar and Planetary Institute, Houston.

Tolan T. L., Anderson J. L., and Beeson M. H. (1989) Origin and characteristics on dextral strike-slip faults within the Yakima fold belt, Columbia River Flood-Basalt Province, USA (abstract). In *MEVTV Workshop on Tectonic Features on Mars* (T. R. Watters and M. P. Golombek, eds.), pp. 63–64. LPI Tech. Rpt. 89-06, Lunar and Planetary Institute, Houston.

Treiman A. H. (1988) Crystal fractionation in the SNC meteorites: Implications for surface units on Mars (abstract). In *MEVTV Workshop on Nature and Composition of Surface Units on Mars* (J. R. Zimbelman, S. C. Solomon, and V. L. Sharpton, eds.), pp. 127–128. LPI Tech. Rpt. 88-05, Lunar and Planetary Institute, Houston.

Turcotte D. L. (1989) Early evolution of the Martian interior (abstract). *Eos Trans. AGU*, 69, 389.

Turcotte D. L. (1989) Thermal evolution of Mars and Venus including irreversible fractionation (abstract). In *Lunar and Planetary Science XX*, pp. 1138–1139. Lunar and Planetary Institute, Houston.

Turcotte D. L. and Huang J. (1990) Implications of crustal formation on Mars from parameterized convection calculations (abstract). In *Lunar and Planetary Science XXI*, pp. 1266–1267. Lunar and Planetary Institute, Houston.

Turcotte D. L. and Huang J. (1990) Implications of crustal fractionation for planetary evolution. *Icarus*, in press.

Van der Laan S. R., Kennedy A., Wasserburg G. J., Wyllie P. J., and Zhang Y. (1990) Preliminary composition of chemical and self diffusion for K and Ca in andesite and rhyolite melt. *Eos Trans. AGU*, 71, 652.

Walsh P. A., Blaney D. L., and McCord T. B. (1988) Martian surface analogs: Laboratory spectral studies in the mid infrared (abstract). In *MEVTV Workshop on Nature and Composition of Surface Units on Mars* (J. R. Zimbelman, S. C. Solomon, and V. L. Sharpton, eds.), pp. 129–131. LPI Tech. Rpt. 88-05, Lunar and Planetary Institute, Houston.

Ward W. R. and Rudy D. J. (1990) Did Mars pass through a secular spin-orbit resonance? (abstract). In *Lunar and Planetary Science XXI*, pp. 1291–1292. Lunar and Planetary Institute, Houston.

Warren P. H. (1989) Primordial global differentiation, Mars-style (abstract). In *MEVTV Workshop on Early Tectonic and Volcanic Evolution of Mars* (H. Frey, ed.), pp. 82–84. LPI Tech. Rpt. 89-04, Lunar and Planetary Institute, Houston.

Watkinson A. J. and Price E. H. (1989) Structural geometry, strain distribution and fold mechanics within Eastern Umtanum Fold Ridge, south central Washington (abstract). In *MEVTV Workshop on Tectonic Features on Mars* (T. R. Watters and M. P. Golombek, eds.), pp. 65–67. LPI Tech. Rpt. 89-06, Lunar and Planetary Institute, Houston.

Watters T. R. (1987) The volcanic plains ridges of the Chryse and Amazonis depressions (abstract). In *Lunar and Planetary Science XVIII*, pp. 1064–1065. Lunar and Planetary Institute, Houston.

Watters T. R. (1987) Volcanic-plains ridges on the terrestrial planets: A comparison of the Columbia and Tharsis Plateaus (abstract). In *Geol. Soc. Am., Abstracts with Progr.*, 19, 463.

Watters T. R. (1987) The origin of volcanic plains anticlinal ridges: The role of reverse and thrust faulting (abstract). *Geol. Soc. Am., Abstracts with Progr.*, 19, 833.

Watters T. R. (1988) Arches, anticlinal ridges, crenulate and sub-crenulate ridges: The wrinkle ridge assemblage (abstract). In *Reports of Planetary Geology and Geophysics Program—1987*, pp. 470–472. NASA TM-4041.

Watters T. R. (1988) The periodic nature and possible origin of anticlinal ridge spacings on the Tharsis and Columbia Plateaus (abstract). In *Reports of Planetary Geology and Geophysics Program—1987*, pp. 473–475. NASA TM-4041.

Watters T. R. (1988) Strain distribution in the anticlinal ridges of the Columbia Plateau: Implications for their origin and the origin of first-order ridges on terrestrial planets (abstract). In *Lunar and Planetary Science XIX*, pp. 1243–1244. Lunar and Planetary Institute, Houston.

Watters T. R. (1988) The wrinkle ridge assemblage (abstract). In *Lunar and Planetary Science XIX*, pp. 1245–1246. Lunar and Planetary Institute, Houston.

Watters T. R. (1988) Wrinkle ridge assemblages on the terrestrial planets. *J. Geophys. Res.*, 93, 10236–10254.

Watters T. R. (1989) Periodically spaced wrinkle ridges in ridged plains units on Mars (abstract). In *MEVTV Workshop on Early Tectonic and Volcanic Evolution of Mars* (H. Frey, ed.), pp. 85–87. LPI Tech. Rpt. 89-04, Lunar and Planetary Institute, Houston.

Watters T. R. (1989) Periodically spaced ridges of the Columbia Plateau. In *Volcanism and Tectonism in the Columbia River Flood-Basalt Province* (S. P. Reidel and P. R. Hooper, eds.), pp. 238–292. Geol. Soc. Am. Spec. Pap. 239.

Watters T. R. (1989) Periodically spaced wrinkle ridges on the Tharsis Plateau of Mars (abstract). In *Fourth International Conference on Mars, Progr. and Abstracts*, pp. 206–207. Univ. of Arizona, Tucson.

Watters T. R. (1989) The origin of periodically spaced wrinkle ridges on the Tharsis Plateau of Mars. *J. Geophys. Res.*, submitted.

Watters T. R. (1990) The nature and origin of periodically spaced wrinkle ridges on Mars (abstract). In *Lunar and Planetary Science XXI*, pp. 1304–1305. Lunar and Planetary Institute, Houston.

Watters T. R. and Chadwick D. J. (1989) Crosscutting periodically spaced first-order ridges in the ridged plains of Hesperia Planum: Another case for a buckling model (abstract). In *MEVTV Workshop on Tectonic Features on Mars* (T. R. Watters and M. P. Golombek, eds.), pp. 68–70. LPI Tech. Rpt. 89-06, Lunar and Planetary Institute, Houston.

Watters T. R. and Golombek M. P., eds. (1989) *MEVTV Workshop on Tectonic Features on Mars*. LPI Tech. Rpt. 89-06, Lunar and Planetary Institute, Houston. 126 pp.

Watters T. R. and Tuttle M. J. (1988) Evidence of a shear system associated with the deformed basalts of the Columbia Plateau: Implications for the ridged plains units on Mars (abstract). In *Geol. Soc. Am., Abstracts with Progr., 20*, A148.

Watters T. R. and Tuttle M. J. (1989) Strike-slip faulting associated with the folded Columbia River basalts: Implications for the deformed ridged plains of Mars (abstract). In *MEVTV Workshop on Tectonic Features on Mars* (T. R. Watters and M. P. Golombek, eds.), pp. 71–73. LPI Tech. Rpt. 89-06, Lunar and Planetary Institute, Houston.

Watters T. R. and Tuttle M. J. (1990) Domains of regional pure shear on the terrestrial planets (abstract). In *Lunar and Planetary Science XXI*, pp. 1306–1307. Lunar and Planetary Institute, Houston.

Watters T. R. and Tuttle M. J. (1990) Origin of curvilinear graben in southwest Lunae Planum, Mars (abstract). In *Lunar and Planetary Science XXI*, pp. 1308–1309. Lunar and Planetary Institute, Houston.

Watters T. R., Tuttle M. J., and Chadwick J. (1988) Mare ridge-highland scarp structures and upland scarps on the Moon, Mars, and Mercury (abstract). In *Lunar and Planetary Science XIX*, pp. 1247–1248. Lunar and Planetary Institute, Houston.

Watters T. R., Chadwick D. J., and Liu M. C. (1990) Distribution of strain in the floor of the Olympus Mons caldera (abstract). In *Lunar and Planetary Science XXI*, pp. 1310–1311. Lunar and Planetary Institute, Houston.

Watters T. R., Tuttle M. J., and Kiger F. J. (1990) Symmetry of inferred stress fields in the Tharsis region of Mars (abstract). In *Lunar and Planetary Science XXI*, pp. 1312–1313. Lunar and Planetary Institute, Houston.

Weiblen P. W. (1990) Simulants for martian surface minerals (abstract). In *Lunar and Planetary Science XXI*, p. 1314. Lunar and Planetary Institute, Houston.

Wells G. L. and Zimbelman J. R. (1989) Extra-terrestrial arid surface processes. In *Arid Zone Geomorphology* (D. Thomas, ed.), pp. 335–358. Belhaven Press, London.

Wentworth S. J. and Gooding J. L. (1990) Pre-terrestrial origin of "rust" in the nakhlite meteorite (abstract). In *Lunar and Planetary Science XXI*, pp. 1321–1322. Lunar and Planetary Institute, Houston.

Wichman R. W. and Schultz P. H. (1989) An ancient Valles Marineris? (abstract) In *MEVTV Workshop on Early Tectonic and Volcanic Evolution of Mars* (H. Frey, ed.), pp. 88–90. LPI Tech. Rpt. 89-04, Lunar and Planetary Institute, Houston.

Wichman R. W. and Schultz P. H. (1990) A model for crustal subduction by large impacts (abstract). In *Lunar and Planetary Science XXI*, pp. 1331–1332. Lunar and Planetary Institute, Houston.

Wichman R. W. and Schultz P. H. (1990) Large scale compression structures in the Eridania-Phaethontis region: More evidence for polar wandering (abstract). In *Lunar and Planetary Science XXI*, pp. 1333–1334. Lunar and Planetary Institute, Houston.

Wilhelms D. E. and Baldwin R. J. (1988) Ridged and gullied terrains in the martian uplands (abstract). In *MEVTV Workshop on Nature and Composition of Surface Units on Mars* (J. R. Zimbelman, S. C. Solomon, and V. L. Sharpton, eds.), pp. 132–134. LPI Tech. Rpt. 88-05, Lunar and Planetary Institute, Houston.

Wilhelms D. E. and Baldwin R. J. (1989) The relevance of knobby terrain to the martian dichotomy (abstract). In *MEVTV Workshop on Early Tectonic and Volcanic Evolution of Mars* (H. Frey, ed.), pp. 91–93. LPI Tech. Rpt. 89-04, Lunar and Planetary Institute, Houston.

Williams S. H. (1990) Possible aeolian megaripples on Mars (abstract). In *Lunar and Planetary Science XXI*, pp. 1339–1340. Lunar and Planetary Institute, Houston.

Williams S. H. and Zimbelman J. R. (1988) Aeolian gradation on Mars: Widespread and ancient (abstract). In *Lunar and Planetary Science XIX*, pp. 1281–1282. Lunar and Planetary Institute, Houston.

Williams S. H. and Zimbelman J. R. (1988) Lowland plains in Utopia Planitia: Evidence of multiple and ancient aeolian events (abstract). *Eos Trans. AGU*, 69, 390.

Williams S. H. and Zimbelman J. R. (1989) Origin of debris flow material: Ismenium Lacus, Mars (abstract). In *Lunar and Planetary Science XX*, pp. 1209–1210. Lunar and Planetary Institute, Houston.

Williams S. H. and Zimbelman J. R. (1989) Preliminary geologic mapping in the western Utopia Planitia region of Mars (abstract). In *Reports of Planetary Geology and Geophysics Program—1988*, pp. 580–582. NASA TM-4130.

Williams S. H. and Zimbelman J. R. (1990) Preliminary geologic mapping near the Nilosyrtis Mensae, Mars (abstract). In *Lunar and Planetary Science XXI*, pp. 1341–1342. Lunar and Planetary Institute, Houston.

Wilson L. and Parfitt E. A. (1990) Widths of dikes on Earth and Mars (abstract). In *Lunar and Planetary Science XXI*, pp. 1345–1346. Lunar and Planetary Institute, Houston.

Witbeck N. E., Tanaka K. L., and Scott D. H. (1990) Geologic map of the Valles Marineris region, Mars. *U.S. Geol. Surv. Misc. Inv. Series Map I-2010*, scale 1:2,000,000, in press.

Woronow A. (1988) Variation in the thickness of ejecta cover on Mars with increasing crater density (abstract). In *MEVTV Workshop on Nature and Composition of Surface Units on Mars* (J. R. Zimbelman, S. C. Solomon, and V. L. Sharpton, eds.), pp. 135–137. LPI Tech. Rpt. 88-05, Lunar and Planetary Institute, Houston.

Wright I. P., Grady M. M., and Pillinger C. T. (1990) A search for carbonate minerals in Chassigny (abstract). In *Lunar and Planetary Science XXI*, pp. 1353–1354. Lunar and Planetary Institute, Houston.

Wu S. S. C. and Howington-Kraus A. (1990) Volumetric distributions of Mars topography (abstract). In *Lunar and Planetary Science XXI*, pp. 1355–1356. Lunar and Planetary Institute, Houston.

Wu S. S. C., Garcia P. A., and Howington-Kraus A. (1990) Volumetric determinations of Valles Marineris of Mars (abstract). In *Lunar and Planetary Science XXI*, pp. 1357–1358. Lunar and Planetary Institute, Houston.

Zent A. P. (1987) The record of martian climatic history in cores and its preservation (abstract). In *Workshop on Mars Sample Return* (M. J. Drake et al., eds.), pp. 153–154. LPI Tech. Rpt. 88-07, Lunar and Planetary Institute, Houston.

Zent A. P. (1988) Coadsorption of $H_2O$ and $CO_2$ on the martian surface (abstract). In *MEVTV Workshop on Nature and Composition of Surface Units on Mars* (J. R. Zimbelman, S. C. Solomon, and V. L. Sharpton, eds.), pp. 138–139. LPI Tech. Rpt. 88-05, Lunar and Planetary Institute, Houston.

Zent A. P. and Fanale F. P. (1987) Are independent models of $CO_2$ and $H_2O$ mutually incompatible? (abstract). *Eos Trans. AGU*, *68*, 1341.

Zent A. P., Fanale F. P., and Postawko S. E. (1987) Carbon dioxide: Adsorption on palagonites and partitioning in the martian regolith. *Icarus*, *71*, 241–249.

Zent A. P., Fanale F. P., and Roth L. E. (1987) Melting in the martian subsurface: An analysis (abstract). *Bull. Am. Astron. Soc.*, *19*, 834.

Zent A. P., Fanale F. P., and Roth L. E. (1989) Analysis of 1971 and 1973 Mars Goldstone data and comparison to plausible melt production models (abstract). In *Fourth International Conference on Mars, Progr. and Abstracts*, pp. 213–214. Univ. of Arizona, Tucson.

Zhang Y., Stolper E. M., and Wasserburg G. J. (1989) The mechanism of water diffusion in silicate melts (abstract). *Eos Trans. AGU*, *70*, 501.

Zhang Y., Stolper E. M., and Wasserburg G. J. (1990) Diffusion of a multi-species component and its role in the diffusion of water and oxygen in silicates. *Earth Planet. Sci. Lett.*, in press.

Zhang Y., Stolper E. M., and Wasserburg G. J. (1990) Diffusion of water in rhyolitic glasses. *Geochim Cosmochim. Acta*, in press.

Zhang Y., Stolper E. M., and Ihinger P. D. (1990) Reaction kinetics of $H_2O+O=2OH$, and its equilibrium revisited. Abstract presented at Goldschmidt Conference, May 1990.

Zhang Y., Stolper E. M., and Wasserburg G. J. (1990) Role of water during hydrothermal oxygen diffusion in minerals (abstract). *Eos Trans. AGU*, *71*, 650.

Zhang Y. (1990) An approximate treatment of uphill diffusion (abstract). *Eos Trans. AGU*, in press.

Zimbelman J. R. (1987) Spatial resolution and the geologic interpretation of Martian morphology: Implications for subsurface volatiles. *Icarus*, *71*, 257–267.

Zimbelman J. R. (1988) Release of volatiles from ancient terrains along the upper portion of Mangala Valles, Mars (abstract). *Eos Trans. AGU*, 69, 390.

Zimbelman J. R. (1988) Erosional outliers of dust along the southern margin of the Tharsis region of Mars (abstract). *Eos Trans. AGU*, 69, 1286.

Zimbelman J. R. (1988) Fault control of volatile transport into Mangala Valles, Mars (abstract). In *Geol. Soc. Am., Abstracts with Progr.*, *20*, A147–A148.

Zimbelman J. R. (1988) High resolution Viking Orbiter images of Mars: Location and distribution (abstract). In *Lunar and Planetary Science XIX*, pp. 1317–1318. Lunar and Planetary Institute, Houston.

Zimbelman J. R. (1988) High resolution Viking Orbiter images: A useful data source for testing the viability of geomorphic processes attributed to martian landforms (abstract). In *MEVTV Workshop on Nature and Composition of Surface Units on Mars* (J. R. Zimbelman, S. C. Solomon, and V. L. Sharpton, eds.), pp. 140–142. LPI Tech. Rpt. 88-05, Lunar and Planetary Institute, Houston.

Zimbelman J. R. (1988) Physical properties of surface materials volcanoes: Dust-covered lava and ash(?). In *NASA MEVTV Program Working Group Meeting: Volcanism on Mars*, pp. 19–21. Lunar and Planetary Institute, Houston.

Zimbelman J. R. (1988) Preliminary geologic mapping in the Memnonia region of Mars (abstract). In *Reports of Planetary Geology and Geophysics Program—1987*, pp. 541–543. NASA TM-4041.

Zimbelman J. R. (1988) Preliminary photogeologic mapping in the Memnonia region of Mars (abstract). In *Lunar and Planetary Science XIX*, pp. 1319–1320. Lunar and Planetary Institute, Houston.

Zimbelman J. R. (1988) Present imaging limitations to providing a geological assessment of potential sample return sites on Mars (abstract). In *Workshop on Mars Sample Return Science* (M. J. Drake et al., eds.), pp. 186–187. LPI Tech. Rpt. 88-07, Lunar and Planetary Institute, Houston.

Zimbelman J. R. (1989) Noachian faulting in the Memnonia region of Mars (abstract). In *MEVTV Workshop on Early Tectonic and Volcanic Evolution of Mars* (H. Frey, ed.), pp. 94–96. LPI Tech. Rpt. 89-04, Lunar and Planetary Institute, Houston.

Zimbelman J. R. (1989) Application of glacier reconstruction techniques to concentric crater fill on Mars (abstract). In *Geol. Soc. Am., Abstracts with Progr.*, *21*, A371.

Zimbelman J. R. (1989) Erosional outliers of dust along the southern margin of the Tharsis region, Mars (abstract). In *Lunar and Planetary Science XX*, pp. 1237–1238. Lunar and Planetary Institute, Houston.

Zimbelman J. R. (1989) Geologic mapping of southern Mangala Valles, Mars (abstract). In *Lunar and Planetary Science XX*, pp. 1239–1240. Lunar and Planetary Institute, Houston.

Zimbelman J. R. (1989) Geologic mapping of southern Mangala Valles, Mars (abstract). In *Reports of Planetary Geology and Geophysics Program—1988*, pp. 578–579. NASA TM-4130.

Zimbelman J. R. (1989) Tectonic influences on the development of Mangala Valles, Mars (abstract). *Eos Trans. AGU, 70*, 388.

Zimbelman J. R. (1990) Geologic mapping of the central Mangala Valles region, Mars (abstract). In *Lunar and Planetary Science XXI*, pp. 1373–1374. Lunar and Planetary Institute, Houston.

Zimbelman J. R. (1990) Henry crater, Mars: Thick layered deposit preserved on a crater floor in the martian highlands (abstract). In *Lunar and Planetary Science XXI*, pp. 1375–1376. Lunar and Planetary Institute, Houston.

Zimbelman J. R. (1990) Outliers of dust along the southern margin of the Tharsis region, Mars. *Proc. Lunar Planet. Sci. Conf. 20th*, pp. 525–530.

Zimbelman J. R. (1990) Thickness estimates for concentric crater fill on Mars (abstract). *Eos Trans. AGU, 71*, 547.

Zimbelman J. R. (1990) Preliminary geologic map of central Mangala Valles, Mars (abstract). In *Reports of Planetary Geology and Geophysics Program—1989*. NASA TM, in press.

Zimbelman J. R. (1990) Thickness estimates for concentric crater fill in the Utopia Planitia region of Mars (abstract). In *Reports of Planetary Geology and Geophysics Program—1989*, NASA TM, in press.

Zimbelman J. R. and Craddock R. A. (1990) An evaluation of the possible extent of bedrock exposure in the Sinus Meridiani region of the martian highlands (abstract). In *Lunar and Planetary Science XXI*, pp. 1377–1378. Lunar and Planetary Institute, Houston.

Zimbelman J. R. and Craddock R. A. (1990) Extent of bedrock exposure in the Sinus Meridiani region of the martian highlands (abstract). In *Reports of Planetary Geology and Geophysics Program—1989*, NASA TM, in press.

Zimbelman J. R. and Craddock R. A. (1991) An evaluation of probable bedrock exposure in the Sinus Meridiani region of the martian highlands. *Proc. Lunar Planet. Sci., Vol. 21*, pp. 645–655.

Zimbelman J. R. and Fink J. H. (1989) Estimates of rheologic properties for flows on the martian volcano Olympus Mons (abstract). In *Lunar and Planetary Science XX*, pp. 1241–1242. Lunar and Planetary Institute, Houston.

Zimbelman J. R. and McBride K. M. (1989) A possible pyroclastic deposit near Elysium Mons, Mars (abstract). In *Lunar and Planetary Science XX*, pp. 1243–1244. Lunar and Planetary Institute, Houston.

Zimbelman J. R. and Wells G. L. (1987) Geomorphic evidence for climatic change lattitudes on Mars (abstract). *Geol. Soc. Am., Abstracts with Progr., 19*, 905.

Zimbelman J. R., Clifford S. M., and Williams S. H. (1988) Terrain softening revisited: Photogeological considerations (abstract). In *Lunar and Planetary Science XIX*, pp. 1321–1322. Lunar and Planetary Institute, Houston.

Zimbelman J. R., Clifford S. M., and Williams S. H. (1989) Concentric crater fill on Mars: An aeolian alternative to ice-rich mass wasting. *Proc. Lunar Planet. Sci. Conf. 19th*, pp. 397–407.

Zimbelman J. R., Solomon S. C., and Sharpton V. L., eds. (1988) *MEVTV Workshop on the Nature and Composition of Surface Units on Mars*. LPI Tech. Rpt. 88-05, Lunar and Planetary Institute, Houston. 144 pp.

Zimbelman J. R., Williams S. H., Greeley R., and Kieffer H. H. (1987) Field observations of albedo contracts associated with wind streaks: Fluvial and botanical effects on aeolian features (abstract). *Eos Trans. AGU, 68*, 1341–1342.

Zimbelman J. R., Solomon S. C., and Sharpton V. L. (1991) The evolution of volcanism, tectonics, and volatiles on Mars: An overview of recent progress. *Proc. Lunar Planet. Sci., Vol. 21*, pp. 613–626.

Zuber M. T. and Aist L. L. (1989) The shallow structure of the lithosphere in the Coprates and Lunae Planum regions of Mars from the geometries of volcanic plains ridges (abstract). In *MEVTV Workshop on Early Tectonic and Volcanic Evolution of Mars* (H. Frey, ed.), pp. 97–99. LPI Tech. Rpt. 89-04, Lunar and Planetary Institute, Houston.

Zuber M. T. and Mouginis-Mark P. J. (1989) The depth of the Olympus Mons magma chamber as determined from the spatial distribution of tectonic features (abstract). In *MEVTV Workshop on Tectonic Features on Mars* (T. R. Watters and M. P. Golombek, eds.), pp. 74–76. LPI Tech. Rpt. 89-06, Lunar and Planetary Institute, Houston.

Zuber M. T. and Mouginis-Mark P. J. (1990) Constraints on the depth and geometry of the magma chamber of the Olympus Mons volcano, Mars (abstract). In *Lunar and Planetary Science XXI*, pp. 1387–1388. Lunar and Planetary Institute, Houston.

# Appendix 3. Abstracts from Special Sessions at LPSC XXI

To mark the end of the MEVTV project, three dedicated sessions were held at the 21st Lunar and Planetary Science Conference in March 1990 at the NASA Johnson Space Center, Houston, Texas. Each session was initiated by an invited overview talk on one of the MEVTV themes; the remaining contributed talks summarized research progress over the course of the project. Following are abstracts of the papers given in or associated with those sessions; abstracts of the three overview talks are given first.

# MARTIAN MAGMAS AND MANTLE SOURCE REGIONS: CURRENT EXPERIMENTAL AND PETROCHEMICAL CONSTRAINTS

John R. Holloway, Departments of Chemistry and Geology, Arizona State University, Tempe, AZ 85287

**Mantle bulk chemical composition** has been based on two constraints, SNC meteorites and the moment of inertia. Recently, the moment of inertia has become highly controversial and cannot be considered useful (1, 2, 3). The SNC compositions provide strong constraints (4, 5), but it has not been conclusively proven that SNC's are of Martian origin. It could reasonably be argued that we do not know the composition of Mars! Never-the-less the following discussion is based on the presumption that SNC's are of Martian origin and that the model for the Martian mantle composition based on SNC geochemistry and the assumption of a chondritic bulk composition is accurate. The primary difference between that Martian mantle composition and the Earth's upper mantle is the ratio of Mg to Fe, expressed as the mg# (=atomic Mg/Mg+Fe).

**Mantle mineralogy** can be calculated from experimental and thermodynamic constraints given the bulk composition. The major mineral mode in the Martian mantle at a pressure of 30 Kbar is (roughly) 50wt% olivine, 25 orthopyroxene 15 Ca-pyroxene and 10 garnet, which is very similar to the Earth's upper mantle (6). A major difference compared to Earth is that garnet is stabilized at lower pressures in Mars (7). A second probable difference which may be important is that the lower mg# will stabilize pigeonite pyroxene relative to clinopyroxene at temperatures below the solidus (8). The presence of pigeonite instead of Cpx could affect partitioning of several trace elements, e.g. REE between source region and primary magmas.

**Volatiles in the mantle source region** are poorly defined. Sulfur is clearly present in significant abundance (9). The $H_2O$ content is based on SNC's which have yielded two very different conclusions, one that the Martian mantle is extremely dry (10), and the other that it is probably at least as wet as Earth's mantle (11). Experimental and petrochemical arguments require at least a two-stage melting history for at least some SNC source regions (which would give erroneously low estimates for mantle $H_2O$), and SNC's themselves are highly fractionated (which would yield high estimates). Carbon in the Martian mantle is unconstrained, but arguments based on planetary accretion would suggest that carbon in the Martian mantle is probably greater than in the Earth's (12).

**Mantle solidus temperatures** are well constrained for a volatile-free mantle at pressures to 30 kbar (230 kms depth)(8, 13). The solidus temperature for a carbonate-bearing mantle is complex (14, 15, 16, 17). At pressures <20 Kbar carbonates are not stable and have little direct effect on solidus temperatures. Above 20 Kbar a very small amount (<<1%) of an alkali carbonate liquid is formed at temperatures <1000°C. At 25 kbar Mg-Fe calcite melts at 1200-1225°C.

**Primary magma characteristics** are dominated by the iron-rich, low mg# character. At low degrees of melting, magmas will be in equilibrium with garnet at pressures above 15-18 Kbar. Compositions are well constrained for a volatile-free mantle at 25 Kbar, where the melt resembles an iron-rich (23wt% FeO), picritic, alkali basalt at low degrees of partial melting (18). With an increase in the degree of melting the primary magmas will trend toward iron-rich komatiites (13). A carbonate-bearing mantle at pressures above 20 Kbar will possibly form a carbonatitic melt at low degrees of melting, and by 1250°C (possibly 2% melting) the melt will have a large silicate component and may resemble a kimberlite magma (17).

**Derivative magmas.** Primary magmas will definitely fractionate olivine during their ascent to the surface; thus, decreasing their mg# and increasing $SiO_2$, $Al_2O_3$ and CaO contents. Primary magmas produced by small degrees of partial melting would have low initial mg#'s and this fractionation would produce magmas with mg#'s far lower than SNC parent magmas. Thus, it is probable that all SNC parent magmas are produced either by large degrees of partial melting, or that their source region has under gone at least one previous melting event (5, 19). The high $H_2O$ content implied for the Chassigny and Shergotty parent magmas (11) suggests a more

complex history for those magmas and their source regions than has yet been envisioned for Mars. The oxygen fugacity estimated from SNC's is close to the quartz-fayalite-magnetite buffer reaction (11, 20). The viscosity of a generalized SNC parent magma has been measured and ranges from 10 to 200 poise over the 1350° to 1250°C temperature range at one atmosphere pressure (21). Those viscosities are only slightly higher than the 1-3 poise viscosity of the 23 kbar primary magma at 1450°C (6).

**$CO_2$ solubility** has been measured in the proposed parent composition of the SNC EETA79001 and found to be similar to the solubility in terrestrial basalts with higher mg#; implying there is little or no mg# effect on $CO_2$ solubility (22). The very low solubility at low pressure means that $CO_2$ evolution will provide a driving force for magma degassing on Mars as it does on Earth.

**Conclusions** which can be reached from the available data are (1) that any Martian magma produced by processes equivalent to those on Earth will have a significantly higher mg# (2) the lower mg# will result in lower liquidus and, in mafic and ultramafic compositions, lower solidus temperatures (3) that Magmas on Mars can have high $H_2O$ contents and hence, erupt explosively, and (4) that magmatism on Mars shows considerable complexity based on just the few SNC samples available.

**Future work** should include continued study of the phase chemistry of SNC's followed by mineral equilibria calculations, melting experiments on hydrous and carbonated mantle mineral assemblages, measurement of combined $CO_2$ and $H_2O$ solubilities, and attempts to recreate the line of descent that produced SNC parent magmas. Much more work is needed on the density and viscosity of the iron-rich melts characteristic of Mars for use in fluid dynamic modelling of magma collection, ascent and eruption.

1. B. G. Bills, *Geophys. Res. Lett.* 16, 385-389 (1989). 2. B. G. Bills, *Geophys. Res. Lett.* 16, 1337-1338 (1989). 3. W. M. Kaula, N. H. Sleep, R. J. Phillips, *Geophys. Res. Lett.* 16, 1333-1336 (1989). 4. G. Dreibus, H. Wanke, *Meteoritics* 20, 367-382 (1985). 5. J. Longhi, V. Pan, *Proc. Lunar Planet. Sci. Conf. 19th* 19, 451-464 (1989). 6. C. M. Bertka, J. R. Holloway, *Lunar Planet. Sci. Conf. Abs.* XX, (1989). 7. E. S. Patera, J. R. Holloway, *J. Geophys. Res.* 87, 31-36 (1982). 8. C. M. Bertka, J. R. Holloway, *This volume* (1990). 9. R. G. Burns, in *MEVTV workshop on the evolution of magma bodies on Mars* (LPI, San Diego, CA, 1989) 10. H. Wänke, G. Dreibus, *Phil. Trans. R. Soc. London* A235, 545-557 (1988). 11. M. C. Johnson, M. E. Rutherford, P. C. Hess, in *MEVTV workshop on the evolution of magma bodies on Mars* (LPI, San Diego, CA, 1989). 12.J. R. Holloway, *Lunar Planet. Sci. Conf.* XIX, 499-500 (1988). 13. C. B. Bertka, J. R. Holloway, V. Pan, in *MEVTV workshop on the evolution of magma bodies on Mars* (LPI, San Diego, CA, 1989). 14. M. E. Wallace, D. H. Green, *Nature* 355, 343-346 (1988). 15. T. J. Falloon, D. H. Green, *Earth Planet. Sci. Lett.* 94, 364-370 (1989). 16. M. I. Odezynskyj, J. R. Holloway, *Lunar Planet. Sci. Conf. Abs.* XX, (1989). 17. M. I. Odezynskyj, J. R. Holloway, *This volume* (1990). 18. C. M. Bertka, J. R. Holloway, in *Proc. Lunar. Planet. Sci. Conf. 18th* (Cambridge University Press, 1988), pp. 723-739. 19. J. Longhi, in *MEVTV workshop on the evolution of magma bodies on Mars* (LPI, San Diego, CA, 1989). 20. E. M. Stolper, H. Y. McSween Jr., *Geochim. Cosmochim. Acta* 43, 1475-1498 (1979). 21. F.J. Spera and D.J. Stein, in *MEVTV workshop on the evolution of magma bodies on Mars* (LPI, San Diego, CA, 1989). 22. V. Pan, J. H. Holloway, in *MEVTV workshop on the evolution of magma bodies on Mars* (LPI, San Diego, CA, 1989).

GEOPHYSICS AT MARS: ISSUES AND ANSWERS; R.J. Phillips, Dept. of Geological Sciences, Southern Methodist University, Dallas, TX 75275

**Introduction.** The tectonic and volcanic evolution of Mars is strongly coupled to the evolution of the martian mantle, which has delivered mass and heat to the martian lithosphere over geological time. Understanding the evolution of the martian mantle and unraveling the tectonic and volcanic history are tightly coupled because in the absence of seismic data, surface information and gravity data are the major ways to constrain interior processes. The overall problem is highly underdetermined, but some progress has been made in the sense that there are not an infinite number of interior models that will satisfy the topographical, gravitational and geological constraints available.

Model results for the Global Dichotomy Boundary (GDB) are limited. There is general agreement that this boundary is isostatically compensated, and any scenario that attempts to explain the gross differences between the two hemispheres must include processes that extend to at least the crust-mantle boundary. The global center-of-figure to center-of-mass offset is explained by a combination of an isostatically compensated GDB and a nearly compensated Tharsis.

Most geophysical modeling of Mars has concentrated on the Tharsis and Elysium provinces. Central to these considerations are the relative roles of structural uplift and volcanic construction in the creation of immense topographic relief [1,2]. The origin, classification, and relative timing of tectonic features has also been a subject of focused study [3,4].

**Stress Modeling.** The observation of grossly organized tectonic patterns associated with Tharsis (and to a lesser extent Elysium) have led to the formulation of a number of theoretical elastic and isostatic models of the interior [5-8]. Such models are constrained by the observed gravity and topography, satisfy the equations of mechanical equilibrium, and are used to predict stress type, magnitude, and direction in the lithosphere. The results depend on the estimate of the non-hydrostatic component of the second zonal harmonic of gravity, $J_2$. This estimate and the corresponding estimate of the mean moment of inertia have been the subject of recent debate [9,10].

If tectonic features on Tharsis can be separated into stratigraphic groups with relative age firmly established [3], and if these groups can be related to specific mechanical models of the interior, then scenarios for interior evolution can be worked out. Generally, three types of mechanical models have been recognized: (i) isostatic, (ii) flexural loading, and (iii) flexural uplift. In model (i) the flexural rigidity $D$ is set to zero and the stress distribution is governed solely by membrane and gravitational forces. Addition of a non-zero $D$ leads to a different stress distribution, which depends on whether the lithosphere is loaded from above [model (ii); e.g., volcanic piles] or loaded from below [model (iii); e.g., buoyant uplift]. Model (i) cannot distinguish isostatic loading from isostatic uplift.

Graben in the Claritas Fossae region of Tharsis are mapped as Early Noachian in age [3]. Flexural uplift models predict extensional stresses at Claritas Fossae [8] that are approximately orthogonal to the mapped tectonic features [11]. This suggests that flexural uplift was an early phase in the tectonic evolution of Tharsis. To first order, radial graben and fractures on the periphery of Tharsis are consistent with flexural loading models [5-7], while tectonic features in the immediate Tharsis area are best explained by isostatic models [6,7]. *Detailed* matching of stress predictions with tectonic features is more problematical. This is partly due to the extremely poor knowledge of martian topography and partly because all modeling efforts have no choice but to use the present-day values of the gravity field and topography to predict ancient stress fields. The most complete modeling to date uses spherical harmonic coefficients of the field quantities to degree and or-

der eight [8]. While this model has more resolution than earlier fourth degree models, it may also be noisier. Locally, predictions are successful in some regions but do not match as well as earlier models do in other regions (e.g., Valles Marineris). Attempts to match stratigraphically assigned fracture/graben sets to either flexural loading or isostatic models have also not been successful because of inadequate azimuthal resolution of the stress trajectories in the two types of models.

**Petrological Models Related to Geophysics.** All of the mechanical models carry an interior density distribution required to match the gravity and topography boundary conditions. Isostatic models, for example, are composed of a low density Pratt-like region in the upper mantle and a thinned crust beneath Tharsis. Flexural loading models carry a thickened crust. The Pratt zone in the isostatic model can be interpreted in terms of a low density mantle residuum formed by partial melting that produced basaltic magmas [12]. Isostatic models have been formulated that satisfy the gravity and topography boundary conditions and conserve mass in a partial melting sequence. More recent work [11] has concentrated on the implications of a requirement for uplift, as suggested by the fault distribution and elevation of Claritas Fossae. While most of the buoyancy for uplift is provided by a low density residuum, a crustal extrusive load will strongly counteract this effect unless it is only a small portion of the melt products generated beneath Tharsis. Thus most of the Tharsis magmas may have ended up as intrusive bodies in the crust and upper mantle. During the period of intense tectonism of Tharsis (Hesperian time and earlier), volcanism was not as active at Tharsis as it was on other parts of Mars [13]. Later (Late Hesperian, Amazonian), Tharsis accounted for about half of the planet's volcanism. The picture that is emerging is that early in the history of Tharsis, massive intrusion led to tectonic disruption of the surface. Subsequently, magmas made their way to the surface and tectonism waned. The reason for this evolution may have been decreasing melt density as the partial melting process evolved toward lower iron content of basaltic magmas. The concept of massive intrusion leading to the immense relief of Tharsis blurs the distinction between uplift and constructional models.

**Future Directions.** While geological mapping of Tharsis has reached a high level of maturity, there are major areas of geophysical modeling yet to be carried out. Time-dependent thermoelastic modeling has not been considered, nor has stress modeling with the majority of the flexural load in the form of intrusive bodies. Considerable work on the spatial and temporal variation of elastic lithospheric thickness [14] and inferred temperature gradient [15] has not been incorporated into the regional-scale stress modeling described above. The accuracy and resolution of stress modeling will undergo marked improvement with the topography and gravity field information to be acquired by Mars Observer. Finally, some of the models for the origin and evolution of Tharsis, which predict specific differences in magma composition as a function of age, can possibly be tested with data acquired by the remote sensing instruments on Mars Observer.

**References.** [1] Solomon, S.C., and J.W. Head, *JGR, 87,* 9755, 1982; [2] Phillips, R.J., *et al.*, *JGR, 78*, 4815, 1973; [3] Tanaka, K.L., and P.A. Davis, *JGR, 93,* 14893, 1988; [4] Tanaka, K.L., *Proc. Lunar Planet Sci. Conf. 20th*, in press, Cambridge Univ. Press, 1990; [5] Willemann, R.J., and D.L. Turcotte, *JGR, 87*, 9793, 1982; [6] Banerdt, W.B., *et al.*, *JGR, 87*, 9723, 1982; [7] Sleep, N.H., and R.J. Phillips, *JGR, 90,* 4469, 1985; [8] Banerdt, W.B., *et al.*, in *Mars*, University of Arizona Press, in press, 1990; [9] Kaula, W.M., *et al.*, *GRL, 16*, 1333, 1989; [10] Bills, B., *GRL, 16*, 385, 1989; [11] Phillips, R.J., *JGR, 95,* in press, 1990; [12] Finnerty, A.A., *et al.*, *JGR, 93,* 10225, 1988; [13] K.L. Tanaka, personal communication, 1989; [14] Comer, R.P., *et al.*, *Rev. Geophys., 23*, 61, 1985; [15] Solomon, S.C., and J.W. Head, *JGR, 95,* in press, 1990.

**MARTIAN GEOLOGIC "REVOLUTIONS": A TALE OF TWO PROCESSES;** **Kenneth L. Tanaka**, U.S. Geological Survey, 2255 N. Gemini Dr., Flagstaff, AZ 86001

The antiquated geologic term "revolution" is defined as "A term formerly popular among geologists for a time of profound orogeny and other crustal movements, on a continentwide or even worldwide scale, the assumption being that such revolutions produced abrupt changes in geography, climate, and environment" [1]. The term is little used today because of changes in our definition of "orogeny" and in our understanding of Earth's geologic history. Herein, I informally resurrect the term for Mars, in modified form, because of its suitability to this planet. My definition is "a time of profound geologic activity resulting in global changes in physiography, climate, or environment."

On Earth, most surface rocks (except the youngest) record a cumulatively complex geologic history, and their landscapes are largely molded by surficial processes. On Mars, however, structure and topography are more directly the results of volcanism and tectonism. Singular, major volcanic and tectonic events dominated in shaping the surface, and they strongly influenced the planet's environment. Impact cratering has also had a major role in the geology of Mars, and geologic revolutions related to cratering events may be proposed. However, here I examine only those revolutions apparently or possibly related to volcanism and tectonism, because I am reviewing the thrust of work from NASA's research project "Mars: Evolution of Volcanism, Tectonism, and Volatiles."

Below I outline three possible revolutions on Mars that are based on geologic evidence. Each includes uncertainties in such fundamental aspects as origin, nature and sequence of events, and environmental significance. Activity of the revolutions overlapped somewhat because of their longevity and planetwide effects. Nevertheless, the concept that revolutions have dominated the surface history of Mars provides a context for evaluating individual geologic events and the interrelation of geologic forces with climate and environment.

**(1) Plate tectonics and the northern lowlands.** Researchers have advocated either impact [2, 3] or tectonic origins [4, 5] for the northern lowlands (which cover about 40% of Mars), and this controversy will likely continue until more definitive data are gathered. Geologic observations and inferences consistent with a plate-tectonic origin [6] include (a) the lowering of a broad section of the crust (possibly through isostatic adjustment of a thinned crust [4]); (b) the possibility that Phlegra Montes (a north-trending ridge complex more than 1,000 km long and about 1,000 km northeast of Elysium Mons) are an extinct spreading center (suggested by their elevation, spreading-ridge morphology, and central location in the northern lowlands); and (c) the appropriate position and orientation of Tharsis Montes for arc-type volcanism relative to Phlegra Montes. Phlegra Montes were heavily degraded during the Late Noachian [7], indicating that any associated volcanic and tectonic activity had ceased by then. If further analysis confirms a tectonic hypothesis, this revolution accounts for major topographic modification of nearly one Martian hemisphere.

**(2) Tharsis tectonism and filling of lowlands.** The Tharsis rise is a complex of tectonic centers that include Tharsis Montes, Syria Planum, Claritas Fossae, the Thaumasia rise, Valles Marineris, Tempe Terra, Alba Patera, and Ceraunius Fossae. It largely developed during Noachian and Hesperian time [8]. Systems of near- to far-ranging radial and concentric grabens formed concomitantly with development of topographic highs [9]. During the Late Noachian and Early Hesperian [8], wrinkle ridges were formed concentric to the Tharsis rise and more than 2,000 km away from its center. The rise and its associated structures stretch out over a hemisphere of the planet. Two profound effects may have resulted from the uplift: (a) the uncompensated mass distribution of the planet

may have been significantly altered [10], which may have resulted in polar wandering [11] and temporarily high obliquity [12] that changed ice-frost depositional environments [13, 14]; and (b) the probable formation of a broad zone of increased hydraulic potential in the ground-water system [15]. Fault activity, earthquakes, and volcanic heating associated with the rise caused breakouts of debris flows and catastrophic floods that carved the outflow channels of Chryse Basin and Mangala Valles [15-17]. These discharges contributed to extensive erosion of large highland areas, resurfacing of much of the northern plains [18], and a major redistribution of the planet's ground water (some likely ended up in the polar caps).

(3) **Centralization of volcanism at Tharsis and Elysium.** By the end of the Early Hesperian, Martian volcanism had changed dramatically. Previously, it had dispersed over the planet fields of broad, simple lava flows originating from fissures (minor central, dominantly pyroclastic volcanism was probably produced by phreatomagmatic eruptions). Now, volcanism began to produce regional fields of elongate, lobate flows and to build large shields or fissure complexes at Tharsis and Elysium [19, 20]. These changes could have resulted from general cooling and thickening of the lithosphere that decreased the magma supply rate [19] and from pronounced hydrothermal circulation that drove away ground water from eruptive centers. Possible related effects of centralized volcanism include (a) further changes in the planet's uncompensated mass distribution, with consequences as noted above; (b) continued discharge of ground water at the peripheries of volcanotectonic rises; and (c) strong localization of heat flow, which would have affected the form of the cryosphere and possibly decreased planetwide small-valley formation by sapping during the Early Hesperian [21].

We are fortunate that the surface of Mars, unlike surfaces of most other photographed bodies in the Solar System, so richly and straightforwardly reflects both the long-term geologic and the environmental histories of the planet. We can thus identify and postulate revolutionary events in Martian volcanic and tectonic history that produced profound changes in the planet's orientation, physiography, climate, ground and surface volatile distributions, and heat flow.

**References**

[1] Bates, R.L., and Jackson, J.A., eds., 1987, *Glossary of Geology, 3rd ed.*, p. 565.
[2] Wilhelms, D.E., and Squyres, S.W., 1984, *Nature*, **309**, 138-140.
[3] Frey, H., and Schultz, R.A., 1988, *Geophys. Res. Lett.*, **15**, 229-232.
[4] Wise, D.U., Golombek, M.P., and McGill, G.E., 1979, *J. Geophys. Res.*, **84**, 7934-7939.
[5] McGill, G.E., 1989, *Abstracts Lunar Planet. Sci. Conf. XX*, p. 667-668.
[6] N.H. Sleep, personal communication, 1989.
[7] Tanaka, K.L., Chapman, M.G., and Scott, D.H., in press, *USGS Misc. Inv. Ser. Map.*
[8] Scott, D.H., and Tanaka, K.L., 1986, *USGS Misc. Inv. Ser. Map I-1802-A.*
[9] Tanaka, K.L., and Davis, P.A., 1988, *J. Geophys. Res.*, **93**, 14,893-14,917.
[10] Reasenberg, R.D., 1977, *J. Geophys. Res.*, **82**, 369-375.
[11] Melosh, H.J., 1980, *Icarus*, **44**, 745-751.
[12] Ward, W.R., Burns, J.A., and Toon, O.B., 1979, *J. Geophys. Res.*, **84**, 243-259.
[13] Schultz, P.H., and Lutz, A.B., 1988, *Icarus*, **73**, 91-141.
[14] Jakosky, B.M., and Carr, M.H., 1985, *Nature*, **315**, 559-561.
[15] Carr, M.H., 1979, *J. Geophys. Res.*, **84**, 2995-3000.
[16] MacKinnon, D.J., and Tanaka, K.L., in press, *J. Geophys. Res.*
[17] Tanaka, K.L., and Chapman, M.G., in press, *J. Geophys. Res.*
[18] Lucchitta, B.K., Ferguson, H.M., and Summers, C., 1986, *Proc. 17th Lunar Planet. Sci. Conf., J. Geophys. Res.*, **91**, E166-E174.
[19] Greeley, R., and Spudis, P.D., 1981, *Rev. Geophys. Space Phys.*, **19**, 13-41.
[20] Tanaka, K.L., 1986, *Proc. 17th Lunar Planet. Sci. Conf., J. Geophys. Res.*, **91**, E139-E158.
[21] Wilhelms, D.E., and Baldwin, R.J., 1989, *Proc. 19th Lunar Planet. Sci. Conf.*, p. 355-365.

**LIMITS ON THE COMPOSITIONAL VARIABILITY OF THE MARTIAN SURFACE.** John B. Adams and Milton O. Smith, U. of Washington, Seattle, WA 98195

We analyzed spectral reflectance data from Viking Landers and Orbiters and from telescopic observations, with the objective of isolating compositional information about the Martian surface and assessing compositional variability. Two approaches were used to calibrate the data to reflectance to permit direct comparisons with laboratory reference spectra of well characterized materials (1-7). In Viking Lander multispectral images (six spectral bands) most of the spectral variation is caused by changes in lighting geometry within individual scenes, from scene to scene and over time. Lighting variations are both wavelength independent and wavelength dependent (1). By calibrating Lander image radiance values to reflectance using spectral mixture analysis (1) we assessed the possible range of compositions with reference to a collection of laboratory samples, also resampled to the Lander spectral bands. All spectra from the Lander images studied plot (in 6-space) within a planar triangle having at the apexes the respective spectra of tan basaltic palagonite, gray basalt and shade. Within this plane all Lander spectra fit as mixtures of these three endmembers; therefore, pure materials that occupy this space cannot be distinguished mixtures of these endmembers. Reference spectra that plot outside of the triangle are unable to account for the spectral variation observed in the images.

In earlier work (1) we concluded that the rocks at the Lander sites could be unweathered basalts or andesites, and that both oxidized and unweathered basaltic fines were present. Laboratory spectra of many basalts and andesites appear similar when sampled with the six Lander bands. The main difference between the two rock groups is that the basalts typically are darker than the andesites. Otherwise, both rock types are spectrally similar, having nearly equal reflectances at all wavelengths ("gray"). If andesitic rocks occur on Mars there also should be andesitic tephra, which, unaltered, has a substantially higher albedo than basaltic tephra. Accordingly, we searched Lander images for gray, moderate albedo rocks and for a light gray component of the fines. In addition, we postulated that aeolian abrasion might produce finely particulate crystalline basalt (unweathered) that would be expected to have a spectrum close to that of andesitic tephra.

Fig. 1 shows the endmember triangle on the plane defined by Lander bands 1 and 3, and illustrates that a small portion of the data encompasses andesites, andesitic tephra, and mixtures of basalt and crystalline basalt powder, giving the impression that these or spectrally similar materials are present in the Lander images and mix with the other spectral endmembers. However, when each spectrum is traced back to the image, the context reveals that this gray "component" always coincides with a specular lighting geometry. To compare image and laboratory spectra the lighting geometries of the measurements must be approximately the same. Bidirectional and total hemispherical laboratory measurements avoid specular reflections, because for most silicates they introduce a "gray" component that increases the overall lightness and reduces spectral contrast. Many Lander images, however, include local areas (especially on dust-free rocks) that have specular (or quasi-specular) reflection from surfaces that are oriented appropriately relative to the sun and the camera. These specular reflections, which occur at both pixel and sub-pixel scales, plot outside the basaltic spectral endmember plane, coincident with the spectra of andesitic materials and their mixtures with the basaltic materials. The specular reflections disappear when the same areas are imaged under different lighting conditions. Thus, there is no spectral evidence for an andesitic or other spectrally similar components at the Lander sites.

A Viking Orbiter image (3 bands) was analyzed of the Chryse Planitia - Kasei Valles - Lunae Planum region that includes the Lander 1 site. The calibrated spectra plot within the central part of the mixing triangle defined by the Lander data, indicating that these Orbiter pixels are consistent with mixtures of the Lander endmembers, and that the reference spectra (basaltic palagonite, basalt and shade) account for the spectral variation at a regional scale. The three broad Orbiter bands, although of limited use for identifying most materials, are sufficient to distinguish a light achromatic component. This component was not detected, therefore, we detected no areas of pure andesite or andesitic tephra, or mixtures of these materials with the modeled basaltic

materials. The basaltic reference spectra also fit the spectral variation in 1969, 1973 and 1978 telescopic spectra.

The spectral detectability of andesite or of any other material on Mars depends on several factors, including the spectral contrast between the material and its background, the spectral and spatial resolution, and the signal-to-noise of the data. Although a few percent of andesitic materials cannot be ruled out, and other Orbiter images and telescopic spectra remain to be analyzed, all of the spectral data examined so far fit the model of the Martian surface consisting primarily of basaltic rocks, unweathered basaltic fines, and chemically weathered basaltic fines.

REFERENCES. (1) Adams J. B., Smith M.O., and Johnson P. E. (1986) *J. Geophys. Res.* 91, 8098-8112. (2) Smith M. O., Adams J. B., and Johnson P. E. (1986) *Lunar and Planetary Science XVII,* 807-808. (3) Smith M. O., Adams J. B., Guinness E. A., and Arvidson P. E. (1987) *Lunar and Planetary Science XVIII*, 934-935. (4) Adams J. B., Smith M.O., Arvidson R. E., Dale-Bannister M. A., Guinness E. A., and Singer R. (1987) In *Mars Evolution of Volcanism, Tectonism and Volatiles*, LPI. (5) Smith M. O. and Adams J. B. (1988) *Lunar and Planetary Science XIX*.. (6) Arvidson R. E., Guinness E. A., Dale-Banister M. A., Adams J. B., Smith M. O., Christensen P. R., and Singer R. B. (1989) *J. Geophys. Res.* 94, 1573-1587. (7) Smith M. O. and Adams J. B. (1989) *Lunar and Planetary Science XX*, 1024-1025.

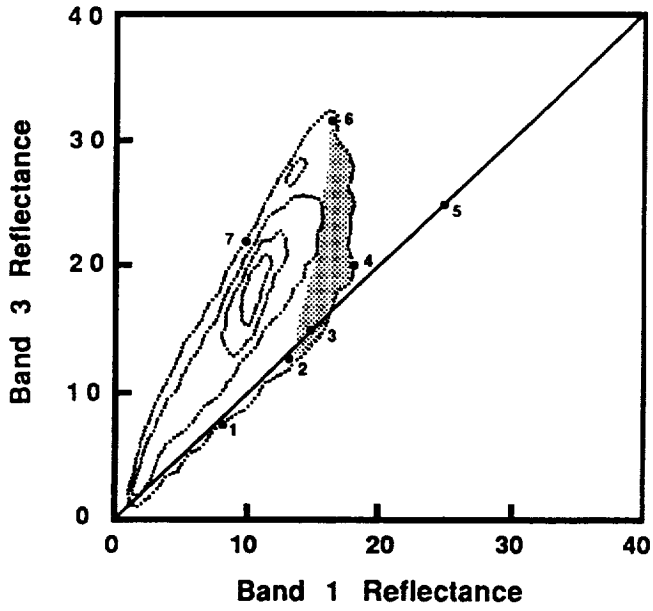


Figure 1. Histogram of six-band spectra from a Viking Lander image (VL1-28) displayed on the two-dimensional plane of bands 1 (blue) and 3 (red). Units are in percent reflectance. Contours show increasing number of pixels toward a maximum near blue = 10, red = 20. Laboratory reference spectra, resampled by the Lander bands, are plotted as filled circles. Basalt tephra (1), basaltic rocks (2), andesitic rocks (3), andesitic tephra (4), and basaltic rock powder (5) plot on or near the achromatic line (blue = red). The stippled region corresponds to specular reflections from a few (mostly rock) surfaces in the image. Basaltic rock (2), fine-grained weathered basaltic palagonite (6) and mixed grain-size basaltic palagonite (7) along with shade (blue = 0, red = 0) model the non-specular parts of the image.

**CONTRIBUTION TO THE STUDY OF THERMAL EROSION ON MARS.**

AGUIRRE-PUENTE, J.** COSTARD, F.M.* and POSADO-CANO, R.**
* "Laboratoire de Géographie Physique (URA D0141)", and
** Laboratoire d'Aérothermique (UP 1301)", CNRS, 92195 Meudon Cédex, France.

Climatic conditions on planet Mars could be mainly described by its mean annual temperature of -60°C and its atmospheric pressure of about 600 Pa (6 mb) which involve a dry periglacial type climate. Even taking into account this low pressure, it could be considered that the water-ice equilibrium temperature is about 0°C ($\Delta T_m \simeq 0{,}00737\ kbar^{-1} x \Delta p$ (1)). Permafrost extends all over planet Mars with a near surface ground-ice at mid and high latitudes. Sublimation of the ice contained in the upper layers at equatorial latitudes implies a deep ground-ice (2, 3).

Like in the coldest terrestrial periglacial regions as Yakutia (Siberia), the important width of some martian outflow channels and the presence of permanent ground-ice lead to the idea that thermal erosion existed during fluvial outbursts (4). The thermal erosion process follows from a thermal action of thawing produced by the heat exhange between the water flow and the frozen ground and a mechanical action of sediment transport. For example, Siberian backwearing of river slopes can reach 25 m/year (5, 6). Due to the poor information about fluvial actions on Mars and to the complexity of the thermal process of change of phase and of the mass transport phenomena, the study of the fluvial thermo-erosion in Mars presents great difficulties.

From the qualitative point of view, this paper proposes some physical models which could describe the interaction of the thermal process and of the sediment transport. From the quantitative point of view, only thermal models are proposed and discuted.

Roughly, it is considered that thermal erosion consists of the wash-out by mechanical action of the unfrozen sediments. The zones undergoing the most efficient erosion are the river banks; in these circonstances, study of twodimensionnal thermal processes with change of phase are necessary. Such a problem will be analysed in other paper. Here, mechanical erosion, of the bottom of wide rivers (martian outflows) is considered using onedimensionnal thermal model. In such models, a semi-infinite soil is considered with an initial temperature equal to the equilibrium water-ice temperature; thawing is supposed existing due to a fluvial flow at Positive Celsius temperature producing a thermal flux on the bottom through the deep ground.

Results on the melting front propagation using the different proposed models are discussed. A strong model which describes extreme conditions supposes constant thermal flux on the ground surface and an immediat removal of unfrozen sediments (fig. 2). Other models don't take into account such a wash-out of unfrozen sediments and consider either a constant flux (fig. 3), or a constant heat transfert coefficient. Determination of this coefficient needs the calculation of dimensionless numbers

(Reynolds, Prandtl, Nusselt) and the consideration of turbulent regime of flow:

Reynolds Number $Re = \frac{Vt}{\nu}$

Prandtl Number $Pr = \frac{\nu}{\alpha}$

Nusselt Number $Nu = \frac{hL}{k} = F(Re, Pr)$

where L is the depth of the river, V the velocity of the flow, $\nu$, $\alpha$ and K are respectivelly the kinematic viscosity, the thermal diffusivity and the thermal conductivity of the water; h is the heat transfer coefficient.

The discussion of results shows the different importance of fundamental parameters involved in the thermal processes and a preliminary choice of the model giving the best satisfaction.

A research programm is proposed in order to take into account interaction of thermal processes and mechanical erosion, for both onedimensional and twodimensionnal models. Concerning futur planetary missions, suggestions are made in order to get more detailled observation of certain physical and morphological interesting aspects.

References: (1): Hobbs, P.V., 1974: Ice Physics, Charendon Press, Oxford, pp.837. (2): Rossbacher, L.A and Judson, S. 1981: Icarus 45:39-59. (3): Battistini, R. 1984: Rev. Geom. Dyn. 33:25-41. (4): Costard, F.M. 1989: 20th LPI, pp. 189-190. (5): Are, F.E. 1983: 4th Int. Conf. Permafrost, Alaska, 24-28. (6): Jahn, A 1975: Problems of the periglacial zone, Washington DC, Warzawa.

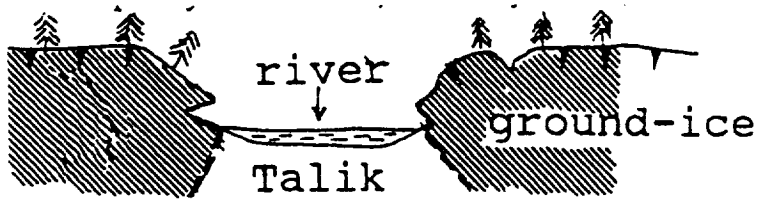


Fig. 1: Thermal erosion in Siberian rivers.

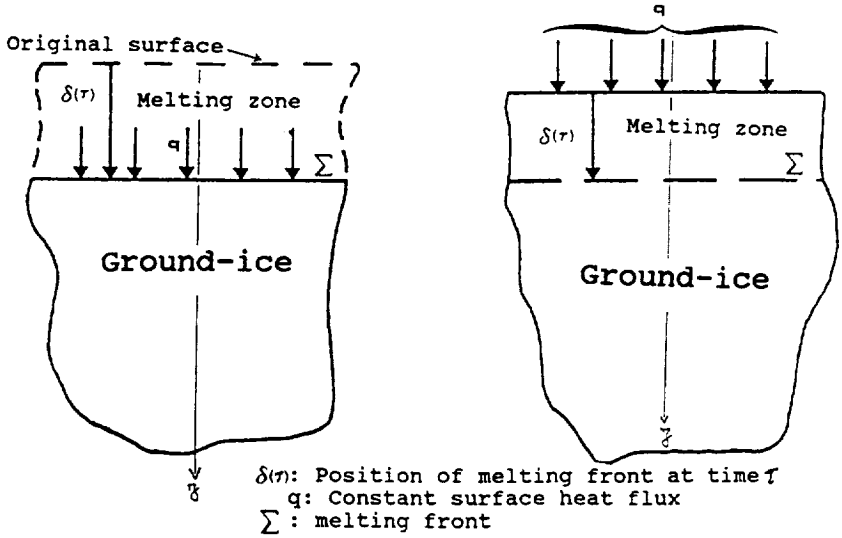


δ(τ): Position of melting front at time τ
q: Constant surface heat flux
Σ : melting front

Fig. 2: Melting semi infinite solid with complete removal of melt from surface.

Fig. 3: Melting semi infinite solid with constant heat flux on the boundary.

CHEMICAL WEATHERING OF BASALTIC ROCKS UNDER COLD ARID CONDITIONS; C. C. Allen, Northwest Environmental Center, Richland, WA 99352 and J. L. Conca, Earth and Environmental Sciences, Washington State University Tri-Cities, Richland, WA 99352.

Chemical weathering of basaltic rocks in the high altitude, ice-free areas of Victoria Land, Antarctica produces etch pits and secondary minerals including illite and quartz. This occurs under some of the driest and coldest conditions encountered on earth. Weathering under cold, arid conditions was investigated as a possible source of the pitted rocks and clay minerals at the Viking landing sites on Mars.

Antarctica Fine-grained, non-vesicular cobbles derived from dolerite (basalt) intrusives are a distinctive feature of the Allan Hills nunatek, Beacon Valley, the Olympus and Asgaard Ranges, and most other high altitude, ice-free areas of Victoria Land, Antarctica. Ubiquitous etch pits in these cobbles range from mm to several cm in diameter (Fig. 1). They are formed by dissolution of the rock by infrequent snow meltwater during the austral summer. Snowfall contributes an undetermined amount of water per year, 1-10 mm maximum, confined to a few storms. Moisture in the etch pits lasts for tens of hours before evaporation. Wind erosion removes weathered material from the pits. Rocks exhibiting etch pits have been exposed to weathering up to 690,000 years (1).

A yellow precipitate lines the upper interior walls and a very thin zone of active weathering underlies the pit bottoms. Infrared spectroscopy indicates a combination of quartz and clays in the illite/montmorillonite series (2). The O-H stretch for structural hydroxyl at 3624 $cm^{-1}$ and the Si-O stretches at 1033 $cm^{-1}$ and 750 $cm^{-1}$ positively identify the clay as non-mixed layer illite (<10% montmorillonite). The yellow precipitate consists of 65% illite, 30% quartz and <5% soluble salts in an intimate mixture.

The presence of well-crystalline, discrete illite was confirmed by transmission electron microscopy. Typical illite particles are subhedral flakes 1-2 microns in width (Fig. 2). Electron diffraction patterns are well-developed and show no evidence of mixed-layering. However, the quartz was very poorly crystalline. The Al/(K+Mg) in the precipitate was 4.6 - 4.7 which is very close to the 4.2 of idealized discrete illite. The illite has the composition $K_{0.4}Mg_{0.1}Al_{2.1}Si_{3.3}O_{10}(OH)_2$.

Illite has never before been described as a surface weathering deposit precipitated directly from solution, although it can occur as a subsurface weathering product of primary micas (3,4). Previous experimental investigations of etch pit solution chemistry during wetting show that the aqueous chemistry is exotic with fluoride, ammonium, sulfate, sodium and nitrate ions occurring in high concentrations of 10 to 30 ppm, buffered by the preexisting secondary minerals (5). However, the F/Cl ration in solution is 2, the same as the basalt substrate. During evaporation-induced precipitation, most of the cations enter soluble salts. $NH_4^+$ and $Ca^{2+}$ precipitate from solution first along with $NO_3^-$ and $SO_4^{2-}$, followed by $Na^+$, $K^+$ and $Mg^{2+}$ along with $F^-$ and $Cl^-$. After complete evaporation, Si, K, Mg and Al are left in a gel that eventually crystallizes as illite and quartz in a nearly constant ratio of 2.2:1. The crystallization takes place at near-freezing temperatures when the rock surface is heated to above 0°C by solar illumination. The occurrence of illite indicates that Na, Ca and Mg are efficiently removed by precipitation in salt phases, and not incorporated into silicates during cold crystallization from solution. Elsewhere in the basalt, montmorillonite and vermiculite clays occur as alteration products of the primary minerals under conditions separated from the etch pit solutions. Therefore, extremely low moisture fluxes together with cold temperatures cause a variety of metastable conditions to occur over small distances.

Fig. 1. Basalt cobble with etch pits formed by chemical weathering

Fig. 2. Illite flake from yellow precipitate. Particle width is 2 microns.

Mars Most of the rocks at the Viking landing sites are coarsely pitted, with pit diameters of 0.3 - 1 cm. They are generally identified as vesicular lavas, though preferential etching of softer minerals in coarse-grained rocks has also been suggested (6).

The surface fines at the two landing sites are thought to be secondary weathering products, predominantly clay minerals. On earth, clays generally form in moist, temperate environments far different from the extreme cold and aridity of the present martian surface. Proposed mechanisms for clay formation on Mars include hydrothermal interactions of water and rock, heated by volcanism or impact (7).

The present investigation of chemical weathering in Antarctica shows that pitting and clay formation can occur in extremely cold and arid climates as a result of mechanisms not operable at higher temperatures under relatively wet conditions. In less than 690,000 years non-vesicular, fine-grained basalt becomes strikingly pitted by exposure to minimal snowfall and wind erosion. Illite and quartz are produced by infrequent, short-term weathering events. Mars, with colder more arid conditions but a much older surface, has also experienced infrequent catastrophic wetting events and occasional surface fog condensation. Such mechanisms may have played a part in forming the striking landscapes at the Viking landing sites.

This work was supported by NASA Grant NAS 7-918 and NSF Grant DPP-8206391.

(1) Cherry, E.M. and Noltimier, H.C. (1986) Ant. J. of U.S., 19, p. 10.
(2) Cariati, F., Erre, L., Micera, G., Piu, P. and Gessa, C. (1981) Clays and Clay Min., 29, p. 157.
(3) Shvartzev, S. L. and Bazhenov, V. A. (1978) Geochemistry International, 15, p. 49.
(4) Boyer, S. J. (1975) N.Z. J. Geol. and Geophys., 18, p. 623.
(5) Conca, J. L. and Wright, J. (1988) Ant. J. of U.S., 22, p. 42.
(6) Carr, M.H. (1981) "The Surface of Mars", Yale Univ. Press, p. 23.
(7) Allen, C.C. et.al. (1982) J. Geophys. Res., 87, p. 10,083.

**Ancient Ocean–Land–Atmosphere Interactions on Mars: Global Model and Geological Evidence.** V.R. Baker, R.G Strom, S.K. Croft, V.C. Gulick, J.S. Kargel, and G. Komatsu, Dept. of Planetary Sciences, University of Arizona, Tucson, AZ 85721.

A great variety of geological evidence indicates that Mars has experienced past climatic epochs characterized by intense fluvial activity (1,2,3,4), glacial, periglacial and permafrost processes (5,6,7,8,22), and phases of intense degradation of impact craters (9,10). The evidence indicates planetwide causative climatological conditions very different from those prevailing today and probably generated several times during early Martian history.

The following model is consistent with a remarkable diversity of geological evidence, some of which is otherwise anomalous with regard to alternative hypotheses. Episodic cataclysmic flood discharges of immense volume emanated almost exclusively from an equatorial zone of fractures peripheral to the Tharsis Bulge, including Memnonia Fossae (Mangala Vallis) and the Valles Marineris system (Kasei and Maja Valles) extending eastward to the Chryse Trough (Shalbatana, Simud, Tiu, and Ares Valles). The huge water volume stored in the fracture system (including ponding in the Valles Marineris) may have had its release triggered by volcanism centered on the fracture system at Tharsis. Concentration of volcanism in short time spans may occur as in terrestrial rifting (11). Based on excavated channel volumes (12), total water debouched to the low-lying Northern Plains would be at least $7.5 \times 10^6$ km$^3$. Allowing for drainage of extensive subsurface aquifers (13), several times this volume could have been discharged, constituting the equivalent of a planetwide layer hundreds of meters deep (14). Concentration of this water in the Northern Plains would comprise a northern hemispheric ocean (Oceanus Borealis), the relic vestiges of which are manifested as ponded sediments (15,16,35), polygonal fractures (17), and ground-ice features (6,7).

Catastrophic invasion of the plains by relatively warm flood water would have vaporized the carbon dioxide ice of the north polar cap. Subsequent evaporation of water and sublimation of the Oceanus Borealis ice cover would have occurred at atmospheric pressures elevated well above present conditions. Addition of water vapor, a greenhouse gas, to the enhanced carbon dioxide atmosphere probably would have triggered additional feedbacks, perhaps releasing adsorbed $CO_2$ (18) from the previously cold regolith. The warming effect would have been further enhanced and/or modulated by optimum periods of obliquity and orbital eccentricity.

The global climate associated with cataclysmic formation of Oceanus Borealis was probably relatively short-lived and analogous to terrestrial glacial climates. Valley networks formed by precipitation related to the last formation of Oceanus Borealis during early Amazonian time are limited to low permeability zones on Alba Patera (19,20). More extensive are the widespread occurrences of periglacial landforms in the cratered uplands (7,8) and along fretted terrain margins of the highlands/lowlands boundary (21). Evidence of alpine-type glaciation in areas of the southern highlands at high latitudes (22) and possible formation of ice masses in outflow channels (23,24) probably reflect this early Amazonian glacial climate. The last glacial epoch may have consisted of an ice sheet extending from the south pole to about -45 degrees latitude.

Precipitation and temperature during the maritime climatic epoch probably fluctuated with the forcing of various orbital parameters. Water from the evaporating/sublimating ocean was gradually sequestered through recharge into the heavily cratered uplands and infiltration into the sea floor. With its disappearance, the ocean could no longer contribute water vapor to the greenhouse warming. This would rapidly lead to a return of the planet to atmospheric conditions similar to those prevailing today.

Although elements of the above sequence are best evidenced during early Amazonian time, the process could have been repeated with variations throughout martian history. Water release from subsurface aquifers was probably most extensive during the Noachian when volcanic activity was widely distributed in the martian highlands. Hydrothermal cycling (25,26,27) could have been important in valley network initiation, subsequently enhanced by precipitation during the maritime climate that followed ocean formation. The global distribution of scapolite (36) may be the result of hydrothermal processes involving $CO_2$. Precipitated water would largely infiltrate the highly permeable martian substrates (megaregolith and lava flows), subsequently emerging as springs, thereby enlarging valleys through sapping. At least one such phase of valley development appears to be post-heavy bombardment (Hesperian) in age (28,29). At the termination of a maritime climatic epoch much of the planetary water recycled from the temporary ocean would be trapped in aquifers of the cratered highlands. There it would reside until released by subsequent temporal/areal concentration of volcanic activity. Because of atmospheric escape processes (30), the initially high endowment of martian water (31) should have been continuously declining through time. This probably contributed to the far greater component of fluvial (valley network) activity during Noachian time versus the predominance of glacial/periglacial features in the early Amazonian. The last phases of outflow

channel activity (Amazonian) from Maja Vallis and Elysium eroded older ocean floor and shoreline forming a much smaller sea. This last smallest sea would be associated with the glacial activity in the southern hemisphere.

**It has not escaped our attention that, given sufficient time, large standing bodies of water under a relatively mild climate could have provided conditions favorable for the inception of life.**

The long-term, cyclic formation and dissipation of Oceanus Borealis and its attendant ramifications obviously have planetwide implications that will require both theoretical modeling and testing against geological constraints. As a preliminary contribution to what will need to be a broad-based interdisciplinary research effort, we note the following points of consistency with the periodic ocean formation and hydrological cycling hypothesized herein.

Basal Scarps Surrounding Volcanoes. Initiation of the Olympus Mons scarp either as a table mountain in vestigial oceanic ice (23) or as a wave-cut margin (as on Hawaiian volcanoes) is readily accommodated, with post-maritime enhancement mainly involving mass wasting. A similar basal scarp around Apollinaris may also be related to Oceanus Borealis.

Layered Terrain in Valles Marineris. This may be lacustrine deposits laid down in lakes which occupied the valley early in its history (33). In some areas, e.g., Ganges Chasma, the source of the water was probably in the subsurface (34). The canyon may have been breached more than once, eroding the sediments and supplying water to the ocean.

Shoreline. Gradational boundary materials at the margin of the southern uplands and northern lowlands are probably best interpreted as sediment deposition in an ocean (15). This boundary probably represents the shoreline of an unfrozen ocean which occupied about 25 percent of Mars' surface.

Runoff Valleys. Drainage networks on Alba Patera, Ceraunius Tholus, and Hecates Tholus could have been caused by precipitation runoff from atmospheric moisture derived from an ocean (19).

Widespread Glacial Features. Widespread glacial features such as eskers, aretes, cirques, kettles, and outwash plains southward of about -45 degrees may be the result of the final ablation of an ice sheet precipitated from water supplied by Oceanus Borealis and cold-trapped as snow in the higher elevations of the southern hemisphere (22).

Impact Crater Degradation. The impact cratering record indicates there was at least one and probably several major episodes of crater obliteration near the end of late heavy bombardment and later (9,10) which could have been caused by fluvial, glacial, and eolian erosion and deposition resulting from a denser atmosphere, at least in part, derived from Oceanus Borealis.

References. 1.Baker,V.R.(1982),The Channels of Mars,Univ. Texas Press. 2.Carr,M.H., and Clow,G.D.(1981),Icarus,**48**,91-117. 3.Mars Channel Working Group(1983),Geol. Soc. America Bull.**94**,1035-1054. 4.Baker,V.R.,Carr,M.H.,Gulick,V.C.,Marley,M.S.,and Williams,C.R. (in press) in Mars,(ed. H.H. Kieffer,B.M. Jakosky, and C. Snyder),Univ. Arizona Press. 5.Squyres,S.W.(1979),J. Geophys. Res.**84**,8087-8096. 6.Lucchitta,B.K.(1981),Icarus,**45**,264-303. 7.Rossbacher,L.A. and Judson,S.,(1981)Icarus,**45**,39-59. 8.Squyres,S.W. and Carr,M.H.(1986),Science,**231**,248-252. 9.Chapman,C.R.,(1974),Icarus,**22**,272-291. 10.Chapman,C.R. and Jones,K.L.,(1977),Ann. Rev. Earth Planet. Sci.,**5**,515-540. 11.McKenzie,D.P. and White,R.S.,(1989),Sci. American,**26(1)**,62. 12.Carr,M.H.,(1986),Icarus,**56**,187-216. 13.Carr,M.H.,(1979),J. Geophys. Res.,**84**,2995-3007. 14.Carr,M.H.,(1987),Nature,**326**,30-34. 15.Parker,T.J., Saunders,R.S. and Schneeberger,D.M.(1989),Icarus,**82**,111-145. 16.Lucchitta,B.K.(1986),Lunar and Planet.Sci.**XVIII**,498-499. 17.McGill,G.E.(1985),Lunar and Planet. Sci.**XVI**,534-535. 18.Fanale,F.P. and Cannon,W.A.,(1979),J. Geophys. Res.,**84**,8404-8414.19.Gulick,V.C.andBaker,V.R.,(1989),Nature,**341**,514-516.20.Gulick,V.C.andBaker,V.R.(in press),J.Geophys.Res.. 21.Kochel,R.C.andPeake,R.T.,(1984),J.Geophys.Res.,**89**,C336-350.22.Kargel,J.and Strom,R.G.,(1990),Lunar and Planet. Sci.**XXI**. 23.Lucchitta,B.K., Anderson,D.M. and Shoji,H.,(1981),Nature,**290**, 759-763. 24.Lucchitta,B.K.,(1982),J. Geophys. Res.,**87**,(B12),9951-9973. 25.Brakenridge,G.R., Newsom,H.E. and Baker,V.R.,(1985), Geology,**13**,859-862. 26.Brakenridge,G.R.,(1989),NASA Tech. Memo.,**4130**,310-312. 27.Gulick,V.C., Marley,M.S., and Baker,V.R.,(1988), Lunar and Planet. Sci.**XIX**, 441-441. 28. Grant,J.A. and Schultz,P.M., (in press) Icarus. 29.Baker,V.R. and Partridge,J.B.,(1986), J. Geophys. Res.,**91**,3561-3572. 30.Hunten,D.M., Donahue,T.M., Walker,J.C.G. and Kasting,J.F. (1989) in Origin and Evolution of Planetary Atmospheres. (ed. S.K. Atreya, J.B. Pollack, and M.S. Matthews), Univ. Arizona Press, 386-422. 31.Pepin,R.O. (1987), J. Geophys. Res., **84**,8061-8074. 32.Hodges,C.A., and Moore,H.J. (1979) J. Geophys. Res.,**84**, 8061-8074. 33.McCauley,J.F. (1978), Geol. Map of the Coprates Quad. of Mars, USGS Map I-897. 34.Komatsu,G. and Strom,R.G. (1990), Lunar and Planet. Sci.**XXI**. 35.Jons,H.-P., Lunar and Planet. Sci.**XVII**, 404-405. 36.Clark, R.B., et al., (1989), 4th Internat. Conf. on Mars Abstract., 82-83.

## THE EVOLUTION OF THARSIS: IMPLICATIONS OF GRAVITY, TOPOGRAPHY, AND TECTONICS:

W. B. Banerdt and M. P. Golombek, Jet Propulsion Laboratory, California Institute of Technology, Pasadena, CA 91109

Introduction: Dominating the western hemisphere of Mars, the Tharsis rise is an elongate area centered on Syria Planum that ascends as much as 8 to 10 km above the datum. It is intensely fractured by long, narrow grabens that extend radially hundreds of kilometers beyond the rise and is ringed by mostly concentric wrinkle ridges that formed over 2,000 km from the center of the rise. Its size, involving a full hemisphere of Mars, gives it a central role in the thermo–tectonic evolution of the planet and has stimulated a number of studies attempting to determine the sequence of events responsible for this unique feature [1–5]. In this abstract I review the constraints that gravity and topography data place on the current structure of Tharsis, along with insights into its development derived from comparisons of detailed regional mapping of faulting with theoretical deformation models. Finally, a self–consistent model for the structure of Tharsis is proposed.

Gravity and Topography: The gravity and topography of Tharsis show a high degree of correlation, with a large proportion of the spectral power contained in the lowest harmonics (degrees 2–3). The apparent depth of compensation derived from the spectral admittance depends strongly on wavelength, ranging from over 1000 km at degree 2 to about 100 km for the shorter wavelengths [6]. Stated plainly, there is a large excess of gravity at long wavelengths relative to that which can be explained by simple compensation models. There are a limited number of ways to realistically accommodate this. One is isostatic compensation utilizing a density dipole, with a shallow positive anomaly overlying a deeper negative anomaly [4,7]. This model requires massive removal of crustal material and static support by a thick (~300–400 km), immobile layer of magmatically depleted mantle. Another approach is dynamic support by mantle convection [8]. This would imply a single immense plume that has not moved significantly with respect to the lithosphere since the Noachian. The third possibility is partial flexural support of the load [2]. In this case a modestly thicker crust is required with a >100 km thick lithosphere that is capable of supporting stresses of several hundred MPa.

Faulting: The timing and extent of faulting around Tharsis is both long lived and varied, involving both local/regional events and full hemispheric events [1,9–11]. For hemisphere-wide patterns relevant to the theoretical stress models, three distinct events have been recognized. In the upper Noachian, a radial system of grabens formed that marks the first unequivocal tectonic event in the formation of Tharsis. This fracture system, centered on Syria Planum [10] can be traced from near the center of the rise to beyond its flanks in exposed Noachian aged units. In the lower Hesperian, massive outpourings of fissure volcanics formed the surface now recognized as Lunae Planum and similarly aged plains surrounding Tharsis (the so–called ridged plains). Shortly after deposition of the plains, concentric wrinkle ridges formed [11] that are also centered in Syria Planum. By upper Hesperian times another enormous radial normal faulting event occurred, this time centered near Pavonis Mons [10]. This was followed by long-lived volcanism (throughout the Amazonian) to form the prominent central volcanoes of Tharsis and their aprons. One other faulting event has been related to stress models. A system of E–W trending normal faults formed in Claritas Fossae, an uplifted horst of Noachian aged terrain that is covered by all Hesperian and Amazonian units [5,9]. These faults are consistent with a Tharsis–concentric pattern, but this fracture system is only found in a limited area, so its regional significance is unclear.

Stress calculations: These two types of information, gravity/topography and surface strain, can be linked in a complementary fashion via theoretical stress modelling [2,4]. In broad terms, three distinct fault patterns can be generated at the surface of a spherical shell that supports a roughly circular, long–wavelength topographic high by static means. If the topography is due to uplift of the lithosphere, circumferentially oriented extensional features within the uplifted portion and radially oriented compressional features in the periphery are predicted. In contrast, a surface load that causes subsidence of the lithosphere predicts the opposite sense of faulting, with circumferential ridges within the load region and radial extensional faulting farther out. Isostatic support of topography generates a stress field that predicts radially oriented normal faulting in a region around the topographic center and circumferential ridge formation near its edges. In

addition, the isostatic stresses are much smaller in magnitude than those for the flexural cases (~50 MPa vs. 200–400 MPa). Stresses due to convective support of topography are still under study, but the patterns are likely to be similar to those of the uplift case.

These results place some strong constraints on the evolution of Tharsis as reflected in its structural record. Only the uplift case (and, possibly, convective support) can form circumferentially oriented grabens. Such grabens have tentatively been identified only in the oldest (early Noachian) units in Claritas Fossae [5,9]. Thus this mechanism can be ruled out for all but perhaps the earliest stages of formation. Circumferentially oriented ridges near the edge of the rise are a feature of both the isostatic and subsidence cases, with the former extending the ridge zone outward and the latter extending it inward. Thus the distribution of ridges tends to marginally favor an isostatic regime. The most clear–cut distinction between these two cases, however, is in the respective regions of radial extensional faulting. Inner radial faulting is possible only in the isostatic case, whereas outer radial faulting can occur only in the subsidence case; the conditions under which these two patterns form are mutually exclusive. However stratigraphic mapping has shown that both inner and outer radial faulting have occurred contemporaneously over a considerable interval of Tharsis history [12]. Thus there is a fundamental contradiction between apparently robust model results and observation.

Proposed model: The stress models described above assume that the load is supported by a homogeneous elastic shell. But the actual rheology of the lithosphere is undoubtedly more complex [e.g., 12–14]. Laboratory and field measurements on Earth indicate that the strength of rocks in the shallow lithosphere is generally limited by frictional sliding on preexisting faults, giving a strength that increases with depth. At the higher temperatures characteristic of the lower portions of the lithosphere ductile creep becomes the strength–limiting factor, with the conductive thermal gradient causing a decrease in strength with depth. In addition, ultramafic minerals characteristic of mantle rocks have a considerably higher creep resistance than those minerals common in crustal rocks. Thus the lithosphere may have two strength maxima separated by a ductile layer in the lower crust. The existence and strength of this ductile layer will depend on the crustal thickness and thermal gradient, with larger values of either of these parameters making such a layer more pronounced.

The gravity observations described above, along with the difficulties inherent in creating a realistic isostatic structure, argue for flexural support of the Tharsis load. Additionally, most of the regional tectonic deformation, with the notable exception of the inner radial faulting, is consistent with subsidence of the lithosphere. We contend that the formation of the inner radial fault pattern is a natural consequence of the thickened crust and higher heat flow resulting from the extrusive and intrusive volcanic construction of the Tharsis rise.

If Tharsis is formed by construction, it acts as a flexural load on the elastic lithosphere. Far from Tharsis the lithosphere consists of both the crust and upper mantle. However, within Tharsis itself, the thickened crust and high heat flow will act to decouple the upper crust from the strong zone in the upper mantle. In this situation the upper mantle strong layer, which constitutes most of the lithosphere in either case, will deform as part of the global shell, transferring flexural stresses and displacements to the rest of the shell. The relatively thin, brittle upper crustal layer will deform not as part of the greater shell, but rather as a spherical cap with a lubricated lower surface and a peripheral boundary which is fixed to the global shell. Thus it will respond primarily to isostatic spreading forces and increases in its radius of curvature [15] induced by the subsidence of the lower lithosphere. Both processes induce circumferential extension within the cap, leading to radial faulting within the highland area. Outside this region of decoupled crust, faulting will be due to flexural stresses caused by the overall lithosphere subsidence. Radial compression is likely to be concentrated near the boundary of the two regions.

References: [1] Wise et al. *Icarus* **38** 456, 1979; [2] Banerdt et al. *JGR* **87** 9723, 1982; [3] Solomon and Head *JGR* **87** 9755, 1982; [4] Sleep and Phillips *JGR* **90** 4469, 1985; [5] Phillips et al. *JGR* in press; [6] Phillips and Saunders *JGR* **80** 2893, 1975; [7] Sleep and Phillips *GRL* **6** 803, 1979; [8] Kiefer and Hager *MEVTV: Early Tect. Volc. Evol. Mars*, 48, 1988; [9] Tanaka and Davis *JGR* **93**, 14893, 1988; [10] Plescia and Saunders *JGR* **87** 9775, 1982; [11] Watters and Maxwell *JGR* **91** 8113, 1986; [12] Banerdt et al. in *Mars* in press; [13] Brace and Kohlstedt *JGR* **85** 6248, 1980; [14] Solomon and Head *JGR* in press; [15] Turcotte *Geophys. J.* **36** 33, 1974.

MARTIAN IMPACT CRATERS: CONTINUING ANALYSIS OF LOBATE EJECTA SINUOSITY.
N. G. Barlow, SN21, NASA/Johnson Space Center, Houston, TX 77058.

The lobate ejecta morphology surrounding most fresh martian impact craters can be quantitatively analyzed to determine variations in ejecta sinuosity with diameter, latitude, longitude, and terrain. The results of such studies provide another clue to the question of how these morphologies formed: are they the result of vaporization of subsurface volatiles (1) or caused by ejecta entrainment in atmospheric gases (2). Kargel (3) provided a simple expression to determine the degree of non-circularity of an ejecta blanket. This measure of sinuosity, called "lobateness", is given by the ratio of the ejecta perimeter to the perimeter of a circle with the same area as that of the ejecta:

$$\Gamma = \text{perimeter}/(4\pi * \text{area of ejecta})^{1/2}.$$

A circular ejecta has a $\Gamma$ of 1; more sinuous ejecta display $\Gamma>1$. Kargel's study of 538 rampart craters in selected areas of Mars led him to suggest that lobateness increased with increasing diameter, decreased at higher latitudes, and showed no dependence on elevation or geologic unit.

Major problems with Kargel's analysis are the limited size and distribution of his data set and the lack of discrimination among the different types of lobate ejecta morphologies (4). Bridges and Barlow (5) undertook a new lobateness study of 1582 single lobe (*SL*) and 251 double lobe (*DL*) craters. Their results are summarized in Tables I and II. These results agree with the finding of Kargel that lobateness increases with increasing diameter, but found no indication of a latitude dependence for *SL* craters. A slight terrain dependence was also detected, contrary to Kargel's results.

The Bridges and Barlow study has now been extended to multiple lobe (*ML*) craters. Three hundred eighty *ML* craters located across the entire martian surface have been studied. *ML* craters provide more complications to lobateness studies than do *SL* or *DL* craters--in particular, the ejecta lobes surrounding the crater are often incomplete (i.e., do not extend completely around the crater). Since the lobateness formula compares the perimeter of the ejecta lobe to that of a circle, we have restricted our analysis only to complete lobes. The lobes are defined sequentially starting with the outermost lobe and moving inward: L1 for the outermost lobe, L2, L3, etc. for inner lobes. Generally only two or three complete lobes are recognizable for *ML* craters.

Median lobateness values for the lobes are 1.18 for L1, 1.13 for L2, and 1.09 for L3. The L1 value is slightly larger than the average *SL* and *DL* lobateness values. L2 lobateness values are comparable to those found for the highland *SL* craters and for the outer lobe (L1) of *DL* craters. L3 lobateness values are equal to $\Gamma$ values of plains *SL* craters and the inner lobe (L2) of *DL* craters. Analysis of individual craters show that 72% of the L2 lobes display smaller $\Gamma$ than their accompanying L1, and, in 77% of craters with three lobes, L3 has a lower $\Gamma$ than L2. Eighty-nine percent of all craters with three lobes show L3 with less sinuous ejecta (i.e., lower $\Gamma$) than L1. This continues the trend seen with *DL* craters. No statistically significant lobateness dependence on latitude is suggested for L1, L2, or L3. Kargel's detection of a latitude-lobateness correlation can be explained by Barlow and Bradley's (6) observation of more *ML* craters (which have higher $\Gamma$) near the equator and more *SL* craters (with lower $\Gamma$) near the poles. Since Kargel did not distinguish among different ejecta morphologies, he inadvertently reported

a lobateness relationship with latitude. Also contrary to Kargel's study, we found that *ML* craters on highlands regions tend to show slightly lower values of lobateness than *ML* craters on plains, at least for the L1 ($\Gamma_h$=1.17; $\Gamma_p$=1.20) and L2 ($\Gamma_h$=1.13; $\Gamma_p$=1.15) lobes. This is opposite the trend seen for *SL* craters, where lower lobateness values are seen for craters on the plains.

The change in $\Gamma$ with increasing diameter suggests that either impact energy or changes in physical properties with depth are reflected in ejecta sinuosity measurements. However the change in $\Gamma$ with general geologic unit and ejecta morphology (which varies with latitude (see 6)) favors a dependence of sinuosity on target properties. This in turn has implications for the distribution of volatiles on Mars, if we accept the theory that fluidized ejecta morphologies result from impact vaporization of subsurface volatiles (1). If increases in $\Gamma$ correspond to higher volatile-to-clast ratios, the correlation of $\Gamma$ with diameter, morphology, and geologic unit implies that the highlands are volatile-rich close to the surface and plains have volatile reservoirs stored at greater depths. Alternately, if *SL* craters form by impact into ice and *ML* craters result from excavation into subsurface aquifers (as suggested by (6, 7)), these same correlations lead us to conclude that the highlands are icier than the plains but the plains contain more near-surface water.

References: (1) Carr, M.H. et al. (1977), *JGR*, **82**, 4055. (2) Schultz, P.H. and Gault, D.E. (1979), *JGR*, **84**, 7669. (3) Kargel, J.S. (1986), *LPS XVII* (abs.), 410. (4) Mouginis-Mark, P. (1981), *JGR*, **84**, 8011. (5) Bridges, N.T. and Barlow, N.G. (1989), *LPS XX* (abs.), 105. (6) Barlow, N.G. and Bradley, T.L. (1990), submitted to *Icarus*. (7) Johansen, L.A. (1979), NASA TM 80339, *Rpts. Planet. Geol. Geophys. Prog. 1978-1979*, 123.

Table I--General Results of Lobateness Studies

| | SL | | DL | | ML | | |
|---|---|---|---|---|---|---|---|
| | P | H | L1 | L2 | L1 | L2 | L3 |
| Number | 370 | 1212 | 251 | 245 | 380 | 363 | 184 |
| Median $\Gamma$ | 1.09 | 1.13 | 1.14 | 1.09 | 1.18 | 1.13 | 1.09 |
| Max $\Gamma$ | 3.33 | 3.81 | 2.27 | 1.38 | 1.74 | 1.47 | 1.33 |
| Min $\Gamma$ | 1.00 | 1.01 | 1.01 | 1.00 | 1.02 | 1.01 | 1.00 |
| Average $\Gamma$ | 1.13 | 1.16 | 1.17 | 1.10 | 1.20 | 1.16 | 1.10 |
| Latitude Dep? | No | No | * | * | No | No | No |

P = Northern Plains H = Southern Highlands

**DL* craters are located primarily within the 40-65°N latitude range, thus latitude dependence studies are not valid.

Table II--Median $\Gamma$ Values by Diameter Range

| Diam (km) | SL | | DL | | ML | | |
|---|---|---|---|---|---|---|---|
| | P | H | L1 | L2 | L1 | L2 | L3 |
| 8.0-11.3 | 1.09 | 1.11 | 1.13 | 1.07 | 1.11 | 1.06 | 1.06 |
| 11.3-16.0 | 1.09 | 1.14 | 1.14 | 1.07 | 1.12 | 1.09 | 1.07 |
| 16.0-22.6 | 1.12 | 1.16 | 1.17 | 1.10 | 1.17 | 1.13 | 1.08 |
| 22.6-32.0 | 1.15 | 1.18 | 1.17 | 1.13 | 1.20 | 1.18 | 1.11 |
| 32.0-45.3 | 1.08 | 1.17 | 1.30 | 1.24 | 1.22 | 1.18 | 1.12 |
| 45.3-64.0 | -- | 1.11 | 1.08 | 1.17 | 1.27 | 1.33 | 1.22 |
| 64.0-90.5 | -- | -- | -- | -- | 1.35 | 1.27 | 1.18 |

**CAN IRON OXIDE/OXYHYDROXIDE MINERALS BE IDENTIFIED ON THE MARTIAN SURFACE FROM GROUNDBASED VIS-NIR SPECTRA?** Jim Bell and Tom McCord, Planetary Geosciences, Univ. Hawaii, Honolulu 96822; BITNET: jimbo@uhpgvax.pgd.hawaii.edu

Visible to Near-Infrared (VIS-NIR) reflectance data of numerous regions on Mars were obtained during the 1988 opposition at Mauna Kea Observatory. A Circular Variable Filter (CVF) spectrometer was used to acquire data of 41 regions on the planet from 0.4-1.0 $\mu$m. The spatial resolution of these observations was approximately 500-600 km, the spectral resolution was $R = \lambda/\Delta\lambda \simeq 80$, and the spectral sampling was $S \simeq 125$ channels/$\mu$m [Bell *et al.*, 1989].

The new CVF data show abundant evidence (some previously observed, some not) of the existence of the $Fe^{3+}$ cation on Mars. First, there is the strong and diagnostic $O^{2-} \rightarrow Fe^{3+}$ near-UV charge transfer absorption edge which is typical of ferric-bearing minerals [*e.g.*, Sherman *et al.*, 1982]. This deep blue absorption is primarily responsible for the red color of Mars and also lead numerous early workers to speculate on the existence of iron oxides on the martian surface. Second, there is a weaker though clearly discernible absorption band from 0.78-0.94 $\mu$m, centered at $\simeq$ 0.85 $\mu$m in many of the spectra. This band has been interpreted by several groups as being due to the $^6A_1 \rightarrow {}^4T_1({}^4G)$ ligand field transition of $Fe^{3+}$ [Singer, 1982; Morris *et al.*, 1989; Bell *et al.*, 1989], indicating the presence of some crystalline iron oxide component in the Mars soil. This contention is further supported by the third piece of evidence, a heretofore undetected weak band or "cusp" at 0.61-0.72 $\mu$m that is interpreted as being due to the $^6A_1 \rightarrow {}^4T_2({}^4G)$ electronic transition of $Fe^{3+}$. This weak feature is typically deepest in spectra of brighter regions on the planet. Thus these new data indicate unambiguous evidence of $Fe^{3+}$ absorption; the question as posed above is whether or not the positions and strengths of these absorptions can be used to identify surface $Fe^{3+}$ mineralogy.

Some of these new data are compared directly to laboratory $Fe^{3+}$-bearing mineral spectra in Figures 1-3. It can be immediately seen that the position and strength of the near-UV charge transfer absorption edge places severe constraints on the abundances of several of these *pure* iron oxides in certain particle size ranges. For example, the hematite powder in Figure 1 exhibits a steep, saturated near-UV absorption with the band edge near 0.55 $\mu$m, typical of most bulk crystalline hematites and a poor match to the martian spectral data. It can be seen that none of the other common iron oxides/oxyhydroxides in Figure 1 reproduce the shape and position of the near-UV absorption either. The less common and also more poorly crystallized $Fe^{3+}$ phases in Figure 2 come closer to matching the absorption edge position and shape, yet there are still discrepancies except for the spectrum of synthetic iron-silica gel which provides a fair match. The similarly poorly crystalline "amorphous" palagonites in Figure 3 also provide a good fit to the absorption edge. Based on this simple examination of these particular lab data, it appears that poorly crystalline (*not* amorphous) materials exhibit the best match to the VIS-NIR martian data based solely on the highly diagnostic near-UV charge transfer absorption.

As mentioned above, however, two *crystalline* $Fe^{3+}$ absorption bands are evident in the new Mars data. Figure 3 clearly shows that most "amorphous Hawaiian soils" such as those examined by Singer (1982) do not exhibit $Fe^{3+}$ bands as deep as those in the Mars data, suggesting then that although poorly crystalline materials constitute an important part of the Mars soils, some component of well crystallized, bulk $Fe^{3+}$-bearing mineral(s) exist and produce those features. A more quantitative estimate of the partitioning of crystalline vs. poorly crystalline $Fe^{3+}$ phases is in progress.

A quick look at the variation in band strengths and positions of the two VIS-NIR $Fe^{3+}$ electronic transition bands in the lab data of Figures 1 and 2 suggests that the answer to the question posed in the title is "yes." The increased spectral sampling of these new data combined with ongoing lab analog studies and refined data calibration suggest that at least hematite, and possibly also goethite, existing in a wide range of particle sizes down to nanometer scales, may be important constituents of the Mars soil. Other possibilities which must not be overlooked without further study include $Fe^{3+}$-bearing sulfates, palagonite-like secondary weathering products, and some of the more exotic, poorly crystalline iron oxides/oxyhydroxides.

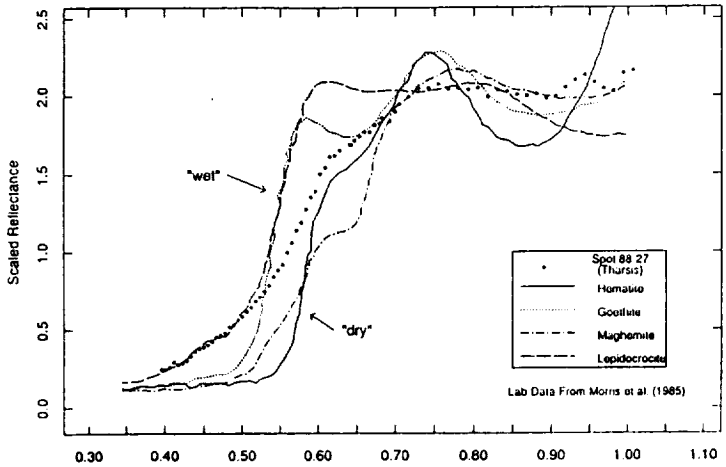


**Figure 1:** Mars CVF spectrum 88-27 (Tharsis region) from Bell *et al.* (1989) compared to four common iron oxides/oxyhydroxides. The lab data are from powdered samples of Morris *et al.*, 1985. The wet/dry distinction simply refers to the presence or lack of $OH^-$ radicals in the mineral structure. Note the poor fit of the Mars data to the lab near-UV charge transfer absorptions and the variation of position of the two $Fe^{3+}$ electronic transitions at 0.65 $\mu$m and 0.86 $\mu$m in the lab data. Data scaled for display purposes.

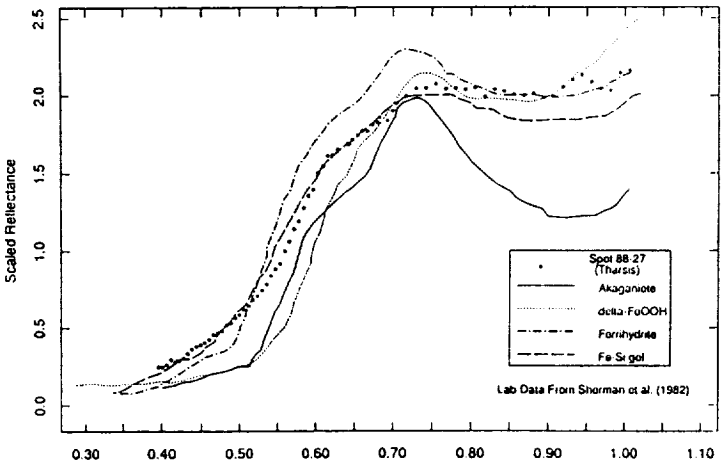


**Figure 2:** Same Mars data as Figure 1 compared to some less common and poorly crystalline iron oxides/oxyhydroxides from Sherman *et al.*, 1982. The near-UV charge transfer edge is more closely matched in these data although there are still discrepancies. Data digitized and scaled for display purposes.

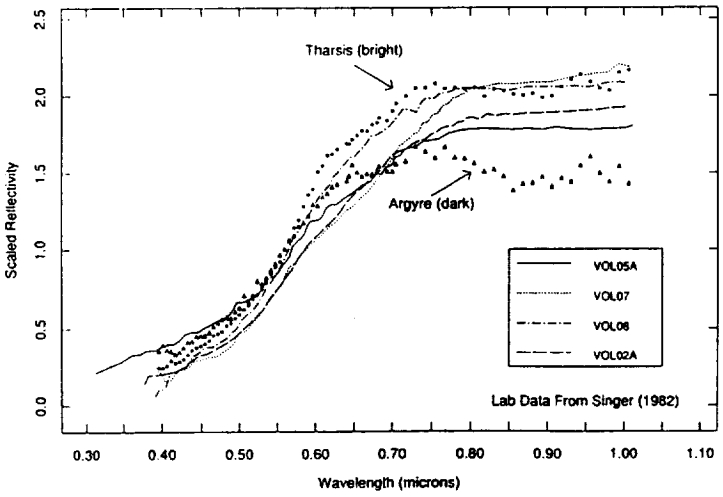


**Figure 3:** Mars CVF data from bright (Tharsis) and dark (Argyre) albedo regions compared to hawaiian palagonite spectra of Singer (1982). The position of the near-UV charge transfer edge is matched nicely, however the palagonites show little evidence of the crystalline $Fe^{3+}$ absorption bands seen in the Mars data. Data digitized and scaled for display.

References:

Bell, Jim, T.B. McCord, and P.D. Owensby (1989) submitted to *JGR, Special Mars Conference Issue.*

Morris, R.V., H.V. Lauer, Jr., C.A. Lawson, E.K. Gibson, Jr., G.A. Nace, and C. Stewart (1985) *JGR, 90,* 3126-3144.

Morris, R.V., D.G. Agresti, H.V. Lauer, Jr., J.A. Newcomb, T.D. Shelfer, and A.V. Murali (1989) *JGR, 94,* 2760-2778.

Sherman, D.M., R.G. Burns, and V.M. Burns (1982) *JGR, 87,* 10169-10180.

Singer, R.B. (1982) *JGR, 87,* 10159-10168.

GROUNDBASED IMAGING SPECTROSCOPY OF MARS DURING 1988 AND 1990: INSTRUMENTATION AND DATA REDUCTION/INTERPRETATION STRATEGIES FOR THE FUTURE OF PLANETARY SPECTROSCOPY: Jim Bell, Paul Lucey, Tom McCord, and Tom Ozoroski, HIG/PGD, Univ. Hawaii, Honolulu 96822; BITNET: jimbo@uhpgvax.pgd.hawaii.edu

Our goals for the 1988 and upcoming 1990 Mars oppositions are to map the surface of Mars at 150-250 km resolution in the 0.4-2.5 μm range using imaging spectroscopy. One of the great advantages of imaging spectroscopy over traditional narrow-band filter imaging or point spectroscopy is its ability to obtain simultaneous information over wide spatial and spectral ranges [1,2]. Such measurements produce enormous quantities of data, on the order of 10-100 Mbytes per night of observing. Obviously, this is a concern that must be addressed by the proper choice of image processing hardware and software. Depending on the size of the array used, $10^4$ - $10^6$ *individual* spectra can be produced from any single dataset. This huge number prohibits traditional methods of spectrum interpretation, and thus techniques must be derived which can automatically analyze vast numbers of spectra and produce maps of the most important quantities.

For example, we obtained imaging spectrometer data of 70% of the martian surface in the 0.4-1.0 μm range from Mauna Kea Observatory during the 1988 opposition [2,3]. Using the U.H. 2.24-m Wide Field Grism Spectrograph and IFA/Galileo CCD, 26 raw Mars and standard star image cubes of dimensions 800 X 200 X 50 (spatial X spectral X spatial) were obtained. Standard spectral and CCD data processing techniques required some 75 hours of continuous processing by a 2 MIPS Sun 3/260 machine just to obtain approximately calibrated reflectance images. After performing this level of reduction we employed several techniques to simplify our analyses. One technique was band-depth mapping. Our 0.4-1.0 μm image cube spectra showed $Fe^{3+}$ absorption bands at 0.65 μm and 0.86 μm which varied spatially on the planet. In a manner similar to lunar spectrum continuum removal, we created an averaged image across the 0.61-0.72 μm region and ratioed that with an image at 0.68 μm. The resulting ratio image shows several classical bright regions on Mars to exhibit up to a 5% deeper 0.65 μm $Fe^{3+}$ band than dark albedo regions, consistent with the idea of bright regions consisting of more weathered (dusty) materials. Possibly of more interest, however, are several regions on the planet where the $Fe^{3+}$ band variations do not correlate well with observed classical albedo boundaries, such as Sinus Sabaeus (Figure 7 in [2]).

A second technique used in data analysis was polynomial fit coefficient mapping [4,5]. In this process, the spectral axis is fit to an $n^{th}$ order polynomial ($y=a_nx^n+a_{n-1}x^{n-1}+...+a_0$), yielding n+2 (including residuals) coefficients for each pixel that can subsequently be displayed as n+2 complete images showing how these coefficients vary across the martian surface. Some examples of this procedure are shown in Figs. 1 and 2. In Fig. 1 the steep near-UV $Fe^{3+}$ absorption edge characteristic of Mars [e.g. 6, 7] was fit by a first order polynomial, and the resulting spectral slope and intercept are plotted as images. The intercept maps correlate very well with albedo (as expected: albedo is just an additive offset), and the spectral slope also shows significant correlation, again consistent with classical bright regions having "redder" spectra. However, several regions near the south polar cap (300-360° W) and west of Sinus Meridiani in Thaumasia (near 30°S, 60-90° W) are anomalous in that they do not show the typical global slope/albedo correlation. In Fig. 2 similar maps are presented for a fit to near-infrared data from 0.735-0.795 μm. Again the spectral intercept is essentially an albedo map, but the slope maps are relatively "bland" and somewhat noisy, consistent with the fact that the martian spectrum is relatively flat to slightly "blue" at these wavelengths [6,7]. For the slope maps, brighter values indicate deeper "near-infrared" absorption. There is some structure in these images associated with the Sinus Meridiani/Sinus Sabaeus region, showing the northern boundary of this dark albedo feature to have a relatively flat spectrum while its southern boundary has a deep (most likely $Fe^{3+}$) absorption. Such anomalous regions may indicate more spectral heterogeneity than once thought in the martian surface fines, and are difficult to detect using standard imaging or point spectroscopy techniques.

Observing plans for the upcoming 1990 opposition (the last in the excellent 1986-1988-1990 triad) include further mapping of the entire planet in the 0.4-1.0 μm and 1.0-2.5 μm regions. For the longer wavelength imaging spectrometer data we will concentrate our efforts on the Tharsis/Valles Marineris region in an effort to directly compare our global dataset with the higher resolution though spatially confined Phobos-2 ISM data [8]. Also, an in-depth analysis of the Syrtis Major/Sinus Sabaeus area will be undertaken in an effort to characterize better the compositional nature of the dark regions (can we really see exposed "bedrock?" [9]) and provide comparisons to high spatial resolution 1988 groundbased images of the same areas [10].

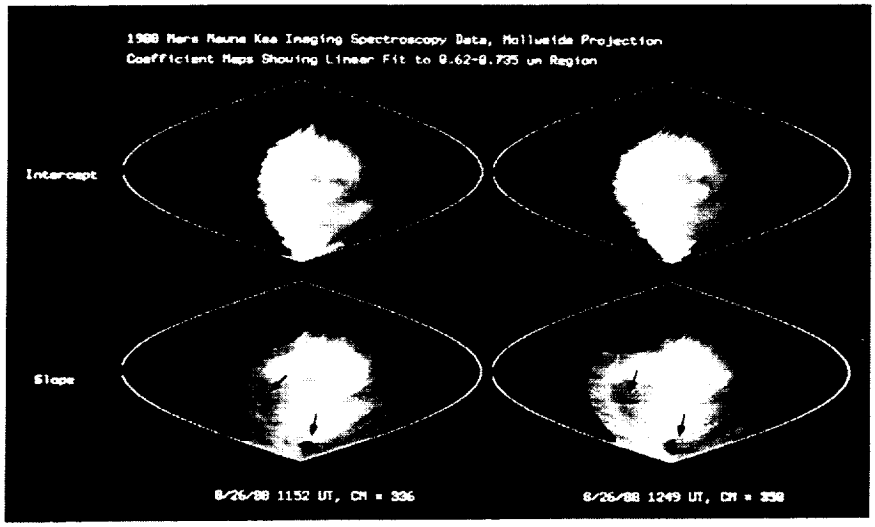


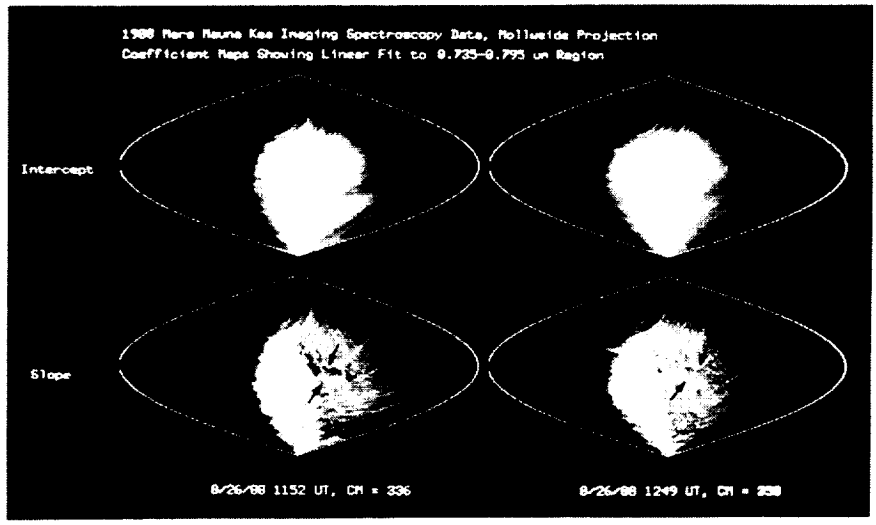


Figure 1 (Top) and Figure 2 (Bottom). See text for explanation.

References: [1] Goetz A.F.H., Vane G., Solomon J.E. and Rock B.N. (1985) *Science, 228,* 1147-1153. [2] Bell III J.F., McCord T.B., and Lucey P.G. (1990) *Proc. Lunar Planet. Sci. Conf. 20th,* 479-486. [3] Bell III J.F., McCord T.B., and Lucey P.G. (1989) *EOS Trans. AGU, 70,* 50. [4] Lucey P.G., Bruno B.C., and Hawke B.R. (1989) *B.A.A.S., 21,* 971. [5] *Ibid* . (1990) *LPSC XXI,* 726-727. [6] McCord T.B. and Westphal, J.A. (1971) *Astrophys. J., 168,* 141-153. [7] Bell III, J.F., McCord, T.B., and Owensby, P.D. (1990) *J. Geophys. Res.*, in press. [8] Bibring, J.-P. and 16 others (1989) *Nature, 341,* 591-593. [9] Zimbelman, J.R. and Craddock, R.A. (1990) *LPSC XXI,* 1377-1378. [10] Pinet P. and Chevrel S. (1989) submitted to *J. Geophys. Res.*

**COMPARISON OF NEW GROUNDBASED AND PHOBOS-2 VSK COLOR RATIO DATA FOR MARS**; James F. Bell III[1,2], Mark S. Robinson[1], Thomas B. McCord[1,3], and Fraser P. Fanale[1] ([1]Planetary Geosciences Division, Univ. of Hawaii, Honolulu 96822; [2]Remote Sensing Lab, Univ. of Washington AJ-20, Seattle 98195; [3]SETS, Inc., Mililani, HI 96789)

Summary: The VSK-FREGAT imaging experiment on the Phobos-2 spacecraft acquired several VIS (0.4-0.61 μm) and NIR (0.7-1.1 μm) image pairs containing both Mars and Phobos during February and March, 1989 [17]. We have analyzed these image pairs and calculated NIR/VIS DN ratios for Mars for comparison with groundbased 0.4-1.0 μm CVF reflectance spectra obtained during August, 1988 [1]. We find that for the particular region imaged (Mare Sirenum, 35°S, 155°W--NE of Newton crater) our telescopic reflectance spectrum convolved to VSK bandpasses yields a NIR/VIS ratio of 1.78. The NIR/VIS DN ratio that we obtained from Phobos 2 image pairs at similar phase angles as the groundbased data is 2.25±0.2, thus suggesting that dividing such Mars (and Phobos) DN ratios by a correction factor of 1.26 yields more accurate values for the true NIR/VIS reflectance ratio. Several sources of error, including near-opposition contrast enhancement in the blue ("blue clearing") associated with possibly variable atmospheric dust loading between August 1988 and February-March, 1989 indicate that this method of calibration could possibly suffer from additional errors of up to 10-15%, although comparison of the Phobos-2 data with Viking results [5] seems to indicate that these effects were minimal or absent during the 1989 encounter.

Discussion: Current efforts to map color variations (and thus perhaps map compositional variations [2,5]) are using calibration methods based on modeled groundbased telescopic narrow-band filter photometer data of Mars (R ≈ 20; [e.g. 3,4]) compared against the spacecraft VIS and NIR image pairs that contain both Mars and Phobos [5]. After having discovered that one of the regions we measured in August 1988 was also serendipitously imaged by Phobos-2 (S. Murchie, personal communication, 1989), we decided to use these new, higher spectral resolution data to better constrain the ongoing color calibration efforts [5,6].

Using the data from [7] we plotted a smoothed solar spectrum for the 0.4-1.1 μm region and multiplied this spectrum by our reflectance data for CVF Spot 88-37 (Figure 1). Thus we obtained a spectrum that we then convolved into the VSK VIS and NIR bandpasses that simulates the response that the Phobos-2 cameras recorded of the same region on Mars some six months later. Ignoring absolute flux levels since we are most interested in obtaining the VIS/NIR channel *ratio* and using a NIR/VIS filter efficiency ratio of 1.395 (B. Zhukov, personal communication, 1989) we determined that if the VSK experiment had been looking at a region on Mars which exhibits a reflectance identical to that of our CVF Spot 88-37, then it would have obtained a NIR/VIS DN ratio of 1.78 (for comparison, [5] obtained NIR/VIS = 2.08). Additionally, we found that given the above parameters and a NIR/VIS bandpass solar flux ratio of 0.806, the NIR/VIS DN ratio of a constant albedo object as viewed by VSK would be 1.125.

Using dark subtracted, flatfielded, and recently re-calibrated [5] VSK images of Phobos and Mars, we determined average DN values and variations for the region of Mars common to our spectral data in images 2300123 and 2300111. Data values for 17X17 pixel regions for the NIR and VIS channels were 62±3.5 and 110±3, respectively. The VIS image had an exposure 4 times that of the NIR, so assuming that the cameras were linear the resulting NIR/VIS image ratio was 2.25±0.19.

A possible source of error in the comparison with groundbased results is the so-called "blue clearing" or near-UV brightening near zero phase. This effect (which is difficult to quantify) is typically strongest during periods near perihelion in southern hemisphere spring and summer ($L_S$≈160-200° and $L_S$≈270-300° [8]). Visual monitoring during our telescopic observations, acquired at $L_S$=250° and a phase angle of 34° did not show any indications of this phenomenon, however imaging spectrometer data that we obtained six weeks later at opposition (near zero phase) did show distinct evidence of increased contrast in the blue [9,10], suggesting that significant changes in reflectivity can occur in global or localized areas on Mars over short timescales. Comparisons of these telescopic spectra (and others such as those of

[3,4]) with the Phobos-2 imaging data, acquired at $L_S$=3°-17°, may exhibit systematic variations of up to 5-10% due to such variations in flux in the visible.

A related source of variability is atmospheric dust load changes between August 1988 and February-March 1989. Variations in column abundance and/or surficial distribution of bright, very red dust particles (which may be the cause of brightening in the blue) are known to occur on both diurnal and seasonal timescales, with the greatest variability typically occurring near and shortly after perihelion when insolation is a maximum [11,12]. $Fe^{3+}$-rich dust will produce systematic variations mostly in the Phobos-2 NIR imaging channel due to its higher reflectance from 0.7-1.1 μm than from 0.4-0.61 μm [1,13]. Although difficult to quantify and highly longitudinally dependent, we estimate that variations in dust opacity over a low albedo region such as Sirenum can easily lead to 10-15% reflectance variations at NIR wavelengths for localized dust storms, or possibly up to 50% reflectivity variations during truly global dust storms that completely obscure the surface below [see also 14,15].

The combined effect of these VIS and NIR variabilities on the final NIR/VIS DN ratios is to introduce possibly significant uncertainty (perhaps as much as 10-15%) in the comparison with groundbased reflectance data which have not been simultaneously obtained. Unfortunately, we know of no 0.4-1.1 μm reflectance spectra of Mars obtained during February-March 1989 other than the Phobos-2 ISM imaging spectrometer data [16], which only extend down to 0.8 μm and did not image the Sirenum region. Preliminary work comparing Viking Orbiter and Phobos-2 color ratios of Phobos [5] seem to indicate, however, that these effects may not be serious for these data, thus allowing increased confidence in color unit mapping efforts.

References: [1] Bell III, James F., T.B. McCord, and P.D. Owensby (1989), submitted to *JGR Special Fourth Mars Colloquium Issue*. [2] Murchie, S., D.T. Britt, J.W. Head, S.F. Pratt, B.S. Zhukov, and A.A. Kuzmin (1989), *B.A.A.S., 21*, 957. [3] McCord, T.B. and J.A. Westphal (1971), *Astrophys. J., 168*, 141-153. [4] McCord, T.B., R.L. Huguenin, D. Mink, and C. Pieters (1977), *Icarus, 31*, 25-39. [5] Murchie, S. and 12 others (1990), *LPSC XXI*, this volume. [6] Bell, Jeffrey F., P.G. Lucey, J.C. Gradie, J.C. Granahan, D.J. Tholen, J.R. Piscitelli, and L.A. Lebofsky (1989), *B.A.A.S., 21*, 991. [7] Allen, C.W. (1973), Astrophysical Quantities, pp. 171-173. [8] Slipher, E.C. (1962), Mars: The Photographic Story, pp. 37-54. [9] Bell III, James F., T.B. McCord, and P.G. Lucey (1989), *Proc. 20th Lunar Planet. Sci. Conf.*, in press. [10] Bell III, James F., T.B. McCord, P.G. Lucey (1989), *EOS, Trans. Amer. Geophys. U., 70*, 50. [11] Martin, L.J. (1974), *Icarus, 23*, 108-115. [12] Zurek, R.W. and L.J. Martin (1989), *B.A.A.S., 21*, 980. [13] Singer, R.B. (1982), *JGR, 87*, 10159-10168. [14] Pollack, J.B., D.S. Colburn, F.M. Flaser, R. Kahn, C.E. Carlston, and D. Pidek (1979), *JGR, 84*, 2929-2946. [15] Briggs, G.A., W.A. Baum, and J. Barnes (1979), *JGR, 84*, 2795-2820. [16] Bibring, J.-P. and 16 others (1989), *Nature, 341*, 591-593. [17] Avanesov, G.A. and 43 others (1989), *Nature, 341*, 585-587.

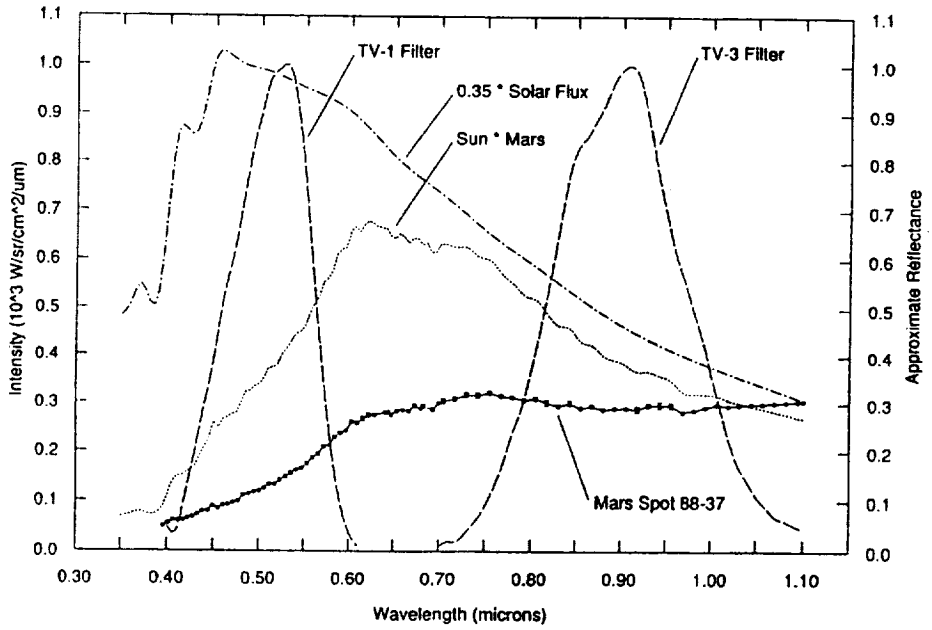


Figure 1: 1988 Mars CVF reflectance data (scale at right), Phobos-2 VSK bandpasses (normalized to 1.0) [17] and Solar Flux [7] and Mars*Solar Flux data (scale at left).

## Iron-enriched Smectite Clays as Mars Soil Analogs - Chemical Reactivity in the Labeled Release Experiment;

**T. Ben-Shlomo and A. Banin, Department of Soil and Water Science, The Hebrew University, Rehovot, Israel.**

On the basis of the martian soil elemental composition directly determined by the Viking landers, and through a computerized modelling-search it was proposed that the soil may contain phyllosilicate minerals of the smectite group mixed with iron oxides, and small amounts of carbonates and sulfate salts (1). Following this model and other data, it was suggested that significant amounts of iron in the martian soil may be associated with the smectite clays as adsorbed-precipitated oxide or oxyhydroxy iron phases (2, 3). In order to further examine this model a series of iron-enriched clays, containing iron at concentrations up to that found in Mars soil (ca. 19% $Fe_2O_3$) was prepared from a standard montmorillonite (SWy-1, the Clay Minerals Society) by the "Quantitative Ion Exchange Method" (4). The chemical and mineralogical properties of the clay and of the iron phase(s) formed in the system have been determined. The clay preparation procedure caused little change in the crystal lattice thus producing purified montmorillonite clay free of soluble salts and minor accessory minerals but with the predesignated proportion of adsorbed iron and precipitated iron oxides and oxyhydroxides, characterized by the chemical analysis and morphological study to be poorly ordered and of low crystallinity (5).

Reflectance spectra in the visible and near-IR wavelength range revealed increasing absorbance below 0.7$\mu$m with the increased iron addition. Such absorbance is characteristic to the Mars spectra. A broad absorbance band around 0.9$\mu$m was also developed as more iron was added . It was also found during recent telescopical observations (6). However, the pronounced spectral features of crystalline smectite in the near-IR (2.1-2.3$\mu$m) and in the IR range (doublet at 20$\mu$m) were not detected in the martian spectra (7, 8), indicating that crystalline smectite may not be a singular silicate phase in the martain soil.

Simulation of the Viking Landers Labeled Release (LR) experiment were carried by the $^{14}C$ absorption method ("Getter Technique") (2) with: (a) Iron enriched clays, prepared by chemical deposition by the quantitative ion exchange method, in which the concentration of added iron ranged from below the exchange capacity of the clay up to ~15%$Fe_2O_3$ bringing the total iron content to that found in the martain soil (Fig. 1). (b) A physical mixture of various crystalline iron oxides (maghemite, goethite and hematite) and short-range-ordered ferrihydrite with iron-saturated clay (Fe-Mont, 7%$Fe_2O_3$) at a constant added concentration of 12%wt $Fe_2O_3$, which add-up to the iron concentration found in the martain soil (Fig. 2). (c) Same as (b) but mixed with the crude SWy-1 montmorillonite (which was found to be nonactive during the LR simulation, probably for increasing the pH values) (Fig 2). (d) Same as (b) but the clay was mixed with 24%wt siderite ($FeCO_3$) (Fig. 2).

The presence of excess non-crystalline or poorly crystalline iron oxides at a high concentration beyond the exchange capacity systematically decreased the reactivity of the mixture (Fig. 1). However, iron-adsorbed clay (~7%$Fe_2O_3$) alone or when mixed with crystalline iron oxides up to 19%$Fe_2O_3$ in series (b), and with siderite (d), exhibited good match to the decomposition rate found on Mars (Fig. 2). The crystalline iron oxides mixed with the crude SWy-1 montmorillonite in series (c) did not simulate the LR reaction (Fig. 2). Levin and Straat reported also that hematite alone was not active in simulation of the LR reaction (9). The effect of the mixing of the less crystallized ferrihydrite with the iron clay in diminishing the reactivity (Fig. 2), is notably similar to that of the amorphous iron-oxides formed in situ (series a, Fig. 1). Addition of siderite to the iron clay did not cause a pronounced change in the decomposition rate (Fig. 2) although the addition of 12%wt magnesite ($MgCO_3$) or dolomite ($CaMg(CO_3)_2$) and only 2% calcite ($CaCO_3$) substantially decreased the decomposition reaction (data not shown).

It was suggested that the formate decomposition mechanism by the iron clay is mainly dehydrogenation, involving electron transfer to adsorbed $Fe^{3+}$ (2). The presence of excess amorphous iron oxide or oxyhydroxide precipitates, may perhaps interfere with this reaction partly by adsorbing the formate to the iron oxyhydroxide.

Thus, the presence of iron oxides per se is not sufficient to drive the decomposition reaction, and the iron phase(s) crystallinity and surface properties affect the kinetics and extent of the reaction. The presence of the reactive surface of iron smectites seems to be essential for the decomposition reaction measured by the Viking landers in the LR experiment.

References:
(1) Toulmin, P. III, Baird A.K., Clark B. C., Keil K., Rose H. J., J.R., Christian, R.P., Evans P.H. and W.C. Kelliher (1977) JGR 82, 4625-4634 (2) Banin, A. and Rishpon J. (1979) J. Mol. Evol. 14, 133-152. (3) Banin, A. (1986) "Clays on Mars", In Clays and the Origin of Life (H. Hartman and A.G. Cairns-Smith, eds.) pp. 106-115. (4) Banin A. (1973) U.S. Patent 3,725,528 April 3,1973 14pp. (5) Ben-Shlomo, T. and Banin A. (1989) submitted to the Proceedings of the 9th International Clay Conference. (5) Singer, R. B. (1982) JGR 87:10,159-10,168 (6) Bell, J. F., McCord T.B. and Owensby P.D. (1989) submitted to JGR special 4th Mars colloquium issue.(7) Roush, T. B., Pollack B. J. and Banin A. (1989) in the Fourth International Conference on Mars, Tucson, Arizona, January, 1989. (8) Ben-Shlomo, T. and Banin A. (1989) in the International Symposium on First Results of the Phobos-Mars Mission and Future Space Exploration, Paris, Oct. 1989. (9) Levin, G. V. and Straat P. A. (1981) Icarus 45:494-516. (This work was supported in part by the NASA Exobiology and Solar System Exploration Programs).

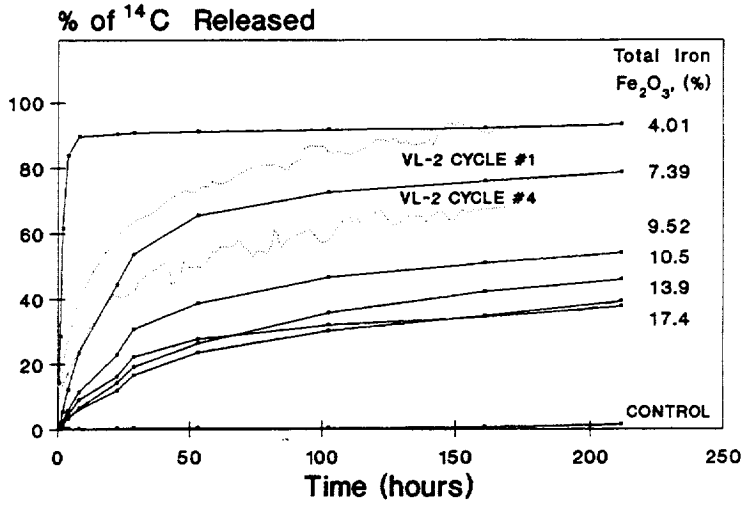


Fig 1: Decomposition of the LR medium by Mars soil in the Viking Labeled Release Experiment (VL-2), and in simulation experiments with sodium formate using H-Mont. (4.01%$Fe_2O_3$), Fe-Mont. (7.39%$Fe_2O_3$) and various iron enriched smectite clay preparations (series a).

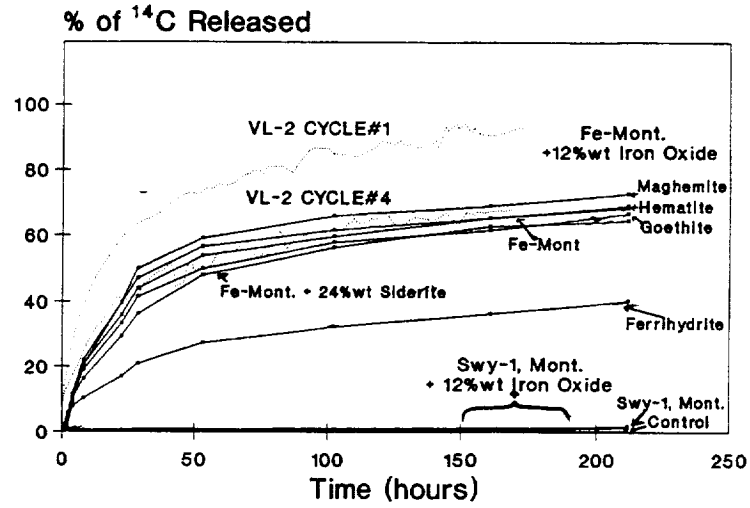


Fig 2: Decomposition of the LR medium by Mars soil in the Viking Labeled Release Experiment (VL-2), and in simulation experiments with sodium formate using iron oxides (maghemite, goethite, hematite and ferrihydrite) and iron carbonate (siderite) mixtures with iron saturated clay (series b and d respectively), and the iron oxides mixed with crude montmorillonite (SWy-1) (series c).

MARTIAN MANTLE PRIMARY MELTS

C.M. Bertka*, and J.R. Holloway Department of Geology, Arizona State University, Tempe, AZ 85287; *also at the Geophysical Laboratory, Carnegie Institution of Washington, 2801 Upton St. N.W., Washington D.C. 20008

INTRODUCTION:

Primary melts are liquid compositions in equilibrium with their mantle source region. Models that attempt to predict the diversity of lavas on a planet or outline the petrogenetic history of lavas require information about the chemical and physical properties of primary melts. These properties are determined by the bulk composition, modal assemblage, volatile content, and oxygen fugacity of the source region and by the degree of partial melting.

Most estimates of the bulk composition of the Martian mantle rely on calculations of mantle density. These calculations suggest that the Martian mantle is denser than the Earth's mantle, a difference that is attributed to an iron-enrichment of the Martian mantle(e.g.,1,2,3). Calculations of mantle density depend on knowledge of the mean moment of inertia of Mars. This value is poorly constrained and recently a lower estimate, which would result in a more Earth-like mantle iron abundance, has been proposed (4). However, if Mars is the parent body of SNC meteorites(5) then these samples help constrain the mantle composition independent of estimates of mantle density. Wanke and Dreibus (6) used element correlations between measured ratios in SNCs and chondritic abundances to predict a SNC parent body with a mantle enriched in iron relative to the earth. The purpose of this paper is to present our experimental melting phase equilibria data for an anhydrous Dreibus and Wanke mantle composition at 10, 20 and 30 kb.

EXPERIMENTAL TECHNIQUE:

Experiments were performed in an end-loaded piston cylinder apparatus with a 0.5" diameter solid-media pyrex-NaCl-AlSiMag cell assembly. Starting materials were synthesized from spec pure oxides ground under ethanol in an agate mortar for one hour , reduced in a gas mixing furnace (1000° C, fO2 at one log unit below QFM) for 24 hours and reground in a carbide container to less than 5um. Approximately 10 mgs of the starting composition was sealed in graphite-lined platinum capsules. Run duration varied from 48 hours at near solidus temperatures to 1 hour at near liquidus temperatures.

RESULTS:

Phase equilibria data for the Dreibus and Wanke, (DW) mantle composition at 10, 20 and 30 kb are shown in Figure 1. Experimental Fe/Mg distribution coefficients for ol / opx and gt / cpx pairs in the subsolidus runs are in good agreement with previously determined values (7,8). A spinel lherzolite assemblage is stable to at least 20kb, but the subsolidus spinel phases are less than 10um in size and exhibit variations of up to 7 wt% in aluminum and chrome contents. Mass balance calculations to express the DW mantle composition as proportions of the analyzed subsolidus phases were performed with a least squares fit technique. In all cases the calculated modes duplicate the starting composition with a total error of less than 1.5 wt%, most of which can be attributed to poor spinel analysis.

Enough melt accumulated at the top of some of the charges run in the opx+ol+liq and the ol+liq fields that the resulting quench crystals + glass material could be analyzed by rastering a 2-um beam across a 20-um x 20-um area. The analyzed melts are komatiitic. Experimental Fe/Mg ol/melt and ol/opx distribution coefficients also compare favorably with previously determined values (9,7) and mass balance calculations duplicate the starting composition with a total error of less than 2.5wt%.

DISCUSSION:

Compared to the earlier model Martian mantle bulk compositions, (i.e. Morgan and Anders(2), Goettel(3) ), and the proposed terrestrial undepleted mantle samples, (PHN 1611 (10), KLB-1(11)), the DW composition has a greater modal abundance of orthopyroxene (12) largely at the expense of olivine or clinopyroxene. Partial melting of a DW lherzolite assemblage produces a larger temperature interval of primary melts in equilibrium with only olivine and orthopyroxene. Our data indicates a minimum interval of 200° C at 10kb and 120° C at 20 kb. Experimental data for KLB-1 at 15kb (13) and PHN1611 at 20kb (14) indicate maximum olivine + orthopyroxene + melt intervals of 100°C. The primary melt compositions produced in this interval will be picritic to komatiitic. Tholeiitic and alkali basalt melts are expected to be produced at lower degrees of partial melting, before clinopyroxene or the aluminous phase are exhausted. However, the relative abundance of these primary magma types compared to the komatiitic

melts can not be evaluated without additional data. Although clinopyroxene is present in subsolidus experimental assemblages it is absent above the solidus except in two experimental charges from the spinel lherzolite field at 15 and 20kb. These charges were equilibrated at temperatures well above the solidus then lowered in temperature to the solidus. Their clinopyroxene compositions are very similar to those found in the subsolidus runs. This data suggest that clinopyroxene may melt out of the spinel lherzolite assemblage within 20° C of the solidus. Our previous experimental work (12) suggested that an iron-rich lherzolite assemblage would yield a picritic alkali basalt at small degrees of melting.

The surface features of Martian lava flows are often attributed to high eruption rates and/or low viscosity magmas (e.g.,16 ). Our previous work (17) suggested that the picritic alkali basalt produced at low degrees of partial melting at 23kb has a viscosity of 3 poise at source region pressure; similar in magnitude to its calculated 1atm. values at the same temperature. This viscosity is much smaller than that measured for a terrestrial tholeiite composition at 20kb and near liquidus temperatures, 25 poise(18) but similar in magnitude to 1atm. calculated values for a terrestrial alkali basalt at its 30kb liquidus temperature. Magma ascent rates or crystal fractionation processes in the two planets for any given primary melt type (i.e, alkali basalt, tholeiite,komatiite) may be more sensitive to gravitational differences between the two planets than to viscosity differences between the melts at their respective liquidus temperatures. Additional near solidus phase equilibria data for the model DW Mars mantle should reveal whether or not the bulk composition and resulting modal mineralogy favor the production of low viscosity picritic and komatiitic primary melts.

References. 1) McGetchin, T.R. and Smyth, J.R. (1978) *Icarus* 34, 512-536. 2) Morgan, J.W. and Anders, E. (1979) *Geochim. Cosmochim. Acta* 43, 1601-1610. 3) Goettel, K.A. (1981) *Geophys. Res. Lett.* 8, 497-500. 4) Bills, B.G. (1989) abst. *Lunar and Planet. Sci. XX,* 74. 5) McSween, H.R. (1985) *Rev. Geophys.* 23, 391-416. 6) Wanke, H. and Dreibus, G. (1988) *Phil. Trans. R. Soc. Lond.* A 325, 545-557. 7) Mori, T. and Green, D.H. (1978) *J. Geol.* 86, 83-97. 8) Ellis, D.J. and Green, D.H. (1979) *Contrib. Mineral. Petrol.* 71, 13-22. 9) Roeder, P.L. and Emslie, R.F. (1970) *Contrib. Mineral. Petrol.* 29, 275-289. 10) Nixon, P.H. and Boyd, F.R. (1973) in *Lesotho Kimberlites*, ed. P.H. Nixon. 11) Carter, J.L. (1970) *Geol. Soc. Am. Bull.* 81, 2021-2034. 12)Bertka, C.M. and Holloway, J.R. (1987) *Proc. lunar Planet. Sci. Conf.* 18, 723-739. 13) Takahashi, E. (1985) *J. Geophys. Res.* 91, 9367-9382. 14) Mysen, B.O. and Kushiro I. (1977) *Amer. Mineral.* 62, 843-865. 15) Schonfeld, E. (1979) abst. *Lunar and Planet. Sci. IX*, 1063. 16) Bertka, C.M, and Holloway , J.R. (1989) abst. *Lunar and Planet. Sci. XX,* 69. 17) Kushiro, I., Yoder, H.S. and Mysen, B.O. (1976) *Jour. Geophys. Res.* 81, 6351-6356. 18) Leshin, L.A., Holloway, J.R., and Bertka, C.M. (1988) abst. *Lunar and Planet. Sci. XIX,* 67.

Figure 1. DW Anhydrous Experimental Phase Assemblages

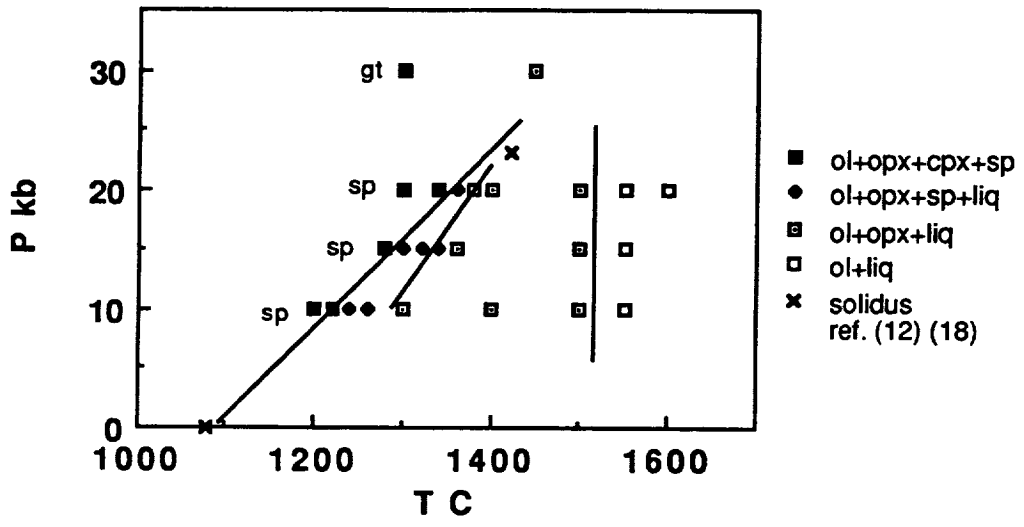

DIGITAL MOSAIC AND ELEVATION MODEL OF CENTRAL VALLES MARINERIS, MARS; L. M. Bertolini, A.S. McEwen, U.S. Geological Survey, Flagstaff, AZ 86001

We have geometrically controlled 143 Viking Orbiter 1 images to produce a digital mosaic of the central Valles Marineris region of Mars. The mosaic covers most of Ophir, Candor, and Melas Chasmata and covers approximately $+1^{o}$ to $-15^{o}$ latitude and $65^{o}$ to $75^{o}$ longitude. The image frames are PICNOS 910A01-917A20, red filter and nadir looking; illumination and phase angles both range from 55 to 65 degrees. Noise removal by box filtering [1], radiometric correction, and all other image processing were done by using the Planetary Image Cartography System (PICS). The image frames were transformed into sinusoidal Equal Area projections at a scale of 1/1024 degree/pixel (approximately 58 m/pixel) prior to mosaicking. The geometric control and format are consistent with those of the Mars Digital Image Model project [2,3].

We obtained measurements of landslides and other features from the controlled images using the photoclinometric program TVPROF (on single images) and the program TVSTEREO on pairs of images. For TVPROF [4], which produces topographic profiles, we used a variety of photometric models and parameters to constrain the slope values. TVSTEREO calculates relative heights. Measurements include those of landslide drops, deposit thicknesses, and slopes of canyon walls. The data will be used to refine estimates and to make additional ones of landslide volumes and yield strengths [5].

In addition, we prepared a digital elevation model of the region from $-3^{o}$ to $-7.6^{o}$ latitude and from $70^{o}$ to $75^{o}$ longitude from a 1:500,000-scale (200-m contour interval) topographic map [U.S.Geological Survey, work in progress]. The topographic map was first digitized into vector format, then transformed into raster format of the same map projection and scale as the digital mosaic; the contour lines were then interpolated to produce the digital elevation model. From the coregistered mosaic and digital topographic data, synthetic oblique views were generated from the north, south, east, and west. When producing an oblique view, we can specify viewpoint elevation and azimuth and vertical exaggeration. The oblique views provide versatile imaging of geologically important areas and their topography. These data will eventually be used to make 3-dimensional movies of the terrain.

REFERENCES

[1] Eliason, E. M., and McEwen, A.S. Adaptive box filters for removal of random noise from digital images. Photogrammetric Engineering and Remote Sensing (in press).

[2] Batson, R.M. (1987) Digital cartography of the planets: New methods, its status, and its future. Photogrammetric Engineering and Remote Sensing 53, 1211-1218.
[3] Edwards, K. (1987) Geometric processing of digital images of the planets. Photogrammetric Engineering and Remote Sensing 53, 1219-1222.
[4] Davis, P.A., and Soderblom, L.A. (1984) Modeling crater topography and albedo from monoscopic Viking Orbiter images. J. Geophys. Res. 89, B11, 9449-9457.
[5] McEwen, A.S. (1989) Mobility of large rock avalances: Evidence from Valles Marineris, Mars. Geology 17, 1111-1114.

PRELIMINARY QUANTITATIVE ASSESSMENT AND ANALYSES OF PHOBOS 88 TERMOSKAN OBSERVATIONS OF MARS; B. H. Betts, T. Svitek, M. L. Santee, B. C. Murray, D. Crisp, California Institute of Technology, D. A. Paige, University of California at Los Angeles, M. Naraeva and A. Selivanov, Institute of Space Devices, Moscow.

In February and March, 1989, the Termoskan instrument onboard the Phobos '88 spacecraft of the USSR acquired a limited set of very high resolution simultaneous observations of the reflected solar and thermal emission from Mars' equatorial region. We have analyzed quantitatively approximately 20% of the entire data set and here present three preliminary analyses: a comparison of Termoskan data with Viking Infrared Thermal Mapper (IRTM) data; an analysis of thermal infrared limb brightening seen on the morning limb and other preliminary limb analysis results; and an analysis of one observation of the shadow of the moon Phobos as observed on Mars by Termoskan.

THE EXPERIMENT: Termoskan was a two channel optical-mechanical scanning radiometer with one visible channel (0.5-1.0 μm and one thermal infrared channel (8.5-12.0 μm). The instrument was fixed to the spacecraft, pointing in the anti-solar direction. Resolution per pixel at nadir was 1.8 km for 3 of the 4 panoramas acquired and 300 meters for the remaining panorama.

COMPARISON WITH IRTM OBSERVATIONS: To determine the absolute accuracy of the Termoskan data set, we compared it with the well calibrated Viking IRTM measurements. We compared brightness temperatures from Termoskan infrared observations to brightness temperatures from IRTM's 11 micron channel (9.8 to 12.5 μm). We constrained the IRTM data to match approximately the Termoskan data in season ($L_s$), longitude, latitude, and local time of day. In order to compare the two data sets, we degraded the Termoskan resolution to a resolution comparable to Viking. Figure 1 shows a representative Termoskan-IRTM comparison which is consistent with other areas that we have compared. We find that the Termoskan brightness temperatures are approximately 3 K warmer than corresponding IRTM brightness temperatures; that relative features correlate very well in the two data sets; and that Termoskan sees thermal variations even at the limit of its spatial resolution.

TERMOSKAN LIMB PROFILES: Limb brightening in the Termoskan thermal infrared channel from the morning limb was consistently observed. Figure 2 shows a sample morning limb profile. We explain the peak in thermal brightness just off the limb as a consequence of an ice or dust haze in equilibrium with the atmosphere, which is warmer than the pre-dawn surface. Paige used a delta-Eddington spherical shell model developed for the Mars Observer limb sounder PMIRR (Pressure Modulator Infrared Radiometer), and found that a water ice haze with a scale height of 5 km (isothermal atmosphere at 200 K, surface at 175 K) could produce a thermal brightness signature matching the one in Figure 2. The visible channel defines a highly scattering atmosphere to extend 60 to 70 km above the limb. Figure 3 shows a sample evening limb profile. The absence of any infrared evening limb brightening is consistent with a surface which is warmer than the atmosphere . On the evening limb a high haze was observed which may correlate well with that seen by the Phobos '88 AUGUST experiment.

PHOBOS SHADOW MEASUREMENTS: Termoskan observed the shadow of Phobos on the surface of Mars during two of its four scans. Due to the scanning nature of the instrument and the similarity of the spacecraft's orbit to that of Phobos, the shadow appears elongated in the images. We have looked at one shadowed region south of Arsia Mons. We used the observed drop in visible flux within the shadowed area to model the solar insolation as a function of both actual time since the beginning of eclipse and position in the scan. We then used this in an adaptation of the Clifford et al., 1987 one dimensional, finite difference thermal model for a homogeneous surface [1]. By comparing the model results with the temperature drops observed in the infrared scan we find thermal inertias varying from 0.7 to 1.1 ($10^{-3}$ cal $cm^{-2}$ $s^{-1/2}$ $K^{-1}$). These values of thermal inertia are lower by factors of 2 to 4 compared to thermal inertias derived from Viking IRTM measurements [2] for the same area. Viking-derived inertias are sensitive to the upper few centimeters of the surface, whereas the Phobos shadow measurements are sensitive only to the upper tenths of a mm of the surface due to the short duration of the

eclipse. Our results imply that there is a thin layer of highly insulating material, for example a thin, loosely packed dust layer, on the surface which overlies a layer of less insulating material.

REFERENCES: (1) Clifford, S.M., C.J. Bartels, and E.P. Rubenstein (1987), Lunar and Planetary Institute; (2) Kieffer, H.H., T.Z. Martin, A.P. Peterfreund, B.M. Jakosky, E.D. Miner, F.D. Palluconi (1977), Journal of Geophysical Research, 82 (28), pp. 4249-4291.

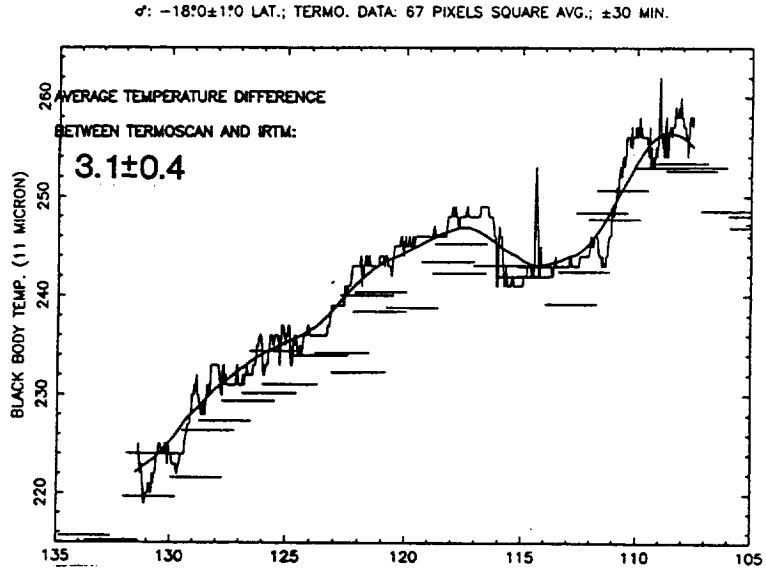


Figure 1: Comparison of Termoskan data with analogous IRTM data for a 2 degree wide strip of constant latitude centered on -18 degrees. The dark line represents a sliding boxcar average of Termoskan data which has been averaged in 2 x 2 degree squares. The lighter line is a 1 pixel Termoskan strip for reference. The points represent IRTM data with the error bars representing the footprint of each IRTM data point. IRTM data is constrained to match the Termoskan data to within ±10 degrees of $L_s$ and to within ±30 minutes of local time. After comparing each IRTM point with the averaged Termoskan point of the same longitude, the average temperature difference between Termoskan and IRTM is 3.1±0.4 K with the Termoskan temperatures being warmer. Local time of day in the data shown ranges from about 8.5 to 10.3.

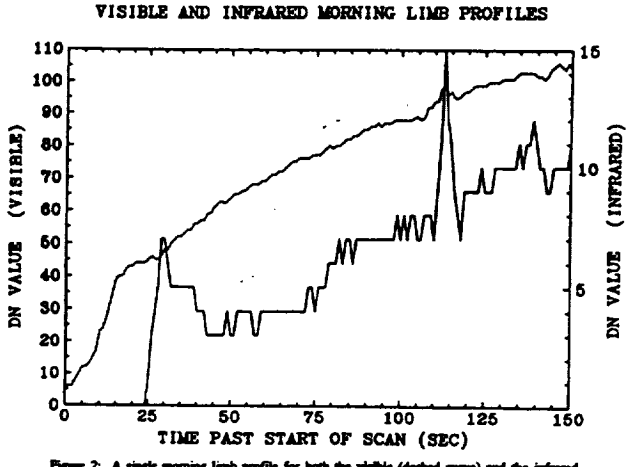


Figure 2: A single morning limb profile for both the visible (dashed curve) and the infrared (solid curve) channels. The solid limb was encountered at approximately 26 seconds after the start of the scan.

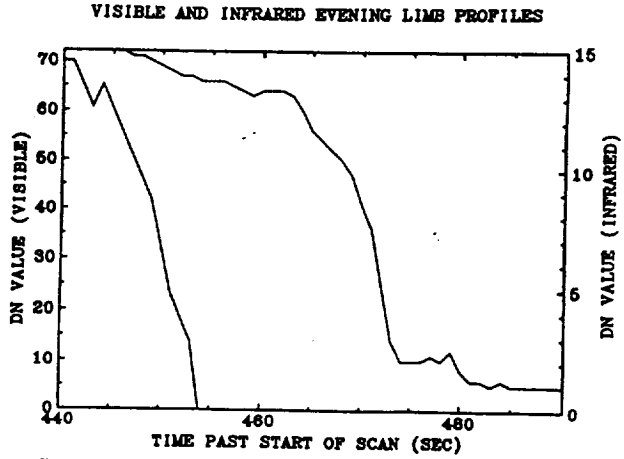


Figure 3: A single evening limb profile for both the visible (dashed curve) and the infrared (solid curve) channels. Note that the times on the horizontal axis are local to the particular data file and do not represent actual times along the scan. Note the peak in visible brightness at 479 seconds which is a distinct cloud feature.

**OBLIQUITY HISTORIES OF EARTH AND MARS: INFLUENCE OF INERTIAL AND DISSIPATIVE CORE-MANTLE COUPLING**; Bruce G. Bills, LPI, Houston, TX

For both the Earth and Mars, secular variations in the angular separation of the spin axis from the orbit normal are suspected of driving major climatic changes (1,2,3,4). There is thus considerable interest in determining, as accurately as possible, the amplitude and timing of these obliquity variations. If the orientation of the orbital plane were inertially fixed, and the planet were to act as a rigid body in its response to precessional torques, the spin axis would simply precess around the orbit normal at a fixed obliquity $\epsilon$ and at a uniform angular rate $\alpha \cos(\epsilon)$. The precession rate parameter

$$\alpha = \frac{3}{2} \frac{(C-(A+B)/2)}{C\omega} \sum \mu_i/(b_i)^3 \qquad [1]$$

depends on the principal moments of inertia ($A \leq B \leq C$) and rotation rate $\omega$ of the perturbed body, and on the gravitational masses $\mu = GM$ and semiminor axes $b = a(1-e^2)^{1/2}$ of the perturbing bodies. For Mars, the precession rate is not well known, but probably lies in the interval 8-10 arcsec/year (5,6,7,8,9,10). The much larger precession rate for the Earth (~50.3 arcsec/year) is partly due to greater proximity to the Sun (which contributes roughly 1/3 of the total), but is mostly due to the presence of the Moon (11).

Gravitational interactions between the planets lead to secular motions of the orbit planes of the form

$$\sin(I)\, e^{i\Omega} = \sum N_j e^{i(s_j t + \delta_j)} \qquad [2]$$

where I and $\Omega$ are the inclination and longitude of the node, and $N_j$, $s_j$ and $\delta_j$ are amplitudes, rates and phase constants (12,13). In the rigid body case, the spin axis still attempts to precess about the instantaneous orbit normal, but now the obliquity varies. A first order solution for the obliquity can be written in a form similar to [2] but with amplitudes $K_j N_j$, where the admittance $K_j$ has the value (14,15,16)

$$K_j = \frac{s_j}{s_j + \alpha \cos(\epsilon)} \qquad [3]$$

As the orbital precession rate constants $s_j$ are all negative and fall within the range {-26.3 arcsec/year $\leq s_j \leq 0$}, while the spin precession rate constants are positive, the potential exists for significant resonant amplification of the obliquity if the denominator of [3] approaches zero (17,18). The possibility of actual singularities in [3] is not too worrisome, as the linear analysis leading to that form of the admittance is no longer applicable in the immediate vicinity of a resonance. However, the physical model of rigid rotation which leads to that formula is almost certainly too simplistic.

The hydrostatic figure of a planet represents a compromise between gravitation, which attempts to attain spherical symmetry, and rotation, which prefers cylindrical symmetry (19). Due to their higher mean densities, the cores of the Earth and Mars will be more nearly spherical than the outer layers of these planets. The direct gravitational torques on the core will thus be inadequate to make it precess at the same rate as the mantle. For the Earth, where the structure is relatively well known, the core oblateness is only about 3/4 that required for coprecession with the mantle (20). However, it is clearly the case that the core and mantle precess at very nearly the same rate (21,22). Two different types of torques contribute to the coupling.

## CORE-MANTLE COUPLING: Bills, B.G.

On short time scales it is appropriate to consider the core to be an invisid fluid constrained to move within the ellipsoidal region bounded by the rigid mantle (23,24). The inertial coupling provided by this mechanism is effective whenever the ellipticity of the container exceeds the ratio of precessional to rotational rates. If the mantle were actually rigid, or even elastic, this would be an extremely effective type of coupling. However, on sufficiently long time scales, the mantle will deform viscously and can accomodate the motions of the core fluid. The inertial coupling torque exerted by the core on the mantle will have the form $T_i = k_i [\omega_m \times \omega_c]$. A fundamentally different type of coupling is provided by electromagnetic or viscous torques (25,26). The dissipative coupling torque exerted by the core on the mantle will have the form $T_d = -k_d [\omega_m - \omega_c]$. This type of coupling is likely to be most important on longer time scales. In each case, the mantle exerts an equal and opposite torque on the core.

The admittance which relates inclination amplitude to obliquity amplitude is now a complex quantity which can be written in the following form (27,28)

$$K(s) = \frac{s(s + a_m + \eta)}{(s + a_m)(s + a_m + \eta) - \Delta a\, \eta_m} \qquad [4]$$

The coupling constants are rescaled ($\beta_m = k_d/C_m$, $\gamma_m = \omega \cos(\epsilon)\, k_i/C_m$) and then combined to form a single complex parameter $\eta_m = \gamma_m - i\beta_m$. Also, $a_m = \alpha_m \cos(\epsilon) + \cos(I)\, d\Omega/dt$. Core parameters ($a_c, \beta_c, \gamma_c, \eta_c$) are defined analogously, and the sum of core and mantle parameters $\eta = \eta_m + \eta_c$ is left unsubscripted, and $\Delta a = a_m - a_c$. Viscous relaxation of the mantle is included by multiplying both $\gamma$ values by $(is\tau)/(1+is\tau)$, where $\tau$ is the effective Maxwell relaxation time of the mantle.

There are several features to note, in comparing [3] and [4]. As is typical of a forced oscillation with damping, the response now lags the forcing by an amount which depends on the frequency of forcing and the strength of the viscous coupling. The most evident difference in response is near resonance, since [4] exhibits no singularities. However, even away from resonance, the inclusion of possible differential precession can modify the obliquity history by amounts that could have climatic significance. Unfortunately, the coupling constants are not well known, even for the Earth, and are almost completely unconstrained for Mars. Thus, some caution is advised in constructing climatic history scenarios which depend on details of the obliquity history.

**References:** (1) M. Milankovitch, Konin. Serbische Akad., 484p, 1941; (2) A.L. Berger et al. (eds.) Milankovitch and Climate, D. Reidel, 1984; (3) O.B. Toon et al., Icarus 44, 552-607, 1982; (4) S.M. Clifford et al., Eos 47, 1585-1596, 1988; (5) P. Lowell, Astron. J. 28, 169-171, 1914; (6) W.M. Kaula, Geophys. Res. Lett. 6, 194-196, 1979; (7) B.G. Bills, Geophys. Res. Lett. 16, 385-388, 1989; (8) B.G. Bills, Geophys. Res. Lett. 16, 1137-1338, 1989; (9) A.T. Sinclair, Astron. Astrophys. 220, 321-328, 1989; (10) T.A. Morley, Astron. Astrophys. (in press) (11) H. Kinoshita, Celest. Mech. 15, 277-326, 1977; (12) P. Bretagnon, Astron. Astrophys. 30, 141-154, 1974; (13) J. Laskar, Astron. Astrophys. 198, 341-362, 1988; (14) S.G. Sharaf, & N.A. Budnikova, Trud. Inst. Teor. Astron. 11, 231-261, 1967. (15) W.R. Ward, J. Geophys. Res. 1974; (16) A. Berger, Celest. Mech. 15, 53-74, 1977; (17) W.R. Ward et al., J. Geophys. Res. 83, 243-259, 1979; (18) W.R. Ward, Icarus 50, 444-448, 1982; (19) Z. Kopal, Figures of Equilibrium of Celestial Bodies, U. Wisc. Press, 1960; (20) M.L. Smith & F.A. Dahlen, Geophys. J. R. Astr. Soc. 64, 223-281, 1981; (21) E.C. Bullard, Proc. Roy. Soc. A197, 433-453, 1949; (22) F.D. Stacey, Geophys. J. R. Astr. Soc. 35, 47-55, 1973; (23) H. Poincare, Bull. Astr. 27, 321-356, 1910; (24) A. Toomre, Geophys. J. R. Astr. Soc. 38, 335-348, 1974; (25) S. Aoki, Astron. J. 74, 284-291, 1969; (26) M.G. Rochester, J. Geophys. Res. 67, 4833-4836, 1962. (27) P. Goldreich & S.J. Peale, Astron. J. 75, 273-284, 1970; (28) W.R. Ward & W.M. DeCampli, Astrophys. J. Lett. 230, 117-121, 1979.

**Implications of the low carbonate abundance in the optical surface of Mars.** **Diana L. Blaney. Planetary Geosciences Division, Hawaii Institute of Geophysics, 2525 Correa Rd. Honolulu, HI 96822.**

There are two major reasons for expecting carbonates on Mars: 1) if Mars underwent a period of climatic warming due to a thicker CO2 atmosphere, carbonates would have formed at a rapid rate (1,2) and 2) the thermodynamically stable weathering products of igneous material on Mars under current conditions also include carbonates (3). Earth-based spectroscopy of the Martian surface in the 4.0 μm region has placed an upper limit on the carbonate abundance of < 1 - 3 wt% in the optical surface of the regions measured based on laboratory mixing models (4,5). The implications for weathering and climate change on Mars using various models to explain the low carbonate abundance are presented.

**Model 1. The observed upper limit on carbonate abundance (i.e. <1 wt%) is representative of the Martian regolith.** A 1 km mega-regolith with 1 wt% carbonate could at most contain 0.6 bars of CO2 (2), well short of the 3-5 bars (2,6,7) needed for global warming by a CO2 greenhouse at average orbital parameters.

A consequence of an early wet warm Mars is that liquid water would be present to remove CO2 from the atmosphere by formation of carbonates would occur at rates of approximately 1 bar CO2 removed every $10^7$ years (1,2). If the low carbonate abundance observed (0.6 bars), accurately reflects the planetwide inventory, then a 3-5 bar early greenhouse lost most of its CO2 by other mechanisms and had a duration of a few million years. A short greenhouse contradicts the geomorphic evidence which shows valley networks (a major geomorphic feature supporting an early greenhouse), forming during throughout the first billion years. Recycling carbonate to replenish the atmospheric CO2, whether by volcanic (2) or by impact (8) processes, may be able to extend the length of the greenhouse, but the last few bars would have to have been stored in the near surface environment (i.e. if you are forming carbonates by surface water, the last carbonates formed must be near the surface).

A low carbonate abundance would also imply that the weathering products observed (i.e. the dust) are not the thermodynamically stable end-members of weathering under current ambient Martian conditions. As an illustration, consider the thermodynamically stable decomposition products from the weathering of basalt of the same composition as Shergotty. Shergotty is a basaltic achondrite from the SNC (S=Shergotty, N=Nakhla, and C=Chassigny) group of meteorites. SNC are thought for a variety of reasons to come from Mars (e.g. 9). The weathering products of a Shergotty-like basalt which has reached thermodynamic equilibrium by gas-solid interactions at 240°K and current Mars atmospheric conditions, based on (3) indicate a total carbonate abundance of 32.48 wt %. If the 1 wt% carbonate in the dust is a reasonable upper limit, then about only about 3% of the dust could have formed by gas solid reactions carried to equilibrium. The majority of the dust would have formed by other processes. Similarly, if liquid water containing dissolved CO2 and O2 from the current Mars atmosphere were involved, again based on (3), the end products would contain 18.07 wt% carbonate, leaving 5.5 wt% of the dust to form by this process. Clearly, either the majority of the dust formed by processes other than surface weathering under current ambient conditions, or the formation process has been halted mid-way by kinetic barriers leaving metastable products.

**Model 2. Carbonate deposits are located at depth.** Carbonates deposits at depth are impossible to detect with spectroscopy, as spectroscopy looks only at the optical surface. Previous models calling for the recycling of carbonates to sustain an early greenhouse (2,8) assume that carbonates are well mixed in the regolith. Carbonate recycling rates from both impact and volcanic burial are too slow to replenish the carbon dioxide fixed as carbonates by liquid water (8). Carr (1989) suggested that the rate of carbonate fixation may have been overestimated. If liquid water was not continuously present on the surface, then carbonate formation would have preceded at a much slower rate. Temperatures, while warmer than the current epoch, would have remained just below the point at which liquid water could exist. Ground water would be close to the surface and under proper hydrostatic conditions would break out and form valley networks. Even with the slower carbon dioxide fixation rates, carbonates would form in the near surface environment where they should be detectable. Thus, a mechanism to for locating carbonates at depth is needed.

An alternative hypothesis calls for stratified carbonate layers. If carbonates exist at depth in stratigraphically localized deposits a possible formation scenario could be: a) Mars is warm, valley networks form; b) carbonates form rapidly, decreasing the atmospheric CO2 pressure until temperatures drop below the temperature needed to keep liquid water around to form carbonates; c) carbonate formation ceases and volcanic and impact processes bury the carbonates; d) carbonates are buried to a depth where rapid decrepitation occurs, releasing a pulse of CO2; e) the released CO2 causes another episode of greenhouse warming and valley network formation, and carbonates begin to form again. If a carbonate decrepitation depth of about 17 km, as suggested by Carr (1989), is valid then the cycle of rapid carbonate formation followed by burial could repeat itself about 10 times in the first billion years according to liquid stirring models (8). Declining impact rates would then slow the burial rates, leaving the carbonate layer stratified somewhere in the Martian crust. There is some geomorphic evidence for a strength discontinuity at about 1 km depth (10) which

could be a carbonate layer. Geochemical arguments which focus on the calcium deficiency of the Viking fines when compared to SNC meteorites also indicate that a carbonate layer may be present at depth (11).

**Model 3. The low carbonate abundance is the result of secondary weathering processes which have removed carbonates from the regolith.** The presence of the sulfate in the Martian fines measured by Viking Landers 1 and 2 (12), may have major implications for carbonate abundance.

The stability of carbonates in the presence of gaseous SO2 has been addressed by (13) and (14) with differing results. Clark et. al. (13) performed laboratory experiments which indicated that carbonates decompose readily in the presence of SO2 leaving sulfates. Sidorov and Zoltov (14) examined kinetic constraints and showed that the reaction encounters a kinetic barrier which would make this reaction negligible. Understanding the possible role of SO2 in destroying carbonates is critical in understanding the composition and evolution of the fines at the Martian surface. Alteration of the surface by airborne reactive components may be a major process in the formation of salts on Mars.

Settle (15) proposed a sulfate aerosol model for the formation of the sulfate duracrust at the Viking sites. The acidic nature of these aerosols would tend to decompose carbonates readily. If carbonates do decompose in the presence of SO2 vapor or sulfate aerosols, CO2 would be released from the decomposed carbonates back into the Martian atmosphere. A terrestrial example of aerosol formed salts are the sulfate and nitrate deposits form in Antarctica from the deposition of stratospheric anions, which react with local rocks which provide the cations to form these deposits (16).

Carbonates and sulfates must be considered together. If carbonates are absent from the surface due to interactions with volcanic aerosols, then the rate of SO2 released by volcanoes on Mars must be greater than the rate of regolith overturn exposing new carbonates. Fresh craters which have occurred after the height of volcanism would be expected to show evidence of carbonates brought up from depth. The rates of both volcanism and cratering were higher during the early portion of Martian history than at the present (e.g. 17, 18). If the sulfur in the Martian regolith is the result of sulfate aerosol deposition throughout Martian history, then the release of CO2 by sulfate aerosols may have played a critical role in the rapid recycling of CO2 throughout Martian history.

**Model 4. Weathering environments on Mars did not form carbonates.** The majority of materials examined on the Martian surface are weathering products formed by unknown mechanisms. As discussed previously, the expected carbonates from surface atmospheric interactions do not seem to be present in large quantities in the optical surface of Mars. Processes unique to Mars may have formed the observed dust. A weathering mechanisms which may have created the dust is impact ejecta from volatile rich targets (19).

In addition to the hydrothermal alteration of material in throughout sheets, Kieffer and Simonds (19) proposed that a fine ash deposit formed by the rapid expansion of silicate melt/vapor by superheated steam from pore water or by carbon dioxide from decrepitated carbonates. The ash formed by the interaction of melt and vapor and would occur at the top of the crater's stratigraphic sequence. Erosion has removed this ash layer from terrestrial craters which, by analogy with melt sheets from impacts into crystalline material, would be 1-5% of the volume excavated. Impacts into volatile rich material provide a way of producing a large volume of fine grained material of unknown composition. The alteration of the melt in the vapor cloud would be controlled by the dominant volatile propelling the expansion of the melt-vapor cloud. Thus, if water was the principle volatile, oxidation and hydration products would dominate and little if any carbonate would form. Due to the speed with which this event would occur, the altered material would be poorly crystalline or crystalline on a small scale.

**References:** 1. Fanale F. P. et al., *Icarus, 50,* 381-407, 1982. 2. Pollack, J. B. et al., *Icarus ,71,* 203-224, 1987. 3. Gooding, J.L., *Icarus, 33,* 483-513, 1978. 4. Blaney, D.L., and T.B. McCord,*J. Geophys. Res., 94,* 10,159-10,166,1989. 5. Blaney, D.L. and T.B. McCord, submitted to *J. Geophys. Res.,* 1990. 6. Pollack, J. B, *Icarus* 37, 479-553, 1979. 7. Postowko S.E. and W.R. Kuhn, *J. Geophys. Res., 82,* 4635-4639, 1986. 8. Carr, M. H., *Icarus*, in press, 1989. 9. McSween, H.Y.,*Rev. Geophys., 23,* 391-416, 1985. 10. Soderblom L.A. and D.B. Wenner, *Icarus*, 34, 622-637, 1978. 11. Warren, P.H., *Icarus, 70,* 153-161, 1987. 12. Clark, B.C. et al., *J. Geophys. Res.,87,* 10,059-10,068, 1982. 13 Clark B.C.e al. *J. Mol. Evol.,* 14, 91-102, 1979. 14. Sidorov Yu. I. and M. Yu Zolotov, In S.K. Saxena (ed.), *Chemistry and Physics of Terrestrial Planets*, Adv. Geochem. Vol. 6, Springer-Verlag, New York, p. 191-223, 1986. 15. Settle, M., *J. Geophys. Res., 84,* 8,343-8,354, 1979. 16. Campbell, I.B., and G.G.C. Claridge, *Antarctica: Soils, Weathering Processes and Environment, Developments in soil science 16*, Elsevier Science Pub. B.V., New York, N.Y., 1987. 17. Greeley, R. and P. Spudis, *Rev. of Geophys. and Space Phys., 19* , 13-41, 1981. 18. Neukum, G. amd K. Hiller, *J. Geophys. Res, 86,* 3097-3121, 1982. 19. Kieffer, S.W., and C.H. Simonds, *Rev.of Geophys. and Space Phys., 18,* 143-181, 1980.

**Earth-Based Telescopic Observations of Mars in the 4.4 μm to 5.1 μm Region. Diana L. Blaney and Thomas B. McCord. Planetary Geosciences Division, Hawaii Institute of Geophysics, 2525 Correa Rd. Honolulu, HI 96822.**

**Measurements.** The telescopic measurements of Mars reported here were made on August 19, 1988 UT at the NASA IRTF facility. Spectra were obtained with the Cooled Grating Array Spectrometer (CGAS) which utilizes a thirty-two element InSb line array with a resolution of R=300. Measurements were made by taking data at two different grating positions, with an eleven channel overlap between positions. Segment 1 covered 4.405 μm - 4.86 μm, and segment 2 covered 4.67 μm - 5.13 μm. Spectra were normalized to unity at 4.71 μm and were reduced using the star BS437 as a standard. A 2.7 arc-second aperture was used, producing a spot size 900 km in diameter at the sub-earth point. The measurements were taken as part of a sequence of measurements which also covered the wavelength region between 3.2 μm and 4.2 μm using three grating positions discussed(1).

The Martian atmosphere has a large number of atmospheric absorptions from both CO and CO2 in the wavelength region between 4.4 μm and 5.1 μm in addition to significant thermal components. These complications must be considered in the interpretation of the spectra.

**Detection of an Absorption Feature at ~4.5 μm--Indication of Sulfates.** A modeled atmospheric spectra (PCO2 =7 mbar, T=240K, CO/CO2=0.002, Airmass = 2.0) based on atmospheric models by Encrenaz is plotted over the spectra from the Argyre region (Figure 1). Note that all the atmospheric absorption features (shown with arrows) are clearly present in the telescopic data and that most features appear to be weaker than predicted by the model. The exception to this is the rise out of the 4.2 μm - 4.4 μm CO2 absorption which has a much shallower slope in the telescopic data than in the model atmosphere spectra. In addition to this gradual slope, an inflection at 4.5 μm is present in all the spectra and is extremely well defined in the Eastern Solis Planum and Argyre spectra (Figure 2). These measurements indicate that a surface absorption, centered near 4.5 μm, is present on the Martian surface.

The wavelength region between 4.4 μm and 5.1 μm contains sulfate absorptions, shown in figure 3a, for anhydrite, gypsum, and MgSO4, with the the 2ν3 vibrational overtone of the SO4-2 anion being centered at 4.5 μm.

The multiband structure seen in the sulfate spectra is produced by the metal cation complexing with the SO4 -2 lowering the symmetry of the sulfate. The lower symmetry causes degeneracy in the ν3 and ν4 modes, and the appearance of the ν1 and ν2 modes which are not infrared active under the tetrahedral symmetry that the SO4 -2 anion occupies. Unfortunately the Mars atmosphere cuts off the short wavelength portion of the absorption. The sulfates shown in figure 3a are shown in figure 3b at the resolution and wavelength of the telescopic data. Note that there does not appear to be any of the structure associated with the sulfates shown above in figures 3 a and b present in the telescopic data.

The location of this feature at 4.5 μm, the 2ν3 SO4 overtone, is especially exciting as the Viking lander sites detected large quantities of sulfur (~7 wt% SO3) in the Martian soils. The sulfur content was highly variable even at a local level. Sulfur abundance ranged from 5.9 wt% to 9 wt% SO3 at Chryse and from 7.6 wt% to 8.5 wt% SO3 at Utopia (2).

**Spatial Variation in the 4.5 μm band depth -- Implications for sulfate distribution.** In order to isolate atmospheric effects from surface absorptions we compared spectra which had the same 3.81 μm band depth. The 3.81 μm band is caused by CO2 with 16O and 17O (1). The isotopically heavy CO2 absorption provides an indicator, independent of possible sulfate absorption, of the similarity of atmospheric conditions of the various spectra. The spectra for the regions Valles Marineris, Argyre Basin, Eastern Solis Planum and Eastern Tharsis (figure 2) all have 3.81 μm band depth between 3.1% and 3.3%.

In comparing the Valles Marineris, Argyre Basin, Eastern Solis Planum and Eastern Tharsis spectra, the 4.5 μm inflection discussed above is probably the strongest indicator of sulfate abundance. In order of strength of deepest absorption to weakest the regions are ordered 1. Eastern Solis Planum, 2. Argyre Basin, 3. Eastern Tharsis, and 4. Valles Marineris, although in no spectrum does the rise out of the carbon dioxide band match the atmospheric model. A note of caution must be offered in taking this approach to estimating relative sulfate abundance as the strength of the 4.5 μm band could indicate not only the abundance but changes in mineralogy and degree of crystallization. However, the four regions do follow a progression due to either sulfate abundance or chemistry and there is significant variation between regions shown in figure 2.

**Conclusions.** The rise out of the 4.2 μm - 4.4 μm CO2 band cannot be matched by solely atmospheric constituents. A surface absorption must be added at roughly 4.5 μm in order to decrease the reflectance rise and produce the 4.5 μm inflection which is present in the data. The known presence of sulfates on the Martian surface and the location of this feature at the 2ν3 overtone of the SO4 -2 anion indicate that the surface absorption is probably caused by sulfates on the Martian surface. An exact match to a terrestrial sulfate mineral has not been made but it is suggested that the mineral has very weak structure and thus a high degree of symmetry . Significant variation exists between the spectra at 4.5 μm. In order of strength of deepest absorption to weakest the regions are ordered Eastern Solis Planum, Argyre Basin, Eastern Tharsis, and Valles Marineris for the four regions measured at similar Mars atmospheric conditions.

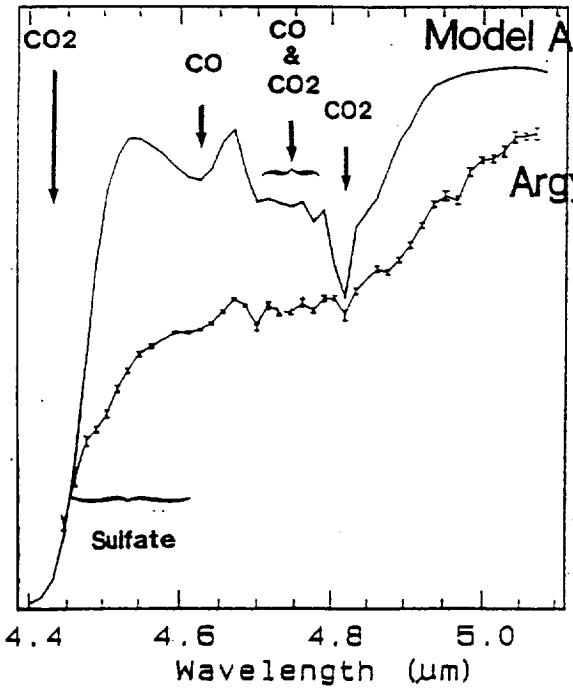


Figure 1. Representative spectra (Argyre region) and Mars model atmosphere of 7 mbar, 2 airmass, 240K, and CO / CO2 with atmospheric and surface absorptions labeled.

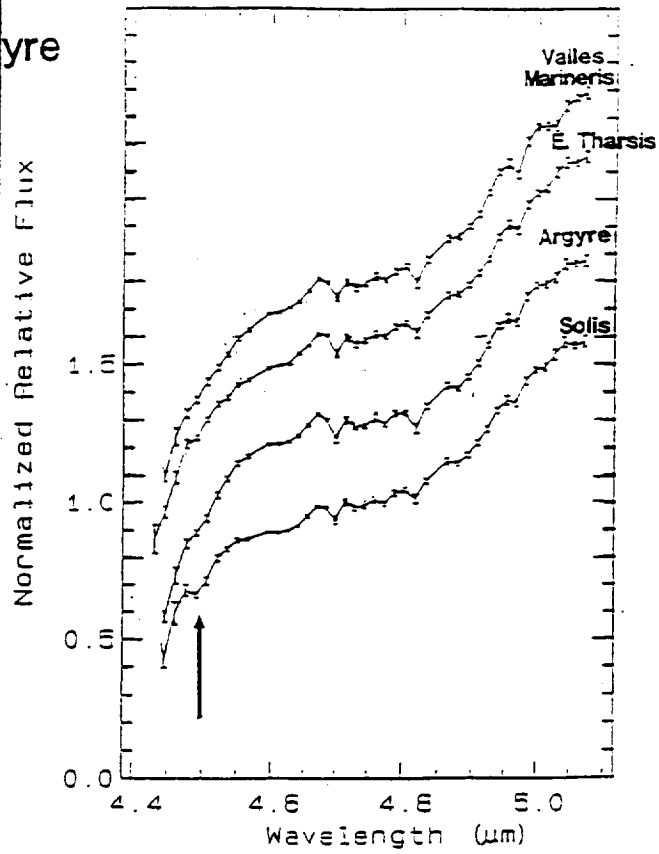


Figure 2. Spectra for four regions with similar 3.81 μm band depths. Regions are Eastern Solis Planum, Ridged Plains, Heavily Cratered Terrain; Argyre Basin; Eastern Tharsis; and Valles Marineris. Spectra are arranged in order of 4.5 μm band depth.

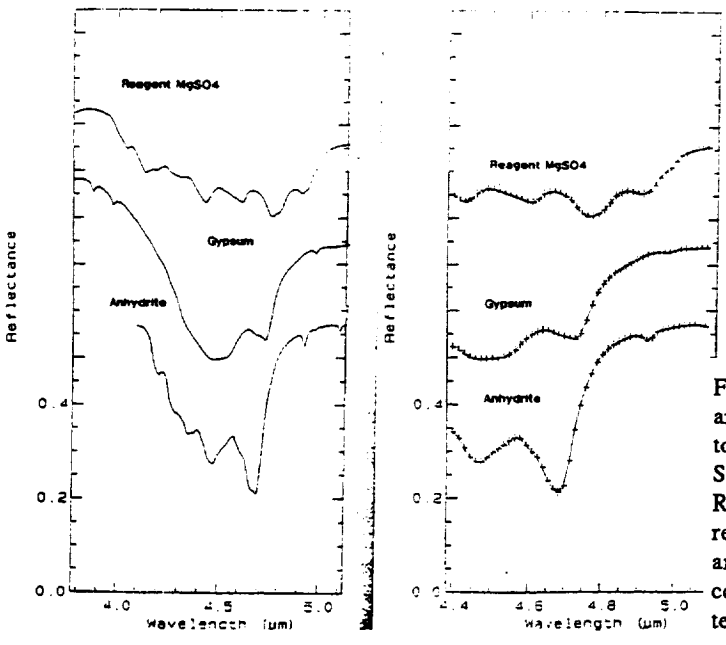


Figure 3 a. Reagent MgSO4, gypsum, and anhydrite reflectance spectra. Spectra are relative to sulfur and have a grain size of <34 μm. Spectra measured at 2 cm $^{-1}$ resolution. b. Reagent MgSO4, gypsum, and anhydrite reflectance spectra. Spectra are relative to sulfur and have a grain size of <34 μm. Spectra convolved and interpolated to wavelengths of the telescopic observations.

**References:** 1. Blaney D.L. and T.B. McCord submitted to *J. Geophys. Res.* 1990. 2. Clark, B.C. et al. *J. G. Res.* 87, 10,059-10,068, 1982.

RADIATION DAMAGE IN GERMANIUM DETECTORS: IMPLICATIONS FOR THE GAMMA-RAY SPECTROMETER OF THE MARS OBSERVER SPACECRAFT;

J. Brückner, M. Körfer, and H. Wänke, Max-Planck-Institut für Chemie, Mainz, F. R. Germany; A. N. F. Schroeder, Universität zu Köln; F. R. Germany; D. Filges and P. Dragovitsch, Institut für Kernphysik, KFA Jülich, F. R. Germany; P. A. J. Englert, San Jose State University, CA, USA; R. Starr and J. I. Trombka, NASA Goddard Space Flight Center, MD, USA; I. Taylor, Princeton Gamma-Tech, NJ, USA; D. Drake and E. Shunk, Los Alamos National Laboratory, NM, USA.

High-purity germanium (HpGe) detectors will be used in space missions to measure gamma-rays emitted by planetary bodies or astronomical sources. The upcoming NASA Mars Observer mission, scheduled for launch in 1992, will explore the surface of the planet Mars for 1 Martian year. One of the scientific instruments on-board the spacecraft will be a gamma-ray spectrometer (GRS) that will utilize a coaxial n-type HpGe detector. The GRS shall make high-resolution energy measurements of gamma rays emitted by the planetary surface. Cosmic-ray bombardment of the planetary surface induces gamma-ray emission due to subsequent primary and secondary nuclear interactions. Gamma-ray measurements made aboard the polar orbiting Mars Observer spacecraft can be used to infer chemical composition of the Martian surface.

Previous experiments [1] and flight experience [2] have indicated that HpGe detectors exposed to cosmic radiation can suffer significant radiation damage. As a result, the energy resolution of the HpGe detector will degrade to such a degree that it is not useful for further measurements.

The purpose of this experiment was to obtain more detailed information on the behavior of HpGe detectors under irradiation with high-energy charged particles in space and to test methods of annealing radiation-damaged HpGe detectors in a closed system. Basic scientific as well as engineering data on detector performance under simulated space exposure and operating conditions were collected. These data will be used to help in the design, control, and understanding of how to maintain the health of HpGe detectors during future space missions.

Several HpGe detectors were exposed to a proton irradiation at the French accelerator facility Saturne (Laboratoire National Saturne, Saclay). One detector was a flight-type version of the Mars Observer gamma-ray HpGe detector with a volume of 130 $cm^3$. Six other HpGe detectors having volumes of 90 $cm^3$ were grouped in pairs, each pair mounted in a special double-cryostat. Each pair consisted of a n-type and a p-type germanium crystal.

Simulation calculations on the interaction of protons with germanium were carried out by using the HERMES code system. Implications from the calculations and space environment conditions led to special requirements for the proton beam and detector setup. At the accelerator a 1.5-GeV proton beam with a cross sectional area of 20 cm in diameter and with an intensity distribution of less than 20 % variation was obtained. The proton flux was as low as about $10^5$ protons $cm^{-2}sec^{-1}$ and was measured with plastic scintillation counters and monitor foils. The HpGe detectors were arranged inside the beam cross section in such a way that no Ge crystal was in the geometrical shade of another. By using a special heating device the detectors were held at operating temperatures of 90 K, 100 K, and 120 K to cover a temperature range expected for a planetary mission. The irradiation of the detectors occurred in several steps until an accumulated fluence of about $10^8$ protons $cm^{-2}$ was reached. The detectors were irradiated in predetermined increments of proton fluence. During irradiation interruptions, gamma-ray spectra of $^{60}Co$ were taken to evaluate the performance of the detectors as a function of accumulated charged particle fluence.

At completion of the irradiation, all detectors were characterized and cooled stepwise to $LN_2$ temperatures. Then, the detectors were transported in special containers to the laboratory at Mainz, where a detailed characterization of their performance was carried out.

A total proton fluence of $10^8$ protons $cm^{-2}$ is about equivalent to one year of exposure in space. At elevated temperatures the observed energy resolution degradation after accumulation of

this fluence would not allow for high-resolution gamma-ray spectroscopy. But, as shown later, annealing can remove the damage.

During the stepwise irradiation, the peak shape of the n-type detectors showed a significant change. Before the irradiation the shapes were either pure Gaussian or showed a little exponential tailing at the low-energy side. During the irradiation the exponential tailing evolved until it dominated the entire low-energy side of the the peak. A Gaussian shape was maintained at the high-energy side. More irradiation produced a new feature depending on the operating temperature: a broad Gaussian peak sitting on top of the exponential tailing (in a logarithmic display visible as a bump).

The full-width-at-half-maximum (FWHM) of the three 90-$cm^3$ n-type detectors is shown in Figure 1 as a function of proton fluence and operating temperature. The detector held at 90 K showed the best resistance against degradation of energy resolution. The detector held at 100 K (further on called "Yellow") exhibited an increase of degradation to 6 keV after being exposed to a fluence of $1.1 \times 10^8$ protons $cm^{-2}$; prior to the irradiation the resolution was 2.1 keV at 100 K. At an accumulated fluence of $6 \times 10^7$ protons $cm^{-2}$, which corresponds to about a half year of exposure in space, the energy resolution of detector Yellow was still below 3 keV. After the irradiation detector Yellow was cooled down to 90 K and its FWHM improved to 4.5 keV. The detector at 120 K showed an almost linear dependence of FWHM vs. fluence in contrast to the curve of Yellow, which led to an resolution degradation from 2 keV before the irradiation to 3 keV at an accumulated fluence of $3 \times 10^7$ protons $cm^{-2}$.

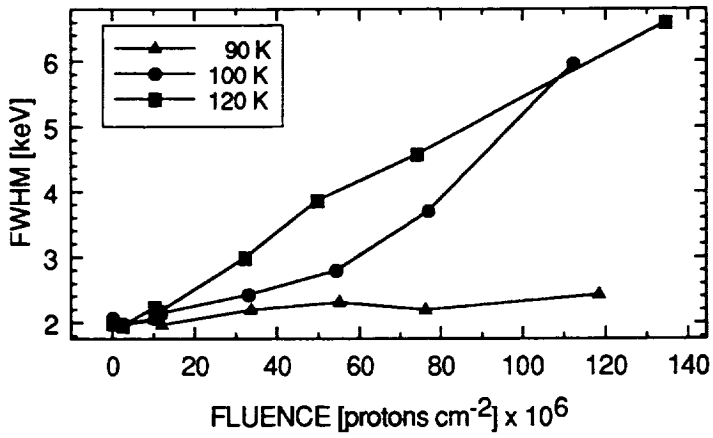


Fig.1 FWHM of the 1.3-MeV line of $^{60}Co$ for 3 n-type HpGe detectors at different temperatures as function of proton fluence.

Temperature cycling of damaged detectors between a reference temperature of 90 K and temperatures up to 130 K proved that irreversible additional loss in detector performance occurred above 120 K. For detector Yellow, it was observed that between 125 and 130 K an irreversible increase of damage occurred, *i. e.* if the detector was cooled down to 90 K after being at 130 K, its energy resolution had increased to 6.7 keV compared to 4.5 keV at 90 K. Heating up to room temperature produced only a small further increase of the resolution degradation (7.2 keV at 90 K).

During annealing (heating up to 100°C or higher) the detectors stayed in their special designed cryostat (the Ge crystal was encapsulated in a vacuum-tight inner can). After having annealed detector Yellow at a temperature of 105°C for 11 hours, almost all damage was removed (resolution improved from 7.2 to 2.4 keV). Further annealing of 50 hours at the same temperature brought the energy resolution back to its original value. A further indication of complete recovery of the annealed detector was the lack of variation in the intrinsic detector energy resolution as a function of temperature in the range 90 K to 120 K.

The irradiation and annealing cycles of the detectors simulated space exposure and operating procedures as closely as possible. The annealing temperatures applied to the detectors are available on the Mars Observer GRS. The study showed that HpGe detectors can successfully be used in long-term space experiments.

References: [1] Pehl R.H., Madden N.W., Elliott J.H., Raudorf T.W., Trammell R.C., and Darken L.S. (1979) IEEE Trans. Nucl. Sci. NS-26, 321-323. [2] Mahoney W.A., Ling J.C., and Jacobson A.S. (1981) Nucl. Instr. Meth. 185, 449-458.

# CHEMICAL EVOLUTION AND OXIDATIVE WEATHERING OF MAGMATIC IRON SULFIDES ON MARS

**Roger G. Burns and Duncan S. Fisher**, Department of Earth, Atmospheric and Planetary Sciences, Massachusetts Institute of Technology, Cambridge, MA 02139

**INTRODUCTION.** Ferric-bearing phases in the martian regolith testify to oxidative weathering reactions near the surface of Mars. A paragenetic link between primary magmatic sulfide minerals on Mars and their weathering products (gossans) has been proposed by us [1-3]. This model is based on petrogenetic associations between komatiitic rock-types, Viking geochemical data, SNC meteorites, and terrestrial magmatic sulfide ore deposits [4]. It appears that unique conditions during the evolution of the martian crust have conspired to generate an acidic groundwater (permafrost) environment that has facilitated chemical weathering of basaltic rocks on Mars.

Some of the steps that have been proposed during oxidative weathering of iron sulfides [1-4] are summarized by reactions formulated in Table 1. Initially, deep-weathering reactions involving dissolved ferric iron in acidic groundwater percolating from the surface converts pyrrhotite to pyrite (reaction {1}). Pyrite is then oxidized either by ferric ions {2} or by groundwater equilibrated with oxygen in the atmosphere {3}, even under an oxygen partial pressure of $10^{-5}$ bar existing in the present-day martian atmosphere. Strongly acidic (pH 1 to 5) and sulfate-rich solutions are generated which stabilize and mobilize a variety of simple and complex ions of Fe, including $Fe^{2+}$, $Fe^{3+}$, $FeSO_4^+$, $FeOH^{2+}$, etc. Above the water table, these dissolved ions become unstable and produce hydronium jarosite {4} or eventually goethite by further oxidation {5}, hydrolysis {6}, and decomposition {7} reactions, each of which liberates $H^+$ ions thereby promoting chemical weathering of basaltic silicate minerals {8}.

To test this weathering model, komatiitic pyrrhotites and olivines have been exposed to sulfuric acid solutions, with and without the addition of ferric iron to simulate deep-weathering processes. We report here measurements made on the reaction products, and summarize tectonic and geochemical processes that might have modified the surface of Mars.

**EXPERIMENTAL PROCEDURES.** Powdered samples of pyrrhotite ($Fe_7S_8$) and olivine ($Fa_{49}$) were reacted in stoppered flasks with sulfuric acid (pH 2) at 60°C, with and without the addition of dissolved 1M ferric sulfate, for time periods ranging from 1 to 5 weeks. Reaction products were filtered, washed with cold distilled water, air-dried and measured by Mossbauer spectroscopy at ambient (295K) and liquid helium (4.2K) temperatures to characterize the X-ray amorphous $Fe^{3+}$-bearing phases formed in the reactions. Correlative Mossbauer spectra were also obtained for pyrite, marcasite, hematite, goethite, and jarosite. The spectra were calibrated against a metallic iron foil standard.

**RESULTS.** Examples of 4.2K Mossbauer spectra of pyrrhotite before and after reaction with pH 2 sulfuric acid are shown in Figure 1. The unreacted pyrrhotite spectrum (Fig. 1a) is complex and consists of 3 or 4 superimposed magnetic hyperfine sextets. After reaction with $H_2SO_4$, additional peaks appear at approx. 0.1 and 0.7 mm $s^{-1}$ (Figs 1b & 1c) attributable to $FeS_2$ (pyrite or marcasite), which are intensified (Fig. 1c) when $Fe_2(SO_4)_3$ is present as a lixiviant. New peaks also occur near -7.75 and +8.5 mm $s^{-1}$ and represent another component sextet, the magnetic hyperfine splitting parameter of which (H = 50.6T) resembles the value of goethite [5]. The breadth (Fig. 1b) or asymmetry (Fig. 1c) of the two goethite peaks suggest that some hydronium jarosite (H = 49.3T) may also be present in the reaction products. The Mossbauer spectra of reacted pyrrhotites, therefore, indicate that sulfuric acid has induced the pyrrhotite → $FeS_2$ (pyrite or marcasite) → goethite (+ jarosite) oxidative reactions formulated in Table 1. Nanophase goethite is also formed during reactions of olivine with $H_2SO_4$ [4], particularly in the presence of dissolved $Fe^{3+}$ ions, hydrolysis of which is unlikely in acidic (pH 2) solutions.

**DISCUSSION.** The experimental results for $H_2SO_4$-degraded pyrrhotites support our proposed model for the oxidative weathering of Fe-S sulfide minerals, in which supergene alteration of pyrrhotite in groundwater and the formation of secondary $FeS_2$ phases precedes the deposition of goethite and jarosite in gossans above the water table [1-4]. Dissolved $Fe^{3+}$ ions clearly promote the formation of supergene pyrite or marcasite, and the acidic groundwater causes chemical weathering of ferromagnesian silicates such as olivine to nanophase goethite. Similar oxidative weathering reactions involving pyrrhotite and olivine in komatiitic basalts are suggested to have occurred on Mars, contributing to the ferric-bearing materials present in the regolith there.

**EVOLUTION OF THE MARTIAN SURFACE.** Oxidative weathering of sulfides on Mars has been largely confined to pyrrhotite, perhaps associated with pentlandite and minor chalcopyrite, which predominate as accessory minerals in mafic igneous rocks and in associated ore deposits. Partial melting of the martian mantle estimated to contain about 4.5 wt. % S [4] produced iron-rich basaltic magma which

reached the surface of the planet via massive shield volcanoes and as fissure eruptions, transporting high concentrations of dissolved $S^{2-}$ and $HS^-$ to the surface. Extrusion of turbulent low viscosity lava, segregation of immiscible FeS liquids during cooling, gravitational settling and fractional crystallization of sulfide minerals in the lava flows, produced thinly disseminated iron sulfide mineralization over large areas of Mars. Massive ore deposits were also deposited locally at the base of structural depressions or in channels eroded by advancing lava flows [6]. Fracturing associated with this volcanism facilitated deep-weathering reactions by permeating groundwater early in the history of Mars. However, because plate tectonic activity appears to have been insignificant on Mars, the apparent absence of spreading centers and subduction zones has minimized acid-buffering of aqueous solutions by wall-rock alteration. Therefore, the acidity of groundwater, now permafrost, has been maintained during the chemical evolution of the martian surface, aiding the chemical weathering of silicates in the basaltic crust when water is present. Furthermore, since tectonic-induced interactions of martian mantle with crust, hydrosphere and atmosphere have been minimal, sulfide mineralization has not evolved on Mars beyond pyrrhotite-pentlandite assemblages associated with mafic igneous rocks. Therefore, common terrestrial ore deposits such as porphyry copper and molydenum, granite-hosted mineralization, and sediment-hosted galena-sphalerite assemblages [7] have not formed on Mars.

REFERENCES. [1] R.G.Burns, *Proc. 17th LPSC, JGR*, 92, E570 (1987); [2] R.G.Burns, *Proc. 18th LPSC*, 713 (1988); [3] R.G.Burns & D.S.Fisher, *LPI Tech. Rept., 88-05* 34 (1988); [4] R.G.Burns & D.S.Fisher, *LPI Tech Rept., 89-04*; 20(1989); [5] E.Murad & J.H.Johnston, in *Mossbauer Spectroscopy Applied to Inorganic Chemistry* (G.J.Long, ed.; Plenum) 2, 507 (1987); [6] A.K.Baird & B.C.Clark, *Nature*, 311, 18 (1984); [7] C.Meyer, *Ann. Rev. Earth Planet. Sci.*, 16, 147 (1988); [8] Research supported by NASA grants NSG-7604 and NAGW-1078.

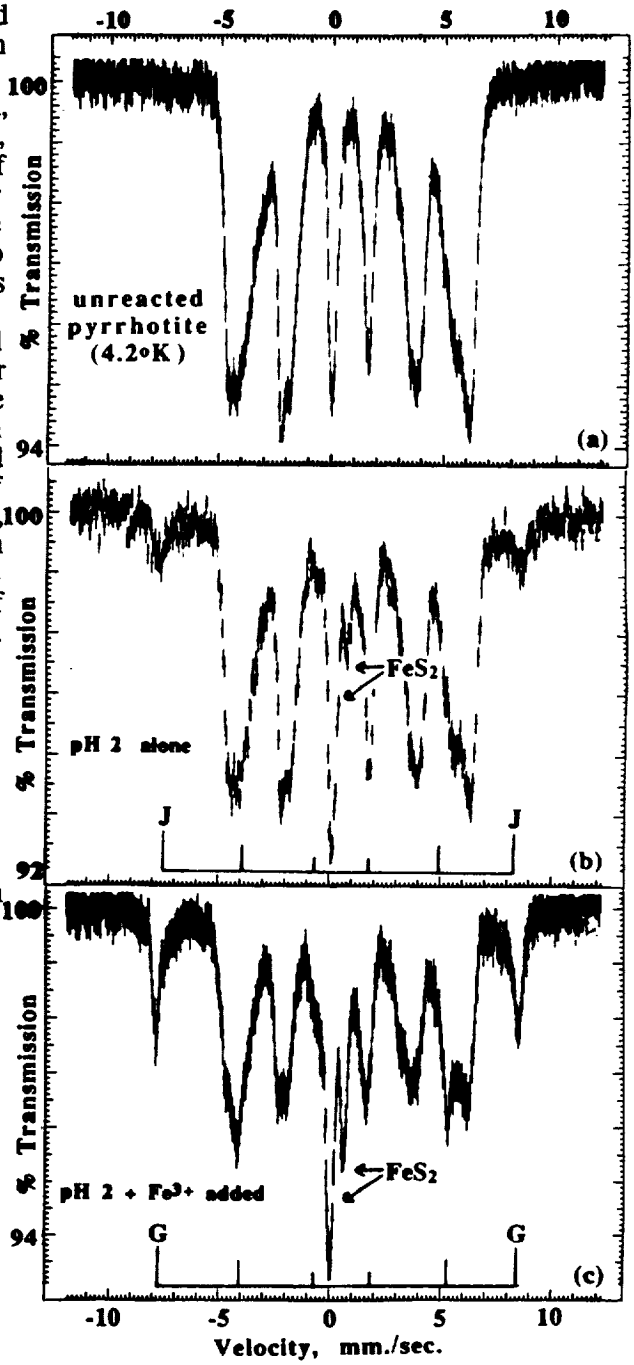


FIGURE 1. Mossbauer spectra measured at 4.2K of pyrrhotite (a) before, and (b,c) after, reaction with pH 2 sulfuric acid for 5 weeks at 60°C, in the absence (b) and presence (c) of dissolved 1M ferric sulfate. Peaks attributed to $FeS_2$ are identified, as are the positions of the goethite (G) and jarosite (J) sextet spectra

TABLE 1. Chemical weathering reactions of iron sulfides and silicates

{1} $Fe_7S_8 + 6\,Fe^{3+} \Rightarrow 4\,FeS_2 + 9\,Fe^{2+}$

{2} $FeS_2 + 14\,Fe^{3+} + 8\,H_2O \Rightarrow 15\,Fe^{2+} + 2\,SO_4^{2-} + 16\,H^+$

{3} $2\,FeS_2 + 2\,H_2O + 7\,O_{2\,(aq)} \Rightarrow 2\,Fe^{2+} + 4\,SO_4^{2-} + 4\,H^+$

{4} $2\,FeSO_4^+ + FeOH^{2+} + 6\,H_2O \Rightarrow (H_3O)Fe_3(SO_4)_2(OH)_6 \Downarrow + 4\,H^+$

{5} $4\,Fe^{2+} + 6\,H_2O + O_{2\,(aq)} \Rightarrow 4\,FeOOH + 8\,H^+$

{6} $Fe^{3+} + 2\,H_2O \Rightarrow FeOOH \Downarrow + 3\,H^+$

{7} $(H_3O)Fe_3(SO_4)_2(OH)_6 \Rightarrow 3\,FeOOH + 2\,SO_4^{2-} + 4\,H^+ + H_2O$

{8} $(Mg,Fe)_2SiO_4 + 4\,H^+ \Rightarrow 2\,(Mg^{2+} + Fe^{2+}) + SiO_{2\,(aq)} + 2\,H_2O$

# MOSSBAUER SPECTRA OF OLIVINE-RICH WEATHERED ACHONDRITES: II. BRACHINA, CHASSIGNY, ALHA 77005, AND NAKHLA

**Roger G. Burns and Sondra L. Martinez,** Department of Earth, Atmospheric and Planetary Sciences, Massachusetts Institute of Technology, Cambridge, MA 02139.

**INTRODUCTION.** Olivine predominates in several SNC meteorites believed to have originated from Mars, including Chassigny (approx. 90 modal % $Fa_{31.5}$; **[1]**) and ALHA 77005 (~52% $Fa_{28-34}$; **[2]**). It is also a significant constituent of Nakhla (15.5% $Fa_{68}$; **[3]**), and is present in minor amounts in EETA 79001 lithology A, Lafayette and Governador Valadares **[4]**. Furthermore, almost 80% of Brachina is olivine ($Fa_{30}$) **[5,6]** (which is related to ALHA 84025; **[7]**), and this meteorite was once grouped with the SNC meteorites. Because olivine is particularly reactive in low temperature environments and forms iddingsite under hydrothermal conditions and during weathering **[8]**, the presence of such ferric-bearing oxyhydroxide and phyllosilicate assemblages may be indicative of oxidative weathering in an aqueous environment on Mars. Since the presence of ferric iron in amounts exceeding 1-2% is usually readily detectable by Mossbauer spectroscopy **[9]**, and because preliminary measurements of weathered meteorites at very low temperatures enabled nanophase hydrated Fe(III) oxide phases to be identified **[9,10]**, we have measured the spectra of several olivine-rich achondritic meteorites and report here 295K and 4.2K Mossbauer spectral data for SNC and related meteorites; an accompanying abstract **[11]** describes similar measurements on a suite of ureilites found in Antarctica.

**SPECIMENS STUDIED.** Achondrites acquired for the Mossbauer spectral measurements included: ~100 mg chips from interior portions of Brachina, Chassigny and Nakhla; homogenized powders from the Antarctic Meteorite Collection of the "dark" (olivine-rich) and "light" (olivine-depleted) fractions of ALHA 77005; and a powdered eucrite (ALHA 80102) showing moderate rustiness, which served to locate pyroxene peaks in the low-temperature spectra. Experimental details are described in the accompanying abstract **[11]**

**RESULTS.** Assembled in Figure 1 are the 4.2K Mossbauer spectra of the six achondrites. It is immediately apparent from Figure 1 that peaks at approx. -7.75 and +8.5 mm $s^{-1}$ are most conspicuous in the Brachina spectrum (Fig. 1a), yielding a value of 50.3T for the magnetic hyperfine field which corresponds to values for goethite. Magnetic ordering of this Fe(III) oxyhydroxide phase is not observed in the 295K spectrum, however, indicating that the ~7% ferric iron present in Brachina occurs as nanophase (<10 nm) goethite. Very weak FeOOH features appear in 4.2K Mossbauer spectra of Nakhla (Fig. 1e) and eucrite ALHA 80102 (Fig. 1f), but not in the spectra of Chassigny (Fig. 1b) or the ALHA 77005 "dark" (Fig. 1c) and "light" (Fig. 1d) fractions, even though the 295K spectra resolved small amounts of ferric iron in Chassigny (2.3% $Fe^{3+}$) and ALHA 77005 (1.7% $Fe^{3+}$; **[10]**) as well as Nahkla (1.6% $Fe^{3+}$; **[9]**). The ferric iron in Chassigny appears to be accomodated in the olivine structure as it is in ALHA 77005 **[12]**, and not in the iddingsite FeOOH phase present in Nakhla and Brachina.

**DISCUSSION.** The presence of goethite in Brachina correlates with the "small amount of limonite produced by terrestrial weathering" reported when the meteorite was found in South Australia **[5]**. Similar terrestrial weathering could not have occurred in Chassigny and Nakhla which were collected as *falls*, so that their ~2.0 $Fe^{3+}$ probably represents preterrestrial oxidation during exposure on Mars. We also conclude that the ferric iron measured in olivine-separates **[12]** and bulk samples **[9]** of ALHA 77005 did not originate in Antarctica but was produced during low temperature alteration reactions on the martian surface.

**REFERENCES.** **[1]** R.J.Floran *et al.*, *GCA*, 42, 1213 (1978); **[2]** H.Y.McSween Jr *et al.*, *Science*, 204, 1201 (1979); **[3]** T.E.Bunch & A.M.Reid, *Meteoritics*, 10, 303 (1975); **[4]** H.Y.McSween Jr, *Rev. Geophys.*, 23, 391 (1985); **[5]** J.E.Johnson *et al.*, *Rec. Sth. Austral. Mus.*, 17, 309 (1977); **[6]** C.E.Nehru *et al.*, *Proc. 14th LPSC, JGR*, 88, B237 (1983); **[7]** P.H.Warren & G.W.Kallemeyn, *Proc. 19th LPSC*, 475 (1989); **[8]** R.A.Eggleton, *Clays & Clay Min.*, 32, 1 (1984); **[9]** T.C.Solberg & R.G.Burns, *Proc. 19th LPSC*, 313 (1989); **[10]** R.G.Burns, *Lunar Planet. Sci.*, XX, 129 (1989); **[11]** S.L.Martinez & R.G.Burns, *Lunar Planet. Sci.*, XXI, this vol. (1990); **[12]** R.Ostertag *et al.*, *EPSL*, 67, 162 (1984); **[13]** Research supported by NASA grants NSG-7604 and NAGW-1078.

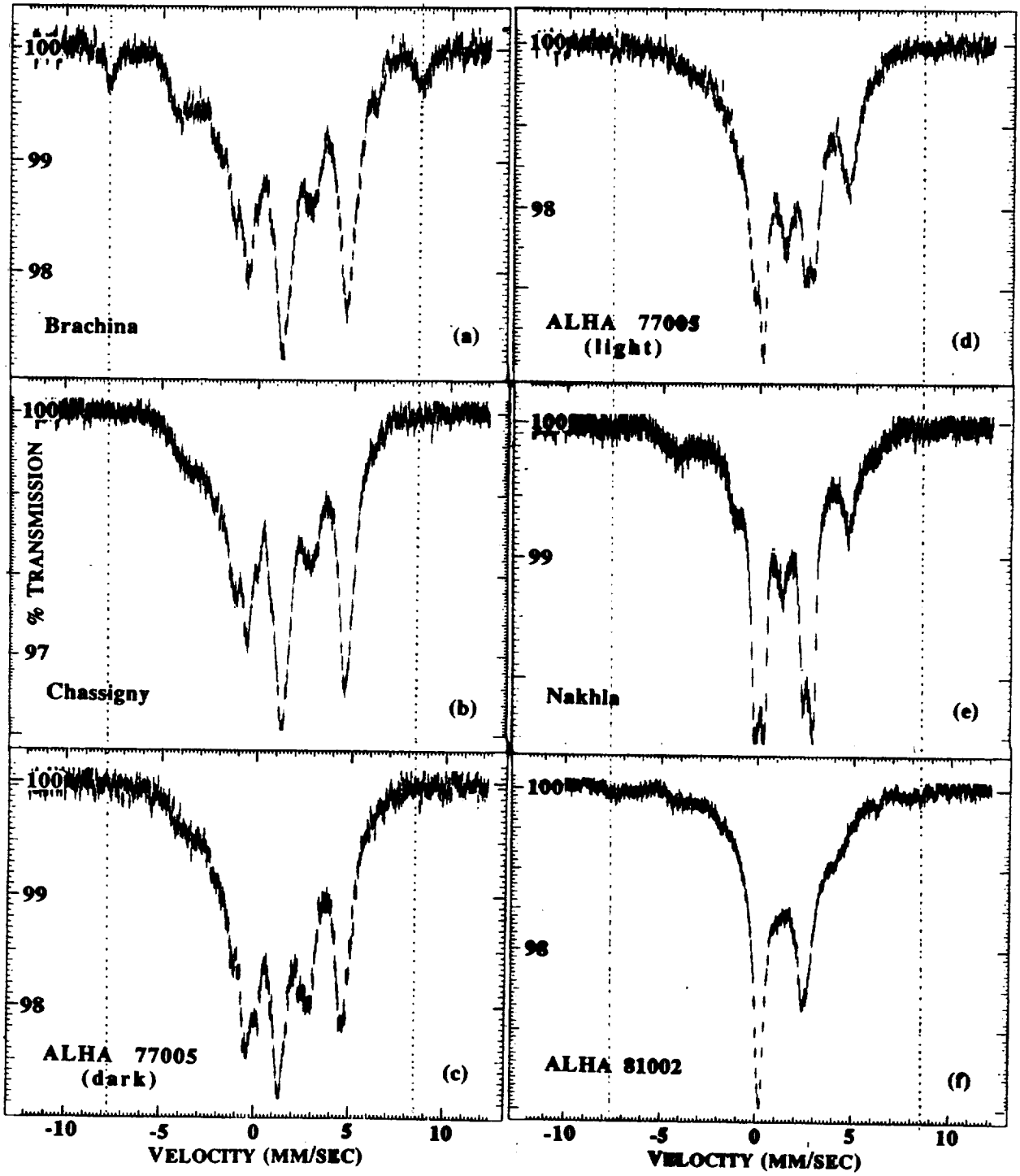


FIGURE 1. Mossbauer spectra measured at 4.2K of a variety of achondrites. (a) Brachina; (b) Chassigny; (c) shergottite ALHA 77005 "dark" (olivine-enriched) and (d) "light" (olivine-depleted) fractions; (e) Nakhla; and (f) eucrite ALHA 81002. Vertical dotted lines indicate the locations of the outermost peaks of the goethite sextet Mossbauer spectrum. This ferric oxyhydroxide phase is present in Brachina, Nakhla and eucrite ALHA 81002. Ferric iron occurring in the olivines, which is resolved in the 295K Mossbauer spectra of Chassigny and ALHA 77005, is obscured by peaks representing the onset of magnetic ordering of ferrous iron.

**PHYSIOGRAPHIC CHARACTERISTICS OF MARTIAN DRAINAGE BASINS.** CABROL, N.A , Lab.Geo.Phys.(UA0141CNRS) and Lab.Phys.Syst.Solaire.Meudon 92195.-France-

In this study, a martian drainage basin is defined by the limit with the environment of a system of thalwegs. These systems are widly distributed on the craterized uplands and display various morphologies and sizes (from 2000 $km^2$ to 50 000 $km^2$). A conceptual model, built up with geometrical data from the 1: 2.000.000 maps, yields to a classification of drainage basins. This classification is based upon the relationship between the perimeter (P) and the area (A) of the basin, and is expressed by two coefficients : *Kd* (drainage density) = $\Sigma Li/A$, where $\Sigma Li$ is the sum of the basin branch lengths. *Kc* (drainage basin compacity, Gravellius coefficient) = $P/2\pi\sqrt{A}$ # $.28P/\sqrt{A}$. P is the length of a drainage basin limit, which is defined in this method by a line located 10 km upstream the headwater system and including the branch systems until the outlet. This 10 km value considers the limited Viking resolution, and the limit of the hydrogeological system of underground water reservoirs. To test this model, 15 well preserved drainage basins are selected between -47° and +19°Lat. in order to cover a representative distribution. The model is calibrated by 8 terrestrial basins, located on 3 different geological units (Bassin Aquitain, Bassin de la Durance and Bassin de la Seine -France-), respectively in 3 rainfall regimes. These coefficients Kc and Kd characterize the basin physiographies. Within the model, a discriminant parameter Kd/Kc = D (drainage intensity) is established. Terrestrial Kc values vary from 1 to 1.5 and Kd from .02 (karsts : scarcely branched areas) to 300 (badlands, high drainage intensity areas). So, terrestrial D is included between 200 (high drainage intensity) and .01(low drainage intensity) with medium compacity value of 1.5. The relationship between Kd and Kc allows to classify martian and terrestrial basins (Fig.1) which are represented on the graph by their parameters Kd and Kc. Three concentrations appear, one for the terrestrial examples, and two for the martian basins. The gravity center for the terrestrial examples is Kd= .05 and Kc= 1.3, so D=.04. For the martian lower concentration I, the gravity center coordinates are : Kd=.1 and Kc=1.6, so D=.06. For the martian concentration II, the gravity center coordinates are : Kd=.05 and Kc=3, so D=.01.The D martian values for the 15 tested basins are closer to the representative value of terrestrial low drainage basins intensity located on geological units of karstic types. The martian drainage basins of $(5^+/-2)$ $.10^6$ $km^2$ correspond to a high compacity value and a low thalweg distribution.Martian drainage basins of $(30^+/-10).10^6$ $km^2$ correspond to a low compacity value and a low thalweg distribution.

A first conclusion is that Kd value varies only between .03 to .15 (Earth .02 to 300). The result is calibrated with 30 other drainage basins on Mars. Because Kd is related to the geological type of the basin, this result indicates a probable undiversified substratum on a wide area (-50°, +10°Lat.) in which local singularities might lead to groundwater occurrences. A second conclusion is : for martian drainage basins, Kc appears as a clear discriminant coefficient.

These conclusions are then correlated with a mapping of headwater branch densities (order 1) on the entire martian surface. The results vary from 100 to 1 per $10^6$ $km^2$, implying a wide interval of variation. These headwater systems are found mainly in the Margaritifer Sinus, Sinus Sabeus, and Iapygia regions. Their dispersion is unconsistant with an organized meteorological feeding origin and with true surface drainage basins. The .03 mean Kd value and the 1.6 to 3 Kc values (corresponding to elongated basins with isolated headwater systems) lead to support the seepage hypothesis.

**PHYSIOGRAPHIC CHARACTERISTICS OF MARTIAN DRAINAGE BASINS.** CABROL,N.A.

The third conclusion is : the limits of martian drainage basins are not divides. The basins are not joined, they are widely spreaded as relatively small units on wide areas. The methodological hypothesis considering these basins as isolated systems is consistant with the observation.

**REFERENCES** : Abrahams, A.D, 1984 Channels networks : a geomorphological perspective. Water.Res.Research, **20**, p161-188. Baker, V.R, and Partridge, J.B, 1986 Small martian valleys : Pristine and degraded morphology. J.G.R 91, p3561-3572. Battistini, R, 1985, in Klinger et al (eds), Hydrolithosphere and problem of subsurface ice in equatorial zone of Mars, Ices in the Solar System, p607-617. Cabrol, N.A, 1988, Compte-rendu des Journées de Planétologie. (CNRS/INSU). Cabrol, N.A, 1988 Morphological variations and evolution of channels on Mars. LPI, XX, p136-137. Carr, M.H, 1986 Mars a water rich Planet? Icarus **68**, p187-216.

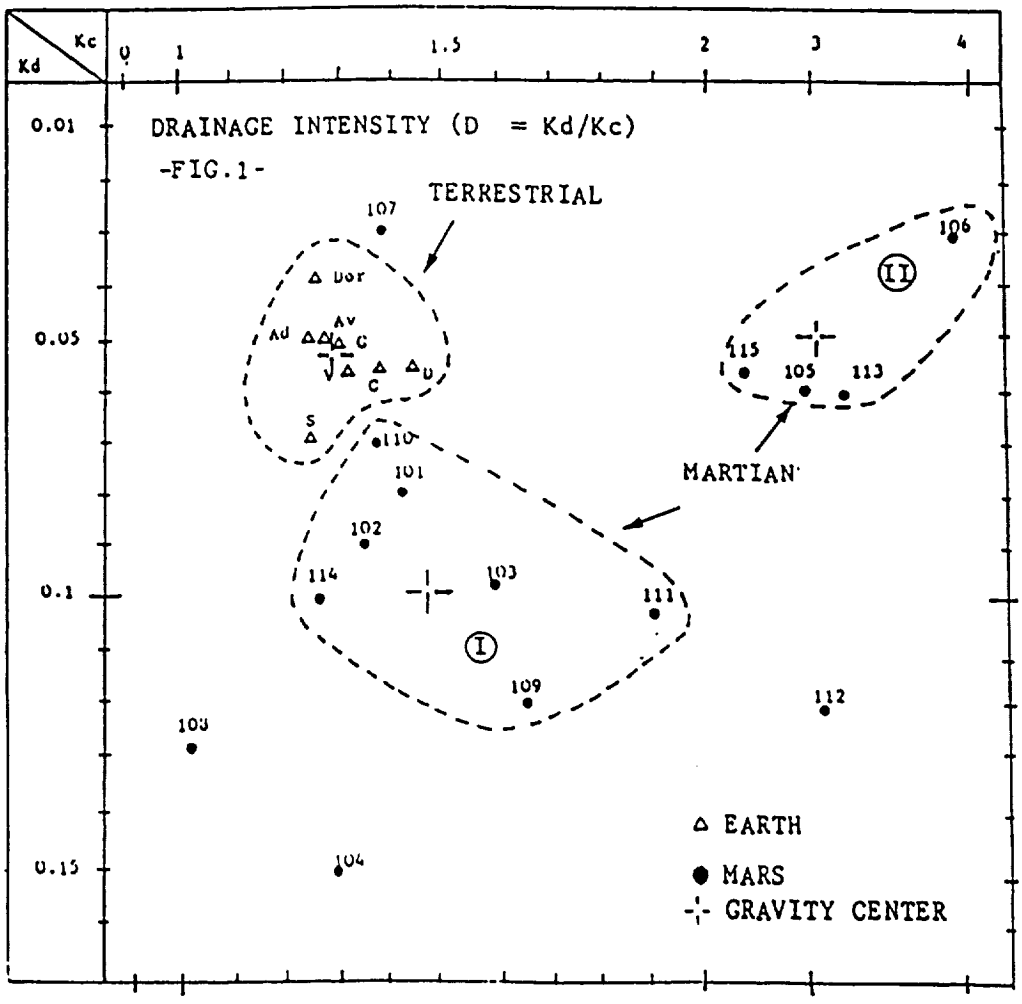

**ANALYSIS OF MARINER 6 AND 7 SPECTRA FOR WEAK ABSORPTION FEATURES FROM 2 TO 6 μm,** Wendy M. Calvin and Trude V. V. King, U. S. Geological Survey, Denver, Colorado 80225

The current study of the Mariner 6 and 7 spectra was undertaken to identify previously unrecognized absorption features and to confirm the results of recent ground-based observation of Mars by Clark et al. (1989), Blaney and McCord (1989), and Pollack et al. (1989). The Mariner data have the advantage that they are not affected by terrestrial atmospheric absorption, have higher spatial resolution than terrestrial observations, and cover the short wavelength infrared region with reasonably high spectral resolution. However, the Mariner data are subject to a variety of other uncertainties which we have attempted to correct for, in as far as is possible twenty years after the original flyby.

The Mariner 6 and 7 infrared spectrometer data set was obtained from Martin (1985), who provided corrections to the current latitude and longitude system and an initial wavelength calibration. The wavelength region from 2 to 6μm is covered by two halves of a circular variable filter wheel. The first wavelength segment is 1.9 to 3.7μm and the second is 3.0 to 6.0μm. In between each half of the filter wheel is a clear aperture which produces a fiduciary spike ostensibly for wavelength calibration. The use of the fiduciary spikes for this purpose was found to yield inaccurate wavelengths, as did corrections using atmospheric bands at one side of a wavelength segment. Apparently the rotation rate of the filter wheel varied nonlinearly and so adjustments at one side of the wavelength segment often will not accurately predict wavelengths on the other side of the wavelength segment. Further wavelength calibrations were performed using atmospheric $CO_2$ bands, where available, and fiduciary spikes. In the 3 to 4-μm wavelength region where no strong atmospheric bands occur a feature caused by an absorption in the filter at 3.4μm (Herr et al., 1972, and Pimentel et al. 1974) was used for calibration.

Other corrections made to the data set include removal of a space background signature, correction for the instrument response as a function of wavelength, removal of the thermal flux to the reflected component and finally correction of the reflected solar response to reflectance. These additional corrections were only made for the 3 to 6-μm wavelength region because at shorter wavelengths the space background did not vary significantly from zero and calibration spectra are not yet available to derive accurate instrument response functions. For the longer wavelength segment space background responses were determined from 6 spectra recorded after the flyby. The average of these was fairly noisy and it was necessary to smooth the response function using a fast Fourier transform. Instrument response functions, determined from black-body calibration spectra included in the flight data set, were also smoothed to eliminate the introduction of noise. In addition, the solar flux was calculated and adjusted for Mars' distance from the sun, and the thermal contribution was calculated using temperatures determined by the original instrument team (Pimentel et al., 1974).

In the wavelength region from 1.9 to 3.6μm, several absorption features that cannot be attributed to atmospheric absorptions are observed in the processed Mariner 6 and 7 data. The most dominant feature is the broad 3μm

absorption associated with hydrated surface minerals which was discussed by Pimentel et al. (1974). An absorption feature is also observed in the 2.3 to 2.4-$\mu$m wavelength region which is in agreement with the Clark et al. (1989) observations. However, the resolution of the instrument is insufficient to verify whether the 2.3-2.4$\mu$m feature is atmospheric or mineralogic in origin. Between approximately 2.45 and 2.62$\mu$m there are two broad absorption bands. The shorter of the two bands is centered on 2.48$\mu$m and seems to be correlated to a band observed by Clark et al. (1989) at 2.45$\mu$m. The 2.48$\mu$m absorption feature in the Mariner data could be shifted in wavelength because the wavelength calibration is fixed at isolated points, the closest of which is at 2.7$\mu$m. The second band is broader (2.5- 2.65$\mu$m) and can possibly be explained by discrepancies between the amount of atmospheric water modeled and observed or the presence of hydrated surface minerals. Removal of the atmospheric signature in the 2.7 to 2.8-$\mu$m region indicated a residual absorption feature at 2.76$\mu$m which can be attributed to the presence of OH-bearing mineral phases. This feature can be seen weakly in some of the original Mariner 7 spectra. Attempts to confirm it with Mariner 6 were unsuccessful as the signal to noise ratio of Mariner 6 data is much worse than that of Mariner 7. Uncertainties associated with removing atmospheric absorptions have precluded a definitive identification of an OH-absorption feature.

In the 3 to 6-$\mu$m region the strongest absorption features result from atmospheric absorptions. However, a broad 3-$\mu$m absorption associated with hydrated minerals is present. The 3.8-$\mu$m feature reported by Blaney and McCord (1989) is confirmed. Over Hellas the 3.8$\mu$m feature is nearly twice as deep as is predicted for a four airmass atmosphere, indicating a mineralogical as well as atmospheric origin. In addition, a weak feature at 5.35$\mu$m, on the edge of the atmospheric $CO_2$ band at 5.2$\mu$m, is observed in both Mariner 6 and Mariner 7 spectra of the Meridiani Sinus region. These absorption features can result from the presence of OH-bearing mineral species and possibly, based on preliminary laboratory spectra, from S-bearing mineral phases or a combination of the two mineral species.

This study confirms the presence of several weak absorption features observed by terrestrial observations and identifies previously unrecognized absorption features in the wavelength regions from 2.5 - 2.65 and 5.35$\mu$m in Mariner 6 and 7 data. These features appear to be mineralogic rather than atmospheric in origin and are believed to result from the presence of OH- or S-bearing minerals on the Martian surface.

## REFERENCES

Blaney and McCord, submitted to *J. Geophys. Res.*, 1989. Clark, Swayze, Singer and Pollack, submitted to *J. Geophys. Res.*, 1989. Crisp, submitted to *J. Geophys. Res.*, 1989. Herr, Forney, and Pimentel, *Appl. Opt.*, 493-501, 1972. Martin, Mariner 6 and 7 data released under the Pilot Planetary Data System, 1985. Pimentel, Forney, and Herr, *J. Geophys. Res.*, 1623-1634, 1974. Pollack et al., *Eos*, *70* 1171, 1989.

THE EFFECTS OF FLOODS, VOLCANISM AND POLAR PROCESSES ON THE D/H RATIO IN THE MARTIAN ATMOSPHERE. M. H. Carr, U. S. Geological Survey, Menlo Park, CA 94025.

Water in the martian atmosphere is 5.1 times more enriched in deuterium than terrestrial water (Owen et al., 1988; Bjoraker et al., 1989). The enrichment has been previously attributed to either massive loss of water early in the planet's history (Owen et al., 1988) or to the presence of only a very small reservoir of water that has exchanged with the atmosphere over geologic time (Yung et al. 1988). However, early massive loss of nearly all the planet's water appears inconsistent with abundant evidence for the action of water throughout Mars history, and exchange of only small amounts of water with the atmosphere is contrary to interpretation of channels as water worn, and interpretation of the poles as a sink for water. Here we examine what effect geologic processes might have on D/H in the atmosphere, and assess whether the geologic model for the evolution of the Mars surface that has been developed over the last two decades needs major revision.

Outflow channels are generally believed to have been formed by large floods. A large flood would immediately inject a substantial amount of water into the atmosphere, then in the long term water would sublime into the atmosphere from the ice rich deposits that must have formed where the water pooled after the flood was over. To estimate the amount of water injected into the atmosphere, a flood was divided into three stages. Assuming present conditions on Mars at the time of a flood, and using previously derived techniques for determining sublimation rates (Toon et al., 1980), it was estimated that roughly $10^{17}$ g of water would evaporate into the atmosphere in the active stage, while the flood was in progress. This water probably would have frozen out rapidly at the poles to form an ice layer a few centimeters thick. In the second stage, the lake that formed at the end of the flood channel freezes, and the thermal anomaly created by the presence of the lake dissipates. It was estimated that in a typical flood the terminal lake would take about one year to freeze solid and the thermal anomaly would take about 6 years to dissipate during which time about another $10^{17}$ gm of water would evaporate into the atmosphere and be precipitated out at the poles. The long term fate of the terminal ice deposits would depend on their latitude and thickness of any superimposed dust. Most of the floods in Elysium and Hellas, and around Chryse Planitia appear to have pooled at high latitudes (McGill, 1985; Lucchitta et al., 1986). Dust would affect the stability of ice deposits by reducing daily temperature excursions and inhibiting movement of water vapor from the buried ice to the surface. These effects were modelled using the techniques developed by Clifford and Hillel (1983). For an ice deposit at $50^{o}$ latitude, covered with a few tens of centimeters of dust, sublimation rates are estimated to be extremely low, in the range of $10^{-7}$ - $10^{-8}$ g $cm^{-2}$ $yr^{-1}$. Sublimation rates at the equator are over 100 times higher. Thus, the immediate effect of a flood on the atmospheric D/H would be to reset the atmospheric D/H to the value for groundwater. The long-term effect would depend on the latitude of the terminal ice deposit. Sublimation rates are so low for high latitude deposits that the D/H in the atmosphere could become enriched with respect to groundwater in response to upper atmosphere losses. If the terminal ice deposit were at low latitude, the atmosphere would be maintained at the D/H value for groundwater until the deposit had fully sublimed.

D/H ON MARS
Carr, M. H.

Volcanism is likely to have episodically introduced water into the atmosphere throughout the history of the planet. Greeley (1987) estimates that 25 to 41 m of water averaged over the whole planet have been introduced onto the surface by volcanism during the last 3.5 Ga. Judging from the size of lava flows, individual eruptions could almost instantaneously introduce $10^{13}$ to $10^{17}$ gm of water into the atmosphere. The larger eruptions would inject enough water into the atmosphere to reset its D/H ratio to that of juvenile water. Much of the erupted water would have rapidly frozen out at the poles without having its D/H ratio changed.

The effect of polar processes on D/H in the atmosphere depends on how actively water at the poles is exchanging with the atmosphere. If the Yung et al. (1988) estimates of loss of hydrogen from the upper atmosphere are correct, and water at the poles has actively interchanged with the atmosphere, then the poles can contain no more than 0.2 m of water averaged over the whole planet. But this conclusion is inconsistent with evidence of introduction of water onto the surface by floods and volcanism, and with the current perception of the polar layered terrains as ice rich. Jakosky (in press) suggested that Yung et al (1988) had underestimated hydrogen loss rates. He suggested that loss rates at high obliquity could be 100 times present rates, and the time averaged value 20 times the present rate. If so, then the reservoir of water at the surface would be correspondingly increased. An alternative explanation of the inconsistency is that exchange of water between the poles and the atmosphere is minimal, and restricted to the upper few centimeters of the polar deposits. Thus, new ice added to the polar deposits as a result of floods or volcanism, retains its initial D/H ratio except for the upper surface. In this case, the D/H in the atmosphere evolves almost independently of the poles, and reveals little about the inventory of water at the surface. Such a scenario is consistent with the crater ages of Plaut et al. (1989), which suggest that the polar layered terrains are older than formerly thought.

We can conclude that the D/H enrichment of the atmosphere is not necessarily that of the bulk of the near surface water. The evolution of D/H in the atmosphere is likely to have been episodic. Floods and eruptions would have periodically reset the atmospheric D/H to the groundwater and juvenile values respectively. Between these events the atmosphere would have become enriched in deuterium at a rate dependent on the rate of interchange of water between the atmosphere and other surface reservoirs such as the poles.

REFERENCES. Bjoraker, G. l., Mumma, M. J., and Larson, H. P., Proc. 4th Int., Conf. on Mars, Tucson, 69-70 (1989). Clifford, S. M., and Hillel, D., J. Geophys. Res., **88**, 2456-2474 (1983). Greeley, R., Science, **236**, 1653-1654 (1987). Jakosky, B. M., J. Geophys. Res. (in press). Lucchitta, B. K., LPSC XVII, 498-499 (1986). Mc Gill, G. E., LPSC XVI, 534-535 (1985). Owen, T., Maillard, J. P., deBergh, C., and Lutz, B. L., Science, **240**, 1767-170 (1988). Plaut, J. J., Kahn, R., Guiness, E. A., and Arvidson, R. E., Icarus, **76**, 357-377 (1988). Toon, O. B., Pollack J. B, Ward, W., Burns, J. A., and Bilski, K., Icarus, **44**, 552-607 (1980). Yung, Y. L., Wen, J., Pinto, J. P., Allen, M., Pierce, K. K., and Paulsen, S., Icarus, **76**, 146-159 (1988).

# CRATER MORPHOLOGY VARIATIONS IN THE ELYSIUM REGION: IMPLICATIONS FOR ICE DISTRIBUTION ON MARS

**Julie A. Cave, U.L.O. Planetary Image Centre, 33–35 Daws Lane, Mill Hill, London NW7 4SD.**

INTRODUCTION: Variations in crater morphology are attributed to differences in target strength, depth of excavation, presence of near-surface volatiles, and environmental conditions (1,2,3,4). Rampart craters and other features which may be a result of the presence of sub-surface ice have been observed in the Elysium Volcanic province (5). The aim of this study is to examine the distribution of various crater characteristics and to evaluate the usefulness of crater morphology as an indicator of sub-surface ice.

METHODOLOGY: Preliminary mapping of the region indicated a great complexity of crater morphologies. The study area (155–245°, 15°S–47.5°N) covers a wide range of latitude, altitude, surface type and age and there are therefore several factors that could have contributed to the observed morphological variations. Using mosaics of Viking frames (at a scale of 1:1 250 000) the co-ordinates of each crater over 1.875 km in diameter were digitised. A comprehensive classification scheme was devised that recorded the characteristics of each component of the crater allowing as much detail as possible to be used in the analysis. The characteristics of the craters' morphology recorded include: profile, central features, rim nature (continuous, buried *etc.*), rim condition (fresh, terraced, degraded *etc.*), ejecta type and surface texture (for each component of multiple blanket ejecta), geological unit according to references (6) and (7), and local target nature (*e.g.* lava flow, crater ejecta, channel floor). A confidence factor was also included since the precision of interpretation varied with resolution, although wherever possible the descriptive details were confirmed by checking the highest resolution images available. These details were incorporated into a homogeneous database which can be searched systematically to highlight the dominant factors. Initial analysis has concentrated on average or dominant crater characteristics as a function of latitude, altitude, geological unit, crater diameter and local target nature. The database is nearing completion, and initial observations presented here come from a preliminary analysis of 3060 craters in the Northern Hemisphere.

OBSERVATIONS:

(a) Approximately one third of the selected craters have discernable ejecta blankets. Plots of maximum ejecta diameter versus crater diameter (hereafter abbreviated to Evs$\Phi$) provide an indication of the mobility of the ejecta which is presumed to reflect the degree of fluidisation. The majority of the ejecta documented showed some degree of fluidisation (even for the smallest craters), and *very* few radial ejecta blankets were observed (this may be due in part to the resolution, since radial deposits are harder to detect). If the fluidisation of the ejecta *is* due to the incorporation of subsurface volatiles, then variations in the gradients of Evs$\Phi$ reflect *changes* in the state or concentration of volatiles rather than a transition from 'dry' to 'wet' materials being excavated (ignoring possible atmospheric effects).

(b) For most geological units there is a well-defined relationship between ejecta diameter and crater diameter. Many units (although the statistics of some are limited) seem to exhibit significantly higher gradients at larger crater diameters. When all the data are combined the resulting graph is a smooth, rising curve, but the data for several units taken individually exhibit gradient discontinuities. The position of such discontinuities, and the gradients appear to depend on the geological unit. The Elysium lava plains, unit AEL1 have a lower gradient of 2.1±0.2, upper gradient of 3.6±3.6, with an assumed break-point occurring at crater diameter 7km. The lower gradient lies between the gradient for similar-sized craters on Elysium Mons itself (AEL2, 2.0±0.1) and that of the channeled deposits AEL3 which originate from the N.W. flanks of the volcano (gradient = 2.9±0.2). This might suggest a *localised* transfer of volatiles from AEL2 to AEL3 driven by the increased thermal gradient of Elysium Mons. Further evidence of volatile enrichment of units AEL3/4 is provided by the marked concentration of double-ejecta craters in this location (see figure 1).

(c) An initial investigation of Evs$\Phi$ has revealed no obvious trend with latitude, except that the previously mentioned relationship breaks down at latitudes greater than about 40° N. Plots of Evs$\Phi$ in this region indicate a wide scatter of the data, which may be due to the high concentration of pedestal craters here.

(d) The precise target nature does appear to have influenced the spread of the ejecta: a linear Evs$\Phi$ relationship occurs for craters that have impacted other crater rims (despite varied geological locations) and a possible linear trend has been observed for craters on volcanic constructs.

## CRATER MORPHOLOGY IN THE ELYSIUM REGION: J. A. CAVE

(e) The location of central features is as shown in Figure 1. The peaked craters are widely distributed on many units, while the pit craters are less frequent and have a more limited distribution. The plot of EvsΦ for these craters indicate similar ejecta fluidities, possibly indicating similar formation conditions. The scarcity of pits may be due in part to the infilling or flooding of many of the larger craters in the sample set.

(f) These observations are currently being checked for statistical accuracy. Altitude, radial distance from Elysium Mons, and estimates of the depth of excavation will also be taken into account. The morphological characteristics of the ejecta will be examined simultaneously with the dimensional data.

The database is a valuable aid in the interpretation of the crater morphology in the area, and will also provide information on the ages and resurfacing histories of the units. This work forms part of a detailed investigation of Elysium in which all possible indications of the presence of ice (craters, channels, chaotic and knobby terrain, volcano eruptive styles) are being assessed. Comprehensive studies of the age, nature and distribution of each ice-related landform will enable further constraints to be placed on the importance, timing and distribution of ice in Elysium. In a future project, the Hellas volcanic region will be investigated using the same technique, allowing comparisons to be made between two volcanic provinces of different ages and geological settings.

REFERENCES: (1) Head J.W., Proc. L.P.S.C. VII 2913–2927, 1976. (2) Carr M.H., Crumpler L.S., Cutts J.A., Greeley R., Guest J.E. and Masursky H., J. Geophys. Res. **82** 4055-4065, 1977. (3) Mouginis-Mark P.J., J. Geophys. Res. **84** 8011–8022, 1979. (4) Bridges N.T. and Barlow N.S., L.P.S.C XX 105–106, 1989. (5) Mouginis-Mark P.J., Wilson L., Head J.W., Brown S.H., Lynn Hall J. and Sullivan K.D., Earth, Moon, and Planets **30** 149–173, 1984. (6) Scott D.H. and Tanaka K.L., Map I-1802-A, U.S.G.S., 1986. (7) Greeley R. and Guest J.E., Map I-1802-B, U.S.G.S., 1987.

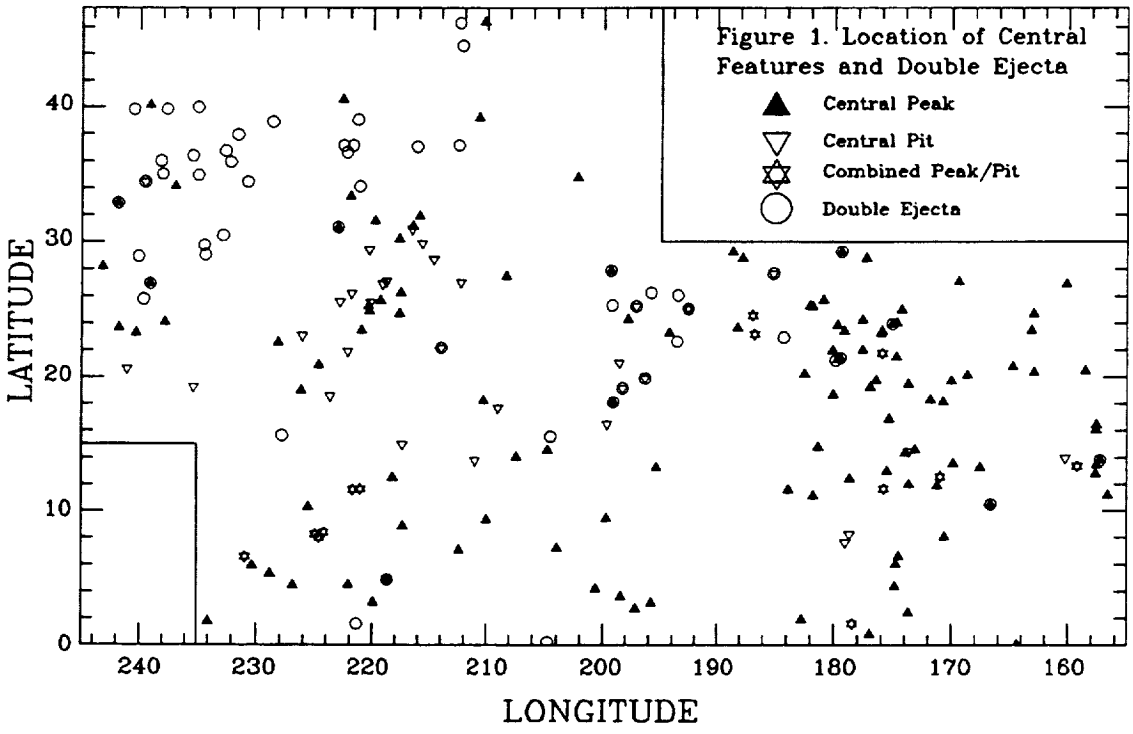

CROSSCUTTING, PERIODICALLY SPACED WRINKLE RIDGES OF HESPERIA PLANUM; D. John Chadwick, Dept. of Geology, Northern Arizona University, Flagstaff, AZ 86001; Thomas R. Watters and Michael J. Tuttle, Center for Earth and Planetary Studies, National Air and Space Museum, Smithsonian Institution, Washington, D.C. 20560

Wrinkle ridges are the long, sinuous anticlinal features which occur on the volcanic plains units of the terrestrial planets and the Moon. Most of these ridges form single, parallel trending groups or concentric patterns within circular basins. The wrinkle ridges of Hesperia Planum on Mars, however, show a much more complex spatial relationship. Two distinct sets of ridges have formed here, crosscutting one another at nearly orthogonal angles, implying a more complex structural history for the region. Termed reticulate ridge patterns (1), these crosscutting ridges are found elsewhere on Mars, but at Hesperia Planum they dominate a very large area to the east and southeast of Tyrrhena Patera.

In this study, the two directional components of the reticulate pattern were separated and ridge spacing was determined using a series of sampling traverses spaced about 20 km apart and oriented perpenducular to the mean ridge trend of both sets. In addition, the two sets of ridges maintain a constant trend over a limited area. Therefore, a large area of Hesperia Planum containing the reticulate pattern was divided into four domains based on the mean trend of the ridges. In each of the domains, the ridge spacings of the two sets were found to be very similar and passed the statistical t-test for equivalency. This test compares two sets of sampled numerical data to determine if they appear to be derived from the same population. The mean spacing for the two ridge sets in each domain are as follows: 38.23 km and 36.13 km for domain one, 32.02 km and 33.75 km for domain two, 36.10 km and 35.58 km for domain three, and 23.80 km and 24.26 km for domain four. The equivalent spacing of both sets of ridges can be explained by two superimposed episodes of buckling at a critical wavelength, governed by the rheological properties and thickness of the plains material in which the ridges formed (2).

The origin(s) of the compressive stresses which formed the reticulate pattern is not readily apparent. The compressional stresses that resulted in the formation of the wrinkle ridges of the Tharsis Plateau may have been in part due to isostatic uplift (3,4,5,6). In the absence of a "Tharsis-like" uplift or load in Hesperia Planum, other mechanisms for the generation of compressional stresses must be found. Compression may have resulted from subsidence due to loading of the volcanic plains material (1), but this mechanism may produce only a single ridge trend related to the shape of the basin. A superimposed regional tectonic event may account for the second ridge set in the reticulate pattern, with local influences accounting for the variable trends of the ridges.

REFERENCES

(1) Raitala, J., Earth, Moon and Planets, 40, 71-99, 1988. (2) Watters, T.R., submitted to JGR, 1989. (3) Banerdt, W.B., M.P. Golombek, and K.L. Tanaka, submitted to Mars, University of Arizona Press, Tucson, AZ, 1989. (4) Banerdt, W.B., R.J. Phillips, N.H. Sleep, and R.S. Saunders, JGR, 87 9723-9733, 1982. (5) Sleep, N.H. and R.J. Phillips, JGR, 90 4469-4489, 1985. (6) Watters, T.R. and T.A. Maxwell, JGR, 91 8113-8125, 1986.

Figure 1. Crosscutting wrinkle ridges of Hesperia Planum; a portion of domain three.

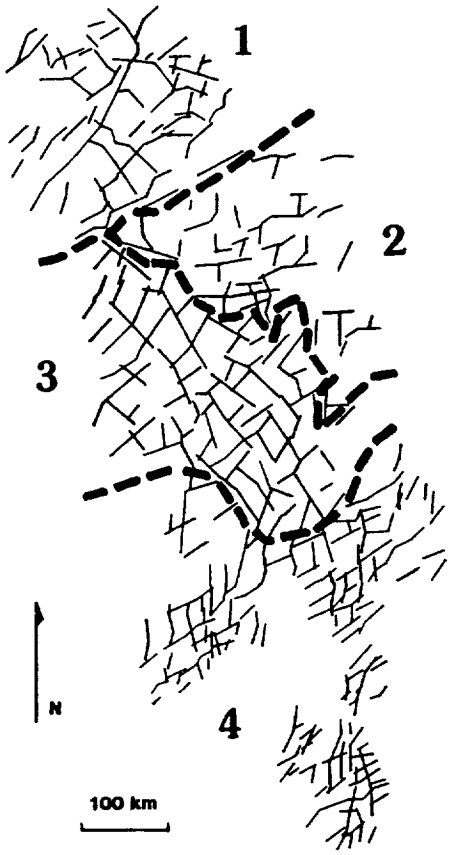


Figure 2. The four domains of eastern and southeastern Hesperia Planum.

GEOLOGIC MAPPING OF LOWER MANGALA VALLES, MARS: EVIDENCE OF FLOODING, SAPPING, DEBRIS FLOW, AND VOLCANISM[1]; Mary G. Chapman and Kenneth L. Tanaka, U.S. Geological Survey, 2255 North Gemini Drive, Flagstaff, AZ 86001.

Two periods of catastrophic flooding are indicated by detailed geologic mapping of the Mangala channel, based on two 1:500,000-scale photomosaics (MTM -05152 and -10151), computer enhancement of Viking images, and photoclinometric channel profiles. The ages of these two episodes are Late Hesperian and Amazonian-Hesperian. Lobate lava flows were erupted during channeling episodes; at least two stratigraphically distinct, resistant lava flows filled the early channels; later flooding eroded the surrounding, less resistant material to leave the lava-capped channels higher than surrounding terrain (i.e. inverted topography). Impact craters that were breached and filled by the earliest phase of flooding formed lakes; some of these ponded areas were covered by lava, others were refilled by the later period of flooding. This flooding period was followed by (1) spring sapping that formed narrow, theater-headed channels (2) debris-flow deposition resulting from chaotic collapse of lava-capped material within breached craters. The direction of drainage was north toward Amazonis Planitia, where the flow materials were partly covered by Middle Amazonian lobate lava flows.

[1]Previously published in GSA Abstracts with Programs, 1989, v. 21, no. 6, p. 4108.

# ESA PLANS FOR THE SCIENTIFIC EXPLORATION OF MARS

Chicarro A.F., Space Science Department, ESA/ESTEC, 2200 AG Noordwijk, The Netherlands.

The exploration of Mars by unmanned spacecraft during the last quarter of a century shows that, although geologically less evolved, Mars is far more Earth-like than any other planet. Its internal evolution, resulting in intense tectonic and volcanic activity, and the exogenic processing of its surface, have extended over several billion years. Aside from the Earth, Mars is the only other planet with surface-temperature conditions in the range of stability of complex organic compounds, and therefore, it is an obvious target in the search for present or extinct lifeforms.

**Specific goals:** The future international exploration of Mars must address major scientific questions, such as: What is the present internal structure, composition and activity of the planet? What are the relative and absolute ages of Mars geologic units? What is the chronology of extensive and compressive tectonic phases? Do SNC meteorites unequivocally come from Mars? What are the most common minerals in volcanic, plutonic and sedimentary rocks? How different were the atmospheric composition, pressure, temperature and dynamics in the past? What is the present surface and subsurface water distribution ? How closely did early Mars resemble the Earth when life appeared on our planet, about 3.8 billion years ago? Are there sediments on Mars containing organic compounds or primitive fossils?

**Strategy:** ESA has identified three possible areas of European participation in the future international exploration of Mars. These options, two of them dealing with science from the surface, the other addressing science from orbit, are as follows:

• Network science: A network of small surface stations, including a combination of 2 hard landers (surface penetrators) and a cluster of 3 semi-hard landers (mini-probes), thus defining a global/local seismological network (Figure 1) designed for an operational lifetime of one Martian year. The scientific objectives (Table 1) would especially concentrate on the internal structure, mineral and chemical composition, surface meteorology, and entry and descent science measurements. The global/regional network concept could be part of a precursor mission to the *Mars Rover Sample Return* and *Manned Exploration* missions.

• Rover science: A sophisticated sample-acquisition subsystem, including intelligent robotic arm(s) to be placed on-board a rover from another space agency, and capable of stereo-vision, handling, sampling and analyzing rocks and soils. It would conduct detailed in-situ chemical and mineralogical analyses of surface samples, subsurface structural studies, biological experiments, and atmospheric studies, at a number of surface locations within a limited area of mobility. This sampling subsystem could be a contribution to a *Mars Rover Sample-Return* mission.

• Orbiter science: A facility on-board an orbiting spacecraft able to: (i) acquire very high-resolution imagery, (ii) provide radar altimetry and subsurface sounding, or (iii) contribute to the identification of the mineralogical and chemical composition of geologic units. This orbital facility would include a very sophisticated imager or a microwave radar instrument, and would have scientific potential for any surveillance mission of Mars.

**International cooperation:** Any of the three selected areas for possible European participation would represent a major and independent contribution to a future international mission to Mars, complementing the already scheduled US *Mars Observer* and the USSR's *Mars-94* missions. However, in-depth technical and scientific assessment studies, with emphasis on a *Network mission*, are currently under way in ESA. Following the cooperative path initiated by *Cassini*, a participation in international planetary missions stands as a sensible and viable approach for Europe, in order to take its proper role in the exploration of the Solar System during the next decade and beyond.

Reference: Chicarro A.F. et al., *Mission to Mars: Report of the Mars Exploration Study Team*, ESA SP-1117, European Space Agency, 138 pp., 1989.

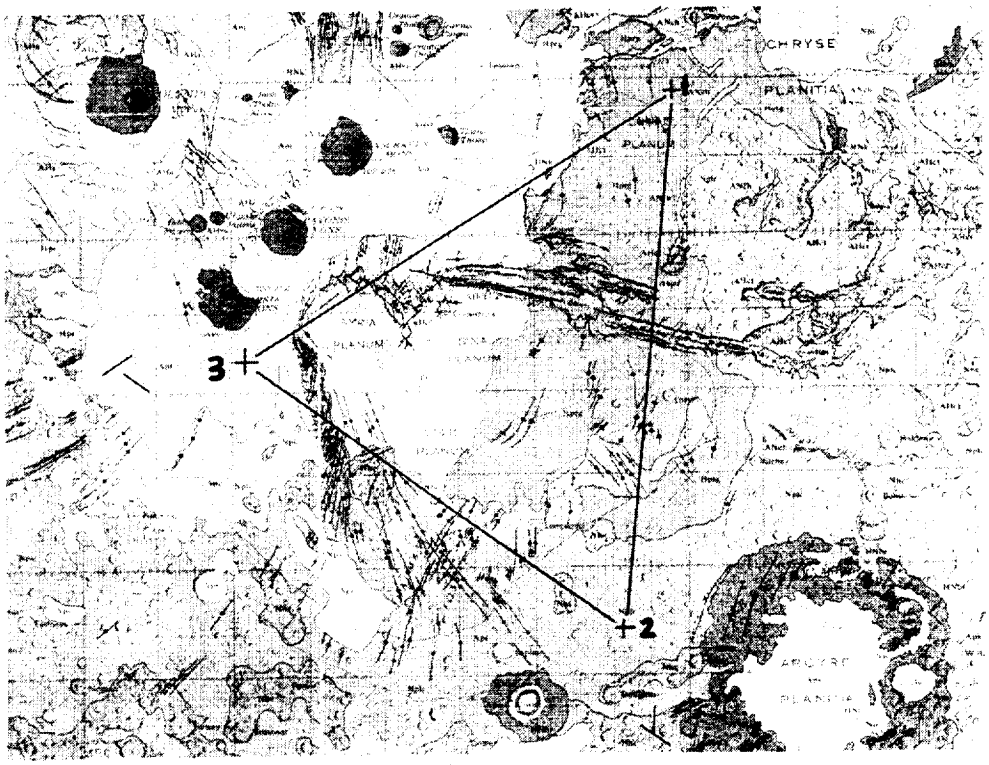


Figure 1: *Location of proposed landing sites in the Tharsis region.*

| Site | Device | Payload | Mass | Scientific interest<br>Geochemistry | Meteorology | Seismology |
|---|---|---|---|---|---|---|
| 1 | Cluster of 3 mini-probes | Total of:<br>1 global seismometer,<br>3 local seismometers (1 axis),<br>3 meteorol. packages,<br>1 camera,<br>chemical analysis (DEG, TPA, PM, GC) | 250 kg including aeroshell and ~5 kg payload on each probe | Analyse ridged plains material and subsurface volatile content | Northern hemisphere site, near Viking Lander-1 in order to compare results | The three sites determine a triangle (of side ~3500 km) which englobes most of the Tharsis uplift and its radial fault system:<br>— likely tectonic activity<br>— good definition of seismic epicentres.<br>Global network: to determine Mars' internal structures<br>Local network: to study the lithosphere's upper layers. In addition, meteoritic impacts do trigger seismic waves: to help determine the planet's internal structure |
| 2 | Independently targetted penetrator | For each penetrator:<br>global seismometer (3 axis),<br>camera,<br>meteorol. package,<br>chemical analysis (DEG, TPA, XRF, GRS, GC, PM, CS) | 100 kg including ~8 kg payload | Analyse most widespread older unit: complex history of weathering and impacting | Southern hemisphere site: study formation and evolution of global dust storms | |
| 3 | Independently targetted penetrator | | 100 kg including ~8 kg payload | Analyse younger volcanic unit: type of volcanic activity.<br>All three sites have simple geology: unmistakable units | Near the equator and higher-altitude site: study formation of clouds in addition to weather patterns and atmospheric circulation | |

Table 1: *Scientific interest of a network of small stations.*

**DERIVATION OF MARS ATMOSPHERIC DUST PROPERTIES FROM RADIATIVE TRANSFER ANALYSIS OF VIKING IRTM EMISSION PHASE FUNCTION SEQUENCES;** R.T. Clancy and S.W. Lee, Laboratory for Atmospheric and Space Physics, University of Colorado, Boulder, CO 80309

During the span of the Viking Orbiter missions, several hundred emission-phase-function (EPF) sequences were obtained, in which the IRTM instrument observed the same area of surface as the spacecraft moved overhead. The IRTM data set as a whole is well calibrated, having been corrected for inter-spacecraft, inter-detector, and temporal calibration variations; a conservative estimate for the absolute uncertainty inherent in this data set is 1-2% [1]. The EPF visual brightness observations (passband of 0.3-3.0 μm , effective wavelength of 0.57 μm ) present very accurately calibrated albedos of a given region and the atmosphere above it versus emission (and to a lesser extent, incidence) angle. Although these observations were designed for the purposes of surface photometric studies, they are quite suitable for the derivation of atmospheric dust opacities.

We have developed a radiative transfer model of the Mars atmosphere and surface based upon a discrete-ordinates radiative transfer code [2]. Input parameters include the atmospheric dust opacity, the single scattering albedo ($\varpi_0$) and particle phase function of the atmospheric dust, and the surface bidirectional reflectance. A 16-stream approximation is adopted to adequately represent the model dust and surface phase functions. The surface photometric function is estimated from EPF sequences at low dust opacities and emission angles, where the effects of scattering by atmospheric dust are minimized. The exact behavior of the bidirectional reflectance at large emission angles and/or high dust loading is not critical since the contribution of atmospheric dust scattering dominates the observed reflectance for these regions.

On the basis of an analysis of ~20 separate EPF sequences spanning low and high latitudes, low and high dust opacities, and a wide range of $L_S$; we find evidence for three distinct aerosol populations. In all three cases it is possible to model the dust scattering with a single dust phase function labelled "IRTM" in figure 1. An empirical phase function representing scattering by non-spherical particles was derived by Pollack et al. [3] to fit the Viking lander observations of dust scattering, and is presented by the solid line in figure 1. The agreement between the "IRTM" and Pollack phase functions is quite good; however the asymmetry factor, g, is 0.55-0.56 rather than the value of 0.79 given by Pollack et al. [3]. A Henyey-Greenstein phase function with g=0.79 is also included in figure 1 to indicate the very large large differences in particle back-scattering implied by g=0.55 versus g=0.79.

We find three separate values of the single scattering albedo, $\varpi_0$, corresponding to the three aerosol populations. At low-to-mid latitudes for moderate dust opacities ($\tau$ = 0.2-1.0), $\varpi_0$=0.88 fits the EPF observations. Figures 2-4 present a subset of model-data comparisons for this case. At high latitudes (70°-80°N) we find $\varpi_0$=1.0, indicating that ice clouds are the likely source of particulate scattering. Figure 5b presents a model-data comparison for this case and a best fit attempt with $\varpi_0$=0.88 (figure 5a). The third aerosol population corresponds to very high dust loading ($\tau$ > 2), in which it is necessary to increase $\varpi_0$ to 0.9-0.92 to fit the data with the "IRTM" dust phase function. Figures 6a and 6b indicate model-data comparisons over Hellas basin in which we attempt to fit the EPF data with $\varpi_0$=0.88 and $\varpi_0$=0.92, respectively.

The primary differences between the EPF IRTM and Viking lander derived dust properties are larger $\varpi_0$ from the EPF analysis ($\varpi_0$=0.88 versus 0.86) and an increase in $\varpi_0$ during the peak of the dust storm as found in the EPF analysis (the Viking lander data indicate no such change, J. Pollack, personal communication). It is possible that the distinction of looking from below with lander data and looking from above with the IRTM data may account for these differences. Finer dust (higher $\varpi_0$ and more backscattering) may be mixed to higher altitudes and may increase during the peak of the dust storms (J. Bergstrahl, personal communication). The downward-looking geometry of the EPF sequences would be more sensitive to a high-altitude, fine component.

This research was supported under NASA Planetary Geology grant NAGW 1378.

**REFERENCES:** [1] Pleskot, L.K., and E.D. Miner (1981). Time variability of martian bolometric albedo. *Icarus 45*, 179-201. [2] Stamnes, K., S.C. Tsay, W. Wiscombe, and K. Jayaweera (1988). A numerically stable algorithm for discrete-ordinate-method radiative transfer in scattering and emitting layered media. *Appl. Opt., 27*, 2502-2509. [3] Pollack, J. B., D. S. Colburn, F. M. Flasar, R. Kahn, C. E. Carston, and D. Pidek (1979). Properties and effects of dust particles suspended in the martian atmosphere. *J. Geophys. Res., 84*, 2929-2945.

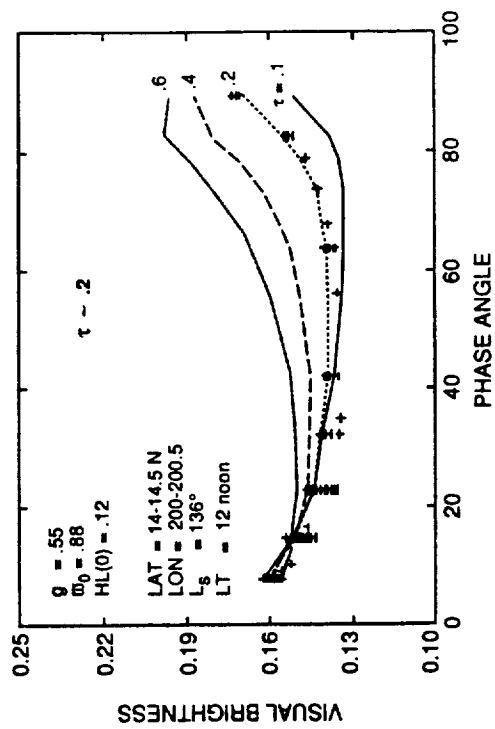


Fig. 2. Observed (crosses) phase function of EPF sequence over Cerberus versus model phase functions with τ=.1,.2,.4, and .6. Best-fit to data gives τ=.2, $\varpi_0$=.88, g=.55.

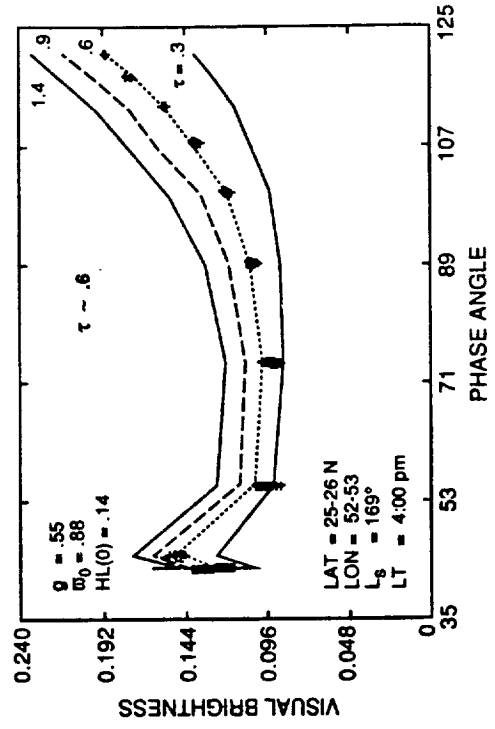


Fig. 4. Observed (crosses) phase function of EPF sequence over Chryse Planitia versus model phase functions with τ=.3,.6,.9, and 1.4. Best-fit gives τ=.6, $\varpi_0$=.88, g=.55.

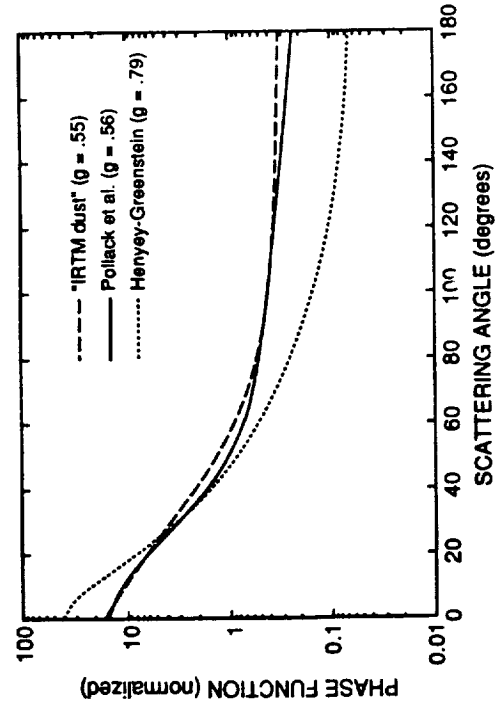


Fig. 1. Mars aerosol phase functions.

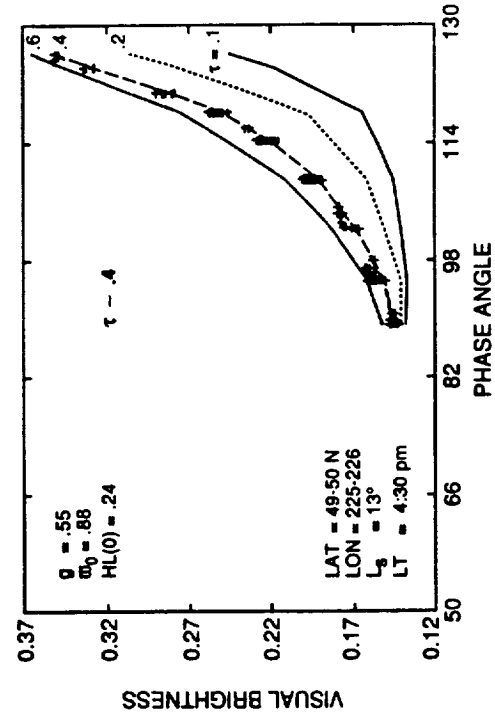


Fig. 3. Observed (crosses) phase function of EPF sequence over Utopia Planitia versus model phase functions with τ=.1,.2,.4, and .6. Best-fit to data gives τ=.4, $\varpi_0$=.88, g=.55.

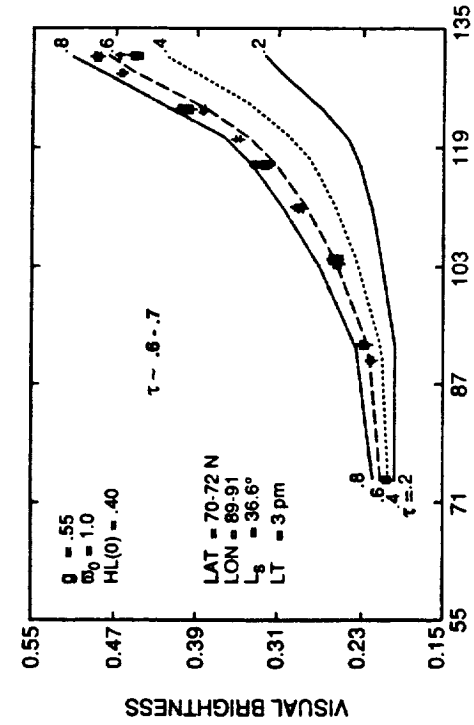


**Fig. 5b.** Observed (crosses) phase function of EPF sequence over the North polar erg versus model phase functions with $\tau$=.2, .4,.6, and .8. Best-fit to data gives $\tau$=.7, $\varpi_0$=1.0, g=.55.

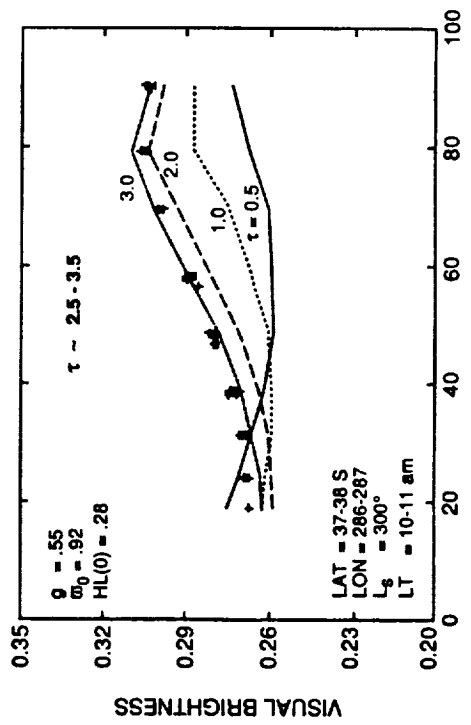


**Fig. 6b.** Observed (crosses) phase function of EPF sequence over Hellas Planitia versus model phase functions with $\tau$=.5,1.0, 2.0, and 3.0. Best-fit gives $\tau$=3.0, $\varpi_0$=.92, g=.55.

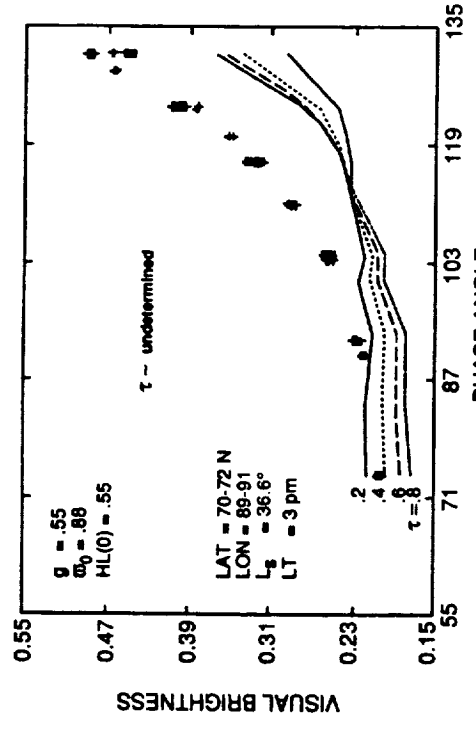


**Fig. 5a.** Observed (crosses) phase function of EPF sequence over the North polar erg versus model phase functions with $\tau$=.2, .4,.6, and .8. No fit is possible for $\varpi_0$=.88, g=.55.

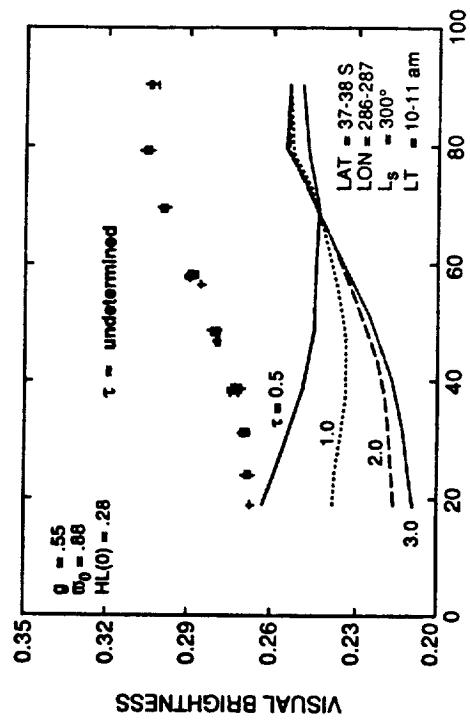


**Fig. 6a.** Observed (crosses) phase function of EPF sequence over Hellas Planitia versus model phase functions with $\tau$=.5,1.0, 2.0, and 3.0. No fit is possible for $\varpi_0$=.88, g=.55.

COLD POLAR DESERTS: WEATHERING RATES, MECHANISMS, AND IMPLICATIONS FOR REMOTE SENSING OF MARS; Edward A. Cloutis, Department of Geology, University of Alberta, Edmonton, Alberta T6E 4S6

Introduction: Polar and alpine desert regions (cold deserts) offer the best terrestrial field analogues to weathering conditions on Mars [1]. A suite of rock samples from the Northwest Territories in Canada has been spectrally characterized in order to better understand the weathering processes prevalent in cold deserts and to examine the implications for remote sensing of Mars. Since these samples have presumably been subaerially exposed only since the last period of glaciation, they are useful for examining how relatively short-term physical and chemical weathering affect spectral properties.

The samples were collected from the Yellowknife Bay area (basalt) and Contwoyto Lake-Point Lake region in the Slave Province. The samples include a basalt (JMP2), an iron formation (5PLJ009), a volcanoclastic (4PLI017), a schist (5PLT001), and a granite (5PLJ001). Both weathered (exterior) and unweathered (interior) surface spectra of each sample were measured. It is known that physical and chemical weathering operate at low rates in cold, dry deserts. The unique environment of these regions affects the relative importance of different weathering processes [2]. The most common alteration phenomona which have been amply documented are the formation of ferric iron oxides/hydroxides, as evidenced by rust-colored staining on rock surfaces and in soils [3,4,5,6], and the formation of clays [3,7,8].

Results: *Basalt:* The weathered and unweathered surface spectra of a basalt are shown in Figure 1. The weathered surface spectrum shows strong evidence of ferric iron at shorter wavelengths- an absorption edge near 0.53$\mu$m, and two broad absorption bands near 0.65 and 0.9$\mu$m. The wavelength position of the latter band ($\tilde{}$0.88$\mu$m) and its broadness are consistent with multiple hydrated ferric species such as goethite, ferroxyhyte and ferrihydrite [9,10]. The interior surface spectrum suggests a greater ferrous iron component and is similar to other unweathered basalt spectra [11,12]. At longer wavelengths both spectra are similar. The various absorption bands can be assigned to clay lattice-OH absorption bands involving both Mg and Al, as expected for a basalt. The presence of these bands in the interior surface spectrum indicates that the interior has been slightly metamorphosed.

*Iron Formation:* Sample 5PLJ009 is composed of magnetite, chert and siderite. The degree of visible weathering is small enough so that the underlying banding is still visible. The weathered surface spectrum is again dominated by ferric iron absorption features. The broad band near 1.9$\mu$m indicates that weathering has produced multiple hydrated species and/or poorly-crystallized phases (Figure 2). The interior surface spectrum is dominated by siderite, which exhibits a broad absorption band between $\tilde{}$1.0 and $\tilde{}$1.4$\mu$m. However, the expected strong carbonate absorption bands at 2.35 and 2.56$\mu$m [13] are absent.

*Volcanoclastic*: The weathered surface spectrum of a felsic-pyritic metatuff is again dominated by ferric iron bands at shorter wavelengths (Figure 3). A broad pyrite absorption band expected near 1$\mu$m is not evident. The weakness of various clay lattice-OH bands suggest that the formation of well-crystalized hydrated species has not been significant. The interior spectrum shows almost no evidence for ferric iron absorption bands. The broad feature centered near 1.05$\mu$m is characteristic of ferrous iron and pyrite.

*Schist:* The weathered and unweathered surface spectra of a cordierite-biotite knotted schist differ markedly from each other (Figure 4). In both cases there is a general lack of diagnostic absorption bands. The general reflectance rise towards longer wavelengths and lack of well-defined absorption bands in the exterior spectrum suggests that weathering has generated a number of poorly crystallized phases which absorb incident radiation over a range of energies, probably through charge transfers.

*Granite*: Granite differs from the other samples in its general lack of iron-bearing minerals. This is reflected in the lack of ferric iron absorption bands in the spectrum (Figure 5). Both the interior and exterior surface spectra show the same types of long wavelength absorption bands, indicative of aluminum.

Discussion: In spite of the presumed low rate and duration of weathering which has presumably affected these samples, exterior (weathered) and interior (unweathered) surfaces of the same sample vary from very similar (Figure 1) to radically different (Figures 4 & 5). It is apparent that significant spectral changes can be effected by even the low weathering rates prevalent in cold desert regions. The formation of ferric iron species results in the appearance of an absorption edge near 0.53$\mu$m, a shoulder or band near 0.64$\mu$m, and an absorption band near 0.9$\mu$m [9,10]. These features are most apparent in the most iron-rich samples such as basalt, iron formation and volcanoclastic. The reflectance spectra amply confirm the physico-chemical and spectral importance of ferric iron oxide/hydroxide formation in cold deserts.

Aluminum- and magnesium-rich lithologies give rise to Al-OH and Mg-OH absorption bands respectively in weathered surface spectra in cases where the absorption bands are resolvable. For example, the absorption bands present in the exterior granite spectrum at 2.20, 2.32 and 2.35$\mu$m can be assigned to Al-OH vibrations. There is no clear evidence for an Mg-OH absorption band expected near 2.4$\mu$m. This is consistent with the aluminum-rich composition of the granite.

A general lack of well-defined absorption bands attributable to specific hydrated phases indicates that cold desert weathering is generally not accompanied by the formation of well-crystallized phases, but that clay formation is nevertheless an important process. The broadness of the ferric iron absorption bands also suggests that poorly-crystallized phases are important. The formation of poorly-crystallized phases in cold deserts is consistent with interpretations of martian telescopic spectra as indicating semi-amorphous or amorphous phases such as palagonite [14].

The spectral changes associated with cold desert weathering include variations in overall spectral slope, the appearance/disappearance of absorption bands, shifts in absorption band minima wavelength positions, and changes in band shapes and intensities. Dramatic spectral differences between interior and exterior surface spectra are present even when weathered surfaces are thin enough so that underlying petrofabrics are still visible.

In spite of the small number of samples in the current suite, the data indicate that cold desert weathering of carbonates may be sufficient to render them virtually indistinguishable. In addition, the oxidation of ferrous to ferric iron proceeds regardless of whether the iron is derived from silicates (basalt), oxides (iron formation), carbonates (iron formation), or sulfides (volcanoclastic). It is clear that unweathered, interior rock sample spectra are generally not useful for the interpretation of remote sensing data for targets such as Mars which are subject to subaerial weathering.

**Acknowledgments:** This study was supported by a Grant-in-Aid of Northern Research from the Boreal Institute for Northern Studies of the University of Alberta (#55-30274) and a Research Grant from the Geological Society of America (#3741-87).

**References:**[1] Agresti, D.G., Morris, R.V., Newcomb, J.A., and Lauer, H.V. Jr., *Lunar Plan. Sci. Conf. XVII*, 3-4 (1986). [2] Ugolini, F.C., *Rates of Chemical Weathering of Rocks and Minerals*, 193-235 (Colman & Dethier, Eds.), Academic (1986). [3] Glazovskaya, M.A., *Sci. Pap. Inst. Geol. Geogr. Sci. Moscow Univ., 1*, 63-76 (1958). [4] Tedrow, J.C.F., *Soil Sci. Soc. Amer. Proc., 30*, 381-387 (1966). [5] Ugolini, F.C., *NAS-NRC Publ. 1278*, 55-61 (1966). [6] Bockheim, J.G., *Soil Sci., 128*, 142-152 (1979). [7] Claridge, G.C.C., *New Zealand J. Geol. Geophys., 8*, 186-220 (1965). [8] Jackson, M.L., Lee, S.Y., Ugolini, F.C., and Helmke, P.A., *Soil Sci., 123*, 241-248 (1977). [9] Sherman, D.M., Burns, R.G., and Burns, V.M., *J. Geophys. Res., 87*, 10169-10180 (1982). [10] Morris, R.V., Lauer, H.V. Jr., Lawson, C.A., Gibson, E.K. Jr., Nace, G.A., and Stewart, C., *J. Geophys. Res., 90*, 3126-3144 (1985). [11] Hunt, G.R., Salisbury, J.W., and Lenhoff, C.J., *Mod. Geol., 5*, 15-22 (1974). [12] Singer, R.B., and Blake, P.L., *Lunar Plan. Sci. Conf. XIV*, 706-707 (1983). [13] Hunt, G.R., and Salisbury, J.W., *Mod. Geol., 2*, 22-30 (1971). [14] Singer, R.B., *J. Geophys. Res., 87*, 10159-10168 (1982).

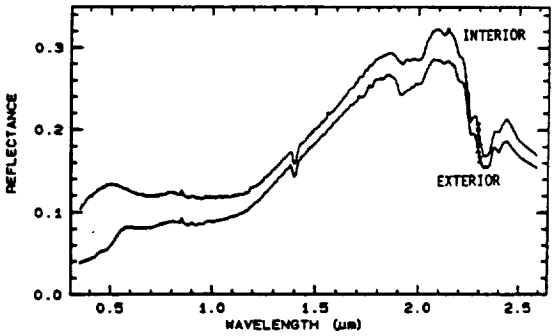


**Figure 1.** Reflectance spectra of interior and exterior surfaces of basalt sample JMP2.

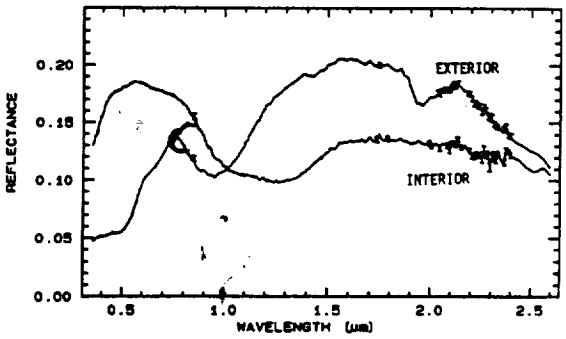


**Figure 2.** Reflectance spectra of interior and exterior surfaces of iron formation sample 5PLJ009.

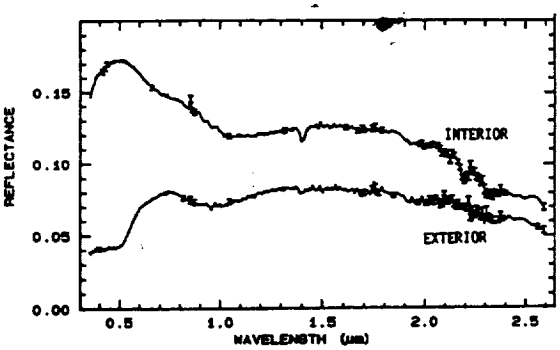


**Figure 3.** Reflectance spectra of interior and exterior surfaces of felsic-pyritic-metatuff (volcanoclastic) sample 4PLJ017.

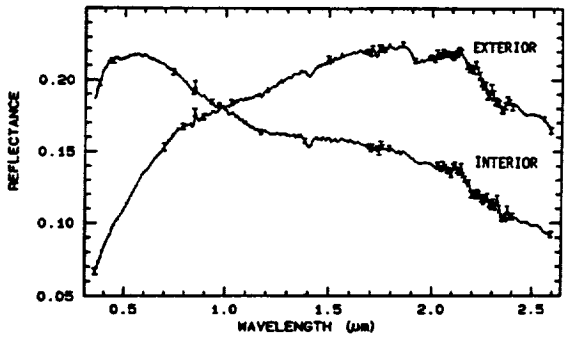


**Figure 4.** Reflectance spectra of interior and exterior surfaces of cordierite-biotite knotted schist sample 5PLT001.

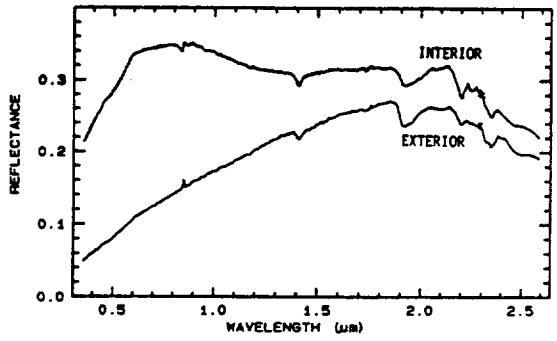


**Figure 5.** Reflectance spectra of interior and exterior surfaces of granite sample 5PLJ001.

**Characteristics of the Martian Atmospheric Surface Layer**; G.D.Clow (USGS, MS946, Menlo Park, CA 94025) and R.M.Haberle (NASA/Ames, Moffett Field, CA 94035)

We extend elements of various terrestrial boundary layer models to Mars in order to estimate sensible heat, latent heat, and momentum fluxes within the martian atmospheric surface ("constant flux") layer. The atmospheric surface layer consists of an interfacial sublayer (#1) immediately adjacent to the ground and an overlying fully turbulent surface sublayer (#2) where wind-shear production of turbulence dominates buoyancy production. Within the interfacial sublayer, sensible and latent heat are transported by non-steady molecular diffusion into small-scale eddies which intermittently burst through this zone. Both the thickness of the interfacial sublayer and the characteristics of the turbulent eddies penetrating through it, depend on whether airflow is aerodynamically smooth or aerodynamically rough, as determined by the Roughness Reynold's number. Within the overlying surface sublayer (#2), similarity theory can be used to express the mean vertical windspeed, temperature, and water vapor profiles in terms of a single parameter, the Monin-Obukhov stability parameter.

To estimate the molecular viscosity and thermal conductivity of a $CO_2$-$H_2O$ gas mixture under martian conditions, parameterizations were developed using data from the TPRC Data Series [1] and the first-order Chapman-Cowling expressions; the required collision integrals were approximated using the Lenard-Jones (12,6) potential. Parameterizations for specific heat and binary diffusivity were also determined. The Prandtl and Schmidt numbers derived from these thermophysical properties are found to range 0.78 - 1.0 and 0.47 - 0.70, respectively, for Mars. Brutsaert's model for sensible and latent heat transport within the interfacial sublayer for both aerodynamically smooth and rough airflow has been experimentally tested under similar conditions [2], validating its application to martian conditions. For the surface sublayer (#2), we modify the definition of the Monin-Obukhov length to properly account for the buoyancy forces arising from water vapor gradients in the martian atmospheric boundary layer. This length scale is then utilized with similarity-theory turbulent-flux profiles with the same form as those used by Businger *et al.* [3] and others.

We find that under most martian conditions, the interfacial and surface sublayers offer roughly comparable resistance to sensible heat and water vapor transport and are thus both important in determining the associated fluxes. Airflow over surfaces similar to terrestrial polar snow (surface roughness length $z_0$ approx. 0.03 cm) is generally found to be aerodynamically smooth at low martian pressures (P<30 mb) but aerodynamically rough at high pressures (P>300 mb); airflow at the Viking Lander sites is aerodynamically transitional under current martian conditions. For aerodynamically smooth airflow, the thickness of the interfacial sublayer is found to be up to 100 times thicker for Mars than is typical for the Earth. At low pressures (P<30 mb) and high temperatures (T>250 K), buoyancy forces due to water vapor gradients can become so high on Mars that the surface sublayer (#2) essentially disappears (the Monin-Obukhov length becomes comparable to the thickness of the interfacial sublayer). At this point, the atmospheric boundary layer transitions to the "free convection" regime [4]. Free convection sensible and latent heat fluxes are smaller than those for the case when the surface sublayer (#2) is present. As expected, friction velocities $u_*$ and the sensible and latent heat fluxes are found to be extremely sensitive to the Monin-Obukhov stability parameter for stable atmospheric conditions and mildly sensitive for unstable conditions.

The ability to predict heat losses across an interfacial boundary layer and to predict the shapes of the windspeed and temperature profiles in the atmospheric surface layer, should prove useful for estimating heat losses from engineering structures deployed on the martian surface and for improving our understanding of water vapor transfer rates from icy surfaces (such as the poles) to the atmosphere.

References: [1] Touloukian,Y.S. (1972) **Thermophysical Properties of Matter: The TPRC Data Series**, vol.3,6,11; [2] Brutsaert,W. (1975) **Water Resour. Res.**,11,543-550; [3] Businger *et al.*(1971) **J.Atmos.Sci.**,28,181-189; [4] Clow,G.D. and R.M.Haberle (1990) **Lunar and Planet. Sci. XXI**, in press.

**Free Convection in the Martian Atmosphere**; G.D.Clow (USGS, MS946, Menlo Park, CA 94025) and R.M.Haberle (NASA/Ames, Moffett Field, CA 94035)

We investigate the "free convective" regime for the martian atmospheric boundary layer (ABL). This state occurs when the mean windspeed at the top of the ABL drops below some critical value $U_c$ and positive buoyant forces are present. Such forces can arise either from vertical temperature or water vapor gradients across the atmospheric surface layer. During free convection, buoyant forces drive narrow plumes that ascend to the inversion height with a return circulation consisting of broad slower-moving downdraughts. Horizontal pressure, temperature, windspeed, and water vapor fluctuations resulting from this circulation pattern can be quite large adjacent to the ground (within the surface layer). These local turbulent fluctuations cause non-zero mean surface stresses, sensible heat fluxes, and latent heat fluxes, even when the mean regional windspeed is zero. Although motions above the surface layer are insensitive to the nature of the surface, the sensible and latent heat fluxes are primarily controlled by processes within the interfacial sublayer immediately adjacent to the ground during free convection. Thus the distinction between aerodynamically smooth and rough airflow within the interfacial sublayer is more important than for the more typical situation where the mean regional windspeed is greater than $U_c$. Buoyant forces associated with water vapor gradients are particularly large on Mars at low pressures ($P<30$ mb) and high temperatures ($T>250$ K) when the surface's relative humidity is 100%, enhancing the likelihood of free convection under these conditions. On this basis, Ingersol [1] postulated the evaporative heat losses from an icy surface on Mars at 273 K and current pressures would exceed the available net radiative flux at the surface, thus prohibiting ice from melting at low atmospheric pressures.

Recently, Schumann [2] has developed equations describing the horizontal fluctuations and mean vertical gradients occurring during free convection. However, his model is limited to the case where free convection is driven solely by thermal buoyancy and the surface is aerodynamically rough. Within these restrictions, model results compare very well with those of a detailed large-eddy simulation (LES) which in turn generally agree with available atmospheric observations [3]. Despite large horizontal wind velocities associated with the updraughts, the LES demonstrates that the time-derivatives for horizontal motion in the surface layer are small, validating the use of Monin-Obukhov theory in the model.

We have generalized Schumann's model to include convection driven by water vapor gradients and to include the effects of circulation above both aerodynamically smooth and rough surfaces. Applying the model to Mars, we find that nearly all the resistance to sensible and latent heat transfer in the ABL occurs within the thin interfacial sublayer at the surface. Free convection is found to readily occur at low pressures and high temperatures when surface ice is present. At 7 mb, the ABL should freely convect whenever the mean windspeed at the top of the surface layer drops below about 2.5 m $s^{-1}$ and surface temperatures exceed 250 K. Mean horizontal fluctuations within the surface layer are found to be as high as 3 m $s^{-1}$ for windspeed, 0.5 K for temperature, and $10^{-4}$ kg $m^{-3}$ for water vapor density. Airflow over surfaces similar to the Antarctic Polar Plateau (surface roughness length $z_0$ approx. 0.03 cm) is found to be aerodynamically smooth on Mars during free convection for all pressures between 6 and 1000 mb while surfaces with $z_0 = 1$ cm are aerodynamically rough over this pressure range.

Free convective latent-heat fluxes are of particular interest because they establish the *minimum* evaporative heat losses that will occur for an icy surface at a given temperature. Fig.1 shows the predicted latent heat fluxes during free convection for the limiting case where the ABL is isothermal and the surface temperature is 273 K. For a surface resembling average terrestrial polar snows (curve A), our predicted fluxes are a factor of 4 smaller than those given by Eq.(1) of Ingersol [1], making it proportionally easier to melt ice on Mars. Fig.2 shows the albedo required for the net radiative flux at the surface to just balance the predicted latent heat losses at 273 K at the time of maximum incoming solar radiation. The lowest albedo that can be achieved for martian ice surfaces is about 0.2 [4]. Hence, atmospheric pressures need to be at least 100 mb at the poles and about 6 mb at the equator before ice can melt under the best of conditions.

References: [1] Ingersol,A.P. (1970) **Science, 168,** 972-973; [2] Schumann,U. (1988) **Boundary-Layer Meteorol., 44,** 311-326; [3] Schmidt,H. and U.Schumann (1989) **J.Fluid Mech., 200,** 511-562; [4] Clow,G.D. (1987) **Icarus, 72,** 95-127.

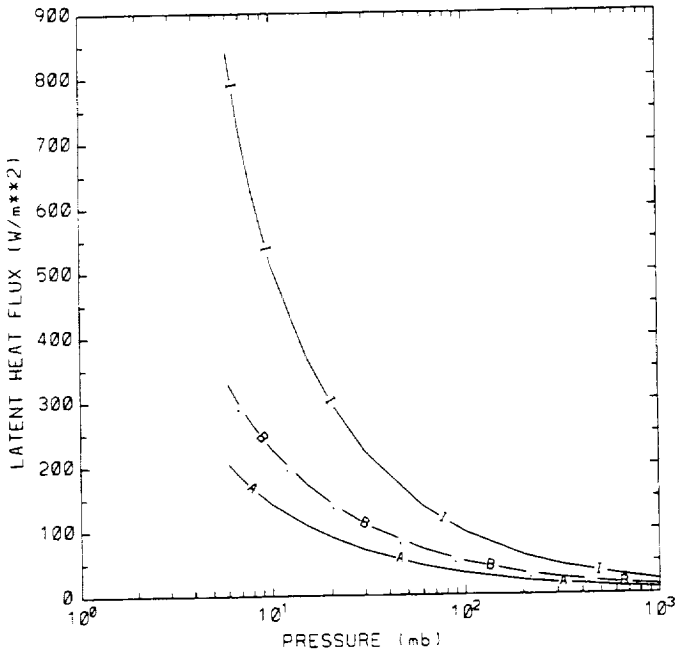


**Fig.1**: Predicted latent heat fluxes at 273 K for a surface with $z_0 = 0.03$ cm (curve A) and $z_0 = 1$ cm (curve B). Shown for comparison are the free convection predictions of Ingersol [1], (curve I).

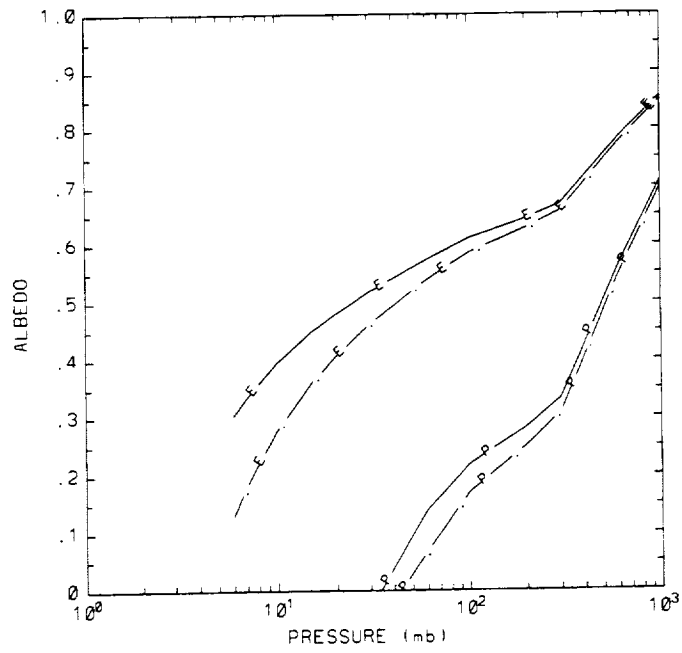


**Fig.2**: Highest albedos for which ice can melt under optimal conditions in the equatorial regions (curves E) and the polar regions (curves P). Solid lines refer to aerodynamically smooth surfaces while dashed lines are for aerodynamically rough surfaces.

# THERMOKARSTIC DEPRESSIONS AT THE MOUTH OF ELYSIUM CHANNELS (MARS): NEW EVIDENCE FOR THE PRESENCE OF MASSIVE ICY BEDS.

F.M. COSTARD, Laboratoire de Géographie Physique URA DO141, CNRS, 92195 Meudon Cédex, France.

The analysis of very high resolution Viking pictures (12 m/pixel) in Utopia Planitia indicates a concentration of thousand of depressions at the mouth of Elysium channels. Their spatial distribution concern an area of 220.000 km² between 237°W to 271°W and 41°N to 50°N. These depressions are 130 m to 3 km in length and 20 m to 45 m in depth and occupy a regional depression whose floor altitud is -2 km (fig. 1). The occurrence in the same area of very high density fluidized ejecta craters implies the presence of a continuous and subsurface ground-ice (1) probably in thick sediment deposits (2, 3, 4). The purpose of this study is to compare these depressions with thermokarstic features of Yakutia (Siberia). An eolian origin would produce elongated shapes and not circular depressions as they are actually observed. A kettle hypothesis is also unlikely because of the lack of moraine like ridges in the vicinity.

a) Circular depressions:

These depressions are the most numerous. They are similar in size and form to thermokarstic depressions (alases) of terrestrial Arctic regions (fig. 2). In Yakutia, alases are well developped in presence of massive icy beds which can be as much as 2 km in length and 40 m in thickness (5). On Mars, the occurrence of alases implies a near surface ground-ice which contains massive icy beds (6). A change in the thermal balance of ground-ice, during a warmer climate or a geothermal heating, would produced melting or sublimation of the ice with an extensive alas development.

b) Annular depressions:

In the same area, a few tens of fluidized ejecta craters exhibit an annular moat at the edge of the ejecta blanket. The complete evolution of these annular moats since their formations until their complete developments will be retraced. A thermokarstic origin is also proposed. Just after the formation of the ejecta lobe, a post-deposition fluid flow produced a concentration of volatiles in the edge of the ejecta lobe (fig. 3-B). Such a mechanism is attested by the occurence of channels on some ejecta blankets (fig. 3-A) as advocated by Mouginis-Mark (7). Under the cold climate conditions of planet Mars, freezing of water involved a modification of the porous structure of ground-ice. Its subsequent melting produced individual alases (fig. 3-C) where slope retreats resulted in a progressive widening around the ejecta lobe (fig. 3-D, E). Finally their intersection produces a complete annular moat (fig. 3-F).

c) Stratified deposits.

As advocated by Zimbelman et al. (8), Utopia Planitia seems to be covered by a stratified deposit. The deepest alases reveal an horizontal deposit with three or four layers. In many places, the layers exhibit a trangressive overlap over a distance of 2 km (fig. 4). Such observations involve a stratification of sediments during different episods of channeling and sedimentation with a kind of cross-bedding. Such an apparent stratification on the alas slopes is not consistent with a collapse process. It is supposed that an aeolian erosional process might reveals locally that stratification after the thermokarst episod. The reduced energy regime at the mouth of Elysium channels may have involved a preferential accumulation of fine grained deposit easily removable by an eolian process. Under a cold climate condition, such sediments might have contained considerable amounts of ice (massive icy beds, ice segregations) which favored intense development of thermokarst features.

Conclusion: The occurence of such circular and annular thermokarstic depressions at the mouth of outflow channels supports the presence of a volatile-rich fluvial sediments which contain major amount of massive icy beds.

This work was supported by INSU (ATP de Planétologie) n°876714.

References: (1) Costard, F.M. (1989): Earth, Moon and Planets, 45: 265-290. (2) Lucchitta, B.K., Fergusson, H.M. and Summers, C. (1986): Proc. 17th Lunar and Planet. Sci. Conf., J.G.R. pp. E166-E174. (3) Mc Gill, G.E. (1985): Lunar and Planet. Sci. Conf. pp. 534-535. (4) Jons, H.P. (1985): Proc Lunar and Planet Sci. Conf., 414-415. (5) Mackay, J.R. (1973): Permafrost Conf., pp.223-228. (6) Costard, F.M. (1988): Lunar and Planet. Sci. Conf. pp. 211-212. (7) Mouginis-Mark, P.J. (1987): Icarus, 71:268-286. (8) Zimbelman, J.R., S.M. Clifford and S.H. William (1989): Proc. 19th Lunar and Planet. Sci. Conf., J.G.R. pp. 397-407.

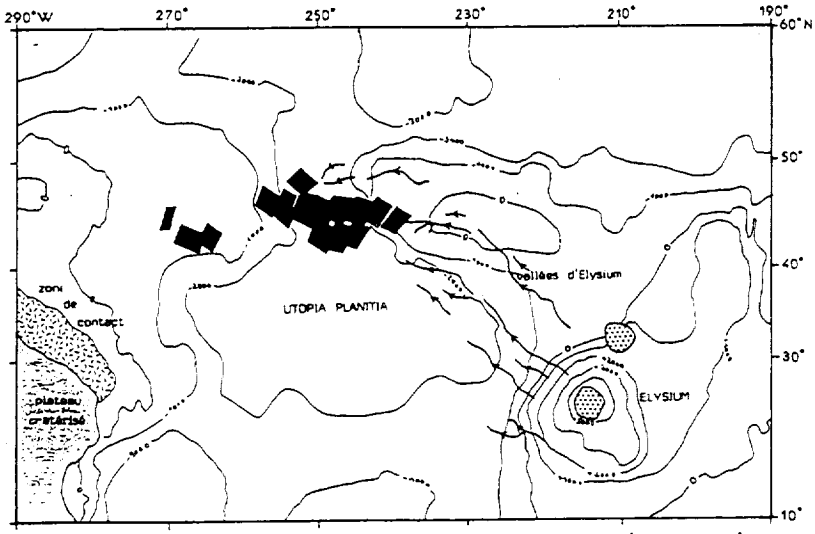


Fig. 1: Location of high resolution Viking images which comprise alas depressions (solid black). Note their association with Elysium channels (solid lines with arrows).

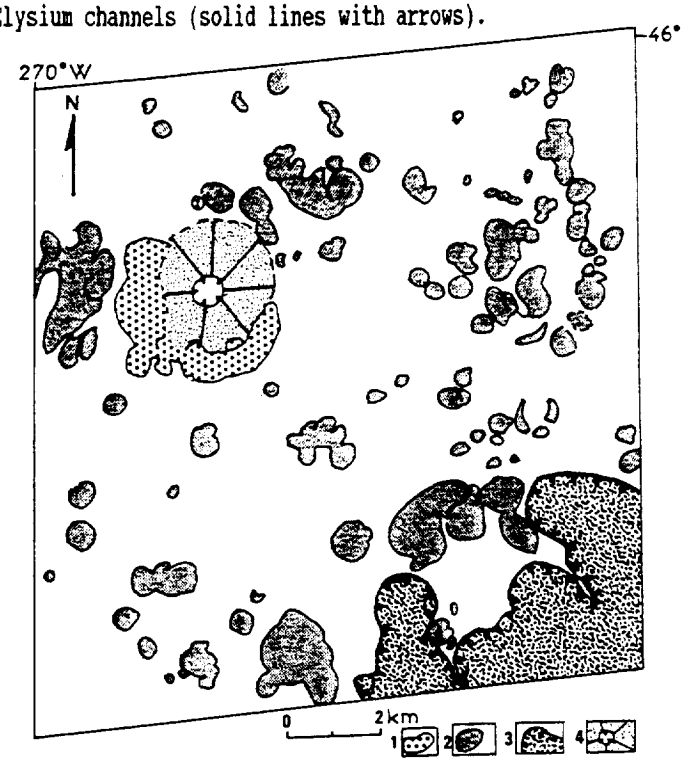


Fig. 2: Alas depressions in Utopia Planitia at the mouth of Elysium channels. (1): annular moat, (2): circular depression, (3): large thermokarst depression, (4): fluidized ejecta crater.

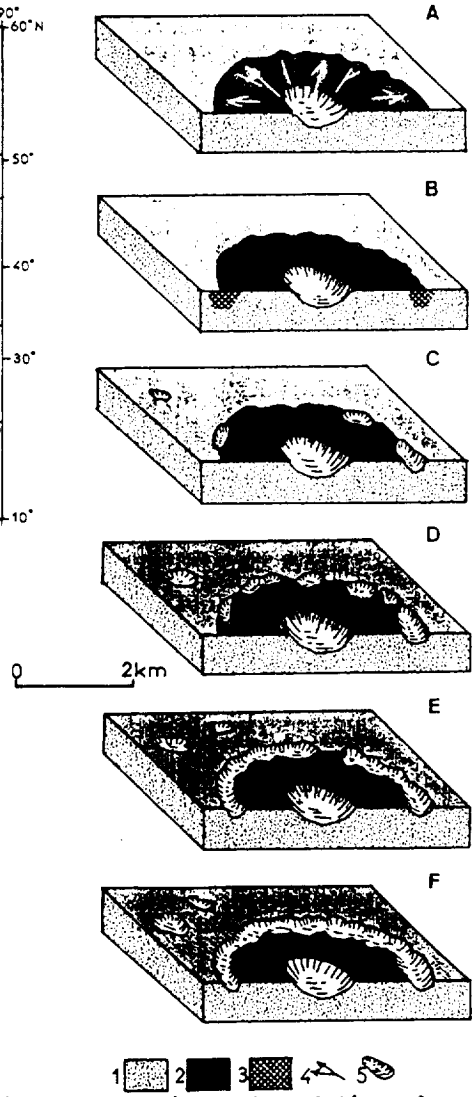


Fig. 3: Formation and evolution of an annular moat around a fluidized ejecta crater. 1: ground-ice; 2: ejecta blanket; 3: volatile concentration; 4: channels; 5: alas.

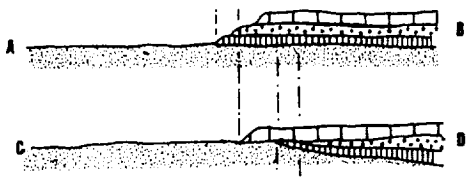


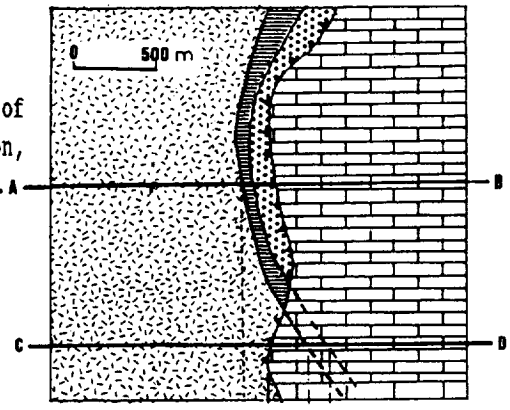


Fig. 4: Map showing a transgressive overlap within stratified deposits of a thermokarst collapse.

RATIONALE FOR A MARS ROVER/SAMPLE RETURN MISSION TO CHRYSE PLANITIA AND THE VIKING 1 LANDER; Robert A. Craddock, Center for Earth and Planetary Studies, National Air and Space Museum, Smithsonian Institution, Washington, DC 20560

As a precursor to a sample return mission and/or manned mission to Mars, landing sites that are both safe and scientifically interesting must be determined. Potential sites could ultimately affect spacecraft design and development and determine the range of scientific objectives possible. The earlier potential sites are selected, the more cost and time efficient mission planning and operations will be. However, Mars has as much land surface area as the continental crust of the Earth and exhibits a wide variety of geologic processes and features thus making site selection an arduous task.

So why go back to Chryse Planitia, an area previously explored by the Viking 1 Lander? One of the best reasons is that we have already been there. Viking 1 landed successfully, proving that it is safe and providing us with valuable ground-truth observations of the martian surface. For example, Viking Lander 1 data have provided information useful in determing the physical properties of the martian surface materials [e.g., 1]. Observations such as these will undoubtingly be incorporated into any future spacecraft design--no matter where the designated landing site is located. In addition, Chryse Planitia still represents one of the lowest spots on the surface of Mars (>2 km below mean Mars datum; 2), providing more atmosphere to slow down a landing vehicle. Its equatorial location (~20° N lat.) allows contact with both polar and equatorial orbiting spacecraft along with direct line-of-site communications with the Earth, an added bonus when sending commands to a moving vehicle. The extensive photographic coverage of Chryse Planitia by the Viking Orbiters and Earth-based radar observations have provided 100 m resolution topography in the vicinity of the Viking 1 Lander [e.g., 2]. Analysis of these data and lander photographs indicate that Chryse Planitia may be unique in that features >50 km away from the lander (such as the rims of Lexington and Yorktown craters) are visible over the horizon [3]. This information could potentially provide a valuable check for determining the location of the spacecraft on the surface and aid in roving vehicle navigation.

Ideally a landing site should include access to as many different geologic units as possible. In addition to the materials debouched into the Chryse basin by the large martian channel complex [e.g., 4], the Hesperian age ridged plains covering much of region [5] may represent the single most important geologic unit needed for age-dating materials on Mars. Composing ~3% of the total Mars surface area [6], the ridged plains are fairly widespread in comparison to other geologic units and, more importantly, are the Hesperian epoch referent [7]. Because the Hesperian epoch represents the interval of time immediately following the period of heavy bombardment (~3.8 Ga; 8), an absolute age determined from a ridged plain sample would allow estimates of the post-heavy bombardment impact flux on Mars to be calibrated. It may then be possible to determine the absolute ages of every younger geologic unit on Mars based on crater statistics. In addition, materials washed down from the highlands may be present in the vicinity of Lander 1. Although the absolute ages of these materials almost certainly correspond to the period of heavy bombardment, analysis of their composition could provide some insight into the early geologic history of Mars. Also the distribution of the materials in Chyrse Planitia as determined by a manned or unmanned traverse may be indicative

of the channel formation mechanism. For example, catastrophic flooding would lead to a Bouma sequence deposit in the Chryse basin [9]; in liquefaction, an accretionary lobe in the debouching area results in larger particles dropping out first with smaller particles being transported greater distances [10].

Because of the likelihood of running water debouching into Chyrse Planitia in the past, the Viking 1 landing site was considered an ideal place to look for complex organic molecules [11]. Although the Viking biological experiments did not identify the presence of organic life [12], controversy still exists as to the meaning of the Label Release Experiment [13]. Knowing the position of Viking 1 on the surface to within 50 m [14], it would be possible to navigate to the landing site and obtain the same soil samples investigated by the lander. Rocks seen in lander images could also be returned to Earth, answering questions concerning their compositional and erosional properties. A piece or pieces of Lander 1 itself could be obtained! Especially easy to recover is the small latch pin released when the lander sampler shroud was jettisoned. This 8.2 cm long and 0.6 cm diameter pin fell within 1 m of the lander, weighs 11.3 g, and has been exposed to the martian environment for a known period of time. No special tools would be needed to obtain the latch pin, and analysis upon return to earth would provide erosion rates and other information useful in understanding geologic processes. In situ erosional analysis of Lander 1 itself could also have implications on the development of future martian spacecraft materials. In addition, it may be possible to navigate from the lander to the crater caused by the jettisoned Viking aeroshell. Ejecta from this fresh crater would represent Chryse stratigraphy at depth, providing a possible alternative if a drill sample is determined impractical for the early sample return missions. Yorktown, a 7.9-km-diameter "rampart" [15] or "fluidized ejecta" crater [16], is ~45 km northwest of the Viking 1 landing site as well. Samples of the ejecta from Yorktown could determine how much volatile material is involved in rampart crater formation [e.g., 15], if any at all [17]. Following the Xanthe Dorsa ridge north for ~34 km from the Viking 1 Lander to the crater San Juan, Yorktown is ~22 km to the west. An active seismic or sounder experiment operated along the Xanthe Dorsa ridge traverse could provide clues to the ridge structure and the underlying Chryse basin stratigraphy.

REFERENCES: [1] Moore, H.J., et al., U.S.G.S. Prof. Paper 1389, 222 pp., U.S. Government Printing Office, Washington, 1987. [2] U.S.G.S. Misc. Invest. Series Map I-1059, Controlled mosaic of the Yorktown region of Mars, U.S. Geol. Surv., Denver, CO, 1977. [3] Craddock, R.A. and J.R. Zimbleman, Lunar Planet. Sci., XX, 193-194, 1989. [4] Greeley, R., et al., J. Geophys. Res., 82, 4093-4109, 1977. [5] Scott, D.H. and K.L. Tanaka, U.S. Geol. Surv. Misc. Invest. Series Map I-1802A, U.S. Geol. Surv., Denver, CO, 1986. [6] Watters, T.R., Abstracts for the MEVTV-LPI Workshop: Early Tectonic and Volcanic Evolution of Mars, 63-65, 1988. [7] Tanaka, K.L., J. Geophys. Res., 91, E139-E158, 1986. [8] Hartmann, W.K., et al., In Basaltic Volcanism on the Terrestrial Planets, Pergamon, New York, 1981. [9] Komar, P.D., Icarus, 42, 317-329, 1980. [10] Nummedal, D., and D.B. Prior, Icarus, 45, 77-86, 1981. [11] Masursky, H. and N.L. Crabill, Science, 193, 809-812, 1976. [12] Klein, H.P., J. Geophys. Res., 82, 4677-4680, 1977. [13] Levin, G.V. and P.A. Straat, J. Geophys. Res., 82, 4663-4667, 1977. [14] Morris, E.C. and K.L. Jones, Icarus, 44, 217-222, 1980. [15] Carr, M.H., et al., J. Geophys. Res., 82, 4055-4066, 1977. [16] Mouginis-Mark, P.J., J. Geophys. Res., 84, 8011-8022, 1979. [17] Schultz, R.A. and D.E. Gault, Third International Colloquium on Mars, 226-228, 1981.

EVIDENCE FOR WIDESPREAD RESURFACING IN THE MARTIAN HIGHLANDS;
Robert A. Craddock and Ted A. Maxwell, Center for Earth and Planetary Studies, National Air and Space Museum, Smithsonian Institution, Washington, DC 20560

The southern cratered highlands of Mars contain a large population of flat-floored, rimless craters which occur on a variety of Noachian geologic materials. Previously these craters have been interpreted to have formed by aeolian mantling [1] or flood volcanism [2]; however, neither of these geologic processes accurately explains the observed morphology or the crater statistics. Determining the distribution of the flat-floored, rimless craters, the timing of the process responsible for their formation, and the actual process involved in their formation is important for understanding the geomorphic evolution of most of the southern cratered hemisphere of Mars. Our initial investigation concentrated on the analysis of the Amenthes and Tyrrhena regions near the dichotomy boundary [3,4,5]. Currently we have begun investigations into other areas including Mare Australe, Eridania, Arabia, Noachis, and Memnonia.

The geologic analysis of these regions was based on the published 1:15M geologic maps of Mars and was limited to two materials: the Noachian cratered unit ($Npl_1$; 6) and the Noachian dissected unit (Npld; 6). Although flat-floored, rimless craters occur on other Noachian geologic materials as well, the interpretations of these units [7,8,9] includes resurfacing by processes we feel are separable from a larger, more extensive process. The Noachian cratered unit ($Npl_1$) and the Noachian dissected unit (Npld) are distinguished by the absence or presence of ancient valley networks (i.e., runoff channels), respectively [6]. Together these units make up a bulk (~70%) of the surface area of the southern cratered hemisphere.

The termination of the resurfacing event represented by the cumulative size-frequency curves of superposed, fresh craters was not a catastrophic, global event (Fig. 1). Resurfacing ceased during the late Noachian to early Hesperian in the regions analyzed. In general, resurfacing ceased in the Npld materials later than in the $Npl_1$ materials, suggesting that the ancient valley networks represent the late stages or a change in the resurfacing process. These observations correlate well with other work suggesting that the ancient valley networks ceased to form by the early Hesperian [6].

A proposed mechanism responsible for martian highland resurfacing must be able to explain not only the morphology of the flat-floored, rimless, craters, but also the timing of the process between regions and the bendover in crater size-frequency distribution curves of highland materials [e.g., 5] as well. Although a bulk of the cratered highlands may be composed of volcanics [e.g., 10], volcanism does not produce flat-floored, rimless craters except in very rare circumstances. Aeolian erosion/deposition is also a very active process on Mars as evidenced by the seasonal dust storms and a variety of landforms [e.g., 11]; however, unlike what has been suggested by Wilhelms and Baldwin (1) aeolian fallout would not only be deposited up to the rim crest of craters but on the rims of craters as well. The result is not to produce a flat-floored, rimless crater, but to subdue the morphology of the crater. Volcanic and aeolian resurfacing do not produce a bendover in the cumulative size-frequency curves either. In both processes a crater is either buried, or it is not, in which case it is still counted. We propose a fluvial process capable of eroding the rims of the craters primarily from the outside, thus reducing the apparent diameter of the craters. The eroded material is

redistributed, inundating the smaller craters before they are eroded completely. Such a complicated process not only explains the morphology of the flat-floored, rimless craters, but also the bendover in the cumulative size-frequency curves and potentially the timing of the process between regions.

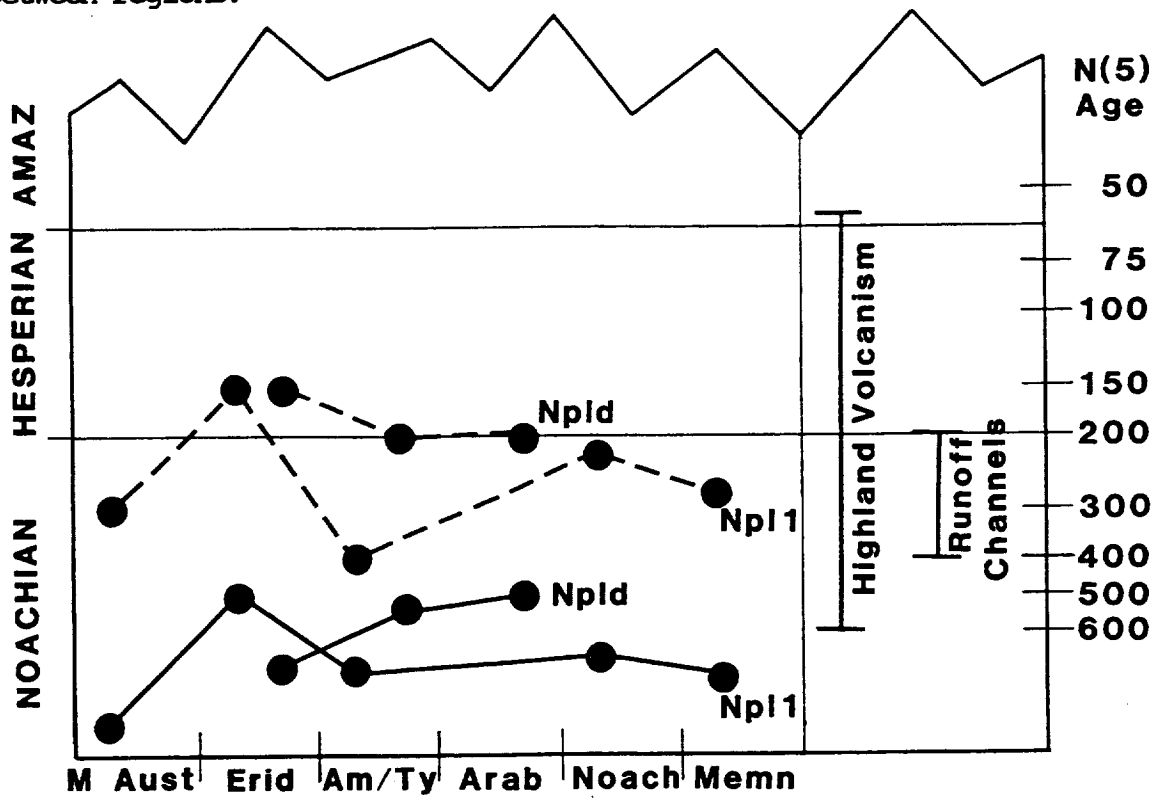


Figure 1. Timing of resurfacing in the areas mentioned in text. N(5) ages represent the number of craters >5-km-diameter per million square kilometers. Solid lines represent age of material based on all craters. Dashed lines represent termination of resurfacing event based on fresh, superposed craters.

REFERENCES: [1] Wilhelms, D.E. and R.J. Baldwin, Proc. Luanr Planet. Sci., 19th, 355-365, 1989. [2] Hartmann, W.K. et al., In Basaltic Volcanism on the Terrestrial Planets, Chap. 8, pp. 1049-1127, Pergamon, New York, 1981. [3] Craddock, R.A. and T.A. Maxwell, Lunar Planet. Sci., 20, 191-192, 1989. [4] Maxwell, T.A. and R.A. Craddock, Lunar Planet. Sci., 20, 646-647, 1989. [5] Craddock, R.A. and T.A. Maxwell, Resurfacing of the martian highlands in the Amenthes and Tyrrhena region, J. Geophys. Res., in review. [6] Tanaka, K.L., Proc. Lunar Planet. Sci. Conf., 17th, in J. Geophys. Res., 91, E139-E158, 1986. [7] Scott, D.H., and K.L. Tanaka, Geologic map of the western equatorial region of Mars, 1:15M scale, U.S.G.S. Map I-1802-A, 1986. [8] Greeley, R. and J.E. Guest, Geologic map of the eastern equatorial region of Mars, 1:15M scale, U.S.G.S Map I-1802-B, 1987. [9] Tanaka, K.L. and D.H. Scott, Geologic map of the polar regions of Mars, 1:15M scale, U.S.G.S. Map I-1802-C, 1987. [10] Greeley, R. and P.D. Spudis, Rev. Geophys. Space Phys., 19, 13-41, 1981. [11] Thomas, P., J. Geophys. Res., 87, 9999-10,008, 1982.

# GEOLOGIC HISTORY OF THE SOUTHERN REACHES OF MANGALA VALLES, MARS;

Robert A. Craddock[1], James R. Zimbelman[1], and Ronald Greeley[2], [1]Center for Earth and Planetary Studies, National Air and Space Museum, Smithsonian Institution, Washington, DC 20560, [2]Department of Geology, Arizona State University, Tempe, AZ 85287

Mangala Valles is unique in that unlike the other large martian outflow channels it does not originate from chaotic terrain, nor does it debouch into a basin such as Chryse Planitia. Deriving the geologic history of Mangala Valles is important for determining the cause of postulated subsurface volatile release and understanding the reasons for martian channel formation. Analysis of Mariner and Viking images and Earth-based radar topography in the Mangala Valles/Memnonia region of Mars as part of the Mars Geologic Mapping program has identified several important steps in the history of Mangala Valles.

As evidenced by the orientation of Imbrium Sculpture-like groves and the circular occurrence of massifs and faults, a 6400-km-diameter, early Noachian basin has been identified in the center of Daedalia Planum [1], confirming observations made by Earth-based radar data [2]. In the Memnonia region, the Daedalia basin caused an eastern slope to the topography and uplifted an arc of highland material, which define an inner ring ("m/r" in Fig. 1). Subsequent radial faulting composing the Memnonia Fossae and associated with the formation of the Tharsis Montes [3] intersected this inner ring, possibly forming conduits for the migration of subsurface volcanic material. We suggest that some the volcanic material extruded to the surface and flowed along the eastern side of the massif ("lf" in Fig. 1). Although the vent for these materials is probably buried, a possible source is the circular depression located along the margin of the ring massif (Fig. 2; "o" in Fig. 1). With time the volcanic heat source also melted a sufficient portion of the volatile resevoir frozen in the eastward sloping highlands, thus allowing a hydrostatic head to develope. Volatiles were released along the cracked tips of en echelon Memnonia Fossae at -18.5°, 149.4° ("x" in Fig. 1). Evacuation of the volcanic material may have also caused rotation of part of the massif (see dashed block in Fig. 1) and induced release of the volatiles under a hydrostatic head at the present source area of Mangala Valles.

Initial flooding associated with the formation of Mangala Valles seems to have been widespread during the late Hesperian. Volatiles partially filled the large crater cross-cut by the source graben [4] and were ponded in the depression adjacent to the massif (Fig. 2). The volatiles ponded by the massif depression may have percolated through the material underlying the lava flow ("lf"), causing sapping and back-wasting along the flow margin (arrows in Fig. 1). Radar-derived topography indicates that southern Mangala Valles has an average gradient of .001 [5], which is comparable to active rivers at similar distances from their sources [6]. This suggests that fluvial activity at Mangala Valles may have been sufficiently longlived to produce a graded profile, while becoming more localized with time. Analysis of available photographs and crater size-frequency data from the Daedalia Planum plains east of the massif suggest that Amazonian volcanic material may have extruded through an extension of the Mangala Valles source graben ("$lf_2$" in Fig. 1). These materials may represent the termination of volcanic activity in the area and associated channel flooding since they appear to post-date the channel materials [7].

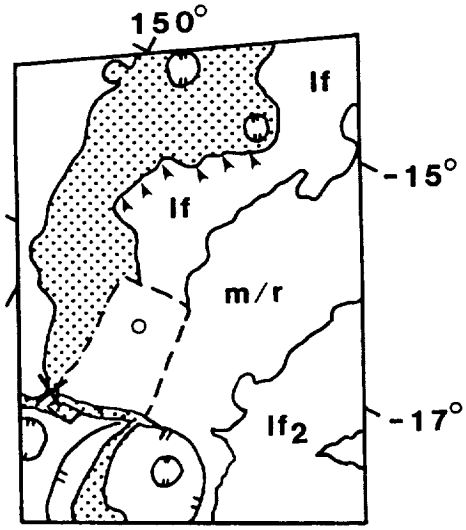


Figure 1 (left). Schematic diagram of features visible in Fig. 2. Stippled pattern represents Mangala Valles channel materials.

Figure 2 (below). Stereoscopic pair showing features discussed in text. Viking orbiter frames 637A82 (left) and 639A11 (right). (Stereoscopic viewers can be found in NASA SP-441 or NASA SP-445.)

ORIGINAL PAGE
BLACK AND WHITE PHOTOGRAPH

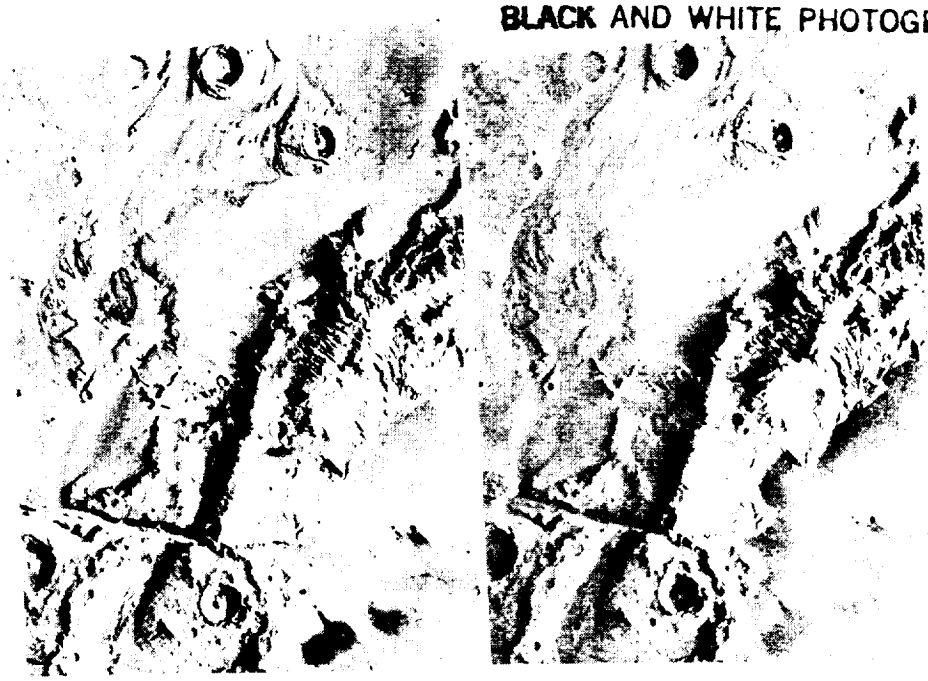

REFERENCES: [1] Craddock, R.A. et al., Evidence for an ancient impact basin in Daedalia Planum, Mars, J. Geophys. Res., in review. [2] Plescia, J.B. et al., Lunar Planet Sci., 11, 891-893, 1980. [3] Plescia, J.B. and R.S. Saunders, J. Geophys. Res., 87, 9775-9792, 1982. [4] Pfau, C.E. and S.R. Saunders, NASA TM-86247, 152-155, 1984. [5] Zimbelman, J.R., Lunar Planet Sci., 20, 1239- 1240, 1989. [6] Leopold, L.B. et al., Fluvial Process in Geomorphology, Freeman & Co., p. 190, 1964. [7] Greeley, R. and R.A. Craddock, Geologic Map of the Southern Mangala Valles Region of Mars, scale 1:500K, in review.

# STYLES OF VOLCANISM, TECTONIC ASSOCIATIONS, AND EVIDENCE FOR MAGMA-WATER INTERACTIONS IN EASTERN HELLAS, MARS

***David A. Crown and Ronald Greeley,*** *Department of Geology, Arizona State University, Tempe, Arizona 85287*

Four of the martian highland paterae (low-relief, areally-extensive features with central calderas and radial channels and ridges [1,2]) are associated with inferred rings of the Hellas basin [3,4] (Figure 1). Their morphometry [5] and the erosional characteristics of Tyrrhena Patera [2] have been used as evidence that they are composed of ash. Analyses of the energetics of eruption and flow processes have shown that the distribution of units at Hadriaca and Tyrrhena Paterae is consistent with an origin by the emplacement of gravity-driven pyroclastic flows and that explosive eruptions driven by magmatic volatiles or groundwater could provide sufficient energy [6-9]. The supply of groundwater for hydromagmatic eruptions has been considered; large volumes of water could accumulate rapidly at flow rates determined for Mars [7,10-11]. The present investigation synthesizes the previous studies of Tyrrhena Patera and results of modeling martian volcanic processes with current photogeologic investigations of the Hadriaca Patera region [6,12] in order to examine the evolution of volcanism in the eastern Hellas region.

In eastern Hellas, Hadriaca and Tyrrhena Paterae are observed in association with the ridged plains of Hesperia Planum. Zones of weakness generated by the Hellas impact event may have produced conduits for the magmas forming these deposits [4]. The structure of Hellas has clearly influenced the shapes of the paterae, which are elongated downslope toward the basin, as well as the positions of the volcanic source vents. The orientations of 243 ridges have been mapped in the Hadriaca [260-275° W, 27.5-42.5° S] and Tyrrhena [247.5-265° W, 15-30° S] regions. The 219 ridges contained within volcanic units have a wide range of orientations but exhibit trends which approximate radial (NE-SW) and concentric (NW-SE) patterns to Hellas. Although orthogonal and parallel alignments between ridges and the regional slope and lava flow directions in the flank flow unit at Tyrrhena are also observed, basin-related tectonism is considered the primary factor governing ridge orientation because the regional slope is a consequence of the basin and has controlled the emplacement of the volcanic units. The NE-SW and NW-SE ridge orientations measured agree with previously documented trends for Hesperia Planum [13] and indicate the effects of the Hellas impact event over a wide region of the southern highlands and the persistence of the tectonic signature of the basin over geologic time.

Photogeologic studies indicate that Tyrrhena Patera consists of basal and summit shield units, the surfaces of which contain channels radiating from the summit caldera region [6-7,12]. Layering is observed in these units, the distal margins of which are highly dissected and form isolated erosional remnant mesas. The large flank flow unit composed of well-defined lava flow lobes and leveed channels, the first definitive evidence for effusive volcanic activity associated with the paterae, extends from near the summit of Tyrrhena for over 1000 km to the SW adjacent to Hadriaca. Hadriaca Patera also exhibits channeled flanks, although the channels are smaller and more closely spaced. Multiple layers and erosional remnants are also observed. The morphologies of these volcanoes suggest that their surfaces have been modified by fluvial erosion (sapping?), and these erosional characteristics in combination with similar morphometry to large terrestrial ash sheets [5] and the absence of primary lava flow features (except in the flank flow unit) suggest that the highland paterae are composed primarily of ash [6,7].

Cross-cutting relationships determined from geologic mapping of eastern Hellas indicate that the ridged plains of western Hesperia Planum and the flank flow unit at Tyrrhena Patera are younger than the basal and summit shield units [7,12], suggesting a transition from explosive to effusive volcanism. The erosion of the flanks of Hadriaca pre-dates the erosion of the channeled plains to the south. The erosion on the plains (presumably by runoff) and the eventual formation of the Dao Vallis outflow system continues through the formation of the flank flow. Thus, the erosional processes affecting Hadriaca and Tyrrhena Paterae and the plains were probably active, at least in some areas, after the emplacement of the flank flow. This relationship supports the interpretation of the dissected units at Hadriaca and Tyrrhena as ash rather than eroded lavas because the flank flow unit should have been subjected to similar degradational processes, at least

in the south near Hadriaca. The presence of volatile-rich surface materials in the region is strongly supported by the morphologies of the channeled plains and Dao Vallis [6,11]. In addition, debris flows and pitted plains associated with Noachian mountains near Harmahkis Vallis illustrate the influence of near-surface volatiles. The transition from explosive to effusive volcanism (from the low shields of the paterae to the flank flow unit and the ridged plains of Hesperia Planum) can be interpreted as the result of the cessation of magma-volatile interactions. Groundwater could have been concentrated by the topography of Hellas and would have moved easily in the fractured highland crust. The interpretation of the caldera-filling materials at the paterae as late-stage lavas [7] is consistent with this scenario, as the rising magma could eventually seal the conduit from further inflow by water [14]. In addition, as the volcanoes increased in size, water would tend to flow away from the structures, and even if contact occurred beneath the surface, explosive eruptions could be suppressed by the increasing weight of the volcano. Explosive eruptions at Tyrrhena would have ceased first due to its distance from Hellas.

The style of eruptive activity in eastern Hellas has implications for the general evolution of martian volcanism. If magmatic eruptions generated the pyroclastic flows forming the paterae, this suggests an evolution in magma types from Hesperian to Amazonian time, when the Tharsis and Elysium volcanics formed, and/or the existence of spatial heterogeneities in the mantle from which the magmas were derived. Hydromagmatic origins for the paterae imply an evolution from volatile-rich to volatile-poor eras in the near-surface environment of Mars, in accordance with proposed global climatic changes [15]. While the observed morphologies and the energetics of explosive eruptions are consistent with both magmatic and hydromagmatic origins of Hadriaca and Tyrrhena Paterae, consideration of the regional geologic setting supports the role of magma-volatile interactions in the volcanism of the eastern Hellas region.

**References:** [1] Plescia, J.B. and R.S. Saunders, 1979, *Proc. Lunar Planet. Sci. Conf., 10th,* 2841-2859. [2] Greeley, R. and P.D. Spudis, 1981, *Rev. Geophys. Space Phys., 19,* 13-41. [3] Peterson, J.E., 1978, *Proc. Lunar Planet. Sci. Conf., 9th,* 3411-3432. [4] Schultz, P.H., 1984, *Lunar Planet. Sci. Conf., XV,* 728-729. [5] Pike, R.J., 1978, *Proc. Lunar Planet. Sci. Conf., 9th,* 3239-3273. [6] Crown, D.A. and R. Greeley, 1990, in *MEVTV Workshop on the Evolution of Magma Bodies on Mars,* L.P.I., in press. [7] Greeley, R. and D.A. Crown, 1990, *J. Geophys. Res.*, in press. [8] Crown, D.A. et al., 1988, *Lunar Planet. Sci. Conf., XIX,* 229-230. [9] Crown, D.A. and R. Greeley, 1988, *LPI Technical Report 89-04,* 29-31. [10] Carr, M.H., 1979, *J. Geophys. Res., 84,* 2995-3007. [11] Squyres, S.W. et al., 1987, *Icarus, 70,* 385-408. [12] Crown, D.A. et al., 1990, this issue. [13] Watters, T.R. and D.J. Chadwick, 1989, *LPI Technical Report 89-06,* 68-69. [14] Sheridan, M.F. and K.H. Wohletz, 1983, *J. Volcanol. Geotherm. Res., 17,* 1-29. [15] Clifford, S.M. et al., 1988, *EOS (Trans. Amer. Geophys. Union), 69,* 1595-1596.

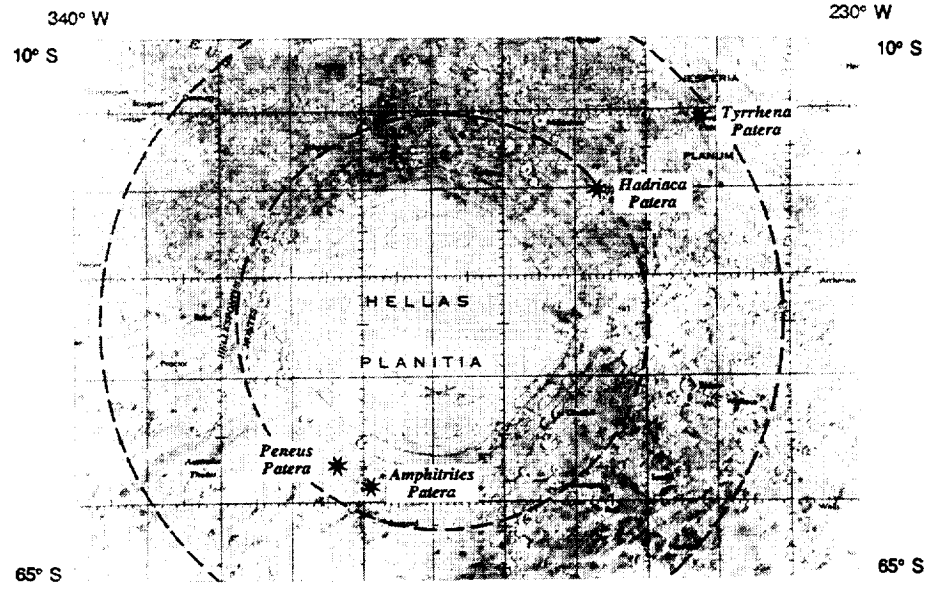


Figure 1. Portion of the *Topographic Map of Mars* showing the locations of 4 martian highland paterae. Positions of inferred basin rings (dashed lines) from Peterson, 1978.

# EVOLUTION OF THE EAST RIM OF THE HELLAS BASIN, MARS

***David A. Crown, Katherine H. Price*, and Ronald Greeley,*** *Department of Geology, Arizona State University, Tempe, Arizona 85287; *Department of Geology & Geography, DePauw University, Greencastle, Indiana 46135*

The Hellas basin, an ~2000 km impact structure with possible rings extending 4260 km in diameter [1], is a dominant feature in the ancient, southern cratered highlands of Mars. Impact basin control of volcanism and tectonism is evident on the Moon [2], and relationships between martian basins and surface processes have been identified [3-4]. The east rim of Hellas is a complex geologic region affected by volcanism, tectonism, and channeling. Remnants of an extensive mantling deposit and smooth deposits filling craters may be indicative of widespread aeolian activity, presumably related to the dust storms originating in the Hellas region [5]. A detailed study of the area between 27.5 - 42.4°S and 260 - 275°W has been initiated to analyze the processes forming surface materials and to decipher the evolution of this geologically important highland area (Figure 1). Major units include Hesperian volcanics associated with Hadriaca and Tyrrhena Paterae in the N and Hesperian and Amazonian channeled plains and outflow channels in the S. Remnants of Noachian mountains and plateaus are found throughout the region [6].

Hadriaca and Tyrrhena Paterae are low relief volcanoes thought to lie on inferred rings of Hellas [1]. The asymmetry exhibited by both volcanoes reflects the regional slope [7] caused by the topography of the basin. Materials associated with Hadriaca (Hvf) are interpreted to be ash deposits on the basis of their erosional characteristics, the low relief of the volcano, and the absence of primary lava flow features [8]. The distribution of units at both Hadriaca Patera and Tyrrhena Patera (located NE of the study area) are consistent with an origin by the emplacement of gravity-driven pyroclastic flows [8-11]. A large flank flow (Hff) containing lava flow lobes and leveed channels extends from Tyrrhena to the SW adjacent to Hadriaca Patera.

Dao and Harmakhis Valles have lengths >500 km and trend ~S45W. Outflow channel deposits have been subdivided into 3 facies: $AHch_1$, irregular materials forming channel floors, associated with channel walls, or forming dissected, low-lying regions connecting channel deposits; $AHch_2$, smooth, featureless deposits forming channel floors; and $AHch_3$, materials with linear to curvilinear features parallel to channel margins. $AHch_1$ materials are interpreted to be remnants of the plains in which the outflow channels formed and occur as sections of incompletely collapsed, dissected plains or as hummocky mounds and blocks on channel floors or slumped from channel walls. $AHch_2$ materials are smooth channel floors resulting from uniform removal of materials or uniform collapse. $AHch_3$ deposits indicate fluvial modification. These facies suggest that water flowed in part of the channels following dissection and collapse. Surrounding the channels in the S part of the mapped area is the channeled plains rim unit ($AHh_5$). Cross-cutting relationships N of Dao Vallis indicate that the channeling pre- and post-dates collapse.

Based upon photogeologic mapping the geologic history of the east rim of Hellas has been derived. Uplift of Noachian mountainous (Nm) and plateau (Npld, $Nh_1$) materials occurred in association with the Hellas impact event. The locations of mountains identify possible basin rings, which may have produced zones of weakness providing access to the surface for the magmas forming Hadriaca and Tyrrhena Paterae in Hesperian time. Erosion by runoff and/or sapping modified the plains and flanks of the volcanoes, followed by the formation of Dao and Harmakhis Valles. The presence of volatile-rich surface materials and possible fluvial or periglacial activity is suggested by the deflation and collapse of the channel deposits [12], the style of erosion of the channeled plains, and the debris aprons (AHda) and pitted materials (AHpp) observed in association with the older units. The origin and extent of the mantling deposit in the S and the role of aeolian processes are current topics of investigation. Crater counts will further constrain the temporal relationships observed.

**References:** [1] Peterson, J.E., 1978, *Proc. Lunar Planet. Sci. Conf., 9th*, 3411-3432. [2] Solomon, S.C. and J.W. Head, 1980, *Rev. Geophys. Space Phys., 18*, 107-141. [3] Schultz, P.H. et al., 1982, *Lunar Planet. Sci. Conf., XIII*, 700-701. [4] Schultz, P.H., 1984, *Lunar Planet. Sci. Conf., XV*, 728-729. [5] Zurek, R.W., 1982, *Icarus, 50*, 288-310. [6] Greeley, R. and J.E. Guest, 1987, *U.S. Geol. Survey Misc. Inv. Series Map I-1802B*. [7] U.S.G.S., 1987, *Topographic Map of Mars-Eastern Region, 1:15M*. [8] Crown, D.A. and R. Greeley, 1990, in *MEVTV Workshop on the Evolution of Magma Bodies on Mars*, L.P.I., in press. [9] Crown, D.A. and R. Greeley, 1988, *LPI*

*Technical Report 89-04*, 29-31. [10] Crown, D.A. et al., 1988, *Lunar Planet. Sci. Conf., XIX*, 229-230. [11] Greeley, R. and D.A. Crown, 1990, *J. Geophys. Res.*, in press. [12] Squyres, S.W. et al., 1987, *Icarus, 70*, 385-408.

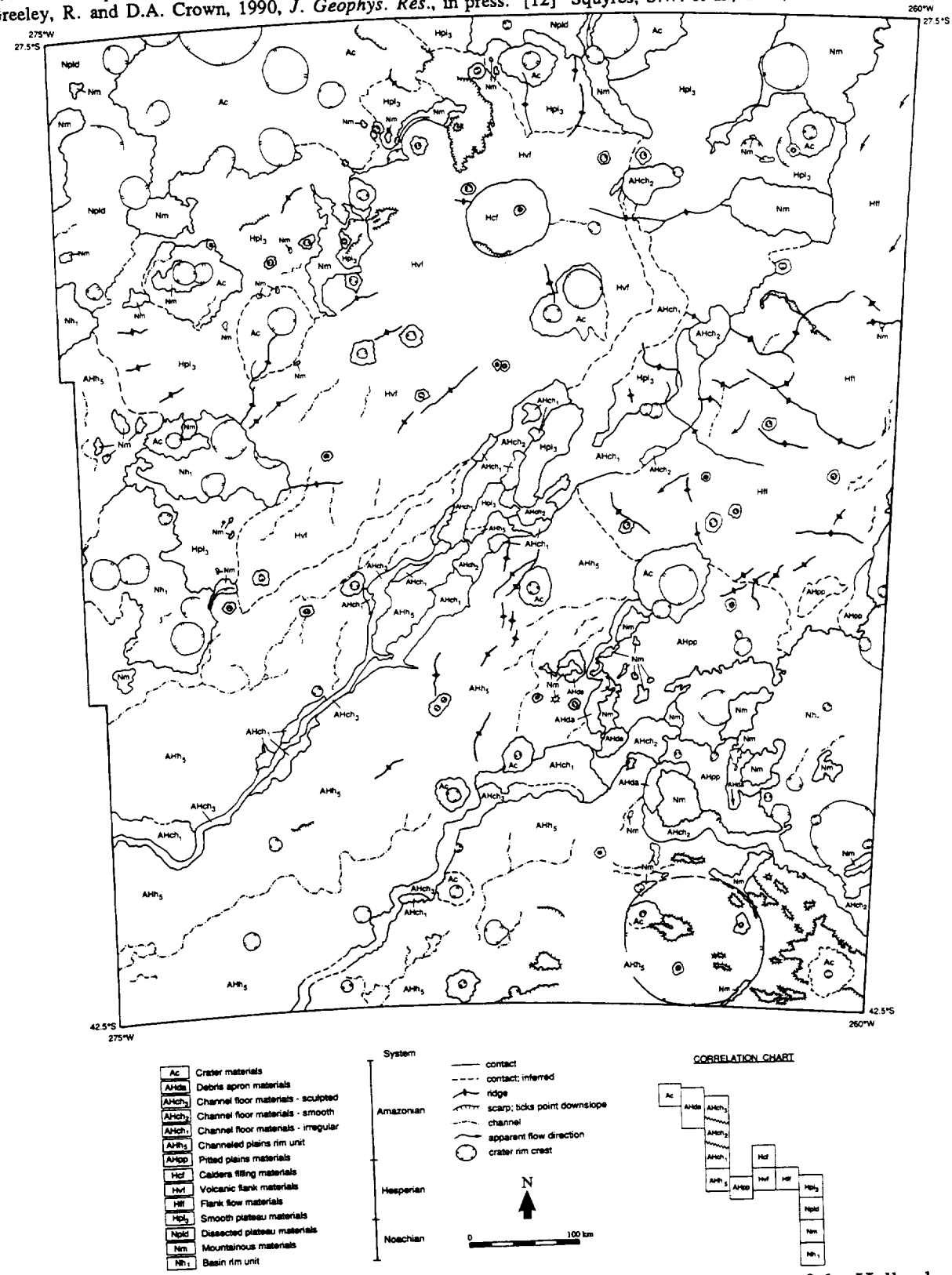


Figure 1. Geologic sketch map of the Hadriaca Patera region on the east rim of the Hellas basin.

CALCULATION OF MARTIAN GAMMA RAY SPECTRA; G. Dagge, P. Dragovitsch, D. Filges, KfA Jülich, Institut für Kernphysik,D-5170 Jülich, Germany, J. Brückner, Max-Planck-Institut für Chemie, Abteilung Kosmochemie,D-6500 Mainz, Germany

Gamma ray spectra from planetary surfaces provide a tool for the investigation of the chemical composition of the planet's surface. Galactic cosmic rays (GCR) penetrate the upper few meters of the soil producing a cascade of hadronic particles and gamma rays. Gamma rays from inelastic neutron scattering or neutron capture are a characteristical fingerprint of the target nucleus, whereas several other gamma ray sources make up a background spectrum. The gamma ray spectrum from a planetary surface thus contains information about the chemical composition of the surface material. The portion of the gamma ray flux transported back through the soil and the atmosphere can be detected from an orbiting spacecraft. Planetary gamma ray spectroscopy can be applied for a chemical mapping of planets with a sufficiently thin atmosphere like Mars, as planned for the Mars Observer Mission (launch scheduled for 1992).

In order to extract information about the Martian surface composition from measured gamma ray spectra simulations of the GCR-irradiation have to be performed. This has to be done for all subsequent processes and for a variety of material compositions and structures (1). The HERMES code system (2) allows a calculation of the complete gamma ray spectrum starting from a realistic GCR-proton (and alpha) spectrum, the supposed material composition and basic nucleon-nucleon cross sections together with cross section data for a coupled n-$\gamma$ transport calculation. Therefore, modeled particle flux profiles which are often not adequate for the particular case under consideration can be circumvented. Furthermore, practically no restrictions concerning the geometry or material are imposed on the calculations.

The HERMES system is basically used for shower calculations of calorimeters and has proved its reliability for a large number of quite different applications. The analog Monte-Carlo code system consists of the four physics modules HETC/KFA-2, MORSE-CG, NDEM, and EGS-4 coupled together with a common geometry input. Particles which can not be treated by one module are stored and can be passed over to another module without loosing information about location, direction or energy. Calculations can be performed for an arbitrary 3D-geometric setup.

For a simulation of a GCR-irradiated planetary surface a proton (and alpha) source with a realistic energy distribution up to 10 GeV (40 GeV) which provides a $2\pi$ irradiation of an infinite disk is used. Since most experimental data are available from Moon, the calculational procedure was developed and tested (3,4) for this body. For the lunar case, the resulting hadronic flux profiles can be checked by calculating several production rates of nuclei such as $^{53}$Mn or $^{60}$Co. The agreement with experimental data is excellent (Fig. 1), which is essential for a subsequent simulation of gamma ray spectra.

For a Martian surface mapping, various gamma ray sources have to be considered. Gamma rays from (n,n'$\gamma$) and (n,$\gamma$) reactions are of main interest. For these reactions, neutrons are produced and transported by the HETC module down to energies of 15 MeV. Below that threshold, the neutrons are passed over to MORSE-CG for a coupled n-$\gamma$ transport which provides the gamma ray line intensities as well as the continuum part reaching

the planet's orbit. The production of photons from inelastic neutron scattering with neutron energies above 15 MeV, spallation or from reactions such as $^{16}O(n,n'\alpha\gamma)^{12}C$ is performed by the NDEM module. This photon source is then passed over to MORSE-CG for a transport calculation. An important background source is the decay of $\pi^0$-mesons. The $\pi^0$-particles are produced by HETC and passed over for immediate decay and transport to the fourth HERMES module EGS4. A calculation for the test case Moon gives a gamma spectrum which is clearly different from earlier semi-empirical estimations concerning both intensity and spectral distribution. This background source will especially influence the investigation of low-energy gamma ray lines. Delayed photons from naturally occuring or GCR-produced radionuclides can be inserted as external source for MORSE-CG for a transport calculation.

The calculational procedure was applied for a typical Martian surface including the thin atmosphere, which proved to attenuate especially low-energy gamma ray lines (see Fig. 2). Furthermore, the HERMES system can be applied for a calculation of the gamma ray background from the GCR-irradiated orbiter at the detector site. This can be achieved by performing the same procedure as described before only by changing the geometric setup. Thus, the highly flexible code system gives access to basic problems of planetary photon production and will be an essential tool for the interpretation of measured gamma ray spectra.

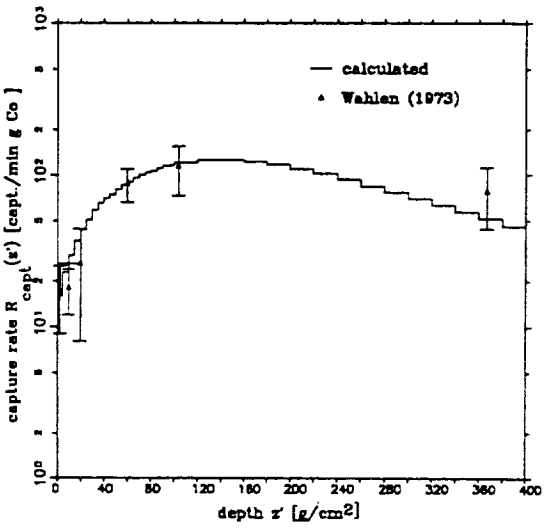


Fig. 1: Calculated depth profile of the capture rate of $^{59}Co$ in a lunar surface compared to experimental data from Wahlen (3).

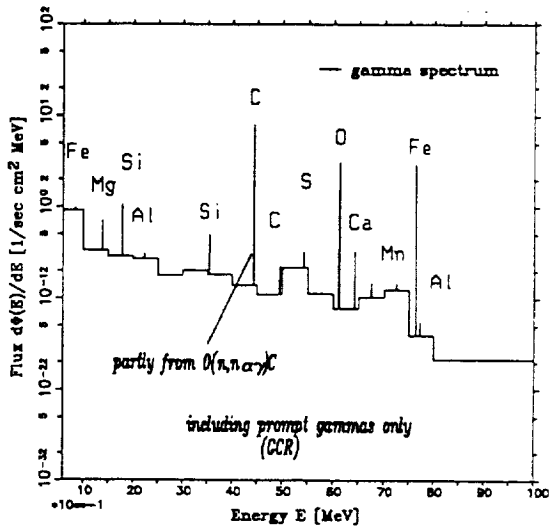


Fig. 2: Calculated spectrum of prompt photons for a typical Martian surface. Some of the most important lines were selected for the calculation.

**Acknowlegdements.** We wish to thank R. Michel (ZfS Universität Hannover) for providing spallation cross section data and several fruitful discussions. This work was supported by the Deutsche Forschungsgemeinschaft.

**References.** (1) L. G. Evans, (1987) J. Geophys. Res. Vol. 91, no. B9, p.9153-9167. (2) P. Cloth et al., (1988) HERMES User's Guide, Jül-2203. (3) M. Wahlen et al., (1973) Earth and Planet. Sci. Lett. 19, p. 315-320. (4) R. C. Reedy, (1978) Proc. Lunar and Planet. Sci. Conf. 9th, p.2961-2984.

HYDRAULIC ROUTING OF THE MAJA OUTFLOW ACROSS XANTHE TERRA:

R. A. De Hon, Department of Geosciences, Northeast Louisiana University, Monroe, LA 71209.

The object of this study is to trace a single flood crest through the Maja outflow system and to evaluate the effects of topography on ponding and multiple channel routing. Maja Valles provides a good model because it has a single source and a well-defined channel system. The 1500 km long Maja Valles originates in Juventae Chasma. The outflow system stretches 1100 km northward along the Lunae Planum--Xanthe Terra boundary, then eastward across the Xanthe Terra highlands. It descends to Chryse Planitia where it extends northeastward toward the middle of the basin.

The Lunae Planum Outflow Complex (1) includes the Maja Valles outflow and related valleys (Maja, Vedra, Maumee, and Bahram Valles) that transect Xanthe Terra and turns eastward toward Chryse Planitia. The Maja flood traveled the first two-thirds of its distance as a semi-confined sheetflood. At the northern end, it ponded on the Lunae Planum surface until the waters rose to spill over the Xanthe Terra revetment onto the lower Chryse Planitia surface. The flow first crossed the highland terrain as sheetflood flow, but broken by irregularities in the rugged highland surface, it incised a complex series of anastomosing channels (Fig.1). Early formed channels were rapidly abandoned as hanging valleys as a few main channels captured most of the drainage (2). Flow from these Xanthe canyons ponded behind the wrinkle ridge system on the western edge of Chryse Planitia (3,4). As the impounded water crested the ridges, the flood continued downslope toward the center of the basin where it lost volume by infiltration and evaporation.

During much of its brief history, the flow is marked by a single flood crest. However, multiple flood crests formed as the flow across Xanthe Terra separated into multiple anastomosing channels, then recombined in the downstream reaches. Modeling the flood surge across Xanthe Terra provides insight into the erosional and depositional history of the flood in the lower portions of the channels.

The distance across the highland is 75 km along the most direct route and ranges up to 150 km along channel routes of greatest diversion. Maumee Valles consists of 118 possible flow routes and a total of 795 km of channel segments with approximately 400 cubic km of channel storage. Vedra consists of 40 possible routes with 250 cubic km of channel storage. The "South" drainage (informal name for valley headed in the crater Dixie) consists of 6 segments and 65 cubic km of channel storage. Maja Vallis (canyon section across Xanthe) was established after the other valleys, but it eventually captured the remaining drainage from Lunae Planum.

As in any flow across a rugged surface, ponding occurred in local basins. The chief impoundments, providing more than 500 cu km of temporary storage, were in the lowland basin at 19.7°; 56.5°, the crater Bahn, the crater Dixie, the crater at 18.7°, 54.5° and the lowland trough at 17.7°; 54.3° near the mouth of Maja canyon. At these impoundments, the flood crest was delayed as the crater or basin filled to capacity. Then, one or more new flood crests formed as flood waters spilled through breaches in the downstream side of impeding basins. In the Maja canyon section, the flow onto Chryse Planitia was impeded by a highland ridge. Initially, the flow ponded in a trough on the highland side of the ridge and was diverted to the south through a 65 km relief channel. However, the flood waters eventually topped the confining ridge and cut the present gorge to allow direct drainage onto the Chryse surface.

# HYDRAULIC ROUTING ACROSS XANTHE TERRA

De Hon, R. A.

Modeled times for the flow to transverse the Xanthe highland region range from 3 to 10 hours depending on flood routing and retardation within impoundments in the valley systems. Hydrographs of the flow at the termini of the chief valleys provide a graphic view of the surges as they reached the end of the valley systems. The initial flood crest was reduced to multiple surges along a prolonged flow at the terminus. Anastomosing flow was primarily responsible for reducing the initial flood crest into a prolonged flow with a series of minor ebb and flows. Ponding and release was responsible for the greatest retardations and the separation of major flood crests at the termini of the canyons.

Thus, flood routing through multiple channels and retardation in local impoundments are responsible for breakup of the initial flood crest and the formation of multiple flood crests. Recombined flow near the mouths of these canyons results in an extended flow regime and multiple flood surges. As a result of ponding along the flood course, depositional sites are localized and renewed erosion downstream (from ponded sites) results in sediment source areas not greatly removed from depositional sites. Some sites, especially at the mouths of the trans-Xanthe canyons, experienced a complex history of deposition and erosion in response to the ebb and flow of multiple flood crests imposed by flood routing and multiple ponding.

References:
1. De Hon R.A.(1987) Lunar Planet. Sci. XVIII, 227-228.
2. Greeley R. et al. (1977) J. Geophys. Res. 82, 4093-4109.
3. Thelig E. and R. Greeley (1979) J. Geophys. Res. 84, 7961-7984.
4. Baker V.R. and R.C. Kochel (1979) J. Geophys. Res. 84, 7994-8010.

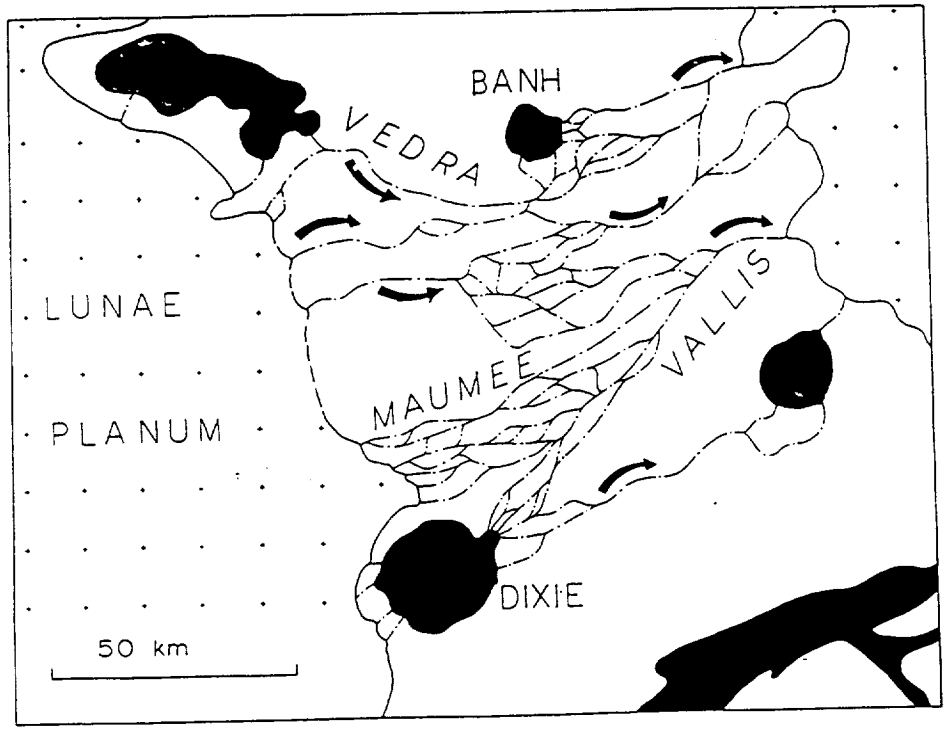


FIGURE 1. Subparallel and anastomosing channels across Xanthe Terra.

**GEOLOGIC MAP OF THE GALAXIAS REGION OF MARS.** R. A. De Hon, Department of Geosciences, Northeast Louisiana University, Monroe LA, 71209, P. M. Mouginis-Mark, and E. E. Brick, Planetary Geoscience Division, Hawaii Institute of Geophysics, University of Hawaii, Honolulu HA 96822.

Introduction: The Galaxias region (MTM 35217) is one of a series of 1:500,000-scale science study areas on Mars sponsored by NASA Planetary Programs. This map is part of an east-west strip which includes Hecates Tholis and a mixture of volcanic and nonvolcanic terrains near the northern limit of the Elysium lava flows. Resolution on the images used in the Viking photomosaic base ranges from 160 to 40 meter per pixel, and the solar illumination angle is not constant. Thus, visible surface detail varies considerably.

Some of the map units (Fig. 1) correspond or are partially equivalent to units of Elston (1), Scott and Carr (2), Greeley and Guest (3), and Tanaka et al. (4). Established terminology is followed where feasible, but the scale of this map requires that some new units be introduced and that some previous terminology be redefined.

Geologic Setting and Physiography: The Galaxias region is located along the transition zone between the broad Elysium Mons rise to the southeast and Utopia Planitia to the northwest. The regional topography consists of a uniform, gentle slope to the northwest upon which is superimposed a moderately smooth to rugged surface consisting of lava plains in the south and a mixture of rolling plains, rugged "badlands", and subdued knobby terrains to the north. The entrenched Hrad Vallis heads in the region and continues 500 km to the northwest. Galaxias Fossae, for which the map is named, consists of a family of parallel, deep fissures in the southern part of the region and a long, linear fissure in the northern part of the map area.

Stratigraphy: The chief stratigraphic units in the region are flows from Elysium Mons and possible volcaniclastic units associated with the Elysium activity (Fig. 1). All materials other than craters are Amazonian in age. The oldest flow material (Unit Ael1) covers much of the southern third of the map. More pristine lobate flows (Unit Ael2) are superposed on the older flows. Coarse and smooth members of the Elysium Formation (Units Aelc and Aels) form much of the surface in the northern part of the map. Smooth materials may be of clastic origin (volcaniclastic, mudflow, loess, fluvial, etc.) based on the apparent ease of dissection. The coarse member is expressed as rugged "badlands" topography that appears to form at the expense of the smooth member. Breakup of older lava flows into polygonal blocks is mapped as polygonally grooved materials (Unit Apg) along the northern edge of the flows. This material grades northward into either knobby plains material (Unit Apk) or a mixture of coarse and smooth members of the Elysium formation. Locally, lumpy plains materials (Unit Apl) consisting of closely-spaced small hillocks overlie grooved materials. Smooth plains-forming material (Unit Aps) forms broad plains and floors some basins. Fluvial materials occur as slope and floor material of the incised Hrad Vallis (Unit Ach) and as floodplain material (Unit Achp). Fluted plains material (Unit Apf) near the head of Hrad Vallis may be a lahar originating from Hrad Vallis. A unique mound of rugged ridge material (Unit Arr) stands above the plains in mid-quadrangle. Gullied or fluted slopes suggest that this material is easily eroded and may be friable volcaniclastic material or gullied domed plains material. A smaller mound is located to the southeast, and a long ridge with similar gullied or scalloped flanks is located to the east.

Craters: Most impact craters within the region are small, fresh-appearing Amazonian craters (Unit Ac). Amazonian craters have sharp rim crests and textured ejecta blankets. Some ejecta blankets extend greater than one crater diameter from the crest. Secondary crater fields are scarce. A few craters, which are partially buried by Amazonian plains-forming materials, have uncertain stratigraphic bases. These craters are designated as Amazonian and Hesperian crater material (Unit AHc).

Structure: The dominant structural trend is parallel to the regional slope. Fissures, graben, and faults trend dominantly northwest with a lesser orthogonal trend. Galaxias Fossae consists of a system of parallel and alined fissures trending northwest in the southern part of the map region and a 300 km long fissure trending west-northwest in the northern part of the region. The northwest trend is accentuated by parallel alinement of other linears such as the long axis of the rugged ridge material, other ridges, valleys, and flow lobes.

Some features present in the region are of undetermined origins. Small (1 to 3 km basal diameter) oval to elongate hillocks with apical fissures are common in the northeastern portion of the region. They may be pingos. Small ridges (less than a kilometer in width) of questionable origin occur along the edge of the smooth plains material near its contact with polygonal plains materials in the eastern portion of the area.

Channels and Hydrologic History: Hrad Vallis and an unnamed flood plain are prominent drainage courses within the map. Both drainages trend parallel to the regional slope and parallel to the dominant structural trend of fissures, faults, and lineaments. In addition, parts of Galaxias Fossae may have carried flowing water.

Hrad Vallis heads in a fissure-like depression that is locally associated with collapsed terrain. The channel is a well-defined, incised, sinuous channel flanked by a broad, paired terrace along most of its course. Slumping along the walls of the valley has left small islands of terrace material within the channel. Cut-off loops attest to an earlier period of channeling before the present channel was fully established.

East of the Hrad Vallis a flat-floored, broad, irregular depression reaches from the southeast portion of the quadrangle to beyond the central northern border. The depression has a smooth floor with some minor scour and channeling that indicates that this depression carried water. The primary source of water is a 10 km diameter depression at the northern limit of the Elysium flows, but water may have been released all along the egde of the polygonally grooved terrain. A delta and levee complex leads from the source basin into the drainage course (5). Locally, the waters embayed isolated blocks of the grooved terrain.

Geologic History: In this region, the interplay of volcanism, near surface volatiles, and surface runoff is evident. Major units were emplaced as lava flows associated with Elysium volcanism and clastic deposition as either sediment or volcaniclastic processes. Surface modification by fluvial processes and possibly by karst/thermokarst action has been responsible for the development of moderately rugged topography.

REFERENCES

(1) Elston, W. E., 1979, Geologic Map of the Cebrenia Quadrangle of Mars: U.S. Geol. Surv. Misc. Inves. Map I-1140 (MC7).

(2) Scott, D. H. and M. H. Carr, 1978, Geologic Map of Mars: U.S. Geol. Surv. Misc. Inves. Map I-1083.

(3) Greeley, R. and J. E. Guest, 1987, Geologic Map of the Eastern Equatorial Region of Mars: U.S. Geol. Surv. Misc. Inves. Map I-1802-B.

(4) Tanaka K. L., M. G. Chapman, and D. H. Scott, 1989, Geologic Map of the Elysium Region of Mars: U.S. Geol. Surv. Misc. Inves. Map I-xxxx (in press).

(5) Mouginis-Mark, P. M., 1985, Volcano/Ground Ice Interactions in Elysium Planitia, Mars: Icarus 64, 265-284.

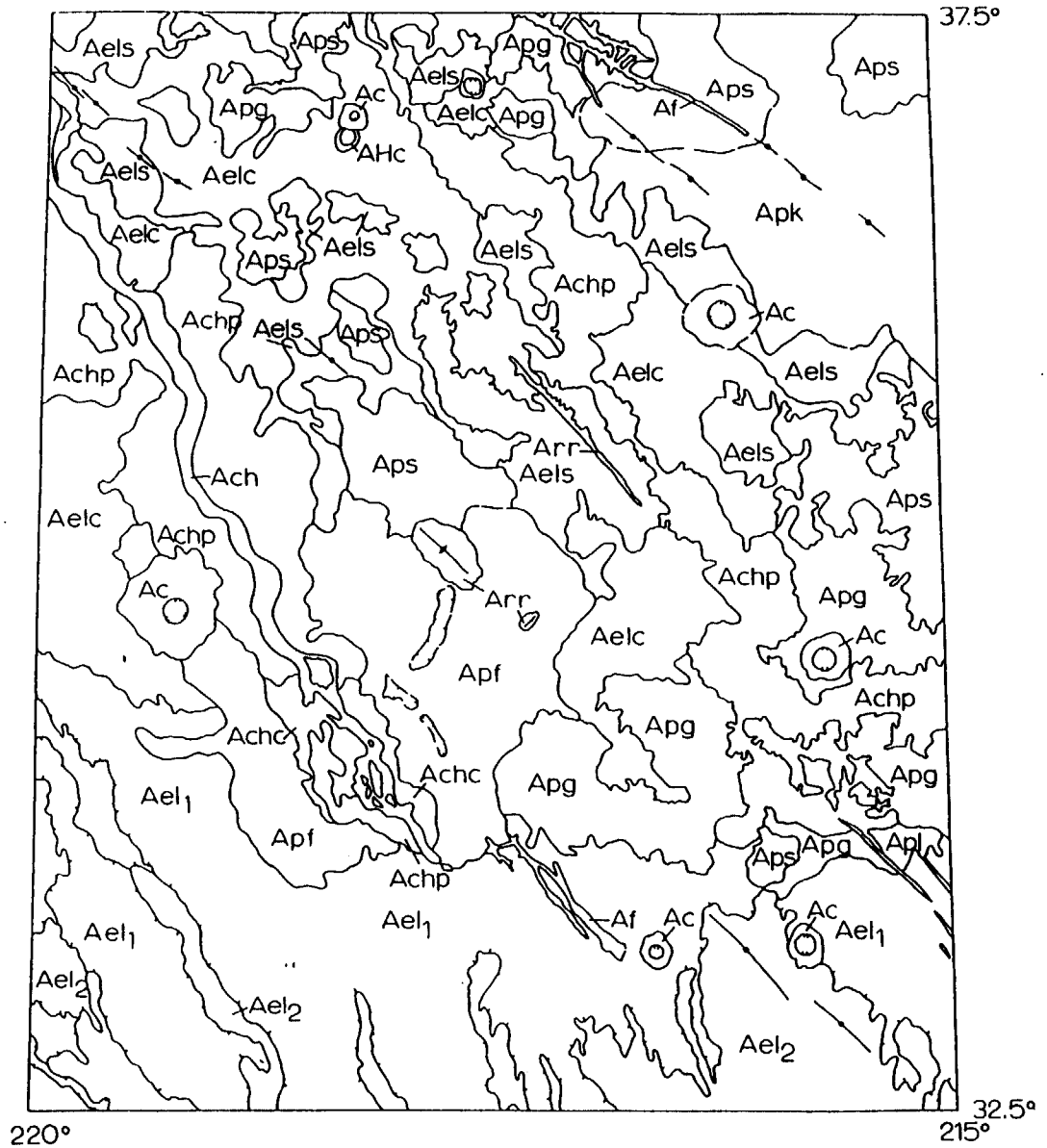


## MAP UNITS

### LOWLAND MATERIALS

| | |
|---|---|
| Aps | Smooth Plains Material |
| Apl | Lumpy Plain Material |
| Apf | Futed Plains Material |
| Af | Fissure Material |
| Arr | Rugged Ridge Material |
| Apk | Knobby Plains Material |
| Apg | Grooved Plains Material |

### EASTERN VOLCANIC ASSEMBLEDGE

Elysium Formation

| | |
|---|---|
| Aelc | Coarse Member |
| $Ael_2$ | Member 2 |
| Aels | Smooth Member |
| $Ael_1$ | Member 1 |

### CHANNEL MATERIALS

| | |
|---|---|
| Ach | Channel Material |
| Achp | Flood Plain Material |
| Achc | Chaotic Channel Material |

### IMPACT CRATER MATERIALS

| | |
|---|---|
| Ac | Amazonian Crater Material |
| AHc | Amazonian and Hesperian Crater Material |

FIGURE 1. Geologic sketch map of the Galaxias Region of Mars (MTM35217).

MINIMUM ESTIMATES FOR VOLUME REMOVAL FROM THE MARTIAN FRETTED TERRAIN BETWEEN 270°W and 360°W, Andrew M. Dimitriou, University of Massachusetts, Amherst, MA 01003.

Martian fretted terrain has been a subject of study since the return of Mariner 9 data (1) and the original morphological description as offered by Sharp (1) has been widely accepted. This description is of a once continuous heavily cratered plateau which has since been subject to extensive erosion. The plateau remnants stand topographically higher as outlying "knobs" and "mesas" amidst onlapping stratigraphically younger plains materials. The best exposed area of fretted terrain on Mars lies between 270°W and 360°W in a 5-10 degree wide zone around 40°N. Work has been done in this area on the nature and origin of the debris aprons and fretted valley floor lineations (2,3) and principal component analysis attempted (4) on the outlying "mesas" in order to explain the observed distribution as a function of structural trends and erosive events. This abstract outlines the method used to estimate the volume of former plateau material that has been removed from this well exposed area of fretted terrain. The method attempts to place relatively hard lower bounds on these estimates. Upper bounds are more uncertain because inferring the extent of plateau material buried beneath plains to the north is difficult. The quantification is important because this region provides a very obvious source of material available for redistribution, and the lowlands to the north have acted as a sink for sedimentary material. The source volumes obtained here can be compared to the sink volumes required to bury large areas of the lowlands with a view to placing this regional contribution into a global context.

Three models are presented for the former extent of a once continuous heavily cratered plateau that has since been dissected and eroded. Within these model areas, outlying "mesas" and "knobs" (hereafter grouped as mountains) are separated for analytical purposes into two groups based on exposed surface area. Mountains >40 $km^2$ are termed large mountains, those <40 $km^2$ small mountains.

The southern and western limit for all three models is identical and well defined by the present boundary between fretted terrain and the heavily cratered plateau. The northern limit for all three models is less well defined because it is gradational. Between 300°W and 350°W, the northern boundary is inferred from the limit of occurrence of larger (>40$km^2$) mountains, which is an irregular east-west trace at about 49°N. East of 300°W, the three models have different NE limits, none of which coincides with the observed limits of fretted terrain. These northeast limits define the different model areas.

The smallest area (model 1) is bounded by a northwestward extension of the northwest trending graben sets visible on the upland surface at about 38°N, 305°W. This extension of a visible upland trend into what is now lowland is based on the postulate that the graben sets are the observable remnants of a series of northwest trending boundary faults that dissected the plateau surface and significantly dropped plateau material to the north and east. Some of the remnant mesas standing in this area of lowland appear to have long axes oriented parallel to this northwest trend. Any assumption of a continuous plateau thickness available for erosion north and east of these faults is not warranted, if this model defines the true initial northern limit of the plateau.

Model 2 includes the model 1 area but its northeast limit is farther eastward and is defined by a northwest-southeast trend at the abrupt limit of occurrence of outlying mountains. This is noted clearly around 43°N, 298°W. The rationale for this model is that this abrupt loss of mountains indicates a rapid drop in basement elevation which could be the limit of a plateau surface that has since been dissected, eroded and embayed by younger materials.

Model 3 includes all of the model 2 area and also an additional zone to the east as far as a northwest-southeast trace defined by the trend of the large irregular mesas centred on 35°N, 280°W. The mesas were identified by Wilhelms and Squyres (5) as rim remnants from their proposed 7700 km diameter Borealis basin. There is no observable evidence to indicate that a continuous thickness of plateau material was available for erosion north and east of this proposed rim boundary.

MARTIAN FRETTED TERRAIN VOLUME REMOVAL: Dimitriou, A.M.

Within all three areas, the exposed surface area of every large mountain was digitised, as was the enclosed area for each model. Shadow measurements were made at 16 locations on the continuous plateau boundary scarp and a mean height of 1.42 ± 0.52 km was determined. The quoted error not only includes the standard deviation, but a 2 pixel vertical error to account for slope rounding and shadow margin location problems as detailed by Parker et al. (6). Shadow measurements were made on 39 large mountains in a similar manner: the mean height of 1.45 ± 0.69 km agrees very well with that obtained from the scarp, strengthening the case that the mountains are remnant outliers of the plateau. In order to account for the volume of residual plateau material remaining within the model areas in the form of small mountains, five representative small subareas were located where the resolution permits a confident assessment of the surface areas and heights of small mountains to be made. An average of 3.3% of these five subareas is covered by small mountains and this is assumed to be a fair estimate across all three of the model areas. A mean height of 0.78 ± 0.41 km was obtained from 45 shadow measurements of small mountains. Ten shadow measurements were made on the margins of debris aprons visible on the extremely high resolution orbit 461B Viking images and a mean height of 0.07 ± 0.02 km was determined. Rather than attempt the extremely difficult task of identifying the percentage of the model areas covered by debris aprons, it was assumed that the entire lowland within each model area was completely buried by a debris blanket of the above thickness.

Estimates of volume removed range from 1.04 ± 0.60 M $km^3$ for model 1 through 1.53 ± 0.80 M $km^3$ for model 2 to 1.99 ± 1.10 M $km^3$ for model 3. This corresponds to a global equivalent sediment layer of between 3 and 21 m. If the northern lowlands is considered as the sole sink for this material a layer of between 9 and 60 m is indicated. These are minimum estimates because: (a) the thickness of plateau material measured does not represent the height above pre-plains basement but the height above the younger plains deposits (b) the northern inferred plateau limit is conservative; more plateau material may lie buried (c) the mountains were assumed to be flat-topped and have vertical cliff faces but are often conical or significantly rounded in cross-section.

As the volume of young material proposed to be present in the northern lowlands is significantly greater than that estimated above, the contribution of sediment from this area of fretted terrain is a small proportion of the lowland total.

(1) Sharp, R.P., J. Geophys. Res., 78, 4073-4083, 1973.
(2) Squyres, S.W., Icarus, 34, 600-613, 1978.
(3) Squyres, S.W., J. Geophys. Res., 84, 8087-8096, 1979.
(4) Kochel, R.C., and R.T. Peake, J. Geophys Res., 89, C336-C350, 1984.
(5) Wilhelms, D.E. and S.W. Squyres, Nature, 309, 138-140, 1984.
(6) Parker, T.J., et al. Icarus, 82, 111-145, 1989.

STRATIGRAPHY OF THE ISMENIUS LACUS SE SUBQUADRANGLE: CLUES TO AN UPLAND/LOWLAND BOUNDARY FORMING EVENT?, Andrew M. Dimitriou, University of Massachusetts, Amherst, MA 01003.

The Ismenius Lacus SE (MC5SE) subquadrangle is located in NE Mars between 292.5$^0$W and 315$^0$W and 30$^0$N and 47.5$^0$N. Within this area, the global boundary between southern heavily cratered upland and northern sparsely cratered lowland is well exposed along a series of northwest trending scarps that approximate 1.4 km in mean height (1). To the northwest and southeast of the boundary defined by the scarps, areas of "fretted terrain" (2) make the upland/lowland boundary difficult to locate precisely. Geologic mapping based on Mariner 9 imagery was done by Lucchitta (3) over the entire MC5 quadrangle at a scale of 1:5M. This area was also covered in the 1:15M scale map of the Martian eastern hemisphere as compiled by Greeley and Guest (4). The purpose of this abstract is to present the initial results of a stratigraphic and tectonic study of this area using the highest available resolution Viking imagery as well as the published 1:2M photomosaic. By obtaining a detailed relative age sequence of the geologic units isolated, the fracturing and tectonic history of this key upland/lowland boundary area can be constrained more precisely than before. The cumulative crater plots generated were compared with the Neukum and Hiller curve (5) and stratigraphic ages assigned with reference to Tanaka (6).

Within the uplands, a distinctive population of "rimless" craters is recognised which has also been noted in Amenthes (7). It is assumed here that these craters represent an old population lying at a relatively uniform depth beneath the present plateau surface units. When relative ages are determined, either by considering the plateau surface as a whole or by separating populations based on the observable geologic units, counts of "rimless" craters yield an Early Noachian age.

Above this ancient surface, a number of geologic units can be identified based on differences in surface morphology. A smooth plateau unit is located along the fretted northern boundary of the plateau and as a capping unit on the outlying mesas. This is interpreted as being volcanic and/or aeolian material and yields a crater age of Early Amazonian. The smooth plateau unit truncates a boundary between two units tentatively interpreted as volcanic, the most extensive of which is identified as ridged plateau. It lies in the central portion of the upland in this subquad and is characterised by the presence of low relief irregular scarps; crater counts yield a Early Hesperian age although the counts also indicate that lava may have continued to flood this surface with decreasing volumes into the Early Amazonian. The ridged plateau is fractured and truncated along its eastern margin by boundary scarps which separate upland from lowland materials. The second unit truncated by the smooth plateau is characterised by a hummocky surface at km scale and is thus identified as hummocky plateau. This is located in the central and eastern portion of the upland where its eastern margin is also dissected and truncated by boundary scarps. Crater counts yield an Late Hesperian age for this unit.

A complexly eroded unit is identified in the southern region of the subquad as etched plateau. The boundary between this and the ridged plateau is characterised by erosional rather than depositional processes. Here, the visible etched unit consists of ridged and possibly smooth plateau material that has been differentially eroded in a complex manner leaving irregular and circular positive relief landforms. Crater ages from this unit yield Early Amazonian ages, but this relative youth is almost certainly due to removal of craters by the complementary processes of erosion and deposition, the stratigraphic age of the materials visible is older. These erosional and depositional processes have neverless allowed a fairly clear boundary to be drawn between the etched and ridged units.

Within the lowland along the upland/lowland boundary, a unit which is characterised by the presence of bright, very sparsely cratered material is identified. This unit includes debris aprons present at the base of the scarp and of many outlying mountains and also bright deposits mantling the floors of fractures and irregular valleys penetrating into the uplands. Crater counts proved impossible on this unit due to the small number of superposed craters present.

North and west of the boundary scarp, three lowland plains units are identified: a smooth plains unit, a very smooth plains unit and an etched plains unit. Crater counts are only possible

on the first two units and yield ages between Early and Middle Amazonian. The latter unit does not have a large enough exposed area within the mapped area to permit crater counting. The morphological differences between the first two units is based on the relative abundance of small mountains that are scattered through the lowland plains. These mountains are inferred to represent inliers of older material. Within the areas where these mountains abruptly decrease in abundance practically to zero the very smooth plains unit was identified. The differences in mountain abundance are taken to represent variations in sub-plains basement elevation. The etched plains unit is characterised by the presence of small (< 10km long axis) cuspate positive relief features that suggest differential erosion of plains materials.

A unit that consists of isolated large groups of mostly rounded mountains scattered in a wide zone roughly paralleling the present trace of the upland/lowland scarp is interpreted to be remnants of an older surface that has been partially buried and embayed by the unconformable younger plains materials. Crater remnants are visible in many cases and counts over these areas yield a population that fits the Neukum and Hiller production curve (5) very well. The age determined is Early Noachian. Therefore, the surface that lies at a shallow depth on the plateau is also present at a shallow depth in the lowlands, an elevation difference of at least 1.4 km.

In order to account for this observation, work is in progress attempting to model this as an area which experienced crustal downwarping, or normal faulting causing downthrow to the northeast. These models must also take into consideration the timing of the event. Because some of fractures cut upland surfaces the faults are inferred to have initiated around the Late Noachian/Early Hesperian boundary, which is significant for the timing of the origin of the dichotomy boundary itself in this region of Mars.

This region is a key area of the upland/lowland boundary, due to the exposure of a wide age range of materials. The work done and the modelling in progress enables better constraints to be placed on the timing and nature of this portion of the global dichotomy.

(1) Dimitriou, A.M., Lunar and Planet Sci. Conf. XXI (abs), this volume, 1990.
(2) Sharp, R.P., J. Geophys. Res., 78, 4073-4083, 1973.
(3) Lucchitta, B.K., Geol. Map Ismenius Lacus Quadrangle of Mars, Map I-1065, 1978.
(4) Greeley, R. and J.E. Guest, Geol. Map of Eastern Equatorial Regions of Mars, Map I-1802B, 1987.
(5) Neukum, G., and K. Hiller, J. Geophys. Res., 86, 3097-3121, 1981.
(6) Tanaka, K.L., J. Geophys. Res., 91, E139-E158, 1986.
(7) Maxwell, T.A. and R.A. Craddock, Lunar and Planet Sci. Conf XX (abs),646-647, 1989.

EXPERIMENTAL SIMULATION OF MARTIAN NEUTRON LEAKAGE SPECTRUM; D.M. Drake, S. Wender, R. Nelson, and E. R. Shunk, Los Alamos National Laboratory, Los Alamos, NM 87545; Winfried Amian, UFA, Julich, FRG; Peter Englert, San Jose State University, San Jose, CA; Johannes Bruckner, Max-Planck Institut fur Chemie, Mainz, FRG; Manfred Drosg, University of Vienna, Vienna, Austria

The boron loaded plastic scintillator that partially surrounds the Gamma Ray Spectrometer (GRS) of the Mars Observer satellite has two functions. First, via anticoincidence, it allows pulses that are caused by energetic cosmic rays to be eliminated from the gamma-ray spectrum, and second, it counts cosmic ray created neutrons that leak from the martian surface. Due to the fact that the plastic shield is divided into four parts similar to the sides of a pyramid, the neutron leakage spectrum can be parameterized by the four counting rates. Because the space craft velocity is larger than that of thermal neutrons, the front face of the counter counts faster than the back face.[1]

In a previous paper[2], we modeled the neutron leakage spectrum using a neutron transport code for various martian surface conditions (dry and wet regolith, layers, and carbon dioxide overlay). These spectra were parameterized into epithermal and thermal parts in order to facilitate identification regolith features.

Although we have a high degree of confidence in the codes used, we thought some experimental verification of the trends predicted would be appropriate.

To this end we filled a large container with pseudo "martian sand" whose composition was similar to that found at Chryse and bombarded it with pseudo cosmic rays, i.e., 800 MeV protons from the Los Alamos LAMPF accelerator.

The LAMPF beam was delivered in pulses whose time duration was less than a nano-second, about twenty time per second. The leakage neutrons were detected by $^{6}$Li glass detectors located at the end of a 30 meter evacuated flight path. The time of flight neutron spectra were converted to energy spectra and corrected for detector efficiency so that they could be compared directly to the calculated spectra.

Preliminary results of this experiment show the neutron spectrum to be considerably harder than calculations using infinite plane geometry. We attribute this difference in part to the finite size of the containers.

References

1) William C. Feldman and Darrell M. Drake, Nuclear Instruments and Methods A245 (1986) 182.

2) D. M. Drake, W. C. Feldman, and B. M. Jakosky, Journal of Geophysical Res. 93 (1988) 6353.

# A GAMMA RAY MODE OF THE ALPHA PARTICLE ANALYTICAL INSTRUMENT

Thanasis Economou* and Anthony Turkevich *#.
* Laboratory for Astrophysics and Space Research, Enrico Fermi Institute,University of Chicago, Chicago, # Chemistry Department, University of Chicago, Chicago, IL 60637.

The Alpha Particle Analytical Instrument provided the first relatively complete analyses of lunar surface material at three locations on the moon during the Surveyor Missions in 1967 and 1968 using only the classical alpha and proton modes of the technique. The capabilities have since been expanded by measuring the fluorescent x-rays produced by the interaction of the source radiations with the sample surface. Such versions of the instrument were flown on the ill-fated Soviet Phobos missions in 1988. The alpha sources used in such instruments are also neutron emitters due to spontaneous fission branches in the alpha decay and due to the interaction of the alpha particles with nearby materials. These neutrons can react with surrounding materials to produce gamma rays. Inclusion of a gamma ray detector in the Alpha Particle instrument can enhance the analytical capabilities of the package by providing a direct sensitivity for hydrogen, by providing a bulk analysis for several elements that are determined in the surface material, and by providing some isotopic information. This possibilitiy of determining several elements by different modes can remove ambiguities about the applicability of a surface analysis to represent bulk composition. Thus, an alpha particle package with alpha, proton, x-ray and gamma modes can provide the most complete in situ chemical analysis of an extraterrestrial body that is presently possible.

In order to test these ideas a 50 mCi $^{244}Cm$ alpha source, mounted on stainless steel, has been used in an arrangement where the alpha ( neutron) source was approximately 20 cm away from a cooled 30 $cm^3$ GeLi crystal. Samples of various materials, varying in mass from 2 to 15 Kg were interposed between the source and detector and the resultant gamma rays measured. The experimental situation differs from that of Bruckner et al (1) in using relatively low energy neutrons (less than 4 MeV cf 14 MeV) and rather thick targets.

As an example of the type of results obtained, Figure 1 compares the response of the gamma detector to a sample of $NaHCO_3$ with that when $Na_2CO_3$ is the sample. Figure 1a shows the energy region between 420 and 500 KeV. Also shown is the detector response when no sample is present. Clearly seen in both carbonate samples is the 439 KeV gamma ray line due to inelastic neutron scattering on $^{23}Na$. In the NaHCO3 sample there is, barely visible, the 472 keV neutron capture line in $^{23}Na$. This line is not seen in the $Na_2CO_3$ sample presumably because of neutron leakage before capture.

Figure 1b shows the spectra in the 2 MeV region. The 2.22 MeV neutron capture line of hydrogen is visible in the bicarbonate sample. The neutron capture lines of H and $^{23}Na$ are greatly enhanced by addition of surrounding paraffin.

Table I lists the samples that have been measured so far, the gamma rays identified and their relative intensities as recorded. These preliminary results should be used with caution since the intensities will depend on the actual geometrical situation which, in this work, was quite different from that to be encountered on either a surface or penetrator type space mission.

The gamma rays detected so far are pretty much those expected by calculations of the type of Evans et al (2) although some significant differences are noted. For example, in the magnesium run, the lines at 1.369, 1.612 and 1.809 MeV are not in the ratios given by Evans et al (2), and the 1.612 MeV line is hardly visible in our measurements. In addition, the detector system used here had a cut off at 6.1 MeV and was too small to have a good efficiency for gamma rays above about 4 MeV.

On a space mission with alpha sources of the strength needed for the alpha and proton modes of the Alpha Particle Instrument, the gamma ray rates should be at least comparable to those expected from cosmic rays. They could easily be enhanced by up to a factor of ten by use of a Be shutter over the alpha sources or with higher intensity, encapsulated, alpha sources.

There are several disadvantages to using such neutron sources for exciting gamma rays for analytical purposes and these have to be investigated. However, advantages would be the presence of a neutron source of constant and known strength and energy distribution, the response to which could be adequately calibrated on earth. This would make the analytical results quantifiable in a way hard to do with cosmic ray activation.

**Acknowledgements**: Support provided by the U.S. National Aeronautics and Space Agency (grant #NAG W 878).

**References**: (1) J. Bruckner, R.C. Reedy and H. Wanke, Lunar and Planetary Sci. XV, Abstract p. 98 (1984). (2) L.G. Evans, J.I. Trombka and W.V. Boynton, Lunar and Planetary Sci. XVI, J. Geophys. Res. 91, D525 (1986).

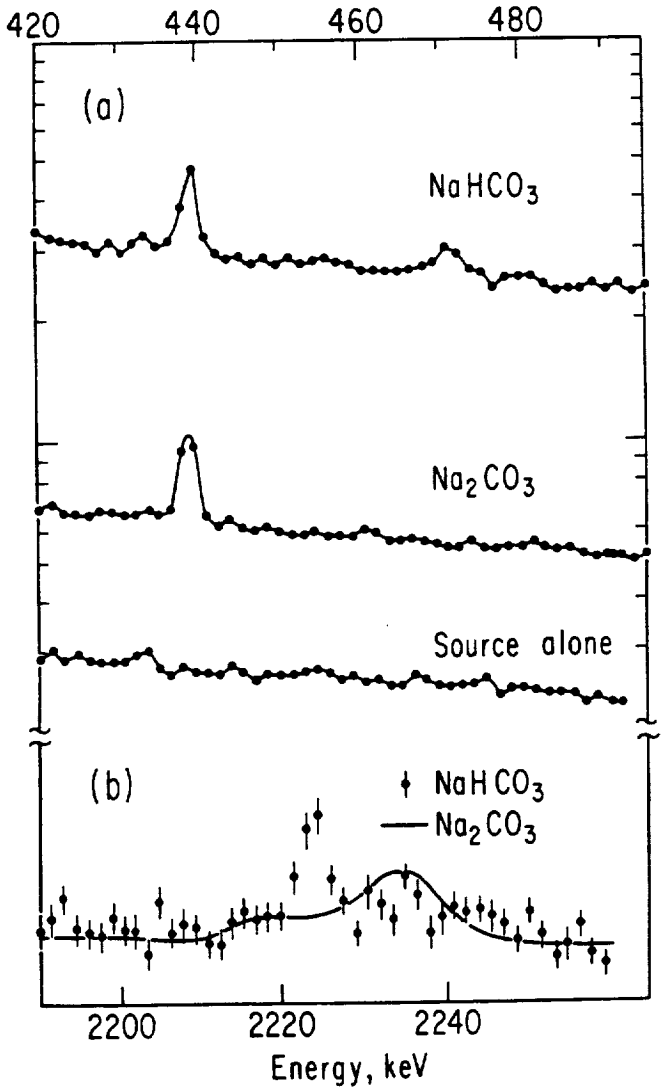


**Fig.1** Response of Ge(Li) detector to carbonate samples exposed to 50 mCi $^{244}Cm$. 1a: Energy region 420-500 keV. 1b: Energy region 2150 -2260 keV

**TABLE I**

| Sample | Weight (kg) | Line | Isotope (keV) | Relative Intensity (c/1000 min) |
|---|---|---|---|---|
| Plexiglas | 5.9 | 2,223 | H | 3936 ± 70 |
| $Na_2CO3$ | 12.0 | 439 | $^{23}Na$ | 5088 ± 146 |
| NaHCO3 | 10.0 | 439 | $^{23}Na$ | 802 ± 52 |
| | | 472 | $^{23}Na$ | 263 ± 47 |
| | | 2,223 | H | 70 ± 13 |
| Mg | 5.4 | 1,369 | $^{24}Mg$ | 1355 ± 74 |
| | | 1,612 | $^{25}Mg$ | 236 ± 22 |
| | | 1,819 | $^{26}Mg$ | 263 ± 47 |
| Al | 15.0 | 2,210 | $^{27}Al$ | 167 ± 16 |
| SiC | 2.8 | 1,779 | $^{28}Si$ | 288 ± 28 |
| | | 1,273 | $^{29}Si$ | 717 ± 47 |
| | | 2,235 | $^{30}Si$ | 746 ± 31 |

# THE X-RAY MODE OF THE ALPHA PARTICLE ANALYTICAL INSTRUMENT

T. Economou*, J. Iwanczyk** and A. Turkevich*

*Laboratory for Astrophysics and Space Research, The University of Chicago,Chicago, Il.60637.
**Xsirius Scientific,Inc. 4640 Admiralty Way, Suite 214, Marina Del Ray, California 90292.

The Alpha Particle Instrument with its alpha, proton, x-ray, and now, the new gamma ray modes, is a versatile analytical instrument that can provide the most complete in-situ chemical analyses of samples on planetary missions. The instrument is based on interactions of radiation with matter that are well understood and it can be easily calibrated in the laboratory before being sent into space. Its performance has been proven during space missions in the past.

The excitation of characteristic x-rays in the Alpha Particle instrument is caused by two mechanisms: 1) by the alpha particles from the curium radioactive source - the same source that is used in the alpha, proton and the gamma modes - and, 2) by the plutonium L x-ray lines ( 14-22 keV) which are more effective than alpha particles in exciting higher Z elements. Such excitation is sufficient to obtain good analyses for all the major elements in relatively short counting periods. To enhance the sensitivity for certain minor and trace elements, additional auxiliary x-ray excitation sources can be utilized ( e.g $^{109}Cd$ , $^{241}Am$, etc).

In the past, ( e.g. on the recent Soviet Phobos mission), the X-ray mode of this instrument was implemented by using a cryogenically cooled Si(Li) detector. However, for many missions, including a mission to Mars, such cooling is impractical or impossible. In such cases ambient temperature x-ray detectors are needed. (J. Iwanczyk et al, 1986, 1989).

We report here the first preliminary results obtained using an x-ray probe containing an ambient temperature $HgI_2$ x-ray detector attached to the Alpha Particle instrument as shown in Fig. 1. The detector used in this work had an area of 5 $mm^2$ with about 500 mm depletion depth . It was biased at -800V. The detector and the first stage FET transistor were slightly cooled to about 0° C by small Peltier coolers. Such cooling will not be necessary for most missions . The detector was exposed to the x-rays from the sample in vacuum and acted therefore as a windowless detector. A 3.5 mm parylene N type film was coated directly on to the $HgI_2$ crystal to prevent contamination and to enable the detector to operate properly in vacuum. The total energy resolution of the x-ray system was 225 eV at 6.04 keV of Fe $K_a$ line The electronic noise was 187 eV.

With this arrangement we were able to detect the very low x-ray energies that even the best laboratory silicon detector with thin Be window have difficulties detecting. Fig. 2 shows the x-ray spectrum obtained from a $Na_2CO_3$ sample. The sodium line at 1.04 keV is clearly above the noise level of the system. Fig.3 shows the x-ray spectrum obtained from a sample of an Allende meteorite There, the 1.25 keV Mg $K_a$ line is well separated from 1.74 keV Si $K_a$ line. With proper line fitting algorithms even a line from about 1.7 % aluminum (1.49 keV ) sample can be detected in the presence of 15% Mg and 13% Si present in the Allende meteorite . The other lines are due to sulphur, calcium, titanium,chromium,manganese,iron and nickel. Notice that the Fe $K_b$ line is very well separated from the Ni Ka line. Fig.4 shows for comparison a similar spectrum obtained with the Phobos x-ray instrument that utilized cooled Si(Li) detectors (Hovestadt et.al.,1988.).

Although the first results of the x-ray mode of the Alpha Particle instrument using ambient temperature $HgI_2$ x-ray detectors were much better than we had expected in terms of

resolution and sensitivity to low energies, it can be seen that the Phobos instrument with similar energy resolution has slightly better sensitivity to elements present in low concentration This is due to the higher background in the present arrangement. As can be seen from Fig.1, the source-sample-detector geometry of the x -ray probe is less than optimal in this experimental setup. By mounting the x-ray detector inside the Alpha instrument, the sample to detector distance can be decreased from the present 65 mm to less than 25 mm. This will increase the useful x-ray counting rate by almost a factor of seven while the background will not change significantly. This will dramatically improve the sensitivity of the instrument to low concentration elements. Future experiments will concentrate on investigating the best design geometries, detector sizes and the best auxiliary excitation sources.

**Acknowledgements**. The present work was supported by the U.S. National Aeronautics and Space Agency ( grant # NAGW-1847 and # NASW-4492 )

**References:** J. S. Iwanczyk, A. J. Dabrowski, G. C. Huth, J.G. Bradley, J.M Conley and A. L. Albee, Low Energy Spectra Measured with Mercutic Iodide Energy Dispersive Spectrometer in Scanning Electron Microscope, IEEE Tran. Nucl. Sci. Vol. No.1, 355-358 (1986).

J.C Iwanczyk, Y.J.Wang,J.G.Bradley,J.M.Conley, A.L.Albee, and T. E. Economou , Performance and Durability of $HgI_2$ X-ray $HgI_2$ Detectors for Space Missions IEEE Tran Nuc Sci, Vol.37, No.1 pp.841-845 (1989).

D. Hovestadt. et all : In-situ Measurements of the Surface Composition on the Phobos Mission. Lunar and Planetary Science XIX (March 14-19,1988), p.511.

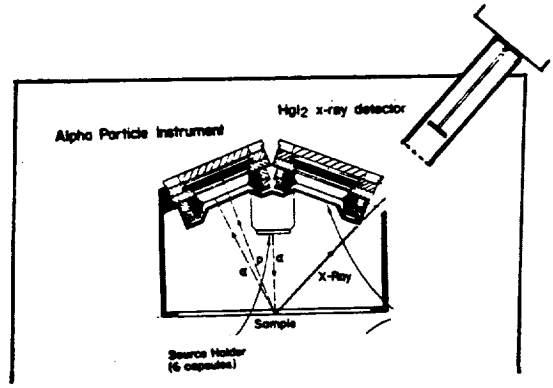


**Fig. 1:** Geometrical relationship of $HgI_2$ detector probe attached to the Alpha Particle Instrument.

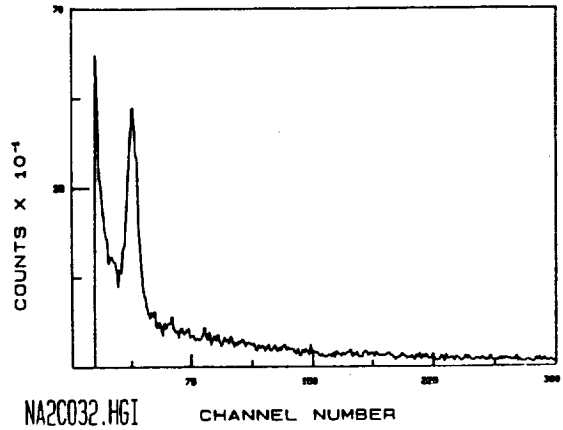


**Fig. 2:** Sodium $K_a$ line at 1.04 keV from $Na_2CO_3$ sample. The resolution of the line is 180 eV.

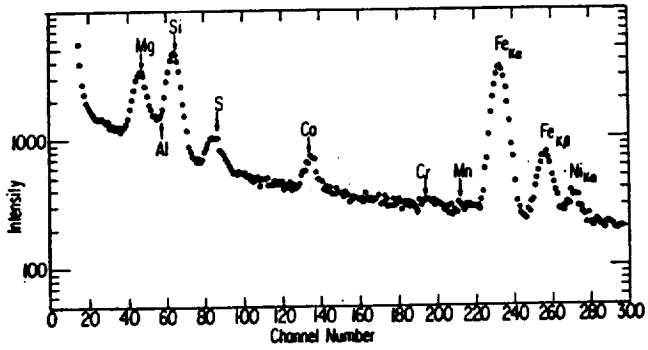


**Fig. 3:** X-ray spectrum from a sample of meteorite Allende, obtained with $HgI_2$ x-ray detectors at ambient temperature . The sample was excited with 40 mCi of $^{244}Cm$ alpha source that is used by the Alpha Particle instrument.

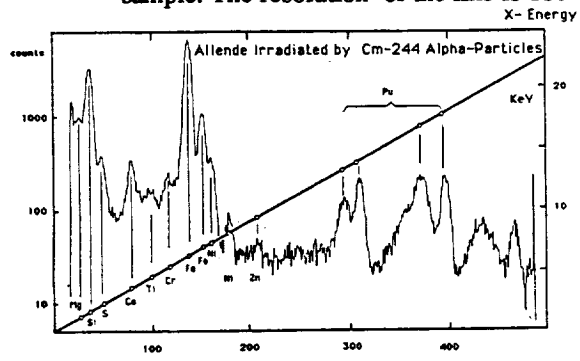


**Fig. 4:** X- ray spectrum from similar Allende sample obtained with Phobos Alpha-X flight instrument that utilized cooled Si(Li) detector and $^{244}Cm$ source excitation.

## POSSIBLE CINDER CONES NEAR THE SUMMIT OF PAVONIS MONS, MARS.

*Kenneth S. Edgett, Department of Geology, Arizona State University, Tempe, AZ 85287.*

**Introduction.** In 1979, Wood [1] mentioned the existence of a possible cinder cone near the summit of Pavonis Mons, and he estimated its dimensions. Examination of medium resolution *Viking* photographs has revealed four additional candidate cinder cones in the summit region. Pavonis Mons has been largely overlooked in the literature concerning the late-stage volcanic activity of the Tharsis volcanoes; and no cones have been found on the other Tharsis Montes [2,3]. The presence of possible cinder cones near the summit implies that volatile-rich pyroclastic activity occured late in the evolution of Pavonis Mons.

**Setting.** The summit region of Pavonis Mons (Fig. 1) was photographed at moderate to high resolution (50 to 75 m/pixel) by both *Mariner 9* and *Viking 1*. The summit is about 18 km above the martian datum [4,5], and has two conspicuous features: a 45 km-diameter caldera and, off-set to the northeast, an 85 km-diameter depression [6-9]. The caldera is about 4 to 5 km deep [4,5,10]; and the walls have numerous vertical, parallel ridges and grooves which are attributed to mass wasting and aeolian modification [11,12]. The caldera floor appears smooth and featureless with the exception of two 500 m-diameter craters. The large depression is bounded by inward-facing arcuate scarps in the west, and both an inward- and outward-facing scarp in the east. There is no surface expression of the southeastern rim of the depression. Six mare-type wrinkle ridges oriented radial to the caldera occur within the depression, none occur within 5 km of the caldera rim, but three of them extend up to 12 km beyond the depression rim. The depression apparently formed before the caldera; and the wrinkle ridges formed before or concurrently with the depression [13]. The wrinkle ridges likely formed by compression [14-16], the depression likely formed by volcano-tectonic collapse [9].

**Cones and Mounds.** Five cones or mounds, labeled "c" in Fig. 1, occur within 5 km of the caldera rim. The best example is a cone with a pit at its summit which occurs on the volcanic shield along the edge of a fissure, about 3.5 km west of the caldera rim. This cone, originally identified by Wood [1], is best seen in an oblique-view photograph from *Mariner 9* (DAS 55663953). It is also visible in *Viking 1* images 210A32 and 210A34. To the north of this cone there is an irregular, rough-textured, raised-relief landform (labeled "m" in Fig. 1) which is bissected by a fissure. Two mounds, approximately elliptical in shape, occur along fissures north of the caldera rim between the rim and the southern end of a wrinkle ridge in the 85 km depression; one of these features appears to have a summit crater. Two additional features, circular mounds with summit pits, are visible near the limits of resolution in *Viking* frame 210A34; they occur in the large depression about 15 km east of the elliptical mounds and about 5 km north of the caldera rim.

**Interpretations and Discussion.** The five cones and the irregular, rough-textured landform are considered to be volcanic constructs, because of their occurence on a volcano and their proximity to both the caldera and to fissures in the summit region. Wood [1] interpreted the cone seen in the *Mariner 9* image as a possible cinder cone with a basal diameter of ~1.1 km, a crater diameter ~0.45 km, and a height of ~0.07 km. Although Wood did not plot this cone [fig. 6 of 1], with these dimensions the cone plots within the cinder cone "field" of Wood's crater diameter/basal diameter diagram for monogenetic volcanoes [13].

Alternative explanations for the cones are: (1) They could be small effusive volcanoes, such as the chain of low shields in the Arsia Mons caldera [17]; or (2) they could be volcanic domes. Short of obtaining very high resolution photographs or thermal infrared measurements, there is no conclusive test to demonstrate that any of the five cones/mounds are cinder cones. One test for the presence of cinders is to look for very high resolution thermal infrared data, which might indicate the presence of cinders because thermal inertia correlates with grain size under martian atmospheric conditions [*eg.* 18]. The highest resolution thermal infrared data from the *Viking* Infrared Thermal Mapper (IRTM) did not indicate the presence of surficial deposits with grain sizes larger than ~0.1 mm (silt-sized) on the Pavonis Mons shield [19]. However, the spot sizes for these data were about 3 to 5 km, while the cones are smaller, about 1 to 3 km.

If the cones are cinder cones, then they indicate that pyroclastic activity occured on Pavonis Mons. Since they appear to be associated with fissures emanating from the caldera, they might post-date the caldera collapse, and would therefore suggest that the last summit volcanic activity involved volatile-rich magmas [*eg.* 20]. Cinder cones form from short-lived strombolian eruptions, usually resulting from eruption of a low-viscosity magma through a narrow fissure or conduit [21]. The fact that these landforms do not resemble the low-profile, several km-wide cinder cone shapes predicted for Mars by McGetchin *et al.* [22] might be explained by their use of terrestrial values for ejecta volumes, escape angles, and velocities.

The possible presence of cinder cones on Pavonis Mons distinguishes it from the other Tharsis volcanoes. Olympus, Arsia, and Ascraeus Montes were photographed at higher resolutions by the *Viking Orbiters*, yet detailed studies of these volcanoes reveal no cinder cones or other evidence for pyroclastic volcanism [2,3]. It should be noted that the Hawaiian basaltic shield volcanoes have numerous cinder cones on them [*eg.* 23]; suggesting that Pavonis Mons has had a similar evolution.

The cone-shaped landforms near the summit of Pavonis Mons are the most likely candidate cinder cones yet identified on Mars, because they occur on a volcano and they occur in the vicinity of a caldera, as do many of the Hawaiian cinder cones. Possible cinder cones have also been identified on Elysium Mons

## CINDER CONES ON PAVONIS MONS? *K.S. Edgett*

[24]. Numerous cone-shaped features with summit pits have been identified elsewhere on Mars [*eg.* 25-27], but their volcanic associations are questionable due to the lack of a definite volcanic context.

**References:** [1] Wood, C.A. (1979) *Proc. 10th Lunar Planet. Sci. Conf.*, 2815-2840. [2] Mouginis-Mark, P.J. (1981) *Proc. 12th Lunar Planet. Sci. Conf.*, 1431-1447. [3] Zimbelman, J.R. (1984) PhD Diss., Arizona State Univ.; reprinted in (1986) *Adv. Planet. Geol., NASA TM 88784*, 271-572. [4] Hord, C.W. *et al.* (1974) *Icarus, 21*, 292-302. [5] U.S. Geol. Surv. (1989) Topographic Maps...of Mars; *Map I-2030*, 1:15M scale. [6] Masursky, H. *et al.* (1972) *Science, 175*, 294-305. [7] McCauley, J.F. *et al.* (1972) *Icarus, 17*, 289-327. [8] Carr, M.H. (1973) *J. Geophys. Res., 78*, 4049-4062. [9] Crumpler, L.S. and J.C. Aubele (1978) *Icarus, 34*, 496-511. [10] Bibring, J.-P. *et al.* (1989) *Nature, 341*, 591-593. [11] Sharp, R.P. (1973) In *Geology, Seismiscity, and Environmental Impact* (D.E. Moran *et al.*, eds.), pp. 115-122, Assoc. Eng. Geol., Univ. Publ., Los Angeles. [12] McCauley, J.F. (1973) *J. Geophys. Res., 78*, 4123-4137. [13] Edgett, K.S. and J.R. Zimbelman (1990) "The Landforms of Pavonis Mons, Mars," (manuscript in preparation). [14] Baldwin, R.P. (1963) *The Measure of the Moon*, Univ. Chicago Press, 488p. (see p. 380). [15] Plescia, J.B. and M.P. Golombek (1986) *Geol. Soc. Am. Bull., 97*, 1289-1299. [16] Watters, T.R. (1988) *J. Geophys. Res., 93*, 10236-10254. [17] Carr, M.H. *et al.* (1977) *J. Geophys. Res., 82*, 3985-4015. [18] Kieffer, H.H. *et al.* (1973) *J. Geophys. Res., 78*, 4291-4312. [19] Zimbelman, J.R. (1986) *Trans. Am. Geophys. U. (EOS), 67*, 1074. [20] Blackburn, E.A. *et al.* (1976) *J. R. Soc. London, 132*, 429-440. [21] Wilson, L. and J.W. Head (1981) *J. Geophys. Res., 86*, 2971-3001. [22] McGetchin, T.R. *et al.* (1974) *J. Geophys. Res., 79*, 3257-3272. [23] MacDonald, G.A. *et al.* (1983) *Volcanoes In The Sea; The Geology of Hawaii*, 2nd ed., Univ. Hawaii Press, Honolulu, 517p. [24] McBride, K. and J.R. Zimbelman (1989) *Lunar Planet. Sci. XX*, 651. [25] Woronow, A. (1980) *Repts. Planet. Geol. Prog.-1979/80, NASA TM 81776*, 187-188. [26] Plescia, J.B. (1980) *Repts. Planet. Geol. Prog.-1980, NASA TM 82835*, 263-265. [27] Frey, H. and M. Jarosewich (1982) *J. Geophys. Res., 87*, 9867-9879. [28] **Acknowledgements:** Comments by J.R. Zimbelman and D.A. Crown were very helpful in refining the discussion presented here.

**Figure 1.** Sketch map of the summit region of Pavonis Mons. Mare-type ridges are shaded. The five cone-shaped features are labeled "c", and are interpreted as *possible* cinder cones. Feature (m) is interpreted to be a volcanic extrusion which post-dates the caldera. The units labled are: (cf)= caldera floor, (s)= wall-slump material, (cw)= caldera walls. Sketch is centered at 0.8°N, 112.7°W; the map base included *Viking 1* images 210A 33-36.

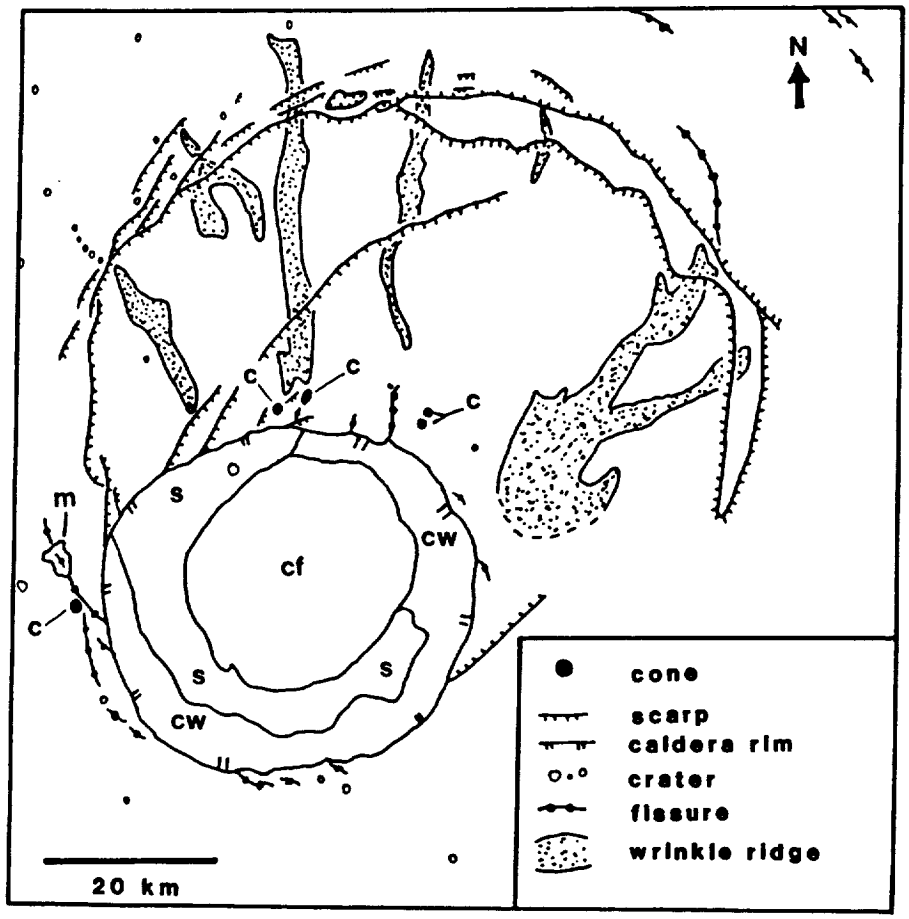

**SAND ON MARS: DARK AEOLIAN DEPOSITS ON CRATER FLOORS RELATED TO REGIONAL WINDS.** ***Kenneth S. Edgett and Philip R. Christensen,*** *Department of Geology, Arizona State University, Tempe, Arizona 85287.*

Intracrater dark features are common on Mars, especially on the floors of craters larger than ~25 km in diameter [1]. They typically occur on the predominant downwind side of the crater, and a number of them are composed of sand dunes [2-6]. The dark features, commonly termed "splotches" [7,8], are also apparently relatively free of incorporated fine dust [6] and coarse rocks [9]. All of the previous work that considered these features suggests that they have an aeolian origin, and that most may be composed of granulometrically unimodal deposits of sand-sized material. The purpose of the present study is to search for regional versus local differences in the properties of materials comprising the dark intracrater features; in order to make inferences concerning the nature and global distribution of martian sands.

The approach of this study involved: (1) examination of the highest resolution *Mariner 9* and *Viking Orbiter* photographs, in an effort to locate dunes, and (2) determination of the thermophysical properties of intracrater dunes, followed by the same for intracrater dark features with no visible duneforms. *Viking* Infrared Thermal Mapper (IRTM) 20 μm brightness temperatures and an assumed surface albedo of 0.15 were used to calculate thermal inertia. (The reader should note that a 0.15 albedo is a more realistic value than the 0.25 used to calculate thermal inertias presented in an earlier abstract [10]). A standard albedo of 0.15 was used because actual albedos for all of the dark intracrater features are not available. The IRTM data were constrained to avoid the effects of atmospheric dust, clouds, surface frosts, surface roughness, and surface emissivity. The best IRTM data for these purposes were taken at night (one reason for using an assumed albedo) and between $L_S$ 344° to 125°. The resolution of the data were constrained, so that only data which lie exactly (or as close as possible) on the dark feature were used. Thermal inertia (expressed in units x $10^{-3}$ cal $cm^{-2}$ $sec^{-1/2}$ $°K^{-1}$), at martian atmospheric pressures and temperatures, can be used to estimate effective particle size of unconsolidated materials [11,12]. This relationship is most useful for examining sand dunes, because they are the most likely martian feature which would be unconsolidated *and* have a unimodal grain size distribution which should be equal to the effective grain size determined by the thermal inertia-grain size relationship.

Compared to terrestrial dunefields, we would expect intracrater dunefields to have an effective particle size in the medium sand range (250 - 500μm, or 6.0 - 7.9 thermal inertia units) [13], or perhaps slightly larger [14]. The best IRTM data avialable for dunes is that of the large Hellespontus dunefields in the craters Kaiser, Rabe, and Proctor. The thermal inertias calculated for these are all ~8.0 (effective grain sizes ~ 550μm). The actual thermal inertias may be slightly less than 8.0, because the actual albedos for these dunes are closer to 0.13 rather than the standard 0.15 used to calculate thermal inertias from predawn data. Regardless of the actual albedo, it is clear that the thermal inertia of these dunes is consistent with an average particle size in the upper-medium or lower-coarse sand size range. Dunefields in the craters Wirtz (-48.5°, 25.6°) and Moreux (+42.1°, 315.5°) yield similar thermal inertias (8.4 and 8.3, respectively) and grain sizes.

Because the effective particle sizes indicated for the dunefields fall within a reasonable, expected range of grain sizes, we believe that the data for intracrater features that do not have visible duneforms also represent the actual effective particle sizes of those deposits. Figure 1 shows the range of thermal inertia values and effective grain sizes for 133 dark intracrater features in 11 geographic regions. The figure shows that there is a different mean thermal inertia for each region, each with a narrow range of variation in thermal inertia among individual dark features within the regions. The regions are identified on the basis of

overall regional albedo patterns [15] and the observed clustering of dark intracrater thermal inertia values reported here. The overall mean thermal inertia is about 8.4 (coarse sand, ~0.65 mm). The finest-grained intracrater deposits occur in Northern Arabia (NA), where the mean thermal inertia is 3.7 (very fine sand, ~0.07 mm), while the coarsest deposits occur in the Margaritifer Sinus (MS) region, where the mean is 13.7 (granules, ~ 2.5 mm). Many of the dark features are apparently composed of sand-sized particles, and might show duneforms when photographed at higher resolutions (most were photographed at resolutions > 150 m/pixel). Some of the deposits with high thermal inertias may be regions where there are barchan dunes with coarser interdune deposits; this is apparently the case for some of the dark deposits in the Oxia Palus region, where barchan dunes are seen in photographs with resolutions of less than 40 m/pixel.

Regions with the highest thermal inertia dark features correlate well with regions of high surface wind stress as predicted by the Mars General Circulation Model (GCM) [16, 17]. Greeley *et al.* (1989) [17] showed that there is a correlation between high surface wind stress and high rock abundance, suggesting that stronger winds remove fine particles from those regions [17, 18]. We speculate that the same may occur on the sandy, rock-free dark intracrater features. In regions where surface wind velocity is high, finer sands are winnowed out, leaving behind very coarse sand and granules. In Northern Arabia, where the dark features effectively consist of very fine sands, the regional winds are correspondingly low. Alternatives include the barchan dunes with coarse interdune explanation, and the possiblity that the coarser sands simply occur nearer to their source.

**REFERENCES:** [1] Arvidson, R.E. (1974) *Icarus, 21*, 12-27. [2] Cutts, J.A. and R.S.U. Smith (1973) *J. Geophys. Res., 78*, 4163-4196. [3] Breed, C.S. (1977) *Icarus, 30*, 326-340. [4] Peterfreund, A.R. (1981) *Icarus, 45*, 447-467. [5] Thomas, P. (1982) *J. Geophys. Res., 87*, 9999-10008. [6] Thomas, P. (1984) *Icarus, 57*, 205-227. [7] Sagan. C. *et al.* (1972) *Icarus, 17*, 346-372. [8] Sagan, C. *et al.* (1973) *J. Geophys. Res., 78*, 4163-4196. [9] Christensen, P.R. (1983) *Icarus, 56*, 496-518. [10] Edgett, K.S. and P.R. Christensen (1990) *Lunar Planet. Sci. XXI*, 313-314. [11] Kieffer, H.H. *et al.* (1973) *J. Geophys. Res., 78*, 4291-4312. [12] Kieffer, H.H. *et al.* (1977) *J. Geophys. Res., 82*, 4249-4292. [13] Ahlbrandt, T.S. (1979) *in* McKee, E.D. (ed), *A Study of Global Sand Seas, U.S.G.S. Prof. Paper 1052*, 21-51. [14] Greeley, R. and J.D. Iversen (1985) *Wind as a Geological Process on Earth, Mars, Venus, and Titan*, Cambridge Univ. Press, 333p (esp. see p. 70). [15] Pleskot, L.K. and E.D. Miner (1981) *Icarus, 45*, 179-201. [16] Pollack, J.B. *et al.* (1981) *J. Atmos. Sci., 38*, 3-29. [17] Greeley, R. *et al.* (1989) *Lunar Planet. Sci. XX*, 359-360. [18] Skypeck, A. (1989) *M.S. Thesis*, Arizona State Univ., Tempe, Arizona.

**FIGURE 1. Regional variation of intracrater dark feature thermal inertia.** The points show the average thermal inertia of dark intracrater deposits in each region shown on the map. The bars represent one standard deviation from the mean. Numbers to the right of the bars indicate the number of data points included in each region. Grain sizes are based on the standard Wentworth scale, the relationship between thermal inertia and grain size is best explained by Kieffer *et al* (1973) [11]. One region not depicted on the map, SP, includes dunes of the south polar region, between latitudes -65° and -75°, and longitudes 145° to 250°. There are a number of uncertainties in the south polar dunes data, and they may not be representative of the acutal thermal inertias.

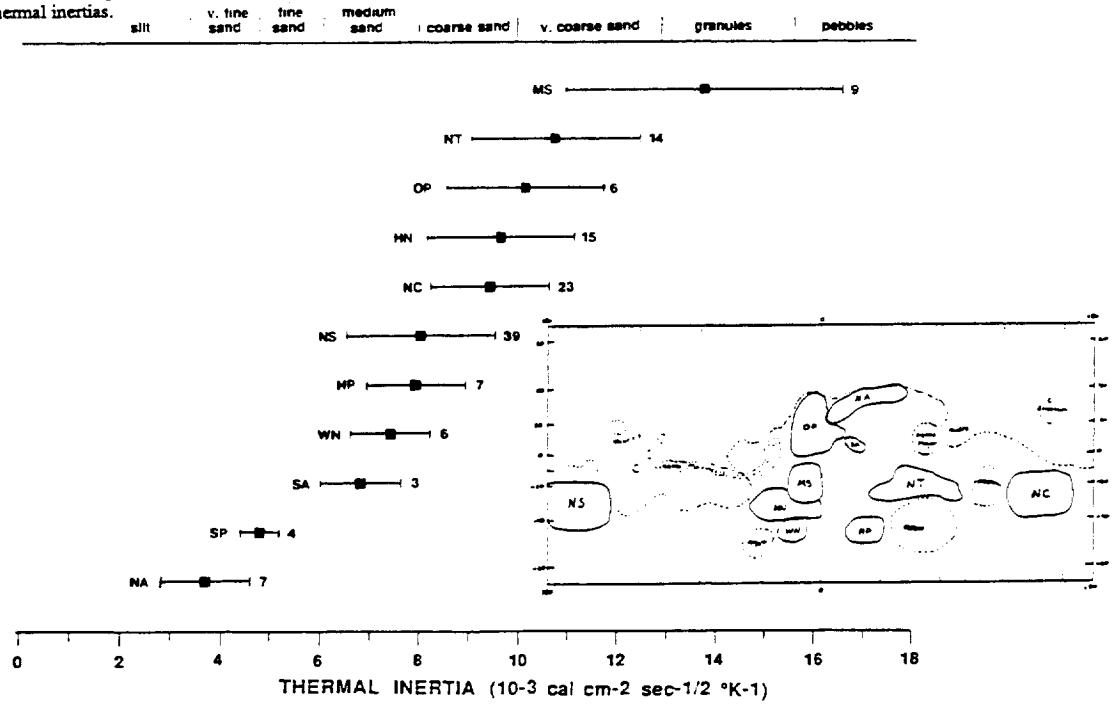

**THE ARSIA MONS-OTI FOSSAE THERMAL ANOMALY: A REGION WITH A HIGHER THERMAL INERTIA THAN THE REST OF THARSIS.** ***Kenneth S. Edgett,*** *Department of Geology, Arizona State University, Tempe, AZ 85287; and* ***James R. Zimbelman,*** *Center for Earth and Planetary Studies, National Air and Space Museum, Washington, DC 20560.*

Global mapping of the thermal properties of the martian surface have shown that the Tharsis region is largely covered by low thermal inertia materials; interpreted to be very fine (clay and silt-sized), unconsolidated particles which may occur in accumulations up to 2 meters thick [1-4]. Tharsis, Arabia, and Elysium are considered by Christensen [4] to be regions of net dust deposition following annual dust storms; and net dust transport is thought to switch from south->north to north->south approximately every million years.

Nearly the entire Tharsis region appears to have a covering of dust; this is seen even in the highest spatial resolution *Viking* thermal infrared data [5-7]. One area in Tharsis, located on the plains adjacent to the east-southeastern margin of Arsia Mons, has a consistently higher thermal inertia than the rest of Tharsis. This region, near the Oti Fossae fracture system, covers approximately 15,700 sq. km. The anomaly was first reported in an analysis of early data from the *Viking* Infrared Thermal Mapper (IRTM)[8], an infrared scanning radiometer sensitive to five mid-IR bands centered on 7, 9, 11, 15, and 20 μm plus a visible/near-IR band from 0.3 to 3.0 μm [9]. Kieffer *et al.* [8] reported that this region east of Arsia Mons is cool during the afternoon and warm in the nighttime. The thermal anomaly appeared in subsequent moderate resolution thermal maps [1,2,10], but none attempted to explain the feature. The Oti Fossae thermal anomaly also appears in high resolution (3-5 km) IRTM data [5] and in a high resolution (2-3 km) *Phobos 2* Thermoscan image obtained on 26 March 1989 [11,12]. It is clearly a surface phenomenon rather than an atmospheric anomaly.

Figure 1 is a sketch of the anomalous region. The shaded area corresponds to a region of slightly lower albedo than its surroundings. We were not able to obtain a reliable figure for the albedo, as daytime observations in the region are commonly hampered by clouds and haze. The contoured track in Fig. 1 is a high resolution map of thermal inertias (units x $10^{-3}$cal $cm^{-2}sec^{-1/2}K^{-1}$) calculated from predawn 20μm brightness temperatures measured by the *Viking 1* IRTM (orbit-sequences 461-5 and 500-1) during Southern Summer after the 1977 dust storm. The highest thermal inertias measured are around 8.0. Application of Christensen's [13,14] two-component block abundance model to the data gives a figure of ~ 0% blocks for all points in the high resolution sequences: on the anomaly, on the adjacent plains, and on the Arsia Mons shield.

*Viking* photographs (Table 1) of the anomalous region do not reveal anything unusual about the area. The region appears as a darker spot relative to its surroundings only in the *Viking* images 641A85, 52A07, and 52A09; the other images are hazy. The dark spot does not appear to be as dark as the upper slopes of Arsia Mons. It is

FIGURE 1: Sketch Of The Eastern Arsia Mons Thermal Anomaly

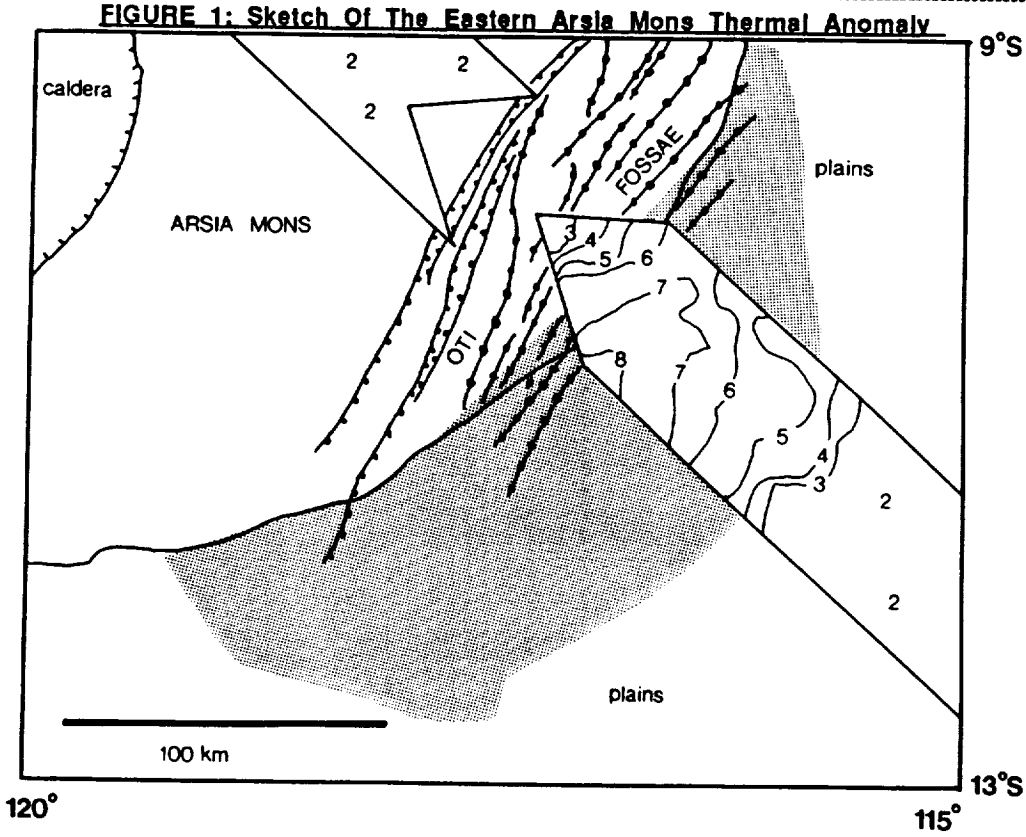

possible that dust in the atmosphere causes the apparent difference between the dark shield surface seen at high elevations relative to the more hazy, dark anomalous feature which occurs at a lower elevation. There are no *Mariner 9* B-frame images of this region.

Zimbelman [15] observed that the thermal properties of the Oti Fossae anomaly are similar to surfaces on Solis Planum to the southeast. Assuming a model where there is cyclic removal and deposition of dust on a scale of one million years [4], both the anomalous surface and the surfaces of Solis Planum could be made up of indurated soils from a previous climatic cycle. Zimbelman [15] suggested that the Oti Fossae anomaly is a "window" through the present dust cover. To test the "window" hypothesis and comparisons with Solis Planum, we chose two 0.1°x 0.1° latitude/longitude bins, each along the high resolution track in Fig. 1, and each with a thermal inertia of 7.9. One location is in the anomalous region centered at -10.8°,116.9°, the other on Solis Planum at -23.3°, 99.8°. We calculated emissivities for the 11 and 20 μm bands, assuming that the 7 μm brightness temperature closely approximates the surface kinetic temperature [13,16]. The 20 μm emissivities were both 0.94, while the 11 μm emissivities were different by 0.04 (0.93 and 0.97, respectively). This is not conclusive evidence that the surfaces at these two locations are made up of similar-composition materials, but neither does it weaken the proposed relationship.

There are three possible explanations for the Oti Fossae region thermal anomaly which are consistent with the observations. The area is definitely a region where there is no net dust deposition. It may be either an indurated soil (commonly termed "duricrust" in the literature [17,18]), a deposit of unconsolidated sand, or a surface where the dust cover is very thin, so that an underlying consolidated surface (bedrock or "crust") contributes to the thermal behavior of the region. Because the region appears somewhat darker than its surroundings, this would argue against the third hypothesis, since only a thin coating of dust is needed to change the surface albedo.

Under martian atmospheric pressure and temperature conditions, thermal inertia ($I = (kpc)^{1/2}$) is strongly dependent upon thermal conductivity (k) [19,20], and both are closely related to unconsolidated particle size [20]. The thermal inertias observed for the Oti Fossae anomaly (5.0 to 8.0) are consistent with a surface of unconsolidated sand. If the anomaly results from sand, it may be difficult to explain the zonation of thermal inertias (Fig. 1), indicating grain sizes increasing toward the center. A large field of sand would explain the presence of the anomaly in Tharsis; saltating grains can remove dust from sand sheets [21]. To determine if the anomalous region is a sand sheet will require images with very high resolution to search for duneforms.

A surface composed of partially cemented fine particles might also be consistent with the observed thermal inertias [*eg.* 22] and low block abundance. Variations in thermal inertia may occur for a constant particle size (*eg.* "dust") if the thermal conductivity can be increased by bonding the grains [*eg.* 18,23]. If the anomalous feature results from intergranular bonding of dust, the zonation of thermal inertias might result if either: (1) the feature results from wind stripping recently accumulated dust off the surface, where removal has been most complete toward the center, or (2) the zonation results from differing degrees of bonding between grains, suggesting that rather than a "window" to a past soil surface, the region could be undergoing cementation at the present. Testing the "duricrust" hypothesis might be more difficult than testing for sand, since it would likely require *in situ* observations for conclusive results. On the other hand, a lack of duneforms might be construed as further evidence for the crust hypothesis. The *Mars Observer* Thermal Emission Spectrometer should be able to detect the composition of the anomalous region, and could provide additional information about its surficial properties.

**TABLE 1: *Viking* Photographs Of The Anomalous Region**

| Frame | resolution (m/pixel) | Notes |
|---|---|---|
| 52A07,09 | 175 m/p | dark spot visible, despite some clouds |
| 210A47-50 | 89 m/p | hazy, spot not visible |
| 641A85 | 287 m/p | spot visible as mapped in Fig. 1 |
| 42B30,46 | 140,170 m/p | hazy, spot not visible |

**Notes and References:** [1] Kieffer, H.H. *et al.* (1977) *J. Geophys. Res., 82,* 4249-4291. [2] Zimbelman, J.R. and H.H. Kieffer (1979) *J. Geophys. Res., 84,* 8239-8251. [3] Palluconi, F.D. and H.H. Kieffer (1981) *Icarus, 45,* 415-426. [4] Christensen, P.R. (1986) *J. Geophys. Res., 91,* 3533-3545. [5] Edgett, K. and J.R. Zimbelman (1986) *Papers Presented 2nd Ann. Summer Intern Conf., L.P.I.,* Houston, L.P.I. Contrib. 602, 9-11. [6] Zimbelman, J.R. (1986) *Trans. Am. Geophys. U. (EOS), 67,* 1074. [7] Zimbelman, J.R. *et al.* (1987) *Lunar Planet. Sci. XVIII,* 1128-1129. [8] Kieffer, H.H. *et al.* (1976) *Science, 194,* 1346-1351. [9] Chase, S.C. *et al.* (1978) *Appl. Opt., 17,* 1243-1251. [10] Christensen, P.R. and M.C. Malin (1989) in (M. Zuber *et al.*, eds.) *Planetary Geosciences-1988, NASA SP- 498,* 6-7. [11] Crumpler, L.S. *et al.* (1990) In *Abs. Pres. to MEVTV Workshop on the Evolution of Magma Bodies on Mars,* San Diego, CA, p. 16-17. [12] Selivanov, A.S. *et al.* (1989) "Phobos Shadow On Surface of Mars," *Papers Presented to the Phobos 2 Conference, Paris* . [13] Christensen, P.R. (1982) *J. Geophys. Res., 87,* 9985-9998. [14] Christensen, P.R. (1986) *Icarus, 68,* 217-238.[15] Zimbelman, J.R. (1984) PhD Diss., Arizona State Univ., Tempe, AZ, see p. 232 (reprinted in *Adv. Planet. Geol., NASA TM-88784* (1986), see p. 516). 16] Christensen, P.R. (1984) *Lunar Planet. Sci. XV,* 150-151. [17] Ditteon, R. (1982) *J. Geophys. Res., 87,* 10197-10214.. [18] Jakosky, B.M. and P.R. Christensen (1986) *J. Geophys. Res., 91,* 3547-3559 [19] Neugebauer, G. *et al.* (1971) *Astron. J., 76,* 719-728. [20] Kieffer, H.H. *et al.* (1973) *J. Geophys. Res., 78,* 4291-4312. [21] Sagan, C. and J.B. Pollack (1969) *Nature, 223,* 791-794. [22] Presley, M.A. and R.E. Arvidson (1988) *Icarus, 75,* 499-517. [23] Kieffer, H.H. (1976) *Science, 194,* 1344-1346.

**PHOTOMETRIC TECHNIQUES FOR LANDER SITE CERTIFICATION.** Nicholas D. Efford, IEBS, Environmental Science Division, University of Lancaster, Lancaster LA1 4YQ, U.K.

In view of the need to safeguard wideranging scientific objectives and a considerable investment of human effort and funding, the certification of an acceptable landing site is of paramount importance in any spacecraft mission involving the deployment of an unmanned lander probe. In the case of Viking, boulders greater than 0.22 m in size represented potentially fatal hazards, yet features smaller than roughly 100 m across could not be recognised in the images used for site certification [1]. As even a cursory examination of the Viking Lander images will illustrate, the techniques employed to circumvent this problem, namely the extrapolation of visible detail down through more than two orders of magnitude coupled with the utilisation of Earth-based radar roughness measurements [2], are of limited value; the assumptions inherent in the former may be unjustified, whilst the latter suffers from poor spatial resolution and ambiguities in interpretation, in that, for example, the penetrating character of electromagnetic radiation may result in the detection of sub-surface roughness not necessarily indicative of unduly hazardous surface topography. Site reconnaissance at extremely high (i.e. 1 m pixel$^{-1}$ or better) resolution, such as that recommended for future Mars missions [3], is a direct yet in many ways impractical solution, given optical system design technicalities and the number of images that must be acquired to adequately cover the areas targetted by landing ellipses. There is thus a need for economical methods of hazard detection that operate at sub-pixel scales and make use of existing, commonly-employed spacecraft instrumentation, such as the imaging system itself.

**Pixel-Scale Feature Detection.** Positive-relief features on a flat plane will in general have a bright sunward-facing side abutting a darker side, which is tilted away from the Sun and possibly in shadow, given a sufficiently high incidence angle. The net effect on pixel reflectance will be minimised if the bright and dark sides of the feature are wholly contained within the projected area of a single pixel. It is statistically likely, however, that some objects will be favourably positioned so as to produce a detectable signature in the image, namely one or more anomalously bright pixels immediately adjacent to one or more anomalously dark pixels. This signature has been identified in a small subregion of a Viking Orbiter frame containing the site of the Mutch Memorial Station, and has been interpreted as signifying the presence of a boulder roughly 10 m across [4].

To determine the limits of detectability for such anomalies, a digital terrain model (DTM) was constructed by the emplacement of randomly-located obstacles, each of uniform size with a parabolic or conic cross-section. An initial synthetic image was generated from the DTM under near-optimum conditions of viewing and illumination (zero emergence angle $e$ and moderate-to-high incidence angle $i$) by the method described in [5], and this was artificially degraded by the enlargement of pixel size to produce images with a range of spatial resolutions. Figure 1 plots the standard deviation of imaging pixel DN against image resolution for a DTM populated by 40 cones with base radii of 1.5 m and heights of 2 m. A Lommel-Seeliger surface scattering law with $i = 60°$ was assumed. The horizontal dashed lines indicate points at which the anomaly becomes statistically insignificant, for a given error in pixel DN. Clearly, if unrealistically-extreme aspect ratios are ignored, this technique is of little use for obstacles smaller by a factor of two or more than the size of an imaging pixel.

**Sub-pixel Scale Feature Detection.** Given suitable images of the potential landing site obtained under a variety of viewing and illumination conditions, it is possible to fit Hapke's bidirectional reflectance equation [6] to photometric measurements in order to derive an estimate of $\bar{\theta}$, a parameter generally corresponding to the mean slope angle of unresolved surface roughness. The principal requirement is the availability of high phase angle data, and since survey images are likely to be acquired at or near $e = 0°$, this translates in practice to the requirement that the maximum value of $i$ is large. Under such conditions, the presence of unresolved shadows will darken a pixel in a manner quantified by $\bar{\theta}$. The relationship between this parameter and the probability of a successful landing was investigated by using the previously-described synthetic topography and modelling the photometric properties of surface material with Hapke's equation, setting $\bar{\theta} = 0°$ and the remaining parameters to arbitrary values. Average DTM reflectance was computed for a range of incidence angles, and the resulting data were used to solve for $\bar{\theta}$ only, as described in [5].

Figure 2 plots $\bar{\theta}$ against both the population of hazardous obstacles, $n$, and the probability of success, $P_{succ}$, the latter being determined for features with a circular base of radius $r$ in a square pixel of size $x$ by the equation $P_{succ} = 1 - (n\pi r^2/x^2)$. Here, $r = 1.5$ m and $x = 50$ m. A clear relationship between $\bar{\theta}$ and $P_{succ}$ exists, but an observed photometric roughness of 15° may imply probabilities of either 96% or 84%, depending on the height of the obstacles. The usefulness of this technique will therefore be somewhat limited without contraints on the morphology and size distribution of obstacles at the proposed site. In the case of Mars, it might be possible (though not necessarily appropriate) to derive these constraints from Viking Lander images. More practical limitations result from the accuracy with which $\bar{\theta}$ can be estimated from inevitably sparse orbital imaging data; restricted phase angle coverage or the assumption of incorrect Hapke parameters in constrained fits of $\bar{\theta}$ can have a serious effect [7]. Recent photometric studies of dust deposits in the vicinity of the Mutch Memorial Station [8] provide Hapke parameter estimates that might be applicable in those cases where it proves necessary to assume values for all parameters other than $\bar{\theta}$, though further careful investigation of the photometric properties of martian terrain is evidently required.

In conclusion, neither technique can be expected to provide accurate quantitative estimates of landing success probabilities, given the large number of potential sources of error that exist. However, it is envisaged that both could usefully supplement existing methods; the cumulative application of a wide range of techniques can only improve the reliability of the certification procedure and hence the likelihood of a successful landing on Mars, or for that matter, other bodies in the solar system.

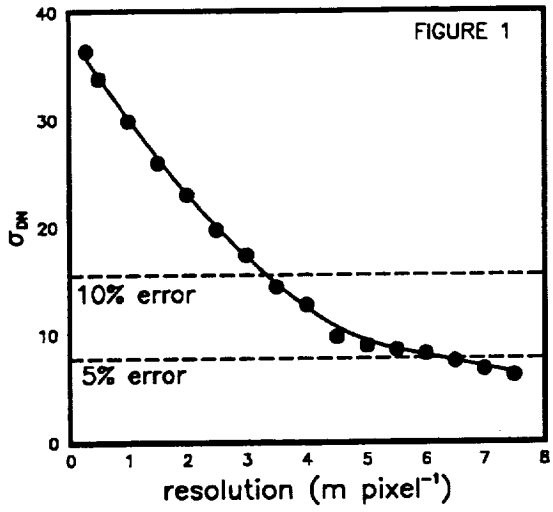


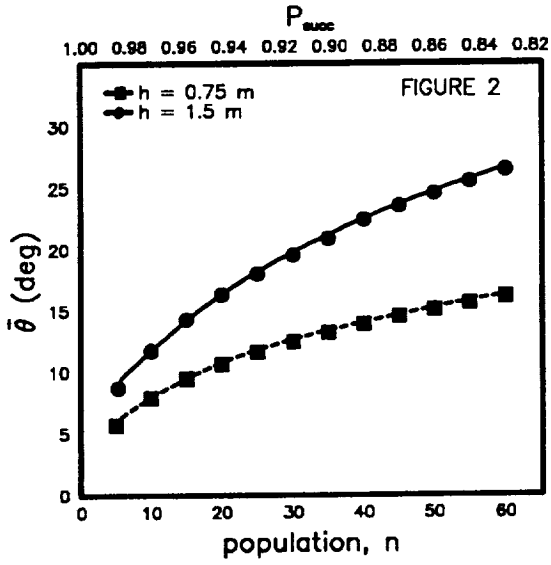


**Acknowledgements:** The author was supported during the course of this work by a SERC research studentship.

**REFERENCES:** [1] Soffen, G.A. *et al.* (1977) *J. geophys. Res.* **82**, 3959–3970. [2] Masursky, H. & N.L. Crabhill (1976) *Science* **193**, 809–811. [3] Henderson, B.W. (1989) *Aviation Week & Space Technology* **131**, no. 5, 85–94. [4] Wilson, L. *et al.* (1984) *Lunar Planet. Sci.* **XV**, 920–921. [5] Helfenstein, P. (1987) *Icarus* **73**, 462–481. [6] Hapke, B. (1984) *Icarus* **59**, 41–59. [7] Efford, N.D. (1989) Ph.D. thesis, in preparation. [8] Arvidson, R.E. *et al.* (1989) *J. geophys. Res.* **94**, 1573–1587.

# DETERMINATION OF SPECTRAL UNITS IN THE SYRTIS MAJOR-ISIDIS PLANITIA REGION FROM PHOBOS/ISM OBSERVATIONS;

S. Erard[1], J-P. Bibring[1], J. F. Mustard[4], Y. Langevin[1], M. Combes[2], J.W. Head[4], S. Hurtrez[3], C. Sotin[3].
[1]Institut d'Astrophysique Spatial, Orsay, 91406, France; [2]Departement de recherches spatiales, Observatoire de Paris-Meudon, France; [3]Laboratoire de Géophysique, Université de Paris-Sud, Orsay, 91405, France; [4]Department of Geological Science, Brown University, Providence, R.I.

**Introduction:** On March 1st 1989, the ISM spectrometer on the Phobos 2 probe observed the Syrtis-Isidis domain. This window contains very different units including Isidis Planitia, its heavily cratered rim, and the dark Syrtis Major shield. It provides an opportunity to observe the crustal dichotomy in the eastern hemisphere. The domain lies between longitudes 240°W and 310°W, and latitudes 2°N and 9°N (Fig. 1). The image is made of 25 x 120 pixels (3000 x 450 km$^2$), each one (20 x 20 km$^2$) being a set of 128 spectral measurements ranging from 0.76 to 3.16 μm (1).
Data correction process is the following : 1) Dark current substraction, 2) Detector temperature correction, 3) Gain correction, 4) Spectral orders overlap removal, 5) Division by the transfert function, and 6) Division by a solar spectrum, taking into account the Sun-Mars distance at this date. Some instrumental effects remain, weak enough to allow mineralogic identifications (2,6).

**First results :** Three simple criteria bearing the most part of the spectral variance were used for quick-look analysis (3). Brightness (Fig. 2) accounts for more than 80% of this variance, the instrument having observed two very different types of terrains. In particular, Syrtis Major is known to be one of the darker parts of Mars. Brightness (Fig. 2) ranges from 0.1 to 0.35, varying by a factor of three between Isidis and Syrtis. In this case, the brightness is very close to albedo, slopes being relatively weak. Hydration was estimated by using the depth of the 2.9 μm $H_2O$ absorption band. The spatial distribution is close to that of the brightness, opposing mainly a very dry Syrtis (25% absorption) to a very hydrated Isidis (40% absorption). Reddening (ratio of intensities at 2.39 μm and 1.79 μm) has a similar spatial distribution. It also exhibits a second order discrepancy within Syrtis. The general slope in the spectra is partly due to atmospheric dust.

**Methods used to determine the spectral units :** In order to use the total spectral information, four principal component analysis (PCA) have ben carried out, one for each set of 32 channels (odd and even, first and second orders). This allows us to avoid major discrepancies in viewing directions. Rough atmospheric corrections are performed with a simple atmospheric spectrum from the Pavonis high resolution track combined with a linear model and based on the strengh of the $CO_2$ 2 μm absorption band (4). Since brightness variation is the major information, each quarter-spectrum has been divided by its own mean value in order to see second order features that define five main units (Fig. 3). Another method has been used to define the different spectral units. Two reference spectra are chosen respectively in the darkest area (Syrtis) and in the brightest area (Isidis). The location of the reference spectra is taken in a homogeneous domain. For each pixel, the spectrum is fit as a linear combination of the two reference spectra. For each pixel, the variance between the theoretical spectrum and the observed spectrum is determined. The spatial distribution of both brigthness and residual variance allows the definition of five units as those defined with the previously described method.

**Results:** Results obtained with the odd and even channels are very consistent : a strong contrast between hydration and a broad absorption band centered at 2.3 μm, attributed to high-Ca pyroxenes; another contrast in the second order between two silicate bands centered around 0.9 and 1.1 μm. Five domains can be defined, which are spatially consistent with observation of images of the surface of Mars. Isidis Planitia (domain 1) bright and hydrated with poor mineralogic features, except an absorption band at 0.9 μm, seems to be covered with a thick dust layer. A smooth plain in the SE, crossing the heavily cratered rim in a NW-SE direction, exhibits similar features. The cratered rim of Isidis in the South (domain 2) and Arabia (domain 3) in the NW corner are a little drier, and exhibit a weak absorption band at 2.3 μm. The Syrtis Major region seems to be free from dust, much darker and drier, with strong absorption features corresponding to mafic minerals, in

particular around 1 μm. The Eastern part of Syrtis Major (domain 4) is bluer and drier than the Western part (domain 5). Also, the shape and position of the 1 μm band are different between these two domains within Syrtis. Differences in slopes is partly due to surface materials, since albedo is about the same, and possibly related to a thin weathered coating (6). In Syrtis Major, several smaller spatial features of particularly interest are observed near the region's topographic crest. Further interpretation of ISM spectra in terms of mineralogy within each of the previously defined units is done in the companion paper (5). A more detailed study on this region and the Valles Marineris domain was carried through (6).

***References*** : (1)Bibring et al., *Nature 341, 6242,591-592*, 1989 (2)Bibring et al., *Lunar Planet. XXI*, 1990 (3)Erard et al., *DPS*, 1989 (4)Bibring et al., *Proceedings of Lunar Planet. XX*, 1990 (5)Mustard et al., this volume, 1990 (6)Erard et al., submitted to *Proceedings of Lunar Planet. XXI*, 1991.

Figure 1. Map of depth of $CO_2$ 2 μm absoption band correlated with topography, and location of the window.
Figure 2. Brightness, computed as a geometrical mean of intensities at 0.99, 1.07, 1.10 μm
Figure 3. Detailed synthetic map with the five spectral units determined from multifactorial analysis. Some sub-units are delimited, with the shading of the principal unit.

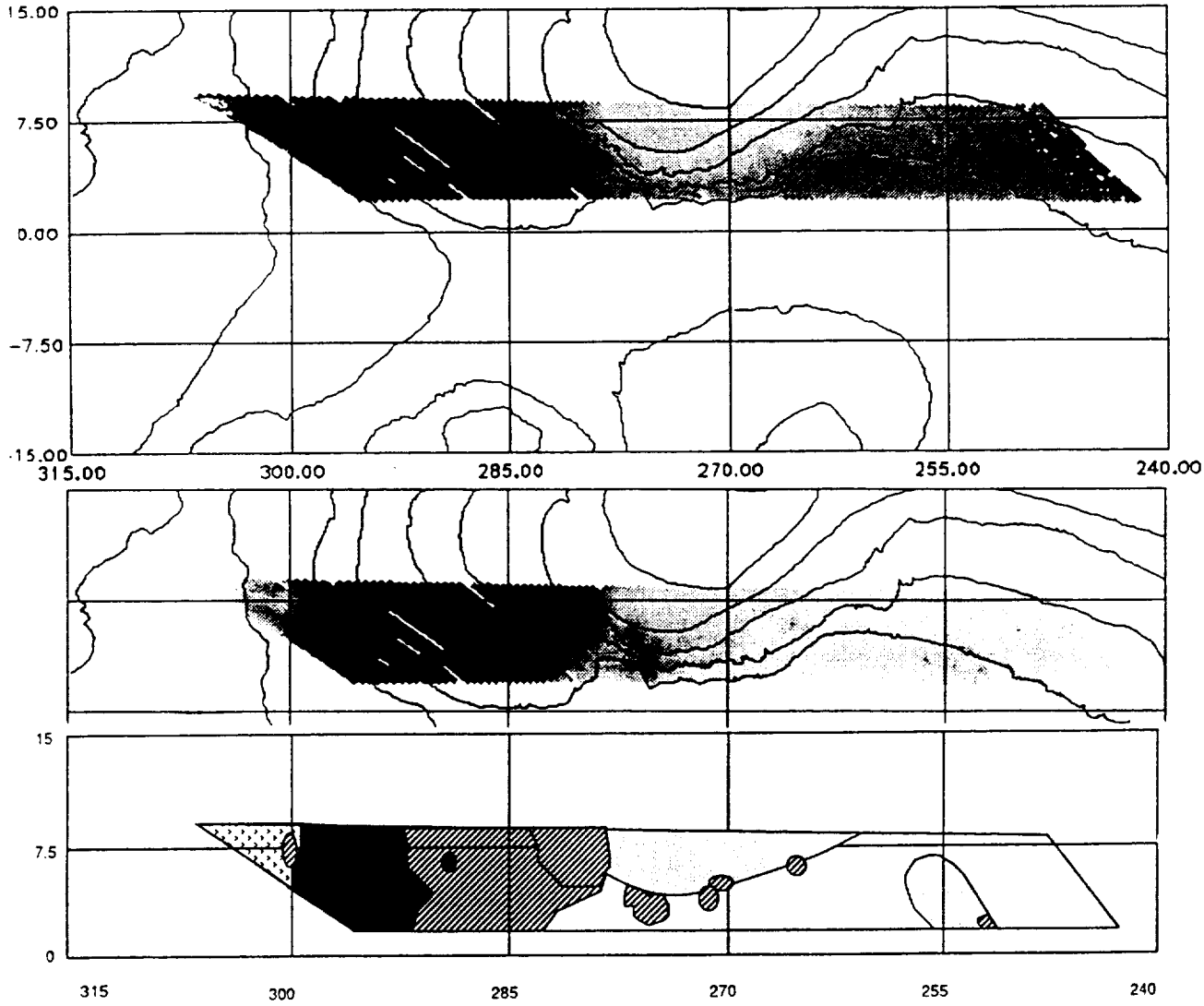

**HEAT FLOW vs. ATMOSPHERIC GREENHOUSE on EARLY MARS.** Fraser P. Fanale and Susan E. Postawko, Planetary Geosciences Div., Univ. of Hawaii, 2525 Correa Rd., Honolulu, HI 96822

Long term climate change on Mars is suggested by an apparent difference in the erosional style exhibited by the ancient cratered terrain as opposed to terrain of later origin. In particular, the morphology and distribution of valley networks on Mars clearly indicates a difference in erosional style ~3.8 billion years ago versus mid-to-late martian history. Liquid water was certainly involved in network formation, although sapping processes rather than rainfall seem indicated. Two major factors could have contributed toward making early conditions more favorable to formation of valley networks:

First, it has been argued (1) that higher internal regolith temperatures, associated with a much higher heat flow 3.8 AE, would cause groundwater to be closer to the surface then than at present. Higher heat flows are expected early in Mars' history primarily because of dissipation of the original heat of formation, although a higher rate of production of radiogenic heat is also a factor.

Second, if enough $CO_2$ is in the atmosphere, surface temperatures could be raised, due to an increased atmospheric greenhouse effect, to near the freezing point of water despite a weak early sun - at least at the equator and for the most favorable part of the orbital and axial cycle. Current greenhouse models indicate that $CO_2$ surface pressures of between about 0.75 and 5 bars are needed to raise the surface temperature on early Mars to the freezing point of water. Only slightly lower pressures characterize greenhouse warmings that are 10 to 20° K cooler.

In fact, the effectiveness of both these mechanisms is dependent on a high early heat flow: In the case of the atmospheric greenhouse, this is because the atmospheric mean residence time (M.R.T.) of $CO_2$ in the presence of fluvial activity is believed to be much shorter than the span of time over which network formation occurred. Thus, the atmospheric $P_{CO2}$ would have been dependent almost exclusively on the recycling time for regolith carbonate rather than the instantaneous supply of juvenile $CO_2$. Both of these parameters can be quantitatively related to the heat flow. The depth to the water table, $\Delta Z_{273}$, also depends on internal regolith temperatures. For a given regolith conductivity, k, the temperature at any depth is determined by the heat flow, which determines the gradient, $\partial T/\partial Z$, and the surface temperature, $T_S$.

We have derived a quantitative relationship between the effectiveness of an atmospheric greenhouse and internal heat flow in producing the morphological differences between early and later martian terrains. Our derivation is based on relationships previously derived by other researchers (2). Thus, while the validity of our derivation is dependent on the validity of these previously derived relationships, no new assumptions or mathematical relationships are necessary - merely algebraic manipulation of relationships already in the literature.

Our reasoning may be stated as follows: The CO2 mean residence time in the martian atmosphere, although not well known, is almost certainly much shorter than the total time span over which early climate differences are thought to have been sustained . Therefore recycling of previously degassed CO2 quickly becomes more important than ongoing supply of juvenile CO2 . If so, then the atmospheric CO2 pressure - and therefore the surface temperature - may be approximated mathematically as a function of the total degassed CO2 in the atmosphere plus buried material and the ratio of the atmospheric and regolith mean residence times. The latter ratio can also be quantitatively expressed as a function of heat flow . Hence, it follows that the surface temperature may be expressed (given assumptions as to regolith conductivity) as a function of heat flow and the total amount of "available" $CO_2$. However, the depth to the water table - again assuming the same regolith conductivity - can simultaneously be expressed as a function of heat flow and the surface temperature (the boundary condition). Therefore, for any given values of total available $CO_2$ and regolith conductivity, there exist coupled independent equations which relate heat flow, surface temperature and the depth to the water table. This means that we can now derive <u>simultaneous</u> values of surface temperature and the depth to the water table for <u>any</u> value of the heat flow. We utilize the derived relationship for two purposes: 1) To evaluate the <u>relative</u> importance of the atmospheric greenhouse effect and the internal regolith thermal gradient in producing morphological changes for <u>any</u> value of the heat flow and

2) to assess the absolute importance of each for values of the heat flow which are thought to be reasonable on independent geophysical grounds.

Figure 1 illustrates that for a given amount of total available $CO_2$, regolith conductivity and atmospheric M.R.T., the relative roles of internal heat flow and atmospheric greenhouse are inextricably interlocked. Figs. 1a and 1b are for a case of a cool early sun, favorable orbital situation, and an equatorial site (after ref. 2). The mean residence time of atmospheric $CO_2$, and regolith conductivity are the same in both figures. The figures show surface temperature ($T_S$) as a function of depth to the water table (z). The numbers in parentheses indicate heat flow in mW $m^{-2}$.

In Figure 1a, total $CO_2$ = 3.5 bars. Note that the internal heat flow predicted by (1) for ~3.8 AE ago, that is ~150 mW $m^{-2}$, is more than sufficient to recycle enough $CO_2$ to keep surface temperature at the freezing point because we have assumed so much total $CO_2$. In this case, the surface greenhouse effect plays a dominant role. However, if one considers that a water table depth of < 350 m is sufficient to permit widespread sapping, it is clear that the internal thermal gradient also plays a major role in widening the latitudes and time bands in which sapping would be prevalent. Thus this case is not very different either in assumptions or result from those discussed by (2).

In Figure 1b total $CO_2$ is only one bar. This case is important because in many plausible versions of the early Mars volatile inventory it is entirely possible that the total available CO2 at 3.8 AE might have been only a bar, or even less. In this case we find that the atmospheric greenhouse effect plays almost no role because the low total $CO_2$ abundance requires incredibly fast recycling in order to keep any significant abundance in the atmosphere. Thus for plausible values of earlier heat flow, the surface temperature changes by only a few degrees. On the other hand, the early heat flow produces an enormous direct effect on the depth to the 273K isotherm despite the near constancy of surface temperature; at Q = 30 mW $m^{-2}$ the depth is over a km, but at Q = 100 mW $m^{-2}$ it is less than 300 m and near the critical depth suggested by (1).

All these calculations are sensitive to the values chosen for the (unknown) regolith conductivity, the $CO_2$ atmospheric mean residence time, and especially total $CO_2$ inventory assumed. Thus it is important to explore the sensitivity of the conclusions to the values chosen. Although our exploration of the parametric space has been limited, the qualitative characteristics of the system are apparent.

We find that if the total available $CO_2$ has always been ~4 bars or more, then the atmospheric greenhouse effect can easily account for the change in erosional style, and the primary role of the heat flow is to raise ground water temperatures. This result is in keeping with the earlier results of (2). On the other hand, if the total $CO_2$ were only ~1 bar, the atmospheric greenhouse effect does not raise the surface temperature by more than a few degrees, but for plausible values of regolith conductivity the change in internal gradient accompanying higher early heat flow can still easily decrease the water table depth by a large factor, from well over a kilometer to less than 350 m, enabling network formation at 3.8 AE.

**REFERENCES:** (1) Squyres, 1989. Fourth International Conf. on Mars, Tucson, AZ. (2) Pollack et al., 1987. Icarus *71*, 203-224. (3) Schubert et al., 1979. Icarus *38*, 192-211.

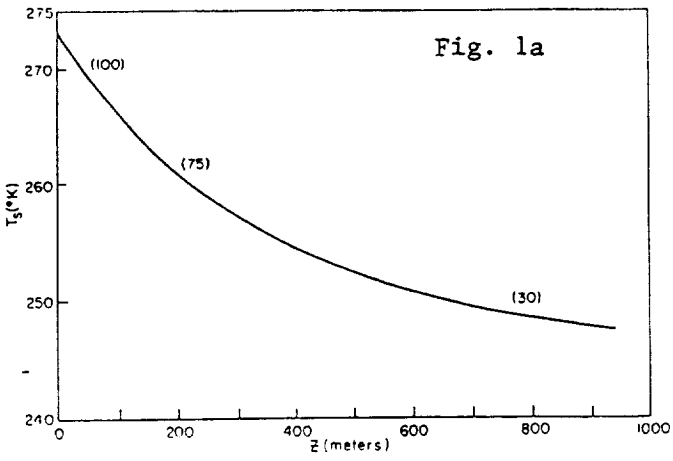


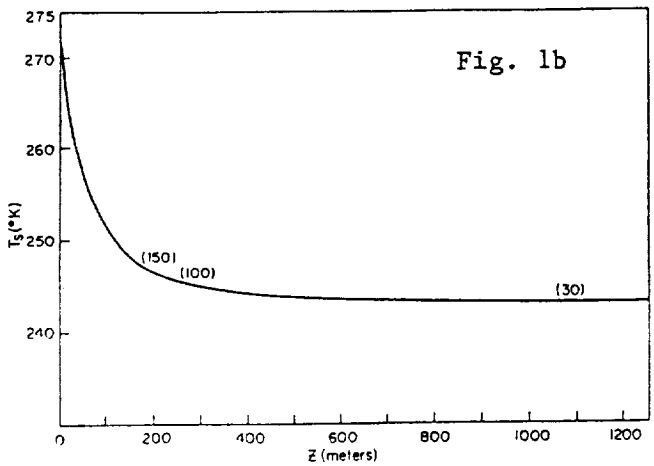

# ANALYSIS OF POORLY CRYSTALLINE CLAY MINERALOGY: NEAR INFRARED SPECTROMETRY *VERSUS* X-RAY DIFFRACTION

William H. Farrand and Robert B. Singer, Planetary Image Research Laboratory, University of Arizona, Tucson, AZ 85721

Clay minerals are arguably the most abundant group of minerals at the Earth's surface, occurring in hydrothermal alteration zones and a host of sedimentary environments. On Mars, the existence of clay minerals has been hotly debated; their existence or absence has important implications for the type of surface processes which have acted through that planet's history and should provide clues to past climate. Given the importance of clay minerals, it is important to know the capabilities and limitations of various analytic methods that can detect and identity clay minerals. This study makes some direct comparisons between two such laboratory analytic methods, X-ray diffraction (XRD) and near infrared (NIR) reflectance spectrometry.

Before the advent of XRD demonstrated the existance of crystalline structure in clays minerals, they were regarded as being composed of amorphous phases [1]. XRD studies showed that any given clay specimen can be thought of as lying somewhere on a continuum between a highly-crystalline end member and an amorphous endmember. Some of the debate about the existence of "clays" vs. "palagonites" on Mars is semantic, since for different researchers these names imply different regions of this continuum. Nevertheless, the degree of crystallinity of a clay is closely related to its formation conditions, information which we very much wish to decipher.

The data for the comparison of techniques presented here are from an ongoing study of basaltic hydrovolcanism on Earth, with applications to Mars. Hydrovolcanism, the explosive interaction of magma with surface or near surface water [2], commonly produces tuff rings and tuff cones when the magma is basaltic in composition. The alteration product of basaltic glass (sideromelane) is termed palagonite, and a tuff in which the sideromelane has been largely altered to palagonite is called a palagonite tuff. The clay size-fraction (< 2 $\mu$m) of such tuffs has, at best, only poorly crystalline clays, and therefore lies toward the "amorphous" end of the continuum discussed above.

For this study, samples from two tuff rings and one tuff cone were analyzed. The tuff rings were Ubehebe Crater, CA and Zuni Salt Lake, NM; the tuff cone was Pavant Butte, UT. The reflectance of ten to twenty powdered samples (grain size < 500 $\mu$m) from each area were analyzed in the 0.3 to 2.7-$\mu$m wavelength range at RELAB [3]. Most of the highly palagonitized tuff cone sample spectra display a 2.3-$\mu$m absorption feature; a typical Pavant Butte palagonite tuff spectrum is shown in Figure 1. The 2.3-$\mu$m feature in these samples is due to a combination of the O-H stretch and Mg-OH lattice modes [4], and is characteristic of trioctahedral Mg-bearing clay minerals. In contrast, several of the less-palagonitized tuff ring sample spectra had 2.2 $\mu$m absorption features. This indicates the presence of Al-OH bonds and is diagnostic of Al-bearing dioctahedral clay minerals. A typical tuff spectrum from the Zuni Salt Lake tuff ring is also shown in Figure 1. Note that, independent of the difference in cation between these two samples, the more heavily altered (palagonitized) tuff cone material has a much deeper band.

It should be noted that our emphasis is on the 2.2- and 2.3-$\mu$m features. These overtones are weaker than the $\nu_{OH}$ stretching fundamental at 2.75$\mu$m and weaker even than the $2\nu_{OH}$ primary overtone at 1.38$\mu$m. However, both of the latter features are obscured by atmospheric water vapor and/or other gases in most remote sensing studies. Consequently, the 2.2- and 2.3-$\mu$m features take on a practical significance belied by their relatively shallow band depth. Details in these relatively weak features have also proven to be very diagnostic of mineralogy.

XRD analyses were performed on our samples that showed the strongest 2.2- and 2.3-$\mu$m features. XRD analyses of the initial bulk samples produced no peaks characteristic of Al-bearing clay minerals. However, the Pavant Butte samples did give a 7 Å peak that is

tentatively assigned to antigorite. The bulk samples were then broken down to sand, silt and clay sized fractions and subjected to XRD analysis in the manner of Starkey et al. [5]. Only in the clay-sized fraction of two of the three tuff-ring samples did even a weak peak in the vicinity of 15 Å appear. This is interpreted as evidence of a smectite and/or mixed layer smectite-illite.

These results demonstrate something that many planetary spectroscopists have noticed for years: reflectance spectrometry is generally a more sensitive indicator of fine-grained and/or poorly crystalline clay-type mineralogy than is the more mature technique of XRD. NIR spectrometry can detect crystalline clays even in bulk samples of poorly crystalline materials. To attempt to detect those minerals with XRD analysis requires time consuming size separation procedures. In fairness, it should also be noted that in one of the Pavant Butte samples, a 15 Å peak indicated the presence of clay minerals whereas the NIR spectrum of that same sample showed no 2.2- or 2.3-$\mu$m band. That particular sample had a low reflectance and the lack of spectral features is attributed to masking by opaque minerals. Reflectance spectrometry is not an entirely mature technique, and more attention needs to be paid to issues such as the role that opaque minerals can play in masking diagnostic absorption features. Nevertheless reflectance spectometry should continue to receive serious consideration not only for laboratory use, but for possible in-situ instrumentation on future planetary rovers.

REFERENCES: [1] Eslinger, E. and Pevear, D. (1988) *SEPM Short Course Notes* **22.** [2] Sheridan, M.F. and Wohletz, K.H. (1983) *J. Volc. Geotherm. Res.*, **17**, 1-29. [3] Pieters, C.M. (1983) *J. Geophys. Res.*, **88**, 9534-9544. [4] Hunt, G.R. and Salisbury, J.W. (1970) *Modern Geology*, **1**, 283-300. [5] Starkey, H.C. et al. (1984) *USGS Bull. 1563.*

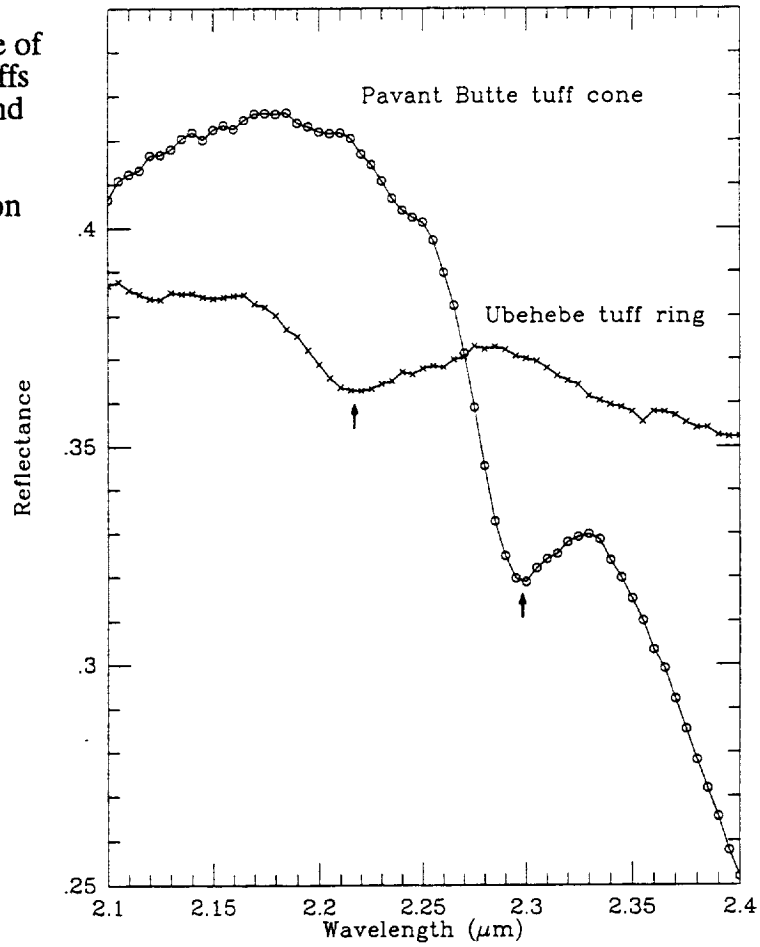


Figure 1. Near infrared reflectance of palagonitized basaltic tuffs from Ubehebe Crater and Pavant Butte. Arrows indicate the presence of 2.2 and 2.3 $\mu$m absorption features.

# THERMAL NEUTRON LEAKAGE FROM MARTIAN CARBONATES.*

**W.C. Feldman**, Los Alamos National Laboratory, MS D438, Los Alamos, New Mexico 87545, and **B.M. Jakosky**, University of Colorado, Laboratory for Atmospheric and Space Physics and Department of Geological Sciences, Boulder, Colorado 80309

Photographic mosaics of Mars have revealed outflow channels, valley networks, and patterned ground that have been interpreted (1,2) to indicate that liquid water once flowed on Mars. The extent of these features has led many researchers to speculate (3) that surface ponds of liquid water may have been stable in early martian history, implying a thicker atmosphere and a warmer climate then than is presently observed. In fact, climatic conditions may have been sufficiently clement over a time period long enough to have supported the development of life.

If this speculation is correct, then an initially thick, predominantly carbon dioxide martian atmosphere should have been gradually transformed to carbonate rocks as the planet cooled (4). Conversely, detection of sizable carbonate deposits near the surface of Mars implies a more clement early environment and provides a focus for a search for fossil remnants of primitive life. Carbonates such as calcite ($CaCO_3$), magnesite ($MgCO_3$), dolomite ($CaMg(CO_3)_2$), and siderite ($FeCO_3$) are expected to be most abundant based on the surface composition measured using Viking instrumentation (5). However, searches for such deposits using infrared reflectance spectra have not been successful (6). Although not encouraging, these results do not imply an absence of such deposits since they would not be visible if buried under a non carbonate aeolian blanket thicker than a few microns. Such an overburden is expected to result from observed recurrent, global dust storms.

Use of neutron and gamma-ray techniques to search for substantial carbonate deposits do not suffer the foregoing limitations since neutrons and gamma rays are more penetrating than infrared photons. It is therefore reasonable to ask whether such deposits have a neutron and gamma-ray signature sufficiently distinctive to allow a unique identification. This report presents results of an initial study confined to the neutron signature of a near-surface carbonate deposit.

A previous study has shown that large, thick deposits of pure calcite and magnesite do indeed generate energy spectra of escaping neutrons that are quite distinct from that generated by regolith having the composition of Chryse Fines with one weight percent of water (7). This type of soil will be referred to simply as regolith in the rest of this report. Specifically, thermal amplitudes of upward neutron currents are increased by factors of 2.8 and 12.2 for calcite and magnesite, respectively. The same study showed no such distinctive signature for siderite because of iron's high thermal-neutron-absorption cross section. However, "global" (radii $\gtrsim$ 1000 km), thick deposits of pure calcite and magnesite are not likely on Mars. We therefore investigated the persistence of measurably enhanced thermal neutron amplitudes for three likely surface configurations. The first corresponds to the burial of a thick, global carbonate deposit under a layer of regolith. The second configuration consists of a thick, global, uniform mixture of carbonate and regolith. Such a deposit could have formed through the gardening of initially stratified layers by meteoroid bombardment or by aeolian deposition and erosion over aeons. The third configuration consists of a circular, thick, pure carbonate deposit surrounded by regolith. This case corresponds to the presence of an ancient pond of standing water that has long since evaporated.

Simulations of leakage neutron energy spectra were made for each of the three carbonate rock types that have measurable thermal amplitude enhancements – magnesite, dolomite, and calcite. In all cases, a 16 g/cm$^2$ atmosphere of predominantly carbon dioxide was included. Resultant thermal and epithermal amplitudes were then sorted as a function of depth of regolith overburden, in g/cm$^2$, in the first configuration, and in terms of percent admixture of regolith into an initially pure carbonate deposit, in the second configuration. Estimates of the detectability of surficially confined deposits were made by calculating the count rate of a neutron sensor that is similar to the Mars Observer Gamma-

MARTIAN CARBONATES USING NEUTRONS
Feldman, W. C. and Jakosky, B. M.

Ray Spectrometer (GRS) anticoincidence shield. The calculations were done assuming the hypothetical neutron sensor is orbiting Mars at the altitude of the Mars Observer, 361 km, but oriented differently than that of the GRS anticoincidence shield, for reasons of simplicity. Here we choose a detector orientation that is pointing radially downward. For this last case, count rates were sorted in terms of the diameter of pure carbonate deposit embedded within a planet-wide regolith domain.

We report only the thermal amplitude results for the first two configurations because the entire differences in epithermal amplitudes calculated between carbonate and regolith deposits reflect the selective inclusion of one weight percent of water in the regolith. This difference therefore has no bearing on the presence or absence of carbonate. In contrast, the enhancement in thermal amplitude displayed by the carbonate deposits stem from the low-to-moderate thermal neutron absorption cross sections of carbon, oxygen, magnesium, and calcium, relative to those for chlorine, titanium and iron. These last three elements are significant constituents of martian regolith.

Plots of neutron thermal amplitude against regolith overburden and percent regolith admixture show that for both, a distinctive neutron signature is detectable for significant deviations from a pure, thick carbonate deposit. Choosing as our identification criterion, a value of thermal amplitude that is 50% higher than that for a globally thick regolith deposit, these calculations indicate that 1) magnesite can be detected even if buried to depths of 59 g/cm$^2$ below the surface or if mixed with as much as 55 mass percent of regolith, 2) dolomite can be detected if buried to depths of 53 g/cm$^2$ or mixed with as much as 46 mass percent of regolith, and 3) calcite can be detected if buried to depths of 44 g/cm$^2$ or mixed with as much as 38 weight percent of regolith. The same identification criterion also yields detection threshold deposit diameters of 240 km for magnesite, 440 km for dolomite and 650 km for calcite.

Although the results of the first two simulations demonstrate the promise of neutrons as a sensitive probe of extensive deposits of carbonate rocks on Mars, the third simulation shows that such a search from orbit will not likely succeed. Sufficiently large diameter deposits are simply not expected. However, this impediment is removed if a search can be conducted on or near the surface such as would be possible using a low-altitude balloon or a rover.

References.
(1) Carr, M.H., *The Surface of Mars*, Yale Univ. Press, New Haven, Conn., 1981.
(2) Squyres, S.W., *Annu. Rev. Earth Planet. Sci.* **12**, 83–106, 1984.
(3) Baker, V.R., *The Channels of Mars*, Univ. Texas Press, Austin, 1982.
(4) Kahn, R., *Icarus* **62**, 175–190, 1985.
(5) Clark, B.C., A.K. Baird, R.J. Weldon, D.M. Tsusaki, L.Schnabel, and M.P. Candelaria, *J. Geophys. Res.* **87**, 10059–10067, 1982.
(6) Singer, R.B., *Adv. Space Res.* **5**, 59–68, 1985.
(7) Feldman, W.C., W.V. Boynton, and D.M. Drake, in *Remote Geochemical Analysis: Elemental and Mineralogical Composition*, Pieters,C.M. and Englert,P.J., eds., LPI, Houston, in press, 1990.
* Work supported by NASA and done at Los Alamos under the auspices of the U.S. Department of Energy.

POLYPHASE NOACHIAN TECTONISM OF THE MEMNONIA/AEOLIS REGION; EVIDENCE FOR GREATER PRE-THARSIS LITHOSPHERIC MOBILITY OF MARS, Randall D. Forsythe, Dept. Geog. and Ear. Sci., UNCC, Charlotte, NC 28223 and Center for Earth and Planetary Studies, National Air and Space Museum, Smithsonian Institution, Washington D.C. 20560.

Contemporary summaries of planetary tectonics state there is no evidence of plate tectonics on Mars (1,2), no strike slip faults (3), and that a large percentage of the planets' tectonic features can be related in some fashion to the development of the Tharsis volcanic province (4,5). From this emerges the view of a Martian immobile lithosphere affected only by low strain contractional features, fractures, and graben systems. However, this view of Martian tectonics becomes much less tenable when consideration is given to a number of observations and inferences concerning Mars' ancient past(6).

Noachian lobate scarps and wrinkle ridges. The Noachian highlands of the Memnonian-Aeolis area contain an array of N to NNE trending lobate scarps that have been argued to pre-date Tharsis-centered tectonism, and which are geometrically incongruous with such an interpretation(6). More detailed mapping (7,8) using Viking imagery has confirmed that at least locally these tectonic features predate outflow channel development in Mangala Valles, and are cut by the Tharsis radial 'fracture' swarm. Kinematically, the lobate scarps have previously been interpreted as normal faults, related either to early thermal stresses(6) or to a major Noachian impact basin (8). Two observations, however, suggest that these scarps are contractional features. First, they are replaced by wrinkle ridge morphologies of similar trend where they intersect major basins, and secondly, there are abundant sharply defined linear NNW-NW and NE-NNE trending offsets of the lobate scarps and wrinkle ridges that are identical in appearance to the strike-slip faults documented in the Valles Marinaris region (9). The wrinkle ridges and inferred strike-slip faults argue for a contractional origin for the lobate scarps.

Transcurrent faults. Work in the western equatorial dichotomy boundary zone argued for the Gordii Dorsum escarpment to represent a lithospheric scale left-lateral transcurrent fault of Noachian age; perhaps indicating greater lithospheric mobility in the ancient past(10). Current analysis of the western equatorial zone has led to the discovery of an additional fault of a probable transcurrent character, here called the Apollinaris fault zone. The fault, like the Gordii Dorsum appears to have fine scale fault sculpture controlled by 2 sets of low angle oblique-trending secondary faults. Also apparent, are several oblique-trending bulges and ridges and an adjacent rhombic-shaped, and fault-limited, depression (rhomb graben?). Finally, adjacent to the rhomb 'graben' is a conspicuous array of regularly spaced assymetric warps that appear truncated and displaced in a left-lateral sense along the edges of the graben structure. The combined set of structures are restricted to what has previously been mapped as Amazonian age materials(11), but are alternatively interpreted as exhumed Noachian units(12). The combined set of structures, can be modelled an with an E-W oriented horizontal maximum compressive stress regime, with the Apollinaris fault zone (>300 km length) representing a major lithospheric-scale left-lateral shear zone like the Gordii Dorsum. Topographic profiles indicate that the NNW to NW trending transcurrent faults of this unique equatorial province (approx. 2500x500 km) parallel large scale trough/swell structures with wavelengths of 375 km and amplitudes between 1 and 3 km. To the west, south, and east highland materials in the immediate vicinity of the Apollinaris fault zone have lobate scarps and wrinkle ridges with 'strike-slip' faults of inferred left-lateral character sub-parallel to the Gordii Dorsum and Apollinaris fault zones.

Polyphase deformed Noachian 'Basement.' Finally, an analysis of the marginal Noachian zone to the south of the dichotomy boundary reveals a number of lines of evidence for erosional resurfacing of a previously deformed(polyphase) basement complex. Here erosional resurfacing in the intercrater plains has etched the surface traces of cross-cutting linear and curvi-linear penetrative fabrics. The fabrics (typically with NW and NE sets represented) have controlled crater basin shapes likely by a combination of primary syncratering excavation, the secondary post-excavation collapse of crater walls, and by later tertiary erosional processes. The fabrics have also controlled dendritic tributary systems within the Noachian intercrater plain areas, as well as the development of outflow channels near the dichotomy boundary. Large craters near the dichotomy boundary reveal internal walls with at least two orientations of fabrics that are seen penetrating at least to the base of crater walls with >1 km relief. Do the fabrics represent bedding, cleavages, or foliations? In one outflow channel (Viking 443S13) erosion reveals the edges of a series of resistant west dipping layers.

Viewed collectively the Noachian data set argues for at least two, if not three, phases of regional tectonism prior to Tharsis development. Penetrative fabrics and upturned layers, appear to be regionally present but largely masked by the highland 'regolith'. Where exposed, however, they provide tantalizing opportunities to gain a glimpse of what appears to be a very different, and more tectonically active phase of Mars' history. The N-S lobate scarps and NW trending transcurrent faults were superimposed on this polyphase deformed basement probably during the late Noachian. Preliminary analysis suggests E-W shortening strains >7.5 % that affected an area >3000 km x 1500 km. This appear larger than that inferred for the circum-Tharsis ridge structures(12) and may reflect a trend towards increasing stabilization (13).


Photomosaic of the Apollinaris Patera region (7S,187W; Approx. scale: 1cm=37 km) AP: Caldera wall of Apollinaris Patera, AF: Apollinaris fault zone (inferred left-lateral transcurrent fault), RG: rhomb 'graben', NAW: northern array of asymmetric 'warps' in the Medusa Fossa Fm., SAW: southern area of warps in the Medusa Fossa Fm., sf: NW-trending offsets of lobate scarps (small strike-slip faults).

REFERENCES (1) Basaltic Volcanism Study Project (1981) Volc. of the Terr. Planets (Pergamon, N.Y.) (2) Carr, M.H. et al. (1984) Geology of the Terrestrial Planets, NASA SP-469, 317 (3) Carr, M.H. (1981) The Surface of Mars, Yale Univ. Press, 232 (4) Wise, D.U., Golombek, M.P. & McGill, G.E. (1979) Icarus 38, 456-472 (5) Phillips, R.J. & Ivins, E.R. (1979) Phys. Earth planet. Inter. 19, 107-148 (6) Schultz, R.A. (1985) JGR 90, 7849-7860 (7) Craddock,R., Zimbelman, J.R., & Watters, T.R. (1989) LPI Tech. Rpt. 89-06, 18-20 (8) Craddock, R. & Zimbelman J.R. (this volume) (9) Schultz, R.A. (1989) Nature 341, 424-425 (10) Forsythe, R.D. & Zimbelman, J.R. (1988) Nature 336, 143-146 (10) Morris, E.C. & Dwornik, S.E. (1978) USGS Map I-1049 (11) Forsythe, R.D. & Zimbelman, J.R. (this volume) (12) Watters, T.R. (1988) JGR 93, 10236-10254.

A DISCUSSION OF MARS' WESTERN EQUATORIAL DICHOTOMY BOUNDARY ZONE; ENIGMAS, ANOMALIES AND CONTROVERSIES, Randall D. Forsythe, UNCC, Charlotte, NC 28223, and James R. Zimbelman, Center for Earth and Planetary Studies, National Air and Space Museum, Smithonian Institution Washington, D.C. 20560.

Mars' equatorial region from the western edge of the Tharsis volcanic province (approx. 135 Long.) west to Apollinaris Patera (approx. 186 Long.) is a transitional realm lying at elevations between 0 and 3000 meters that separates young, low lying, deposits of the northern hemispheres' plains, from high and old intensely cratered materials of the southern hemisphere (1). The region, which corresponds to the classical high albedo areas of Zephria and Mesogaea contains deposits of unusual morphologic, structural, and geophysical characteristics.

A morphologic enigma: Following Mariner 9 data analysis the unusual deposits of the area were characterized as rolling or undulating plains of 'layered' and/or lineated deposits that were suggested to be a succession of lava flows younger than the highlands to the south(2). Viking images permitted detailed mapping, defining a number of units within what has been called the Medusa Fossa Formation(3), and led to a suggestion that they may represent a unique sequence of ignimbrite and tuffaceous units(4,5). A recent interpretation, based on a comparison to layered deposits of similar morphological character surrounding Mars' residual ice caps has led to the suggestion that they may represent an eastward younging track of paleopole deposits, begging the corollary of Martian polar wander(6).

A structural anomaly: Maps of the Zephyria and Mesogaea region show a number of NW to NNW trending structural elements within the layered and lineated deposits that are defined as linear depressions, grabens, or scarps(3). One of these, the Gordii Dorsum, has been recently argued to represent a major left-lateral transcurrent shear zone within the Martian lithosphere(7). Our analysis of Viking imagery reveals similar secondary structures along an equally pronounced NW trending fault zone at the extreme western edge of the belt, that runs along the northern base of Apollinaris Patera. This zone is tracable for some 300 kilometers; diagonally cutting across the transitional province to NW where it disappears under undeformed cover of Elysium Planitia. The Gordii Dorsum and the Apollinaris fault bracket on the east and west sides, respectively, a province that stretches for a minimum 2300 kilometers and appear divisible into 5 to 7 major NW-NNW trending trough/swell couplets with an average wavelength of 375 km and amplitudes of 1 to 3 kilometers. From Gordii Dorsum in the east to Apollinaris Patera in the west there is also a gradual counterclockwise shift of 15 to 20 degrees from NNW to NW orientations, which is opposite that expected from Tharsis models.

An age paradox: While early mapping efforts mapped the transition or dichotomy boundary zone in this region as having materials of intermediate (Hesperian) ages(2), subsequent revisions reversed stratigraphic relations between deposits of this zone and the northern plains materials(3), making them Amazonian. The hypothesis of a layered track of paleopole deposits accepted Amazonian chronologies but argued for an east to west younging pattern(6). The structural arguments paradoxically contradict the relative ages suggested by crater statistics, and would require yet a third revision in the relative age of the province as a whole with respect to surrounding terranes. However, an analysis of crater statistics in the boundary zone to the west (8), as well as our analysis of crater statistics in the this transitional region indicated extensive resurfacing. Cumulative crater frequency v.s. log diameter curves for 200,000 sq km windows of high and low topographic regions of the transition zone suggest a positive correlation of resurfacing effects with topography, not

easily modelled with the ignimbrite or paleopole deposit hypotheses.

Evidence for extensive erosion: Erosional processes that have operating in the dichotomy boundary zone include wind, mass wasting, surface runoff, and possible karst. The minimum depths of erosion are calculated from preserved erosional features in the zone, along the margin with the highlands to the south, and from features within the highlands but still within the marginal region where crater statisical analysis and morphologies document the north to south retreat of the dichotomy boundary. Within the zone mesas, cuestas, and pedestal craters document erosional down-cutting up to 1.1 km; cliffs and canyon walls, along the boundary, document an erosional base level approximately 1 kilometer below perched intercrater plains. Retreat of the highlands from north to south is further supported by the tracing of intrahighlands structural fabrics across the boundary into the transitional province.

Radar & thermal imaging: Thermal inertia of the region is low (9) and is equivalent to an average particle size of >40um for an assumed homogeneous particle surface of one particle size (10). Materials with this value of thermal inertia will completely mask any underlying material (including solid bedrock) if the layer is >2 cm thick on the surface. 3.5 cm radar measurements made during the 88 Mars opposition showed zero depolarized radar echo power in the equatorial region to the west of Tharsis, and strong echo power in the volcanic provinces surrounding the region to its south and east (11). Cursory inspection of a published version of the synthetic radar imaging centered along the 133 and 147 meridian shows an apparent correlation with the transitional zone along the dichotomy boundary(12). Also noted here were discernable echoes from the region surrounding the residual southern polar ice cap, where the modern day equivalent of the postulated paleopole deposits are found. Echo power in the RCP transmitted/LCP received signal is due to multiple surface reflections or multiple subsurface scatterers, and for the equatorial deposits has been interpreted (accommodating thermal data) as an area of fine grained deposits with the absence of volume scatterers to a depth of several meters(11).

A chemical boundary layer hypothesis: An alternative interpretation which may accommodate the combined set of observations (structural, morphologic, crater statistics, and geophysical data) is that the western equatorial region represents an elogate (2-3000 km), 300-500km wide, arch of previously deformed and cratered material that sat initially in excess of 1 to 1.5 km depth beneath the cratered highlands. Exhumation and erosional retreat of the dichotomy boundary brought the earlier intra-highlands erosional base level (?water table) with its attended salt-cemented formations to the surface. The chemical processes attendent with the paleowater table gives a mechanism for masking large craters, the formation of the apparent molds of barchan dunes(13), and explaining crypic cross-cutting layering in the 'layered' sequences. Like the salt-cemented ranges of the Atacama Salar (Chile)(14) uplift initiates a process of decementation leaving an upper fine grained residual layer upwards of 2 meters thick. Such a decemented layer would explain the concurrence of the radar "stealth" zone and low thermal inertias with the exhumed basement arch.

References: (1) Scott, D.H. & Carr, M.H. (1978) USGS Map I-1083 (2) Morris, E.C. & Dwornik, S.E.(1978) USGS Map I-1049 (3) Scott, D.H. & Tanaka, K.L.(1986) USGS Map I-1802A (4) Scott, D.H. & Tanaka, K.L.(1982) JGR 87,1179-1190 (5) Scott, D.H. & Tanaka, K.L.(1981) USGS I-1280 (6) Schultz, P.H. & Lutz, A.B. (1988) Icarus 73, 91-141 (7) Forsythe, R.D. & Zimbelman, J.R.(1988) Nature 336, 143-146 (8) Craddock, R.B. & Maxwell, T.A. (1989) LPSC XX, 191-192 (9) Kieffer, H.H., et al. (1977) JGR 82, 4249-4291 (10 Kieffer, H.H., et al. (1973) JGR 84, 8252- 8262 (11) Butler, B., et al. (1989) EOS 70, 1171 (12) Anonymous (1989) Astronomy 17, 12 (13) Rhodes, D.D. & Neal, T. (1981) NASA Tech. Mem. 84211, 232-234 (14) Stoertz, G.E. & Ericksen, G.E. (1974) USGS Prof. Paper 811

**MEVTV STUDY: EARLY TECTONIC EVOLUTION OF MARS - CRUSTAL DICHOTOMY TO VALLES MARINERIS;** H. V. Frey and R. A. Schultz, Geodynamics Branch, Goddard Space Flight Center, Greenbelt MD 20771

In this study we addressed several fundamental problems in the early impact, tectonic and volcanic evolution of the martian lithosphere: (a) origin and evolution of the fundamental crustal dichotomy, including development of the highland/lowland transition zone; (b) growth and evolution of the Valles Marineris; and (c) nature and role of major resurfacing events in early martian history. Below we briefly summarize our results in these areas.

***(a) Origin and Evolution of the Martian Crustal Dichotomy***

Both internal and external processes have been invoked to explain this fundamental characteristic of the martian lithosphere. We suggest that major, basin-forming impacts have played a prominent role in the origin and development of the crustal dichotomy (1,2,3). Our study revealed little direct support for the single giant impact hypothesis (4), but did suggest a number of new, previously unrecognized large impacts basins (5). Independent evidence for the Daedalia, Utopia and Elysium Basins has been presented by others (6,7,8). Most of the largest recognized basins are in the northern or western hemispheres; we believe that the overlap of these basins is responsible for the lower topography and prolonged volcanism which characterizes the northern lowland plains, and perhaps also for the growth of major volcano-tectonic complexes such as Elysium and Tharsis (3,9). A speculative model for the evolution of the northern lowlands in the Utopia-Elysium region was developed within this context (9,10). More work needs to be done to refine the inventory of major impact basins for Mars and to relate these basins to the earliest crustal development of the planet. We have found evidence in the cumulative frequency curves as well as in the morphology of the basins for a signficant change in properties at Argyre-sized basins (D~1850 km) and at Chryse size basins (D~3600 km) (5). These changes may be related to lithospheric structure at the time of basin formation or to fundamental differences in the impacting population.

***(b) Growth and Evolution of the Valles Marineris***

Valles Marineris is a complex system of ancient grabens that were modified by erosion and deposition. Our detailed studies addressed several fundamental issues on trough origin and growth. Relative orientations of Coprates Chasma and wrinkle ridges and grabens located on the adjacent southern plateau suggest that the ridges and grabens grew under multiple stress states and probably predate Coprates Chasma itself (11). New structural mapping of the region (12,13) details the discontinuous distribution and interrelationships of wrinkle ridges, grabens and pit-crater chains around the troughs. Although the trough system is often assumed to have nucleated as small pit-craters, pit-crater chains appear to be distinct structures, not trough precursors (14). Unambiguous evidence for strike-slip faulting was found in Early Hesperian ridged plains materials to the south in Coprates (15,16,17). Detailed mapping of the echelon set of plateau grabens located on Ophir Planum and the adjacent Coprates trough bounding faults is unravelling the sequence of faulting in central Valles Marineris. The curving geometries of grabens in Ophir and trough faults near Melas Chasma indicate that the local stress state was spatially variable, but probably regionally uniform, during early trough growth (18). Our work reveals unexpected complexities in the growth and tectonic development of the Valles Marineris region.

***(c) Major Resurfacing Events in Martian History***

Resurfacing has been a major process during most of martian history, but detailing the characteristics of major events has been difficult. We have adapted the Neukum and Hiller technique (19) for larger crater diameters in order to study older terrains and the resurfacing which has modified them. We showed that a major resurfacing event within and around the highland/lowland transition zone occured at the time of ridged plains emplacement in Lunae Planum and elsewhere (20). Similar study of the Tempe Terra region in western Mars shows

that comparable resurfacing at about the same time occurred there (21) as well as in Xanthe Terra, Lunae Planum and Coprates (22,23). It appears that there was a major, perhaps planet-wide resurfacing on Mars corresponding to the eruption of Lunae Planum Age (LPA) ridged plains. We also find evidence for an older resurfacing event which can be related to intercrater plains development (cratered plateau material) recognized in geologic studies (24). In the Tempe region a common-age resurfacing event younger than LPA affecting the cratered terrain and adjacent plains-forming lowland units appears to correlate with the Vastitas Borealis Formation (21,24). We have also extracted information on the thickness of materials associated with different resurfacing events from the cumulative frequency curves. Thicknesses associated with the major LPA resurfacing vary greatly depending on location: in the Lunae Planum, Tempe and Coprates ridged plains 350-600 m is common (21,23,25) but in the adjacent cratered terrain in Xanthe Terra, Tempe Terra and elsewhere the correpsonding value is less than 100 m. These results can provide an independent stratigraphy based on major resurfacing events correlated at many places around Mars, which can both date the resurfacing events and also locate the depth to older, now buried surfaces.

In a related study (26) we find evidence that what have been mapped as Noachian age ridged plains in Memnonia and Argyre may be Early Hesperian in age. These plains are sufficiently thin that a large number of medium-sized craters show through from an older surface below. This may mean that the eruption of ridged plains was more temporally confined than previously thought, which would have important implications for the thermal history of Mars.

**References**: (1)Frey, H. and R. A. Schultz, GRL 15, 229-232, 1988. (2)Frey, H. and R. A. Schultz, MEVTV Workshop on Early Tectonic and Volcanic Evolution of Mars, LPI Report 89-04, p35-37, 1989. (3)Frey, H. and R. A. Schultz, 4th Internat. Conf. on Mars, 106-107, 1989. (4)Wilhelms, D. E. and S. W. Squyres, Nature 309, 138-140, 1984. (5)Schultz, R. A. and H. V. Frey, JGR submitted, 1989. (6)Craddock, R. A., R. Greeley and P. R. Christensen, JGR in press, 1990. (7)McGill, G. E., JGR 94, 2753-2759, 1989. (8)Schultz, P. H., LPS XV, 728-729, 1984. (9)Frey, H. and R. A. Schultz, LPS XX, 315-316, 1989. (10)Frey, H. and R. A. Schultz, JGR submitted, 1989. (11)Schultz, R. A. and H. V. Frey, EOS Trans. Am Geophys. Un. 69, 389-390, 1988. (12)Schultz, R. A. and H. V. Frey, 4th Internat. Conf. on Mars, 183-184, 1989. (13)Schultz, R. A. and H. V. Frey, LPS XX, 974-975, 1989. (14)Schultz, R. A., MEVTV Workshop Tectonic Features on Mars, 12-22, 1989. (15)Schultz, R. A., MEVTV Workshop Tectonic Features on Mars, 23-25, 1989. (16)Schultz, R. A., Nature 341, 424-426, 1989. (17)Schultz, R. A., LPS XXI(this volume), 1990. (18)Schultz, R. A., LPS XXI(this volume), 1990. (19)Neukum, G. and K. Hiller, JGR 86, 3097-3121, 1981. (20)Frey, H. V., A. M. Semeniuk, J. A. Semeniuk and S. Tokarcik, Proceed. LPSC 18th, 679-699, 1988. (21)Frey, H. V. and T. D. Grant, JGR submitted, 1989. (22)Grant, T. D. and H. V. Frey, EOS Trans. Am. Geophys. Un. 68, 1342, 1987. (23)Frey, H. V. and T. D. Grant, LPS XX, 313-314, 1989. (24)Tanaka, K. L. Proceed. LPSC 17th, JGR 91, E139-E158, 1986. (25)Frey, H. V., J. A. Semeniuk and T. D. Grant, MEVTV Workshop on Early Tectonic and Volcanic Evolution of Mars, LPI Report 89-04, p38-40, 1989. (26)Frey, H. V., C. E. Doudnikoff and A. M. Mongeon, LPS XXI(this volume), 1990.

**ARE NOACHIAN-AGE RIDGED PLAINS (*Nplr*) ACTUALLY EARLY HESPERIAN IN AGE?** H. V. Frey, C. E. Doudnikoff and A. M. Mongeon, Geodynamics Branch, Goddard Space Flight Center, Greenbelt MD 20771

***Ridged Plains of Noachian Age?***

The prominant ridged plains of Lunae Planum, Coprates, Hesperia Planum and elsewhere are generally considered to have erupted in the Early Hesperian (1,2) and are generally taken to define the base of that stratigraphic system (3). These plains are widespread, covering over 4 x $10^6$ $km^2$ in western Mars alone (1) and are broad, planar surfaces with some flow lobes and parallel, linear to sinuous ridges similar to lunar mare ridges with a spacing of 30 to 70 km. The general interpretation is that the ridged plains (unit *Hr*) are due to relatively rapid eruptions of low viscosity lavas (1,2), and their occurance at the base of the Hesperian represents a major volcanic episode in martian history (3).

In some areas these plains are gradational with another ridged plains unit, mapped as *Nplr*. The ridges of these apparently Noachian-age plains are generally further apart with rougher, more heavily cratered inter-ridge areas (1,2). *Nplr* terrains are widely distributed in both hemispheres of Mars but cover much less area than the more common *Hr* unit. The type area in Memnonia lies southwest of Tharsis in heavily cratered terrain (*Npl1*, *Npl2*). Other major occurances are further south in Sirenum, between the Argyre and Hellas Basins in Noachis, in the southern portion of Cimmeria Terra and in the northeastern portion of Arabia (1,2). The Noachis and Cimmeria outcrops are distributed roughly concentrically about the Hellas impact basin at approximately 1 and 2 basin diameters, respectively.

The stratigraphic position of these apparently older ridged plains is **Middle Noachian**; in the current geologic maps the unit does not extend into the Upper Noachian and appears temporally unrelated to the more common Hesperian ridged plains (*Hr*) even though these two units are sometimes gradational. The assignment of stratigraphic position is based on superposition relationships and total crater counts; the high density of impact craters on *Nplr* would certainly suggest a Noachian age.

But total crater counts can be misleading: if multiple resurfacing or other crater depopulation events occur and successfully compete with crater production, a given terrain may have an apparently young total crater age even though very old surfaces remain partially exposed in the form of very large craters. Inefficient resurfacing events allow older surfaces to show through and give old crater retention ages based on total crater counts, which may not accurately reflect the age of the major terrain unit. In this paper we examine whether or not the *Nplr* units in Memnonia and Argyre truly represent ridged plains volcanism of Noachian age or are simply areas of younger (Early Hesperian age) volcanism which failed to bury older craters and therefore have a greater total crater age than really applies to the ridged plains portion of those terrains.

***Resurfacing in Memnonia and Argyre***

We used the Neukum and Hiller (4) technique to determine the number of preserved crater retention surfaces in the Memnonia and Argyre regions where Scott and Tanaka (1) show *Nplr* units to be common. The Memnonia outcrops are the type example of this unit, and we subdivided the study area in MC 16 into two broad units: cratered terrain *Npl* (mostly *Npl1* and *Npl2*) and the ridged plains *Nplr*. Our mapping is similar to but not identical with that previously done (1). We counted craters larger than 3 km in diameter and plotted cumulative frequency curves for each terrain unit, then broke these curves into separate branches where they departed from a standard production curve (4, 5). This departure is interpreted to be due to resurfacing, and breaking the curves into separate branches allows determination of the crater retention age of each post-depopulation "surface" independent of previous history (the survivors are subtracted and remaining craters compared independently to the crater production curve). Table 1 summarizes the results for cratered terrain (*Npl*) in Memnonia and for ridged plains (Nplr) in both Memnonia and Argyre, and compares these with similar results obtained by us for Tempe

Terra (6) and Lunae Planum (the type area for the Lunae Planum Age [LPA] ridged plains [*Hr*] resurfacing).

In Lunae Planum no craters larger than 50 km exist within the ridged plains; in Memnonia and Argyre there are craters as large as 117 and 100 km that survive in the *Nplr* unit. The population of old, large craters contributes to the total crater counts which suggest the *Nplr* unit is of Noachian age. We find the cumulative frequency curves for the ridged plains in Argyre/Memnonia can be broken into four branches which have remarkably similar crater retention ages N(1): an oldest branch ~[121,000/115,000], a branch with N(1) = [80,200/76,500], a "Lunae Planum Age" branch at [28,100/22,100], and a still younger branch at N(1) = [6700/6200]. Note that the Argyre ages for *Nplr* are consistently slightly older. These ages compare with resurfacing ages for the cratered terrain *Npl* in Memnonia of N(1) = [226,900], [76,000], [27,900], and [6300]. For all but the oldest (and most poorly determined) branch, the crater retention ages for the different branches are extremely similar from one area to the next.

The craters which determine the ridged plains resurfacing age (those superimposed on the ridges as opposed to showing through the plains) define the N(1) = [25,000 +/- 3000] age branch for both Memnonia and Argyre. This age is nearly identical (with the precision this technique affords) with the oldest branch we find for Lunae Planum: N(1) = [25,700], even though the craters which define this age branch (10-20 km in Argyre, 8-15 km in Memnonia) are significantly smaller than in Lunae Planum (25-50 km). This implies that the thickness of the *Nplr* ridged plains in Argyre and Memnonia is significantly less than we estimate (4,5) for Lunae Planum (350- 600 m). This reduced thickness is what allows the older craters to show through, preserving the older crater retention surfaces at N(1) = [78,000 +/- 2000] and [118,000 +/- 3000]. These older preserved craters contribute to the high total crater counts that suggested the *Nplr* were of Noachian age.

We suggest that for these two areas at least the *Nplr* ridged plains are the same age as those (*Hr*) in Lunae Planum, Tempe and elsewhere: N(1) = [25,000 +/- 3000]. If this conclusion holds in general for the other outcrops of those units mapped as *Nplr*, it may imply that the eruption of ridged plains volcanism was more restricted in time than previously thought. This would have interesting implications for models of the thermal history of Mars, and would make the ridged plains even more important as a stratigraphic marker in martian history.

Table 1. Resurfacing Ages for Memnonia and Argyre

| AREA | UNIT | CRATER RETENTION AGE N(1) | | | |
|---|---|---|---|---|---|
| Memnonia | Npl | 226,858 | 75,980 | 27,866 | 6,343 |
| Memnonia | Nplr | 115,221 | 76,445 | 22,062 | 6,223 |
| Argyre | Nplr | 121,300 | 80,200 | 28,100 | 6,700 |
| Lunae Planum | Hr | -- | -- | 25,700 | 10,100 |
| Tempe | Hr | -- | -- | 22,100 | 6,500 |

**References**: (1) Scott, D. H. and K. L. Tanaka, Geol. Map Western Equatorial Region of Mars, USGS Map I-1802-A, 1986. (2) Greeley, R. and J. E. Guest, Geol. Map Eastern Equatorial Region of Mars, USGS Map I-1802-B, 1987. (3) Tanaka, K. L., Proceed. LPSC 17th, JGR 91, E139-E158, 1986. (4) Neukum, G. and K. Hiller, JGR 86, 3097-3121, 1981. (5) Frey, H., A. M. Semeniuk, J. A. Semeniuk and S. Tokarcik, Proceed. LPSC 18th, 679-699, 1988. (6) Frey, H. and T. D. Grant, submitted to JGR, 1989.

# DARK MATERIALS IN VALLES MARINERIS: INDICATIONS OF THE STYLE OF VOLCANISM AND MAGMATISM ON MARS

Paul E. Geissler, Robert B. Singer (Planetary Image Research Laboratory, L.P.L., University of Arizona) and Baerbel K. Lucchitta (U.S. Geological Survey, Flagstaff, Arizona)

Rifting on the equatorial canyon system of Valles Marineris provides a unique view of the interior of the martian crust to depths reaching 7 kilometers, exposing several in-situ bedrock units which testify to past volcanic and magmatic processes on Mars. Dark, relatively gray materials, believed to be among the least altered of martian crustal components, are found in a variety of geologic settings in Valles Marineris. These include in-situ wall-rock layers exposed during the formation of the canyon system, canyon floor covering deposits such as eolian dunes, and volcanic materials, possibly indicating relatively recent volcanism in the Valles [1]. Using Viking Orbiter apoapsis color images, we have studied the spectral reflectance and spatial distribution of these materials in an attempt to understand their relation to past episodes of volcanism, tectonism, igneous intrusion, and eolian redistribution in the canyon system.

A series of cliffs in the Ophir Chasma wallrock is interpreted to be exposures of resistant bedrock; the spectral signature of this massive and uniform unit most closely resembles that of terrestrial mafic rocks altered to or coated by crystalline hematite. These Ophir Chasma cliffs may be erosional scars exposing fresh bedrock beneath more weathered wallrock of a similar composition, or they could be a physically and compositionally distinct unit, produced, for example, by igneous intrusion prior to the formation of the Valles.

Application of multispectral mapping techniques to probable young volcanic materials in the Central Troughs yields an inferred distribution of volcanic activity consistent with an interpretation of extrusion along faults near the margins of the canyon floors. Terrestrial examples of similar relationships between tectonism and volcanism include the African Rift Valleys and the Basin and Range Province in the southwest of the U.S., both areas of crustal extension. Since there is no a-priori reason to expect this relationship to occur if the Valles were generated by fluvial erosion or by subsidence of karst or thermokarst, the inferred distribution of volcanism appears to support the hypothesis [2] that the Valles originated through tectonic extension and graben subsidence. While the age of this volcanism is at present poorly constrained, photogeologic indications that it may be relatively recent [1] could suggest that tensional rifting and canyon formation may be ongoing processes.

A thick, regionally extensive deposit observed in outcrops in Juventae Chasma and in a wallrock layer in Coprates is interpreted to be composed of mafic glass on the basis of spectral reflectance, incompetent erosional morphology and marked tendency for eolian redistribution, indicating that the material is easily broken down into sand-sized grains capable of saltation. Multispectral mapping suggests that the eolian floor-covering materials in the lower canyons several hundred kilometers to the east are derived from sources in Juventae and

Coprates Chasmata. The interpretation of this unit as volcanic ash requires that the deposits were produced in pyroclastic eruptions at what was once the surface of the planet, and later buried by almost 3 kilometers of plains materials including the 400 to 600 meters of Hesperian lavas believed to resurface the Lunae-Sinai Planum region. The deposits in Coprates and Juventae Chasmata are thus probably among the oldest of martian volcanic materials.

Voluminous regional deposits of basaltic ash have no terrestrial analogue, although they are common on the Moon [3-8] and may be present on Mercury as well [9]. If we tentatively accept the identification of massive mafic ash deposits on Mars, the Moon and Mercury, then the absence of such deposits from the inventory of present day crustal materials on Earth requires explanation. One possibility is that the processes which produce large pyroclastic eruptions from mafic magmas are confined to smaller terrestrial planets, perhaps because of their reduced gravitational acceleration and atmospheric pressure [10]. Another possibility is that these processes could be confined to the early stages of planetary evolution. By analogy with the lunar mantling deposits, the materials exposed in the layer in Coprates Chasma and in Juventae may represent a relatively volatile-rich phase of volcanism early in the history of Mars, possibly even the late stages of planetary outgassing. The absence of extensive deposits of mafic glass associated with more recent volcanism on Mars and the Moon (and, perhaps, the Earth) might then be due to a diminishing supply of juvenile volatiles. It is interesting to speculate that massive basaltic ash deposits might once have been common on Earth, and later obliterated from the geologic record along with the evidence for an early period of heavy bombardment by impactors.

References cited:

[1] Lucchitta, B.K., Science, 235, 565-567, 1987.
[2] Carr, M.H., J. Geophys. Res., 79, 3943-3949, 1974.
[3] Wilhelms, D.E., U.S. Geol. Survey Prof. Paper 599-F, 1970.
[4] Wilhelms, D.E. and J.F. McCauley, U.S. Geol. Survey Misc. Geol. Inv. Map I-548, 1971
[5] El Baz, F., Lunar Science IV, 217-218, 1973.
[6] Heiken, G.H., D.S. McKay, and P.W. Brown, Geochim. Cosmochim. Acta, 38, 1703-1718, 1974.
[7] Head, J.W., Proc. Lunar Sci. Conf., 5th, 207-222, 1974
[8] Gaddis, L.R., C.M. Pieters, and B.R. Hawke, Icarus, 61, 461-489, 1985.
[9] Schultz, P.H., Phys. Earth Planet. Int., 15, 202-219, 1977
[10] Wilson, L., and J. W. Head, Nature, 302, 663-669, 1983.

# DOES WRINKLE RIDGE FORMATION ON MARS INVOLVE MOST OF THE LITHOSPHERE?;

M. Golombek[1], J. Suppe[2], W. Narr[2], J. Plescia[1], and B. Banerdt[1]; [1]Jet Propulsion Laboratory, Caltech, Pasadena, CA 91109, [2]Dept. Geological and Geophysical Sciences, Princeton University, Princeton, NJ 08544.

Recent work on the origin of wrinkle ridges suggests that they are compressional tectonic features whose subsurface structure is not understood. In this abstract, we briefly review some characteristics of Martian wrinkle ridges which suggest that they are the surface expression of thrust faults that extend through much of the lithosphere.

Photoclinometric profiles across wrinkle ridges in Lunae Planum show an average regional elevation offset across the ridges (plains on one side of the ridge are at a distinctly different elevation than plains on the other) of about 100 m. The offset in regional elevation extends for many kilometers on either side of the ridge and suggests a fault beneath the structure; simple fold structures or faults that flatten into a decollement do not readily explain the elevation offset. A combination of folding and thrust faulting, however, can produce both the observed ridge morphology and the offset in regional elevation. The lateral extent of the regional elevation change requires a planar fault that does not shallow with depth, because the regional elevation change would decrease to zero above the point where the fault flattens to a decollement (1).

A number of attempts have been made to identify kinematic models capable of explaining the salient characteristics of wrinkle ridges. In particular, fault-bend and fault-propagation folding have been suggested as possible models for the development of wrinkle ridges (2, 3). Fault-bend folding (4) can produce an anticlinal fold when surficial rocks are translated over a surface-flattening bend in a thrust fault. Fault-propagation folding (5, 6, 7) occurs when displacement along a reverse fault at depth is accommodated by folding of overlying layers. Both types of structures are capable of producing surface folds with complex near surface faulting, similar to wrinkle ridges. More detailed considerations suggest, however, that the gross structure of wrinkle ridges is different from typical fault-bend and fault-propagation folds. In particular, faults responsible for both fault-bend and fault-propagation folds most commonly shallow out into horizontal decollements at bedding-plane contacts between rocks with distinct mechanical properties. In addition, where observed on the earth, the step-up ramps associated with these types of structures are sharp, rather than gradual, making a gradually changing fault dip (for example a thrust fault gradually shallowing with depth) unlikely. If the fault dip shallowed or completely flattened with depth, the offset in regional elevation would also decrease or disappear and abrupt changes in fault dip would produce correspondingly abrupt changes in surface elevation away from wrinkle ridges. Furthermore, the shortening across wrinkle ridges is small (hundreds of meters; 1), much less than that likely by formation of these structures by fault-bend or fault-propagation folding. For these types of folds, the long rear limb of the fold is produced by translation of rocks above the thrust ramp. This in turn requires that the slip across the structure be roughly equal to the width of the rear limb. The rear limb of most wrinkle ridges is many kilometers wide, which is an order of magnitude greater than the shortening that can be reasonably accommodated across them (1). Thus, the lack of evidence for horizontal decollements beneath wrinkle ridges and the excessive strains suggested for fault-bend and fault-propagation folds suggest that a different deep subsurface structure might be more applicable for the overall geometry of planetary wrinkle ridges, although fault-bend and fault-propagation folding could still be responsible for near-surface folding and faulting.

In northwestern Lunae Planum wrinkle ridges are spaced about 50 km apart and consistently have an uplifted eastern side. The regional elevation change appears to persist laterally for many kilometers away from the ridges. There is no evidence for tilted blocks between the ridges (dips of 1° or greater would have been detected), and no evidence for any folding or warping of the surface between the ridges. To first approximation, the faults beneath these ridges must dip to the east, to produce the uplifted eastern side, and continue at least 50 km to the next ridge. If the fault dips at roughly 25°, then the fault is roughly 25 km beneath the surface at this distance. Steeper dips would result in greater depths of penetration; a 45° dipping fault would be at

50 km depth beneath the adjacent ridge. Note that even if the surface between adjacent wrinkle ridges was tilted at less than a degree, the underlying fault must still continue laterally to the next ridge, at which point it would probably be tens of kilometers below the surface (e.g., 8). This suggests that the faults responsible for wrinkle ridges clearly involve a significant thickness of the Martian lithosphere and are not simply surface folds affecting the upper few kilometers of the crust.

There is strong evidence that faults beneath foreland basement uplifts, such as the Rocky Mountains, are underlain by planar faults that root in the weak ductile lower crust near the Moho. Best known of these basement thrusts is the Wind River thrust (9), which dips about 40°, has slipped about 5-7 km, and is clearly imaged on seismic profiles to about 20 km depth. Geometric considerations indicate the fault zone flattens near the Moho at about 35 km depth. Numerous other basement thrusts have been documented in the Rocky Mountain foreland and elsewhere worldwide in the course of petroleum exploration (e.g., 10, 11). Many of these basement thrusts have small offsets on the order of hundreds of meters and have a change in elevation across the structure similar to wrinkle ridges. Some of the best documented examples are in the Wind River basin (11). The deformation is entirely by fault slip in the basement, but as the fault enters the 1-3 km thick sedimentary cover, fault-bend folding, wedging and fault-propagation folding produce structures that are quantitatively similar to the kilometer-scale aspects of wrinkle ridges.

On Mars, a number of supporting arguments and models also permit the rooting of faults responsible for wrinkle ridges in a weak ductile lower crust or lithosphere. The flexure of volcanic loads on the Martian surface (12) and the magma source region required beneath the giant Tharsis volcanoes (13, 14) both suggest a lithosphere on the order of 50 km thick at the period in Tharsis history when wrinkle ridges formed. Assuming a 50 km thick lithosphere, with a basaltic crust 30 km (15) to 100 km thick (16, 17, 18) and an olivine mantle (19, 20), requires thermal gradients of 9°/km to 16°/km from ductile creep properties of basalt and olivine. Thermal evolution models of Mars (21) also predict a present average crustal thermal gradient of 9°/km, which is a likely minimum as thermal gradients were undoubtedly greater during Tharsis volcanic and tectonic activity. Given these constraints, we have assumed 9°/km, 15°/km, and 20°/km and various crustal thicknesses for the construction of lithospheric strength envelopes (brittle and ductile yield stress versus depth curves) to gain a better understanding of likely lithospheric strong and weak zones at depth.

Results show that even under the coolest conditions a lower crustal weak zone is present below 40 km, assuming a minimum 50 km thick crust. Under the warmer conditions more likely for Tharsis, lower crustal weak zones begin at about 20 km depth, with all strength in the upper mantle gone at 40-60 km depth. These calculations indicate that under conditions likely during Tharsis deformation, weak zones at fairly shallow depths existed within the crust and mantle in which thrust faults could root, analogous to faults beneath foreland basement uplifts on the earth. These results suggest a mechanism that links wrinkle ridge formation with much of the lithosphere.

**REFERENCES** **1** Golombek, Plescia, Franklin, 1988, Lunar Plan. Sci. XIX, 395. **2** Plescia & Golombek, 1986, Geol. Soc. Amer. 97, 1289. **3** Watters, 1989, J. Geophys. Res. 93, 10,236. **4** Suppe, 1983, Amer. J. Sci. 283, 684. 5 Suppe, 1985, Principles of Structural Geology, Prentice-Hall, 537p. **5** Reidel, 1984, Amer. J. Sci. 284, 942. **6** Suppe & Medwedeff, 1984, Geol. Soc. Amer. Abst. Prog. 16, 670. **7** Woodward, Boyer, Suppe, 1985, An Outline of Balanced Cross Sections, Univ. Tenn. Dept. Geol. Sci., Studies 11, 170p. **8** Erslev, 1986, Geology 14, 259. **9** Smithson et al., 1979, J. Geophys. Res. 94, 5955. **10** Gries, 1983, Amer. Assoc. Petrol. Geol. Bull. 67, 1. **11** Gries & Dyer, 1985, Seismic Exploration of the Rocky Mtn. Region, Rocky Mtn. Assoc. Geol., 299p. **12** Comer, Solomon, Head, 1985, Rev. Geophys. 23, 61. **13** Carr, 1973, J. Geophys. Res. 78, 4049. **14** Blasius & Cutts, 1976, Proc. Lunar Sci. Conf. 7th, 3561. **15** Bills & Ferrari, 1978, J. Geophys. Res. 83, 3497. **16** Sjogren & Ritke, 1982, Geophys. Res. Lett. 9, 739. **17** Sjogren and Wimberly, 1981, Icarus 45, 331. **18** Janle & Ropers, 1983, Phys. Earth Planet. Int. 32, 132. **19** Francis & Wood, 1982, J. Geophys. Res. 87, 9881. **20** Wood & Ashwal, 1981, Proc. Lunar Planet. Sci. Conf. 12B, 1359. **21** Toksoz et al., 1978, Moon & Planets 18, 281.

# VOLATILE COMPOUNDS IN SHERGOTTITE AND NAKHLITE METEORITES.

James L. Gooding[1], Kwesi E. Aggrey[2,3], and David W. Muenow[2]
[1] SN21/Planetary Science Branch, NASA/Johnson Space Center, Houston, TX 77058. [2] Department of Chemistry and Hawaii Institute of Geophysics, University of Hawaii, Honolulu, HI 96822. [3] School of Theoretical and Applied Science, Ramapo College of New Jersey, Mahwah, NJ 07430.

**INTRODUCTION.** Since discovery of apparent carbonate carbon in Nakhla [1], significant evidence has accumulated for occurrence of volatile compounds in shergottites and nakhlites. Gooding and Muenow [2] showed that at least one shergottite (EETA79001) contains substantial sulfur in a highly oxidized form and that the oxidation must have occured on the shergottite parent planet. Burgess et al. [3] also found oxidized sulfur in ALHA77005, Shergotty, Nakhla, and Chassigny. Kerridge [4] reported carbon and deuterium of apparent pre-terrestrial origin in Shergotty and Lafayette (a nakhlite). In addition, discrete grains of salt minerals have been documented in EETA79001 and Nakhla [5-7]. Here we present final results from our study of volatile compounds [8] in three shergottites, one nakhlite, and three eucrite control samples.

**SAMPLES AND METHODS.** Antarctic meteorites included Allan Hills specimens ALHA77005 (shergottite) and ALHA81001 (eucrite), as well as Elephant Moraine specimens EETA79001 (shergottite; lithologies A, B, and C), and EETA79004 (eucrite). A Pasamonte eucrite specimen (USNM-897) was obtained from the U. S. National Museum and a Nakhla specimen (BMNH-1911,369) from the British Museum (Natural History). A Shergotty specimen (GSI-179) was sub-divided from material allocated by the Geological Survey of India to Duke [9]. Samples from the exterior (0-0.5-cm depth, including fusion crust) and interior (> 1-cm depth) of each meteorite were individually analyzed so that terrestrial weathering and contamination could be recognized and not misinterpreted as parent-body effects. Each sample (20-80 mg) was pyrolyzed by continuous heating to 1500 K at 5-6 K/min under $10^{-7}$ torr vacuum in a Knudsen cell fitted with a high-purity aluminum oxide liner. Evolved gases were analyzed by a quadrupole mass spectrometer that was continuously scanned over m/e = 2-100 to simultaneously measure abundances of $H_2O$, $CO_2$, CO, $SO_2$, $S_2$, $H_2S$, HCl, Cl, and hydrocarbons.

**RESULTS.** *WATER.* For interior samples of shergottites, $H_2O$-release profiles and total water concentrations (< 0.1%), are not obviously correlated with similar data for other volatile species. A typical $H_2O$-release profile consists of a single broad peak at 350-700 K that suggests desorption of loosely bound water. Although Nakhla was previously suspected to contain hydrous phases [7,10,11], its measured water content was less than anticipated and its $H_2O$-release profile was similar to those of shergottites. As discussed below for chlorine, however, it is possible that much of Nakhla's indigenous water reacted to form HCl during pyrolysis. Therefore, the actual water content of Nakhla may be significantly higher than the 0.007% measured as evolved $H_2O$. Kerridge [4] reported a total of 13.3 ppm H in Shergotty and 58.3 ppm H in the nakhlite, Lafayette, but discarded as terrestrial contamination all gases extracted at < 723 K. Judging from our results for Nakhla, however, HCl evolution (and, by inference, water loss) begins at < 700 K in nakhlites. Therefore, it is possible that Kerridge underestimated the nakhlite water content. *CARBON.* Carbon-containing species included $CO_2$, CO, and both saturated and unsaturated hydrocarbons ($C_1$-$C_4$ compounds). The contrast between exterior and interior samples is not always obvious although there are differences between shergottites/Nakhla, as a group, and eucrites. In addition, comparatively low hydrocarbon contents of Antarctic interior specimens distinguish them from non-Antarctic museum specimens. Evolution of $CO_2$ from shergottite and Nakhla samples occurs as peaks centered near 750 K or 900 K, the same temperature range over which $CaCO_3$ decrepitates under vacuum [12]. Because $CaCO_3$ has been independently identified as discrete mineral grains in both EETA79001 [5] and Nakhla [7], the evolved $CO_2$ is attributable to $CaCO_3$. Shergotty shows a surprising abundance of $CO_2$ but, unlike other shergottite specimens, the $CO_2$ evolution is closely correlated with the release of hydrocarbons. Therefore, it is likely that some or all of the "apparent carbonate" in Shergotty is associated with terrestrial organic contamination. Two different $CO_2$ peaks in the Nakhla profile suggest two different $CO_2$ carriers. Both of the Nakhla carriers must be inorganic, however, because the Nakhla sample in question is virtually free of hydrocarbons. For interior samples of shergottites and Nakhla, there exists an inverse correlation between $CO_2$ and oxidized sulfur (correlation coefficient, r = -0.71 for 11 samples). Kerridge [4] reported a total of 69.3 ppm C in Shergotty and 112.0 ppm C in Lafayette. His procedure discarded as contamination all gases extracted at < 723 K and interpreted as pre-terrestrial the gases extracted above 1023 K (Lafayette) or 1073 K (Shergotty). Judging from our results for Shergotty and Nakhla, however, Kerridge's procedure might not have excluded some of the hydrocarbon contamination in Shergotty and might have sacrificed some of the carbonate in Nakhla. Our results indicate an intrinsic 210 ppm C in Nakhla.

*SULFUR.* Most sulfur from interior samples of eucrites, and mildly weathered exterior samples of eucrites, evolves as $S_2$ with minor $H_2S$, consistent with a chemically reduced carrier such as pyrrhotite or troilite (FeS). In contrast, large fractions of the sulfur in shergottites and Nakhla evolves as $SO_2$. The fraction of sulfate in interior samples of eucrites is nearly zero and exhibits a maximum value of about 21% in a moderately weathered interior sample of EETA79004; the fraction of sulfate in shergottite and Nakhla interior samples is 17-100% (Fig. 1). The least oxidized shergottite material is bulk Lith-A from EETA79001 whereas the most oxidized material is Lith-C from the same meteorite; other shergottite and Nakhla samples fall between those limits. Evolution of $SO_2$ from interior samples of shergottites and Nakhla, which show little evidence of terrestrial weathering, is attributable to decrepitation of indigenous sulfates. Calcium sulfate of apparent pre-terrestrial origin has been independently documented for EETA79001 [5] and both Ca- and Mg-sulfate have been found in Nakhla [6,7]. Evolution of $SO_2$ from EETA79001/Lith-C is attributable partly to sulfates and partly to a more refractory component that probably occurs as sulfate ions dissolved in glass [2]. In some samples, such as Nakhla, $SO_2$ evolution at 800-1000 K is correlated with $CO_2$ evolution. In terms of total abundances, however, $CO_2$ and $SO_2$ are inversely correlated, as discussed for carbon results. *CHLORINE.* Most of the chlorine evolved from interior shergottite samples consists of nearly equal concentrations of Cl and HCl although a few samples favor the latter. Exterior samples of terrestrially weathered eucrites, which also contain hydrous weathering products, show HCl as the dominant chlorine species. Therefore, it is likely that HCl evolution from all samples is fostered by pyrolysis reactions involving hydrated phases. Nakhla represents a special case in which HCl and Cl profiles are staggered in temperature, possibly indicating two different chlorine carriers. In addition, evolution of Cl at 800-1150 K is strongly correlated with evolution of monatomic Na (and K). The correlated Cl/Na evolution is attributable to decrepitation of sodium chloride that has been previously identified in Nakhla [6]. Production of HCl can be tentatively attributed to decrepitation of hydrous "rust" that contains trace Cl [7]. For interior samples of shergottites and Nakhla, total chlorine (Cl + HCl) varies inversely with total sulfur but varies directly with the abundance of oxidized sulfur (Fig. 2). No such correlations exist for interior samples of eucrites.

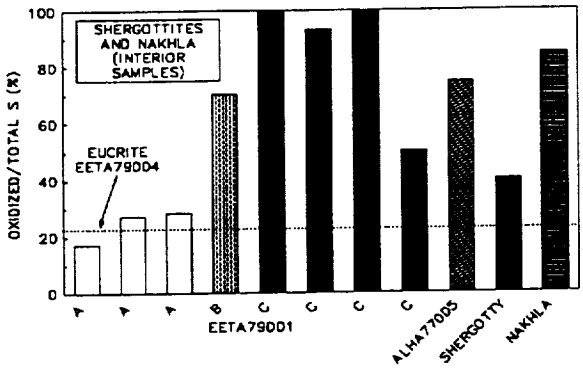


Figure 1. Relative abundances of sulfate in interior samples.

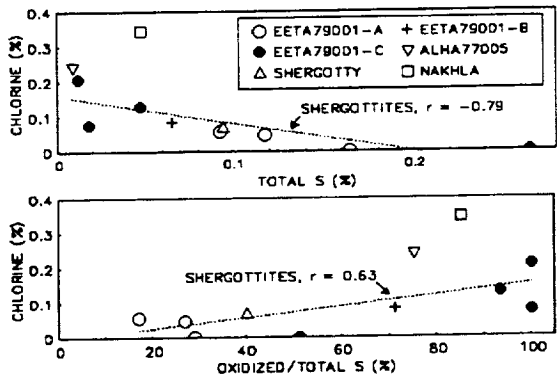


Figure 2. Chlorine-sulfur correlations in interior samples.

**CONCLUSIONS.** Shergottites ALHA77005, EETA79001, and Shergotty, and the nakhlite Nakhla, all contain oxidized sulfur (sulfate) of pre-terrestrial origin; sulfur oxidation is most complete in EETA79001/Lith-C. Significant bulk carbonate was confirmed in Nakhla and trace carbonate was substantiated for EETA79001, all of which appears to be pre-terrestrial in origin. Chlorine covaries with oxidized sulfur, whereas carbonate and sulfate are inversely related. These volatile compounds were probably formed in a highly oxidizing, aqueous environment sometime in the late-stage histories of the rocks that are now represented as meteorites. They are consistent with the hypothesis that shergottite and nakhlite meteorites originated on Mars and that Mars has supported aqueous geochemistry during its history.

**References.** [1] Carr R. H. et al. (1985) Nature, 314, p. 248-250. [2] Gooding J. L. and Muenow D. W. (1986) Geochim. Cosmochim. Acta, 50, p. 1049-1059. [3] Burgess R. et al. (1989) Earth Planet. Sci. Lett., 93, p. 314-320. [4] Kerridge J. F.(1988) Lunar Planet Sci. XIX, LPI, Houston, p. 599-600. [5] Gooding J. L. et al. (1988) Geochim. Cosmochim. Acta, 52, p. 909-915. [6] Wentworth S. J. and Gooding J. L. (1988) Lunar Planet. Sci. XIX, LPI, Houston, p. 1261-1262. [7] Wentworth S. J. and Gooding J. L. (1989) Lunar Planet. Sci. XX, LPI, p. 1193-1194. [8] Gooding J. L., Aggrey K. and Muenow D. W. (1987) Meteoritics, 22, p. 191. [9] Duke M. B. (1968) In B. M. French and N. M. Short (Eds.), Shock Metamorphism of Natural Materials, Mono, Baltimore, p. 613-621. [10] Ashworth J. R. and Hutchison R. (1975) Nature, 256, p. 714-715. [11] Bunch T. E. and Reid A. M. (1975) Meteoritics, 10, p. 303-315. [12] Kotra R. K. et al. (1982) Icarus, 51, p. 593-605.

**VALLEY DEVELOPMENT ON MARS: A GLOBAL PERSPECTIVE**; V.C. Gulick and V.R. Baker, Departments of Geosciences and Planetary Sciences, University of Arizona, Tucson, Arizona 85721.

Several periods of fluvial valley activity have so far been documented on Mars. These periods span Mars' geologic history with widespread episodes occurring during the Noachian, and localized episodes continuing into the Hesperian and Amazonian (Figure 1). Each fluvial event produced valleys which are distinct in overall morphology and network pattern, therefore providing information about the environment in which they formed. The formational environments required are consistent with those in the global model presented by Baker *et al.* [1].

By far the most widespread fluvial valley development is located in the heavily cratered uplands. These valleys form laterally extensive networks which are highly degraded. Headwater regions frequently cannot be traced with the quality of the existing images [2]. However, in areas where they can be traced, tributaries often originate on crater slopes. Lower reaches appear buried and later reactivated by the formation of less extensive pristine valleys in the intercrater plains. The resulting degraded and pristine compound valley morphology has important implications for the environment in which they formed. Because the degraded networks are more laterally extensive and have relatively higher drainage densities than the pristine networks [2], more water was probably available at the surface during the period when the degraded networks formed. In contrast, the pristine valleys which formed in the intercrater plains units appear to be structurally controlled. These networks seem to follow either pre-existing valleys (*e.g.* Margaritifer Sinus Region) or underlying fracture patterns (*e.g.* Nirgal Vallis, Nanedi Vallis) suggesting a subsurface water source was more important in the formation of these valleys.

Fluvial valleys are also present on Ceraunius Tholus and Hecates Tholus [3,4], two Noachian age volcanoes located in the northern plains region [5]. These valleys have drainage densities that are one to two orders of magnitude higher than those in the southern highlands and are equivalent to drainage densities of terrestrial runoff valleys [3,4]. Valleys on Ceraunius and Hecates exhibit a similar compound network morphology as the Noachian valleys in the southern highlands. However, the pristine valley segments on Ceraunius and Hecates are not structurally controlled, in that they do not follow pre-existing fractures. Instead they have exploited and subsequently enlarged or reactivated pre-existing fluvial valleys.

The overall morphology of valleys formed on Noachian age surfaces seems to suggest that surface runoff was at least initially important in the formation of the degraded valleys. However, these valleys probably never developed into highly integrated valley systems, because of the relatively high permeablity of the Martian surface. With the emplacement of the intercrater plains, the style of valley formation changed to a more sapping dominated system where pre-existing valleys or fracture systems provided the locus for subsequent valley formation. Carr [6] noted that the rates of early valley development correlate with cratering rates. We add that the style of valley formation is also consistent with declining impact rates. Cratering rates were still fairly high when the degraded valleys were forming, releasing much of the trapped subsurface water into the surface environment and producing runoff in regions where surface permeabilities were low enough. At any given crater, surface water was probably initially fairly plentiful as a result of vigorous impact-induced hydrothermal circulation [7,8]. With time, hydrothermal circulation became increasingly restricted to the subsurface environment and valley development continued largely as a result of subsurface sapping processes. If the emplacement of the intercrater plains was at least partly volcanic in nature (the result of subsurface magmatic activity *e.g.*, sill intrusions) as suggested by Wilhelms and Baldwin [9], then even longer ($\geq 10^6$ years) hydrothermal circulation would be produced [8]. Near surface aquifers would be recharged with warm, upwardly migrating mineral-rich water and sapping processes would proliferate, reactivating existing valleys or forming new ones where underlying fractures and ground- water flow intersected with the surface environment. Some of this water would be lost to the atmosphere but much of it would infiltrate back into the permeable subsurface in local ice-free regions.

While widespread valley development on Mars ceased soon after the end of heavy bombardment, local areas of fluvial valley activity continued into the Hesperian in the Tempe, Electris and Casius regions [10] and probably also in the Mangala Vallis region [11]. Valley development in these regions appears to be controlled

largely by fractures. Valleys are enlarged, flat-floored and have extremely low drainage densities [10] which is consistent with a sapping origin. These networks probably formed initially as a result of locally intense volcanic activity [10]. Since these valleys are all located near the shore of the putative ocean, subsequent aquifer recharge could have been provided by earlier episodes of outflow channel discharges. The period of ancient glaciation [12] in the southern hemisphere appears to have occurred during this time.

The latest period of fluvial valley development documented so far occurred on the northern flank of Alba Patera. These valleys are Amazonian in age and are morphologically similar to those formed by rainfall-runoff processes on the Hawaiian volcanoes [3,4]. According to the model presented in Baker *et al.* [1], the last major episode of ancient ocean formation resulting from outflow channel discharges was relatively short-lived ($\leq 10^4$ years) and is concurrent with the formation of the Alba valleys [3,4]. Thus the brevity of this episode and the generally high Martian surface permeabilites precluded the formation of fluvial runoff valleys by atmospheric precipitation in all regions except in the lowest permeability, easily eroded zones on Alba Patera [3,4].

**REFERENCES** [1] Baker, V.R. *et al.* (1990), *LPSC XXI.*; [2] Baker, V.R. and Partridge, J.B. (1986) *J. Geophys. Res.* **91**, 3561–3572. [3] Gulick, V.C. and Baker, V.R. (1989) *Nature* **341**, 514–516. [4] Gulick, V.C. and Baker, V.R. (in press) *J. Geophys. Res.* [5] Barlow, N.G. (1989) *Icarus* **75**, 285–305. [6] Carr, M.H. (1989) *Icarus* **79**, 311–327. [7] Brakenridge *et al.* (1985) *Geology* **13**, 859–862. [8] Gulick *et al.* (1988) *LPSC XIX*, 441–442. [9] Wilhelms, D.E. and Baldwin, R.J. (1989) *LPSC XIX Proc.*, 355–365. [10] Grant, J.A. and Schultz, P.M. (1989) *NASA Tech. Memo.* **4130**, 382–383. [11] Chapman, M.G. *et al.* (1989) *USGS Map I-1962.* [12] Kargel, J. and Strom R. (1990), *LPSC XXI.*

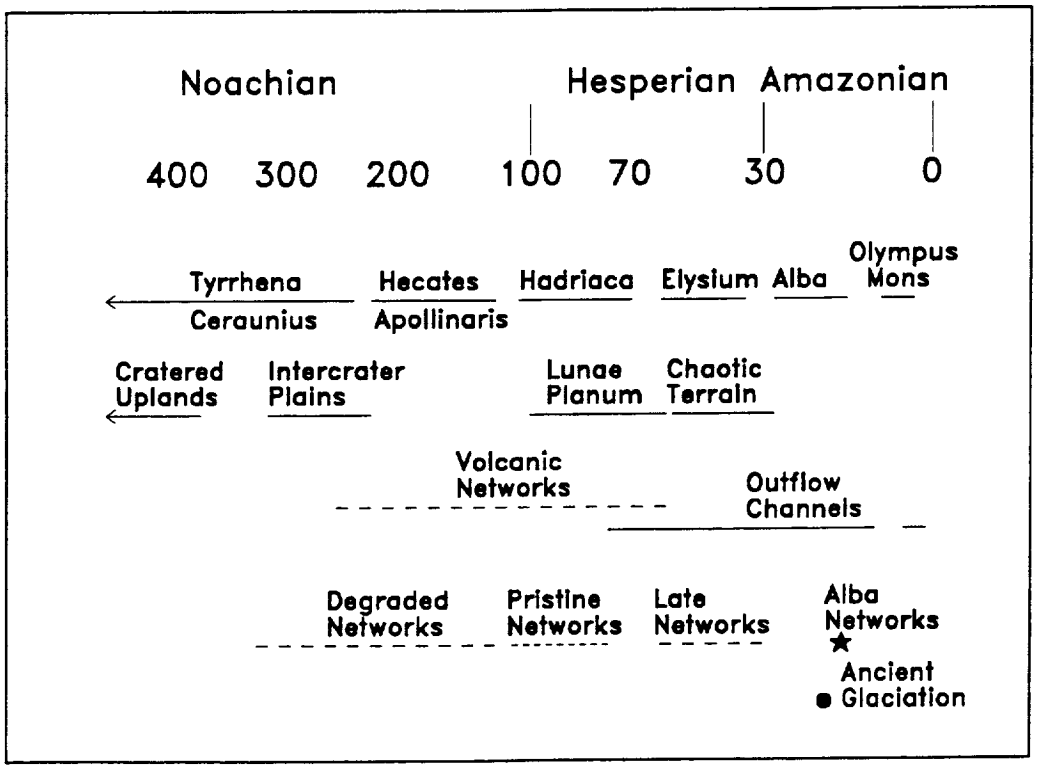


**Figure 1.** Relative ages of volcano, valley, and channel formation in Mars' history. Numbers represent crater densities, where crater density is defined as the number of craters $\geq$ 8 km diameter/$10^6$ km$^2$. Relative age data (crater densities) of volcanoes and terrain units taken from Barlow [5]. Relative age of ancient glaciation taken from Kargel and Strom [12]. Figure modified from Gulick and Baker [4].

## MORPHOMETRY OF FRESH IMPACT CRATERS IN HESPERIA PLANUM, MARS:

Joan Hayashi-Smith and Peter J. Mouginis-Mark, Planetary Geosciences Division, SOEST, University of Hawaii, Honolulu, HI 96822.

**INTRODUCTION:** We explore a concept originally proposed by Cintala and Mouginis-Mark (1) that martian impact craters display a gradual transition with increasing crater size from larger depth/diameter ratios at small diameters to lower values for larger craters. This correlation was interpreted to be the consequence of a pronounced stratification of volatiles within the target. Recent developments in the ability to use PICS software to make quantitative measurements of crater geometry have enabled us to test the hypothesis using craters located in a single region of Mars on the ridged plains materials of Hesperia Planum (~21 - 34°S, 233 - 248°W).

The origin of the ridged plains materials and their thickness within Hesperia Planum are currently unknown. Because of their similarity to the lunar maria, it is likely, however, that these materials comprise a series of flood lavas that partially infilled topographic depressions within the martian highlands. Measurements of crater diameter and the preserved heights of partially buried crater rims, provide estimates that these lava flows within Hesperia Plánum are between 200 - 400 meters thick (2). What is not clear is the spatial distribution of flow thickness or the physical characteristics of the buried terrain.

**SHADOW MEASUREMENTS:** Our sample contains 61 craters in the diameter range 2.00 - 48.72 km. Of these craters, 26 are morphologically very fresh, possessing complete rims, well preserved ejecta blankets with radial striations or sharp distal ramparts, and have no superposed impact craters. These freshest craters are 2.44 - 14.28 km in diameter, and are used here to investigate the possible role of volatiles in influencing impact crater geometry. Crater depth/diameter measurements were made using digital versions of the Viking Orbiter images and the PICS image processing software (Fig. 1). The resolution of each frame (~95 m/pixel) and the lighting geometry (incidence angle = 64 - 72°) of the crater center were used to convert measurements, in the number of pixels, into distances and shadow lengths and, hence, rim heights. Visual analysis of these images identified that some of the SEDR solar azimuth angle files are incorrect, so that we estimated the solar azimuth (i.e., the perpendicular to rim shadows for near-circular impact craters) for each frame. The average of three crater diameters was used for each crater, one diameter being measured in the same direction as the sun angle and two at about ± 45° to the solar azimuth. In all cases, the rim crest of the crater was taken to be the point where there was a rapid variation in the data number (DN) values (in PICS this typically corresponded to a change of 3 - 5 times the variation observed for illuminated terrains). The rapid increase in DN values was also used to determine the edge of the shadow and, from simple trigonometry, the height of the crater rim. For a few of the craters larger than ~4 km diameter, it was also possible to obtain measurements of the height of the far rim above the surrounding terrain (Fig. 2).

**DISCUSSION:** The original premise (1) was that sub-surface volatiles had a variable distribution with depth beneath the surface, but that either water or ice was distributed in fixed proportions over the age of the exposed surface. Clearly, as it is likely that volatiles were driven towards the poles over martian history (3), this concept of a constant volatile concentration with depth is unlikely to be valid. Our preliminary analysis of the Hesperia Planum craters fails to identify the gradual transition from small craters formed within a shallow (top 100 m?) permafrost layer within the target to larger craters formed with deeper, volatile-poor, strata below the permafrost (perhaps at depths of a few hundred meters). Based on our estimates of depth and rim height, several of the freshest craters would penetrate the entire 400 m thickness of the ridged plains materials (Fig. 3), excavating the crater floor within the basement materials. Although ejecta deposits are likely to originate from within the near-surface layers (based on analogy with the ejecta deposits associated with Ries Crater in West Germany; ref. 4), the slumping of the inner wall of the crater and the degree of floor rebound may be significantly affected by this strong stratification of the target materials. Although we cannot at this time identify the reason for this disparity between our results and earlier ideas (1), we offer two possible explanations:

1) Cintala and Mouginis-Mark (1980) measured craters on a variety of geological units, some of which may have contained fewer volatiles than did other units.

2) Our analysis has concentrated on the youngest, best-preserved craters within Hesperia Planum, specifically to avoid complications in crater geometry that may have been caused by erosion or subsequent infilling. Our criteria for recognizing these craters will thus bias our sample to preferentially include only the most recent craters, which may have formed at a time when the ridged plains materials of Hesperia Planum had become dessicated. By studying craters of different degradation states, it may still be possible to investigate the temporal evolution of the hypothesized volatile layer provided that subaerial modification processes can be accounted for.

**REFERENCES:** 1) Cintala, M.J. and Mouginis-Mark, P.J. (1980). Geophys. Res. Lttrs, 7, p. 329 - 332. 2) De Hon, R. A. (1985). Rpt. Plan. Geol. Prog., 1984, NASA TM-87563, p. 242 - 244. 3) Fanale, F.P.et al. (1986). Icarus, **67**, p. 1 - 18. 4) Horz, F. et al. (1983). Revs. Geophys. Space Phys., **21**, p. 1667 - 1725.

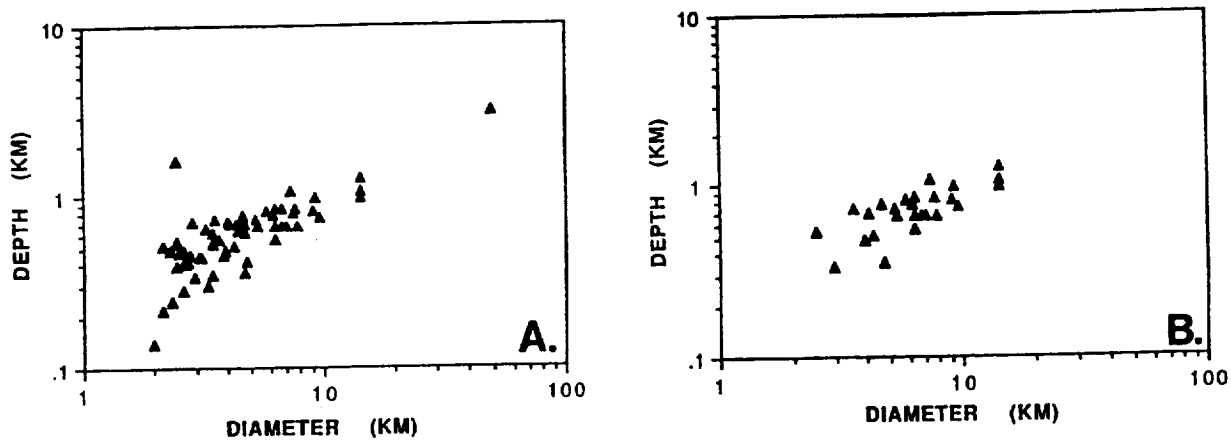


Fig. 1 A) Depth - diameter plot of all craters measured in this analysis. B) Depth - diameter plot of only those craters considered to be "pristine" in this analysis.

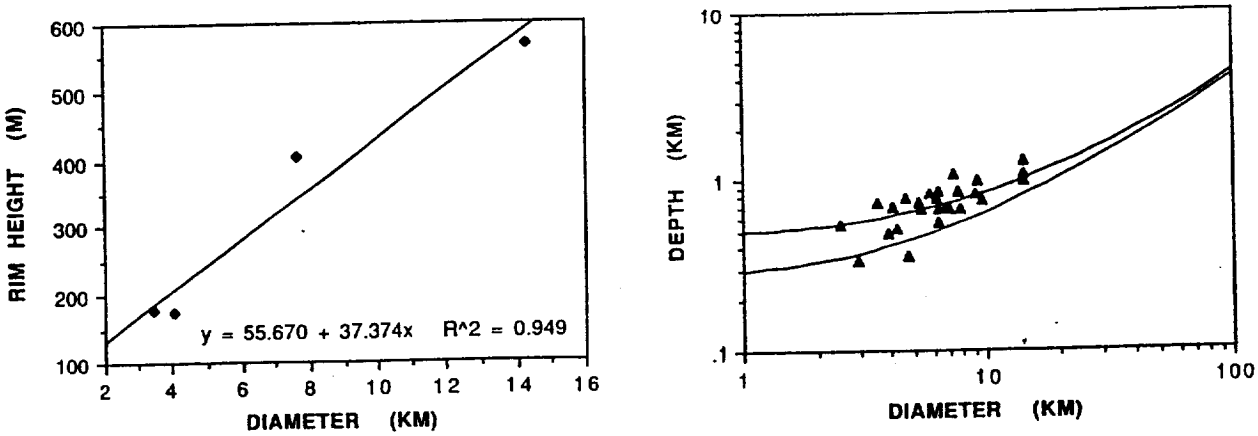


Fig. 2 (Left) Four of the studied craters possess measurable rim heights, permitting a linear least squares fit and, hence, the rim height to crater diameter relationship to be obtained. Fig. 3 (Right) Using the relationships between depth (Fig. 1) and rim height (Fig. 2) to crater diameter, the minimum depth of a crater that is required to penetrate the average thicknesses of the ridged plains materials can be inferred (2). Bottom curve - 200 m; top curve - 400 m plains thickness.

# WEATHERING AND EROSION OF THE POLAR LAYERED DEPOSITS ON MARS

K. E. Herkenhoff, Jet Propulsion Laboratory 183-501, Pasadena, CA 91109

The Martian polar layered deposits are widely believed to be composed of water ice and silicates, but the relative amount of each component is unknown. The "conventional wisdom" among Mars researchers is that the deposits were formed by periodic variations in the deposition of dust and ice caused by climate changes over the last 10 to 100 million years [1]. It is assumed here that water ice is an important constituent of the layered deposits, that the deposits were formed by eolian processes, and that the origin and evolution of the north and south polar deposits were similar.

Calculations of the stability of water ice in the polar regions of Mars [2,3] indicate that ice should not currently be present at the surface of the layered deposits. The present water ice sublimation rate is high enough to erode the entire thickness of the deposits in about a million years. This result suggests that sublimation of water ice from the layered deposits results in concentration of non-volatile material at the surface of the deposits. Such a surface layer would insulate underlying water ice from further sublimation, stabilizing the layered deposits against rapid erosion.

The color and albedo of the layered deposits suggests that bright, red dust is the major non-volatile component of the deposits. However, the differences in albedo and color between mantling dust and exposures of layered deposits in the south polar region [4] and the association of dark dune material with the north polar layered deposits [5] indicates that there is at least a minor component of dark material in the deposits. The dark material may be either sand or dust; each possibility is examined below. The dark material must either be intimately mixed with the bright dust in the layered deposits or occur in layers or lenses less than a few meters in size, or they would be visible in high-resolution Viking Orbiter images.

The presence of small amounts of dark sand in the layered deposits can account for the dark dunes that appear to have sources in the north polar deposits [5]. Poleward circulation during the summer is then required to transport sand into the layered deposits. The most significant problem with this hypothesis is the eolian codeposition of sand and dust in the polar regions. It is unlikely that sand can be carried in suspension by even a much denser Martian atmosphere, so that sand must be transported by saltation [5]. Saltating sand would eject dust into suspension, hindering codeposition of sand and dust. Although small amounts of sand may have saltated over frozen, cemented dust toward the poles, the difficulties with this scenario prompt consideration of alternative hypotheses. A theory for layered deposit formation and evolution involving only dust (bright and dark) and ice is proposed below.

How can dark dust in the layered deposits form the dunes observed in the polar regions? Sublimation of dust/ice mixtures has been shown to result in the formation of filamentary sublimation residue (FSR) particles about 100 microns in size [6]. Such particles can saltate along the Martian surface, and may therefore create dunes [7]. In order to form saltating material by this mechanism that is at least 3 times darker (in red light) than the bright dust that mantles much of Mars, dark dust grains must preferentially form FSR particles. Magnetic dust grains would be expected to form FSR more easily than non-magnetic dust, and are probably much darker. Experimental formation of FSR with magnetic material has not been attempted, and should be the subject of future research.

There is direct evidence for 1-7% magnetic material in the surface fines at the Viking lander sites [8]. In addition, analysis of Viking lander sky brightness data indicates that suspended dust over the landing sites contains about 1% opaque phase, perhaps of the same composition as the magnetic material on the surface [8,9]. Within the uncertainties of these measurements, the percentages of magnetic material given above are identical to the volume of dark dune deposits in the polar regions expressed as a percentage of eroded layered deposits (Table 1). This comparison indicates that the presence of magnetic material in the layered deposits is likely, and that formation of sand dunes from dark FSR particles is plausible.

In summary, weathering of the layered deposits by sublimation of water ice can account for the geologic relationships observed in the polar regions. The non-volatile component of the layered deposits appears to consist mainly of bright red dust, with small amounts of dark dust or sand. Dark dust, perhaps similar to the magnetic material found at the Viking Lander sites, may preferentially form filamentary residue particles upon weathering of the deposits. Once eroded, these particles may saltate to form the dark dunes found in both polar regions. Eventual destruction of the particles could allow recycling of the dark dust into the layered deposits via atmospheric suspension. This scenario for the origin and evolution of the layered deposits is consistent with the available data.

## REFERENCES

[1] Carr, M. H. (1982). *Icarus* **50**, 129-139.
[2] Toon, O. B., J. B. Pollack, W. Ward, J. A. Burns, and K. Bilski (1980). *Icarus* **44**, 552-607.
[3] Hofstadter, M. D. and B. C. Murray (1990). *Icarus*, in press.
[4] Herkenhoff, K. E. and B. C. Murray (1990). *J. Geophys. Res.*, in press (Mars polar processes issue).
[5] Thomas, P. C. and C. Weitz (1989). *Icarus* **81**, 185-215.
[6] Storrs, A. D., F. P. Fanale, R. S. Saunders, and J. B. Stephens (1988). *Icarus* **76**, 493-512.
[7] Saunders, R. S., T. J. Parker, J. B. Stephens, E. G. Laue, and F. P. Fanale (1985). *NASA Tech. Mem.* **87563**, 300-302.
[8] Hargraves, R. B., D. W. Collinson, R. E. Arvidson, and P. M. Cates (1979). *J. Geophys. Res.* **84**, 8379-8384.
[9] Pollack, J. B., D. Colburn, F. M. Flasar, R. Kahn, C. Carlston, and D. Pidek (1979). *J. Geophys. Res.* **84**, 4479-4496.
[10] Thomas, P. (1982). *J. Geophys. Res.* **87**, 9999-10008.

Table 1

| Quantity | Fraction | Reference |
|---|---|---|
| Magnetic material in surface fines | 1-7 % | [8] |
| Opaque phase in atmospheric dust | 1 % | [9] |
| Volume of dark dunes/volume of eroded polar deposits | 1-10 % | [10] |

**WHAT'S WRONG WITH PHOTOCLINOMETRY?** D. G. Jankowski and S. W. Squyres, Department of Astronomy, Cornell University, Ithaca, NY 14853

Topographic data on surface features of planets and satellites are useful in the study of these bodies. Direct measurements of topography are rare. Due to its simplicity and speed, the technique of photoclinometry, which determines surface slopes from brightness variations on spacecraft images, continues to be very popular (1-6). However, photoclinometry will not give reliable results in all cases. Thus it is important that topographic data derived from photoclinometry, like any other data, are not used without associated error estimates.

Photoclinometrically determined slopes contain errors from the following sources:

i. Image noise: Image noise is a source of error because it produces spurious intensity fluctuations from pixel to pixel.
ii. Digitization: The digitization of brightness levels in all spacecraft images results in an inherent slope uncertainty.
iii. Background: An incorrect dark current will introduce systematic errors.
iv. Photometric function uncertainties: An an improper photometric function is obviously a source of error.
v. Albedo errors: The surface albedo can be a source of error both due to uncertainties in the mean regional albedo (often assumed constant) and due to albedo variations.
vi. Atmospheric effects: An atmosphere can be a source of error due both to uncertainties in the mean contribution of light scattered and due to fluctuations of this contribution across the image.
vii. Scanline misallignment: Most photoclinometry techniques are one-dimensional, determining the topography only along a specified line. Such techniques are typically restricted to scanlines that travel directly up or down all slopes. Hence slope errors can also occur due to the misallignment of scanlines.
viii. Viewing and lighting geometry uncertainties: The errors associated with viewing and lighting geometry uncertainties associated with recent spacecraft are for the most part insignificant compared to other errors, and will not be discussed.

We have performed an investigation of the quantitative effect of each of these error sources on the photoclinometric method. The error contributions due to the above sources are modelled under conditions appropriate for spacecraft images of Ganymede and Mars. The characteristics of Viking Orbiter images are used for modelling Mars and the characteristics of Voyager images are used for Ganymede. The noise characteristics of the Galileo camera are included as a comparison with the Voyager cameras. The Lommel-Seeliger photometric function is used to model grooved terrain on Ganymede (1), and the Minnaert function is used to model the surface of Mars (5).

Photoclinometric slope uncertainties due to the above sources have been plotted on photometric latitude-longitude grids for phase angles of 30°, 60°, and 90°. Slope errors are investigated for "actual" slopes of 0°, 10° (sloping away from the sun), and -10° (sloping towards the sun). Slope errors are also investigated for rotation angles (the angle subtended by the scanline direction and the local photometric latitude line) ranging from 30° to -30°.

At small incidence angles, the photometric functions change very slowly; thus small brightness variations in this region correspond to large topographic slopes. Hence the effects of albedo variations, atmospheric variations, noise, and digitization are all enhanced near the subsolar point. This is clearly seen in Figures 1a and 1b, which show contours of the slope error due to a 5% albedo variation on Mars and Ganymede, respectively. The errors in Figure 1 were calculated for a point with 0° slope along a scanline with a rotation angle of 0°. The phase angle is 60°. Albedo variations are inevitably a significant error source in photoclinometry.

The noise levels characteristic of the Viking and Voyager cameras result in significant slope errors at low incidence angles. The errors associated with Viking images are the largest, near 2° at the subspacecraft point at 60° phase. The errors associated with the Galileo camera are still uncertain, primarily due to uncertainties in the effects of the harsh radiation environment. Using noise values characteristic of the CCD detector suggests that the slope error attributable to Galileo noise will be essentially negligible. For all images considered, errors associated with digitization and incorrect dark currents are negligible compared to noise errors.

The Martian atmosphere clearly can not be ignored when doing photoclinometry. However, with the help of resolved shadows (5), the contribution of the atmosphere can be estimated fairly well in many Viking images. The atmospheric contribution can often be estimated with less than 10% error. Fluctuations within a given image are small, usually much less than 5%. The errors associated with these uncertainties are less than 1°.

Errors due to uncertainties in the Minnaert K parameter are generally not larger than 1°. However, for large slopes and large rotation angles, this error source can become much more significant, even at large incidence angles, where other errors sources disappear.

Errors due to misallignment can be significant if the misallignment angle is larger than about 10°. The errors tend to be larger for the Minnaert function than for the Lommel-Seeliger function, and they tend to be smaller for lower rotation angles (scanline directions chosen parallel to lines of photometric latitude) for both functions. For the Minnaert function, scanlines pointing away from the sun are more accurate when pointing away from the photometric equator at a given angle than when pointing towards the equator at the same angle.

Slope errors are usually larger for sun-facing slopes than for slopes facing away from the sun. This effect is generally stronger for the Lommel-Seeliger photometric function than it is for the Minnaert function. The errors associated with uncertainties in the Minnaert K parameter and with scanline misallignment both increase significantly with increasing slope.

Slope errors decrease with increasing phase angle. The optimal phase angle for photoclinometry is about 60°. Smaller phase angles result in larger errors, while larger phase angles result in smaller adequate surface areas and larger geometric foreshortening.

Slopes determined using photoclinometry contain errors from a number of different sources. The size of the error varies significantly depending upon the imaging system used, the lighting and viewing geometry, and the nature of the surface imaged. Hence, photoclinometry codes should always include error estimates with each topographic profile to help determine their reliability.

**References:** (1) Squyres, S. (1981) *Icarus* **46** 156-168. (2) Davis, P., Soderblom, L. (1984) *J.Geophys.Res* **89** 9449-9457. (3) Moore, J., McEwen,A., Albin,E., Greeley,R. (1986) *Icarus* **67** 181-183 (4) Jankowski, D., Squyres, S., (1988) *Science* **241** 1322-1325. (5) Tanaka, K., Davis, P. (1988) J.Geophys.Res **93** 14893-14917. (6) Schenk, P. (1989) *J.Geophys.Res* **94** 3813-3832.

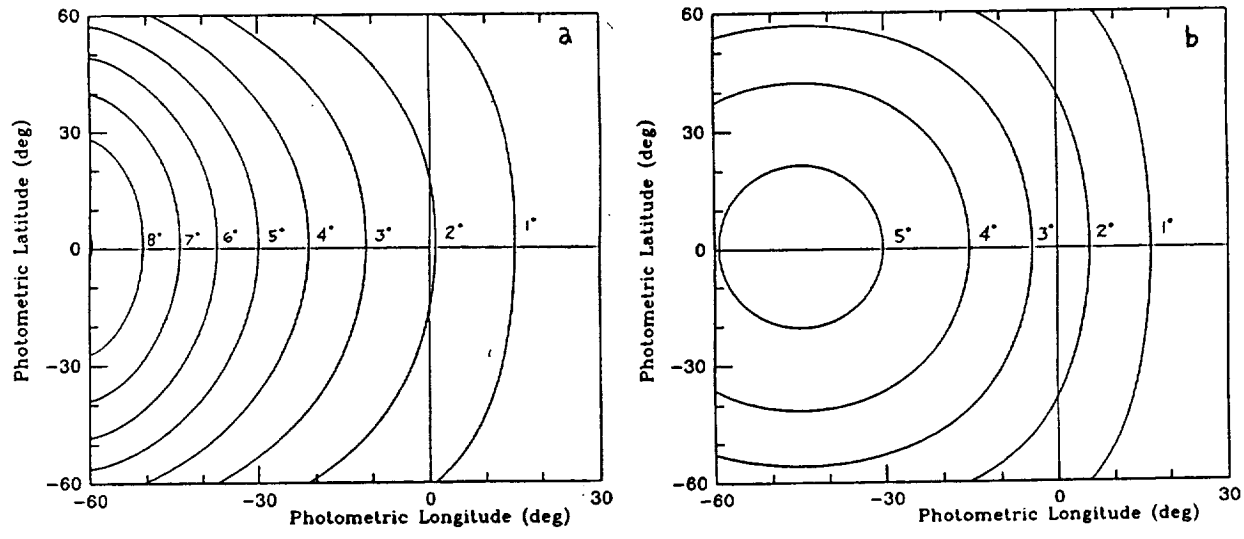


**Figure 1.** a) Contours of slope errors due to a 5% albedo error on Mars. b) Contours of slope errors due to a 5% albedo error on Ganymede.

FURTHER EVIDENCES FOR HORIZONTAL BLOCK-/PLATE MOVEMENTS AND/OR NAPPE TECTONICS WITHIN THE TANOVA - UPDOMING AND ALONG ITS MARGIN,MARS

Heinz - Peter Jöns, Geologisches Institut der T.U. Clausthal; Leibnizstrasse 10; 3392 Clausthal-Zellerfeld; F.R.Germany

Earlier investigations of the relief of the martian uplands led to the discovery of an old volcanicprovince south of the Tharsis-dome and the Claritas Fossae (1). Additional detailed investigations of the relief of the entire area of the martian uplands led to the discovery of the existence of at least about one more dozen very old unclassified volcanoes (shield- or stratovolcanoes?) which are situated exclusively within the oldest parts of the martian uplands. These volcanic edificies are predominantly arranged along ancient linear or curvilinear zones of weakness. The spatial distribution of these very old volcanoes is of special interest and allows the identification of four groups:

-) The first group which has been described as new volcanic province is clustered along arcuate zones of weakness east and west of the Claritas Fossae and is arranged concentrically with respect to the Noctis Labyrinthus-dome.
-) The second group consists of volcanoes which are clustered along very old linear features (grabens?).
-) The third group is probably impact-related, because these features are situated along concentric features in the vicinity of Hellas and probably in the vicinity of Isidis as well.
-) The remaining volcanoes of this type seem to occur with a random distribution in the oldest parts of the martian uplands. A relation of these structures to any tectonic feature(s) is so far not detectable (2).

Detailed studies of the area which containes these volcanoes led to the conclusion that block movements and/or nappe tectonics have happened in the early martian history which led to the formation of an arcuate zone of collisional features in the surrounding of the TaNoVa-updoming(3, 9 ). The most important and most obvious hints for the existence of a probable zone of collision east of the Claritas Fossae is indicated by:

a) subparallel compressional features (narrow ridges),
b) rows of so called flat irons,
c) features of overthrusting (nappe tectonics),
d) and a cuesta landscape which runs parallel to the latter features (Fig. 1).

All these features are arranged concentrically with respect to Syria Planum. They form a belt which is appr. 100 - 200km wide.

As the boundary of the TaNoVa- Updoming is clearly indicated along its eastern and southern margin between the Valles Marineris and the Claritas Fossae (sector A) it is a task which suggests itself to look for similar features along its western margin within sector B. Although the western boundary is less clearly indicated by the relief it is noteworthy that the same set of features with the same spatial distribution which is typical for sector A can be detected between $-30^{\circ}$ and $-55^{\circ}$ lat. and between $160^{\circ}$ and $190^{\circ}$ long. as well:

a) arraged concentrically with respect to Arsia Mons/Syria Planum wrinkle ridges,
b) arranged concentrically compressional ridges together with series of so called flat irons and probable thrust fronts,
c) a prominet radial shear zone which has cut and reshaped a large mountain into a unique set of lamellar ridges,
d) rows of very old unclassified volcanoes (4),
e) many compressed impact structures the longer axis of which runs tangential with respect to the margin of the TaNoVa-updoming within sector B, (Fig. 2).

It is noteworthy that the large impact basin Orcus Patera which is situated along the northern continuation of this area is highly deformed as well with the same orientation of its longer axis (5).

Due to the spatial distribution of the described features (c o n c e n t r i c a l l y with respect to Syria Planum, the most elevated area of the TaNoVa-updoming with a maximum elevation of about 10 000) the supposition seems to be justified that the whole set of concentric features can be interpreted as a fossil embryonic mountain range which probably indicates plate and/or block tectonicstogether with younger nappe tectonics along the border of the southern half of the TaNoVa-updoming.

The distribution of large-scale r a d i a l features reveals additional hints for block/ plate margins in that area. The young (recent?) volcanism in the Valles Marineris (6) could indicate a probably still active spreading axis. A similar type of endogenic activity is imaginable with respect to the origin of Alba Patera and its remarcable rift-like features (7). If this hypothesis is right it seems to be an obvious conclusion that the northern branch of the Kasei Valles may be interpreted as indicating an axis of descending material (8). In this context it should be pointed out that Tharsis Tholus which is situated exactly on the southwest extension of the northern branches of the Kasei Valles is the only martian volcano which has been cut and sheared along linear features. Hence, intensive tectonic stresses must have acted along that axis. The Claritas Fossae which are the boundary between sector A and B of the TaNoVa-updoming remain a mystery. But the ancient volcanoes along the southern part of that prominent linear structure justify the supposition that this feature indicates a block boundary as well (Fi. 3).

References

1) Scott, D.H. and Tanaka, K.L. (1981), Proceedings of the XIIth Lun. and Plan. Sci. Conf., 1449 - 1458.
2) Jöns. H. - P. (1990), The Mars, Global Map of Mars, in press.
3) Jöns, H. - P. (1982), ESA SP - 185, (Proceedings), 89 - 105.
4) Scott, D.H. and Tanaka, K.L. (1986), Geologic Map of the Western and Equatorial Region of Mars, U.S.G.S., I - 1802-A.
5) Jöns, H. - P. (1984), Lun. and Plan. Sci. XV, Abstracts, Part 1, 415 - 416.
6) Lucchitta, B.K. (1985), Lun. and Plan. Sci. XVI, Abstracts, Part 2, 503 - 504.
7) Raitala, J. (1988), Earth, Moon, and Planets 42, 277 - 291.
8) Jöns. H. - P. (1989), Lun. and Plan. Sci. XX, Abstracts, Part 2, 486 - 487.
9) Jöns, H. - P. (1989), Lun. and Plan. Sci. XX, Abstracts, Part 2; 484 - 485.

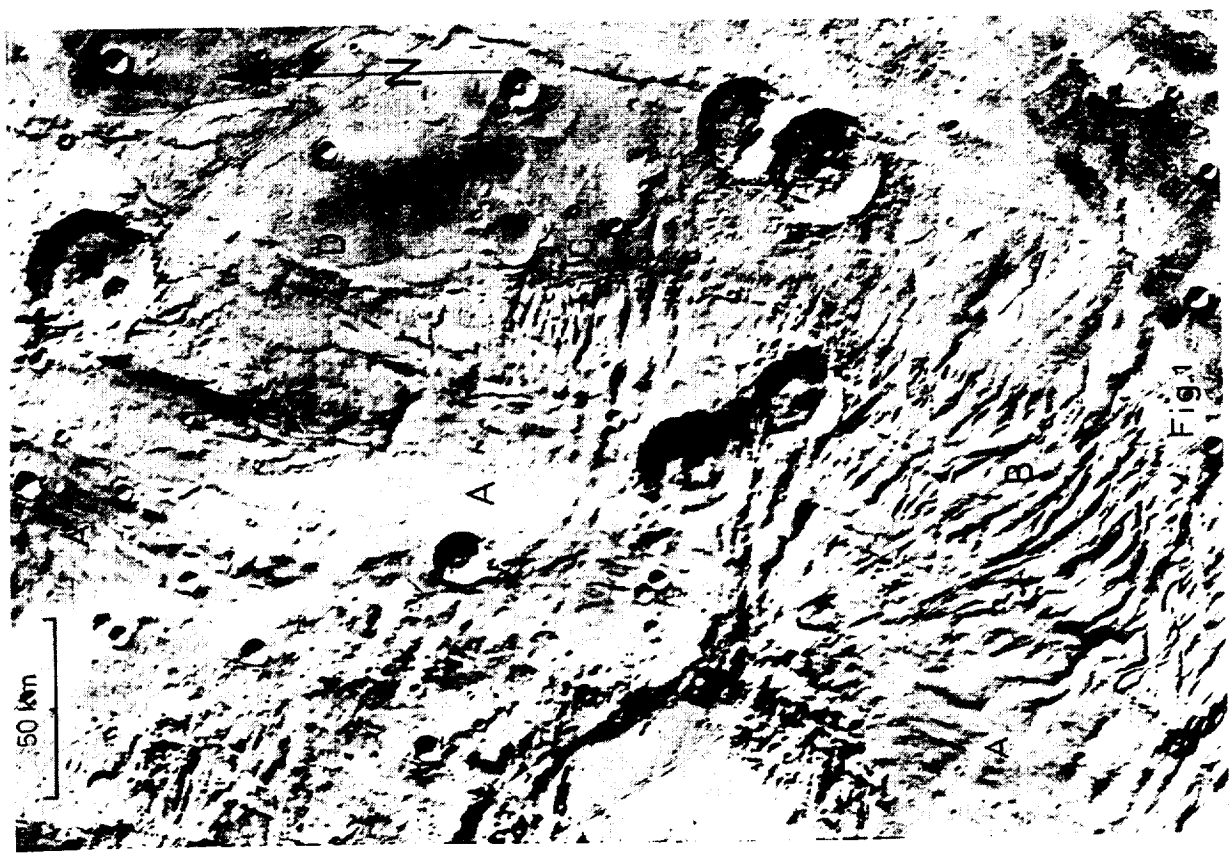


LEGEND (Fig.3)

Ancient martian uplands (undivided) with prominent impact structure

Fronts of compression with embryonic (collisional?) mountain ranges and very old unclassified volcanoes; arranged concentrically with respect to Syria Planum and Alba Patera, resp. Arrow indicates direction of compression. Note gap behind obstacles (P), i.e. pressure shadow!

Presumed (fossil?) axis of probable spreading

Presumed (fossil?) axis of probable descending of material

Fig. 1
Eastern margin of the TaNoVa - Updoming in sector A: Compressional ridges (A); rows of so called flat irons (B); cuesta landscape (C); and front of overthrusted material (D).

Western margin of the TaNoVa - Updoming in sector B: Thrust front (arrow 1); vergency of wrinkle ridges, same vergency as in the case of the thrust front! (arrow 2); rows of so called flat irons (arrow 3); subparallel compressional ridges (arrow 4); and sheared mountain with lamellar ridges (5).

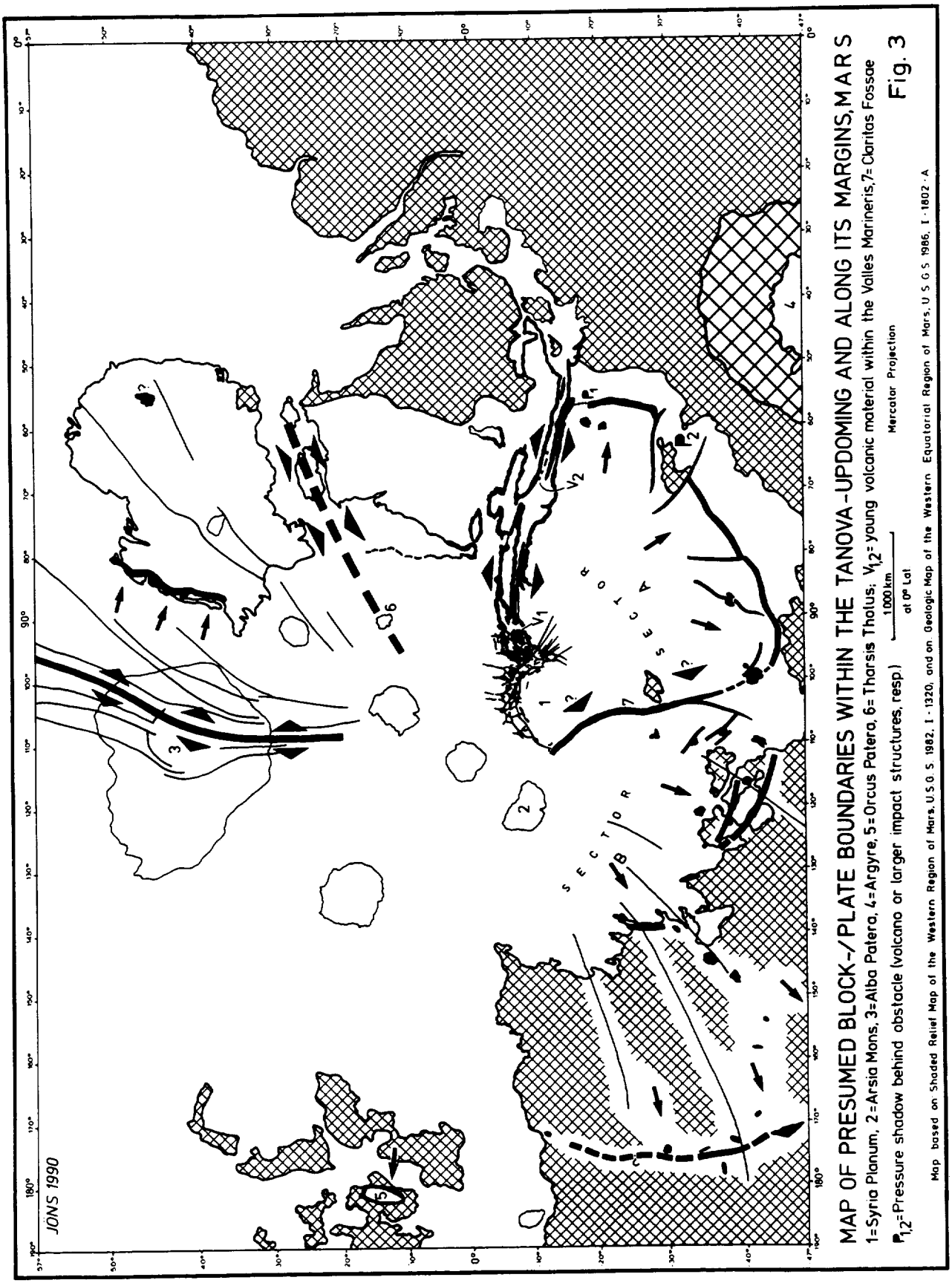
JONS 1990
MAP OF PRESUMED BLOCK-/PLATE BOUNDARIES WITHIN THE TANOVA-UPDOMING AND ALONG ITS MARGINS, MARS
1=Syria Planum, 2=Arsia Mons, 3=Alba Patera, 4=Argyre, 5=Orcus Patera, 6=Tharsis Tholus; V1,2= young volcanic material within the Valles Marineris, 7=Claritas Fossae
P1,2=Pressure shadow behind obstacle (volcano or larger impact structures, resp.)
1000 km at 0° Lat
Mercator Projection
Map based on Shaded Relief Map of the Western Region of Mars, U.S.G.S. 1982, I-1320, and on Geologic Map of the Western Equatorial Region of Mars, U.S.G.S. 1986, I-1802-A
SECTOR B
CHASMA
Fig. 3

# THE PLANET MARS: PRESENTATION OF A GLOBAL MAP

Heinz - Peter Jöns, Geologisches Institut der T.U. Clausthal; Leibnizstrasse 10; 3392 Clausthal - Zellerfeld; F.R. Germany

A global map of Mars will be presented at a scale of 1:30 Mill. with the projection of HAMMERś equal area planisphere. Four main sets of morphologic units have been outlined on this map - beside the most prominent impact structures Argyre, Isidis, and Hellas which form units of its own:

1) The ancient martian uplands (predominantly southern hemisphere),
2) the updomings of Tharsis, Noctis Labyrinthus, and Valles Marineris (= TaNoVa), and Elysium,
3) the lowlands of Mars (predominantly northern hemisphere), and
4) the polar caps.

The main purpose of this map is to demonstrate the relief genesis, the relief dynamics, and (as a result of both) the now existing relief division. It is obvious that the bulk of activities which reshaped the planets primitive relief has happened in the area of the TaNoVa - and the Elysium - updomings and along their margins.

Large - scale depressions which occupy the centre of the TaNoVa - updoming have been interpreted as a result of melting of permafrost and/or ground ice which led to the origin of giant progressive chaotic terrains. During their activity these features delivered their mobilized material (mud, aqueous slurry, debris, water) into the already existing circumpolar depression of the northern hemisphere of Mars which led to the origin of some generations of fossil (mud) oceans in that area (1).

A reactivation (or simply continuation?) of the Tharsis (and Elysium?) volcanism resulted in a large - scale flooding of the adjacent permafrost - related depressions (meltplains) with younger lavas. But remnants of these meltplains have been preserved along the border of the Tharsis - updoming (arcuate escarpments and a set of special morphologic features northwest of Olympus Mons). Smaller (catastrophic?) outflow events happened into the Chryse Planitia, within Isidis Planitia, probably into Hellas Planitia, and in the vicinity of the South Pole and from that area into Argyre Planitia (2). The youngest fossil (mud) ocean within the lowlands of the northern hemisphere was probably the result of polar basal melting (3).

The general border of the TaNoVa - updoming south of the equator is indicated by a special set of morphologic features (wrinkle ridges, zones of compression, rows of so called flat irons, a cuesta landscape, and numerous very old unclassified relatively small volcanoes) which are mainly arranged concentrically with respect to Syria Planum, the most elevated area of the TaNoVa - updoming. That set of features -together with the much younger giant shield volcanoes and the large linear tectonic features to wich they are closely related- offers the possibility to identify areas of nappe tectonics (mainly together with concentrically arranged features) as well as (fossil?) embryonic block/plate boundaries (mainly with radially arranged linear features), (4).

This global map will show for the first time the dynamic events and their results described above together with many other important features of the planetś entire surface. The map will be printed at the Lithographisches Institut, Potsdamer Str. 91, Berlin, F.R.Germany; it will be available from August 1990 from that institute.

References

1) Jöns, H. - P. (1990), Geologische Rundschau, 79/1, 131 - 164.
2) Jöns, H. - P. (1987), Lun. and Plan. Sci. XVIII, Abstracts, Vol.2, 470 - 471.
3) Clifford, S.M. (1987), J. of Geophys. Res., 92, No, 89, 9135 - 9152.
4) U.S. Geological Survey (1979 - 1985), Atlas of Mars, 1:2 Mill. Topographic Series, 140 sheets of the "Controlled Photomosaic" - version.

SCIENTIFIC AND ENGINEERING APPLICATIONS OF THE MARS-GLOBAL REFERENCE ATMOSPHERIC MODEL (MARS-GRAM): Justus, C.G. and James, Bonnie

Results and applications for a new model of the Martian atmosphere are discussed. The Mars Global Reference Atmospheric Model (Mars-GRAM) is based on parameterizations to approximate, as realistically as possible, the temperature, pressure, density and winds of the Martian atmosphere, and their latitudinal, longitudinal, diurnal, seasonal and altitude variation, from the surface through thermospheric altitudes. Parameterizations are also included for the effects of global-scale dust storms on the variations of the thermodynamic and wind properties of the Martian atmosphere. Mars-GRAM is written in Fortran 77, and is designed to run on an IBM-PC or compatible microcomputer. With the planned addition of radiation budget parameterizations, Mars-GRAM will have a variety of possible scientific applications as a "poor man's global circulation model" for the atmosphere of Mars. Among these are: (1) an ability to provide realistic, geographically and seasonally-dependent backgrounds of temperature and wind for studies of tides and atmospheric propagation of other wave disturbances (e.g. gravity waves, mountain lee waves, etc.); (2) similar background fields of temperature and pressure for other environmentally varying physical processes (e.g. cloud nucleation process models, temperature-dependent chemical rate models, etc.); (3) studies of surface radiation budget, boundary layer dynamics, and synoptic and global-scale dynamics; and (4) investigations of the surface-atmosphere flux of dust and the zonal and meridional transport of dust during local-scale and global-scale dust storms. In addition, a number of mission-oriented engineering applications are envisioned for Mars-GRAM (e.g. aerocapture mission profile studies, Mars Rover Sample Return mission planning and design studies, Mars 94 balloon heating loads and trajectory studies, etc.). Figures 1-4 show samples of the output which can be produced by the Mars-GRAM program.

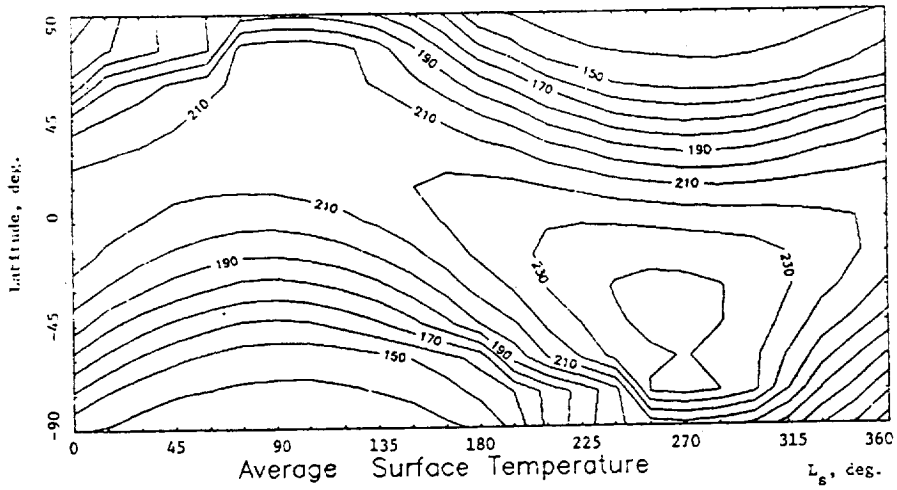


Figure 1 - Seasonal and latitudinal variation of daily average surface temperature, computed by the Mars-GRAM model. $L_S$ is the areocentric longitude of the sun.

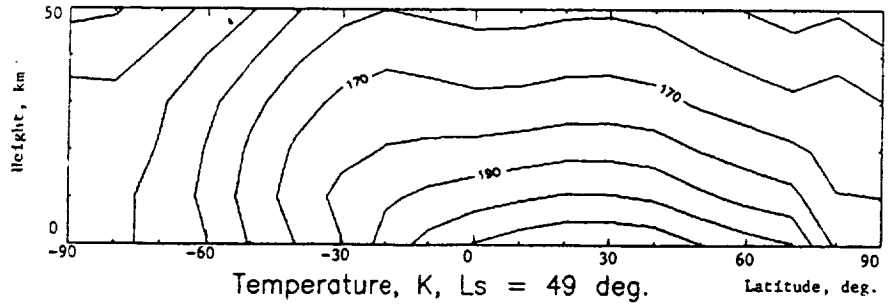


Figure 2a - Cross section of temperature (K) at 9 am local time for $L_s$ = 49°.

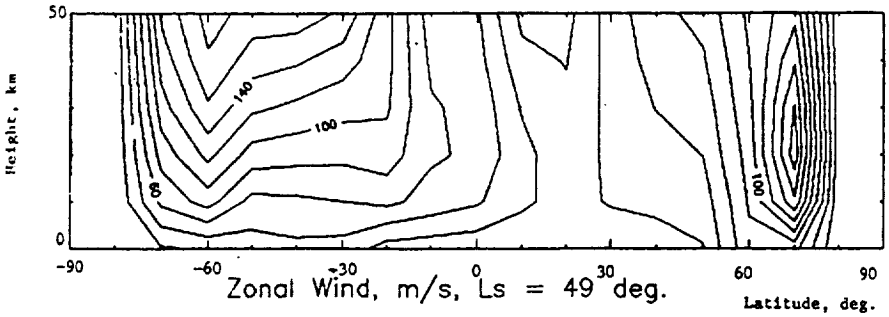


Figure 2b - Cross section of zonal wind (m/s) at 9 am local time for $L_s$ = 49°.

Figure 3 - Progression of simulated dust-storm effect on daily average, maximum and minimum temperature versus latitude and $L_s$ value (degrees) for the 1977b storm.

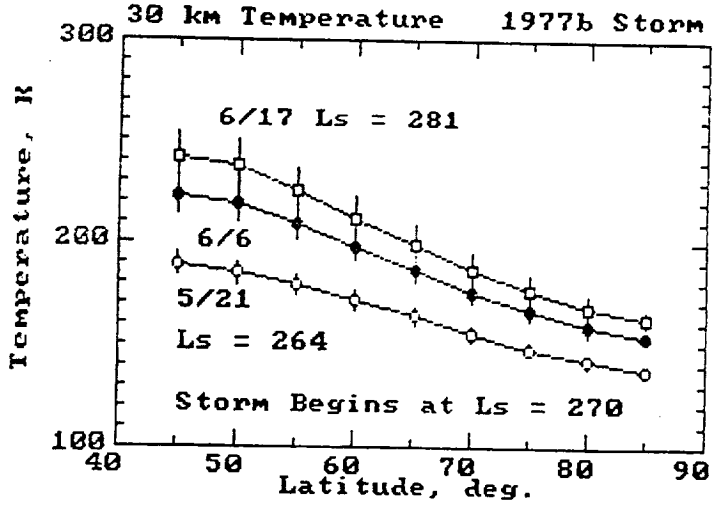


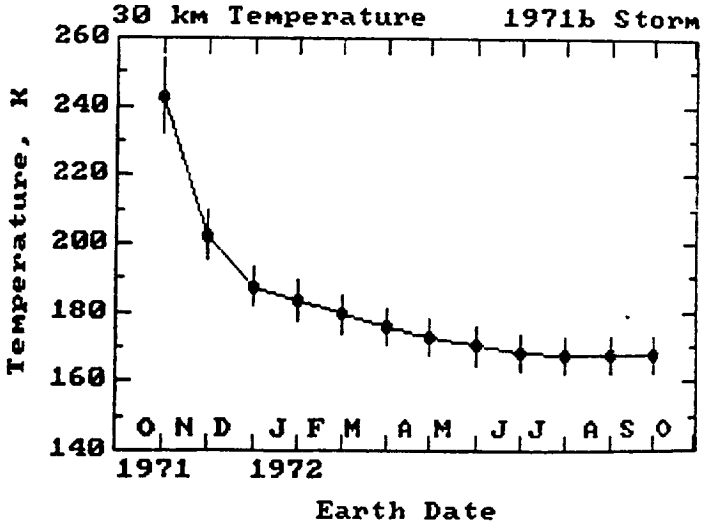


Figure 4 - Progression of simulated dust-storm effect on daily average, maximum and minimum temperature versus time at latitude at 25°S for the 1971b storm.

**Ancient Glaciation on Mars** J.S. Kargel and R.G. Strom, Lunar and Planetary Laboratory, University of Arizona, Tucson, AZ 85721

Photogeologic evidence for widespread ancient episodes of glaciation has been discovered in Viking spacecraft images of Mars. The principal image base used for this study consists of the USGS 1:2 million scale photomosaics of the MC-26 Quadrangle and the Viking Orbiter images obtained on orbits 349S, 352S, 567B, 568B, 569B, and 574A. We recognize that non-glacial mechanisms may adequately explain certain individual types of landforms discussed below. However, we believe that a glacial hypothesis provides a more acceptable unified explanation, and is consistent with the emerging outlines of a global hydrologic model [1].

Figure 1 is a glaciological map of a region the Charitum Montes and the adjoining Argyre Planitia. The most startling feature in this region is an anastomosing system of sinuous ridges, noted previously [2-5]. The plan of this ridge system (Viking Orbiter frames 352S34 and 567B30-35) is fluvial in character and must therefore have an underlying fluvial explanation (volcano-tectonic processes can not generate this pattern). The possibility that similar ridge systems elsewhere on Mars are glacial eskers has been previously noted [2](eskers are stream deposits of sand and gravel originally layed down on the surface of, within, or beneath stagnant, melting glaciers). The esker hypothesis is lent support by the similarity in length, height, width, overall structural plan, and detailed structure of the Martian features compared to large terrestrial eskers associated with the melting of Late Pleistocene and modern ice sheets on Earth [6, 7].

Figure 1 also shows the characteristic structure of the mountainous inner ring of Argyre, including numerous valleys separating sharp linear to semi-circular ridges. The characteristics of this mountain range, if considered with a terrestrial perspective, are diagnostic of alpine-type glacial erosion. The Charitum Montes appear to be a classic glacial assemblage of horns, cirques, and aretes, with intervening valleys mantled by lobate debris aprons. A prominent cirque near 54°30'S. Lat. 31°30'Long. is intimately associated with a region of fluvial deposition and erosion interpreted to be a glacial outwash deposit (sandur plain). Another region of fluvial erosion and deposition, near 54° S. Lat. 37° Long., emanates from a large glacially modified valley in the Charitum Montes and is interpreted as a glacio-lacustrine delta.

Large-scale glacial fluting was severe in Argyre Planitia during the height of the ancient ice age. The scouring of several large impact crater rims (e.g., frame 568B33) demonstrates that a considerable interval of time elapsed between the Argyre impact and the glacial epoch. In the area mapped in Figure 1 (450,000 $km^2$) there are seven fresh impact craters larger than 10 km in diameter displaying fresh ejecta and sharp rims and lacking any signs of glaciation, suggesting an early Amazonian termination of the glacial epoch. The extensive ejecta blanket of the large crater Galle (not one of the seven) covers about a third of Argyre Planitia, and clearly mantles many glacial grooves and ridges (e.g., frame 352S39). However, the delta-like fluvial system mentioned above erodes and elsewhere embays the ejecta blanket of Galle; further, smooth layered deposits, interpreted as glacio-lacustrine sediments associated with the esker system, embay Galle's ejecta blanket (frames 567B36 and 568B09); finally, a channel, either glacial or possibly fluvioglacial, incises the rim of Galle (frame 352S24). Hence, Galle dates from the glacial epoch (or an interglacial). Impact into an ice sheet is suggested by the extensive occurrence of ice disintegration features (e.g., kettle holes) on the ejecta blanket of Galle (frame 568B12). Possibly an underlying ice sheet, or perhaps anomalously large quantities of ice entrained in the ejecta itself, later melted or sublimated.

Kettle fields outside the area of Galle's ejecta testify to the retreat of the ice sheet and the stranding of large blocks of ice on Argyre Planitia (frame 568B53). Together with the eskers and outwash deposits these landforms record the melting of the Argyre ice sheet, *indicating a period of relatively warm climate even at moderately high elevations and latitudes.* However, the absence of super-imposed fluvial systems (other than those plausibly related to the melting of ice) indicates that *humid conditions following the ablation of the ice sheet were short-lived.* We note that the northern rim escarpment of Argyre has been fluvially modified and lacks evidence of glaciation, as if it rained there probably at the time that it snowed at higher latitudes.

We have made a preliminary search for possible glaciogenic landforms elsewhere on Mars. The single most diagnostic glaciogenic landform on Mars probably is the esker. Eskers are widespread in the Southern Hemisphere of Mars, often occurring in close association with polar layered deposits and etched (kettled and/or glacially scoured?) terrains; these probably indicate that a vast ice sheet once enveloped much of the Southern Hemisphere down to about 40° S. Lat. Eskers also occur more sparingly in the Northern Lowlands north of 26° in close association with the "thumbprint terrains" (recessional moraine fields?), and in one tropical location.

The final ablation of the southern ice sheet must have occurred under much warmer conditions and under a denser atmosphere than currently prevail. Glaciation and de-glaciation may have been two steps

in a global hydrologic cycle. Possibly Oceanus Borealis [1] supplied the atmosphere with water vapor which then was cold-trapped as snow or frost in the high elevations of the Southern Hemisphere. As the climate warmed due to climatic perturbations related to the formation of Oceanus Borealis the ice sheet eventually melted, charging the cratered uplands with groundwater. Given sufficient permeability this groundwater may have flowed northward to re-charge the equatorial region. Volcanism-driven outbursts of groundwaters may have re-filled Oceanus Borealis, completing the cycle, possibly on a repeating basis [8, 9].

Finally, we suggest that the nature and significance of the lobate debris aprons at high- and mid-latitudes on Mars [10] should be re-evaluated. It is generally thought that these debris aprons are rock glaciers. The outstanding issue is whether they are purely periglacial rock glaciers where down-slope motion is generated by gelifluction (surficial freeze-thaw), or whether the debris aprons are ice-cored rock glaciers where a rocky lag has accumulated on the surfaces of old glaciers by processes of melting and/or sublimation [11]. Figure 1 shows that debris aprons are commonly associated with individual cirques, suggesting a glacial origin.

References. 1) V. Baker et al., 1990, *LPS XX*. 2) M.H. Carr et al., 1980, *Viking Orbiter Views of Mars*, U.S. Gov't. Printing Office, Washington, D.C., p. 136. 3) P.H. Schultz and D. Britt, 1986, *LPS XVII*, p.775. 4) T.J. Parker, 1989, *LPS XX*, p. 826. 5) C.A. Hodges, 1980, Geologic Map of the Argyre Quadrangle of Mars, USGS Map I-1181. 6) R.J. Price, 1973, *Glacial and Fluvioglacial Landforms*, Oliver & Boyd, Edinburgh, 242 pages. 7) H. Lee, 1965, *Geol. Surv. Can. Pap. 65-14*, 1-17. 8) V. Gulick and V. Baker, 1990, *LPS XXI*. 9) G. Komatsu and R.G. Strom, 1990, *LPS XXI*. 10) S.W. Squyres and M.H. Carr, 1986, *Science 231*, 249-252. 11) J.R. Giardino, J.F. Schroder, Jr., and J.D. Vitek (eds.), 1987, *Rock Glaciers*, Allen & Unwin, Boston, 355 pages.

Figure 1. Glaciological map of a portion of Argyre Planitia and the adjoining Charitum Montes.

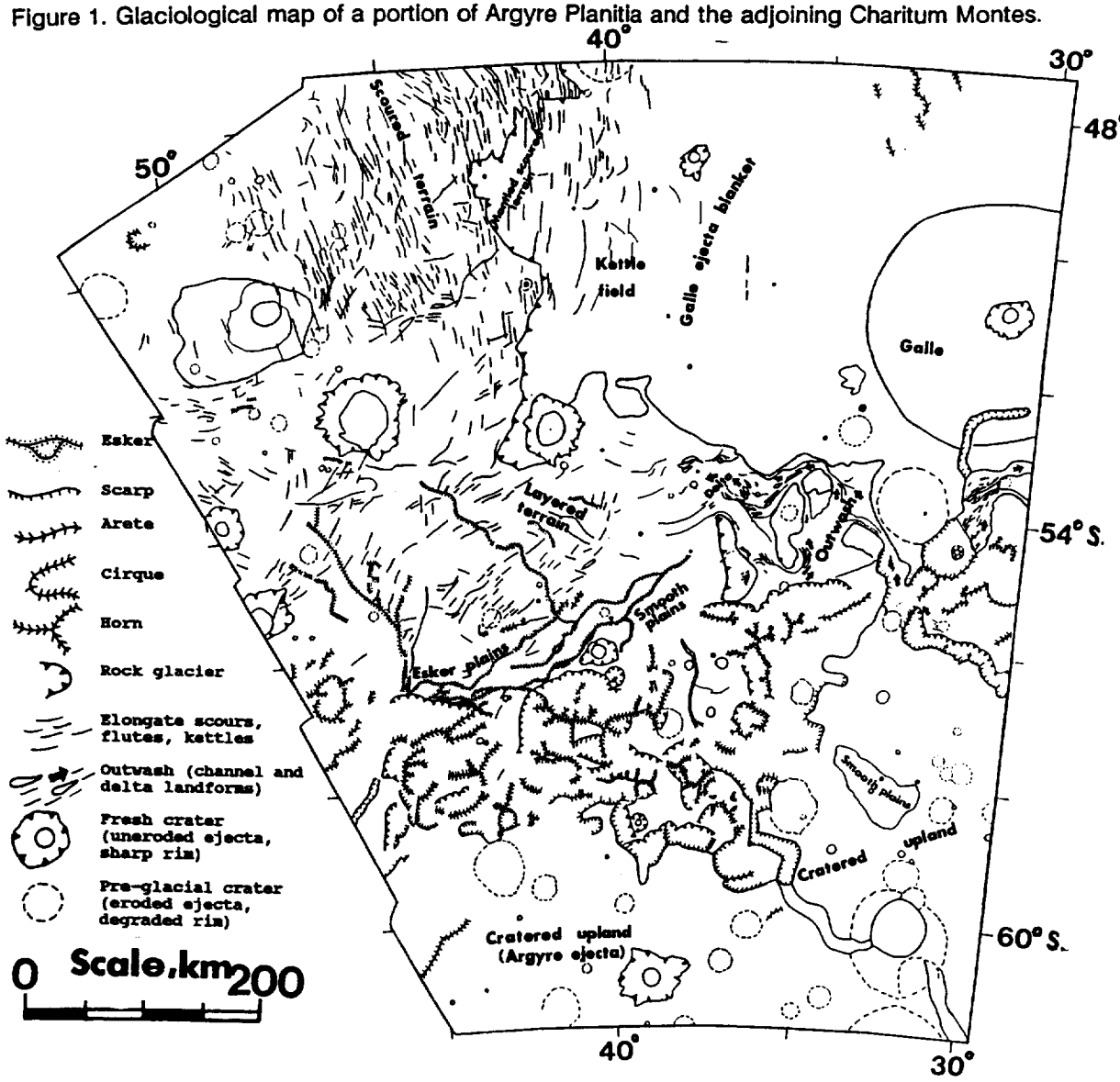

# POST-FLOODING MODIFICATIONS TO CHRYSE BASIN CHANNELS, MARS: IMPLICATIONS FOR SOURCE VOLUMES AND EVOLUTION OF THE CHANNELS

R. Craig Kochel, Department of Geology, Bucknell University, Lewisburg, PA 17837 and Jerry R. Miller, Quaternary Sciences Center, Desert Research Institute, Reno, NV 89506

The mid-latitude Chryse Planitia basin on Mars is host to a complex of large-scale outflow channels along its southern margin. The Chryse channels have been interpreted by most investigators as the erosional product of catastrophic floods which eminated from equatorial source regions characterized by chaotic terrain. Foremost among the unresolved questions concerning channel evolution is an apparent disparity between the volumes of the proposed source areas and downstream channel reaches. In addition, there has been considerable speculation regarding mechanisms which have the ability to release water at rates and volumes consistent with the large-scale flooding dictated by the interpretation of erosional and depositional landforms within the channels. Most source areas have exceedingly small volumes compared to the estimates of discharges required to produce their downstream geomorphology.

Systematic interpretation and mapping of margins along the Chryse outflow channels indicates that degradation of channel walls and floors has been significant. Post-channeling volume enlargement of downstream channel reaches has significant implications regarding the estimates of discharges required in their formation. Post-channeling modification appears to have been dominated by rockfall, debris-flow, slumping, and groundwater sapping processes. The importance of these modification processes varies spatially along individual channels and between systems. These patterns may provide important clues to variations in the composition of host terrains or regional geothermal conditions in the Martian regolith.

Deeply incised channels such as Kasei Vallis have undergone the most extensive post-channeling enlargement, while less incised systems like Maja Vallis exhibit present channel dimensions likely to be very close to their original character. The variation in geomorphic style and degree of incision of the Chryse outflow channels may have important implications regarding formative processes and sources of water. Kasei Vallis is the most deeply incised channel system, with escarpment heights of 2 - 3 km common between its channel floor and the host terrain surface of Lunae Planum. The extreme incision and concommittent large volume of Kasei Vallis may not all be attributable to flood erosion. Schumm (1974) suggested that Kasei Vallis may be a structural landform associated with extension related to the Tharsis Uplift west of the channel. Orientations of geomorphic features within the Kasei channel conform with the trends of regional structural features in the area (Kochel and Burgess 1983, Chapman and Scott 1989), providing support for the suggestion that the Kasei Vallis floods may have used and modified a preexisting structural trough similar to Valles Marineris. This would help explain the anomalous depths of the channel compared to others along the Chryse basin margin.

The disparity between source area and channel volumes varies signifcantly between individual channel systems. The disparity is greatest for Kasei Vallis and its assumed Echus Chasma source and least for Maja Valles and its Juventae Chasma head. The proximity of upstream segments of Kasei Vallis to the Tharsis volcanic complex presents another possible mechanism for explaining the exaggerated development of the Kasei channel system and apparent insignificance of Echus Chasma to supply needed the volumes of outflow necessary to erode the channel. Geothermal heating eminating from early stages of Tharsis volcanic activity could have produced diffuse but widespread regional thermal degradation of the western portions of Lunae Planum. Water released from the formerly frozen regolith would likely have ponded in large lakes upstream from the incised reaches of Kasei Vallis (upstream of the major eastward bend in the channel). Once lake levels overtopped the divide

catastrophic flooding could have ensued down the structural trough of Kasei Vallis. It is likely that numerous floods would have occurred as ice dams may have formed and failed repeatedly as the degradation of Lunae Planum continued along its western margin. This proposed scenario suggests that flows eminating from Echus Chasma played a minor role in the erosion of the Kasei Vallis complex compared to water originating from more diffuse sources downstream.

In contrast to Kasei Vallis, Maja Vallis exhibits much less incision into the host rocks of Lunae Planum and has substantially less disparity between potential source flows and channel volumes. The increased distance from the Tharsis volcanic center may have precluded wholesale degradation of ground ice in Lunae Planum beyond the present location of its westernmost escarpment (approximately 73° W longitude). The style of channel margin degradational features subsequent to channeling along Kasei Vallis appear to change systematically across this longitudinal zone; thus, providing support for this interpretation. East of the Kasei region, potential channel sources related to geothermal processes were probably limited to more localized intrusive activity of the scale represented by the chaos in the Juventae Chasma source area for Maja Vallis. Geomorphic evidence of multiple flow events (DeHon 1989, Baker and Kochel 1979) in downstream reaches of Maja Vallis and associated overflow channels to the north indicate that there is little disparity between source and channel volumes for this system. Similar arguments may be made for the development of Shalbatana Vallis along the southern Chryse margin.

The complex of channels (notably Ares, Tiu, and Simud Vallis) along the southeastern margin of Chryse basin exhibit incision into their host terrain intermediate between Kasei and Maja Vallis. Evidence of structural control is lacking, indicating that the incision is entirely due to flood erosion and will have to be accounted for in consideration of the evolution of these channel systems. Detailed geomorphic studies of this region by Grant (1987) showed that channel evolution was exceedingly complex and involved numerous flood events from multiple sources. Zones of chaos occur at numerous locations within the upper reaches of the channels. Their morphology indicates that the channel systems developed by progressively extending their head regions southward toward Valles Marineris with successive appearance of source chaos areas. As the channels grew, the most recent flows eroded downstream chaos regions. Eventually, headward extension breached the divide and allowed ponded water within eastern Valles Marineris to empty catastrophically into the channels. The combination of flow events is likely to be great enough to explain the substantial downtream volume of material eroded to form these channels. Whether the mechanism for release of water to these source areas is related to localized intrusions or associated with the failure of overpressured aquifers (Carr,1979) is unclear.

Given the scenario of events suggested above to explain the flood flows for the Chryse basin outflow channels in combination with channel volumes adjusted for reasonable estimates of post-channeling enlargement by mass wasting and sapping processes, there may be much less disparity between source area and channel volumes than previously assumed in models for creating these channels by flood processes.

References Cited:

Baker, V.R., and Kochel, R.C., 1979, J. Geophys. Res., 84, p. 7961-7983.
Carr, M.H., 1979, J. Geophys. Res. 84, p. 2995-3007.
Chapman, M.G., and Scott, D.H., 1989, Proc. 19th Lunar Planet Sci. Conf, p. 367-375.
DeHon, R.A., 1989, Abs. 20th Lunar Planet. Sci. Conf., p. 230-231.
Grant, J.A., 1987, NASA Tech. Mem. 89871, p. 1-268.
Kochel, R.C., and Burgess, C.M., 1983, NASA Tech. Mem. 85127, p. 288-290.
Schumm, S.A., 1974, Icarus, 22, p. 371-384.

## Layered deposits with volcanic intrusions in Gangis Chasma, Mars.

G. Komatsu and R.G. Strom. Lunar and Planetary Laboratory, University of Arizona, Tucson, AZ 85721.

Layered terrains on the floor of Valles Marineris were first recognized in the Mariner 9 Images. They are about 100-200km long, 50km wide and 1-5km high, and characterized by well-developed, near-horizontal layers. Proposed origins are summarized by the following hypotheses:

1.Erosional remnants of the surrounding plains. This hypothesis is probably incorrect because the erosional style is very different than that of the canyon walls ([1],[2]). 2.Eolian deposits. Peterson [1] suggested that crossbedding in the Candor and Ophir layered terrains could be explained by global dust storm deposition, but Nedell, et al. [2] argued against this idea because of the lack of similar deposits on the surrounding plains and walls. 3.Pyroclastic deposits. A pyroclastic origin by ash fall or flow is based on the similarity between the erosional pattern of terrestrial ash flow and welded tuff and that of the resistent layer in the Hebes layered terrain [1]. However, because there are no similar deposits on the surrounding plains and no evidence for an associated caldera, Nedell, et al. [2] rejected this hypothesis. 4.Lacustrine deposits. This hypothesis is favored because it can explain the location, near horizontality, lateral continuity, great thickness and stratigraphic relationship ([2],[3],[4]). Moreover, a substantial subsurface aquifer system may have supplied water to fill or partially fill the canyons at or near the time of outflow channel and canyon formation [2].

**Geologic setting of Gangis layered terrain.** The area surrounding the Gangis layered terrain show a variety of geologic features relevant to its origin (Fig. 1). The canyon walls are about 2km high and show gully and spur topography and landslides. Fewer craters on the canyon floor than on the surrounding plains suggests that the floor is younger, possibly as a result of fluvial or eolian processes. A large crater on the southern upper plain shows evidence of ponding and outburst of water to the east forming an outflow channel. On the western part of the canyon floor are blocky mesas a few to 20km across and about 1km high. Their morphology is similar to the mesas of chaotic terrains thought to be the source of outflow channels. To the south and southeast of the layered terrain there are clusters of small hills 1-5km wide and a few hundreds of meters high. These may also be eroded remnants of chaotic terrain or they could be volcanic constructs. Their color is similar to the canyon floor.

**Gangis layered terrain.** The approximate size of Gangis layered terrain is 100km, 40-50km wide, and 1.5-2.0km high. To the west, the terrain seems to have been more eroded than to the east. The relatively gentle south- facing side has a slope of a few degrees, and is conspicuously fluted. This fluting could be due either to wind scouring or to the seepage of ground water. On the eastern part of the south-facing side are two blocky slabs, each about 10km wide. Their blocky nature and fold-like texture in them suggest they may be large landslide masses that have been subsequently shaped by erosion. Extending in a north-south direction from the summit of the layered terrain to near its base are several lines of darker domes and ridges. In some cases, areas of dark material surround the domes. These structures may be volcanic domes and dikes intruded into the layered deposits and subsequently exposed by the erosion which shaped the present-day layered terrain. The associated dark deposits could be erosional products from the structures or pyroclastic material. Part of slope has texture smoother than the fluted area. This region could be covered by the pyroclastic material suggesting volcanism could have been active until recently. The layered terrain itself can be divided into three main stratigraphic units (A,B,C in Fig.1) based on the erosional morphology. Each main unit consists of other less well-defined units not shown in Fig.1. The upper two layers are relatively thin and have steeper slopes than the lower unit. Strata within the middle unit(B) appear to thin and pinch out against the upper unit(C) suggesting an angular unconformity (arrow 1). Similarly, a dark layer within the lower unit (A) appears truncated by the middle unit indicating another angular unconformity (arrow 2). To the west, these three main units disconformably overlie a heavily eroded base rock that might be ancient cratered terrain. The angular conformities between the main stratigraphic units suggest that there were at least two intervals of erosion between the deposition of these three units. Domes, ridges and dark materials suggest that volcanism has modified the Gangis layered terrain. Whether Gangis layered terrain was laid down in a lake is still controversial, but assuming it originated as sedimentary deposits in the lake and the angular unconformaties are real, then the following sequence of events appears to apply.

**1.**Formation of early closed Gangis Chasma and filling with water from subsurface. Hills and mesas may be remnants of chaotic terrain associated with this event. **2.**Layer A deposited. **3.**Draining or evaporation of lake and erosion of layer A during minor tectonic tilting. **4.**Refilling of canyon with water from subsurface and deposition of layer B uncomfomably on layer A. **5.**Draining or evaporation of lake and erosion of layer B during minor tectonic tilting. **6.**Refilling of canyon with water from subsurface and deposition of layer C unconformably on layer B. **7.**Intrusion of volcanics into layered deposits. **8.**Catastrophic draining of lake to the east and erosion of layered deposits to expose volcanic intrusions.

Layered terrains may provide important clues for understanding the history of canyon formation and the Martian hydrologic cycle. Our current interpretation suggests multiple cycles of canyon filling and draining. This may be consistent with the proposed cycles of ancient oceans in the northern plains [5].

REFERENCES [1]Peterson, C. (1981). Proc. Lunar Planet. Sci. 12B, p.1459-1471. [2]Nedell, S.S., et al. (1987). Icarus, 70, 409-441. [3]Lucchitta, B.K. (1982). Report of Planetary Geology Program, p.233-234. NASA- TM 85127 [4]McCauley, J.F. (1978). Geologic map of the Coprates quadrangle of Mars. U.S. Geological Survey, Misc. Inv. Map I-897. [5]Baker, V.R., et al. (1990). Lunar and Planet. Sci. XXI.

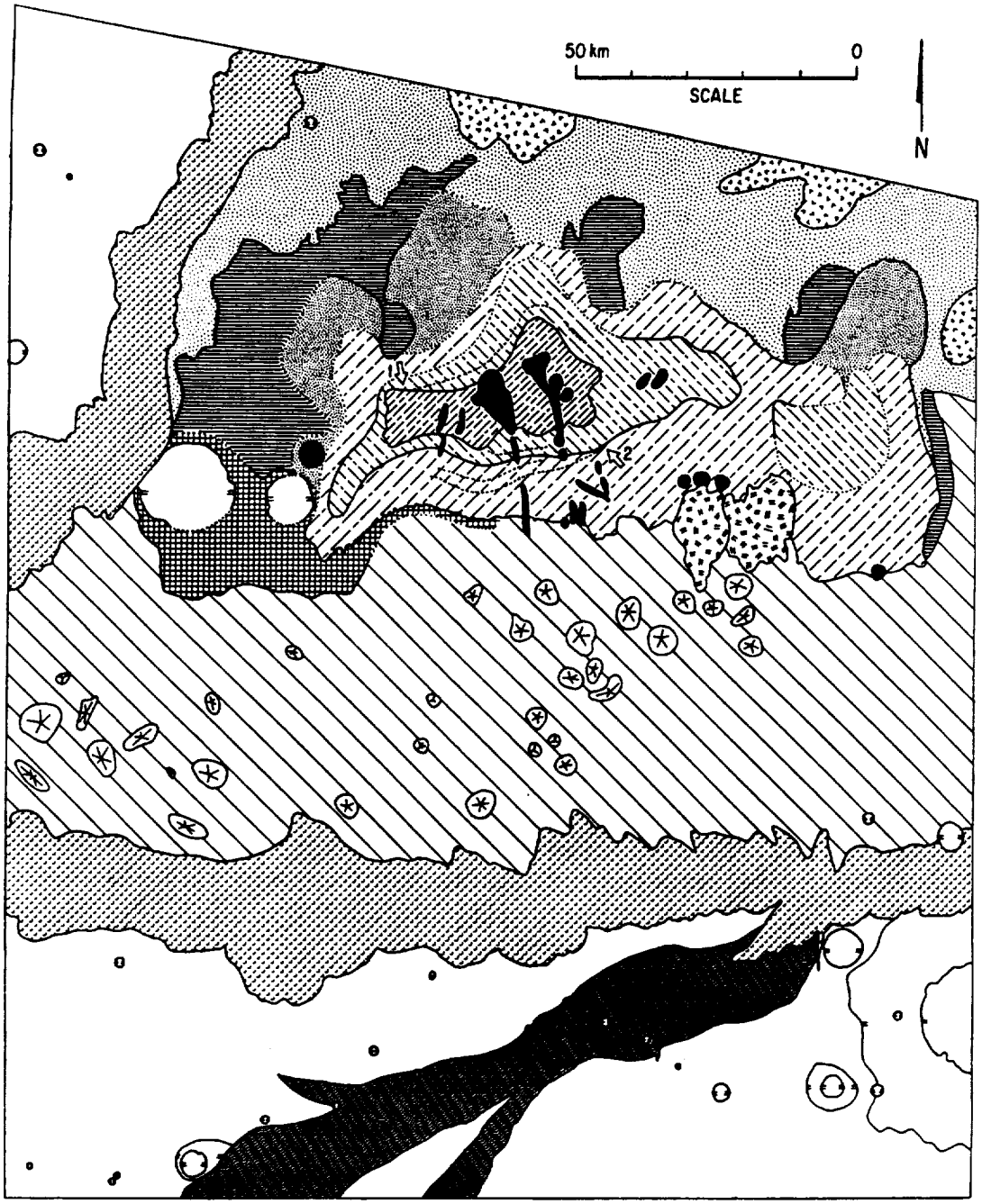


Figure 1. Geologic map of western Gangis Chasma.

# VARIATION OF THE BOUND WATER CONTENTS ON THE MARTIAN SURFACE FROM ISM-EXPERIMENT DATA ON PHOBOS-2: PRELIMINARY RESULTS

R.O.Kuzmin. Vernadski Inst.USSR Academy of Sciences,Moscow 117975 USSR,V.I.Moroz, A.V.Grigoryev, Y.V.Nikolsky, N.F.San'ko, I.V.Khatuntsev, A.V.Kiselev.IKI USSR Academy of Sciences,Moscow 117485 USSR, J.P.Bibring, Y.Langevin, A.Soufflot.IAS/LPSP/University,Orsay,France, M.Combes.Observatore de Meudon, France.

The spatial variations of the bound water in the martian soil were studied on the example of the fourth regins of the Mars:1-Melas and Ophir Chasmata(5-10°S,59-94°W);2-Pavonis Mons(5°S-3°N,95-126°W);3-Ascraeus Mons(5.5-13°N,95-117°W);4-Olympus Mons(12-18°N,112-146°W).The mapping of the bound water contents (in conventional values) was done using the spectral measurements in the absorption band 2.7-3.14μm with the spatial resolution 20×30 km[1].As turned out from all four regions the highest values of the bound water contents( or the hydration degree) were found in the Olympus Mons region - 23% more than those in the Melas and Ophir Chasmata.The hydration degree fluctuations in the martian soil within the studied regions are not identical and are estimated 26%,11%,6% and 9% for Regions 1,2,3,4 respectively.

Within each region the appreciable correlation between the spectral measurements in the band absorption by atmospheric $CO_2$(an equivalent of the altitudes) and mapped values of the soil hydration is not observed.However a certain tendency to clustering is visible.In each region the altitude range in which there is a certain range of the most widespread values of the bound water contents stands out(Fig.1).For Regions 1,2,3,4 such clusters values( into the contour 20 on Fig.1) are equal 35.2%,44.6%,27.8% and 56.7% of all the mapped values respectively.Using the new topographic map of the Mars[2],the mapped values of the spectral data for $CO_2$ atmospheric abundence and bound water contents in the surface materials conform with all altitude range for four regions.As a result the united scale of the conventional values of the bound water contents was worked out and tied to the hypsometric scale of the Mars.

As demonstrated in Fig.2, a tendency to increasing of the clusters values of the hydration degree is observed in direction from the Region 1,through Region 2-3 to Region 4.Moreover,it was found that the clusters values are just on the shield surface only in the case of Pavonis Mons.In the other regions the clusters values of the hydration degree are usually on the surface around Ascraeus Mons,Olympus Mons and on the upper surface levels of Melas and Ophir Chasmata.It is typical that the succesive increasing of the hydration degree of the soil from Region 2,through Region 3 to Region 4 is accompained by the altitude fall of the terrain surface.Alternatively to such tendency,the dependence of the maximum values of the hydration degree from altitude is inversely(Fig.2).The region of Melas and Ophir Chasmata stands as exeption.Here the lots of the higher hydration degree mostly relate to the sedimentary deposits(possibly lake-like deposits [3]), which filled the inner parts of Melas and Ophir Chasmata and its landslide slopes disposed on the lower hypsometric levels. Moreover,the clasters and the maximum values of tne surface material hydration in the region of Ascraeus Mons are only on the shield surrounding surface, while the material directly on the shield surface is less hydrated. The fact,that the surface of this volcanic shield is covered by much coarser materials in comparison with the material of the surraunding plain[4] may be one of the reasons of such hydrated material distribution.

The visible tendency to the increasing of the surface material hydration from Region 1 to Region 2-4 is probably connected with the change(in the same direction) of the physical properties by surface material. For the surface material of Tharsis Montes area had lover thermal inertia values and lighter albedo [5], we believe that the weathering product portion in the surface material of Region 2-4 may be much higher then in Region 1.

On the whole it is not excluded that the found geographical and hypsometrical positions of the clasters and maximum values of the martian material hydration are defined by the possible dependence of the hydrated minerals phases on the geographical latitudinal( and altitudinal) zonality. In our case, the geographical latitude of the regions studied changes from 10°S to 18°N in direction from the fiest to the fourth regions. According to thermodynamic prediction of the stability of the salt hydrates in the modern environments of the Mars[6], increasingly hydrated phases must became more stable with latitude increase(exampie $MgCl_2 \cdot H_2O$ on equator and $MgCl_2 \cdot 4H_2O$ in moderate latitudes).Possibly the continuation of the more detailed analysis of the whole data from ISM-experiment may allow to examine the thermodynamic prediction.

REFERENCES:[1] Bibring J.P. et.al,Nature,1989,V.341,N 6243,p.591-593.[2] Atlas of Mars 1:15 000 000 Topographic series,M15M 0/90T,M15M 0/270,1988.[3] Nedell S.S. et.al,Isarus,1987,V.70,N 3,p.409-441.[4] Zimbelman J.R.,Greeley R.,3-d Int.Colloq.on Mars,1981,p.291-293.[5] Kieffer H.H. et.al, J.Geophys.Res.,1977,V.82,N 28, p.4249-4292.[6] Zolotov M.Yu.,LPSC,XX,1989,p.1257-1258.

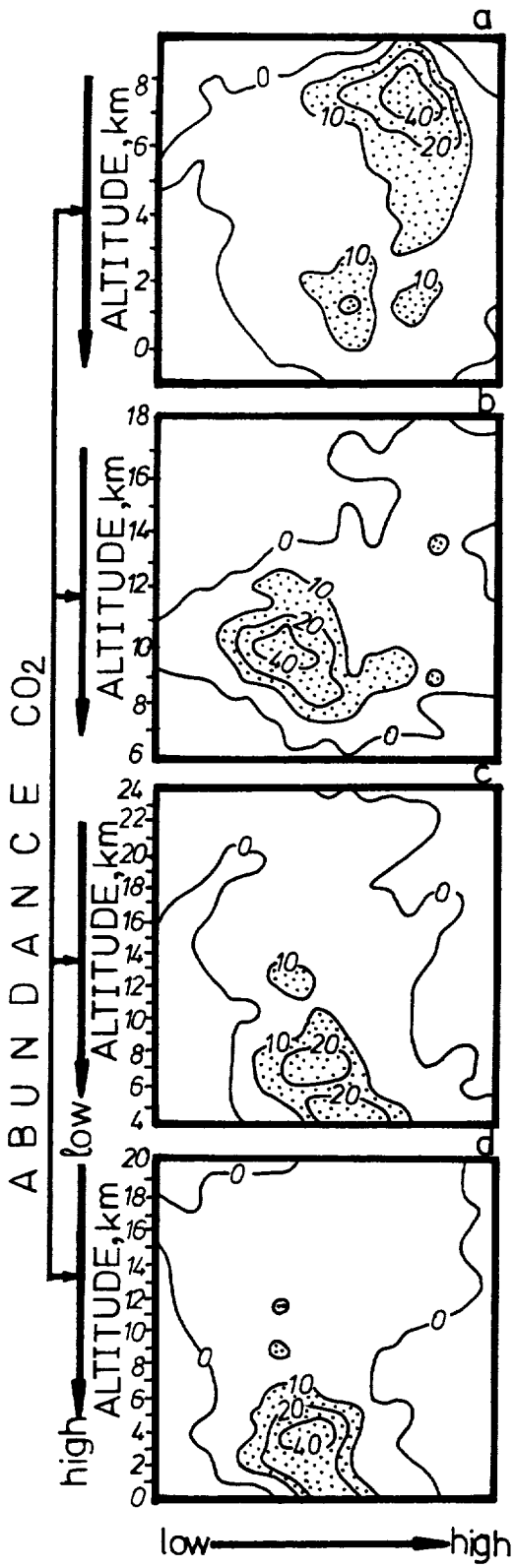


Fig.1. Spectral measurements of $CO_2$-abundence in atmosphere versus the bound water contents(in conventional values) as a contour map.Regions: A-Melas and Ophir Chasmata; B-Pavonis Mons; C-Ascraeus Mons;D-Olympus Mons.

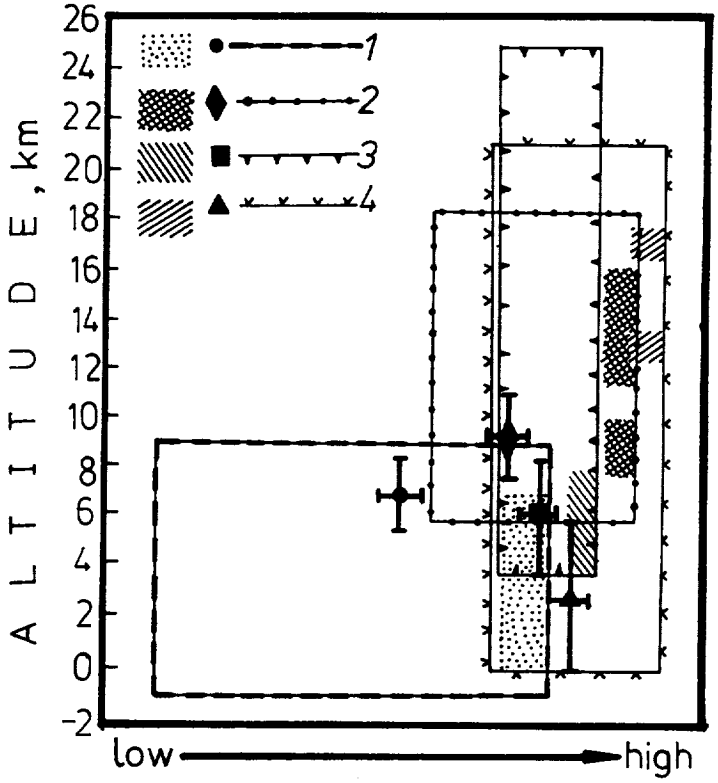


Fig.2.Altitude range of the regions studied(1,2,3,4) and corresponding clusters(symbols) and maximum(shadied areas) hydration values of the surface materials.

**THE EFFECTS OF ATMOSPHERIC DUST ON OBSERVATIONS OF THE SURFACE ALBEDO OF MARS;** S.W. Lee and R.T. Clancy, Laboratory for Atmospheric and Space Physics, Univ. Colorado, Boulder, CO 80309

The Mariner 9 and Viking missions provided abundant evidence that aeolian processes are active over much of the surface of Mars [1; 2]. Past studies have demonstrated that variations in regional albedo and wind streak patterns are indicative of sediment transport through a region [3; 4], while thermal inertia data [derived from the Viking Infrared Thermal Mapper (IRTM) data set] are indicative of the degree of surface mantling by dust deposits [5; 6; 7; 8; 9]. The visual and thermal data are therefore diagnostic of whether net erosion or deposition of dust-storm fallout is taking place currently and whether such processes have been active in a region over the long term. These previous investigations, however, have not attempted to correct for the effects of atmospheric dust loading on observations of the martian surface, so quantitative studies of current sediment transport rates have included large errors due to uncertainty in the magnitude of the "atmospheric contamination".

We have developed a radiative transfer model which allows the effects of atmospheric dust loading and variable surface albedo to be investigated [see related abstract, 10]. This model incorporates atmospheric dust opacity, the single scattering albedo and particle phase function of atmospheric dust, the bidirectional reflectance of the surface, and variable lighting and viewing geometry.

The Cerberus albedo feature has been examined in detail using this technique. Previous studies have shown the Cerberus region to have a moderately time-variable albedo [4]. IRTM observations obtained at ten different times (spanning one full martian year) have been corrected for the contribution of atmospheric dust in the following manner:

- A "slice" across the IRTM visual brightness observations was taken for each time step. Values within this area were binned to 1° latitude, longitude resolution.
- The atmospheric opacity ($\tau$) for each time was estimated from [11]. As the value of $\tau$ strongly influences the radiative transfer modelling results, spatial and temporal variability of $\tau$ was included to generate an error estimate.
- The radiative transfer model was applied, including dust and surface phase functions, viewing and lighting geometry of the actual observations, and the range of $\tau$ [10].
- Offsets were applied to the visual brightness observations to match the model results at each $\tau$ (Figure 1).
- The "true surface albedo" was determined by applying the radiative transfer model to the offset brightness values, assuming $\tau = 0$ and a fixed geometry (0° incidence, 30° emission). Repetition of this technique for each time step allows values of albedo for specific locations to be tracked as a function of time (Figure 2).

The initial results for Cerberus indicate the region darkens prior to the major 1977 dust storms, consistent with erosion of dust from the surface (possibly contributing to the increasing atmospheric dust load). There is some indication of regional brightening during the dust storms followed by a general darkening, consistent with enhanced dust deposition during the storms followed by erosion of the added dust. There is only minor variability during the second year, consistent with little regional dust transport during that period.

The results of this study indicate that atmospheric dust loading has a significant effect on observations of surface albedo, amounting to albedo corrections of as much as several tens of percent. This correction is not constant or linear, but depends upon surface albedo, viewing and lighting geometry, the dust and surface phase functions, and the atmospheric opacity. It is clear that the quantitative study of surface albedo, especially where small variations in observed albedo are important (such as photometric analyses), needs to account for the effects of atmospheric dust loading. Our future work will expand this study to other regional albedo features on Mars.

This research was supported under NASA Planetary Geology grant NAGW 1378.

**REFERENCES:** [1] Veverka, J., P. Thomas, and R. Greeley (1977). A study of variable features on Mars during the Viking primary mission. *J. Geophys. Res. 82*, 4167-4187. [2] Thomas, P., J. Veverka, S. Lee, and A. Bloom (1981). Classification of wind streaks on Mars. *Icarus 45*, 124-153. [3] Lee, S.W., P.C. Thomas, and J. Veverka (1982). Wind streaks in Tharsis and Elysium: Implications for sediment transport by slope winds. *J.Geophys. Res. 87*, 10025-10042. [4] Lee, S.W. (1986). Regional sources and sinks of dust on Mars: Viking observations of Cerberus, Solis Planum, and Syrtis Major (abstract), In *Symposium on Mars: Evolution of its Climate and Atmosphere* (V. Baker et al., eds.), pp. 71-72, LPI Tech. Rpt. 87-01, Lunar and Planetary Institute, Houston. [5] Kieffer, H.H., T.Z. Martin, A.R. Peterfreund, B.M. Jakosky, E.D. Miner and F.D. Palluconi (1977). Thermal and albedo mapping of Mars during the Viking primary mission. *J. Geophys. Res. 82*, 4249-4295. [6] Christensen, P.R. (1982). Martian dust mantling and surface composition: Interpretation of thermophysical properties. *J. Geophys. Res. 87*, 9985-9998. [7] Christensen, P.R. (1986). Regional dust deposits on Mars: Physical properties, age, and history. *J. Geophys. Res. 91*, 3533-3545. [8] Christensen, P.R. (1986). The distribution of rocks on Mars. *Icarus 68*, 217-238. [9] Jakosky, B.M. (1986). On the thermal properties of martian fines. *Icarus 66*, 117-124. [10] Clancy, R.T., and S.W. Lee (1990). Derivation of Mars atmospheric dust properties from radiative transfer analysis of Viking IRTM emission phase function sequences. *Reports of Planetary Geology and Geophysics Program*, this volume. [11] Martin, T.Z. (1986). Thermal infrared opacity of the Mars atmosphere. *Icarus 66*, 2-21.

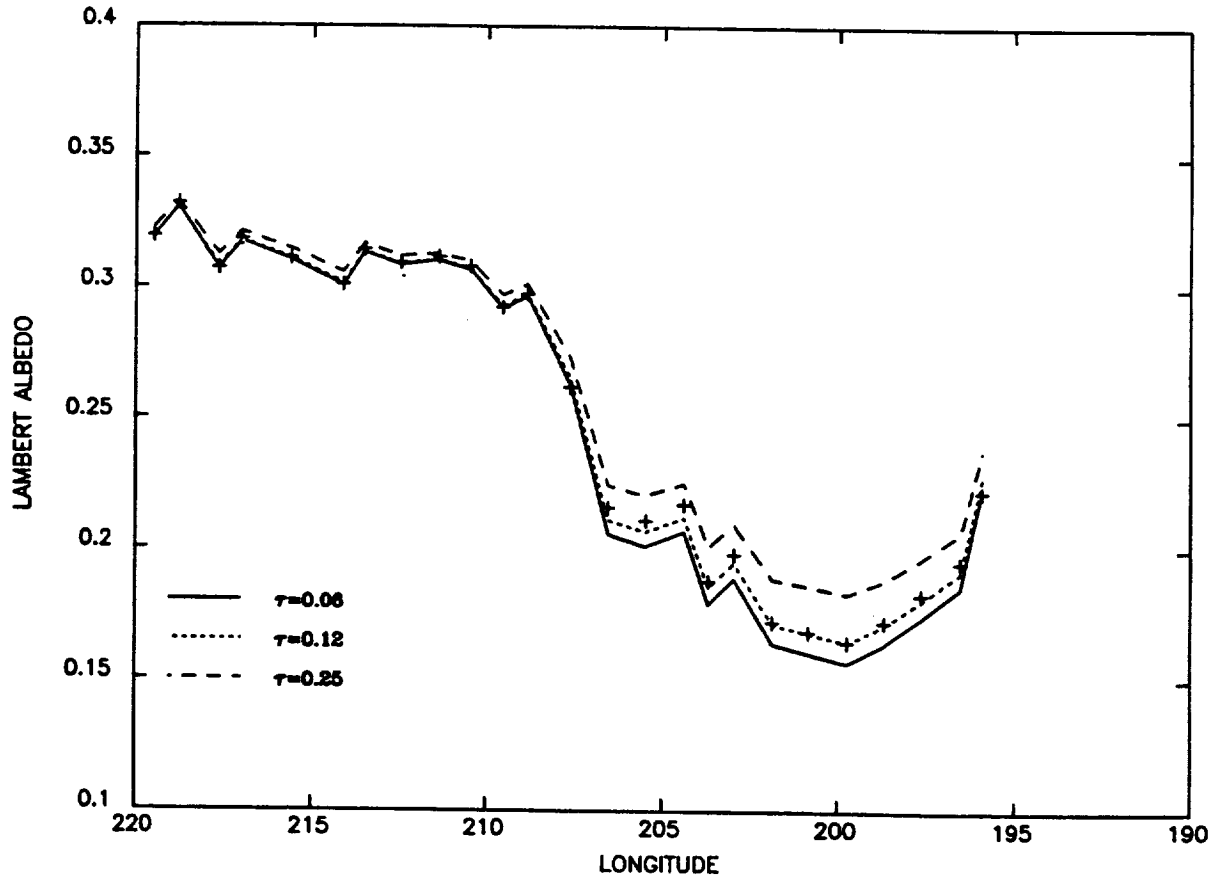


**Figure 1:** Results of the radiative transfer modelling for an albedo slice across Cerberus (latitude 13° – 14°) at $L_s$ 124°. Crosses indicate the actual observations, and lines denote the model results for three different opacities.

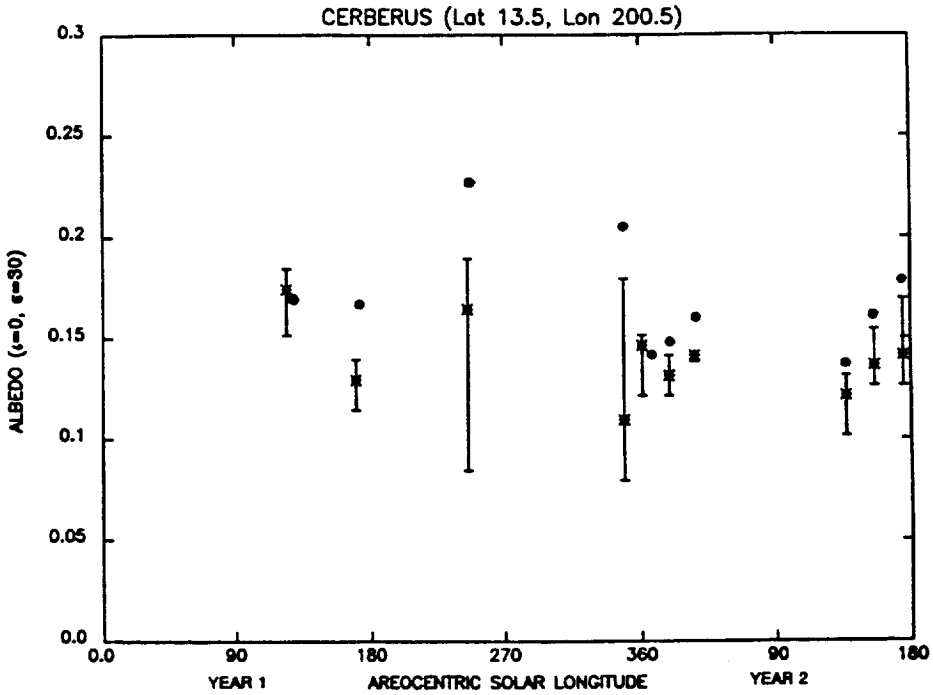


**Figure 2a:** Temporal behavior of a dark area in Cerberus. "True surface albedos" are denoted by asterisks; error bars indicate uncertainty in $\tau$. Uncorrected albedos are denoted by dots.

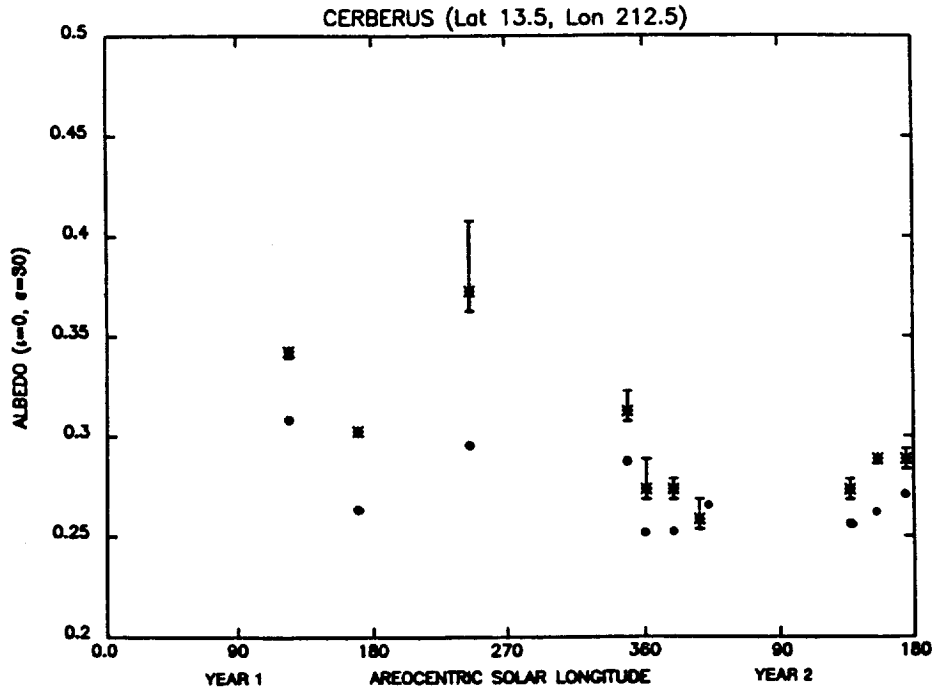


**Figure 2b:** Temporal behavior of a bright area in Cerberus. "True surface albedos" are denoted by asterisks; error bars indicate uncertainty in $\tau$. Uncorrected albedos are denoted by dots.

N91-22995

AN EFFICIENT AND ACCURATE TECHNIQUE TO COMPUTE THE ABSORPTION, EMISSION, AND TRANSMISSION OF RADIATION BY THE MARTIAN ATMOSPHERE. Bernhard Lee Lindner, AER Inc., 840 Memorial Drive, Cambridge, MA 02139; Thomas P. Ackerman, Dept. of Meteor., Penn. State Univ., University Park, PA 16802; and James B. Pollack, NASA/ARC, Moffett Field, CA 94035.

INTRODUCTION. $CO_2$ comprises 95% of the composition of the martian atmosphere [1]. However, the martian atmosphere also has a high aerosol content. Dust opacities vary from less than 0.2 to greater than 3.0, primarily on a seasonal basis with the occurrence of global dust storms during southern spring [2]. Ice-cloud opacities vary from 0 to greater than 1, with large amounts occurring at winter polar latitudes [3]. $CO_2$ is an active absorber and emitter in near-IR and IR wavelengths; the near-IR absorption bands of $CO_2$ provide significant heating of the atmosphere, and the 15 $\mu$m band provides rapid cooling[4-7]. However, dust and ice-cloud aerosols have high scattering albedoes in solar wavelengths, and are highly absorbing at infrared wavelengths, and are as important as $CO_2$ in the atmospheric energy budget [5].

Including both $CO_2$ and aerosol radiative transfer simultaneously in a model is difficult. Aerosol radiative transfer requires a multiple-scattering code, while $CO_2$ radiative transfer must deal with complex wavelength structure, as shown in Fig. 1. The problem can be solved exactly by inserting the $CO_2$ absorptance for each spectral line into a multiple-scattering code, but the 15$\mu$m band alone has on the order of 10,000 lines, making such a computation tedious and expensive. It is this difficulty of simultaneously treating aerosol multiple scattering and the banded absorption structure of $CO_2$ that prompts most radiative-transfer studies of the martian atmosphere to consider either a pure-$CO_2$ or pure-dust atmosphere. This approximation simplifies treatment, but is inaccurate.

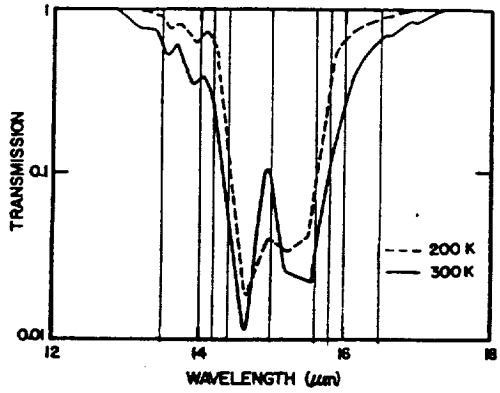


Figure 1. $CO_2$ 15 $\mu$m band transmission at 20 km altitude looking upward, at temperatures of 200 and 300K [25]. Also shown are the sub-intervals used for the 8 term and 16 term fits.

One alternative technique that has recently been developed for atmospheric applications is the exponential-sum or k-distribution approximation [8-21]. The transmission of a homogeneous atmosphere is actually independent of the ordering of the absorption coefficient, k, in frequency space within a spectral interval, depending only upon the percentage of the spectral interval that has a particular value of k. The percentage of the spectral interval which has values between k and k + $\Delta$k can be formulated in a probability density function f(k) shown schematically in Fig. 2. The chief advantage of the exponential-sum approach is that the integration over k space of f(k) can be computed more quickly than the integration of $k_\nu$ over frequency. The exponential-sum approach is superior to the photon-path-distribution and emissivity techniques for dusty conditions [22, 19, 23]. Our work is the first application of the exponential-sum approach to martian conditions.

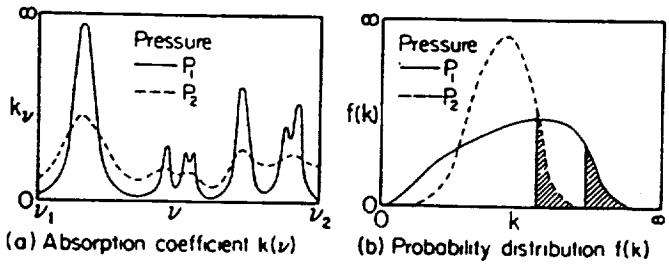


Figure 2. A schematic illustration portraying the essence of the exponential-sum approach. (a) shows a schematic of absorption line spectra at two different pressures. In (b) the two probability density functions f(k) associated with (a) are illustrated. The shaded area depicts the strongest absorption (i.e., largest k) for the same spectral interval (i.e., f(k) for different pressures are correlated). Integration of f(k) over k replaces the integration of $k_\nu$ over $\nu$ (modified from [28], [29]).

THEORETICAL APPROACH. The transmittance of the 15 $\mu$m band and the near-IR bands of $CO_2$ was computed using the FASCOD line-by-line transmittance model [24], modified for martian conditions. Computations with the modified FASCOD model were made at 3 temperatures (125K, 200K, 300K) and 5 pressures (100 mb, 10 mb, 1 mb, 0.1 mb, 0.01 mb); these cover the range of temperature and pressure currently observed in the atmosphere at all latitudes, seasons, and altitudes up to 40 km, and also can be used for early Mars, dense atmosphere studies. The near-IR and 15$\mu$m bands were broken into spectral sub-intervals (see Fig. 1), and the

transmittance for each layer, Tr, as a function of $CO_2$ column abundance within that layer, u, was fit with a series of weighting coefficients, $a_i$, and exponential coefficients, $b_i$:

$$Tr(u) \approx \sum_{i=1}^{n} a_i \exp(-b_i u) \quad (1)$$

We tried fitting procedures based on Wiscombe and Evans [14] and an improved version of Ackerman et al. [13], and found both yielded similar results. Both of these procedures avoid the ill-conditioning of earlier exponential-sum routines, and produce more accurate and unique solutions [13,14]. The exponential-sum fit reproduced the FASCOD transmittances to better than $10^{-4}$ for all $CO_2$ abundances considered. The frequency sub-intervals are picked to try to minimize the variation in line strengths within the sub-interval. As shown in Fig. 1, 2 sub-intervals covered the band center, 2 covered the far line wings, 2 covered the near line wings, and 2 covered the transition from wings to band center. The vertical inhomogeneity of the atmosphere is treated by using homogeneous layers, with the absorption coefficients k for all layers correlated in frequency space, i.e. the sub-intervals of the spectral band which have the maximum absorption also have the largest k values (Ackerman et al., 1976). An interpolation is used for temperatures and pressures which fall in between the values at which the exponential-sum coefficients were computed. We compared a logarithmic interpolation to a linear interpolation, and found the logarithmic interpolation to be more accurate.

INCORPORATION IN MULTIPLE-SCATTERING MODELS. Vertical optical depths of $CO_2$ absorption for each term number, frequency sub-interval, and atmospheric layer are $b_i u$. $CO_2$ is combined with dust and cloud in that the total optical depth $T_i$, single-scattering albedo $\tilde{\omega}_i$, and phase function P for each term, frequency sub-interval, and layer are given by[16]:

$$T_i = b_i u + \tau^R + \tau_s^D + \tau_a^D + \tau_s^C + \tau_a^C \quad (2)$$

$$\tilde{\omega}_i = (\tau^R + \tau_s^D + \tau_s^C) / T_i \quad (3)$$

$$P = \frac{\tau_s^D P^D + \tau_s^C P^C + \tau^R P^R}{\tau_s^D + \tau_s^C + \tau^R} \quad (4)$$

where: $\tau^R$ - Rayleigh scattering optical depth for that layer

$\tau_{s,a}^{D,C}$ - Dust (D) and Cloud (C) scattering (s) and absorption (a) optical depth for that layer

$P^{D,C,R}$ - dust (D), cloud (C), and Rayleigh scattering (R) phase function

The multiple-scattering code is run once for each term in the sum using the T, $\tilde{\omega}_i$, and P appropriate to that term, and the resultant fluxes, $F_i$, (or intensities) are then summed and weighted by $a_i$ to give the total flux, F, (or intensity) over the frequency sub-interval:

$$F = \sum_{i=1}^{n} a_i F_i(b_i u) \quad (5)$$

Tables of the exponential-sum coefficients, $a_i$ and $b_i$, can be obtained from the authors.

NUMERICAL STUDIES. The number of terms in the series of exponentials (n in equation 1) and the number of sub-intervals into which the spectral band is broken can be varied to increase the desired accuracy. Figure 3 shows a comparison between the 15 $\mu$m cooling rates computed using various numbers of frequency sub-intervals and terms within each sub-interval. The temperature of the atmospheric model rose linearly from 150K at the surface to 160K at 10km altitude, and then fell linearly to 130K at 40km altitude. These temperatures are typical of the winter polar atmosphere on Mars. Using 4 terms and 4 sub-intervals results in an error of less than 10% in the lowest 10 km, but results in substantial errors at higher altitudes. The explanation is that the 4 term fit could not capture the effects of both the band center and the wings at all altitudes, and in this case we emphasized the wings, which are more important at lower altitudes where the band center is saturated (see Fig. 1). Adding additional terms from 8 to 16 is far less noticeable.

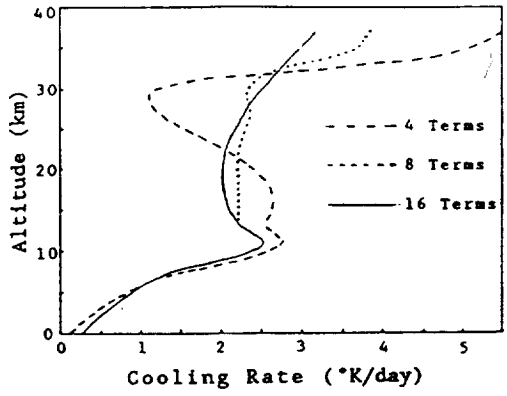


**Figure 3. 15 $\mu$m band cooling rates calculated with an exponential-sum approach using 4 frequency sub-intervals and 4 terms in the sum, 10 sub-intervals and 8 terms, and 10 sub-intervals and 16 terms. A winter polar temperature profile is used (see text), but only 200K exponential-sum coefficients are used for comparison purposes.**

We also separately derived exponential-sum coefficients based on the Gal'tsev and Osipov [25] line-by-line calculations of the 15 μm band. The number of terms in the fit (n in equation 1) were varied, to confirm our FASCOD work on the number of terms required to give an accurate fit. Figure 4 shows cooling rates computed with several fits to the Gal'tsev and Osipov parameterizations, as well as to the FASCOD transmittances. Cooling rates compare favorably in the lower atmosphere (below 10 km altitude). Gal'tsev and Osipov only considered temperatures as cold as 200K. We extrapolated the temperature dependence to colder temperatures [26]. Discrepancies between the Gal'tsev and Osipov and FASCOD cooling rates are due to the inaccuracy in the temperature extrapolation, particularly at the higher, colder altitudes. Again, note that the 4 and 5 term fits become inaccurate above 10 km altitude, as in Fig. 3. Also, the 15 term fit yields no marked improvement over the 8 term fit, as also shown with the FASCOD fits in Fig. 3.

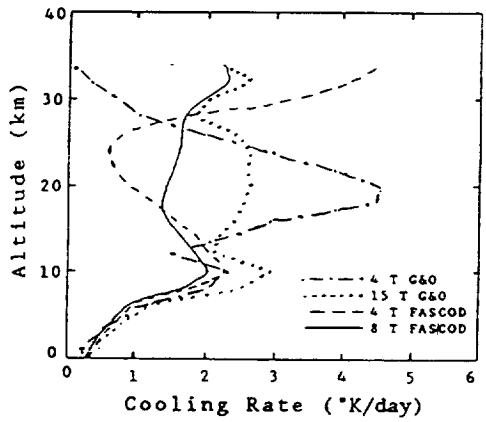


Figure 4. 15 μm band cooling rates calculated with 4 types of exponential-sum coefficients: 4 and 15 term fits to the transmission parameterizations of [25] (abbrev. G&O), and 4 and 8 term fits to the FASCOD transmission model. The winter polar atmosphere model is used, with logarithmic temperature interpolation for the exponential coefficients.

Cooling rates computed using the FASCOD exponential-sum transmittances also compared well below 10 km altitude with cooling rates computed using the Pollack et al. [27,4] parameterizations of $CO_2$ transmittance. At higher altitudes, discrepancies exist due to the use of the strong-line approximation by Pollack et al, which emphasizes the effects of the line wings. However, comparisons of our exponential-sum transmittances with techniques commonly used for the terrestrial atmosphere have indicated that our exponential-sum transmittances could be in error above 20 km altitude. J. Pollack is seeking to modify our exponential-sum approach to use two sets of sums, one applied to the line centers and one applied to the line wings. Initial tests seem to show better agreement in the upper atmosphere of Mars.

B.L. Lindner acknowledges support by NASA contract NASW-4444.

REFERENCES. [1]Owen, T. et al., J. Geophys. Res., 82, 4635, 1977. [2]Pollack, J. et al., J. Geophys. Res., 84, 2929, 1979. [3]Briggs, G. and C. Leovy, Bull. Amer. Met. Soc., 55, 278, 1974. [4]Gierasch, P. and R. Goody, Planet. Space. Sci., 15, 1465, 1967. [5]Kondratyev, K. et al., Sov. Phys. Dokl., 24, 81, 1979. [6]Pollack, J. et al., J. Atmos. Sci., 38, 3, 1981. [7]Lindner, B.L., The aeronomy and radiative transfer of the martian atmosphere, Ph.D. Dissertation, 470 pp., University of Colorado, Boulder, 1985. [8]Kondratyev, K., Radiation in the Atmosphere, Academic Press, 1969. [9]Arking, A. and K. Grossman, J. Atmos. Sci., 29, 937, 1972. [10]Raschke, E. and U. Stucke, Beitr. Phys. Atmosph., 46, 203, 1973. [11]Liou, K. and T. Sasamori, J. Atmos. Sci., 32, 2166, 1975. [12]Kerschgens, M. et al., Beitr. Phys. Atmosph., 49, 81, 1976. [13]Ackerman, T. et al., J. App. Meteor., 15, 28, 1976. [14]Wiscombe, W. and J. Evans, J. Computational Phys., 24, 416, 1977. [15]Morcrete, J., Beitr. Phys. Atmosph., 51, 338, 1978. [16]Freeman, K. and K. Liou, Adv. Geophys., 21, 231, 1979. [17]Evans, J. et al., Math. of Computat., 34, 203, 1980. [18]Chou, M. and A. Arking, J. Atmos. Sci., 38, 798, 1981. [19]Zdunkowski, W. et al., Beitr. Phys. Atmos., 55, 215, 1982. [20]Slingo, A. and H. Schrecker, Quart. J. R. Met. Soc., 108, 407, 1982. [21]Wang, W. and G. Shi, J. Quant. Spectrosc. Radiat. Transfer, 39, 387, 1988. [22]Bakan, S. et al., Beitr. Phys. Atmosph., 51, 28, 1978. [23]Wiscombe, W., Rev. Geophys. Space Phys., 21, 997, 1983. [24]Clough, S. et al., Proceedings of the Sixth Conference on Atmospheric Radiation, Williamsburg, VA, 1986. [25]Gal'tsev, A. and V. Osipov, Bull. (Izv.) Acad. Sci. USSR. Atmos. Ocean. Phys., 15, 767, 1979. [26]Lindner, B.L., The martian polar cap: Radiative effects of ozone, clouds, and airborne dust, J. Geophys. Res., 95, 1367, 1990. [27]Pollack, J. et al., Geophys. Res. Lett., 3, 479, 1976. [28]Stephens, G., Mon. Wea. Rev., 112, 826, 1984. [29] Hansen, J. et al., Mon. Wea. Rev., 111, 609, 1983.

# MAGMATIC PROCESSES ON MARS: INSIGHTS FROM SNC METEORITES;

J. Longhi, Lamont-Doherty Geological Observatory, Palisades, NY 10964 .

The composition and petrology of the SNC (shergottites-nakhlites-Chassigny) meteorites reveal a surprising diversity of magmatic processes on their parent body, which the weight of evidence suggests is Mars (1). There is evidence for large scale mantle heterogeneities, multi-stage melting, extreme fractionation of REE, assimilation of a long-term light REE-enriched component (a 'granitic' crust?), mantle metasomatism, and possibly $CO_2$-fluxed melting. In some respects the style of martian magmatism is intermediate between that of the Moon and the Earth, with the terrestrial component having some of the geochemical character of hot-spot and arc basalts.

Estimates of the major element composition of the SNC parent magmas show them to be hpyersthene-normative, high-Fe, low-Al liquids (2). As might be anticipated, calculated densities of these liquids are high (2.75-2.96) and viscosities are low (4-128 poise). These compositions are consistent with the petrography: olivine and pyroxene crystallize early, plagioclase crystallizes late (1); this crystallization pattern is different from terrestrial MORB's and continental tholeiites in which plagioclase crystallizes early. These low-Al liquids require either large degrees (~50%) of partial melting of an undepleted source or smaller degrees of melting of a depleted source. Geochemical and isotopic data discussed below show the latter certainly to be the case for Nakhla and probably to be the case for the shergottites. This depletion may be accomplished by the accumulation of olivine and pyroxene (lunar style) or extraction of basalt (terrestrial style).

Figure 1 illustrates some important aspects of SNC trace element and isotopic composition. Figure 1A shows the REE concentrations of two calculated parent liquid compositions for Nakhla. Chassigny parent liquids have similar patterns. Nakhla is an unusual rock consisting of large cumulus augite and minor olivine crystals set in a rapidly crystallized matrix (5). The 'closed system' calculation assumes that no net changes in the intercumulus liquid took place after accumulation of the pyroxene, but does allow for partial equilibration of the cumulus crystals and trapped liquid. The 'open system' calculation is a direct calculation based upon the composition of Nakhla augite (6) and the partition coefficients of (7); this calculation allows for the possibility of migration of intercumulus liquid. Both patterns are similar and show dramatic light REE enrichment. This fractionation is truly remarkable in light of the $\varepsilon_{Nd}$ value of +16 (6) which requires that the source had a long term pattern of light REE depletion, i.e. something similar to the EETA79001A pattern in Fig. 2B. Compounding the situation is the low Al content of the Nakhla parent liquid (N) evident in Fig. 1 (Pl is the Al bearing component). The Al content is sufficiently low that garnet, which is the most effective REE fractionating agent, cannot have been a residual phase in the parent magma's source region; niether is there much allowance for removal of augite at low pressure. The problem of deriving strongly light-REE enriched magmas from light-REE depeleted source regions is common to terrestrial hot spots, such as Hawaii (8). Single-stage models require prohibitively small degrees of partial melting (<1%), so multi-stage melting models have been invoked to spread the REE fractionation over two or more steps (e.g., 9). Some sort of multi-stage melting process thus seems necessary to explain the Nakhla parent magma composition with the condition that garnet not have been a residual phase in the last stage of melting. In addition to low-Al the Nakhla parent magma also had an unusually high concentration of CaO (~14 wt% (2)). The combination of low-Al and high-Ca requires either that the source was dominated by augite or that $CO_2$, which has the potential of drastically increasing the CaO content of melts coexisiting with olivine and pyroxene, fluxed the melting at pressures > 25 kb (2). Since partial melting of pyroxene dominated sources produces small negative Eu anomalies in the liquid (10) and since there is no evidence of such an anomaly in Fig. 2A, the presence of $CO_2$ in martian melting processes must be seriously considered.$CO_2$ is also an effective carrier of light REE (11), so $CO_2$ may have affected both trace and major elements during melting.

Fig. 1B illustrates very different REE patterns for the shergottites. The Shergotty pattern is the 70% ICM model taken from (12). The EETA79001A pattern is the bulk rock analysis of (13). EETA79001A is a fine-grained basaltic rock with 10-15 % mafic xenocrysts (14). These xenocrysts will likely have only a minor diluting effect on incompatible elements, so the pattern in Fig. 1B is believed to close to, albeit slightly lower and steeper than, the true parent liquid pattern. The crystallization ages of the shergottites are controversial because of variable shock effects on the isotopic systems and consequentlythe values of $\varepsilon_{Nd}$ are model dependent. The values shown in Fig. 1B are consistent with the 180 m.y. age advocated by (15). This age is chosen here because only the younger ages, which yield $\varepsilon_{Nd} > 0$, are petrologically reasonable, and because the 350 m.y. age reported by (16) has been shown to be a mixing line (12). Given these qualifications, the low-Al content, the depleted light-REE pattern, and $+\varepsilon_{Nd}$ of EETA79001A have a straightfoward explanation: partial melting of a low-Al source region with a long term light-REE depletion. In this regard, the source region was similar to that of Nakhla although the EETA79001A magma genesis was apparently much simpler. The $\varepsilon_{Nd}$ values for Nakhla and EETA79001A are much higher than typical terrestrial basaltic values, but are more typical of lunar mare basalts. This similarity suggests that Mars was more like the Moon in its ability to maintain long term isotopic heterogeneities in its mantle. Lack of crustal recycling on Mars and/or less vigorous mantle convection than the Earth are probable explanations.

Given the similarity of mineral compositions in Shergotty to those in the groundmass of EETA79001A, it is likely that their parent magmas lay along similar liquid lines of descent, as suggested by Fig. 1, and hence they were derived from similar primary magmas and source regions. If so, then REE pattern and $\varepsilon_{Nd}$ of the Shergotty

Shergotty parent magma in Fig. 2B are readily explicable as those of a magma derived from a depleted source region like EETA79001A, but subsequently contaminated by a low-temperature, long-term, light-REE enriched component. The slight U-shape in the light REE is especially indicative of such a contamination. This component probably is crustal, but whether it is older basalt, like the Nakhla parent magma (Fig. 2A), or 'granitic' is not clear; the physics of assimilation favors an evolved composition with a low melting point, however. One thing that is clear is the absence of a negative Eu-anomaly in the Shergotty REE pattern. Consequently, this crustal component was unlike lunar KREEP, which has a prominent negative Eu-anomaly (17).

Fig. 2A contains REE concentrations for the Nakhla parent ('closed system') and the bulk data for EETA79001A taken from Fig. 1 plus additional calculated and measured concentrations of some high-field-strength elements (HFSE) arranged in order of incompatibility. Fig. 2A shows that there are complementary anomalies for Ta, Hf, and Zr in the Nakhla and EETA79001A patterns, thus supporting the hypothesis that the shergottites were generated by remelting a source depleted in a Nakhla-like component. Fig. 2B schematically illustrates typical incompatible element patterns for basalts from terrestrial oceanic islands (OIB), volcanic arcs (ARC), and mid-ocean ridges (MORB). Despite the fact that there is no evidence of plate tectonics on Mars, the Nakhla parent magma pattern appears more similar to the ARC pattern than to OIB or MORB. This similarity is probably due to similar fractionations of the REE from the HFSE during transport by a $CO_2$-rich vapor phase, rather than similar tectonic styles.

REFERENCES: (1) McSween, H. Y. (1985) *Revs. Geophys., 23*, 391-416. (2) Longhi, J. and Pan, V. (1989) *Proc. Lunar Planet. Sci. Conf. 19th*, p. 451-464. (3)Toulmin, P., III, Baird, A. K., Clark, B. C., Keil, K., Rose, H. J., Jr., Christian, R. P., Evans, P. H., and Kelliker, W. C. (1977) *J. Geophys. Res. 82*, 4625-4634. (4) Bertka, C. M. and Holloway, J. R. (1988) *Proc. Lunar Planet. Sci. Conf. 18th*, 723-739. (5) Treiman A. H. (1986) *Geochim. Cosmochim. Acta, 50*, 1061-1070. (6) Nakamura, N., Unruh, D. M., Tatsumoto, M. and Hutchinson, R. (1982) *Geochim. Cosmochim. Acta, 46*, 1555-1573. (7) McKay G., Wagstaff J., and Yang S.-R. (1986) *Geochim. Cosmochim. Acta, 50*, 927-937. (8) Chen C.-Y. and Frey F.A. (1985) *J. Geophys. Res., 90*, 8743-8768. (9) Ribe N.M. (1988) *Earth Planet. Sci. Lett., 88*, 37-46. (10) Shearer C.K. and Papike J.J. Proc. (1989) *Lunar and Planet. Sci. Conf. 20th*, in press. (11) Wendlendt R.F. and Harrison W.J. (1979) *Contrib. Minerl. Petrol., 69*, 409-419. (12) Lundberg L.L, Crozaz G., McKay G., and Zinner E. (1988) *Geochim. Cosmochim. Acta, 52*, 2147-2163. (13) Burghele A., Dreibus G., Palme H., Rammensee W., Spettel B., Weckwerth G., and Wanke H. (1983) *Lunar Planetary Science XIV*, 80-81. (14) McSween H.Y. and Jarosewich E. (1983) *Geochim. Cosmochim. Acta, 47*, 1501-1513. (15) Jones J.H. (1986) *Geochim. Cosmochim. Acta, 50*, 969-977. (16) Jagoutz, E. and Wänke, H. (1986) *Geochim. Cosmochim. Acta, 50*, 939-953. (17) Warren P. H. and Wasson J.T. (1979) *Rev. Geophys. Space Phys., 17*, 73-88.

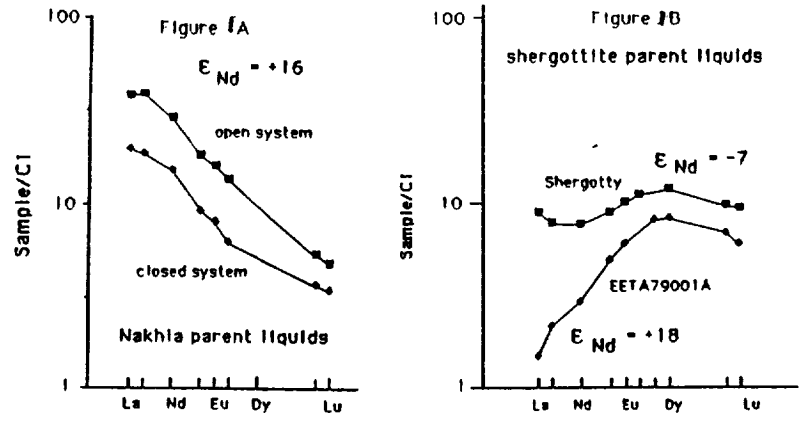


Figure 1. REE in Nakhla and shergottite parent magma compositions. Nakhkla - calc.,this study; Shergotty - calc(12); EETA79001A - bulk (13).

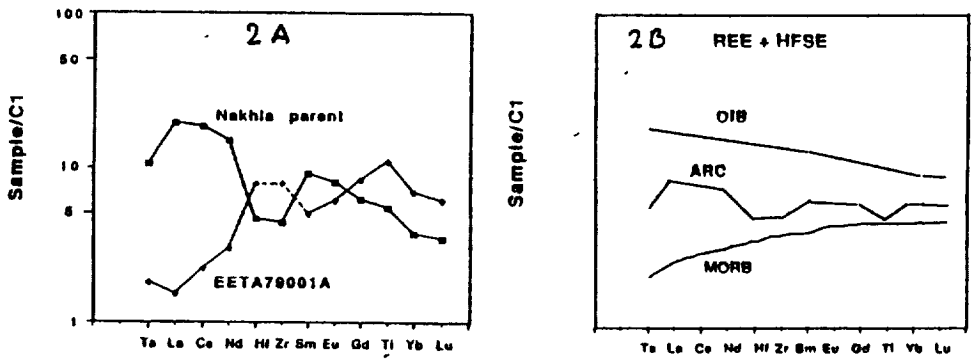


Fig. 2 A. Calculated REE and HFSE in Nakhla parent magma and bulk EETA79001A. B. Typical (schematic) patterns for terrestrial basalts.

VALLES MARINERIS, MARS: ARE PIT CHAINS FORMED BY EROSION AND TROUGHS BY TECTONISM?; B.K. Lucchitta, R.A. Balser, and L.M. Bertolini, U.S. Geological Survey, Flagstaff, AZ 86001.

The origin of the Valles Marineris remains controversial. Erosional [1], tectonic [2], and hybrid processes [3] have been proposed. Erosional processes appeared attractive because a morphologic continuum was thought to exist from pit chains of probable erosional origin to larger troughs. Schultz [4], however, refuted the existence of this continuum. To clarify these contradictions, we compared the widths and depths of pit chains and troughs and found that the features do not form a continuum. Rather, results are consistent with the hypothesis that pit chains formed by surficial collapse and troughs by deeper seated and coherent failure.

We classified by inspection all pit chains and linear depressions in the Valles Marineris region into six morphologic categories: (1) pit chains (linear arrays of small pits), (2) floored chains (arrays of pit chains having flat or hummocky floors), (3) scalloped troughs (wider linear depressions with scalloped wall segments), (4) narrow troughs (depressions of intermediate width with straight wall segments), (5) wide troughs (broad, linear depressions), and (6) chaotic troughs (more irregular depressions displaying some channel morphologies). We drew topographic profiles across the classified depressions at each degree of longitude between long 45° and 90°, on the basis of 1:2,000,000-scale topographic maps of MC 18 NW [5] and 18 NE and SE (work in progress). For each profiled depression, we determined the erosional width between plateau margins, the depth from the surrounding plateau level to the deepest part, and the geologic unit (modified from Witbeck et al. [6]) exposed at the deepest point.

Depths and widths are shown in Figs. 1 and 2. Fig. 1 shows measurements of all troughs. Fig. 2 is the same but with omissions of three types: (1) chaotic troughs, which are genetically linked to outflow channels; (2) troughs east of long 61°, which are transitional to chaotic troughs; and (3) troughs whose maximum depth is not likely to reflect the approximate structural depth because of thick fill from landslides or interior deposits.

Results of the study, as deduced from the figures, are as follows:

1. Pit chains, floored chains, and scalloped troughs lie along a continuously ascending trend that suggests a common origin. Surficial erosional collapse into linear subsurface voids or tension cracks [3] is compatible with this observation. The limiting depths of about 4 km may be due to a discontinuity at that depth or to restricted size of the underlying voids.

2. Narrow and wide troughs form a continuum that suggests their formation by similar processes. The straight scarps bordering these troughs suggest control by faulting rather than surficial collapse.

3. A gap in data occurs at widths of 20-35 km, separating pit chains, floored chains, and scalloped troughs from narrow and wide troughs. Only two transitional points are located within this gap. The gap suggests an abrupt change in physical conditions or processes. Apparently, deep-seated, more coherent failure was activated for troughs wider than about 35 km.

4. Most troughs bottom out at 8-9 km regardless of width, perhaps implying a controlling discontinuity or limit in the amount of extension.

REFERENCES

[1] McCauley, J.F., M.H. Carr, J.A. Cutts, W.K. Hartmann, Harold Masursky, D.J. Milton, R.P. Sharp, and D.E. Wilhelms (1972) Icarus 17, 289-327. [2] Blasius, K.R., J.A. Cutts, J.E. Guest, and Harold Masursky (1977) Jour. Geophys. Res. 87, 9723-9733; [3] Tanaka, K.L. and M.P. Golombek (1989) Proc. 19th Lunar and Planet. Sci. Conf., 383-396; [4] Schultz, R.A. (1989) MEVTV Workshop on Tectonic Features on Mars, 21-22; [5] U.S. Geological Survey (1986) U.S. Geol. Surv. Misc. Inv. Map I-1712; [6] Witbeck, N.E., K.L. Tanaka, and D.H. Scott (in press) U.S. Geol. Surv. Misc. Inv. Ser. Map I-2010.

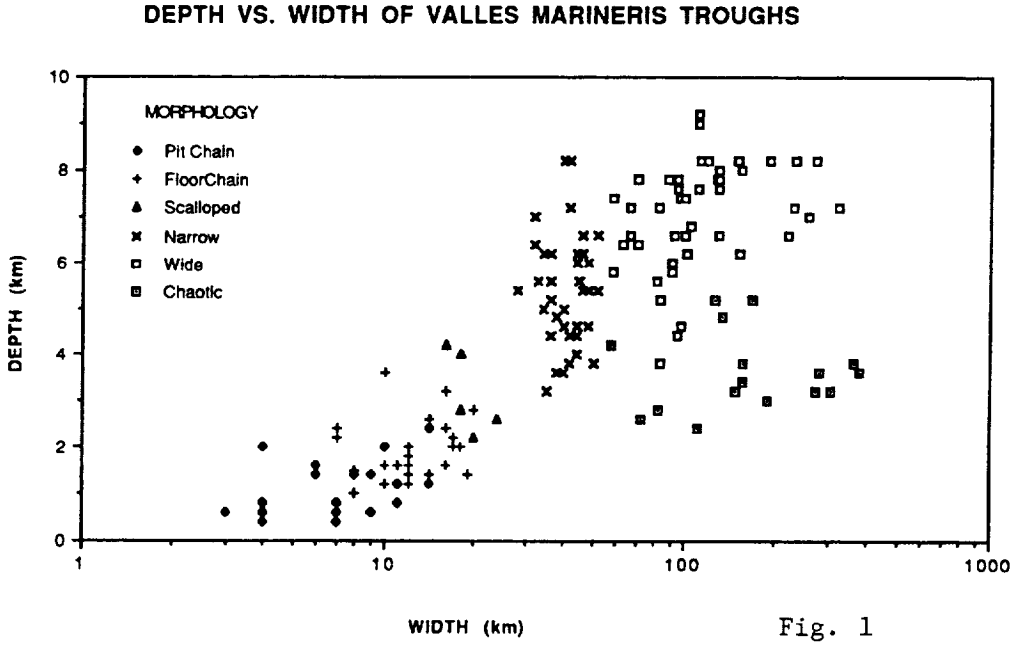


Fig. 1

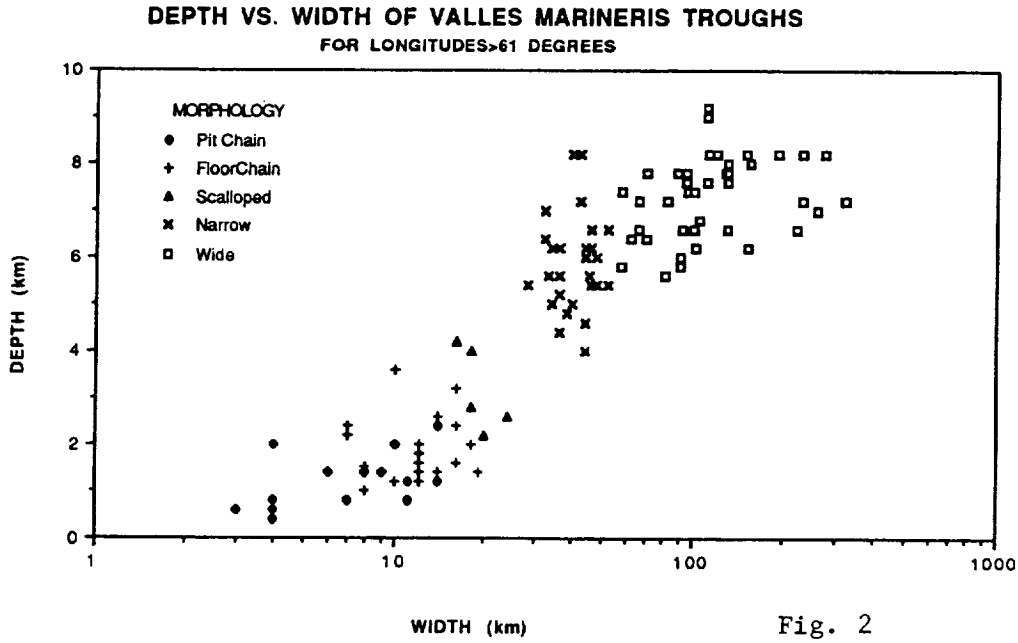


Fig. 2

**A PHYSICAL MODEL OF THE IMPACTED MARTIAN CRUST: HYDROLOGIC AND MECHANICAL PROPERTIES AND GEOLOGIC IMPLICATIONS;** *David J. MacKinnon and Kenneth L. Tanaka, U.S.G.S., 2255 N. Gemini Dr., Flagstaff, AZ 86001*

Photogeologic evidence suggests a close association of many outflow [1,2], intermediate [3], and sapping [4] channels with regions affected by uplift, fracturing, and geothermal heating [1, 5]. The magnitude and diverse morphology of the channeling are impressive by terrestrial standards, especially because there is little evidence that significant rainfall has occurred on Mars [6]. By the end of the heavy bombardment, outgassed water probably had been emplaced in the upper crust [7]. Nearly all the channels originated from or are associated with ancient cratered terrain, some of which has been resurfaced by lava flows and eolian processes. Because high impact fluxes during bombardment probably fragmented most of the materials that resurfaced the impacted surface, we believe that a simple physical and structural model of the impacted, ancient cratered terrain can reasonably describe physical properties fundamental to interpreting subsequent channel formation, as well as other geologic activity.

On this basis, we developed a two-layer model for the impacted crust: an ejecta (impact breccia) zone overlying a zone of fractured basement rock [see 8, 9]. The proposed ejecta zone is 1 to 2 km thick and consists of well-mixed, very poorly sorted impact breccia that grades into the fractured zone. The fractured zone is composed of meter-size or larger blocks of basement rock, and it extends to the depth of lithostatic closure (10 km or more, depending on pore-water pressure [10]). The porosity and permeability of these zones depend on the size distribution and packing of the breccia and fractured blocks. From the results of measurements from terrestrial impact and explosion craters, laboratory analyses, and experimentally verified theoretical models for porosity and permeability, we determined that in such an impacted crust, clast size and degree of sorting increase with depth. These trends cause (1) porosity to decrease with depth throughout the affected crust, (2) permeability to increase with depth to the top of the fractured zone and then to decrease as fracture width and frequency decrease with depth, and (3) material strength to increase with depth from cohesionless to that of solid bedrock. Extrapolating from typical size distributions and packing among ejecta and fractured blocks, we estimate the porosity of the ejecta zone as 10-20 percent and the porosity of the upper part of the fractured zone as less than a few percent; the permeability of the ejecta zone would be less than 0.01 darcys, and the permeability of the upper part of the fractured zone would be about 1000 or more darcys.

We recognize two major limitations of our model: (1) few terrestrial impact and explosion craters provide empirical data for the analysis of the effects of single and multiple impacts on rock structure, and (2) the subsurface stratigraphy of Mars is poorly known. Thus some of our basic assumptions are speculative, allowing for different possibilities regarding the nature of the Martian crust. In one alternative view [10], the crust is more heterogeneous than we have portrayed; thus its hydraulic properties may be more varied, and impact fractures in the basement rocks, if filled, would appreciably lower the bulk permeability.

In spite of such problems, we feel that our two-layer model is generally valid, because it can account for a great diversity of Martian geologic phenomena. Photogeologic evidence suggests mechanical discontinuities in the Martian crust at 1- to 3-km depths, which in some places may form the contact between the ejecta and the fractured zones. Generally, lower layers of the ancient crust have progressively greater resistance to erosion. Within the deeply eroded Kasei Valles, for example, erosional discontinuities in the

channels are evident at depths of 1.0 and 2.6 km. The upper discontinuity has been interpreted as the ejecta/basement contact [11], the interface between ice-laden and dry or wet regolith [12], or the zone between pristine and cemented regolith [13]; the lower discontinuity is consistent with the depth to the base of sapping channels along the Valles Marineris and has been interpreted as the ejecta/basement contact [12]. Such discontinuities are consistent with observed graben widths and collapse pits proposed to originate by collapse of cohesionless material into tension fractures at depth in basement rocks [12, 14].

The Chryse channels may be explained by high pore pressures and fluidization of the base of the ejecta zone by the fractured zone, causing enormous retrogressive debris flows [15]: after removal of the overburden, floods from the fractured zone could have easily eroded ejecta-zone breccia. Late-stage debris flows, sapping channels, and landslides along the channel margins completed the morphology seen today. If debris flows played a central role in the formation of the large outflow channels, their mobilization would require much less water [16] than the flood model [7]. The breccia of the ejecta zone is poorly sorted and rich in clay-size particles, analogous to the clast distributions of terrestrial debris flows [9]. An explanation for the great runout distances of debris flows over very low gradients, however, has not yet been offered.

Other geologic features consistent with our model include (1) outflow channels produced by catastrophic floods erupted from joints or faults that tap the fractured zone and act as high-volume conduits [13,17]; (2) sapping channels where the permeability of the ejecta zone was sufficient to promote sapping of exposed, saturated ejecta; (3) chaotic terrain, possibly formed by liquefaction of breccia at depths of hundred of meters to more than a kilometer [18]; (4) complex channels such as Nirgal Vallis, which can be explained as a combination of outflow along a tension fracture that taps the fracture zone (lower part of channel) and sapping from the ejecta zone (upper part of channel); and (5) high-latitude debris aprons and channels with modest wall slopes (e.g., Auqakuh Vallis) composed of ice-rich impact breccia of low yield strength [19].

Our physical model for the ancient, impacted Martian crust, coupled with local volcano-tectonic histories, enables a more complete understanding of the formation of many common geologic features on Mars. Previously, catastrophic flood models have not addressed the dependence of permeability on clast and fracture distributions and the cohesion of the cratered terrain material, and debris-flow models have not addressed the physical mobility of the material. Furthermore, the ejecta/fractured zone stratigraphy explains many observations of Martian erosional and structural discontinuities.

**References:**

[1] Tanaka, K.L. and MacKinnon, D.J. (1987) (abs.) LPSC 18, 996-997;[2] Tanaka, K.L. and Chapman, M.G. (in press) PLPSC 20;[3] MacKinnon, D.J. and Tanaka, K.L. (1987) (abs.) LPSC 18, 588-589;[4] Kochel, R.C. and J.F. Piper (1986) JGR 91, E175-E192;[5] Mouginis-Mark, P.J. (1985) Icarus 64, 265-284;[6] Pieri, D.C. (1980) NASA TM 81979, 1-160;[7] Carr, M.H. (1979) JGR 84, 2995-3007;[8] MacKinnon, D.J. and Tanaka, K.L. (1987) (abs.) LPSC 19, 707-708;[9] MacKinnon, D.J. and Tanaka, K.L. (1989) JGR 94, 17,359-17,370;[10] Clifford, S.M. (1984) Ph.D. dissertation, U of Mass., 285 p;[11] Robinson, M.S. and Tanaka, K.L. (1987) (abs.) LPI Tech. Rep. 88-05, 106-108;[12] Davis, P.A. and M.P. Golombek (in press), JGR, MEVTV Special Issue;[13] Soderblom, L.A. and D.B. Wenner (1978), Icarus 34, 622-637;[14] Tanaka, K.L. and Golombek, M.P. (1989) PLPSC 19, 383-396;[15] Numedal, D. and D.B. Prior (1981) Icarus 45, 77-86;[16] Rodine, J.D. and A.M. Johnson (1976) Sedimentology 23, 213-234;[17] Tanaka, K.L. and MacKinnon, D.J. (1989) (abs.) 4th Mars Conf., 200-201;[18] Tanaka, K.L. (1987) (abs.) LPSC 19, 1175-1176;[19] MacKinnon, D.J., Tanaka, K.L., and Winchell, P.J. (1987) (abs.) LPI Tech Rep. 88-05, 82-85.

# MARTIAN CRATER COUNTS ON ELYSIUM MONS

Kathleen McBride, Univ. of Houston-Clear Lake, 2700 Bay Area Blvd., Houston, Tx, 77058 and Lunar and Planetary Institute, 3303 NASA Rd. 1, Houston, Tx, 77058, and Nadine G. Barlow, SN 21, NASA Johnson Space Center, Houston, Tx, 77058.

Without returned samples from the martian surface, relative age chronologies and stratigraphic relationships provide the best information for determining the ages of geomorphic features and surface regions. We measured crater-size frequency distributions of six recently mapped geologic units of Elysium Mons to establish their relative ages [1,2].

Most of the craters on Elysium Mons and the adjacent plains units are between 500 and 1000 meters in diameter. However, only craters 1 km in diameter or larger were used because of inadequate spatial resolution of some of the Viking images and to reduce probability of counting secondary craters. The six geologic units include all of the Elysium Mons construct and a portion of the plains units west of the volcano. The surface area of the units studied is approximately 128,000 $km^2$. We used four of the geologic units to create crater distribution curves. There are no craters larger than 1 km within the Elysium Mons caldera. Craters that lacked raised rims, were irregularly shaped, or were arranged in a linear pattern were assumed to be endogenic in origin and not counted.

Three of the crater distribution curves (Figs. A,B,C) show that the ages of the surface units of Elysium Mons are near the heavy bombardment-post heavy bombardment transition. This is consistent with the ages found by Barlow [3]. These three units appear to have been emplaced at nearly the same time. The fourth curve (Fig. D) indicates that the upper flank material is slightly younger; this unit shows considerably fewer craters in the 1.0 to 2.8 km diameter size range. This lack of small diameter craters could have resulted from unusual erosion on the upper eastern flank of Elysium Mons or from the burial of the surface by a later volcanic deposit. In contrast to the undifferentiable, braided lava flows of the western flank, the upper flank is smooth and slightly hummocky at 150 m/pixel. A few craters appear mantled by some surficial deposit. The upper eastern flank has been interpreted as an ash deposit by Mouginis-Mark [4] and McBride and Zimbelman [2] because of its smooth, mantled appearing morphology.

Additional crater frequency distribution analysis is in progress and includes relative age chronologies for adjacent surface units, west of Elysium Mons, to determine the geologic history of Elysium Mons.

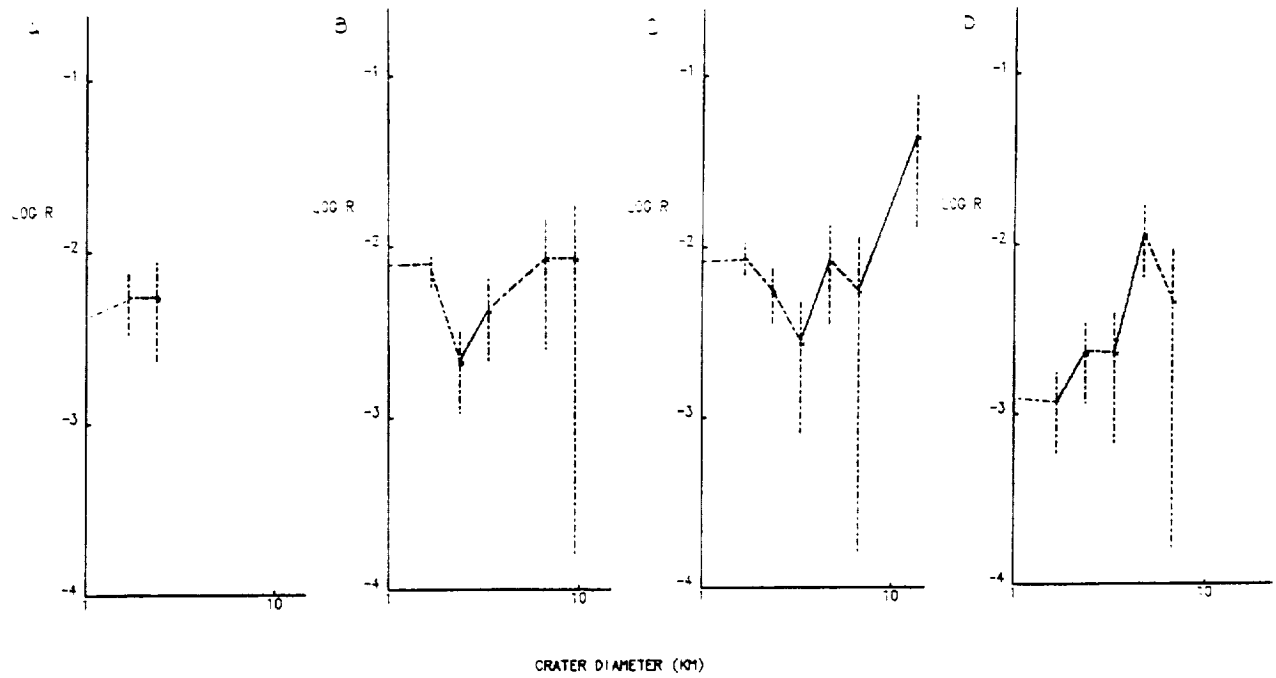


Figures: Relative crater-size frequency distribution curves. (A) Lower/Middle Flank Material. (B) Undifferentiated Flow Material. (C) Plains Unit. (D) Upper Flank Material.

REFERENCES: [1] McBride et al., LPI Tech. Rpt., 89-04, p. 56-58, 1989. [2] K. McBride and J. R. Zimbelman, LPSC 20, p. 651, 1989. [3] N. G. Barlow, Icarus 75, p. 285-305, 1988. [4] P. J. Mouginis-Mark, LPSC 12, p. 726-728, 1981.

DEVELOPMENT OF THE SOUTHWEST ELYSIUM CANYON COMPLEX, MARS; J.H.McDonnell, Consulting Geologist, 5400 Las Trampas Way NW, Albuquerque, New Mexico 87120

A photogeologic study of a large system of depressions (1) on Mars, 320 kilometers west of Elysium Mons (2,3,), reveals component structures of varying age and morphology (1). This system, referred to as the Southwest Elysium Canyon Complex, is one of a number of large depressions found west of Elysium Mons and is distinct in its orientation and form.

Analysis involved stereoscopic and low magnification study of Viking Orbiter images at scales ranging from near 3 km/cm. to about 18 km/cm. and photomosaics at 1:2 million and 1:500,000. Descriptions were made along with measurements and overlay maps. Classification, evolutionary sequence, and genetic interpretations follow.

The Southwest Elysium Canyon Complex comprises the Elysium Chasmata, Hyblaeus Chasma, Stura Vallis, and certain Elysium Fossae (4), along with various pits and graben. The complex is dominated by the Elysium Chasmata and related fosae which provide the predominent NNW-SSE orientation and near 240 kilometer overall length. The overall width is variable, around 30 to 50 kilometers. Individual components, for the most part, range from less than five to 15 kilometers across.

The Elysium Chasmata and related fossae are a series of large, deep, elongate depressions which trend N36W to N20W, more or less tangentially to Elysium Mons, but which become radial at the extreme north end. Hyblaeus Chasma and Stura Vallis, on the other hand are broad, shallow depressions which align radially to Elysium Mons, normal to the Elysium Chasmata. A fossa at the north end of the complex is also radial to Elysium Mons.

All more or less linear depressions having discernible widths are considered fossae. Their classification is based on form (1,5), distinguishing characteristics, and inferred genesis. Chasmata in this instance are simply larger versions and do not represent a distinct morphologic class. All fossae here are closed (1,5). Within this division they are classified as being either floored or floorless (1). Floored fossae have wide smooth floors, steep sides, and somewhat trapezoidal cross sections. Floorless fossae have sloping interiors and founded, U-shaped, cross sections. Elysium Chasmata and related fossae are floorless. Hyblaeus Chasma and Stura Vallis on the south and certain fossae at the north end of the complex are floored. This contrast follows orientation, and inferred relative age and genesis.

Elysium Chasmata and related fossae are some of the youngest features in the region and are the deepest components of the complex. They intersect and displace virtually all features encountered. The northernmost projection down drops the floor of the northern radial floored fossa. Deep northern fossae slice across shallower, floored fossae which trend in nearly the same direction. The southernmost chamsa cuts of the ends of Hyblaeus Chasma and Stura Vallis, and is depressed well below them.

SOUTHWEST ELYSIUM CANYON COMPLEX: McDonnell, J.H.

Both of the southern chasmata follow and truncate intersecting arcuate graben (3), which are also found along side them.

The radial, floored fossae are older, but not necessarily the oldest structures. The floor of Hyblaeus Chasma is off set by graben, while the rim in stepped back between faults; suggesting the graben are older, but have seen successive movement. Conversely, the chasma may have down dropped differentially between faults in the manner of rim set back. Hyblaeus structurally off sets near by pits, making the latter older. But others are inferred to be younger or penecontemporaneous on the basis of convexity of separating wall.

Aligned, floorless pits at the northeast end of the complex are among the oldest depressions. They are intersected by the northern radial fossa which has dropped below them. Fossae on the northwest and opposedly concave east are thought to be intermediate in age as they tend to be shallow and floored and are intersected by more recent fossae. Finally the long gouge-like fossa west of the Elysium Chasmata, between Hyblaeus and the northern fossae, is inferred to be penecontemporaneous with the Elysium Chasmata. It also intersects and cuts through all features encountered.

In summary, the depressions which make up what is called the Southwest Elysium Canyon Complex show a decided dichotomy in form and orientation and a definite sequence of formation. All are topographically closed (1,5) and are otherwise characterized by the presence or absence of well discernible floors. Graben and some pits are early, followed by radial and other floored fossae. These latter developed either as graben or by subsidence along irregular lines of weakness. Most recent are the deep floorless fossae running diagonally to Elysium Mons, which have developed along the earlier graben. The problem of material removal remains, but the draining and collaps of large shallow magma chambers (6) may be called for along with the interaction of near surface ice (1).

References

(1) Mouginis-Mark, P.J.(1985), Icarus 64, 265-284.
(2) Malin, M.C.(1977) GSA Bull. V.88, 908-919.
(3) Tanaka, K.L., Scott, D.H.(1985) Geologic Map of the Elysium Region of Mars, U.S.Geolgoical Survey Miscellaneous Investigation Series Map I-xxxx, Version 10/8/85.
(4) U.S. Geological Survey (1985), MTM-20217 &25217, Atlas of Mars, 1:500,000 topographic series.
(5) Sharp, R.P., Malin, M.C.(1975) GSA Bull. V.86, 593-609.
(6) Decker, R., Decker, B.(1981) Volcanoes, W.H.Freeman & Co.

**VALLES MARINERIS LANDSLIDES: EVIDENCE FOR MECHANICS OF LARGE ROCK AVALANCHES**; A. S. McEwen, U. S. Geological Survey, Flagstaff, AZ 86001.

The mechanism of transport of large rock avalanches has been the subject of considerable interest and controversy in recent decades. On Earth, the observed runout lengths (L) for large rock avalanches, relative to the height of drop (H), are much greater than can be explained by either sliding or dispersive grain-flow mechanisms. Most natural rock types have coefficients of friction (either sliding or internal friction) of 0.6 or higher, so movement is expected only over terrain with an average slope of at least 30° (or H/L at least 0.58); this expectation is confirmed for rock avalanches of relatively small volume and for other flows of dry, granular material. However, as rock avalanches increase in volume, H/L decreases to values as low as 0.1 or less, and a log-log plot of H/L versus volume shows a linear correlation [1,2].

Planetary comparisons under different conditions of gravity, atmospheric pressure, and volatile inventory may prove essential to resolving this question of mechanism. Mars is the only planetary body other than Earth known to have long-runout landslides; they are abundant in the equatorial canyon system of the Valles Marineris. Were the Valles Marineris landslides "wet" or "dry"? ("Wet" is taken to mean that the mass was saturated with water, thus eliminating or greatly reducing grain-to-grain contacts.) Lucchitta [3] thought that they were probably wet, whereas McEwen [4] concluded that they were probably dry. It has even been suggested that the landslides were subaqueous, collapsing into lakes [5]. However, the landslides are among the geologically youngest features on Mars [6]; they clearly postdate the interior layered deposits (of possible lacustrine origin), and there is no evidence for liquid water on the surface of Mars at the time of their formation.

Landslide properties were measured in three regions of Valles Marineris, where 1:500,000-scale topographic maps with 200-m contour intervals are available: (1) the Tithonium and Ius Chasmata region from about lat -9° to -4°, long 83° to 88° [7]; (2) an additional part of Tithonium Chasma from lat -7.5° to -4°, long 80° to 85°; and (3) a region including Ophir Chasma and part of Candor Chasma from lat -7.6° to -3°, long 70° to 75.1°. (Work on maps of the last two regions is in progress by the U.S. Geological Survey.) Within these regions, 25 landslides having identifiable source locations and avalanche deposits were studied. All of the relatively high resolution (200 m/pixel or better) Viking Orbiter images of these areas were utilized.

Landslide volumes were estimated by two methods. For the large landslides with well-defined slump scars, the volume missing from the scars was estimated. For the smaller landslides, the scars are too small relative to the topographic data for the missing volume to be estimated, but the deposits appear to have uniform thicknesses; thus the volumes were estimated from the landslide-deposit area times the estimated height of the flow front. The errors in the volume estimates are small compared

with the variations in landslide volume (more than 5 orders of magnitude.

If we assume a Bingham rheology for the avalanche and uniform, steady flow conditions, then the yield strength, K, may be estimated by $K = pgDsin\beta$, where p is the flow density, g is the gravitational acceleration (3.72 m/s for Mars), D is the height of the flow front, and ß is the ground slope at the flow front. For p, 2000 $kg/m^3$ was assumed, which is characteristic of terrestrial rock avalanches. Yield-strength estimates range from $10^4$ to $10^5$ Pa. Terrestrial dry-rock avalanches are characterized by yield strengths near $10^4$ Pa, whereas water-saturated debris flows have yield strengths typically from $10^2$ to $10^3$ Pa. Therefore, even with an uncertainty in the yield-strength estimates of an order of magnitude, the values are clearly consistent with the yield strengths typical of dry rock debris.

Trends of decreasing H/L with increasing volume are obvious from both the terrestrial and the Valles Marineris observations. Least-square fits to the datasets give linear correlation coefficients of 0.82 for the terrestrial points and 0.90 for the Valles Marineris points. The slopes of the two trends are nearly identical. These relations are very different from those seen in wet debris flows, where H/L is almost always less than 0.1 irrespective of volume. If the Valles Marineris landslides were either wet debris flows or subaqueous flows, then the points would be expected to plot below the terrestrial values for dry rock avalanches. Instead, the Valles Marineris trend plots above the terrestrial trend.

Although the slopes of the terrestrial and Valles Marineris trends are nearly identical, there is clearly an offset between the trends. At a given value of H/L, the Martian landslides are typically about 50 to 100 times more voluminous than the terrestrial counterparts, or, at a given volume, H/L is typically about two times larger on Mars. The offset might be explained by the effect of a lower g on flows with high yield strengths. Although this explanation does not answer the more fundamental question of how friction is overcome in large dry-rock avalanches, it does suggest that the correct model should be consistent with the presence of high yield strengths in the moving flows. Fluidization by a gas, for example, eliminates the yield strength in an active flow and is not consistent with the evidence presented here.

[1] Scheidegger, A. E., 1973, Rock Mechanics 5, 231-236.
[2] Hsu, K. J., 1975, Geol. Soc. America Bull. 86, 129-140.
[3] Lucchitta, B. K., 1987, Icarus 72, 411-429.
[4] McEwen, A. S., 1989, Geology 17, 1111-1114.
[5] Shaller, P. J., Murray, B. C., and Albee, A. L., 1989, Lunar and Planetary Science XX, 990-991.
[6] Lucchitta, B. K., 1979, J. Geophys. Res. 84, 8097-8113.
[7] U. S. Geological Survey, 1980, Misc. Inv. Ser. Map I-1294.

POLYGONAL TERRANE OF MARS: STRESSES FROM DRAPE FOLDING, George E. McGill and L. Scott Hills, University of Massachusetts, Amherst, MA 01003.

The giant polygons of Acidalia and Utopia planitiae pose a fascinating mechanical problem: all of the earth analogues that come readily to mind are almost certainly invalid. Polygonal structures on the earth demonstrate a roughly 10:1 relationship between polygon diameter and the depth of the bounding fractures (1). Transferring this relationship to the giant polygons of the martian northern plains, which are 5-20 Km in diameter, requires that fracturing driven by cooling or desiccation penetrate to depths as great as 2 Km. This is mechanically unlikely, as is convincingly argued by Pechmann (2), who concludes that only deep-seated tectonic stresses could account for the fracture depth required to form such large polygons. But the giant martian polygons do not resemble any known tectonic structures (2,3). Polygonal terrane corresponds in age to large outflow channels that drain from the highlands into the lowlands (4), and it occurs in the topographically lowest parts of the lowlands (5). It also can be shown that the polygonal troughs formed almost immediately following deposition of these materials (3), a timing that does not rule out a tectonic origin, of course, but which does strongly suggest a link between deposition and fracturing. Geological evidence thus favors a model for polygon formation that involves shrinkage stresses due to desiccation of wet sediment. However, most similar structures on earth have dimensions on the order of centimeters to meters; rare large polygons with diameters up to 300m are known from a few playas (6).

The martian polygonal terrane was deposited unconformably on top of a rugged surface characterized by knobs, mesas, fragments of ancient crater rims, and scattered fresh craters (3,7). This rugged surface is exposed south of the polygonal terrane of Utopia planitia. Northward, the surface is increasingly obscured by younger plains deposits until it disappears completely beneath polygonal terrane (7). Circular troughs present among the more irregularly shaped polygons within polygonal terrane occur above buried fresh craters similar to those exposed to the south. The complete burial of a crater population that includes craters as large as 40 Km in diameter requires that polygonal terrain be at least 450m thick (8). Moreover, the sediments also must be thick enough to cover the crater rims to depths greater than the apparent depths of the circular troughs, implying a thickness on the order of 600m. The presence of rugged topography beneath a thick layer of wet sediment will result in the development of drape anticlines and synclines as the sediment compacts because the total downward displacement of an originally horizontal plane within the sediments will vary directly with the thickness of compacting underlying material. These drape folds will superpose bending stresses onto the pervasive tensile stresses due to desiccation shrinkage. The objectives of this research are 1) to test the feasibility of this model by estimating the magnitudes of the stresses involved, and 2) to continue developing an hypothesis for polygon formation that considers both geological and mechanical data.

Because crater morphology is well known (8), and because of the geometric simplicity provided by radial symmetry, our mechanical analysis considers the specific case where the rim of a crater 10 km in diameter is covered by sediments thick enough to bury the rim to a depth of 400m. For purposes of analysis, it is convenient to consider the lower part of the sedimentary layer filling the crater as an "older fill", and the upper part as a "younger cover". This may actually represent the true geological history of the deposit, but the analysis does not depend on this.

Two quantitative models are attempted, one based on plate-bending theory, the other using finite-element methods. Both models draw on the literature of soil mechanics to estimate the rheological properties of polygonal terrane materials. Most normally consolidated sand- and clay-rich soils exhibit Young's moduli in the range 5-75 MPa, and Poisson's ratios between 0.25 and 0.40 (9). Cohesive strengths commonly are negligible, and shear failure is governed by angles of internal friction averaging $30^{\circ}$. The plate bending model considers all material above the crater rim to be an elastic plate that is bent as the underlying older fill compacts under the load of the younger cover. Because boundary conditions impose a sinusoidal shape on the bent plate, this

approach does not predict a very realistic shape for a drape fold formed over the upward-concave slope of a crater wall. However, the sinusoidal shape underestimates bending stresses, and thus is conservative. The finite-element model considers the three-dimensional elastic deformation of older fill and younger cover as a function of position and time. The buried crater rim is modeled using a cubic spline, hence the shape of the resulting drape fold seems very realistic. Because of the flexibility of the finite-element method, various depth-dependent combinations of elastic properties and extent of preconsolidation can be modeled. The assumption of purely elastic compaction, although probably not very realistic, also is conservative.

The two approaches yield similar results. Even when very conservative estimates of compaction of older fill are used (<10%), failure by brittle fracture or by shear is predicted to depths of the right order to account for the troughs bounding the martian polygons. This result is obtained without considering the tensile stresses due to desiccation shrinkage. If these are of the same order as the bending stresses, as seems likely, then not only are the total stresses available adequate to cause failure to the requisite depth, but superposition of these two stress systems will produce significant differences in total tensile stresses available to initiate fracturing at the surface; the probability of fracturing will be enhanced by drape anticlines and domes above crater rims and knobs/mesas, and suppressed by drape synclines between these features. Thus the scale of the polygons relates to the spacing of buried topographic features rather than to the strength/thickness characteristics of the sediment layer.

Compaction and bending must occur quickly enough for elastic strains to build up faster than they can be relaxed by pseudoviscous creep. Equivalent viscosity of soil is rarely determined, but in slow landslides it is estimated to be about $10^5$-$10^6$ MPa-s (10). Maxwell times for materials with equivalent viscosities of $10^6$-$10^8$ MPa-s and Young's moduli of about 10 MPa are months to years. Very large Maxwell times (order of $10^6$ years) would thus seem to require unrealistically high equivalent viscosities. Consequently, it appears as if the formation of the martian polygons must be a geologically rapid process.

(1) Lachenbruch, A.H., J. Geophys. Res., 66, 4273-4292, 1961.
(2) Pechmann, J.C., Icarus, 42, 185-210, 1980.
(3) McGill, G.E., Geophys. Res. Letts., 13, 705-708, 1986.
(4) Neukum, G., and K. Hiller, J. Geophys. Res., 86, 3097-3121, 1981.
(5) Lucchitta, B.K., et al., J. Geophys. Res., 91, E166-E174, 1986.
(6) Neal, J.T., , et al., Bull. Geol. Soc. America, 79, 69-90, 1968.
(7) McGill, G.E., J. Geophys. Res., 94, 2753-2759, 1989.
(8) Pike, R.J., and P.A. Davis, Lunar Planet. Sci. XV, 645-646, 1984.
(9) Hunt, R.E., Geotechnical Engineering Analysis and Evaluation, McGraw-Hill, 1986.
(10) Iverson, R.M., in Abrahams, A.D., Hillslope processes, Allen & Unwin, 1986.

**STATE OF STRESS AND ERUPTION CHARACTERISTICS OF MARTIAN VOLCANOES.** Patrick J. McGovern and Sean C. Solomon, Dept. of Earth, Atmospheric, and Planetary Sciences, Massachusetts Institute of Technology, Cambridge, MA 02139.

*Introduction.* The growth of a large volcano exerts a load on a planetary lithosphere that can give rise to flexural deformation and faulting. Lithospheric stress, in turn, can influence the state of stress within the volcano and thus the characteristics of eruptions and the deformation and growth of the construct. Previous studies of the stress state within and beneath terrestrial volcanoes have been of two main types: (1) models of plate flexural stresses in isolation [1,2], or (2) finite element models of volcanic bodies with rigid lower boundary conditions [3,4]. We seek a model which couples the stress and displacement fields of both the plate and volcano structures, in order to understand the behavior of Martian volcanoes and the relationship of eruption styles to evolving local and regional stress.

*Method.* We use the finite element code TECTON, written by H.J. Melosh and A. Rafesky [5,6], to construct axisymmetric models of volcanoes resting on an elastic lithospheric plate overlying a viscoelastic asthenosphere. This code can model buoyancy forces supporting the plate, thus allowing a proper representation of plate flexure. Several values of the ratio of volcano size to lithospheric thickness were considered. The thickness of the strong upper lithosphere was taken from flexure models [7]. The viscoelastic layer was taken to extend to a sufficient depth so that a rigid lower boundary has no significant influence on the results. The code first calculates elastic deformations and stresses and then determines the time-dependent viscous deformations and stresses. Time in the model scales as the Maxwell time in the asthenosphere.

*Results.* The deviatoric stress field (principal stress directions) resulting from the elastic deformation induced by a volcano 20 km in height and 400 km in diameter on a strong lithosphere 40 km thick (parameters appropriate to Ascraeus Mons) is shown in Fig. 1. The stress field after the plate has flexed under the volcanic load is shown in Fig. 2. We note two effects of plate flexure with increasing time: (1) the deviatoric stresses in the surface region grow quite large; and (2) the area where the principal compressive direction is parallel to the surface extends progressively deeper, eventually reaching into the crust beneath the construct. Also, at large times, the boundary between the area of rotated stress directions and the underlying area of 'normal' stress orientations (compression axis vertical) is a region of low deviatoric stress. We find that plate deflections and stresses within the lithosphere are in qualitative agreement with those of flexural models [7].

*Discussion.* The above effects of flexure on the volcano stress field may have important implications for the history of volcanic events. It has been suggested [1] that time-dependent flexural stresses at the top of the elastic lithosphere beneath the Hawaiian volcanic chain control the history of eruptions at individual volcanoes, with eruptions ceasing during intervals when the two principal horizontal stress deviators are compressive and of significant magnitude. Applied to our model, this would imply that at early times after an interval of significant shield-building eruptions, the horizontal stress deviators within and beneath the volcano are tensional, so magma ascent to high-level chambers within the construct is favored. At later times, the stress directions in and beneath the volcano rotate such that the most compressive axis is nearly horizontal, so high-level magma bodies and summit eruptions would not be expected unless the ascending magma is significantly overpressured. In contrast, given that magma propagates through conduits oriented perpendicular to the least compressive stress, the stress orientations shown in Fig. 2 imply that flank eruptions are preferred at this stage of development. The young ages of the volcanic units surrounding Olympus Mons and Tharsis Montes are consistent with such an evolution in eruptive style [8].

*Conclusions.* These initial models suggest that the state of stress during volcano growth and lithospheric flexure can have an important influence on volcano evolution on Mars. Further models are planned to examine the roles of magma chamber overpressure and evacuation and near-surface faulting on the stress orientations presented here.

*References.* [1] U.S. ten Brink and T.M. Brocher, *JGR, 92,* 13687, 1987; [2] C.H. Thurber and A.E. Gripp, *JGR, 93,* 4721, 1988; [3] L. Chevallier and W.J. Verwoerd, *JGR, 93,*

4182 1988; [4] J.H. Dieterich, *JGR, 93,* 4258, 1988; [5] H.J. Melosh and A. Rafesky, *GJRAS, 60,* 333, 1980; [6] H.J. Melosh and A. Rafesky, *JGR, 88,* 515, 1983; [7] R.P. Comer et al., *Rev. Geophys., 23,* 61, 1985; [8] D.H. Scott and K.L. Tanaka, *Icarus, 45,* 304, 1981.

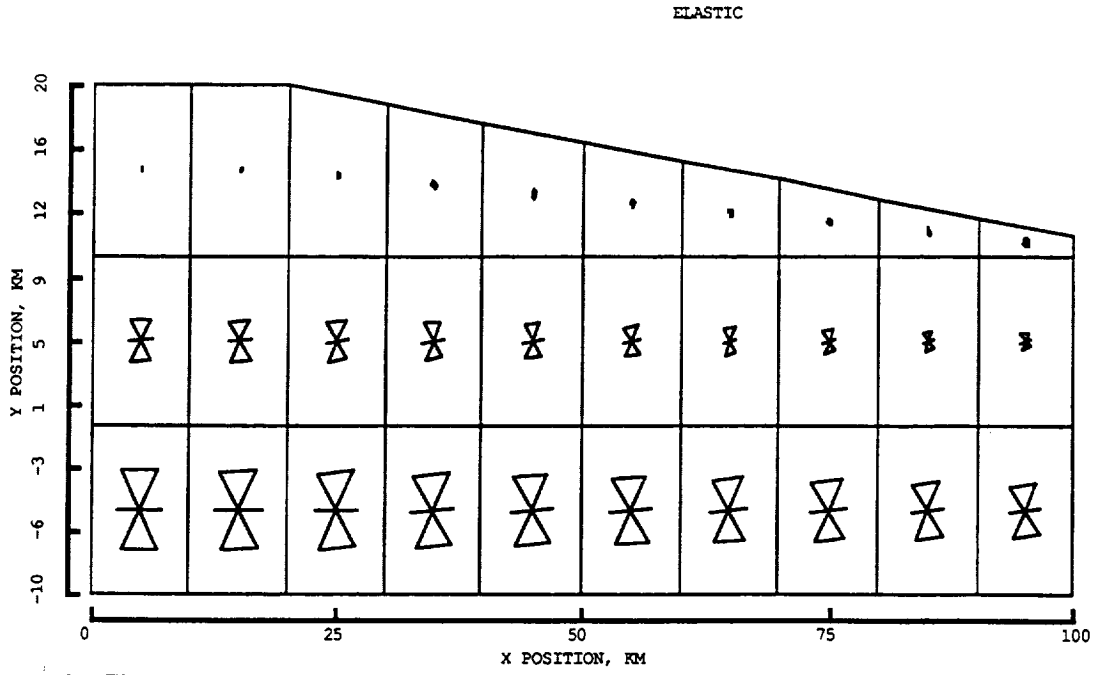


Figure 1. Close-up view of the deviatoric stress field in the volcano after the initial elastic deformation. An hourglass shape denotes the principal axis of compression, a bar denotes the principal axis of tension; the size of each symbol is proportional to deviatoric stress magnitude. The axis of rotational symmetry is x=0.

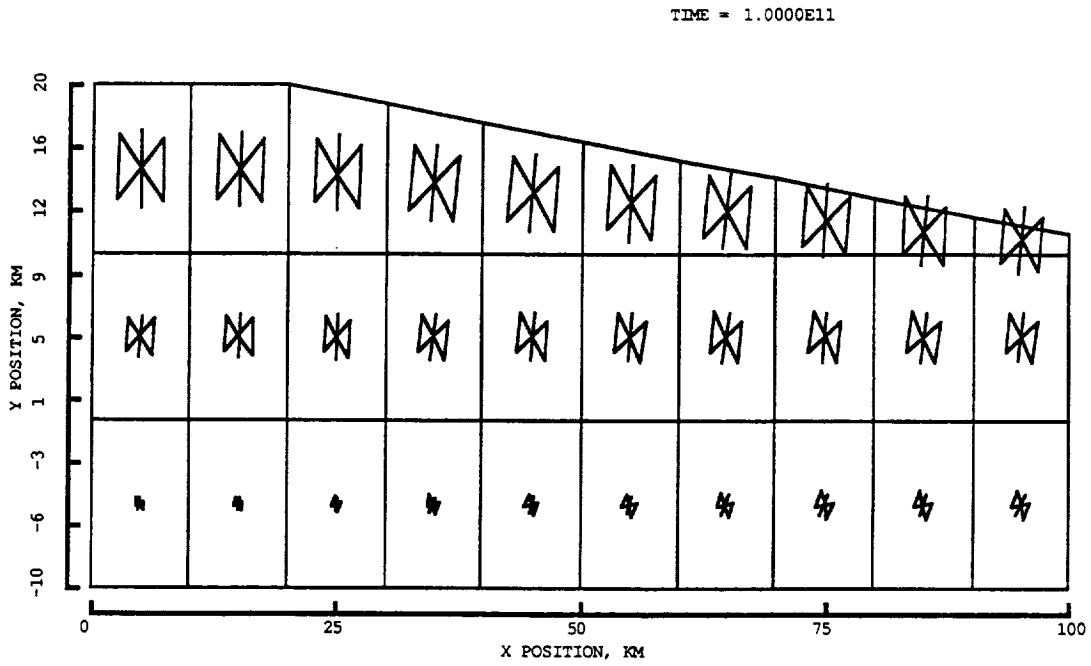


Figure 2. Deviatoric stress field in the volcano after flexure. The time elapsed is on the order of 100 Maxwell times. Rotation of the stress axes extends downward to the top layer of the plate (below y=0).

ANALYSES AND MORPHOLOGY OF A LAVA FLOW, ASCRAEUS MONS, MARS; H.J. Moore, U.S. Geological Survey, Menlo Park, CA, 94025 and P.A. Davis, U.S. Geological Survey, Flagstaff, AZ, 86001.

We have obtained some 32 profiles of lava flows on Mars using photoclinometry [1]. These photoclinometric profiles were leveled by adjusting them until the levee crests had the same elevations. Here, we compare our lava-flow dimensions and rheologic analyses for one profile on Ascraeus Mons with previous results using dimensions from images and shadow techniques [2, profile E5] (fig. 1, Table 1). In our rheological analyses, we use a wide-flow model [3], Hulme's model [4], and model 1 of Baloga and Crisp [5]. Effusion rates are estimated by using an unmixed-cooling model [6] and calibrated by using Hawaiian flows [7] and a Graetz-number model [4,8]. Our Graetz-number effusion rates are about 3.9 times larger than previous ones [7] because of a corresponding increase in thermal diffusivity.

In general, our results are compatible with the previous ones [2] (Table 1). Yield strengths are about 1 to 10 kPa, and Bingham viscosities are about 1 to 10 MPa*s. Newtonian viscosities for the wide-flow model are about 4 times larger than Bingham viscosities. Rates of shear are very small ($5 \times 10^{-8}$ $s^{-1}$). Both Newtonian viscosities and rates of shear are comparable to those expected for basaltic flows just before they stop [9,10].

Morphologies of flow E (fig. 1) and of many other flows near the summit of Ascraeus Mons are complex and similar to those of Hawaii [11] and Etna [12]. For both types of flows, morphologies indicate the presence of overflow levees, sheets, and lobes, breached lava ponds and breakouts; locally, channels appear clogged (profile A, fig. 1) and, in other places, drained (profile B, fig 1); and tips of flows are commonly multilobed (fig. 1). Interpretation of these flows introduces uncertainties into the appropriate flow dimensions to be used in the rheologic models. Additional uncertainties exist that are related to effusion-rate models and parameters, flow lengths and areas, and measurement techniques. Thus, the compatibility of the results from our rheologic analyses and the previous results [2] is surprising.

REFERENCES

[1] Davis, P.A., et al., 1984, J. Geophys. Res., v. 89, p. 9449-9457. [2] Zimbelman, J.R., 1985, J. Geophys. Res., v. 90, Suppl. D, p. D157-162. [3] Moore, H.J., et al., 1975, Proc. 6th LSC., p. 101-118.. [4] Hulme, G., 1974, Geophys. J. Roy. Astron. Soc., v. 39, p. 361-383. [5] Baloga, S.M. and Crisp, J., 1988, unpubl. rept., 35 p. [6] Pieri, D.C., et al., 1986, J. Volc. Geotherm. Res., v. 30, p. 29-45. [7] Moore, H.J., et al., 1989, Repts. Planet. Geol. Geophys. Prgm.-1988, NASA TM 4130, p. 387-389. [8] Hulme, G., et al., 1977, Phil. Trans. Roy. Soc., Lond., ser. A, v. 285, p. 227-234. [9] Moore, H.J., 1987, USGS Prof. Paper 1350, p. 1569-1588. [10] Walker, G.P.L.,

1967, Nature, v. 213, p. 484-485. [11] Lipman, P.W., et al., 1987, USGS Prof. Paper 1350, p. 1527-1567. [12] Kilburn, C.R.J., et al., 1988, J. Geopys. Res., v. 93, p. 14759-14772.

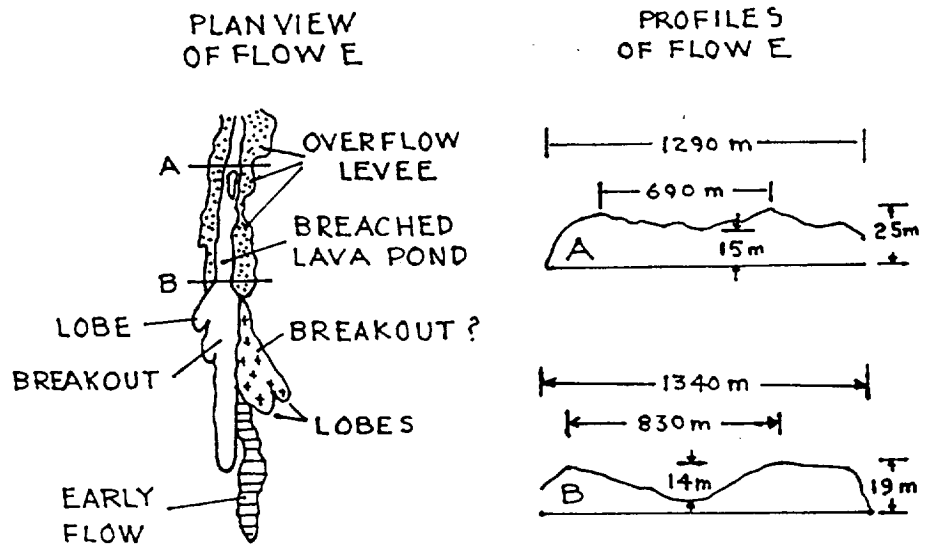


Figure 1. Plan view and photoclinometric profiles of Flow E of Zimbelman [2]. Profile B is same as E5 of Zimbelman [2]; Zy=15 m in Table 1 estimated from profile A.

Table 1. Comparison of dimensions and rheologies for profile E5 of Zimbelman [2] and this work. Equations used to calculate yield strengths (Y1, Y2, and Y3) and Bingham viscosities are given in Zimbelman [2].

| Source | Flow Dimensions | | | | | | Slope Angle | Effusion Rates | |
|---|---|---|---|---|---|---|---|---|---|
| | Zy m | Zl m | Zf m | Yc m | Yf m | Xf km | Theta deg. | Fc $m^3/s$ | Fg $m^3/s$ |
| Zimbelman | 25 | 25 | na | 470 | 1350 | 14.8 | 5.0 | 59 | |
| This work | 15 | 19 | 29 | 830 | 1340 | 15.4 | 3.8 | 120 | 96 |

| | Yield Strength (kPa) | | | | Bingham Viscosity (Mpa) Graetz (Fc) | | | Cooling (Fc) | | |
|---|---|---|---|---|---|---|---|---|---|---|
| | Y1[1] | Y2 | Y3[2] | Y4[3] | E1[2] | E2[2] | E3[2] | Ew[1] | Eh[2] | E4[3] |
| Zimbelman | 21 | 4 | 63 | | 12 | 3 | 36 | | | |
| This work | 8 | 2 | 19 | 4 | 12 | | 19 | 9 | 14 | 4 |

[1] Wide-flow model. [2] Hulme model. [3] Baloga and Crisp Model.

SURFACE-MATERIAL MAPS OF VIKING LANDING SITES ON MARS; H.J. Moore, U.S. Geological Survey, Menlo Park, CA, 94025; J.M. Keller, Stanford University, Stanford, CA, 94309.

We have mapped the surface materials at the Viking landing sites because a review of the literature reveals that such maps have not been made and better information on the types of materials and their abundances should lead to a better understanding of the geology and remote-sensing signatures of the sites. The maps extend to 9 m in front of each lander and are about 15 m wide -- an area comparable to the area of a pixel in the highest resolution Viking Orbiter images of the Lander 1 site.

The maps are divided into near and far fields. Data for the near fields are from: 1/10-scale maps [1], unpublished maps, and lander images. Data for the far fields are from: 1/20-scale contour maps [2], lander camera mosaics with overlain contours [2], and lander images. Rocks were located on these maps using stereometric measurements and the contour maps. Rocks form the control for delineation of other surface materials.

Map units are: (1) fine, (2) soillike, and (3) rock materials. Coordinates, length (l), width (w), and height (h) for each rock are recorded in a file for computational purposes. For many rocks, l or w was estimated. The rocks are assumed to be ellipsoids. Size-frequency and area-covered distributions of rocks are derived from the file according to the surrounding map unit, field, and size. All rocks mapped within fine material and all rocks >0.25 m in the near and far fields are included in the distributions, but rocks <0.25 m in the far fields are assumed to have the same distribution as rocks <0.25 m in the near fields. Areas covered by fine materials and rocks and soillike materials and rocks are measured on the maps. Areas covered by fine and soillike materials are obtained by subtraction of the area covered by rocks.

The forms of our size-frequency distributions of rocks are similar to previous ones [1,3]. Frequencies of rocks >0.18 m are larger at Lander 2 than Lander 1, but the reverse is true for smaller rocks. Fractions of area covered by the larger rocks in logarithmic size-bins are irregular and yield no simple relations for extrapolations to larger sizes of rocks, but the areas covered by small rocks diminish rapidly with decreasing size. Our fractions of area covered by centimeter-size and larger objects and rocks are about 11.5% at Lander 1 and about 16% at Lander 2. Outcrops of rock cover an additional 4.5% of the area at the Lander 1 site. At Lander 1, about 18% of the surface is covered by thick deposits of fines and 40% by both thick and thin fines. At Lander 2, about 30%

of the surface is covered with fine material.

Although there are questions about the physical properties of the materials mapped beyond the sample fields, we assume that the fine materials are loose fine-grained powders with a small thermal inertia like that previously assumed for drift material [4]. If this assumption is correct, our results suggest that the thermal inertias of crusty to cloddy and blocky materials [1] may be larger than previously estimated [4] and that the amounts of $SO_3$ plus chlorine in the soillike materials [5] are directly proportional to their thermal inertias. These differences do not substantially alter the previous conclusions of Moore and Jakosky [4].

Preliminary analyses of our data suggest that polarized- and depolarized radar-echo cross sections and normal radar reflectivities for the Lander 1 site should be about the same at 3.5- and 12.5-cm wavelengths. For Lander 2, polarized- and depolarized-echo cross sections are smaller and the quasi-specular cross section is larger at 3.5-cm wavelength than at 12.5-cm wavelength. These relations are chiefly related to the area distributions of rocks and the model used to calculate the radar cross sections [5,6]. For Lander 2, the fraction of area covered by "wavelength-size" rocks, or diffuse scatterers, is smaller for the 3.5-cm wavelength than the 12.5-cm wavelength; for Lander 1, these areas are about the same for both wavelengths. For Lander 2, the fraction of area of large rocks contributing to the quasi-specular echo is greater at the 3.5-cm wavelength than at the 12.5-cm wavelength; for Lander 1 these areas are about the same at both wavelengths. Finally, the three types of surface materials and "wavelength-size" rocks contribute to the bulk quasi-specular radar echoes in complicated ways.

## REFERENCES

[1] Moore, H.J., et al., 1987, U.S. Geol. Prof. Paper 1389, 222p. [2] Liebes, S. Jr., 1982, NASA CR 3568, 290p. [3] Binder, A., et al., 1977, J. Geophys. Res., v. 82, p. 4439-4451. [4] Moore H.J. and Jakosky, B.M., 1989, Icarus, v. 81, p. 164-184. [5] Evans, J.V. and Hagfors, T., 1964, Icarus, v. 3, p.151-160. [6] Campbell, M.J. and Ulrichs, J., 1969, J. Geophys. Res., v. 74, p. 5867-5881.

N91-22997

IRON MINERALOGY OF A HAWAIIAN PALAGONITIC SOIL WITH MARS-LIKE SPECTRAL AND MAGNETIC PROPERTIES. [1] Richard V. Morris, [1]James L. Gooding, [2]Howard V. Lauer, Jr., and [3]Robert B. Singer. [1]Code SN, NASA-JSC, Houston, TX 77058; [2]LESC, Houston, TX 77058; [3]Lunar and Planetary Laboratory, Univ. of Arizona, Tucson, AZ 85721.

## INTRODUCTION

Visible and near-IR spectral data for some palagonitic soils from Mauna Kea, Hawaii, are similar to corresponding spectral data for Mars [e.g., 1-3]. It is important to understand the composition, distribution, and mineralogy of the ferric-bearing phases for the best spectral analogues because the correspondence in spectral properties implies that the nature of their ferric-bearing phases may be similar to those on Mars. In order to constrain interpretations of the martian data, a variety of palagonitic soils should be studied in order to establish to what extent differences in their spectral data correspond to differences in the mineralogy of their ferric-bearing phases. Reported here are spectral (350-2100 nm), Mossbauer, magnetic, and some compositional data for one of a suite of Hawaiian palagonitic soils we are studying. The soil (HWMK1) was collected below the biologically active zone from the sides of a gully cut at 9000 ft elevation on Mauna Kea. The soil was wet sieved with freon into seven size fractions less than 1 mm.

## RESULTS AND DISCUSSION

Reflectivity spectra (Figure 1) for the 500-1000 $\mu$m and <20 $\mu$m size separates are, respectively, reasonable analogues for the composite martian dark and bright region spectra [e.g., 4]. The positions and shapes of the ferric adsorption edges generally correspond, and the relative difference in the near-IR reflectivity compare favorably with the martian case. The negative near-IR spectral slope that is a characteristic of martian dark regions (but not martian bright regions) is present for the 500-1000 $\mu$m size separate, but not for the <20 $\mu$m separate.

The Mossbauer spectra (Figure 2) show that there is a large difference in the iron mineralogy of the two size separates. One sextet and two doublets are readily apparent in the spectra. Sextet S1 is reasonably assigned to titanomagnetite, which is present based on petrographic and electron microprobe data of soil particles from HWMK1. The position of the ferrous D1 doublet and petrographic observations of olivine both imply assignment of the D1 doublet to olivine. Doublet D2 results from ferric iron, but its mineralogical assignment is not possible with available data. It is, however, likely that a nanophase (superparamagnetic) ferric oxide/oxyhydroxide phase that is the pigment for the soil. As shown by the change in the peak area ratio D2/(D1+S1) from 0.64 for the 500-1000 $\mu$m size separate to 0.93 for the <20 $\mu$m size separate, the latter separate is more highly oxidized and is probably derived by weathering from less oxidized material like the 500-1000 $\mu$m separate.

An important difference between the spectrum of the <20 $\mu$m size separate and the composite martian bright region spectrum is that the latter has a shallow band centered near 870 nm. This band and the other ferric spectral features in the martian data are consistent with the presence of hematite mostly as pigmentary particles having diameters in the range less than ~10 nm (nanophase hematite; np-Hm) but with some larger diameter hematite particles (bulk-Hm) to account for the shallow 870 nm band [5,6]. The absence of the band for HWMK1(<20) implies that, optically speaking, bulk-Hm is relatively more important for the composite martian spectrum. Although the spectral

properties of np-Hm are known, those for other nanophase ferric oxides/oxyhydroxides are not. If they are all nearly equivalent, the nanophase pigment on Mars and for HWMK1(<20) can be fundamentally different but appear to be the same on the basis of spectral data. That this may be the case is suggested by $H_2O$ analyses. The $H_2O$ released from HWMK1(<20) at high temperature (>100°C) is ~18%, which is considerably more than the ~1-3% apparently present in martian soil [7]. This may suggest FeOOH nanophases for the palagonitic soil and $Fe_2O_3$ nanophases soils for Mars.

Palagonitic soil is also a reasonable magnetic analogue for martian soil. The saturation magnetization ($J_s$) of 0.98 $Am^2/kg$ for <1 mm HWMK1 is at the low end of the 1-7 $Am^2/kg$ range estimated for martian soil [8]. Mossbauer and magnetic data for magnetic separates show that the observed $J_s$ results primarily from titanomagnetite, which is a result of primary basaltic volcanism as opposed to subsequent weathering processes. Because potential weathering products (e.g., maghemite and np-Hm) are strongly magnetic, the magnetic nature on martian soil could result from strongly magnetic phases whose origins are primary crystallization, weathering products, or both.

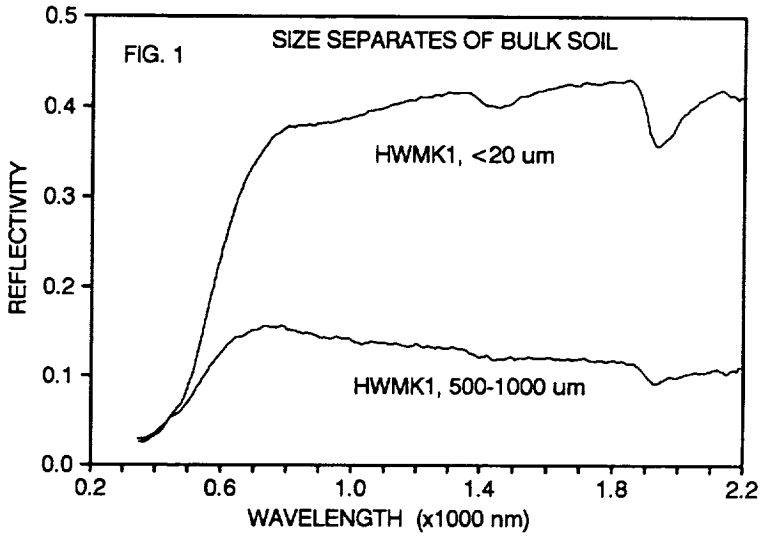


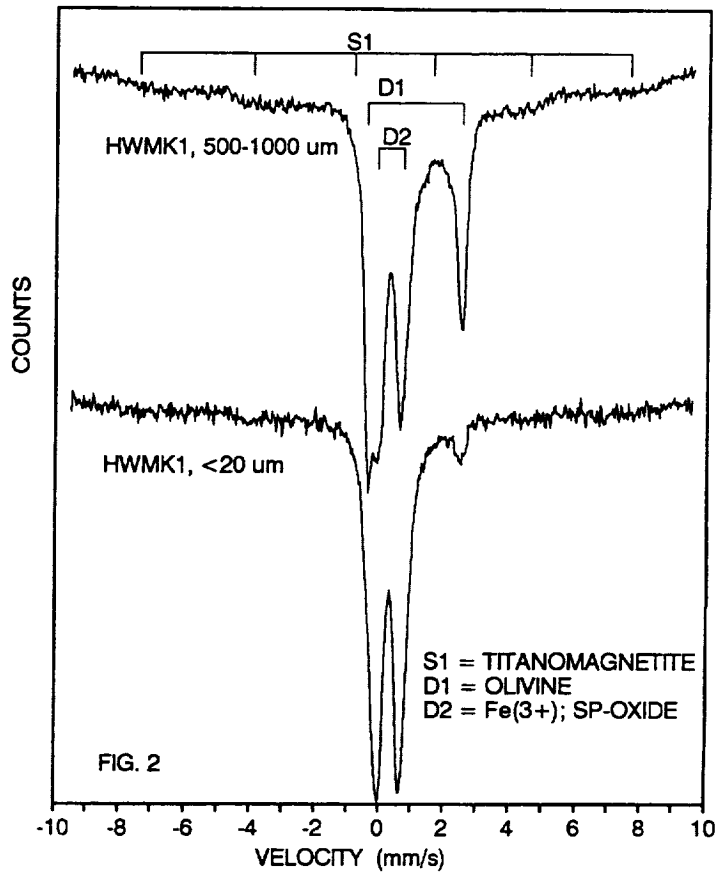


**References:** [1] Evans and Adams, *PLPSC11*, 757, 1980; [2] Singer, *JGR*, *87*, 10159, 1982; [3] Adams et al., *JGR*, *91*, 8089, 1986; [4] Singer, *Adv. Space Res.*, *5*, 59, 1985; [5] Morris et al., *JGR*, *94*, 2760, 1989; [6] Morris and Lauer, *JGR*, accepted, 1990; [7] Anderson and Tice, *J. Mol. Evol.*, *14*, 33, 1979; [8] Moskowitz and Hargraves, *JGR*, *87*, 10115, 1982.

# EVOLUTION OF THE OLYMPUS MONS CALDERA, MARS

Peter J. Mouginis-Mark[1]; Mark S. Robinson[1]; and Maria T. Zuber[2]. 1: Planetary Geosciences Division, SOEST, Univ. Hawaii, Honolulu, HI, 96822; 2: Code 621 Goddard Space Flight Center, Greenbelt, MD 20771.

Extensive high-resolution (15 - 20 m/pixel) coverage of Olympus Mons volcano permits the investigation of the sequence of events associated with the evolution of the nested summit caldera, thereby extending our previous study (1). The sequence of intra-caldera events is well illustrated by image data collected on orbits 473S and 474S of Viking Orbiter 1 (Fig. 1a). These data cover both the oldest and youngest portions of the caldera floor. Our observations permit the following chronology for the caldera floor to be inferred, which in turn can be interpreted in terms of the internal structure of the volcano (i.e., magma chamber depth, existence of dikes; ref. 2, 3):

**Stage 1**: The first preserved summit event was the catastrophic collapse and subsequent partial infilling of crater #1 (Fig. 1b). Our own shadow length measurements of the preserved wall (Viking frame 890A68, 156 m/pixel) indicate that at least 1,100 ± 60 m of collapse took place. Wall material from this collapse is now buried beneath younger materials. **Stage 2**: Subsidence across the entire caldera floor promoted the formation of the radial and concentric ridges similar to lunar mare ridges (Fig. 2). Continued subsidence (~1,300 ± 120 m of displacement) of the central portion of crater #1 created an extensional environment close to caldera wall and a compressional environment closer to caldera center. Concentric graben and ridges formed on the floor (Fig. 2). The transition from graben to ridges (local extension to compression) occurs at a radial distance of ~17 km from the center of the 65 km diameter caldera, and has been used to infer the magma chamber depth (2, 3). **Stage 3**: New collapse events occurred to the west, forming crater #3. A similar episode of circumferential graben formation took place within this portion of the caldera. **Stage 4**: Additional new collapse events just south of the caldera center post-date graben formation within craters #1 and 3. **Stage 5**: On the basis of morphologic evidence for resurfacing, during (or just after) its formation, the combined floor of craters 4 and 5 was probably occupied by a large lava lake. Linear ridges formed on surface that are interpreted to be compressional features produced by local convergence (rafting) on the lake surface. These ridges (Fig. 3) cross boundaries of craters 4 & 5, indicating that both craters were flooded (and, by inference, were convectively overturning) at the same time. **Stage 6**: Partial drainage of the lava lake surface produced a bench around perimeter of crater 4. **Stage 7**: Continued subsidence of entire summit area produced a compressional environment that promoted the formation of large (>3 km wide) wrinkle ridges in craters 1, 2 and 5 (Fig. 3). The numerous linear ridges formed in Stage 6 are now preserved on top of these larger wrinkle ridges. **Stage 8**: Final collapse event of ~350 m displacement produces crater #6. There is no evidence of surface features that could be associated with dynamic overturn of the lava lake on this crater floor. Nor is there any evidence of subsequent tectonic deformation.

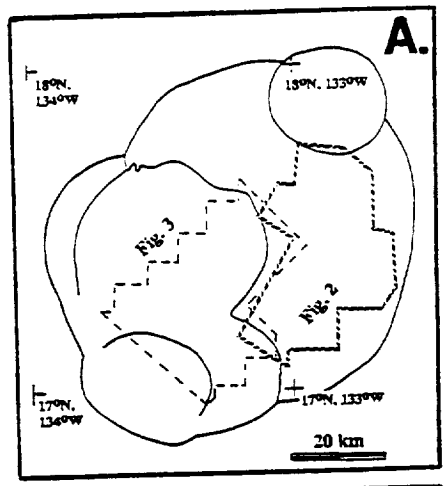


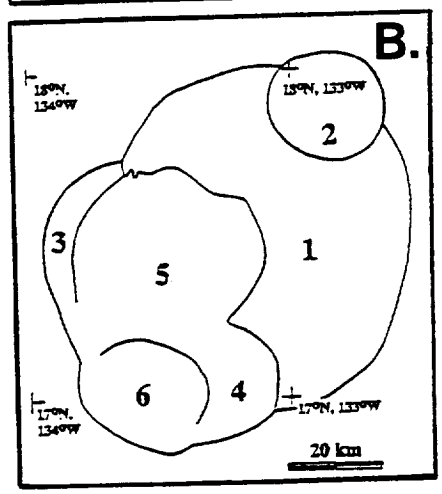


Fig. 1a (Top): Data coverage from Orbits 437S (Fig. 3) and 474S (Fig. 2). Fig. 1b (Bottom): Sequence of caldera collapse episodes. "1" oldest, "6" youngest (ref. 1).

This sequence of events demonstrates that Olympus Mons underwent a protracted period of summit activity. While all segments of the caldera floor possess craters that are interpreted to be impact in origin, no pronounced difference in crater size/frequency curves has been observed for different segments of the caldera floor, implying that all of the observed events probably occurred in a relatively short period of martian history.

References:
1) Mouginis-Mark, P. J. (1981), Proc. Lunar Planet. Sci., **12B**, p. 1431 - 1447. 2) Zuber, M. T. and Mouginis-Mark, P.J. (1989). *Proc. MEVTV Conf. on Tectonic Features on Mars*, LPI, Houston. 3) Zuber, M.T. and Mouginis-Mark P.J. (1990) This vol.

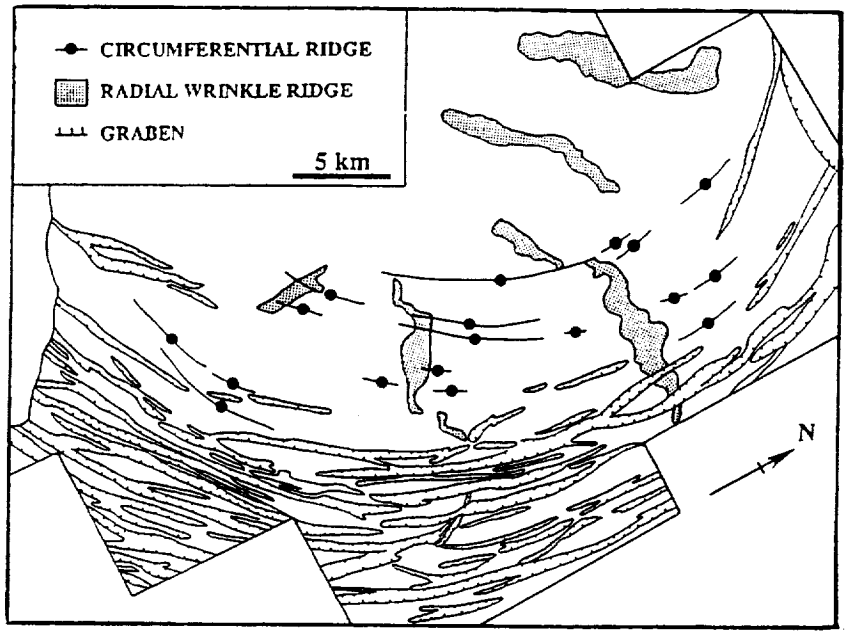


Fig. 2 (Top): Distribution of circumferential graben and ridges within the oldest portion (crater #1) of the Olympus Mons caldera. Note that these graben are truncated by the wall to crater #4. See Fig. 1a for location. Mapped from Viking Orbiter frames 473S27 - 29, 474S25 - 30.

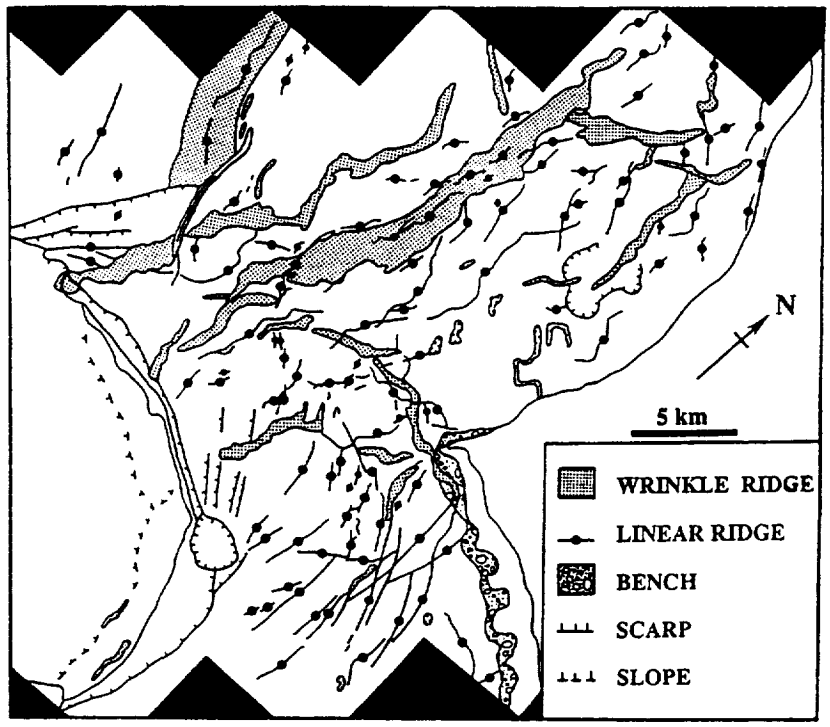


Fig. 3 (bottom): A complex series of linear ridges is seen on the floor of craters 4 and 5, indicating that a large over-turning lava lake may have existed soon after the initial collapse event. Note that these linear ridges are superposed upon the younger wrinkle ridges. See Fig. 1a for location. Mapped from Viking Orbiter frames 473S17 - 26.

Acknowledgement: The help of Eric Eliason at USGS Flagstaff in recovering the digital data used here for frame 860A68 is much appreciated.

**Interpretation of Spectral Units of Isidis-Syrtis Major from ISM-Phobos-2 Observations.** John F. Mustard[1], J-P. Bibring[2], S. Erard[2], E. M. Fischer[1], J. W. Head[1], S. Hurtrez[3], Y. Langevin[2], C. M. Pieters[1], C. J. Sotin[3] (1) Dept. Geol. Sci, Box 1846, Brown Univeristy, Providence RI (2) Institut d'Astrophysique Spatiale, 91405, Orsay France (3) Labratoire de Geodynamique Interne, 91405 Orsay, France

**Introduction:** During the encounter of Phobos-2 at Mars between January and March of 1989, imaging spectrometer data were obtained by the ISM instrument for several areas on Mars. These are the first high spectral and spatial resolution data for Mars and provide important information for identifying the composition of the atmosphere and surface (1). Data obtained for the Isidis-Syrtis Major region are examined here to determine and interpret the spectral features which characterize surface units defined in a companion abstract by (2). The area of the Martian surface covered by these data is shown in outline on the Viking orbiter photomosaic in Figure 1. A diverse range of geologic and geomorphic terrains are contained in this window and it is anticipated that careful analysis of these data will provide information on the composition of the Syrtis Major volcanic materials, basin rim materials of Isidis, and the cratered terrains of Arabia and Amenthes.

**Unit Definition:** Surface spectral units shown in the schematic map in Figure 2 were defined by (2) on the basis of spectral variation using the first 51 even channels. In this approach, each pixel in the image data is modelled as a linear combination of 2 endmembers chosen from within the window. One endmember is selected from the bright materials in the Isidis basin and one from the dark materials on the eastern part of Syrtis Major indicated by E1 and E2 in Figure 1. Pixels most accurately modelled by these endmembers (low total variance, random error as a function of wavelength) comprise the Isidis and Syrtis East units. The other units have high variance and/or show non-random variations in error as a function of wavelength (residual spectra). Careful examination of the residual spectra and the magnitude of the variance led (2) to define the other 3 units shown in Figure 2.

The correlation of the spectral units with the broad scale surficial geologic and geomorphic features is discussed in in detail by (2). Briefly, the Isidis unit is associated with bright deposits in the Isidis basin, the Cratered unit is associated with the rim of the Isidis basin, and the Arabia unit in the extreme north-west corner of the window corresponds with the edge of the cratered highlands. Two distinct units are recognized on the Syrtis Major plateau; an eastern and a western unit. Although the residual spectra are used to define these units, all spectral features identified are relative to the endmember spectra and direct compositional interpretations are difficult.

**Calibration of ISM Spectra:** The ISM data are initially calibrated using pre and inflight engineering data, an assumed average spectral response of Phobos and applying a preliminary atmospheric correction based on the strength of the 2.0 μm $CO_2$ absorption band (3). An additional calibration was applied to these data by assuming regions of homogeneous bright surface material have the same spectral properties as average bright terrain measured telescopically (4). Average telescopic data for bright regions were smoothed and resampled to ISM wavelengths. The region of the ISM data selected for this calibration is indicated by STD in Figure 1. This calibration approach is not an absolute measure of reflectance and subject to possible errors in the choice of reference spectra and the spectral properties of the surface calibrated to. This procedure surpresses features common to all surfaces but not in the reference spectrum.

**Interpretation of Spectra Units:** Typical spectra from each of the spectral surface units shown in Figure 2 are presented in Figure 3. The primary spectral features which distinguish these units are albedo, slope and the nature of the absorption band between 0.8 and 1.2 μm. The character of the absorption band is particularly important because it provides information regarding the composition of the surface. In the spectra of the bright terrain units, the band shape and position (near 0.9 μm) is relatively constant and is characteristic of $Fe^{3+}$ absorptions observed in predominantly dust covered regions (4, 5). The primary spectral differences between the bright terrain units are the slope of the spectrum and slight variations in the position and shape of the 0.9 μm ferric absorption band. Whether the sources of the observed spectral variations are compositional, textural, or otherwise is unclear, however they do define spatially coherent units which are associated with morphologic and geologic features (2).

The shape and position of the absorption centered near 1.0 μm in the spectra of the Syrtis Major units is indicative of $Fe^{2+}$ crystal field absorptions in mafic minerals. To de-emphasize albedo relationships and visually enhance absorption features, the spectral segments for the Syrtis Major units and the Isidis unit are divided by a simple straight line continua and are presented in Figure 4. The shape of the 1.0 μm band for the Syrtis units, and in particular the width of the bands, suggest that multiple mafic minerals contribute to the measured reflectance. In addition to the 1.0 μm band, there is a broad band centered near 2.1 μm. The presence of this feature together with the 1.0 μm band is strong evidence that high calcium pyroxene is present in the volcanic materials of Syrtis Major, the presence of which was previously proposed by (6) based on the shape of the 1.0 μm band alone. A principal distinguishing feature of the Syrtis Major units is the slope of the spectra towards long wavelengths; Syrtis East has

a decrease in reflectance towards longer wavelengths while Syrtis West is relatively flat. It is unknown at this time whether this is a weathering or surface coating phenomenon, or a fundamental mineralogic difference.

A significant degree of spectral variation exists in these data which was used to define units by (2). The principal distinguishing spectral characteristics between units are albedo, slope, and nature of the 1.0 μm band. In the units of Syrtis Major, the presence of clino pyroxene is clearly indicated as well as additional unresolved mafic mineral. We are currently in the processes of refining the calibration and also incorporating odd channels into the analysis to increase the spectral resolution and help resolve some of the remaining compositional ambiguities.

*References:* (1) Bibring et al, *Nature 341*, 1989. (2) Erard et al, *LPSC XXI* (this volume) 1990. (3) Erard et al, *Bull. Am. Astron. Soc. 21*, 1989 (4) McCord et al, *JGR 87*, 1982 (5) Singer, *JGR 87*, 1982 (6) Singer, *LPSC XI*, 1980.


Figure 1. Area covered by the ISM data for the Isidis-Syrtis Major window. The actual image is 26 by 116 pixels and a typical pixel to scale is indicated by the white arrow. The location for the reference spectra (E1 and E2) and the standard area (STD) are also indicated.

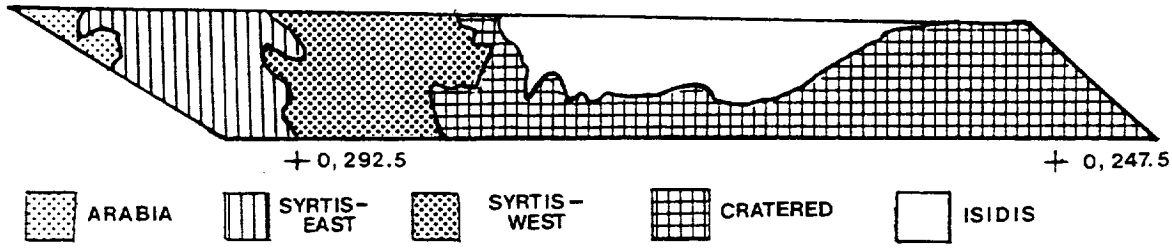


Figure 2. Schematic map for the above window of spectral units defined by (2) using the spectral characteristics of the first 51 channels of the ISM data.

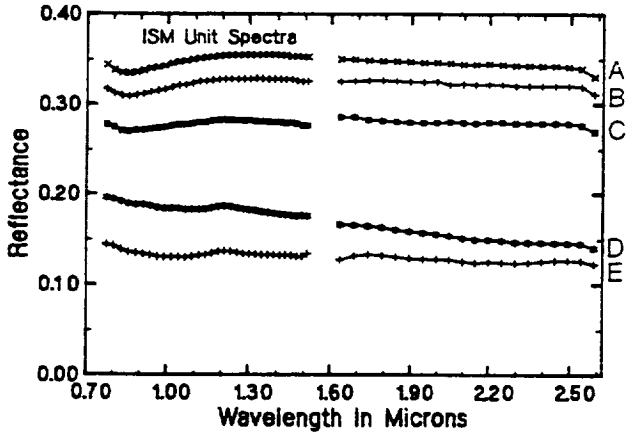


Figure 3. Calibrated ISM spectra typical of the units shown in Figure 2. A) Isidis B) Cratered Highlands C) Arabia D) Syrtis East E) Syrtis West.

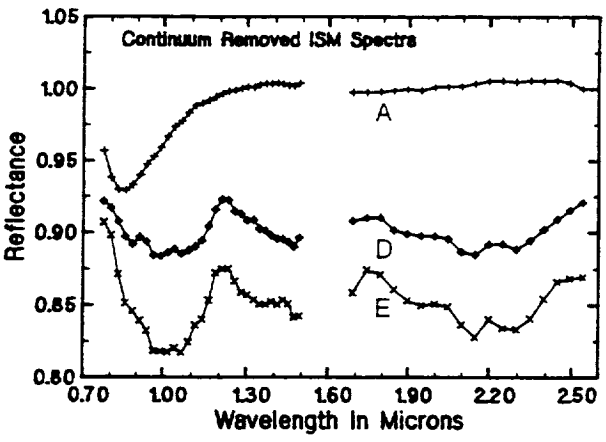


Figure 4. Spectra of the units Isidis (A), Syrtis East (B) and Syrtis West (C) after removing a simple straight line continuum for each segment. These spectra are offset 5% relative to each other for clarity.

# IMPACT CRATERING ON MARS AND THE FORMATION OF CRATER LAKES: A POSSIBLE ENVIRONMENT FOR THE ORIGIN OF LIFE;

H.E. Newsom and G.E. Brittelle, Institute of Meteoritics and Department of Geology, University of New Mexico, Albuquerque, NM 87131.

Liquid water, required for the origin and growth of life, could have been present in two environments on Mars, lakes or in shallow groundwater, including near surface expressions of groundwater, such as springs. Under present climatic conditions on Mars, liquid water is not likely to exist in either environment. Liquid water on Mars requires either a warmer climate, which could have been present early in the history of Mars, or a source of heat, such as volcanism or impacts, which could be present throughout martian history. In this abstract we will discuss the effects of impacts and volcanism on the existence of liquid water on Mars, including the formation of crater lakes and liquid ground water systems. We will show that suitable environments for the origin of life on Mars may have existed, even in the absence of a significantly warmer climate in the past.

The large extent of biologic activity in groundwater systems on the Earth is well known [1]. The interaction of water or ice and hot rock due to volcanic activity could produce liquid groundwater even under present conditions on Mars. A similar environment near or within slowly cooling impact melt sheets, would have been common early in the history of Mars. Over the last ten years, an ongoing investigation of the hydrothermal alteration of impact melt sheets on the Earth has demonstrated that the presence of water plays an important role in the cooling of deposits containing impact melt [2]. Investigations of the cooling and alteration of suevite (melt-bearing breccia), at the Ries Crater in West Germany, has shown that most of the alteration and clay formation occurred during a long period of slow cooling below the boiling point of water [3]. Paleomagnetic techniques have confirmed that alteration and clay formation were probably connected with cooling of the melt sheet rather than being due to alteration under ambient conditions over the 15 m.y. since the formation of the crater [4]. On Mars, impact melt deposits outside of craters and basins could produce widespread shallow aquifers by melting of ground ice. Such shallow aquifers could even be connected with the formation of small valley networks on Mars [5]. The resulting small valleys may not even be closely associated with nearby craters because the distribution of impact melt from very large craters and basins may be very widespread and variable. Also, the liquid groundwater produced by melting ground-ice could flow for significant distances without a surface expression.

An even more important environment for biologic activity on Mars may be lakes, including impact craters which have become flooded with groundwater. The early presence of lakes in low lying areas such as Valles Marineris has been suggested as a site for biological activity [6]. An important question is whether such lakes would be liquid. McKay et al. [7] investigated the thickness of ice on perennially frozen lakes in the Antarctic and on Mars and the calculations for Mars were extended by Squyres [8]. Assuming present conditions, predicted ice thicknesses (> 200 m) are unlikely to allow liquid water to exist in martian lakes [8]. We have investigated the effects of heat from a cooling melt sheet, buried beneath a crater lake, on the thickness of ice on the surface of such a lake. As an example, we have used the calculated conductive cooling profiles for the 200 m thick impact melt sheet from the 65 km diameter Manicouagan crater in Quebec [9]. The calculated heat flow is shown in Fig. 1. This is compared with the other major source of heat within frozen lakes, the latent heat of freezing of water. The assumption is that the ice maintains an equilibrium thickness, with ablation from the surface and freezing at the ice-water interface [7]. Because of the low ablation rates expected for Mars under current conditions, this latent heat of freezing is much less than the heat from the melt sheet for the time interval indicated in the figures. The predicted thickness of ice on the crater lake, indicated in Fig. 2, will be less than 50 m for several thousand years, for ablation rates estimated by Squyres [8] for the present atmospheric pressure of 7 mbar. Eventually, as the heat from the melt sheet is lost, the thickness of the ice will increase to equilibrium values ranging from 200 m to 600 m for ablation rates of 3 cm/yr and 1 cm/yr respectively. Ablation rates higher than 3 cm/yr are unlikely under present conditions [8]. With atmospheric pressures as great as 300 mbar the ice thicknesses will be significantly less. The main conclusion from these calculations is that heat from a buried melt sheet will sustain a liquid crater lake for thousands of years, even under present climatic conditions on Mars. The duration of the cooling will undoubtedly be significantly shortened because of hydrothermal circulation of water through the melt sheet, but the existence of such crater lakes may still be recorded in the deposits within the craters.

## Conclusions

Liquid groundwater or lakes could exist early in Martian history, even without a significantly warmer climate, with heat available from volcanism or impacts, especially from cooling melt sheets in large craters. Even though the liquid state of a martian crater lake would be short on an evolutionary time scale, hundreds of such lakes may have formed, including lakes within basins much larger than those modelled here. In addition, according to Stanley Miller [10], the time scales needed for the origin of life may be as little as $10^4$ years. The dispersal of life-forms around Mars is also possible by impact processes, including spallation [11]. Other aspects of impacts that could be favorable to the origin of life include the possible presence of hot springs at the surface, within or near large craters associated with cooling melt sheets [5], the presence of shocked minerals, which could provide a source of chemical energy [12], and the formation of abundant clays and zeolites, which could catalyze organic reactions.

## References

[1] Back Groundwater 27, 618-622, 1989. [2] Newsom Icarus 44, 207-216, 1980. [3] Newsom, Graup, Sewards, and Keil Proc. Lunar Planet. Sci. Conf. 17th, J. Geophys. Res. 91, E239-E251, 1986. [4] Iseri, Geissman, Newsom and Graup Abstracts for the 52nd Meteoritical Society Meeting, Lunar and Planetary Inst., p. 95, 1989. [5] Brakenridge, Newsom and Baker, Geology 13, 859-862, 1985. [6] McKay and Stoker Rev. Geophys. 27, 189-214, 1989. [7] McKay, Clow, Wharton, Jr., and Squyres Nature 313, 561-562, 1985. [8] Squyres Icarus, 1989. [9] Onorato, Uhlmann and Simonds, J. Geophys. Res. 83, 2789-2798, 1978. [10] Miller in Aspects of Chemical Evolution, John Wiley, 85, 1984. [11] Melosh Lunar and Planet. Sci. XVI, 550-551, 1985. [12] Boslough and Cygan Proc. Lunar Planet. Sci. Conf. 18, 443-454, 1988.

## Figure captions

Fig. 1 The heat flow from a 200 m thick impact melt sheet has been estimated from the calculations of Onorato et al. [9] assuming a constant heat capacity. Even slower cooling times were obtained using a temperature dependent heat capacity [9].

Fig. 2 The ice thickness for two different assumptions about the ablation rate at the surface of the ice, which is assumed to be equal to the amount of ice crystallizing at the base of the ice. The solidification of the ice releases latent heat. The other parameters used in the calculation are: average temperature -43 °C, albedo 0.75, solar flux 180 W $m^{-2}$, extinction path length 1.0 m.

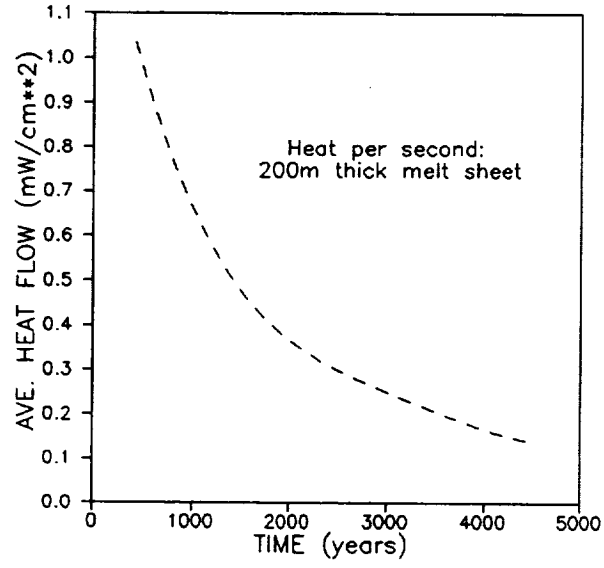


Figure 1

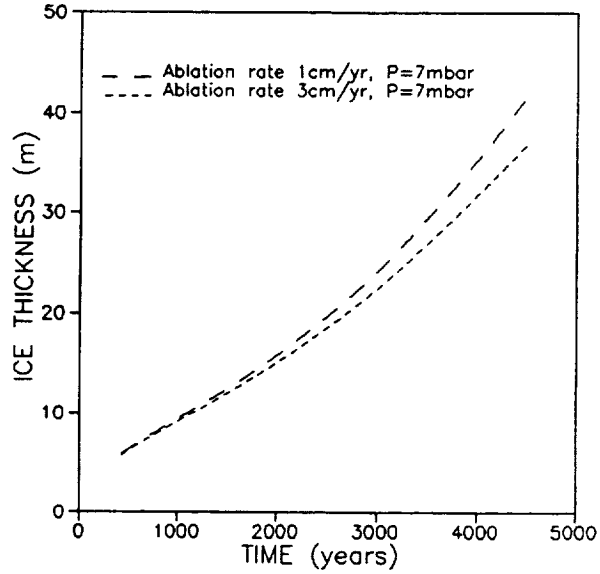


Figure 2

**A MODEL FOR CHEMICAL EVOLUTION OF LIFE ON MARS**, V. R. Oberbeck, NASA Ames Research Center, Moffett Field CA 94035, J. R. Marshall, Arizona State University, Tempe AZ 85287, D. E. Schwartz, SETI Institute, Mountain View, CA 94043

Geological and atmospheric models of Mars strongly suggest the presence of liquid water and a significant atmosphere prior to 3.8 Gyr. Early conditions favorable for life on Mars may have been similar to those on Earth at the time when life began on this planet. It has recently been recognized that the path of prebiotic chemistry (and of life itself) on the early Earth was probably interrupted, or at best retarded, by giant impacts[1]. The time between such impacts (just before the oldest evidence of life on Earth, 3.8 Gyr ago) has been used to estimate the maximum time required to originate life[2,3]. When the same calculations are applied to Mars, it appears that the time windows available for the development of life are longer than those for Earth[3]. Consequently, conditions on Mars conceivably could have been more favorable to life than were those on early Earth. Thus, Mars remains the most likely extraterrestrial setting for the origin of life. However, no specific model for *prebiotic* chemical evolution has yet been developed for Mars.

We now consider the geologic environment during Noachian time in order to develop a realistic model for the planetary processes that could have been involved in the chemical evolution of life on Mars. During the first 800 My of the Solar System, the terrestrial planets accreted planetesimals and experienced an exponential decay of impacting objects. Based on knowledge of the lunar uplands[4], impacting objects produced a thick megaregolith of crushed silicate minerals. Volatiles from comets were also delivered in sufficient quantities to produce terrestrial oceans similar in size to those present today and water, of exogenous origin, 10 m to 100 m in depth may have been retained on Mars[5] very early in its history. Because certain classes of meteorites contain clay minerals believed to have been formed in hydrated regoliths on planetary surfaces[6], we believe that it is likely that clay minerals existed in the ancient megaregoliths of both Mars and Earth. The existence of valley networks formed by sapping in the ancient cratered terrain suggests that surface water had a very limited distribution during the Noachian period. Intermittent precipitation fed subsurface aquifers which in turn fed springs at the heads of sapping channels formed by intermittent flowing water[7]. We believe that the geologic and meteorologic conditions during this period on Mars were at least as favorable (and perhaps more so) for the origination of life as they were on Earth.

We propose the following model for chemical evolution of life on Mars. Important prebiotic organic reactants were supplied by comets, IDPs, carbonaceous chondrites, and photochemical reactions.These compounds would have included amino acids, such as those recently discovered in clays at the KT boundary[8]. Monomers in the atmosphere were scavenged by precipitation or brought to the surface by sedimentation. During the time when reactants where incorporated in rain drops, some were polymerized to produce more complex prebiotic materials.

Seepage of these materials into the megaregolith then provided an ideal environment for the attachment of such monomers and polymers to clay particles. Percolation/filtration processes and fluctuating groundwater levels permitted dehydration of monomers and redistribution of reaction-product polymers. Fluctuations in water content are known to promote the formation of macromolecules[9]. Over a long period of time, the megaregolith acted as a large chemical processing column to form organic polymers of increasing complexity.

The next stage of biochemical organization, the formation of cell-like structures, occurred in the bottoms of sapping channels and lakes fed by sapping channels. Groundwater percolating through the megaregolith emerged as springs at the amphitheater heads of the channels. These were abundant on the surface of the ancient cratered terrain. Complex polymers emerging with the groundwater developed cellular organization on the level of coacervate droplets in this environment, and this permitted some interchange of biochemical compounds with the environment. Solar energy was available as an energy source to drive further chemical organization. Eventually, life may have originated in concentrated aqueous solutions at the bottoms of sapping channels and lakes in a way similar to that proposed for the terrestrial oceans.

Such a model for the chemical evolution of life on Mars compares favorably with the existing model for the origin of life on Earth. For this planet, life is believed to have originated in the primordial soup of organic compounds in the ocean. Monomers were produced in, or supplied to, the atmosphere in the manner referred to above and ultimately settled into the ocean. On Earth, the concentration of monomers in the oceanic "soup" would have taken longer than the time required to concentrate monomers in the megaregolith of Mars. In addition, movement of groundwater through the megaregolith would have provided more efficient absorption of monomers on clay particles. Thus, chemical evolution of life may have proceeded more rapidly on Mars.

References: (1) Maher K. A. and D. J. Stevenson (1988) *Nature* **331**, 612-614 (2) Oberbeck V. R. and G. Fogleman (1989a) *Origins of Life and Evolution of the Biosphere,* in press. (3) Oberbeck V. R. and G. Fogleman, (1989) *LPSC* **XX**, 800 (4)Aggarwal H. R. and V. R. Oberbeck (1978) *LPSC* **IX**, 829 (5) Chyba C. F. (1989) *Nature,* in press, Cornell University CRSR 930 revised. (6) Bunch T. E. and S. Chang (1980) *Geochim. Cosmochim. Acta* **44**, 1543 (7) Carr M. (1989) *Icarus* **79**, 311 (8) Cronin J. R. (1989) *Nature* **339**, 423 (9) Lahav N., D. White and S. Chang (1978) *Science* **201**, 67.

**SEARCH FOR LIFE: A SCIENCE RATIONALE FOR A PERMANENT BASE ON MARS**, V. R. Oberbeck, NASA Ames Research Center, Moffett Field CA 94035, J. R. Marshall, Arizona State University, Tempe AZ 85287, D. E. Schwartz and R. L. Mancinelli, SETI Institute, Mountain View CA 94043

Results of the Viking mission to Mars provided no compelling evidence for extant life, but oxidants could have masked evidence for biological activity[1]. The search for evidence that life originated on Mars remains a primary reason for further scientific exploration of the planet. Even if there was no extant life at the Viking sites, extant life may exist because most of the promising potential Martian habitats were not explored. It is noteworthy that prebiotic reactants and liquid water probably existed at the surface until about 3.8 Gyr ago(2). During this period, Mars was subject to impacts that would have frustrated the origin of life. The time available between these planet-sterilizing events was longer than the time required to originate life on Earth[2]. Thus, there would have been sufficient time for life to originate on Mars before 3.8 Gyr ago. If life existed, it may either have become extinct at the surface, leaving behind fossils, or migrated into the groundwater after 3.8 Gyr ago. This implies that evidence for extant life should be sought beneath the surface and that evidence of extinct life should be sought in the older surface terrain. Mars remains the most promising extraterrestrial setting where life may have originated. The discovery of evidence for either extant or extinct life on Mars would profoundly affect mankind because it would suggest the possibility that life may have originated in many other places in the universe.

The National Research Council recommended searching for four types of indirect evidence for extant life during space missions. These include liquid water, organic compounds, electrolytes, and biogenic gases. However, they point out that none of these is proof that life exists. Conclusive evidence for life cannot be sought with Viking style missions(3) that search for these types of evidence nor do we believe can it be sought with other types of unmanned craft. For example, penetrators could conceivably deploy instruments that could search for this indirect evidence of extant life beneath the surface, but penetrators can only deploy limited payloads to a limited depth in a limited number of places. At best, the results obtained would only provide inconclusive evidence for life on Mars. Therefore, we believe that the search for extant life beneath the surface will be difficult indeed. The search for fossil evidence of life at the surface will also be extremely difficult to undertake. Such fossil evidence is likely to be very old[2] and the volume ratio of fossils to rock will probably be very small; only a centimeter layer of fossiliferous material may exist in hundreds of meters of sedimentary rock. The search for such layers could be quite time-consuming and would require the knowledge and experience of a well-trained geologist. Artificial intelligence techniques that could be used on unmanned surface vehicles (e.g., rovers) could easily mistake inorganic artifacts for fossil remains.

Because the positive results of a search for conclusive evidence for life on Mars would have profound implications for mankind, and because of the difficulties inherent in the search, we believe that this search is compelling justification for a permanent science base on Mars. In the event that extant organisms are found, a semi-permanent presence permits examination of extant life forms in order to prevent possible harmful forward and backward contamination. It is recognized that the same results may be achieved in carefully prepared clean rooms and planetary protection facilities on Earth, a semi-permanent facility on Mars would provide added protection of great value. Additionally, if extant lifeforms are found, they are best studied *in situ*.

The search for extant life should concentrate on subsurface locations. The disappearance of an appreciable atmosphere and associated liquid surface water about 3.8 Gyr ago[4,5] may imply that organisms, as we know them, could not now exist at the surface. It has recently been discovered that a large biomass of microorganisms extends to great depths within terrestrial aquifers[6] and Mars may have analogous environments. However, great effort must be expended in searching for such organisms and in keeping the samples pristine. On Mars, it may be

possible to sample groundwater at selected sites near sapping channels. This would require complex drilling operations in rugged Martian terrain that can only be performed by humans in semi-permanent bases with laboratory facilities. Also, the careful field analysis of groundwater systems, required before extensive drilling is done, is not possible with unmanned landers.

The search for fossil evidence of past Martian life will require painstaking field analysis and detailed examination. Long drill cores may need to be examined, and large volumes of debris searched, for minute traces of extinct life. It is difficult to envision how a successful search for fossils could be carried out without preliminary geological field surveys followed by exhaustive on-site laboratory investigations.

A careful examination of ecosystem dynamics can only be accomplished by humans inhabiting a Mars base equipped with a laboratory. Interrelationships between organisms and their environments are so complex that one is compelled to study organisms in their natural habitat. For example, two elements that are important to organisms are nitrogen and sulfur. In terrestrial ecosystems, we know that cycling of these elements requires a community of co-existing organisms working in concert with the environment. Changing the environment leads to significant changes in the cycling. The types of *in situ* studies that would be required to determine biogeochemical cycles in these ecosystems would be virtually impossible with robotic missions. Such studies, performed by scientists on the surface of Mars, will expand our knowledge of nutrient cycling in an extraterrestrial planetary context. If we can learn how an extraterrestrial biota interacts with its environment, it would greatly expand our knowledge of the limits that planetary environments place on the existence of life. This, in turn, would provide additional evidence regarding the possibility of life elsewhere in the universe. The history of comparative planetology tells us that it is precisely the opportunity for the study of physical and chemical processes in different planetary settings that has offered completely new insights into planetary processes acting within our own terrestrial environment. The presence of humans in a semi-permanent base on Mars will permit similar new perspectives on the importance of processes that are integral with the possibly of origination of life elsewhere.

References: (1) Klein H. P. (1978) *Icarus* **34**, 666 (2) Oberbeck V. R. and G. Fogleman (1989) *LPSC* **XX**, 800 (3) Hartman H., J. G. Lawless and P. Morrison (eds.) (1985), NASA SP-477. (4)Carr M. H. and G. D. Clow (1981) *Icarus* **48**, 91-117 (5) Pollack J. B., J. F. Kasting and S. M. Richardson (1987) *Icarus* **71**, 203-224 (6) Phelps T. J., E. G. Raione, and D. C. White (1988) U. S. Dept. of Energy, DP-MS-88-100.

STABILITY, COMPOSITION AND PHASE RELATIONS OF MARTIAN MANTLE CARBONATES Maria Odezynskyj, Dept. Geo., ASU, Tempe, AZ 85287-1404, John R. Holloway, Depts. Chem. and Geo., ASU, Tempe, AZ 85287-1404.

This abstract introduces further results from a study of Martian mantle carbonates: their stability and composition, and qualitative information about their phase relations during a partial melting event. Data were collected from piston-cylinder experiments conducted on model Martian mantle compositions at 25 kb. and a range of temperatures from 1150°C to 1250°C. Graphite lined Pt capsules were loaded with a basalt + dolomite mixture which was sandwiched between peridotite + basalt + dolomite. The peridotite was composed of synthetic olivine, ortho- and clinopyroxenes, all with mg# 75 (atomic Mg/(atomic Mg + atomic Fe)); natural garnet with mg# 74; natural basalt with mg# 50; and a pure, natural dolomite. Run times were 24 hours. Oxygen fugacity conditions, calculated from Fe solution into Pt (Gudmundsson and Holloway, 1989), are constrained to be within $\pm 0.9$ $\log_{10}$ units relative to NiNiO at 1 atm. and run temperature.

The carbonates in this study fall into two compositional categories. The first, a water soluble 'alkali' carbonate, is present in all experiments at temperatures < 1250°C; its approximate composition is given in Table 1. Figure A is a backscatter image of a region containing the carbonate. Its texture and occurrence suggest that it could be a quench product of an alkali carbonate liquid. Such an interpretation is consistent with the results of Wallace and Green (1988). In contrast, a Ca-Mg-Fe carbonate crystal phase has a stable appearance (see Figure B) up to a temperature between 1200°C and 1225°C. X-ray diffraction studies and Transmission Electron Microscopy indicate that this carbonate has a calcite structure. Above the given temperature range, Mg-Fe calcite contains veins of alkali carbonate and frequently occurs near vugs. (See Figure C.) The average composition of the calcite at different temperatures is given in Table 2.

Silicate phases present in the run products are: olivine, pyroxenes, garnet $\pm$K feldspar. Also present is fine-grained silicate material with a texture and composition that suggest a melt phase. Distinct regions of quench crystals may represent immiscibility between the silicate and carbonate liquids up to ≈1250°C. Average structural formulae of the minerals are listed in Table 3. The Fe/Mg partitioning among phases varies: e.g. 2.27 between cpx and gt, or 0.08 between opx and cpx, in a 25 kb, 1200°C run. (Values from 21$^{st}$ run.) An approach, rather than achievement, of equilibrium is apparent from a comparison of the experimental partitioning with published values. Ellis and Green, 1979, report 2.26 for Fe/Mg partitioning between cpx and gt, and Mori and Green, 1978, report 0.93 for opx and cpx under comparable P and T conditions.

At temperatures $\leq$ 1200°C, alkali carbonate 'melt' coexists with Mg-Fe calcite. Microprobe analyses (see Table 2) show that alkalis do not readily enter the calcite structure. Falloon and Green (1989) approximated the solidus for alkali carbonate at ≈1025°C at 25 kb. Our data place the Mg-Fe calcite solidus between 1200-1225°C at 25 kb. These observations suggest a eutectic melting relationship for mantle carbonates as shown in Figure D.

**References:**

Ellis D J and Green D H (1979) Contrib Min Pet **71** 13. Falloon T J and Green D H (1989) EPSL **94** 364. Gudmundsson G and Holloway J R (1989) EOS **70** 1402. Mori T and Green D H (1978) Jour Geo **86** 83. Wallace M E and Green D H (1988) Nature **335** 343.

Table 1
Alkali Carbonate 'Melt' Composition

| | 1200°C | 1225°C |
|---|---|---|
| SiO2 | 5.5 | 6.5 |
| TiO2 | 1.2 | 1.9 |
| Al2O3 | 0.5 | 0.6 |
| FeO | 23.4 | 18.7 |
| MnO | 0.1 | 0.1 |
| MgO | 11.2 | 10.3 |
| CaO | 8.0 | 10.2 |
| Na2O | 3.7 | 5.6 |
| K2O | 7.1 | 5.1 |
| P2O5 | 9.4 | 9.9 |
| (diff) CO2 | 30.0 | 31.4 |
| mg# | 32.4 | 35.5 |

Table 1: Averaged compositions (in weight percent) of alkali carbonate. 1200°C values from 21st run; 1225°C values from 19th run.

Table 2
Average Compositions of Mg-Fe Calcite

| | 1175°C | 1200°C | 1225°C | 1250°C |
|---|---|---|---|---|
| SiO2 | 0.02 | 0.36 | 0.04 | 0.21 |
| TiO2 | 0.01 | 0.13 | 0.04 | 0.04 |
| Al2O3 | 0.02 | 0.04 | 0.03 | 0.06 |
| FeO | 5.81 | 10.49 | 10.96 | 11.18 |
| MnO | 0.01 | 0.13 | 0.12 | 0.14 |
| MgO | 10.33 | 12.37 | 12.40 | 13.05 |
| CaO | 41.95 | 33.58 | 32.32 | 33.29 |
| Na2O | 0.02 | 0.20 | 0.16 | 0.18 |
| K2O | 0 | 0.44 | 0.18 | 0.26 |
| P2O5 | n/a* | 0.73 | 0.44 | 0.41 |
| (diff) CO2 | 41.85 | 41.53 | 43.30 | 41.18 |

Table 2: Averaged compositions (in weight percent) of Mg-Fe calcite. 1175°C values from 5th run; 1200°C from 21st, 1225°C from 19th and 1250°C from 20th runs.

* -not analyzed

Table 3
Structural Formulae of Run Product Silicates

| phase | structural formula |
|---|---|
| | 1175°C (run 5) |
| olivine | $Mg_{1.47}Fe_{0.55}Si_{0.98}O_4$ |
| Lc.pyx* | $Na_{0.01}Al_{0.06}Ca_{0.09}Mg_{1.47}Fe_{0.46}Si_{1.93}O_6$ |
| clinopyx | $Na_{0.0}Al_{0.0}Ca_{1.01}Mg_{0.92}Fe_{0.14}Si_{1.96}O_6$ |
| garnet | $Ca_{0.69}Mg_{0.82}Fe_{1.57}Al_{2.06}Si_{2.89}O_{12}$ |
| | 1200°C (run 16) |
| olivine | $Mg_{1.52}Fe_{0.53}Si_{0.97}O_4$ |
| Lc.pyx* | $Na_{0.01}Al_{0.07}Ca_{0.08}Mg_{1.58}Fe_{0.38}Si_{1.95}O_6$ |
| clinopyx | $Na_{0.03}Al_{0.03}Ca_{0.68}Mg_{1.05}Fe_{0.29}Si_{1.96}O_6$ |
| garnet | $Ca_{0.92}Mg_{0.69}Fe_{1.38}Al_{1.88}Si_{2.75}O_{12}$ |
| | 1225°C (run 13) |
| olivine | $Mg_{1.46}Fe_{0.53}Si_{1.00}O_4$ |
| Lc.pyx* | $Na_{0.01}Al_{0.01}Ca_{0.14}Mg_{1.44}Fe_{0.43}Si_{1.98}O_6$ |
| clinopyx | $Na_{0.02}Al_{0.03}Ca_{0.55}Mg_{1.11}Fe_{0.32}Si_{1.98}O_6$ |
| garnet | $Ca_{0.84}Mg_{0.75}Fe_{1.36}Al_{1.91}Si_{2.95}O_{12}$ |

*Lc.pyx = low calcium pyroxene

Figure A: Alkali Carbonate 'Melt'


Figure A. Backscatter image of alkali carbonate melt. See text for discussion.

Figure C: Quenched Mg-Fe Calcite


Figure C. Quenched Mg-Fe calcite with veins of alkali carbonate.

Figure B: Stable Mg-Fe Calcite

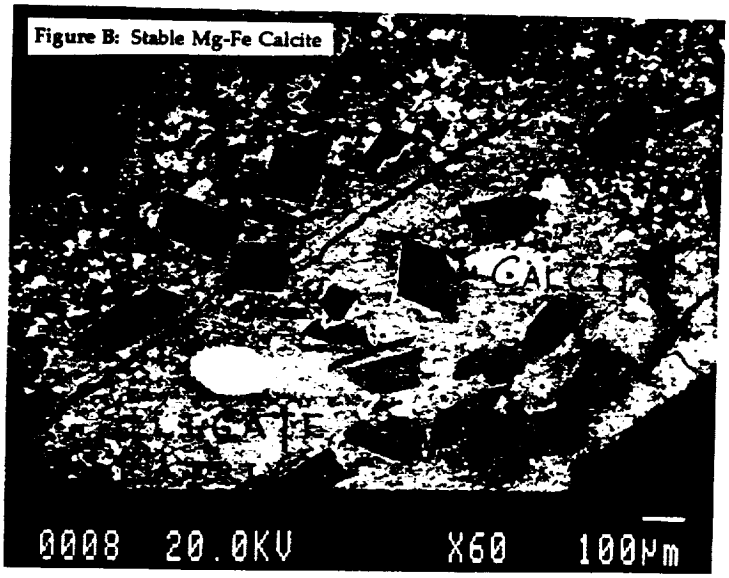


Figure B. Backscatter image of Mg-Fe calcite crystals within run product.

Figure D

A Schematic Diagram of Mantle Carbonate Phase Relations at 25 kb.

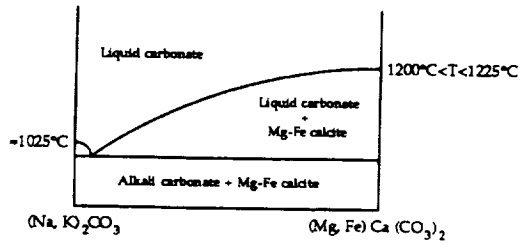


Figure D: Schematic projection of carbonate melting relations onto the alkali carbonate–Mg-Fe calcite join. Silicate relations not shown, but this diagram is for a phase assemblage which includes olivine, two pyroxenes and garnet.

**SPECTRAL EMISSIVITY OF THE SILVER AND LUNAR LAKE PLAYAS - RELEVANCE TO ANALYSES OF MARS TIR DATA**; S.B.Petroy and R.E.Arvidson, McDonnell Center for the Space Sciences, Earth and Planetary Sciences Department, Washington University, St.Louis, MO, 63130

Analyses of existing Viking IRTM data have focussed on providing broad compositional and textural constraints for martian sediments. The higher spectral and spatial resolution data to be acquired from the upcoming MO-TES mission will help to narrow these constraints, thus allowing for more detailed mapping of the martian surface. To prepare for these data, portions of two remote sensing field experiments (MFE-1988, GRSFE-1989) [1,2] were conducted to test procedures used to extract surface property information from TIR data. What follows is a report of initial results from the analyses of Thermal Infrared Multispectral Scanner (TIMS) data, field emission spectra, and field observations with respect to the physical characteristics (composition, emissivity, etc.) of two playas in CA and NV. These areas were selected because they are small and fairly homogeneous, but exhibit variability in surface texture and composition.

Silver Lake, north of Baker, CA, is bounded on the west by the Soda Mtns. The western shore of the playa consists of beach ridges and wave cut cliffs; the eastern shore is marked by a well-sorted quartz sand berm. The 26 $km^2$ floor of Silver Lake is fairly flat but slopes gently to the south. Lunar Lake, 100 km east of Tonopah, NV, is bounded to the northeast by the Lunar Crater Quaternary basaltic flows and tephra cones and to the southwest by uplifted Tertiary ryholite tuffs. The western shore of the playa abuts volcanic flows and tephra cones while the remaining shoreline is marked by a well sorted, quartz-rich sand berm. The floor of the playa is ~10 $km^2$ and is also extremely flat. Several areas at the southern end of the playa are covered with locally derived basaltic cobbles (2-10 cm). Both playas consist of fine-grained, hardpacked silt and clay, but vary widely in degree of compaction and mud-crack morphology.

In February and July of 1989, emission data were collected at both playas with the JPL Portable Field Emission Spectrometer (PFES) [3]. In addition, data were collected at the Cima basalt flows (CA) and Kelso dunes (CA) to provide information on compositional endmembers (see Figure 1).

The emissivity of the Kelso sample is typical for quartz-rich sands with an absorption minima centered near 9.0 µm [4]. Generally, the depth and position of the absorption minima shifts from left to right as the total silicate content within the sample decreases. This trend is observed in the Cima spectra; the emission curve of the I-flow (youngest) is typical of basalts with an absorption minima centered near 10.0 µm. The remaining flow surfaces are older and have accretionary mantles of aeolian sediments. This added silicic material pulls the overall emission curve down and shifts the minima more to the left.

Emission spectra were collected at two sites on Silver Lake - site 1 (south) consists of fine-grained clays (20-40 µm) and deep mudcracks and site 2 (north) of slightly coarser sediments and shallow mudcracks. The emission curves for Silver Lake are higher and flatter than the Kelso curve, and exhibit broad absorptions around 9.0 µm characteristic of fine-grained, quartz-rich materials [4]. The emissivity of site 2 exhibits a deeper absorption at 9.0 µm which is probably due to the slightly coarser nature of the sediment. At Lunar Lake emission spectra were collected at three sites - sites 1 and 3 consist of fine-grained clays and shallow mudcracks and site 2 of basaltic cobbles overlying the playa surface. The cobble site emissivity is similar to that of the Cima mantled flows; the absorption minima is broad and centered between 9.0 and 10.0 µm. The two playa sites exhibit essentially identical emissivities but show a marked contrast from the Silver Lake emission curves. The sediments at Lunar Lake appear to contain a significant mafic component which results in a broader emissivity minima and higher values at smaller wavelengths.

These field observations can be empirically related to color composites using TIMS bands 1, 3, and 5. The green areas on both images correspond to the wettest and lowest

points on the playas; they consist of the finest clays, deepest mudcracks, and densest vegetation cover. At Silver Lake, the general color trend across the lake (west-east) is light blue and red grading into purple, suggesting an overall decrease in particle size away from the source (Soda Mtns). The reddish tint across the lake is due to the more silicic origin of the clays. In constrast, Lunar Lake is dominantly purplish-red due to the more mafic origin of the clays. The red rims around both playas correspond to the well-sorted, quartz rich sands berms observed in the field.

Based on qualitative interpretations of the TIMS data and the field emission spectra, subtle compositional and textural differences across the two playas can be recognized. The next phase of this study is to model the data to more precisely estimate the texture and composition of these surfaces.

References

[1] Wall, S., et al. (1988) Bull. Am. Astr. Soc., 20, p. 809. [2] Arvidson, R.E. and D.L. Evans (1989) GSA Abst. with Prog., p. A121. [3] Hoover, G. and A.B. Kahle (1987) Phot. Eng. and Remote Sen., vol.53, p. 627-632. [4] Conel, J.E. (1969) JGR, vol.74, p.1614-1634.

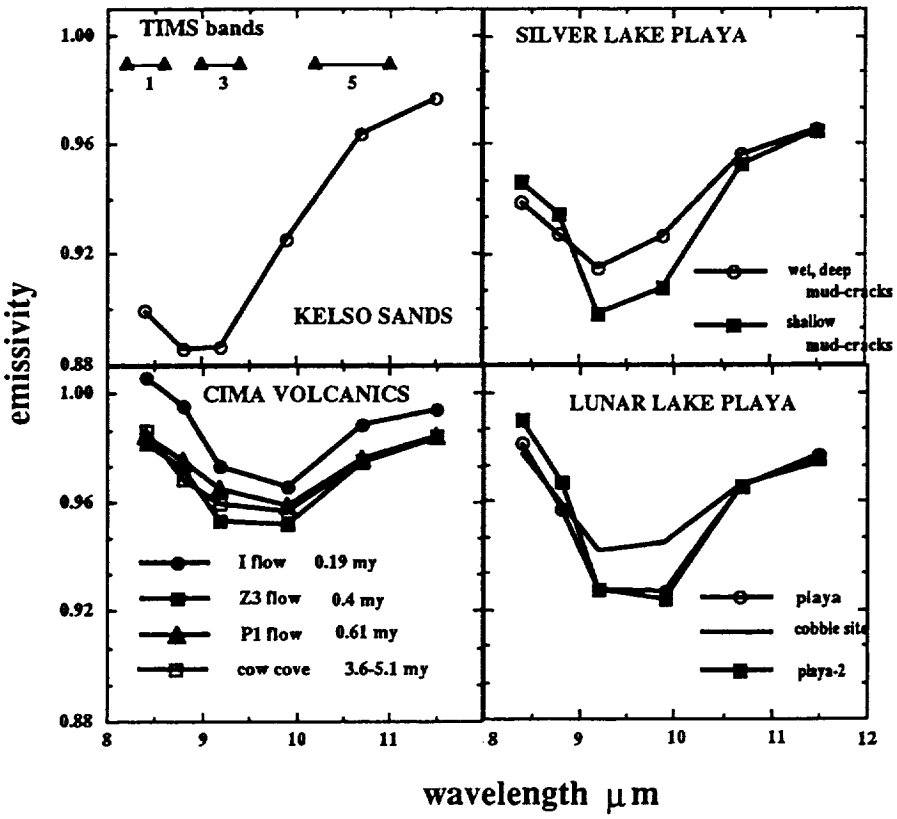


Figure 1. PFES data resampled into TIMS bandpasses and plotted as emissivity against wavelength.

EROSIONAL LANDFORMS AND MORPHOTECTONIC DEVELOPMENT IN VALLES MARINERIS (MARS): MELAS CHASMA; J.P. Peulvast, Laboratoire de Géographie Physique, CNRS, F 92195 Meudon, France.

Evaluating the respective influences of erosional and tectonic processes in the formation of the Valles Marineris troughs is decisive in their widened parts, where long wall segments display arcuate or irregular patterns which are not clearly related to faults (e.g. South Melas Chasma). Nevertheless strong tectonic control on the outlines of the walls and of the "bench" (layered rock plateaus) margins inside the troughs has been suggested in Candor and Melas Chasmata (1). By constructing detailed morphological maps (2), geological cross-sections and block-diagrams (fig. 1) it is possible to obtain more precise data on morphostructural and tectonic patterns in the same area.

The high dissected wall that overlooks the floor of Melas Chasma, i.e. the northern part of the trough, is controlled by faults west of Melas Labes, as demonstrated by stepped patterns with oblique hanging valleys or gullies. A downfaulted part of the main plateau forms a low bench above the floor (3). East of Melas Labes wide steps were probably faulted below a slightly arcuate wall but later landslides prevent easy identification of fault lines. WNW-ESE faults control the northern wall of Coprates Chasma (4), with hanging landslide scars developed from a probable former pit chain intersected after exaggeration of the fault scarp. Though wall rock remnants or small eroded horsts, occur in West Coprates Chasma, low mesas and alternate smooth and mottled surfaces in NW Melas Chasma seem to be underlain by layered deposits, surmounted by a few volcanic hills.

Thick layered deposits are more easily identified in the bench of South Melas Chasma, whose surface is 2-3 km or more above the floor. Whatever their origin is (volcanic, sedimentary or both: 5), the beds were formed in a confined area, during or after basin formation (which implies a subsidence of 6 or 7 km at least in SW Melas Chasma). Dissected walls and a few younger landslide scars overlook this 135 km wide bench or a deep discontinuous moat (SE Melas Chasma). Except in this last case the deposits extend into arcuate reentrants and embayments in the Sinai Planum edge, where no fault can be identified in spite of local parallelism with the Nia Fossae grabens. The SN ridge protruding from this edge is an erosional remnant of the plateau. It is therefore probable that wall backwearing occurred during the basin beds emplacement, even if complex downfaulting of blocks along oblique directions prepared this configuration (1).

The contrast between the southern and northern walls of Melas Chasma is best explained by later tectonic movements (downthrow: 1 or 2 km) along the continuations of the main faults of Ius and Coprates Chasmata through Melas Chasma, with a slight dextral offset. The faulted northern wall faces the bench margin,which appears as a fault scarp, especially if basin beds also underlay the floor: little or no erosion seems to be involved in the formation of this lower part (which would be the case if wall rock remnants were found in it, as suggested by (1).

Downfaulting of the floor, and possibly of parallel and oblique grabens inside the present bench and moat of SE Melas Chasma, resulted in landslides in the exaggerated northern wall (Melas Labes-Coprates Chasma) and in limited dissection and retreat of the edges of interior tectonic blocks, accompanied by differential erosion in alternate soft and hard layers. The occurrence of multiple cuesta-like bluffs and anticlinal hollows (east of the SN ridge) implies the presence of other structures: a long NW-SE monocline along the margin, possibly formed along the former edge of a southern deeper part of the basin before tectonic inversion, and several widely spaced NNW-SSE shallow synclines and low anticlines which formed only in the basin beds, probably as a response to differential vertical movements or strike-slip with weak compressional component in the narrow and weakened offset zone between Ius and Coprates Chasmata.

These deformations seem to predate the late faulting. They probably began during the formation of basin beds or its last stages, as suggested by possible unconformities and flexuring along wall contacts (SW Melas Chasma). They might be partly related to an old stage of volcano-tectonism (6) in a complex of caldera-like depressions along a wide graben or fracture set; deflection of Tharsis radial grabens around Melas Chasma (Nia Fossae) might be the same as observed around Alba Patera or Syria Planum. The basins were partly filled by volcanics and waste from highly erodable walls. Nevertheless this accumulation did not compensate subsidence and erosion induced by heating of volatile-rich wall rocks or tensional fracturing at depth (7).

Late faulting occurred mainly along the Ius-Coprates faults, i.e. in the northern half of Melas Chasma, resulting in increased total trough volume but also in narrowing of the main zone of tectonic activity, which became a simple graben with limited volcanism. Erosional widening became much less efficient than during the first stages, with a few landslides and limited erosion of faulted basin beds, probably for environmental as well as geological reasons (decreasing thermal activity and volatile content of wall rock, lithology of basin beds). Such a multistage tectonic activity probably occurred in the whole trough complex.

**References:** (1) Lucchitta 1989, LPSC XX, 590; (2) Peulvast and Costard 1989, LPSC XX, 840; (3) Witbeck et al 1988, USGS MIS Map I-XXXX, 55 p; (4) Schultz and Frey 1989, 4th Int. Conf. Mars, 183; (5) Nedell at al 1987, Icarus 70, 409; (6) Lucchitta 1987, LPSC XVIII, 572; (7) Tanaka and Golombek 1989 19 LPSC Proc. 383.

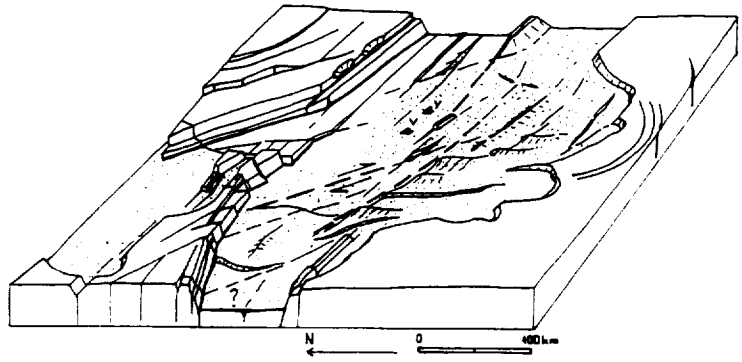


**Figure I.The last morpho-tectonic stage in Melas Chasma. Dots: basin beds.**

## PHOTOCLINOMETRIC ANALYSIS OF WRINKLE RIDGES ON LUNAE PLANUM, MARS

J. Plescia, Jet Propulsion Laboratory, MS 183-501, Pasadena, CA 91109

Wrinkle ridges are common morphologic features on Mars. Both volcanic and tectonic mechanisms have been suggested to explain their origin (e.g., Quaide, 1965; Strom, 1972; Scott, 1973, Muehlberger, 1974; Lucchitta, 1976, Bryan, 1973); recent work has focused on a compressional origin (Maxwell et al., 1975; Lucchitta, 1977; Sharpton and Head, 1982, 1988, Watters, 1988; Plescia and Golombek, 1986). Analysis of terrestrial analogs has greatly influenced and aided the understanding of wrinkle ridge formation (Plescia and Golombek, 1986). An important aspect necessary to interpret structure is topography. Topographic profiles across ridges can provide important constraints for models of internal structure and analyzing deformation associated with ridges.

Topographic maps for Mars are too coarse (contour interval 1 km) to resolve the topography of individual ridges, therefore, monoscopic photoclinometry (Davis and Soderblom, 1984) was used to derive topographic profiles for the ridges in. Profiles spaced a few kilometers apart were obtained for each ridge; the number depended on ridge length, morphology and albedo variation. Photoclinometry relies on pixel brightness variations which results from topography (the assumption of the technique), albedo, or both. Because of the albedo variations, photoclinometric profiles can not be extended across large distances, such as between adjacent ridges (about 20-80 km). However, the technique is applicable to shorter distances, such as the distance across typical ridges. Profiles were measures across the ridge and extended a few kilometers on either side, including all visible components of the ridge.

The data indicate that ridge relief varies from 27-370 m; average relief is 130±74 m; mean width measured is 5±2 km; the maximum width measured is 14 km. The superposed hill and crenulation are well-defined by the topographic profiles of the wrinkle ridges. The superposed hill and crenulation have slopes of 1° to 9°; in a few locations the slopes locally exceed 10°. The profiles are generally asymmetric, with slopes steeper on one side than on the other. Lunae Planum ridges are characterized by an elevation offset, that is, the plains on one side of the ridge have an elevation distinctly different from the elevation of the opposite side. The offset is similar to that observed for lunar ridges. Measured offsets vary from 0 to as much as 250 m; the average offset is about 30 m to 100 m, with a mean of 57±46 m. The sense of offset does not change abruptly or randomly. Locally, changes in the direction of offset are observed, but these are characterized by a corresponding change in the ridge morphology and a decrease in both ridge relief and width. The elevation offset is generally continuous away from the ridges for at least several kilometers (the length of the photoclinometric profiles).

The elevation offset is an important point in the consideration of models of their internal structure (c.f. Watters, 1988 and Plescia and Golombek, 1986). The offset is most easily explained by a fault beneath the ridge separating structural blocks at different elevations. The study of earth analogs suggests that the broad, low-relief structure characteristic of wrinkle ridges is most compatible with folding and faulting over thrust faults. In this model, a thrust fault at depth dips beneath the high side of the ridge producing the elevation offset. Since the elevation offset persists away from the ridge, the fault producing the offset must be uniform over these scales (kilometers to tens of kilometers) and the fault dip can not decrease at a shallow depth. The complex surface morphology of wrinkle ridges in which different morphologies are observed for each ridge and at different points along the same ridge is interpreted to be the result of splays from the master thrust fault. These splays have a variety of dips and senses of displacement and deform the surface in a unique manner.

Using such a model for the internal structure and the topographic profiles it is possible to estimate the shortening due to folding and faulting (Table 1). Shortening due to folding is estimated by simply unfolding the surface profile across the ridge, assuming conservation of line length; shortening due to faulting at depth is proportional to fault dip. Although the fault dip at depth is not directly observable, theoretical failure criteria and observed angle of normal faults on the moon and Mars suggest a dip of about 25° for thrust faults.

Data (Table 1) indicate that folding shortening varies from <1m-75m; mean 10±10 m. Assuming fault dips of 25°, faulting shortening varies from 0-540m, mean 122±98 m. The average ratio of shortening due to faulting versus folding is about 12. Shortening due to faulting significantly exceeds that due to folding; shortening due to faulting would exceed that due to folding by a factor of 3 to 6 even for fault steeper dips (i.e., 35°). These estimates suggest that a model wherein the fault breaks the surface and a substantial portion of the shortening is expressed by slip on faults at the surface is appropriate for martian ridges.

The shortening data can be used to estimate strain. Individual ridges exhibit a local (single ridge) folding strain of 0.05% to 0.5%, a faulting (displacement) strain of 1.0% to 5.0%, to produce a total strain of 1.4% to 5%. These estimates are broadly consistent with previous estimates of strain of a fraction of a percent to a few percent (e.g., Bryan, 1973; Muehlberger, 1974; Watters, 1988). Ridges on Lunae Planum generally trend north-south indicating an east-west compressional stress field. At 20°N latitude, there are 12 major ridges between Echus Chasma-Kasei Vallis on the west and the heavily cratered terrain on the east. Assuming each ridge is typical (131 m total shortening/ridge), the total shortening across Lunae Planum is 1600 m; corresponding regional compressive strain is 0.2% to 0.5%.

References: Bryan, W. B., *Proc. 4th Lunar Sci. Conf.*, 93-106, 1973. Davis, P., and Soderblom, L. A., , *J. Geophys. Res.*, **89**, 9449-9457, 1984. Lucchitta, B. K., *Proc. 7th Lunar Sci. Conf.*, 2761-2782, 1976. Lucchitta, B. K., *Proc. 8th Lunar Sci. Conf.*, 2691-2703, 1977. Maxwell, T. A., F. El-Baz, and S. H. Ward, *Geol. Soc. Amer. Bull.*, **86**, 1273-1278, 1975. Muehlberger, W. R., *Proc. 5th Lunar Sci. Conf.*, 101-110, 1974. Plescia, J. B., and M. P. Golombek, *Geol. Soc. Amer. Bull.*, **97**, 1289-1299, 1986. Quaide, W., *Icarus*, 4, 374-389, 1965. Scott, D. H.,*Apollo 17 Prelim. Sci. Rep., NASA SP-330*, 31/25-31/28, 1973. Sharpton, V. L., and J. W. Head, *J. Geophys. Res.*, **87**, 10,983-10,998, 1982. Sharpton, V. L., and J. W. Head III, *Proc. 18th Lunar Planet. Sci. Conf.*, 307-317, 1988. Strom, R. G., The Moon, IAU Symposium no. 47, 187-215, 1972. Watters, T. R., *J. Geophys. Res.*, **89**, 10,236-10,254, 1988.

TABLE 1

| RIDGE LOCATIONS (number of profiles) | HEIGHT (M) | WIDTH (KM) | OFFSET (M) | HIGH SIDE | SHORTENING FOLD (M) | SHORTENING FAULT (M) | SHORTENING COMBINED (M) |
|---|---|---|---|---|---|---|---|
| MC10NW | | | | | | | |
| 20.5°N; 71°W (27) | 204±52 | 5.3±1.0 | 105±44 | E | 17±10 | 225±95 | 242±101 |
| 20.5°N; 70.5°W (26) | 197±81 | 5.0±1.5 | 94±65 | E | 22±19 | 209±142 | 232±153 |
| 20°N; 69°W (13) | 152±31 | 6.4±1.5 | 58±32 | E | 9±3 | 25±52 | 134±52 |
| 17°N; 71.3°W (23) | 146±41 | 6.8±1.9 | 75±32 | E | 7±3 | 160±70 | 168±71 |
| MC10NE | | | | | | | |
| 20.5°N; 66°W (13) | 69±29 | 5.1±2.4 | 30±22 | E | 3±1 | 63±47 | 65±48 |
| 21°N; 65°W (6) | 102±20 | 4.7±1.3 | 48±28 | E | 5±2 | 103±61 | 108±62 |
| 21°N; 64.5°W (7) | 131±106 | 5.0±3.9 | 52±38 | W | 9±9 | 112±81 | 121±87 |
| 21.5°N; 62.5°W (6) | 55±14 | 3.0±0.8 | 19±12 | W | 3±2 | 41±2 | 44±24 |
| 22°N; 62°W (7) | 147±46 | 5.8±1.5 | 64±22 | E | 8±5 | 136±48 | 142±49 |
| 22°N; 59.5°W (4) | 169±41 | 4.0±1.0 | 68±45 | E | 10±5 | 90±6 | 100±2 |
| 17°N; 66.2°W (6) | 79±36 | 3.7±0.9 | 33±16 | W | 5±4 | 71±31 | 76±33 |
| MC10SE | | | | | | | |
| 14°N; 66.5°W (7) | 75±19 | 3.3±1.1 | 39±20 | W | 3±1 | 84±44 | 87±44 |

(±standard deviation of measurements around means)

**YOUNG FLOOD LAVAS IN THE ELYSIUM REGION, MARS**, J. B. Plescia, Jet Propulsion Laboratory, Pasadena, CA 91109.

The nature and origin of a smooth plains unit (the Cerberus Plains) in southeastern Elysium and western Amazonis is reported here. The Cerberus Plains cover >100,000 $km^2$ and extend an east-west distance of nearly 3,000 km; the plains are about 700 km wide in a north-south direction near longitude 195°. The unit is uncratered and exhibits lobate albedo patterns and embayment relations with older terrane. Morphologic characteristics suggest fluidized emplacement and the unit is interpreted to be formed by the eruption of large volumes of very low viscosity lava. A volcanic origin for this unit was also suggested by Schaber (1980), but he felt that the unit had been heavily modified by aeolian processes and he did not discuss its origin in detail. Tanaka and Scott (1986) and Tanaka (1986) reached a different conclusion and interpreted the material to be sedimentary, deposited during a fluvial episode.

The Cerberus Plains are one of the youngest units on Mars, crater numbers of 89 ±15 craters >1 km/$10^6$ $km^2$ were measured during this study. Carr and Clow (1981) cite 1 km crater numbers of <600; and Scott and Tanaka (1986) cite numbers of <50. Embayment relations indicate the Cerberus Formation overlies all other units in the Elysium region and western Amazonis (Greeley and Guest, 1987; Scott and Tanaka, 1986).

The Cerberus Plains are characterized by distinct linear albedo patterns independent of the wind streaks associated with aeolian processes. These patterns suggest an eastward flow across the Cerberus Plains, then a northeastward flow through a topographic low in the knobby terrane (exploiting a series of older channels carved into knobby terrane and ridged plains during an earlier period), and then out into Amazonis Planitia. In the east the albedo patterns are regionally organized forming bands up to 40 km wide; in the western areas, the albedo patterns are complex and intricate with high-frequency digitate boundaries varying from narrow, meandering patterns to broad, equant "ponded" shapes.

Small-scale surface texture of the plains is difficult to resolve; only in the highest resolution images are the relevant morphologic details observable. Near 19°N, 174°W the unit fills a channel cut through older plains and knobby terrane; here the channel floor appears smooth whereas the surrounding terrane has significant texture and numerous 400-600 m diameter craters. Apparently the original floor is covered by material younger than the surrounding plains. At the southern margin of the Cerberus Plains the surface shows a myriad of surface details indicative of a lava flow--pressure ridges, flow fronts, and flowage around obstacles; a festoon pattern is observed locally indicative of flowage up against the topographically higher areas. Morphology suggestive of a volcanic origin is also observed in western Amazonis Planitia (near 22°N, 170°W) where the distribution of material indicates flow and where the material terminates in a series of digitate and lobate fronts about 10 m high.

Six eruptive vents have been identified; the morphology of these features is suggestive of low shields--constructional volcanic features a few hundred meters high having lava flows emanating both as floods from a central vent and through a tube and channel system (e.g., Mauna Ulu and Mauna Iki; Greeley, 1982). Some of the Cerberus shields are elongate having elliptical vents; others are more symmetric. Summit vents range from 1-2 km diameter for circular vents; up to 15 km in length for elongate vents.

The morphology of the Cerberus Plains suggests it is an example of flood basalt volcanism; the morphology of western part indicates plains style volcanism. Terrestrial examples of flood basalts include the Deccan Traps and the Columbia Plateau (specifically the Yakima Basalt). Flood basalt provinces (Greeley, 1976, 1982) are characterized by flows 5-45 m thick extending over large areas and exhibiting little relief. Eruption rates for flood basalts are many times greater than for central volcanoes and the vents are fissure systems typically tens to hundreds of kilometers long in zones several kilometers wide. Western Cerberus Plains (near longitude 200°) appears to be a basaltic lava plains style of volcanism (e.g., the Snake River Plains of Idaho; Greeley, 1976, 1982). Plains volcanism is characterized by a overlapping and coalescing low shields with intervening tube-fed flows The

low eruption rates and intermittent nature of eruptions favors the construction of low shields and the development of channelized and tube-fed flows. Plains volcanism eruption rates are lower than for flood volcanism.The bulk of the volcanics were probably erupted from linear fissures, which may correspond to the present location of Cerberus Rupes. The eruptive fissures were probably relatively narrow; for example the lunar mare fissures are probably 10-25 m wide (Schaber et al., 1976). Typically, in both lunar and terrestrial flood basalt provinces the fissure vents are hidden.

A fluvial origin for the Cerberus Plains, as proposed by Tanaka and Scott (1986) and Tanaka (1986), appears inconsistent with the observed morphology. Although a fluvial episode did occur in the area, it predates the formation of the Cerberus Plains. The absence of a recognized source region for the fluid (presumably water); the absence of a recognized sink; and the burial of channel floors and the channels themselves by the Cerberus Plains are not consistent with a fluvial origin. Channels cut into the knobby terrane can not be traced to the southwest into their source region, nor to the northeast into the debouchment area; presumably they are overlain by the younger plains. In western Cerberus Plains, narrow channels (a few kilometers wide) are cut into exposures of older plains. However, these channels are traceable only for short distances and only on the older plains; the channels abruptly end at the contact with the Cerberus Plains.

The interpretation that Cerberus Plains results from flood plains style volcanism late in martian history carries implications for martian thermal history and volcanic evolution on a global scale. Although central construct volcanism (e.g., Olympus Mons) has long been recognized as occurring late in time, flood volcanism has not. Flood volcanism in the period <700 Ma indicates that, at least in the Elysium region, sufficient heat remained to generate large quantities of lava having low viscosity and erupted at high rates. Flood volcanism has been suggested as the origin of the ridged plains units (e.g., Lunae Planum, Solis and Sinai Planum). This type of volcanic activity generally occurred early, and in Tharsis the style of volcanism evolved from flood eruptions into centralized eruptions which built the large Tharsis Montes and Olympus Mons shields. Volcanism in the Elysium region seems to have followed a similar trend from flood eruptions to central construct building. But, the Cerberus Plains indicate that the volcanic style returned to flood eruption again after central constructional volcanism had ended.

REFERENCES: Carr, M., and Clow, G. (1981) *Icarus*, **48**, 91-117. Greeley, R. (1976) *Proc. 7th Lunar Planet. Sci. Conf.*, 2747-2759. Greeley, R. (1982) *J. Geophys. Res.*, **87**, 2705-2712. Greeley, R. and Guest, J. E. (1987) U. S. Geological Survey Miscellaneous Investigation Series Map I-1802B. Schaber, G. G., (1980) *Icarus*, **42**, 159-184. Schaber, G. G., Boyce, J. M., and Moore, H. J. (1976) *Proc. 7th Lunar Planet. Sci. Conf.*, 2783-2800. Scott, D. H., and Tanaka, K. L. (1986) U. S. Geological Survey Miscellaneous Investigation Series Map I-1802A. Tanaka, K. L. (1986) *Proc. 17th Lunar Planet. Sci. Conf., Part I, J. Geophys. Res.*, **91**, E139-E158. Tanaka, K. L., and Scott, D. H. (1986) *Abstracts, 17th Lunar Planet. Sci. Conf.*, 865-866.

FORMATION OF RHYOLITIC RIDGES ON MARTIAN BASALTS. T.K. Porter and P.H. Schultz, Dept. of Geology, Brown University, Providence, RI 02912

**Introduction**: Martian lava flows centered at approximately 3° N, 140° W are characterized by steep, thick flow fronts, large areal extents, and distinctive textures. These flows are strikingly different from other martian flows (see Figures 1a and b). The texture has been interpreted as festoon or pressure ridges [1] like those on terrestrial pahoehoe basalts - yet the martian ridges are the same scale as those on terrestrial rhyolite flows [2]. As discussed in [3], the height and spacing of the ridges is controlled by the thickness of the chilled upper margin of the flow and the viscosity ratio (the viscosity of the chilled crust of the flow vs. the viscosity of the flow interior). A thick crust and high viscosity ratio are conditions that favor the formation of high ridges with long wavelengths. Here, analytical modeling and preliminary experimental results suggest that the martian flows could not have developed a crust sufficiently thick to form the observed ridges if the flows were emplaced subaereally, and that instead the flows may have been emplaced under a unit of ice-rich dust.

**Viscosities of Martian Flows**: We used high resolution Viking Orbiter photographs to determine an average ridge spacing of 175.5m and an average ridge height of 13.9m. These dimensions are one to two orders of magnitude greater than the ridge dimensions of typical terrestrial basalts and are similar to ridge dimensions found on terrestrial rhyolites ([2], [3]). They are unlike any lunar basalts. We inserted the values found in Table 1 into analytical models ([1], [2], [3]) to obtain viscosities (Table 2). The lower viscosities are high for terrestrial basalts ([1], [4]) while the larger viscosity values approach the terrestrial rhyolite viscosities [2]. But these flows are undoubtedly basaltic: observed lava channels and abundant evidence for tube-fed flow are distinctive characteristics of basalts [5]. The long flow distances (up to 6000km$^2$) over low gradients combined with the large areal extent of these flows (1000 to 4000km$^2$) indicate a low-viscosity lava; paradoxically, the steep flow fronts, ridge dimensions and analytical models suggest a high-viscosity lava [6]. Recent experiments with molten carbowax [7] indicate that ridge creation is favored if the flow rate is "sufficiently slow" and the ambient temperature is "sufficiently low." Therefore, forming a thick chilled crust on the martian lavas may impart a high-viscosity appearance to a low-viscosity flow. A low-viscosity lava can form steep, thick flow fronts if the flow cools quickly enough. Icelandic table mountains, for example, are basalts that erupted subglacially, producing steep-sided, flat-topped mountains ([8], [9]). The slopes of the steeper terrestrial table mountains are approximately 32° [8]. For comparison, we derive flow front slopes of about 36° for the martian lavas (see Fig. 1a.), in contrast to the thickest lunar flows which have flow front slopes of about 14°.

**Apparent High Viscosity from Low Viscosity Flows**: The high-viscosity appearance of the martian flows might be produced by quickly and efficiently cooling the surface of a low-viscosity flow. Rapid cooling of the flow surface could be achieved by emplacing the flow under a material with high heat capacity and high thermal diffusivity This would create a thick chilled crust and, by exerting a downward force, could increase the drag component on the surface; both conditions enhance ridge formation. Many of the observed flows are surrounded by easily eroded deposits and the surfaces of some flows exhibit heavily eroded impact craters indicating differential removal of a friable surface deposit at least 300m thick. Models of the rate of cooling of terrestrial lava flows [7] permit calculating the thermal diffusivity of the boundary environment for the martian flows. Using this model and the parameters in Table 1, and then solving for the thermal diffusivity yields a value that is a hundred times too high for air, water or ice and is a hundred times too low for most rock. An ice-rich dust may produce the appropriate thermal diffusivity.

Preliminary experimental results suggest that overburden pressure on the lava flow may play an important role in creating the observed textures. By simulating lava flows with molten carbowax, we have found that efficient cooling alone is not enough to produce the large-scale ridge texture and the steep flow fronts at this scale. To determine the first-order trends of ridge formation, we have emplaced the molten wax in varying conditions such as: subaeral with ambient temperatures varying from -2° to 20° C; under water varying from 0° to 25° C; under powdered dry ice, snow and foam to simulate a material with high heat capacity but low thermal diffusivity. Cooling the wax flows with dry ice or 0°C air is not as efficient at producing large ridges and steep flow fronts as is cooling the flows with ice water - even though the thickness of the chilled margin is roughly the same in all cases.

**Conclusion**: The observed martian flows have large areal extents and flow lengths, indicating a fluid basalt; the same flows paradoxically have steep flow fronts and a long ridge wavelength, indicating a highly viscous (almost rhyolitic) lava. A low-viscosity basalt may resemble a high-viscosity lava if the flow cools quickly and efficiently enough to produce a thick surface crust, and if thereby exerting drag force on the crust once formed. Preliminary experimental results suggest that overburden pressures also may be important to ridge formation. If emplaced under a mantle of ice-rich dust, then the martian flows could have cooled quickly and have been sujected to sufficient overburdon pressure

**References**: [1] Theilig and Greeley (1986) *Proc. LPSC XVII.* [2] Fink (1980) *Geology*, **8**. [3] Fink and Fletcher (1978) *Jour. of Volc. and Geotherm. Res.*, **4**. [4] *Basaltic Volcanism Study Project* (1981). [5] Greeley (1980)

*Volcanic Features of Hawaii.* [6] *Hawaiian Planetary Conference.* (1974). [7] Fink and Griffiths (1989) *LPSC XX.* Abs. [8] Allen (1979) *Jour. Geoph. Res.* [9] Hodges and Moore (1979) *Jour. Geoph. Res.*, 84.

| Parameter | Number of Samples | Avg. Value |
|---|---|---|
| Ridge spacing | 1840 | 175.5m |
| Ridge height | 8 | 13.9m |
| Flow thickness | 16 | 62.5m |
| Flow front slope | 8 | 36° |

Table 1. Parameters obtained using high-resolution VO photographs.

| Model | Viscosity in Pa•s | |
|---|---|---|
| | Interior | Exterior |
| Fink and Fletcher (1978) | $5.4 * 10^4 - 8.7 * 10^6$ | $3.4 * 10^5 - 5.5 * 10^8$ |
| Fink (1980) | $1.5 * 10^6 - 2.3 * 10^8$ | $9.7 * 10^6 - 1.5 * 10^9$ |
| Theilig and Greeley (1986) | $1.4 * 10^7 - 2.3 * 10^9$ | $1.5 * 10^8 - 2.5 * 10^{10}$ |

Table 2. Viscosities obtained from the parameters in Table 1 and the models in [1], [2] and [3].



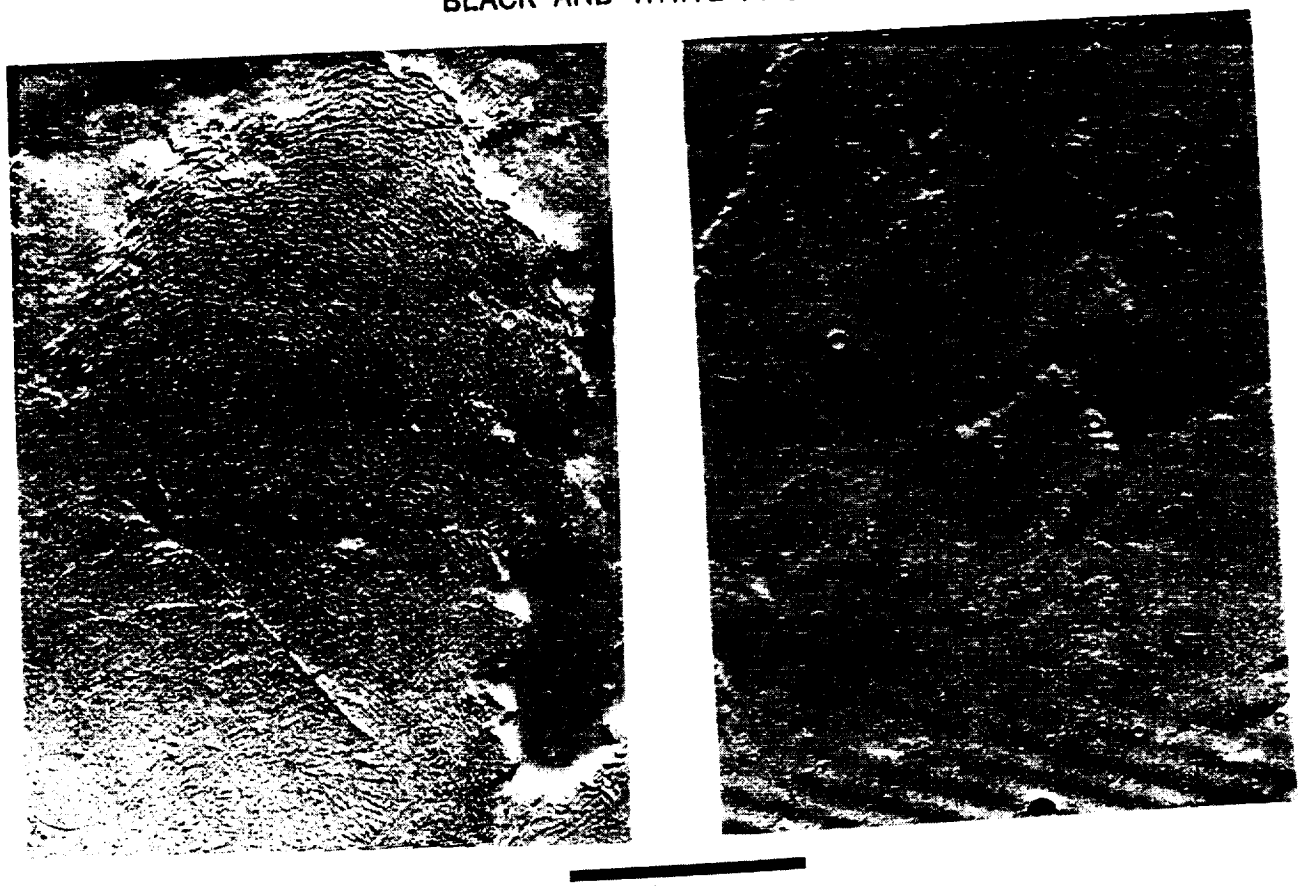

1a. 1b.

Figures 1a. and b. Fig. 1a is a mosaic of 731A03 and 731A04; INA = 75.4°. Note relief and spacing of ridges and steep flow fronts. Fig. 1b. is a portion of 387B13; INA = 72.0°. Here, note flow fronts with less abrupt termini and absence of texture. Scale bar is 10 km for both figures.

# MID-INFRARED SPECTRA OF KOMATIITE VS. BASALT

David P. Reyes and Philip R. Christensen, Arizona State University, Tempe,AZ 85287

Komatiite is an ultramafic extrusive containing > 20% weight MgO, and composed mainly of olivine, with lesser pyroxene, and little or no feldspar. On the Earth komatiites were mainly emplaced during the Archean (>2.7 Ga), were erupted at viscosities of 0.1 to 1 Pa, and at temperatures of 1400-1700° C [1,2]. Komatiite was generated at a depth of 150 to 200 km by massive partial melting of the Archean mantle [3]. Their unique character and origin make komatiite excellent indicators of the early composition and development of the Earth's mantle [4]. Komatiites may also be important constituents on Mars [5], and their discovery would provide important constraints on the composition and temperature gradients of the Martian mantle. In addition, determination of the variation in composition of Martian basalts with time can be used to study the evolution of Martian mantle conditions.

The purpose of this study is to determine the mid-infrared spectral properties of komatiite and to compare these to other basalt types. A suite of samples were selected from the Arizona State University petrology collection which were typical of their rock type. The komatiite samples were originally obtained from one of the best preserved komatiite locations in the world, Munro Township, Ontario, Canada [6]. The basalt samples came from various locations and represent a compositional suite from tholeiitic basalt, to alkali basalt, to basaltic andesite. A total of 8 komatiite and 10 basalt samples were analyzed.

Spectra were obtained using a commercial Fourier transform interferometer at a resolution of 4 $cm^{-1}$ in emissive mode. Emission measurements were used because they are appropriate for comparison to remotely gathered planetary data. Samples were heated to 80° C in an oven for 24 hours in order to achieve thermal equilibrium and eliminate thermal gradients. Samples were removed from the oven and analyzed in open air within 10 seconds to minimize thermal gradients due to cooling. Samples were also analyzed on their flat, freshly broken surfaces. Emissivity was calculated relative to a blackbody with > 99 % emissivity and adjustable to > 0.1° C.

The spectra shown in Figures 1 and 2 were selected for presentation because they are typical of all the samples surveyed for their respective groups. Figure 1 shows a comparison of komatiite and olivine. Olivine is a major mineral constituent of komatiite and should, therefore, be discernable in its spectrum. In Figure 1 komatiite show absorption bands at approximately 10.75, 11.25, and 16.5 μm which are due to olivine. Other olivine bands at 9.5, 24.5, 20, and 29 μm are present in the komatiite spectrum but are not clearly discernable, due to overlaping absorption bands of other minerals.

Komatiite spectra from 7 to 30 μm are easily distinguished from basalt spectra as seen in Figure 2. In the 8 to 12 μm region basalts have broad and shallow absorption features. This region results from a concentration of the absorption bands of constituent silicate minerals in basalt, typically olivine, pyroxene, and feldspar. In this same region, komatiite has several narrow, deep bands due primarily to olivine. In the 15 to 30 μm region basalt spectra show a broad region of shallow and indistinct absorption bands. Conversely, in this same region, komatiite show distinctly expressed absorption bands, again due to the predominance of olivine in the komatiite. These spectral features clearly separate ultramafic komatiite from less ultramafic tholeiite basalt and other basalts.

Previous work has shown that there is a detectable and quantifiable shift in the character of spectra in the 8 to 12 μm region as a result of the depolymerization of $SiO_2$ tetrahedron over large $SiO_2$ ranges in igneous rocks (ie. rhyolite to basalt) [7]. The results discussed here indicate that this distinction is applicable even to small ranges of $SiO_2$ content such as from basaltic

andesite to tholeiitic basalt. These shifts can be seen as a discernable difference among the basalt spectra in Figure 2, and are consistent with the general shift of the Si-O absorption band to shorter wavelengths with increasing $SiO_2$ content. This information is significant in that it indicates that subtle lithologic distinctions can be made from remotely sensed data. This capability is particularly important for Mars, where large variations is $SiO_2$ content may not occur.

In summary, preliminary data show that in the 7 to 30 μm region komatiite is easily distinguished from all other major basalt types, based on the detailed spectral signature of its constituent minerals, particularly olivine. In addition, subtle variations in basalt composition can be detected and related to variations in bulk rock composition and mineralogy. Future work will focus on a detailed interpretation of the mid-infrared spectra to identify mineral components in all of the basalt samples and quantify the composition variations apparent in Figure 2. These results will be directly applicable to Mars following the receipt of Mars Observer Thermal Emission Spectrometer (TES) data, which will acquire spectra from 6.25 to 50 μm at a spectral resolution comparable to the spectra illustrated in Figures 1 and 2.

**References** [1] Huppert, H.E., Sparks, S.J., Turner, J.S., and Arndt, N.T., (3/1984), Nature, V. 309, pp.19-22. [2] Arndt, N.T., Francis, D., and Hynes, A.J., (1979), Canadian Mineralogist, V. 17, pp. 147-163. [3] Takahashi, E. and Scarfe, C.M. (6/1985), Nature, V. 315, pp.566-568. [4] Jahn, B.M. and Gruau, G., (1989), LPI Tech Rpt 89-05, LPI,Houston, pp.47-49. [5] Burns, R.G. and Fisher, D.S., (1989), LPI Tech Rpt 89-04, LPI, Houston, pp.20-22. [6] Pyke, D.R., Naldrett, A.J., and Eckstrand, O.R., (3/1973), GSA Bulletin, V. 84, pp 955-978. [7] Walter, L.S. and Salisbury, J.W., (7/1989), JGR, V. 94, N. B7, pp. 9203-9213.

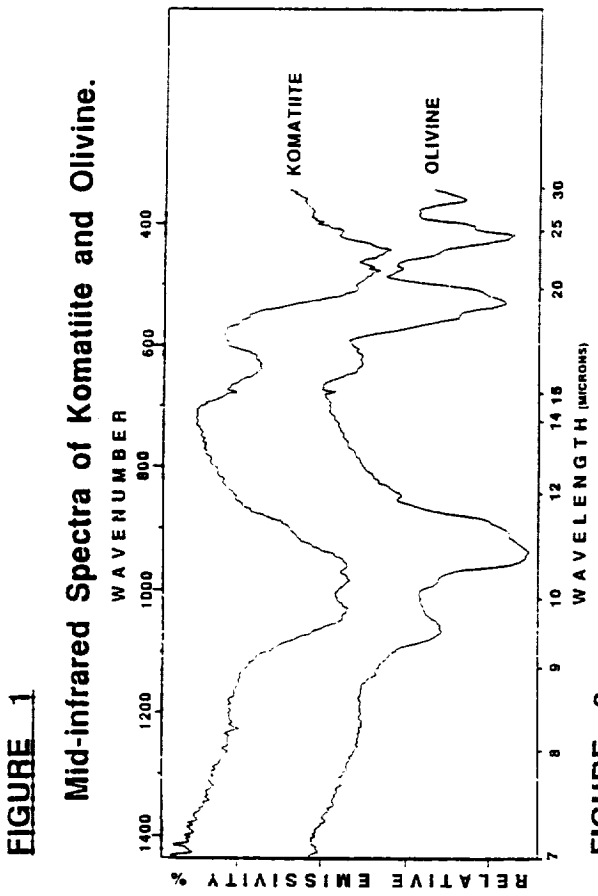


FIGURE 1

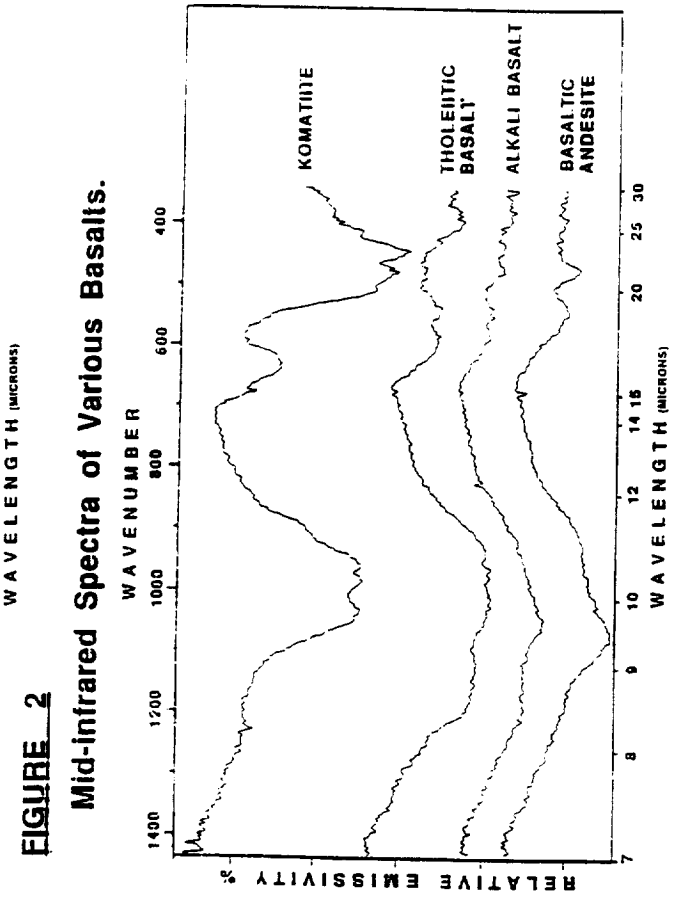


FIGURE 2

THE HIGHLAND-LOWLAND BOUNDARY FORMED ON MARS BETWEEN THE LATE NOACHIAN AND THE EARLY HESPERIAN; Cordula Robinson, ULO Planetary Image Centre, 33-35 Daws Lane, London, NW7 4SD.

The Martian elevation difference has been considered an ancient, stable feature originating early in martian history (3,4,5). Stratigraphical mapping suggests this conventional view needs revision. Further support comes from gravitational data (1) and structural evidence (2).

Detailed stratigraphical mapping provides three pieces of evidence that place constraints on the age of formation of the highland-lowland boundary.

First the plateau material shows volume loss at boundary regions where it acquires a "mesa and butte" form. The confinement to boundary regions suggests volume loss is a consequence of formation of the elevation difference. The volume loss postdates the Middle to Late Noachian plateau material putting a lower limit on the age of boundary formation. Conversely, the "mesa and butte" form is not found in material younger than the plateau material putting an upper limit on the age of boundary formation.

Second the Isidis Basin - formed during the period of bombardment - straddles the boundary. The absence of the north-eastern rim of Isidis implies that the elevation difference came about subsequently.

Finally the absence of large subsurface "ghost" craters in the scarp regions of the boundary, indicates that the early cratering record was obliterated here by destruction and breakage of the palaeosurface.

This work supplements that of McGill (1). He presents new evidence on the age of formation of the highland-lowland boundary, based on detailed analysis of the Viking LOS gravity data. This suggests a weak negative anomaly associated with the boundary region, implying it is not yet fully compensated, as would be expected if it had formed immediately after accretion. McGill supports his proposal with structural data (2) arguing that the boundary in the Eastern Hemisphere was formed as a discrete structural event between Late Noachian and Early Hesperian times. He also proposes that the elevation difference formed in association with the aeolian, fluvial and volcanic resurfacing rates that peaked at these times (6).

Thus, it appears that the elevation difference was attained in a geologically short time interval between the Late Noachian to Early Hesperian; later adjustments are relatively slight. The results suggest that the martian dichotomy stems from endogenic processes and hence mantle differentiation must be a fundamental process in the history of Mars.

References:

(1) McGill G.E. (1988) LPI Tech. Rpt. 89-04 pp.59-61.
(2) Maxwell T.A. and McGill G.E. (1988) Proc.LPSC 18 pp.701-711.
(3) Wise D.U. et al (1979) JGR 84 pp.7934-7939.
(4) Wilhelms D.E. and Squyres S.W. (1984) Nature 309 pp.138-140.
(5) Frey H. and Schultz R.A. (1988) Geophys. Res Letts. 15 pp.229-232.
(6) Tanaka K.L. et al. (1987) Proc.LPSC 18 pp.665-678.

# PRECISE TOPOGRAPHIC MEASUREMENTS OF APOLLINARIS AND TYRRHENA PATERAE, MARS.

Mark S. Robinson, Hawaii Institute of Geophysics, Planetary Geosciences Division, 2525 Correa Road, Honolulu Hawaii, 96822.

## Introduction

Topographic measurements have been used to classify and interpret both terrestrial and martian volcanoes in previous studies [1-6]. However, the topography for most martian volcanos is not constrained to a high precision, making classification and interpretation difficult. To derive precise topography for martian volcanoes I have taken shadow measurements and photoclinometric profiles from Apollinaris and Tyrrhena Patera. Apollinaris Patera has been classified as a shield, while Tyrrhena Patera is classified as a highland patera [1]. Although the two volcanos have been classified differently (according to morphology) they share some gross morphologic and geographic features. Both occur in the southern hemisphere away from the two major martian volcanic provinces - Tharsis and Elysium, and both are roughly 200 km across. The major difference between the two is their relief, Apollinaris Patera is approximately 5 km high while Tyrrhena Patera is lower (~ 2 km). Based on its low relief and style of erosion previous workers have interpreted Tyrrhena Patera to be the result of dominantly pyroclastic activity [1], resulting in an ash shield, while Apollinaris Patera has been interpreted to be built from effusive activity [1], although others [7] have classified Apollinaris as a composite (pyroclastic + effusive).

## Methods

**Shadow measurements** can provide very precise height determinations if the following conditions are met; 1) low sun angle above the horizon, 2) pixel size is much smaller than the size of the feature being measured and 3) relatively distortion free viewing geometry (low emission angle). Fortunately, Viking images exist of Apollinaris and Tyrrhena Paterae that meet these criteria. To determine accurate shadow lengths actual DN values from calibrated Viking images [8] were observed. Measuring shadows from photographic prints can be difficult due to contrast stretches that can make determination of the shadow edge inaccurate. Error reported on the shadow measurements is determined from the assumption that the top and bottom of the shadow can each be located to within 3/4 pixel accuracy (total error, 1 1/2 pixels).
**Photoclinometry** [8,9] was employed to measure flank slopes of Apollinaris Patera and Tyrrhena Patera. For the method to determine an accurate slope, all changes in brightness must be the result of a change in slope, not albedo. Inspection of Viking images from multiple passes (in multiple wavelengths) over Apollinaris Patera (8 orbits) and Tyrrhena Patera (5 orbits) revealed no gross change in brightness other than that due to change in slope (across the measured profile). Current work includes the reduction and analysis of Viking color data from 4 different orbits to determine any subtle albedo changes that may be affecting the photoclinometry. Estimation of a flat field (DN value of a flat surface) was done by examining the DN values of caldera floors and at breaks in slope (caldera rim, impact crater rim). Incorrect determination of the flat field introduces serious error to a given profile. However the validity of the flat field can be checked by taking a profile across a fresh bowl-shaped crater, or by comparing photoclinometricly derived heights with shadow measurements. If the profile across a fresh bowl shape crater determines that the two rims are of the same height and shadow measurements correspond to profile height, then a high confidence level can be put on the flat field value. These checking procedures were carried out whenever possible.

## Results

**Apollinaris Patera:** Shadow measurements (635A57 INA=79.5°, Res= 250 m/pix) indicate a minimum relief of 5100 ± 90 m for the west flank of the volcano (Fig. 1). The slope of the volcano under the shadow must be greater than the angle of the sun above the horizon, 10.5°. Shadow measurements were also taken of the caldera wall, determining a height of 770 ± 90 m. Photoclinometric profiles show a distinct break in slope approximately 12 km from the summit plateau. The lower flanks have a minimum slope of 3.7° ± 0.4° while the upper regions have a minimum slope of 5.7° ± 0.6° (actual slopes are greater due to the oblique angle of the profile to the topographic slope). This change in slope may reflect a change in eruptive style (effusion rate, chemistry, volatile content). **Tyrrhena Patera:** Both high and moderate resolution low-sun angle images of the Tyrrhena Patera region were used to determine flank slopes and caldera scarp heights. Shadow measurements from orbit 445A (INA=68°, res=60 m/pix) indicate that the caldera scarp (Fig. 1) is typically 400 m high, with the maximum relief being 470 ± 35 m. Photoclinometric profiles (image 087A14, res=230 m/pix) indicate that the maximum slope on the measured flank is 3.6° ± 0.5°. The accuracy of the photoclinometric profiles was checked using shadow measurements from the high resolution images.

## Conclusions

The lower slopes of Apollinaris Patera are comparable to the slopes measured for Tyrrhena Patera suggesting a similar evolution. The break in slope on Apollinaris may reflect a change in the style of eruption from an early stage activity similar to Tyrrhena Patera to a later stage, effusive episode. The basal scarp that skirts Apollinaris may reflect the interface between a relatively unconsolidated, and easily eroded, base (pyroclastic) and an overlying resistant cap (effusive). This model is similar to that proposed by Mouginis-Mark et al [10] for the evolution of Alba Patera. The measured depths of the caldera will be used as a constraint on the geometry of the magma chamber underlying each volcano. Future work will include similar measurements for other martian volcanos to allow for a global interpretation, at a greater precision than previously possible, of volcanic processes on Mars.

## References

[1] Greeley, R. and Spudis, P.D. (1981) *Revs. Geophys. and Spa. Phys.* vol. 19 no. 1, pp 13-41. [2] Blasius, K.R. and Cutts, J.A. (1981) *Icarus* 45, pp 87-112. [3] Pike, R.J. (1978) *Proc. LPSC 9th*, pp 3239-3273. [4] Pike, R.J. et al (1980) *NASA TM-81776*, pp. 192-194. [5] Davis, P.A. and Tanaka, K.L. (1987) *MEVTV Workshop on the Nature and Composition of Surface Units on Mars*, pp 49-50. [6] Wu, S.S.C. (1979) *JGR* vol 84 no B14, pp 7955-7959. [7] Plescia, J B. and Saunders, R.S. (1979), *Proc. LPSC 10th*, pp 2841-2859. [8] USGS Astrogeology (1987), *Planetary Image and Cartography System Manual* [9] Davis P. (1984) *JGR* vol 98 no B11, pp 9449-9457. [10] Mouginis-Mark, P.J. et al (1988) *Bull. of Vol.* 50, pp 361-379.

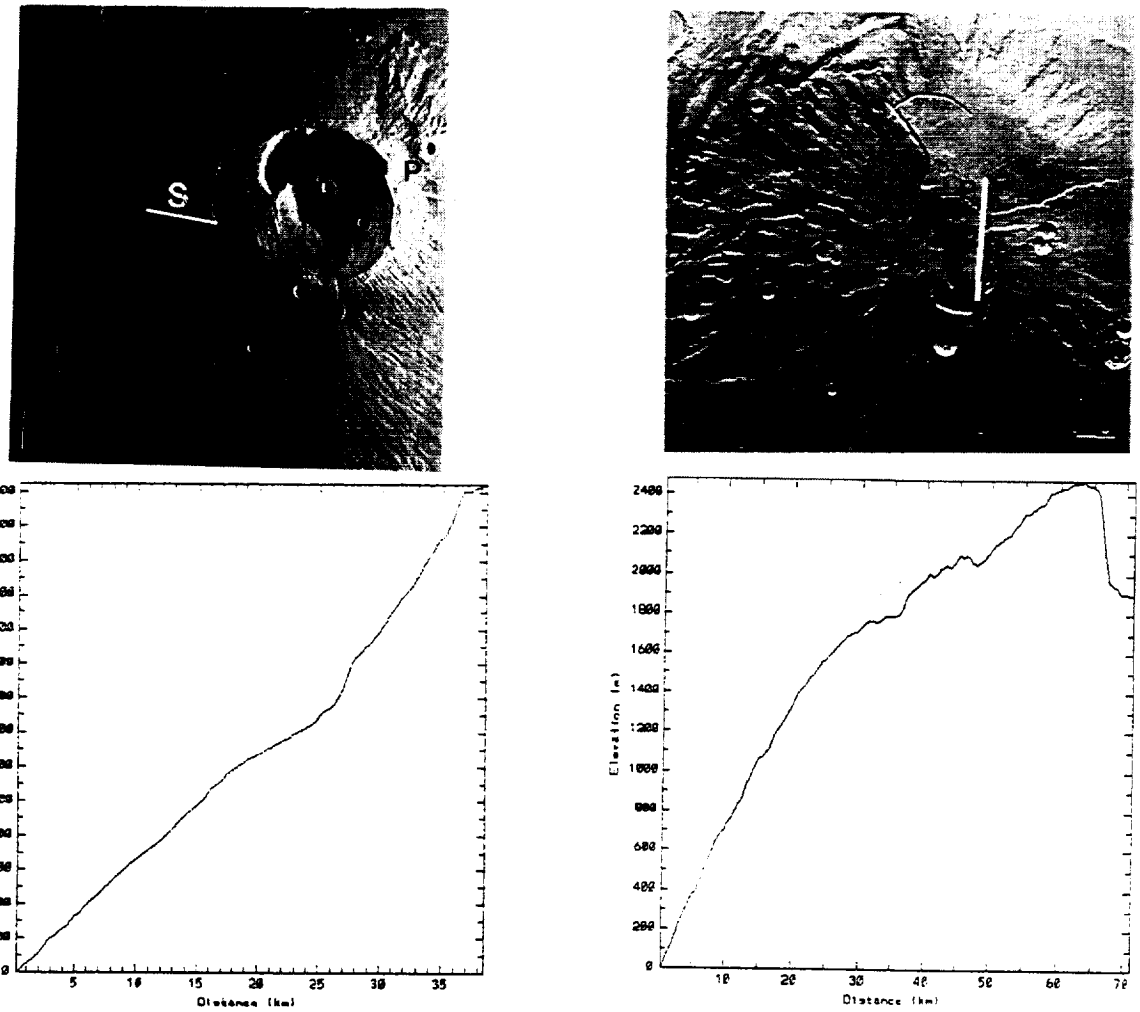


**Figure 1.** UL - Apollinaris Patera, Viking 635A57 INA=79.5 res=250 m/pix, P indicates photoclinometric profile plotted at LL, S indicates shadow measure of edifice height - 5100 m, scale bar = 50 km. UR - Tyrrhena Patera, Viking 087A14 INA=67°, res=230 m/pix, P indicates photoclinometric profile plotted at LR, scale bar = 46 km.

# SINUOUS RIDGES OF THE SOUTH POLAR REGION, MARS: POSSIBLE ORIGINS;

*S.W. Ruff and Ronald Greeley, Department of Geology, Arizona State University.*

Ridges with sinuous, dendritic, and braided morphologies have been identified in the Dorsa Argentea region near the martian south pole and in the Argyre Planitia (Figure 1). They are < 1 km wide, 100-200 m high, and lengths can exceed 200 km. In planform they vary from relatively straight, solitary features to complex, dendritic and braided patterns. In the Dorsa Argentea region, bifurcating and intersecting relationships of ridges give rise to the dendritic patterns. Some ridges are observed to cross medium-sized, partly buried craters while others cross over each other. Ridge intersections are of two types: merging/bifurcating and overlapping. The first type occurs at most Y-junctions where a single ridge bifurcates or two ridges merge into one. Overlapping intersections occur at X-junctions, the result of an apparent intersection of two ridges at different elevations to each other. The overlapping intersections appear to arise when stratigraphically separated ridges are exhumed, giving the appearance of an intersection. The origin of these ridges remains enigmatic and only two brief interpretations have been proposed, eskers (1) and unusual lava-flow features (2). Other possibilities include linear dunes, inverted topography, and clastic dikes.

Howard (1) proposed a fluvial origin by basal melting of ground ice to account for the dendritic and braided characteristics of the ridges. This model suggests that the ridges are eskers, the depositional product of meltwater channels within ice. Terrestrial eskers have similar morphological characteristics which compare favorably to those of the martian ridges. In planform eskers are often braided as well as dendritic features which are a few to 100 m high, up to 6 km wide, and several meters to 400 km long (with breaks) (3). The difficulty with this interpretation is that it requires the presence of large quantities of ice which, on Earth, produce a host of associated glacial landforms. These are not readily apparent in the region where ridges occur.

Tanaka and Scott (2) offered a brief interpretation of the ridges as part of their mapping of the polar regions. They suggested that the ridges could be an unusual lava-flow feature. Known ridge forming features associated with lava flows include, among others, basaltic pressure ridges (e.g., 4), wrinkle ridges (e.g., 5), and flow lobes. However, none of these have morphologies which can explain the forms seen in the martian sinuous ridges. An as yet unexplained and unobserved style of lava flow must be proposed then to account for the ridges.

Another possibility, suggested by Malin (personal communication), proposes that the ridges are dunes. Some linear dunes in Australia bare a striking resemblance to the martian ridges. Australian dunes can be sinuous, bifurcating, and irregular in their occurrence (6). Some parts of these dunes have a braided appearance. They are several meters to 1 km wide and up to 190 km long (7). A dune interpretation for the martian ridges is supported by the fact that aeolian processes on Mars are well documented (e.g.,8) and the adjacent polar layered deposits could represent a ready supply of sediment which could be reworked into dunes. The difficulty with this interpretation is that linear dunes on Earth do not have such complex intersecting and bifurcating patterns as the martian ridges.

An alternative suggestion by Howard (1) includes the possibility of inverted topography to explain the ridges. He discarded this idea due to a lack of favorable morphological comparison to known inverted topography at other martian locales as well as on Earth. But, the preservation of channel deposits produced during fluvial or volcanic activity could, following differential erosion, produce ridge forms. This idea is weakened in the case of the martian ridges by the presence of geometries that are not indicative of flow channels. Namely , many of the ridges have V's which open in opposing directions rather than a single upstream direction.

A final hypothesis that was examined came from Malin (personal communication). He suggested clastic dikes as a possible ridge former. Clastic dikes occur where extraneous material invades a crack within a host rock (9). These features are from 2 cm to 10 m thick and a meter to 15 km long. Perhaps differential erosion could result in a ridge form, but this is not a common attribute of clastic dikes. The relatively small size and lack of topographic relief of terrestrial clastic dikes does not favor them as an analog of the martian ridges.

Additional study is required before making final conclusions. Many of the ridges mapped by Tanaka and Scott (2) have not been inspected in detail, nor has a planetwide inventory of similar appearing features been made. Finally, a complete study of morphometric features associated with the martian ridges and terrestrial analogs must be undertaken. If thermal inertia and/or spectral data with fine enough resolution are available in ridge areas, information concerning the composition of the ridges could be elucidated and could help to constrain certain hypotheses.

REFERENCES

(1) Howard, A.D. 1981. Etched plains and braided ridges of the south polar region of Mars: Features produced by melting of ground ice? *Reports of Planetary Geology Program-1981*, NASA TM 84211, 286-289.

(2) Tanaka, K.L. and Scott, D.H. 1987. Geologic map of the polar regions of Mars. U.S. Geol. Surv. *Misc. Invest. Series*, Map I-1802-C 1:15,000,000.

(3) Price, R.J. 1973. *Glacial and Fluvioglacial Landforms*, Hafner Publishing Co., New York, 242 pp.
(4) Theilig, E.E. 1986. Formation of pressure ridges and emplacement of compound basaltic lava flows. PhD thesis, Arizona State University, Tempe.
(5) Maxwell ,T.A, El-Bas, R., and Ward, S.H. 1975. Distribution, morphology, and origin of ridges and arches in Mare Serenitatis. *Geol Soc. Am. Bull.*, **86**, 1273-1278.
(6) Mabbutt, J.A. and Sullivan, M.F. 1968. The formation of longitudinal dunes: evidence from the Simpson Desert. *Austr. Geogr.*, **10**, 483-487.
(7) Breed, C.S. and Grow, T. 1979. Morphology and distribution of dunes in sand seas by remote sensing. In *A Study of Global Sand Seas*, E.D. Mckee, editor. U.S Geol. Surv. Prof. Paper 1052, 253-302.
(8) Greeley, Ronald, Leach, R.N., Williams, S.H., White, B.R., pollack, J.B., Krinsley, D.H., and Marshall, J.R. 1982. Rate of wind abrasion on Mars. *Journ. Geophys. Rev.*, **87**, 10,009-10,024.
(9) Pettijohn, F.J. 1975. *Sedimentary Rocks*. Harper and Row, Publishers, 628 pp.



Figure 1. *Viking photomosaic showing sinuous ridges in Dorsa Argentea.*

CHEMICAL EVOLUTION OF THE EARLY MARTIAN HYDROSPHERE; M. W. Schaefer, University of Maryland and Goddard Space Flight Center, Greenbelt, MD

Mars today is a cold, dry planet, with a thin atmosphere, largely consisting of carbon dioxide. It may not always have been that way, however. Values of total outgassed $CO_2$ from several to about 10 bars are consistent with present knowledge (18), and this amount of $CO_2$ implies an amount of water outgassed at least equal to an equivalent depth of 500 to 1000 meters (3). Pollack et al. (18) have made extensive calculations deriving the amount of carbon dioxide necessary to achieve a strong enough greenhouse effect to raise the surface temperature of Mars above the freezing point of water, and have determined that, for different values of surface albedo, latitude, and orbital position, pressures of from 0.75 to 5 bars are necessary. The geological evidence suggests that any such warm, wet period in Mars' history must have been over by about 3.5 billion years ago.

One may model the early Martian ocean as a body of relatively pure water in equilibrium with a dense (several bars) carbon dioxide atmosphere. The juvenile water outgassed by Mars should have been extremely acidic, based on Earth analogy. In such waters all common components of ordinary rocks are highly soluble, with the exception of $SiO_2$ and $Al_2O_3$ (10). The chemical weathering of lavas, pyroclastic deposits, and impact melt sheets would have the effect of neutralizing the acidity of the juvenile water. Equilibrium would be achieved when the weathering rate of the rocks was equal to the dissolution rate of the carbon dioxide in the atmosphere (which dissolution would itself require the water to be quite acidic, with a pH no greater than about 5). There was also an extensive groundwater system at this time (2), which acted to weather even those parts of the regolith far distant from the ocean. On the Earth, about 30% (9) of the outgassed water is thought to be geochemically bound in the crust. One might take this figure as an upper limit to how much of the Martian water budget might have become bound in its regolith during the relatively restricted time available for such processes to occur (no more than about 1 billion years, compared to the 4.5 billion years available on the Earth). Assuming then a total value for outgassed water on Mars of 500 - 1000 m, averaged over the entire planet, and only a few meters of that lost to space through thermal escape (12), at the time when enough carbon dioxide was lost from the atmosphere such that temperatures dropped below the freezing point of water on Mars, there should have been at least 350 - 700 m of water still free and unbound. The formation of the highland-lowland dichotomy is believed to have taken place by the time of the decline of the heavy meteorite bombardment (7), thus providing a natural basin into which this water could collect. The lowland terrain takes up roughly 30% (± 5%) of the surface of Mars; therefore, if the available water was concentrated in the lowland terrain, it would have a depth of some 1000 - 2800 m. This depth is comparable to the height of the boundary scarp between the highland and lowland terrains, similarly (though probably coincidentally) to the way in which water on the Earth is largely contained by the continents to within the lowlands formed by the oceanic crust. There may be geological evidence for such an ocean on Mars (3, 13, 11, 15-17).

As calcium and other cations are added to the water by chemical weathering, they are quickly removed by the precipitation of calcium carbonate and other minerals, forming a deposit of limestone beneath the surface of the ocean. Even in the deepest parts of this ocean, pressure effects will not be enough to prevent the precipitation of carbonates, unlike the present situation on the Earth, where carbonate deposits only form in relatively shallow water. By this process, carbon dioxide is removed from the atmosphere. The time scale on which this occurs can be as little as $10^7$ years (3, 6, 18), assuming no reworking of deposited carbonates, or when such reworking is postulated, a time scale of up to about a billion years is reasonable (18). As the carbon dioxide is removed from the atmosphere, the heat trapped due to the greenhouse effect becomes unimportant, the planet's surface cools to below the freezing point of water, and the surface of the ocean freezes. When the surface of the ocean freezes, the removal rate of carbon dioxide from the atmosphere is decreased, due to the decreased rate of regolith weathering caused by the lesser mobility of water through the atmosphere-regolith system, but it is not halted. The ice layer will act to trap beneath it an artificially high concentration of dissolved carbon-bearing species, brought in by the percolation of groundwater. The freezing of the water will have the additional effect of further increasing

the cation concentration in the remaining liquid, due to the exclusion of cations from the crystal structure of the ice. This behavior is observed in frozen lakes in the terrestrial Arctic (8) and Antarctic (14), and there results in the precipitation of carbonates on the lake beds.

As the atmospheric carbon dioxide pressure and the temperature continue to decrease, there should come a time when the Martian ocean is almost completely frozen, perhaps overlying a layer of salts or concentrated brines above the carbonate layer. Due to the high expected ratio of calcium (or other cation) concentration relative to $HCO_3^-$ concentration in the water, calcium carbonates are preferentially deposited, and the remaining fluid gradually evolves to form a Ca-Na sulfate-chloride brine (5). If the entire Martian $CO_2$ budget of, say 1 - 10 bars, were to be used to form this carbonate deposit, it would imply an average thickness for the deposit of 100 to 1000 meters.

Once the ocean is completely frozen, the sublimation and ablation of ice from the uppermost surface of the ocean is no longer compensated for by the freezing of the water below; the ice itself gradually disappears, starting at the warmest areas near the highland-lowland boundary, migrating into the regolith and leaving only a residual cap at the north pole. Or it could be that the ocean would be so reduced in volume by the time it froze completely that it would be not significantly larger than the present polar cap. Also at this time, carbon dioxide from the atmosphere may be adsorbed onto the cold regolith. Eventually, through the action of freezing and the removal of water from the atmosphere-regolith system by irreversible geochemical weathering, the entire water budget of Mars will be tied up in its present reservoirs in the polar caps and regolith.

Given the preceding scenario for the geochemical evolution of the northern lowland plains of Mars, it should be possible to draw a few conclusions about the expected mineralogy and geomorphology of this region. The basement material should be a highly-altered regolith, though it is impossible to say with any certainty whether the original material was mostly basalt flows, ash deposits, or some other volcanic product. One would expect, however, that it should have been highly brecciated by the early, heavy meteorite bombardment of the planet. It should contain a significant proportion of clays and other hydrous minerals. Overlying this basement, and covering most of the northern plains, are carbonate deposits, several hundred meters thick or more. Likely to be primarily calcium carbonate, these deposits would be progressively more sulfate- and salt-rich in their upper layers. The topmost layers of these deposits would be primarily gypsum ($CaSO_4 \cdot 2H_2O$) or mirabilite ($Na_2SO_4 \cdot 10H_2O$), and assorted salts (5). Continued meteoritic impacts, and dust storms, have acted to mix these sedimentary materials with the volcanic materials common over most of the rest of the planet, to form a surficial mantling of dust of uniform composition. Viking chemical analyses indicate that the surficial deposits in Chryse Planitia and Utopia Planitia may contain as much as 8 - 15% sulfates, and up to 10% carbonates (4), consistent with such a volumetric mixing model. It has also been suggested by several researchers that brines may be at least metastable at present in the regolith of Mars (1), particularly in the region of Solis Lacus, where anomalous radar reflectivity has been observed (19,20).

(1) Brass, G. W., *Icarus 42*,20, 1980; (2) Carr, M. H., *JGR 82*, 4039, 1979; (3) Carr, M. H., *Icarus 68*, 187, 1986; (4) Clark, B. C., Van Hart, D. C., *Icarus 45*, 370, 1981; (5) Eugster, H. P., Hardie, L. A., Ch. 8 in *Lakes: Chemistry, Geology, Physics*, Springer-Verlag, 1978; (6) Fanale, F. P., Salvail, J. R., Banerdt, W. B., Saunders, R. S., *Icarus 50*, 381, 1982; (7) Greeley, R., *Planetary Landscapes*, Allen and Unwin, 1985; (8) Hall, D. K., *Arctic 33*, 343, 1980; (9) Holland, H. D., *The Chemical Evolution of the Atmosphere and Oceans*, Princeton, 1984; (10) Loughnan, F. C., *Chemical Weathering of the Silicate Minerals*, Elsevier, 1969; (11) Lucchitta, B. K., Ferguson, H. M., Cummers, C., *JGR 91*, E166, 1986; (12) McElroy, M. B., *Science 175*, 443, 1972; (13) McGill, G. E., in *Lunar and Planetary Science XVI*, Lunar and Planetary Institute, 534, 1985; (14) McKay, C. P., Nedell, S. S., *Icarus 73*, 142, 1988; (15) Parker, T. J., Schneeberger, D. M., Pieri, D. C., Saunders, R. S., *NASA TM-89810*, 319, 1987; (16) Parker, T. J., Schneeberger, D. M., Pieri, D. C., Saunders, R. S., *NASA TM-89810*, 322, 1987; (17) Parker, T. J., Saunders, R. S., *LPI Tech. Rept. 88-05*, 100, 1988; (18) Pollack, J. B., Kasting, J. F., Richardson, S. M., Poliakof, K., *Icarus 71*, 203,1987; (19) Zent , A. P., Fanale, F. P., *JGR 91*, D439, 1986; (20) Zisk, S. H., Mouginis-Mark, P. J., *Nature 44*, 735, 1980.

**GLOBAL RELATIONSHIPS BETWEEN VOLCANIC VENTS AND FRACTURES RADIAL TO LARGE IMPACT BASINS ON MARS.**

Byron D. Schneid and Ronald Greeley, Department of Geology, Arizona State University, Tempe, AZ 85287.

The relation of volcanic vents on Mars to impact basins has been studied previously (1,2,3,4,5,6). It has been asserted that the concentric fractures around impact basins extend into the crust and might localize some features, including volcanoes (e.g. 4). In this study, we assess the possibility of radial fractures inferred to be associated with impact basins as an additional control on the location of volcanoes on Mars. Geologic mapping at 1:2 million scale enabled 250 central vents and fissure vents to be identified. Patterns of vent distribution (fig. 1) superimposed on a globe show that most are located on three distinct circles. The first is a great circle which passes through Arsia Mons, Pavonus Mons , Ascreaus Mons, and Tempe Fossae, along Protonilus Mensae (an area of fractured terrain), through Syrtis Major, Hadriaca Patera, and a series of fissure vents southwest of Tharsis. A similar great circle trends SW to NE from the Hellas basin, through Hadriaca Patera, Tyrhenna Patera, Elysium, Alba Patera (which is approximately antipodal to the Hellas basin), southern Tempe Fossae, the eastern Valles Marineris chaotic region, and the Amphitrites Patera vents on the southwest rim of the Hellas basin. The third series of vents is on a small circle ~4800 km in diameter centered at ~ 104°W, 2°N. This site is near the center of the Tharsis gravity anomaly (7) and the loci of associated tensile stresses (8). Most fissure vents not located on the Tharsis trend of volcanics are on this small circle, as are Alba Patera and other central vents.

There are two more possible great circles which may be superimposed onto the martian globe. The first can be traced along the escarpment dividing the northern lowlands from the southern highlands, across Isidis Planitia (the site of a possible impact basin at ~ 273°W, 13°N), fractured terrain in Solus Planum (a possible fissure vent source area), and through Juventae Chasma. This circle may reflect the role of inferred radial fractures in modifying the surface without associated volcanism. The second possible great circle passes through the Hellas impact basin, some large unnamed central vent volcanoes (at ~ 205°W, 48°S) , Apollonaris Patera, the escarpment north of Alba Patera and the Tempe Fossae region, and into Acidalia Planitia. Acidalia Planitia is also along the trend of the Tharsis chain of volcanoes and may indicate an impact site centered near 30°W, 60°N.

Although concentric fractures of smaller impact basins may influence local vent sites, the global setting appears to be governed by radial fractures associated with major impact basins. This is supported by the association of one or perhaps two great circles with the Hellas impact basin, and possible great circles associated with the Isidis basin and Acidalia Planitia. The distribution also suggests that larger impacts produce larger fractures and can, therefore, accommodate more

**VOLCANIC VENTS AND FRACTURES RADIAL TO IMPACT BASINS**
Schneid,B.D. and Greeley,R.

volcanic vents. Isidis, Argyre, Procellarum, and Hellas basins in that order, have an increasing number of vents inferred to be associated with them.

REFERENCES: (1) Albin, E.F. and Greeley, R., Proc. LPSC XVII, pp. 7-8, 1986. (2) Albin, E., Masters Thesis, Arizona State University Press, 1986. (3) Craddock, R.A., Greeley, R., and Christensen, P.R., Journal of Geophysical Research, in press. (4) Schultz, P.H., Schultz, R.A., and Rogers, J., Journal of Geophysical Research, 82, B12, pp.9803-9820, 1982. (5) Schultz, P.H., Proc. LPSC XV, pp.728-729, 1984. (6) Wichman, R. and Schultz, P.H., NASA TM-89810,pp.474-475, 1987. (7) Phillips, R.J. and Lambeck, K., Reviews of Geophysical Space Research, 18, pp. 27-76, 1980. (8) Phillips, R.J. and Ivens, E.R., Physics of Earth and Planetary Interiors, 19, pp. 107-148, 1979.

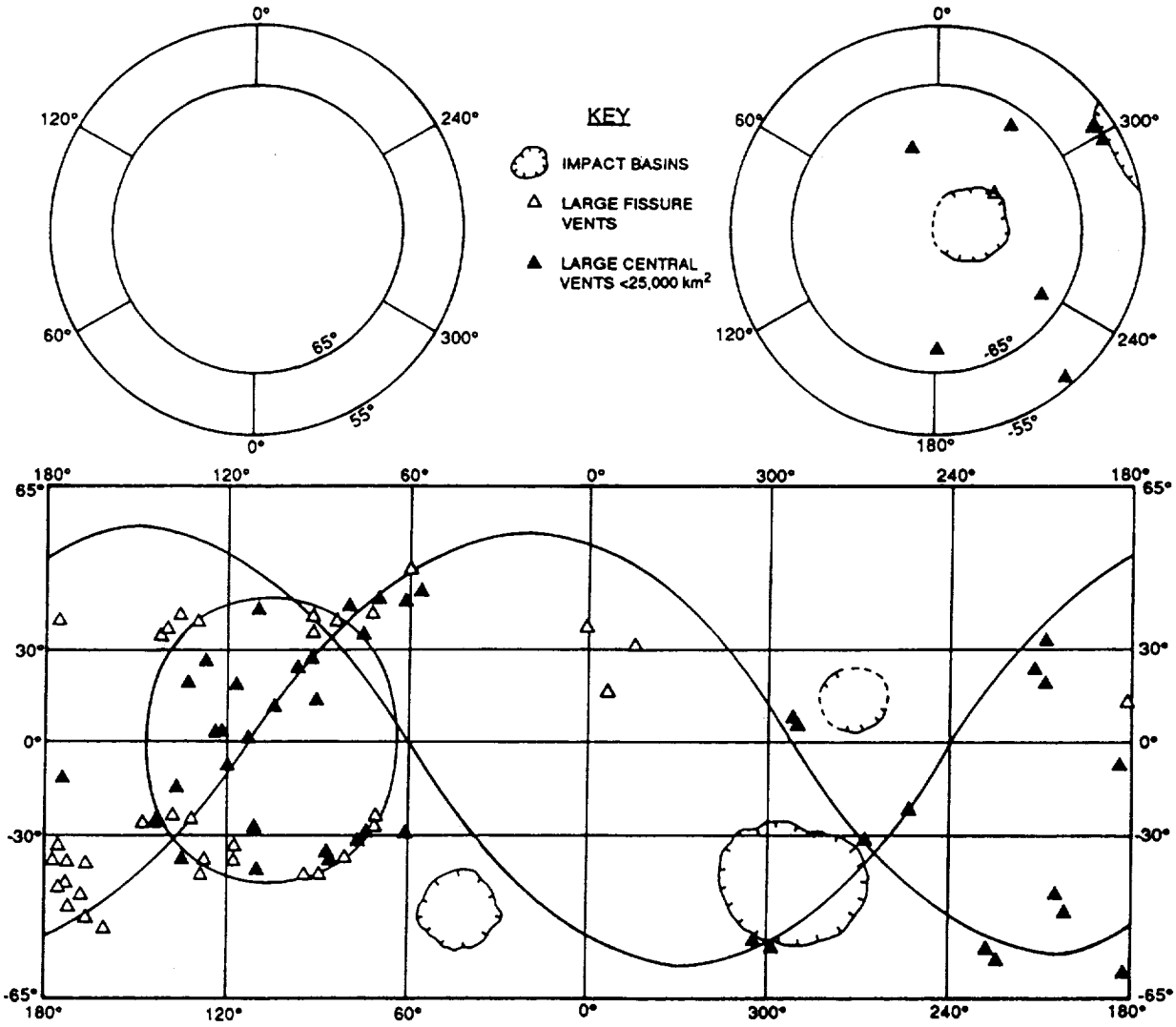


Figure 1. Vent locations, impact basins, and great and small circles.

## COMPLEX EARLY RIFTING IN VALLES MARINERIS: RESULTS FROM PRELIMINARY GEOLOGIC MAPPING OF THE OPHIR PLANUM REGION OF MARS, 1:500,000 SCALE.

*Richard A. Schultz, Geodynamics Branch, NASA Goddard Space Flight Center, Greenbelt, MD 20771.*

Ophir Planum is a relict plateau bounded on three sides by Valles Marineris troughs (Coprates, Melas, and Candor/Ophir Chasmata). The plateau is deformed by a distinctive array of grabens whose orientations differ by as much as 30° from the overall trend of the troughs. Photogeologic mapping of the Ophir Planum quadrangle (MTM -10067; Fig. 1) was undertaken to solve two main problems: (1) What controlled the location, orientation, and growth of Ophir Planum grabens? and (2) How are the grabens and trough faulting related?

Geology within the quadrangle is surprisingly diverse (Fig. 2). The Ophir Planum plateau is capped by plains materials that embay more rugged and densely cratered materials. New crater counts suggest that these plains materials are correlative to Early Hesperian ridged plains on Lunae Planum to the north [1] but significantly, no wrinkle ridges are found on Ophir Planum. The densely cratered materials are probably Noachian (Npl2?) in age, as is the trough wall rock beneath the plateau. Five units are identified in Coprates Chasma: cratered plains (Hpf in Fig. 2), 2 facies of basin beds (Hvl), landslide materials (As), and young possible volcanics (Avsd; see [2]). A third facies of basin bed is distinguished in Ophir Chasma to the north. Crater counts suggest that Hpf in Coprates is also of Early Hesperian age, implying that the Coprates trough floor is structurally lowered caprock of "Lunae Planum" age.

Well defined fault scarps divide Ophir Planum from Coprates Chasma. These trough bounding normal faults change strike from nearly east-west in the eastern part of the quadrangle (Fig. 1) to northwest. The orientations of grabens on Ophir Planum plateau mirror this change and plateau faults locally merge with trough bounding faults. These relationships suggest that plateau grabens are as old as the trough bounding normal faults and that they probably formed under the same stress regime. Ophir Planum grabens probably did not result from either lateral unloading due to landsliding or sliding of caprock into the troughs [3] because (a) their age is older than the periods of landsliding or development of spur-and-gully topography on trough walls, which occurred after downfaulting in the troughs; (b) they do not always parallel the plateau bounding scarp, as required by the mechanisms of [3]; and (c) stress analysis of lateral unloading shows that the grabens occur too far from bounding scarps to have resulted from scarp retreat.

The grabens on Ophir Planum define an echelon set and their changing orientations within the stepover are consistent with mechanical interaction between grabens as they grew into the echelon array [e.g., 4] (Fig. 3). The overall orientation of Valles Marineris troughs is consistent to first order with a spatially uniform, Tharsis generated remote stress state in the region containing the troughs [e.g., 5]. The curving geometries of Ophir Planum grabens and trough bounding faults in Coprates both indicate that the local stress state in this area was spatially variable during the time of Valles Marineris faulting and trough growth. The cause of this spatial variability is still uncertain although stress pertubation by growing troughs that also interact mechanically is an attractive possibility.

The rich geologic history of the Ophir Planum quadrangle (Table 1) underscores the fundamental importance of faulting in the early growth of Valles Marineris.

**REFERENCES**: [1] Tanaka, K.L., *Proc. Lunar Planet. Sci. Conf., 17th*, in *JGR, 91*, E139-E158, 1986. [2] Lucchitta, B.K., *Science, 235*, 565-567, 1987. [3] Witbeck, N.E., K.L. Tanaka, and D.H. Scott, Geologic map of the Valles Marineris region, Mars, *USGS Map I-2010*, in press. [4] Pollard, D.D. and A. Aydin, *JGR, 89*, 10,017-10,028, 1984. [5] Banerdt, W.B. et al., *JGR, 87*, 9723-9733, 1982.

# DEFORMATION OF OPHIR PLANUM, MARS

*Schultz, R.A.*

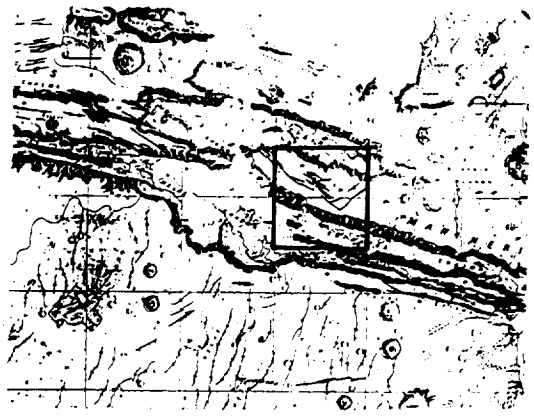

*Fig. 1. Quadrangle location.*

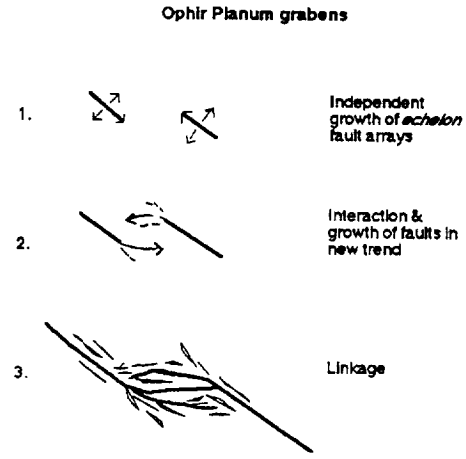


*Fig. 3. Growth model for Ophir Planum grabens.*

*Fig. 2.*

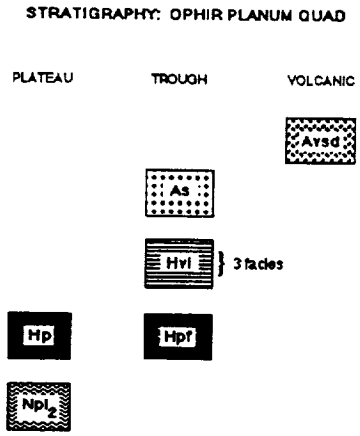


*Table 1: Geologic Synopsis.*

**1. FORMATION OF OLDER NOACHIAN UNITS**
- ◊ $Npl_2$, Noachian wall materials

**2. DEPOSITION OF OPHIR PLANUM PLATEAU UNIT**
- ◊ Resurface and embay $Npl_2$
- ◊ No wrinkle ridges

**3. FAULTING**

*Trough Formation*
- ◊ Growth of Coprates, bounding faults- linear to concave NE
- ◊ Ophir Planum relatively undeformed
- ◊ Minor faulting & volcanism (pits, flows) on OP // to Coprates

*Deformation of Ophir Planum*
- ◊ Growth of oblique graben arrays on & beyond OP
- ◊ Graben depth ~1 km < D < 5 ?? km

**4. TROUGH MODIFICATION**
- ◊ Erosional retreat of wall scarps
- ◊ Deposition of regional & local floor layers (Hvf)
- ◊ Faulting of basin beds, wall scarps (?)
- ◊ Erosion of most Hvf in Coprates, minor in Melas
- ◊ Landslides; mafic volcanism (?)

**POSSIBLE DEFICIENCY OF LARGE MARTIAN CRATERS AND RELATIVE CRATERING OF THE TERRESTRIAL PLANETS.** *Richard A. Schultz, Geodynamics Branch, NASA Goddard Space Flight Center, Greenbelt, MD 20771.*

The relative size-frequency distribution of impact craters and basins on Mercury, the Moon, and Mars is remarkably similar [1], suggesting that all three bodies were bombarded by the same population of objects early in solar system history [2]. However, Mars appears to be deficient in large craters relative to Mercury and the Moon [3,4]. Part of this difference appears to be observational because large partly buried or eroded craters may not always be included in crater inventories [e.g., 5]. The relative deficiency of large craters on Mars conflicts with the interpretation of a common population of impactors within the early inner solar system [1,2] and suggests either of two possibilities. If the apparent deficiency of martian craters is real then the population of impactors at Mars differed significantly from that closer to the Sun. If the apparent deficiency is not real then the complete crater inventory of Mars should be similar to those of Mercury and the Moon, supporting the interpretation of a single population of impactors. These alternative possibilities can be tested by comparing revised inventories that include partly buried or eroded craters to an estimate of Mars' possible relative crater deficiency.

The number of "deficient" martian craters was estimated by subtracting binned lunar crater counts from the binned martian counts and propagating their uncertainties [6]. All counts were normalized by the surface area of Mars. Comparison of *Barlow's* [5] crater and basin inventory for Mars to the lunar one shows the apparent deficiency [3,4] of large martian craters having diameters ~100 km < $D$ < 1000 km relative to the Moon (Fig. 1a, b). The mercurian curve (not shown) is indistinguishable statistically from the lunar curve [1]. All three bodies contain the same relative number of large basins ($D$ > 1000 km). Lateral shift of the martian curve to the next larger diameter bin in order to compensate for lower relative impact velocity [3] eliminates the deficit for craters less than 250 km ($log\ D$ = 2.4) in diameter (Fig. 1b). Revision of the multi-ring basin record [4] does not affect the deficit significantly. The difference between the lunar and martian crater counts shows that a considerable number of large martian craters may remain uncounted.

Best-fit polynomials to cumulative size-frequency crater distributions have been used to define 'standard crater curves' [e.g., 7]. These curves are somewhat artificial because they incorporate crater data from geologic units having different counting areas and absolute ages. Nevertheless, they can be useful for interplanetary comparisons and resurfacing studies. The *Neukum and Hiller* 1981 and *Neukum* 1983 fits were determined by using smaller craters (< 20 km in diameter), and the revised 1983 fit increased the order of the best-fit polynomial from 7 to 11. However, neither curve fits martian crater data at diameters larger than 100-300 km. A new "Mars reference curve" was obtained by converting the binned crater data [5,4] into log-log cumulative form and obtaining best-fitting polynomials by using weighted least squares. The martian crater and basin record can be adequately represented by either a single cubic equation (1) or two equations (2) (see Fig. 2):

$$\Sigma N = 3.40 + 3.47\,D - 2.68\,D^2 + 0.42\,D^3 \qquad 8 \le D < 5000 \text{ km} \qquad (1)$$
$$\chi^2 = 16.8$$

or

$$\Sigma N = 4.67 + 0.70\,D - 0.77\,D^2 \qquad 8 \le D < \sim 500 \text{ km} \qquad (2)$$
$$\chi^2 = 21.2$$
$$\Sigma N = 4.96 - 1.21\,D \qquad D > 500 \text{ km}$$
$$\chi^2 = 0.646$$

These best-fit curves are simpler than previous fits that were restricted to small crater data. Equation (1) or something similar would be appropriate if the apparent crater deficiency is

observational; additional counts of large craters may reduce the knee near 200 km (Fig. 2a: *log D* = 2.3). Equations (2) would be appropriate if the apparent crater deficiency is real and the associated impactor population thereby different than that for Mercury and the Moon. Equations (1) and (2) are better fits to the data than a simple $D^{-2}$ distribution (Fig. 2c). These results provide a means to test the interpretation of a common source of impactors within the early solar system once more complete crater counts for older martian terrains become available.

**REFERENCES**: [1] Strom, R.G., *Icarus, 70*, 517-535, 1987. [2] Wetherill, G.W., *Proc. Lunar Sci. Conf., 6th*, 1539-1561, 1975. [3] Strom, R.G., S.K. Croft, and N.G. Barlow, in *Mars*, Univ. of Arizona Press, in press. [4] Schultz, R.A. and H.V. Frey, *J. Geophys. Res.*, submitted, 1989. [5] Barlow, N.G., *Icarus*, 75, 285-305, 1988. [6] Bevington, P.R., *Data Reduction and Error Analysis for the Physical Sciences*, p. 60-61, 1969. [7] Neukum, G. and K. Hiller, *J. Geophys. Res.*, 86, 3097-3121, 1981.

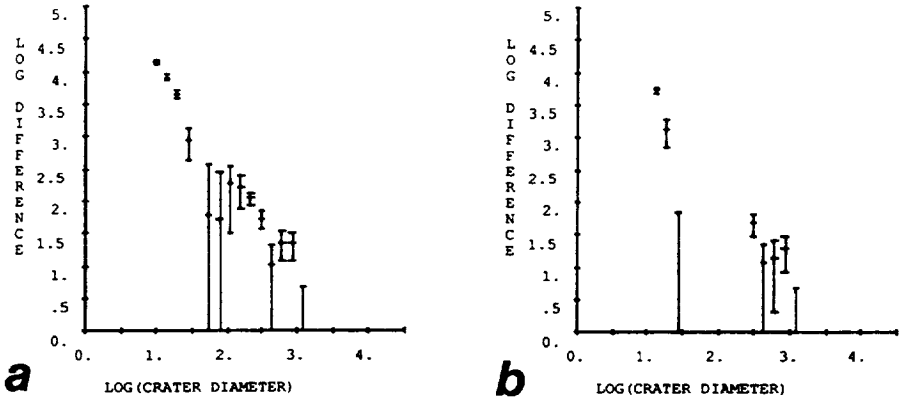


*Fig. 1. Plots of difference between number of lunar and martian craters vs. binned crater diameter. All data normalized to surface area of Mars. (a) Direct subtraction. (b) Subtraction after correction for suggested differences in heliocentric impactor velocity.*

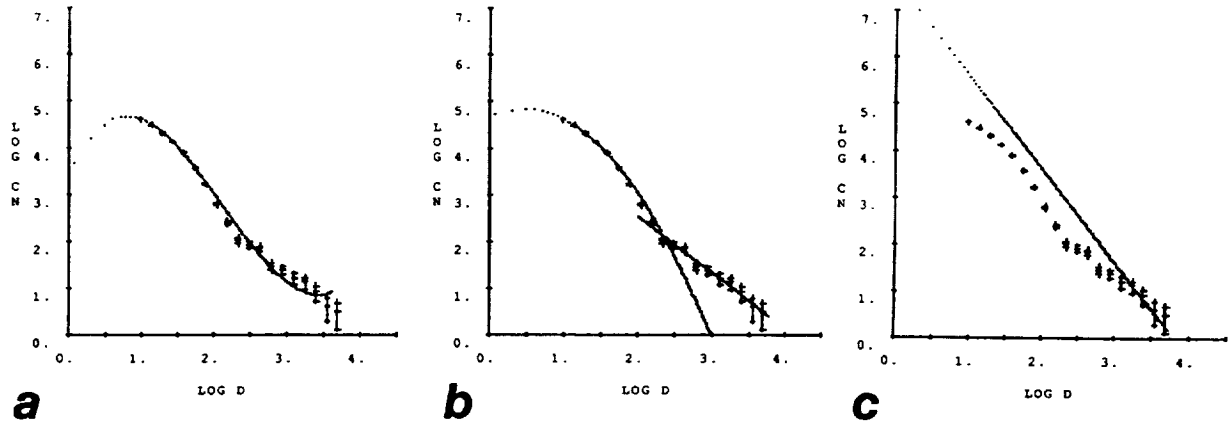


*Fig. 2. Cumulative frequency plots of martian craters and basins; data from [5,4]. (a) Cubic best fit, equation (1). (b) Best fit if two impactor populations are defined; equations (2). (c) $D^{-2}$ curve with intercept $a_o = 7.6$.*

**STRIKE-SLIP FAULTING, WRINKLE RIDGES, AND TIME VARIABLE STRESS STATES IN THE COPRATES REGION OF MARS.** *Richard A. Schultz, Geodynamics Branch, NASA Goddard Space Flight Center, Greenbelt, MD 20771.*

The existence of strike-slip faults has recently been documented in two locations on Mars [1,2]. In this abstract I review two clear examples located southeast of Valles Marineris and present preliminary evidence for more widespread strike-slip deformation elsewhere in Coprates.

Strike-slip faults and wrinkle ridges both deform Early Hesperian plains materials in eastern Coprates between 20-25° S and ~55° W [2]. The strike-slip faults are defined by echelon arrays of linear structures that bound polygonal or rhombohedral plateaus located within their stepovers. The faults are oriented obliquely (~60°) to the overall, north-south trend of the wrinkle ridges. The plateaus were probably formed within contractional strike-slip stepovers rather than by simple lateral or vertical offset of pre-existing markers. Crustal shortening along each echelon fault array may exceed 1-2 km. Northwest trending strike-slip faults in this area are left lateral, as inferred by their sense of step and type of stepover, whereas northeast trending faults are right lateral. The lack of orthogonal fault-ridge intersections implies that the faults did not serve as passive transforms during wrinkle ridge deformation. Indeed, some wrinkle ridges located at fault terminations occur in the fault's compressional quadrants and have angular relationships to the strike-slip faults suggesting that they may have nucleated as a result of the localized strike-slip activity. Strike-slip faulting in this part of Coprates may have predated or overlapped episodes of wrinkle ridge growth and was probably also driven by Tharsis generated stresses.

Strike-slip faulting becomes more complex near 26-28° S in Coprates (Fig. 1). Here, northeast trending linear zones that look like wrinkle ridge material appear to be closely spaced strike-slip faults. Wrinkle ridges that cross these zones are not noticeably offset, suggesting that the zones occurred before the ridges. In contrast, left lateral strike-slip faults occurring in the same area appear to offset at least one ridge, and portions of many other ridges appear defined by scarps of similar orientations to these faults. Inferred remote stress states for the three sets of structures (Fig. 1a, b) are comparable to those predicted from Tharsis deformation models. It appears that right lateral strike-slip faulting first occurred in the curvilinear zones, then was replaced by coeval left lateral strike-slip faulting and wrinkle ridge growth.

Most wrinkle ridges south of Valles Marineris trend northeast but older, northwest trending ridges are also present [e.g., 3]. Fig. 3 shows the geometry of some large ridges southeast of Melas Chasma. Crosscutting relations indicate that northwest ridges formed first (Fig. 2a), so a change in remote stress orientation over time is implied. A resolved shear stress may have acted along or within northwest trending ridges during superposition of the second wrinkle ridge producing stress state. This would explain the growth of short oblique "crenulations" on the southern ridge (Fig. 2b) and growth of some northeast trending ridges in the inferred compressional stress quadrants of older ridges (see [2]). This example differs from the previous two in that discrete strike-slip faults are not observed. Instead, the lateral growth of wrinkle ridges appears to have been locally influenced by the relative orientations of ridges and remote principal stresses [e.g., 4-6]. Interestingly, the older northwest trending ridges with inferred left lateral shear strain parallel the left lateral strike-slip faults to the east [2, Fig. 1].

The first two examples show that strike-slip faulting occurred in a broad zone east of the Coprates Rise spanning ~400 km east-west by perhaps 1000 km north-south. The last example suggests that the growth of major wrinkle ridges throughout Coprates may have been influenced by horizontally directed shear stresses and that more than one generation of ridges was produced. Thus, "compressional" deformation of ridged plains south of Valles Marineris was spatially heterogeneous and a temporal change in stress state may have been involved.

**REFERENCES:** [1] Forsythe, R.D. and J.R. Zimbelman, *Nature, 336*, 143-146, 1988. [2] Schultz, R.A., *Nature, 341*, 424-426, 1989. [3] Watters, T.R. and T.A. Maxwell, *Icarus 56*, 278-298, 1983. [4] Tija, H.D., *Geol. Soc. Am. Bull., 81*, 3095-3100, 1970. [5] Raitala, J., *Moon Planets, 25*, 105-112, 1980. [6] Aubele, J.C., *Lunar & Planet. Sci., XIX*, 19-20, 1988.

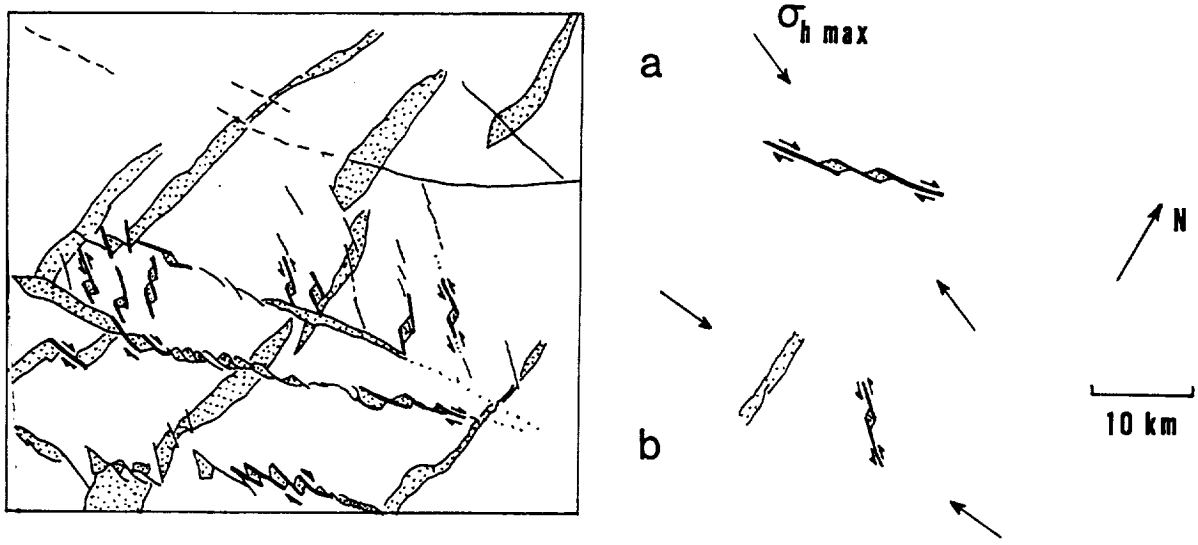


*Fig. 1. Sketch map showing relationships between strike-slip faulting and wrinkle ridge growth in Coprates. Wrinkle ridges are stippled. Deformation inset (a) preceeded deformation (b). Viking orbiter images 610A27, A44.*

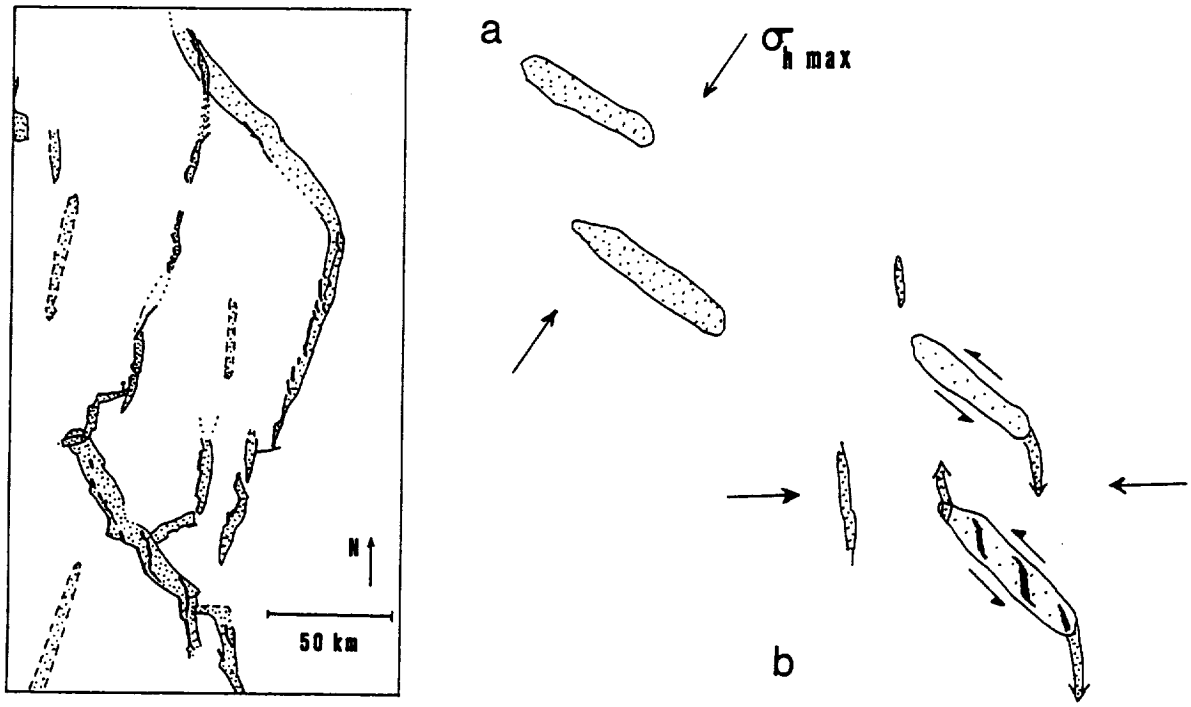


*Fig. 2. Northeast trending regional set of wrinkle ridges are superimposed on northwest trending ridges. Insets show inferred time variation of associated stress states. Viking image 608A51.*

**GEOLOGY, STRUCTURE, AND STATISTICS OF MULTI-RING BASINS ON MARS.** *Richard A. Schultz and Herbert V. Frey, NASA Goddard Space Flight Center, Greenbelt, MD 20771.*

Multi-ring basins define the fundamental tectonic framework upon which subsequent geologic and geophysical processes of many planets and satellites are superimposed. For example, most volcanic and tectonic activity on the Moon was localized by pre-existing impact basins [1]. Control of volcanism, tectonics, erosion, and perhaps even volatile dynamics on Mars by multi-ring basins can be discerned in many areas [2] even though endogenic processes were quite vigorous over the planet's history. On the other hand, the family of impacting objects that produced these basins is probably related to planetary accretion [3], and size-frequency characteristics of impactor populations can be estimated given an accurate inventory of impact craters and basins [4]. Thus the record of multi-ring basins on Mars provides a fundamental link between the planet's accretion and its later development.

We have compiled and evaluated available data on martian multi-ring basins [5] using the new 1:15 milion scale geologic maps of Mars [6] and revised global topography [7] as base maps. Published center coordinates and ring diameters of martian basins were plotted by computer and superimposed onto the base maps. In many cases we had to adjust basin centers or ring diameters or both to achieve a better fit to the revised maps. We also found that additional basins can explain subcircular topographic lows as well as map patterns of old Noachian materials, volcanic plains units, and channels in the Tharsis region [8].

Smaller impact basins on Mars such as Ladon (D = 975 km) are comparable dimensionally, morphologically, and structurally to Orientale (D = 930 km) on the Moon. In contrast, Orientale-type morphology can be recognized only for martian basins smaller than Argyre (D = 1850 km). Larger basins such as Isidis, Argyre, and Hellas typically show a rugged, blocky annulus with concentric grabens surrounding a central depression. Still larger structures show either multiple rings reminiscent of Valhalla on Callisto (Chryse) or persistent depressions surrounded by poorly expressed concentric structure (Elysium [9], Utopia [10]). Basin relief relative to diameter becomes progressively shallower with increasing basin diameter. Thus, the morphology and structure of martian multi-ring basins changes significantly as basins increase in size.

The formation of concentric ring structure and post-impact viscous relaxation of basin topography can differ for spherical, rather than planar, targets [11,12]. Diameters of martian multi-ring basins can be significant fractions of Mars' radius. For example, ratios of basin diameter to planetary radius are: Elysium, 1.46; Utopia, 1.39; Chryse, 1.06; Hellas, 0.68; Argyre, 0.55; and Ladon, 0.29. The value for Argyre is comparable to that of Orientale normalized by lunar radius, 0.53, or Caloris on Mercury, 0.53. Because Argyre, Orientale, and Caloris have similar normalized diameters but different morphologies, planetary curvature by itself probably did not control the morphology of these moderate sized basins. Structures larger than Chryse may have been influenced by spherical target geometry.

R-plots of basin diameters (Fig. 1) show that the martian multi-ring basin population dovetails into the smaller crater population [13] near 500 km diameter. The relative abundance of basins >1000 km in diameter is comparable on Mars and the Moon, perhaps suggesting an inner solar system source for the larger impactors [e.g., [4]). R-plots and weighted least squares fit to cumulative frequency data (Fig. 2) both indicate that basins follow a shallow production function. Basins 500 to 1500 km in diameter show the characteristic Orientale morphology and a best-fit slope of $D^{-0.75}$. Basins larger than Argyre define a $D^{-1.7}$ slope. The slope change may in part reflect the size-frequency population of the largest impactors. Formation of large multi-ring basins on early Mars may be more analogous mechanically to impacts on icy satellites (e.g., [14,11]) than to late forming lunar basins. Thus, Orientale morphology may not scale linearly to the largest diameters on Mars.

**REFERENCES**: [1] Solomon & Head (1980) *Rev. Geophys., 18*, 107-141. [2] Schultz, Schultz, & Rogers (1982) *JGR, 87*, 9803-9820. [3] Wetherill (1977) *Proc. Lunar Sci. Conf., 8th*, 1-16; Wetherill (1981) in Multi-ring Basins, *Proc. Lunar Planet. Sci. 12A*, 1-18. [4] Strom (1987) *Icarus, 70*, 517-535. [5] R. Schultz & Frey (1989) *JGR*, submitted. [6] Scott & Tanaka (1986) USGS *Map I- 1802-A*; Greeley & Guest (1987) USGS *Map I-1802-B*; Tanaka & Scott (1987) USGS *Map I-1802-C*. [7] Wu et al. (1986) PGPI-1985, NASA TM-88383, 614-617. [8] Frey & Schultz (1989) 4th Mars Conf., 106-107. [9] P. Schultz (1984) Lunar Planet. Sci., XV, 728-729. [10] McGill (1989) *JGR, 94*, 2753-2759. [11] Melosh (1982) *JGR, 87*, 1880-1890. [12] Thomas & Squyres (1988) *JGR, 93*, 14,919-14,932. [13] Barlow (1988) *Icarus, 75*, 285-305. [14] McKinnon & Melosh (1980) *Icarus, 44*, 454- 471.

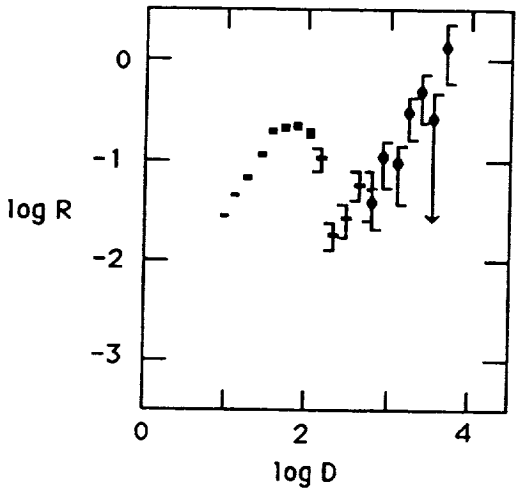


*Fig. 1. Relative frequency (R-plot) diagrams of martian craters and basins. Data for basins < 500 km in diameter from Barlow [1988].*

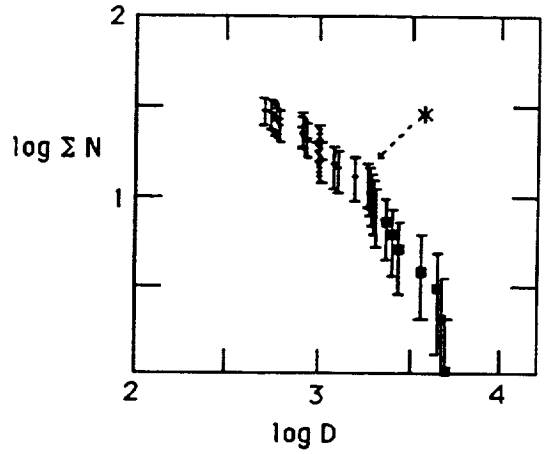


*Fig. 2. Cumulative frequency distribution of martian multi-ring basins > 500 km in diameter (unbinned data). Data normalized by surface area of Mars. Basins > 2300 km in diameter shown by dots; Argyre shown by *.*

EVIDENCE FOR MULTIPLE FLOODING EPISODES IN KASEI VALLES, MARS;
D.H. Scott and James M. Dohm, U.S. Geological Survey, Flagstaff, AZ 86001.

Kasei Valles make up one of the largest systems of outflow channels on Mars. They were a major contributor of water into the Chryse basin during the Late Hesperian and possibly Early Amazonian Epochs. The walls and floors of the valleys are terraced and grooved, closely resembling the Channeled Scablands of eastern Washington State that were formed by catastrophic floods probably lasting no more than a few days [1,2]. Previous geologic mapping [3] of parts of Kasei Valles was not conclusive as to whether water levels varied markedly during a single flood and erosional event or whether flooding was episodic and marked by intermittent periods of scouring. This problem--whether one or several flood episodes occurred within individual water courses--has been a continuing issue in studies of Martian channel formation [4]. Recent large-scale geologic mapping [5] of Mangala Valles, another large outflow channel system in the Memnonia region of Mars, shows deposits of two periods of flooding, which are separated stratigraphically by an intervening lava flow. In other areas around the Chryse basin, geologic studies, e.g., [4] have indicated that more than one episode of channel formation occurred or, less likely, that flooding was of very long duration.

Our present mapping of flood-deposited materials in Kasei Valles on high-resolution photomosaic bases (1:500,000 scale) shows cross-cutting flow and scour lines along water courses that may indicate separate flood events (Fig. 1); more definitively, morphologies of craters clearly distinguish them as having formed before, between, and after separate flood stages (Figs. 2-3). Counts of craters (≥2-km rim-crest diameter) made on smooth and grooved parts of the Kasei floor also indicate floods of at least two different ages: $253\pm96/10^6$ km$^2$ (Early Amazonian) and $910\pm148/10^6$ km$^2$ (intermediate Hesperian); previous crater counts in Kasei Valles [6,7], though less directed toward specific events, generally confirm our results.

REFERENCES

[1] Baker, V.R. and D.J. Milton (1974) Icarus 23, 27-41.
[2] Baker, V.R. and R.C. Kochel (1979) Jour. Geophys. Res. 84, 7961-7983.
[3] Chapman, M.G. and D.H. Scott (1989) Proc. 19th Lunar and Planet. Sci. Conf., 367-375.
[4] Greeley, R., E. Theilig, J.E. Guest, M.H. Carr, Harold Masursky, and J.A. Cutts (1977) Jour. Geophys. Res. 82, 4093-4109.
[5] Tanaka, K. and Chapman, M.G. (1990) Jour. Geophys. Res., in press.
[6] Carr, M.H. and G.D. Clow (1981) Icarus 48, 91-117.
[7] Neukum, G. and K. Hiller (1981) Jour. Geophys. Res. 86, 3097-3121.

KASEI VALLES REGION FLOOD FEATURES

Figure 1. Scoured and grooved channel floor; arrows show three directions of water flow possibly indicative of separate flood events (Viking image 226A10, centered near lat 25° N., long 61°).

Figure 2. Impact crater in channel; crater was formed before and degraded by early catastrophic flooding that scoured channel floor (Viking image 664A07, centered near lat 23° N., long 74°).

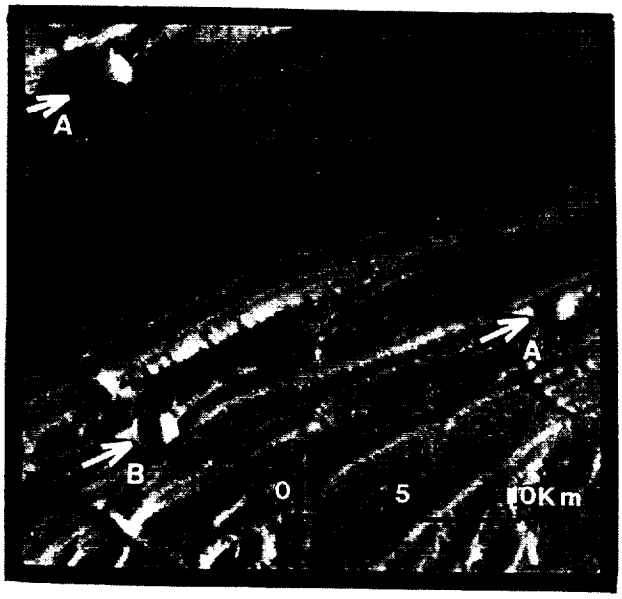


Figure 3. Impact craters (arrows at A) formed after early high-water stage that deeply eroded terraces; craters have been truncated by later floods along lower part of valley floor. A post-flood crater is shown at B (Viking image 665A20, centered near lat 27° N., long 68°).

MOTTLED TERRAIN: A CONTINUING MARTIAN ENIGMA; D.H. Scott and J.R. Underwood, (1) U.S. Geological Survey, Flagstaff, Ariz. and (2) Kansas State University, Manhattan, Kansas

The northern lowlands of Mars are largely covered by plains materials that overall are mottled light and dark, a characteristic that is apparent on both Mariner and Viking images. The mottled terrain material (1) that makes up most of the northern lowlands is probably the most ambiguous material on all Martian images (2). Early studies, e.g., (3), used Mariner 9 images, which showed a hummocky, mottled surface encircling the planet between about lat 50° and 70° N. The Mariner pictures were degraded in this zone by atmospheric haze and high sun angles, which blurred them and produced high albedo contrasts; because significant morphologic variations were not recognized, the entire region was mapped as mottled plains material, a single geologic unit. Although image quality was poor, the mottling of the plains could be seen to result from albedo contrasts between numerous bright crater-ejecta blankets and dark intercrater plains material; also contributing to this effect were many dark-crested knobs, some having long, narrow, bright windstreaks or summit craters with bright interiors. The mottled plains were variously interpreted to consist of lava flows and knobby remnants of the highlands to the south (3), eolian and volcanic materials (4,5,6), ancient terrain and pedestal craters exhumed by wind erosion (7), eolian material cemented by permafrost (8), or volatile-rich deposits (9).

Debris mantles, suggested by (1) to have been derived from polar deposits, are distributed more or less symmetrically around the poles, extending as far as 30° toward the equator. These authors further suggested that the northern hemispheric mantle blankets the mottled plains and masks small (≤10-km diameter) craters on both young and old terrains.

I have described several geologic problems in the Martian northern plains, including that of the origin of the mottled material (2); I suggested that the plains "... may be an eroded remnant of the highlands that have survived a tectonic period of crustal separation caused by drifting or downfaulting followed by erosion."

The presence of lobate debris aprons, concentric crater fill, and terrain-softening poleward of lat 30° N. and S. suggested to (10) that topography in these regions has relaxed through quasi-viscous flow in ice-rich surface and near-surface materials. Support for this idea was provided by theoretical studies (11), which showed that ground ice should be present on Mars at middle and high latitudes. Dial (12) thought that permafrost and highly altered volcanic materials form the mottled plains.

Recent global geologic mapping of Mars (13,14,15), using high-resolution and high-quality Viking images, has subdivided the mottled terrain as originally mapped (3) into four members that constitute the Vastitas Borealis Formation of Late Hesperian age. The members intergrade and are largely distinguished by secondary morphologic characteristics, such as pronounced albedo contrasts, whorled patterns of ridges, knobby hills, and irregular troughs having polygonal outlines in places. Although the formation has been postulated to consist of lava flows, fluvial

deposits, and eolian materials within a permafrost zone (13), its surface is highly degraded, and the composition and origin of its component members remain uncertain.

Mapping problems still exist where image quality and resolution are adequate to determine textural characteristics of individual units but do not reveal the nature of their boundaries, stratigraphic relations, modes of formation, and processes responsible for their characteristic morphologies. The mottled plains material, as originally mapped and recently subdivided into members of the Vastitas Borealis Formation, continues to remain the most enigmatic geologic material in the northern hemisphere of Mars. Clarification of the origin of the mottled plains is critical, because this large, low, comparatively flat and unobstructed region may well provide the most suitable locations for successful landing and sample-return missions on Mars.

REFERENCES

(1) Soderblom, L. A., J. J. Kreidler, and H. Masursky (1973) J. Geophys. Res., 78, 4117-4122.
(2) Scott, D. H. (1979) Proc. Lunar Planet. Sci. Conf. 10, 3039-3054.
(3) Scott, D. H., and M. H. Carr (1978) U.S. Geol. Surv. Misc. Inv. Ser. Map I-1083.
(4) Greeley, R., and J. E. Guest (1978) U.S. Geol. Surv. Misc. Inv. Ser. Map I-1038.
(5) Lucchitta, B. K. (1978) U.S. Geol. Surv. Misc. Inv. Ser. Map I-1065.
(6) Morris, E. C., and K. A. Howard (1981) U.S. Geol. Surv. Misc. Inv. Ser. Map I-1286.
(7) Underwood, J. R., Jr., and N. J. Trask (1978) U.S. Geol. Surv. Misc. Inv. Ser. Map I-1048.
(8) Elston, W. E. (1979) U.S. Geol. Surv. Misc. Inv. Ser. Map I-1140.
(9) Wise, D. U. (1979) U.S. Geol. Surv. Misc. Inv. Ser. Map I-1154.
(10) Squyres, S. W., and M. H. Carr (1986) Science, 231, 249-252.
(11) Fanale, F. P., J. R. Salvail, A. P. Zent, and S. E. Postawko (1986) Icarus, 67, 1-18.
(12) Dial, A. (1984) U.S. Geol. Surv. Misc. Inv. Ser. Map I-1640.
(13) Scott, D. H., and K. L. Tanaka (1986) U.S. Geol. Surv. Misc. Inv. Ser. Map I-1802-A.
(14) Greeley, R., and J. E. Guest (1987) U.S. Geol. Surv. Misc. Inv. Ser. Map I-1802-B.
(15) Tanaka, K. L., and D. H. Scott (1987) U.S. Geol. Surv. Misc. Inv. Ser. Map I-1802-C.

THE RELATION OF THE LAVA COMPLEXES OF THE OLYMPUS MONS ON MARS. I.V. Shalimov, Moscow State University, Moscow, USSR.

The geological map of western equatorial region of Mars by David H.Scott and Kanneth L.Tannaka[I]shows the older ade of the shield lava complex of the Olympus Mons then the plain one. This conclusion is based on the crater density analysis. The detailed geolodical mapping gives us the possibility to obtain the contrary interpretation.

On the northeastern periphery of the shield complex one can observe the plain lava complex, partialy flooding the broken relief of the Olympus Mons aureole. Lavas from the shield complex overly the plain one and flood completely the broken relief of aureole(fig.2[2]). In the southeast one can observe lavas from the plain complex, flooding the Olympus Mons scarp. Lavas from the shield complex flow down from the scarp and form the flows on the surface of the plain complex(fig.3 [3]). In the southwest one can observe the shield lava complex overlying the plain one. In this case plain lavas flooding the depressions of the Olympus Mons aureole relief are isolated from their main area(fig.4[4]).

In addition along the all contact line one can observe the identity of lava flow directions in two complexes. It is known on the orientation of lava flow lobes. If the shield complex is older one should observe another ratio.

This consideration leads to the conclusion that the crater date analysis can give some incorrect results if it is applied to the small surface area. In this case it is necessary to preper the visual investigations and the detailed mapping been more objective analysis.

REFERENCES:

I.D.Scott and K.Tannaka Geology, western equatorial region of Mars. U.S. Geol. Surv. I986 I:I5000000, mapI-I802-A.
2.Atlas of Mars, topografic series, I:2000000: Tharsis northwest, M 2M 22/I24 CM I985,I-I62I /MC-9NW:revised/.
3.Atlas ofMars, ibid; Tharsis southwest, M 2M 7/I24 CM I985, I-I622 /MC-9SW:revised/.
4.Atlas of Mars, ibid;Amasonis southeast, M 2M 7/I46 CM I98I, I-I33I /MC-8SE/.

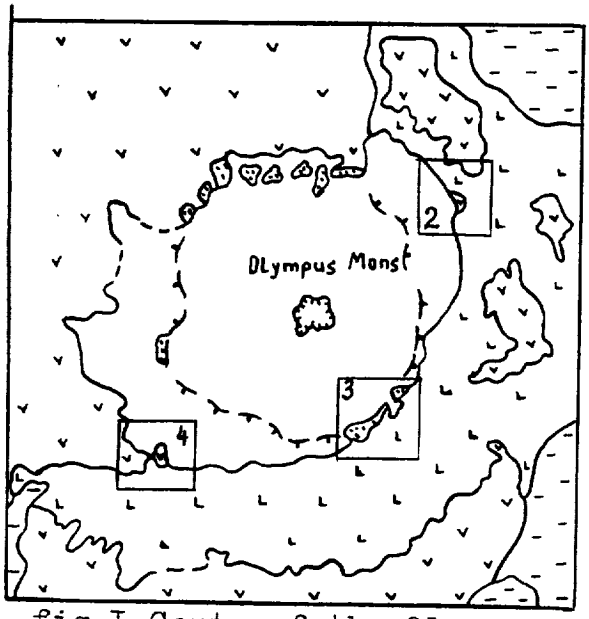


fig.I Centr of the Olympus Mons. The places of fig.2,3,4.

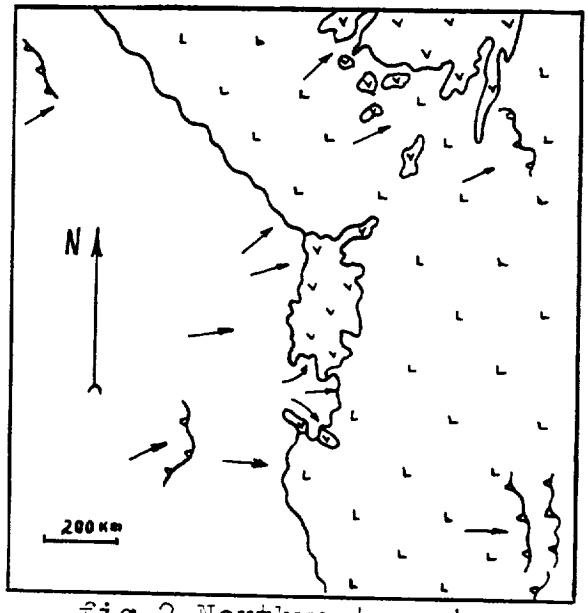


fig.2 Northwest part.

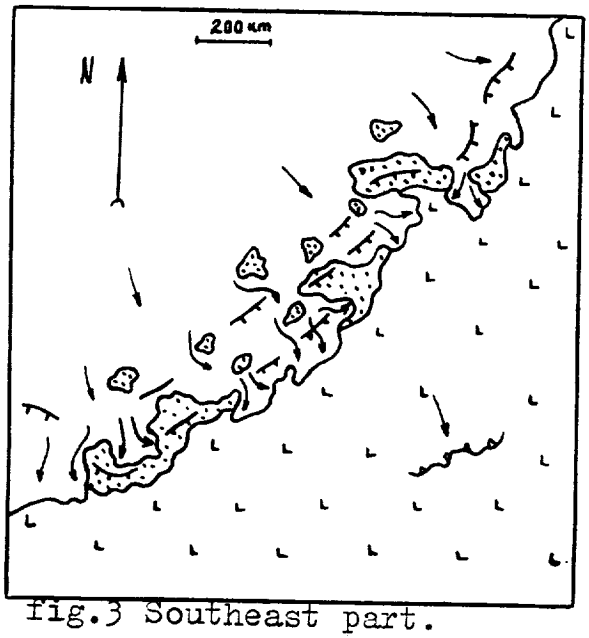


fig.3 Southeast part.

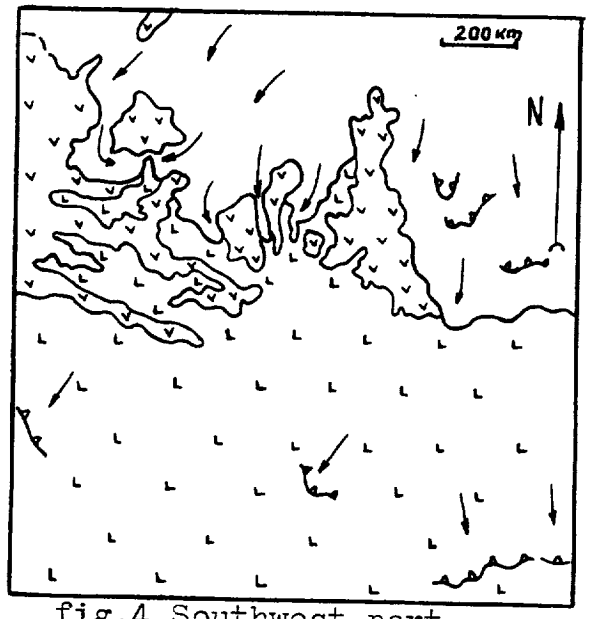


fig.4 Southwest part.


I-shield complex, 2-plains complex, 3-aureole complexes, 4-socle of Olympus Mons, 5-otherwise rocks, 6-direction of flow, 7-lobe of lava flow, 8-scarp of Olympus Mons, 9-caldera.

## VISIBLE AND NEAR-IR SPECTRAL IMAGING OF MARS DURING THE 1988 OPPOSITION.

Robert B. Singer, Jeffrey S. Miller, Kent W. Wells, and Ellen S. Bus, *Planetary Image Research Laboratory, Planetary Sciences Dept., University of Arizona, Tucson AZ 85721*

We conducted a major program of spectral imaging of Mars in the visible and near-IR (0.44-1.05$\mu$m) centered around the excellent 1988 opposition. The objective was to produce detailed reflectance spectra for contiguous, spatially resolved surface elements covering most of the planet. In this abstract we present some initial results from these observations.

A total of 6 observing runs, of 3-4 days duration each, were conducted on the University of Arizona's 1.5m telescope on Mt. Bigelow. Nearly all of Mars south of 40°N was observed at least once. Instrumentation consisted of the LPL Echelle Spectrograph (D. Hunten) and the LPL CCD system (U. Fink). A prism in the spectrograph gave spectral resolution of 2nm in the blue and 10nm in the near-IR. The best-case spatial resolution is 250km by 150km per pixel. Careful standard star observations were made to facilitate accurate spectrophotometric calibrations. Differential refraction in the Earth's atmosphere was also properly accommodated for. A photographic record of the slit position on Mars was made for every CCD exposure to allow the locations of our observations to be calculated accurately. These spectral images will eventually be calibrated to radiance factor ($R_F$) [1] through the solar analog star 16 Cyg B. The data presented here are calibrated in a relative sense to solar analog star HD1835: the zero reflectance level is accurately known, and the relative signal level from all observed areas is correct. At present these data have some narrow residual atmospheric and stellar spectral features which will be removed as the calibrations are refined.

Figure 1 shows a range of spectral and albedo types observed for a number of regions on Mars. As expected, the steep visible slope is relatively smooth, in contrast to ferric-oxide minerals with long-range crystalline structure. However, definite slope changes are visible near 0.53$\mu$m and 0.63$\mu$m, related to incipient ferric-iron crystal-field absorptions. These features indicate a slightly greater degree of crystallinity for the common weathered soil on Mars than seen for the least-crystalline Hawaiian palagonites. The low-albedo region Margaritifer Sinus has a well-developed $Fe^{2+}$ band with a minimum near 0.95$\mu$m, indicating low-Ca, high-Fe clinopyroxene [2]. Slightly different pyroxene band depth and position are seen for Meridiani Sinus in Figure 4. Spectral differences related to $Fe^{3+}$ mineralogy and/or crystallinity are seen in the other figures. The Acidalium spectrum in Figure 2 is less absorbing in the visible than a typical dark region (Margaritifer) but more highly absorbing at longer wavelengths. We interpret these spectral differences as indicating a somewhat more-crystalline ferric oxide at this location on the planet [e.g. 3]. In Figure 3 spectra for Margaritifer Sinus and a region at the southern extreme of Acidalium overlay very well except at wavelengths between roughly 0.8 and 0.9$\mu$m. Such a difference is best explained by variation in a *different* $Fe^{3+}$ crystal-field absorption as seen in the previous example.

These new results, as well as those of others [4], are refining our knowledge of Mars surface composition on a local to regional scale. Greater variation has been observed, related to differing compositions and processes. It should be noted, however, that most of the spectral differences we have seen so far are relatively subtle. Typical high-albedo regions such as Arabia still indicate limited long-range $Fe^{3+}$ crystalline structure in the common weathered soils and dust.

[1] Hapke, B. (1981) **JGR**, **86**, 3039.
[2] Adams, J.B. (1974) **JGR**, **79**, 4329.
[3] Singer, R.B. (1982) **JGR**, **87**, 10159; Sherman, D. *et al.* (1982) **JGR**, **87**, 10169.
[4] Bell, J.F. III *et al.* (1990) **JGR**, in press.

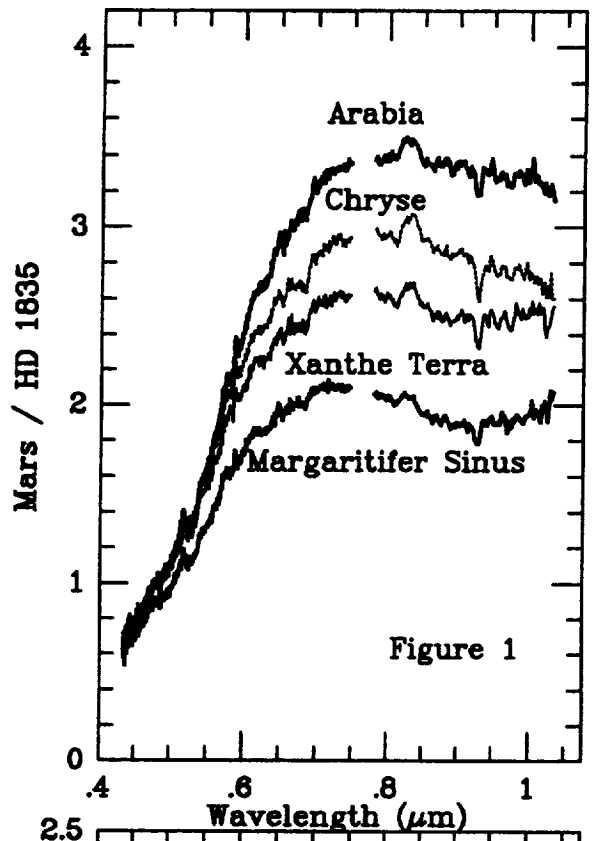
Arabia
Chryse
Xanthe Terra
Margaritifer Sinus
Mars / HD 1835
Wavelength (μm)
Figure 1

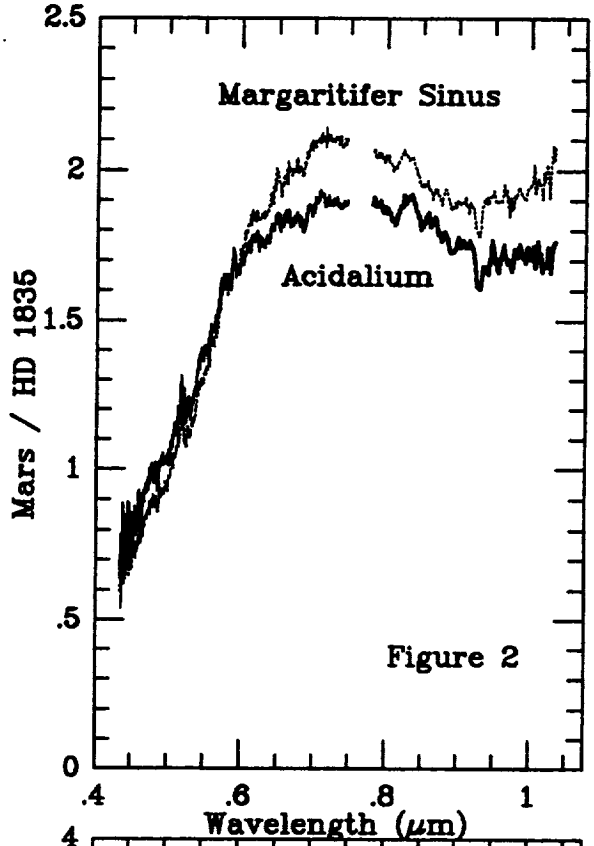
Margaritifer Sinus
Acidalium
Mars / HD 1835
Wavelength (μm)
Figure 2

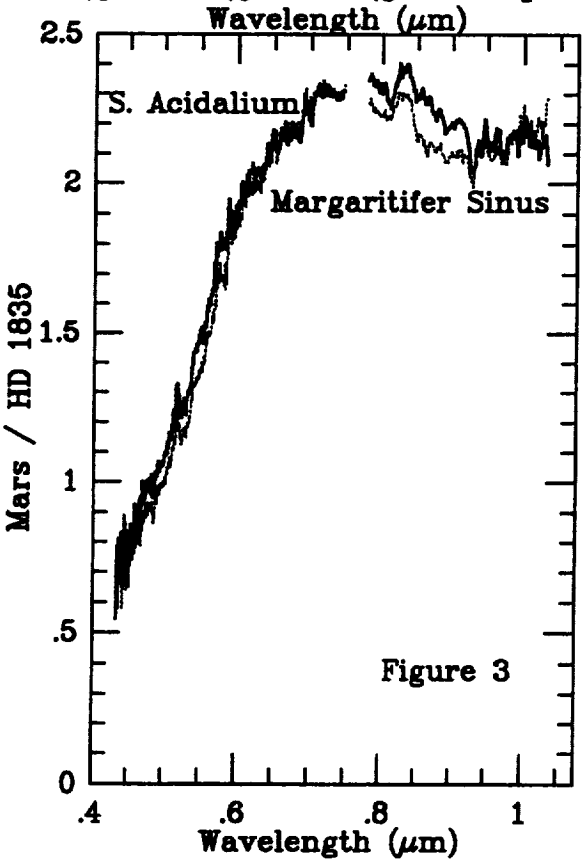
S. Acidalium
Margaritifer Sinus
Mars / HD 1835
Wavelength (μm)
Figure 3

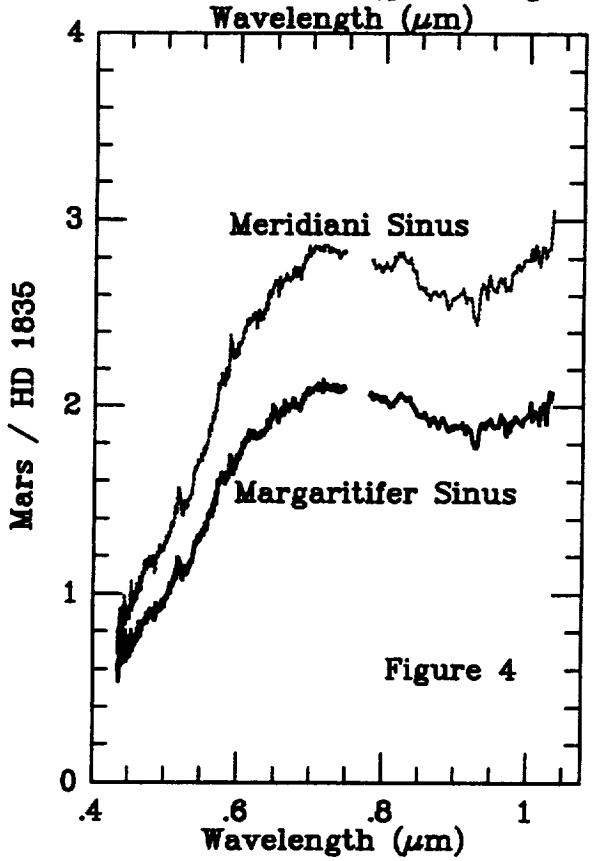
Meridiani Sinus
Margaritifer Sinus
Mars / HD 1835
Wavelength (μm)
Figure 4

DRY CARBONATE FORMATION ON MARS: A PLAUSIBLE SINK FOR AN EARLY DENSE $CO_2$ ATMOSPHERE? Stuart K. Stephens and David J. Stevenson, Division of Geological and Planetary Sciences, California Institute of Technology, Pasadena, CA 91125.

The Problem. Morphological features on the present surface of Mars suggest to many observers [1-5] that Mars once had an atmosphere with a pressure greater than the ~1 bar thought to be required for an atmospheric greenhouse. Pollack et al. (1987) [4], among others, have discussed models of carbonate formation and recycling to buffer the early $CO_2$ pressure in such an atmosphere. However, since carbonate formation is usually assumed to require standing liquid water at the surface, there is a problem with such carbonate cycles, in that the transition from a greenhouse atmosphere to a pressure of a few millibars (too cold for liquid water) would seem to require an additional mechanism for reducing the atmospheric pressure.

Alternative sinks for the early atmosphere (to bring the pressure below ~1 bar) include impact erosion of the atmosphere [6] and adsorption in the regolith [7]. However, impact erosion would have been most important before the end of the late heavy bombardment (3.8 Gyr); thus, its dominant effect may have preceded a greenhouse atmosphere which lasted until later. Also, adsorption in the regolith is thought to be only marginally capable of storing 1 bar of $CO_2$, and this is a sink that would necessarily have been filled -- and therefore unavailable for further use -- during the time of greenhouse conditions.

This work investigates another alternative sink for an early dense $CO_2$ atmosphere on Mars: dry carbonate formation.

Booth and Kieffer's Experiment. An experiment performed by Booth and Kieffer (1978) [8] seemed to demonstrate that carbonate will form on silicate grains under Martian conditions in the absence of liquid water. Their result was $10^{12-13}$ molecules of carbonate evolved per $cm^3$ per second -- yielding much less than a monolayer of carbonate on ~40 μm grains in the span of several days. The authors show that this reaction rate more than accounts (by several orders of magnitude) for a $CO_2$ inventory of 1 bar over geologic time. However, their study had a major limitation, namely that there is no reliable basis for extrapolation, since less than a monolayer was formed, and the nature of the "rind" formed was not closely examined.

We attempted to find published results where the carbonate formed by $CO_2$ interaction with silicates in the absence of water was actually examined (e.g., with a scanning electron microscope), but without success. Unfortunately, a precise theoretical approach holds little promise either, since the exact nature of any rind formed on a substrate of uncertain character (glass vs. crystals? mono- vs. polyminerallic?) is poorly constrained a priori.

Present Theoretical Work. In the absence of experimental results, then, we considered the worst case -- that in which the formation of a rind limits the effectiveness of the rapid reaction reported by Booth and Kieffer. Namely, we considered the question: Is the process (of dry carbonate formation) reaction-limited or diffusion-limited? This involves comparing: (1) the thickness of the reaction layer formed, assuming infinite diffusivity, with (2) the thickness of the product layer formed (which is a multiple of the diffusion distance $(Dt)^{1/2}$ -- see 2 paragraphs below), assuming infinite reactivity. The result is that the diffusion-limited case requires the diffusivity D to be $< 10^{-9}$ $cm^2$ $s^{-1}$.

Next, the diffusivity of $CO_2$ through carbonate was required. Again, no directly pertinent experimental reports were found in the literature, so we used results of Bhatia and Perlmutter (1983) [9] for diffusion of $CO_2$ through

carbonate formed on lime (CaO). Their experiments were performed at high temperature (> 600 K) and must be extrapolated (using an Arrhenius relation) to low temperature, but this probably results in a conservative (i.e., low) estimate of the diffusivity since diffusion mechanisms other than the one fitted by their data probably operate in the low-temperature regime (i.e., mechanisms with smaller activation energies, thus giving higher diffusivities upon extrapolation). The extrapolated diffusivity is $D \sim 10^{-27}$ $cm^2$ $s^{-1}$, implying a diffusion-limited reaction.

The amount of carbonate formed in such a diffusion-limited case is determined by consideration of tarnishing reactions [10,11], for which the thickness of product formed on a solid by a gas reacting with it is given by a relation involving the densities of gas ($CO_2$) and product (carbonate) -- it reduces to $\ell(t) \sim 0.06\ (Dt)^{1/2}$.

Results. Over geologic time, this diffusion-limited dry carbonate formation is capable of forming a layer ~60 Å thick on silicate grains. For a 1 km regolith and 40 μm particles, this means that ~0.05 bar $CO_2$ can be stored. This is a conservative estimate, since: (1) D is probably higher, and (2) we've assumed that the rind is non-porous. Note, however, that our estimate of the diffusivity places us eighteen orders of magnitude on the diffusion-limited side of the inequality. Even if this estimate is wrong by many orders of magnitude, it implies that the Booth and Kieffer results are irrelevant, because we are in the diffusion-limited regime.

Discussion. The possibility that a significant amount of $CO_2$ can be stored by dry carbonate formation on early Mars has implications for the evolution of atmospheric $CO_2$ pressure after bodies of liquid water were no longer available for aqueous carbonate formation. However, whether the $CO_2$ pressure would have declined gradually or very quickly depends on the precise behavior of the diffusivity, which is a function of temperature and therefore time. The answer awaits further work.

Note that if the carbonate is indeed produced in thin (<< μm) layers, as described above, then it may not be readily observable by current remote sensing techniques. Thus, the proposed $CO_2$ storage mechanism cannot be said to be inconsistent with the latest near-infrared telescopic observations [12] which do not reliably detect carbonate.

Conclusions. Thus, we have used assumptions concerning the validity of published experimental work, and conservative estimates of parameters and mechanisms, to arrive at the result: Dry carbonate formation is almost certainly diffusion-limited and the results of Booth and Kieffer are irrelevant. Even with a very low diffusivity, the tarnishing process may provide a significant sink for atmospheric $CO_2$ on early Mars. It may therefore help explain the transition from an early dense atmosphere to the present low pressure.

References. [1] J.C. Walker (1978). In Comparative Planetology, C. Ponnamperuma, ed. Academic Press, New York. [2] J.B. Pollack (1979), Icarus, 37, 479-553. [3] R. Kahn (1985), Icarus, 62, 175-190. [4] J.B. Pollack et al. (1987), Icarus, 71, 203-224. [5] C.P. McKay and C.R. Stoker (1989), Rev. Geophys., 27(2), 189-214. [6] H.J. Melosh and A.M. Vickery (1989), Nature, 338, 487-489. [7] F.P. Fanale et al. (1982), Icarus, 50, 381-407. [8] M.C. Booth and H.H. Kieffer (1978), J. Geophys. Res., 83, 1809-1815. [9] S.K. Bhatia and D.D. Perlmutter (1983), AIChE J., 29(1), 79-86. [10] F. Booth (1948), Trans. Faraday Soc., 44, 796-801. [11] J. Crank (1956). The Mathematics of Diffusion. Clarendon Press, Oxford. [12] D.L. Blaney and T.B. McCord (1989), J. Geophys. Res., 94, 10159-10166.

WHY EXISTING TERRESTRIAL PLANET THERMAL HISTORY CALCULATIONS SHOULD NOT BE BELIEVED (AND WHAT TO DO ABOUT IT); David J. Stevenson and Seth S. Bittker, 170–25, Caltech, Pasadena, CA 91125.

*Introduction.* Beginning in the late 1970's, many workers have used simple parameterized convection recipes for analyzing the thermal history of a terrestrial planet [1–3]. These calculations assume that thermally derived density differences are the only important contribution to convective instability. However, all planets undergo irreversible differentiation and the resulting density effects are locally far larger than thermal effects. This is not a novel observation, but the past response has usually been that the total gravitational energy release which accompanies irreversible differentiation is smaller than that associated with thermal convection and hence energetically less important. Although the latter statement is true (excluding core formation which is believed to be completed very early in all cases [4]), it does not get to the heart of the issue, which is this: This correct parameterization of convection requires a *boundary layer* analysis and it is precisely in this layer where compositional effects can be large because of partial melting. Since the residue left from partial melting is generally less dense than the undepleted mantle below (mainly because the melt is relatively Fe-rich), volcanism can *stabilize* the convective system and even shut the convection off, at least temporarily. This is an especially serious effect on one-plate planets because the lithosphere is not fully participating in the return flow.

*Background and Input.* Compositional effects associated with basaltic production play a role in the subductability of the Earth's oceanic lithosphere [5], the dynamics of matrix flow and melt migration beneath mid-ocean ridges [6] and in the mantle wedge above subduction zones [7], and in the global contraction or expansion of a planet [8]. We can identify the following regimes of interest:

I. The convective temperature profile (conductive lid and adiabatic interior) never intercepts the mantle solidus. Conventional parameterized recipes will then apply; however, this is an uninteresting case, even in smaller planets, since one plate planets usually "run hot" (because one plate planets are less efficient in eliminating heat) and do not lie in this regime, except when all the basaltic component has been flushed out.

II. Adiabat extends into the supersolidus region, though only to a small extent and not so as to deplete all basalt from the material in that region. Here, we can modify the "local" Rayleigh number and devise the following computational scheme, analogous to those used in the past for purely thermal buoyancy (e.g., ref. 3). We set $F = k\Delta T/\delta$, $Ra \equiv g(\alpha\Delta T - \beta f)\delta^3/\nu(T - \Delta T/2)\kappa$, $d(Ra)/d\delta = 0$, and $Ra = 10^3$ at this extremum. Parameters have their usual meanings (F = heat flow, k = thermal conductivity, g = gravity, $\alpha$ = coefficient of thermal expansion, $\delta$ = boundary layer thickness, $\nu$ = temperature-dependent viscosity, $\kappa$ = thermal diffusivity, $\Delta T$ = temperature drop across the boundary layer) and the crucial change is the $\beta f$ term representing the density effect arising from a degree of melting f, averaged within the boundary layer. The value of $\beta$ is a material property that will vary among planets (see below), and allowance must also be made for the *fertility*: the extent to which the mantle still has the "primordial" basaltic (i.e., pyroxene-rich) component.

III. Large excursion of the adiabat into the supersolidus region. In this case, a secondary convection pattern can initiate within the zone of partial melting since all of this zone is denuded of basalt but has an unstable temperature gradient. This convection will *not* penetrate into the deeper mantle, which is intrinsically more dense (more iron-rich). The analysis so far has, however, ignored phase boundaries which will surely complicate these considerations.

*Applications.* We have done a detailed analysis of regime II, and made some analysis of the implications for Mars. In the Figure, we show total heat flux vs. mantle temperature for a variety of values of $\beta$. (Ignore the flat curve at $T < 1600$ K which corresponds to pure conduction.) The smooth upward curvature at small $\beta$ corresponds to the usual expectation

that heat flow increases dramatically with increasing "mantle temperature" (here defined as the zero pressure extrapolation of the mantle adiabat). But at sufficiently large $\beta$ ($\geq$0.04), we find a turnover in the curves, reflecting the increasing stabilization of convection. What is a reasonable value for $\beta$? On Mars, where most estimates of mantle iron content are high, the implication of the work of Finnerty *et al.* [9], for example, is $\beta \approx 0.1$, very large and easily enough to have an *enormous* effect on the convection. The result is that the mantle heats up, enters regime III, and begins to form convective *layers*. The value of $\beta$ on Earth, Venus, and possibly Mercury is smaller by a factor of about 2, but still big enough to be very important. (Remember, however, that the model is not meant to apply to Earth.)

*Implications.* Although detailed models of the resulting thermal evolution have not been completed (they are much harder than previous simple models), it is clear that they will be markedly different from previous work. Here are the main differences: (1) A tendency for the interior to *heat up* at depth even in early history, because volcanism stifles convection. This is in contrast to the trend toward monotonic cooling models and volcanism histories [e.g., 10]. (2) A tendency for episodes of volcanism, separated by long periods of time associated with the merging of convecting layers operating in regime III. (3) Delayed heat loss and the likelihood of continued volcanism on Mars.

## References


1. Schubert, G., Cassen, P., and Young, R.E. (1979). *Icarus* **38**, 192.
2. Stevenson, D.J., Spohn, T., and Schubert, G. (1983). *Icarus* **54**, 466.
3. Solomatov, V.S., Leontjev, V.V., and Zharkov, V.N. (1987). *Gerlands Beitr. Geophysik* **96**, 73.
4. Stevenson, D.J. (1990). In *Origin of the Earth*, in press.
5. Oxburgh, E.R. and Parmentier, E.M. (1977). *J. Geol. Soc. London* **133**, 343.
6. Scott, D.R. and Stevenson, D.J. (1989). *J. Geophys. Res.* **94**, 2973.
7. Davies, J.H. and Stevenson, D.J. (1990). *J. Geophys. Res.*, submitted.
8. Kirk, R.L. and Stevenson, D.J. (1989). *J. Geophys. Res.* **94**, 12,133.
9. Finnerty, A.A., Phillips, R.J., and Banerdt, W.B. (1988). *J. Geophys. Res.* **93**, 10,225.
10. Schubert, G. *et al.* (1990). In *Mars*, Univ. Arizona Press, in press.


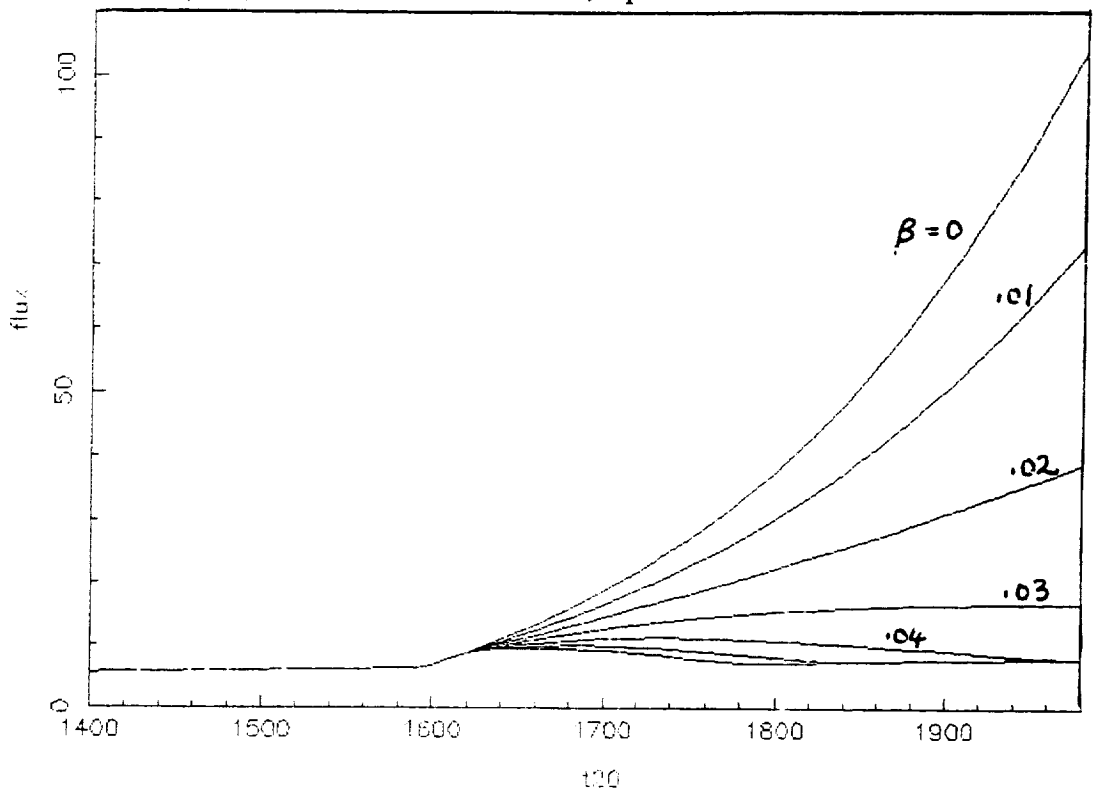

# FERROLYSIS OF IRON-BEARING MARTIAN BRINES: ORIGIN OF DUST-STORM PARTICULATES ON MARS

**D'Arcy W. Straub and Roger G. Burns**, Department of Earth, Atmospheric and Planetary Sciences, Massachusetts Institute of Technology, Cambridge, Massachusetts 02139.

**INTRODUCTION.** Brines have been proposed on Mars [1] to explain salt weathering erosional features [2], regions of high radar reflectivity [3,4], and the high concentrations of S and Cl in Viking Lander XRF measurements of the regolith [5]. These elements were interpreted to be present as chlorides and sulfates in evaporites [6] and gossans [7]. The formation of such evaporite and gossaniferous deposits implies that oxidative weathering reactions in an aqueous environment must have occurred sometime during the evolution of the martian surface. However, such water environments are not conspicuous on the surface of Mars now, except perhaps in the Solis Lacus region (14°-22°S; 84°-120°W) and other areas of comparable latitudes [8] having high radar reflectivities [3] from which local and global dust storms appear to originate [9,10]. Attention on possible martian brine compositions has focussed on eutectic temperatures of salt mixtures containing chlorides and sulfates of Na, K, Mg and Ca [1,4]. However, other dissolved cations must also be present in such brines, particularly ferric and ferrous iron, which are stabilized in aqueous solutions at relatively low values of pH (acidity) and Eh (redox potential) [7].

Ferrolysis, the process of oxidation of ferrous iron accompanied by the hydrolysis of ferric iron, is the ultimate fate of dissolved iron and is likely to occur during sublimation and melting of the permafrost on Mars [11], leading to the precipitation of iron phases which could be transported around the planet in dust storms. This has led to a study of residues formed during the oxidation and precipitation of iron phases from evaporated salt solutions. We report here preliminary results on the nature of ferrolysis products that might have been deposited from martian brines and be constituents of dust storms on Mars.

**EXPERIMENTAL PROCEDURES.** A number of mixed-salt solutions were prepared from sulfates and chlorides of Mg, K, and Na, to which were added ferrous sulfate. During the experiment, air was bubbled through the solutions to increase the rate of oxidation. In some cases, solutions were acidfied to stabilize ferric iron, or the pH was adjusted to produce a precipitate. Other solutions were allowed to evaporate at ambient temperatures. Precipitates from the solutions and products of evaporation were examined by Mossbauer spectroscopy to determine the formation of ferric iron and to identify the ferric hydrolysates. Measurements made at liquid helium temperature (4.2K) proved to be particularly useful for characterizing the nanophase precipitates.

**RESULTS.** For nearly every experiment performed, regardless of length, akaganéite (β-FeOOH) was at least one of the observed ferrolysis products. These results seem to violate formerly observed trends concerning ferric hydrolysis products. For brine compositions containing $SO_4$, goethite (α-FeOOH) or hematite ($\alpha$-$Fe_2O_3$), depending upon the $SO_4$ / Fe ratio, are the expected hydrolysis products [12]. Generally, β-FeOOH is expected in solutions where Cl or F is present [13]. In the presence of Na and K, jarosite [$(K,Na)Fe_3(SO_4)_2(OH)_6$] is another potential hydrolysis product [14].

Acidified solutions, where the $Fe^{3+}$ ion is stabilized, produced complex ferrolysis reactions when evaporation neared completion. Mossbauer spectra at 4.2K of several samples exhibited two magnetic sextets. In the case where Na was present in the brine, magnetic sextets correponding to β-FeOOH and jarosite were observed. Only one magnetic sextet, corresponding to β-FeOOH, was observed when K was present in the brine though.

The experiments performed to present indicate that in high ionic strength solutions, representative of the brines on Mars, the ferrolysis products on Mars may not be easily inferred. First, β-FeOOH appeared in most reactions, regardless of the compostion of the brine solution. Second, under the influence of evaporation, jarosite often appeared. Further studies are needed, however, to

determine if β-FeOOH is always a product in high ionic strength solutions and to better characterize the conditions under which jarosite is formed when evaporation occurs.

**ORIGIN OF DUST STORM PARTICULATES.** Experimental measurements described in an accompanying abstract **[15]** and geochemical models published elsewhere **[7,11,16]** suggest that acid weathering has been a significant surface process on Mars and that groundwater, now permafrost, may be acidic. Such low pH solutions dissolve significant concentrations of silica, Al, Mg, Fe, and other ionic species. They also hold in suspension considerable amounts of monodispersed sols of hydrous oxides and sulfates of Fe and Al **[11]**. These ions and sols are precursors to clay silicate, oxyhydroxide and hydroxo sulfate minerals which form as precipitates in response to changes of temperature, pH and salinity.

On the surface of Mars, volatilization of $H_2O$ during sublimation of permafrost or evaporation of the brine eutectic will induce the precipitation of dissolved salts of Na, Ca, Mg, $Fe^{2+}$, etc. and cause the flocculation of colloidal ferric-bearing aluminosilicate, oxide, oxyhydroxide and hydroxo sulfate phases. These nanophase materials may constitute the particulates of local and global dust storms when they are generated in the Solis Lacus and similar regions of low radar reflectivities on Mars. During aeolian transport, any unoxidized ferrous salts liberated from volatilized permafrost will be completely oxidized, while dessication of ferric hydrolysis products to $Fe_2O_3$ phases **[17]** will be facilitated. Such ferric oxides include the formation of maghemite from lepidocrocite **[18]** considered to be the magnetic phase on Mars **[19]**, as well as the occurrence of nanophase hematite believed to be present in bright regions of Mars **[20]**.

**REFERENCES.** **[1]** G.W.Brass, *Icarus*, 42, 20 (1980); **[2]** M.C.Malin, *JGR*, 79, 3888 (1974); **[3]** S.H.Zisk & P.J.Mouginis-Mark, *Nature*, 44, 735 (1980); **[4]** A.P.Zent & F.P.Fanale, *JGR*, 91, D439 (1986); **[5]** P. Toulmin *et al.*, *JGR*, 82, 4625 (1977); **[6]** B.C.Clark & D.C.Van Hart, *Icarus*, 45, 370 (1981); **[7]** R.G.Burns, *Proc. 18th LPSC*, 713 (1988); **[8]** L.E.Roth *et al.*, *Lunar Planet.Sci.*, XVI, 712 (1987); **[9]** G. De Mottoni, *Icarus*, 25, 296 (1975); **[10]** S.W.Lee, *Lunar Planet.Sci.*, XVI. 483 (1987); **[11]** R.G.Burns, *Proc. 17th LPSC, JGR*, 92, E570 (1987); **[12]** J. Dousma *et al.*, *J. Inorg. Nucl. Chem.*, 41, 1565 (1979); **[13]** M. Ohyabu and Y. Ujihira, *J. Inorg. Nucl. Chem.*, 43, 3125 (1981); **[14]** J. Dutrizac and S. Kaiman, *Can. Mineral.*, 14, 151 (1976); **[15]** R.G.Burns & D.S.Fisher, *Lunar Planet. Sci.*, XXI, 145 (1990); **[16]** R.G.Burns & D.S.Fisher, *LPI Tech. Rept.*, 88-05, 34 (1988); *JGR*, in press; **[17]** J.L.Gooding, *Icarus*, 33, 483 (1978); **[18]** J.Posey-Dowty *et al.*, *Icarus*, 66, 105 (1986); **[19]** R.B.Hargraves *et al.*, *JGR*, 82, 4547 (1977); **[20]** R.V.Morris *et al.*, *JGR*, 94, 2760 (1989); **[21]** Research supported by NASA grants NSG-7604 and NAGW-1078.

# OXIDIZED PYROXENES AND DEGRADATION OF THEIR VISIBLE - NEAR INFRARED SPECTRA: IMPLICATIONS TO REMOTE-SENSING OF MARS

**D'Arcy W. Straub and Roger G. Burns**, Department of Earth, Atmospheric and Planetary Sciences, Massachusetts Institute of Technology, Cambridge, Massachusetts 02139.

**INTRODUCTION.** Pyroxenes and olivines in basaltic magma extruding onto surfaces of terrestrial planets such as Mars, Earth and Venus are vulnerable to atmospheric oxidation during cooling of the igneous rocks. Ferrous iron in these ferromagnesian silicates may be oxidized to structural $Fe^{3+}$ ions or form a veneer of ferric oxide phases that might obliterate the diagnostic $Fe^{2+}$ crystal field (CF) spectral features used to identify pyroxenes and olivines. Previous measurements of oxidized olivines [1] demonstrated that the appearance of $Fe_2O_3$ phases (hematite, maghemite) obscure the characteristic olivine bands at 0.85, 1.05 and 1.20 μm. The 1 micron and 2 micron regions used to identify pyroxene structure-types and compositions in telescopic spectral measurements [2,3] may be similarly compromised. We report here measurements made on heated pyroxenes to assess the effects of aerial oxidation on their visible-near infrared spectra.

**PYROXENE SPECIMENS.** A suite of well-characterized pyroxenes [4] representative of different structure-types and compositions was chosen for the spectroscopic measurements and consisted of orthopyroxene, $Fe_{29}Mg_{70}Ca_1$; pigeonite, $Fe_{37}Mg_{47}Ca_{16}$; augite, $Fe_{10}Mg_{41}Ca_{46}$; a hedenbergite, $Fe_{42.5}Mg_{10}Ca_{47.5}$ containing 10% $Fe^{3+}$ [5]; and a Mn hedenbergite, $Fe_{40}Mn_{10}Mg_{0.5}Ca_{49.5}$. The specimens were selected to encompass different site occupancies of iron cations in the pyroxene crystal structure, particularly the M2 position, since $Fe^{2+}$ ions in this highly distorted non-centrosymmetric site are responsible for the positions and intensities of the diagnostic pyroxene "1 micron" and "2 micron" absorption bands [3]. Ferrous ions located in less distorted pyroxene M1 sites contribute relatively weak absorption bands centered near 0.9 and 1.15 μm [3,6,7]. In magnesian orthopyroxenes and pigeonites, the $Fe^{2+}$ ions are strongly enriched in the M2 positions with relatively small proportions in the M1 positions [8]. In calcic clinopyroxenes, although the $Fe^{2+}$ ions are more concentrated in the M1 positions, they preferentially fill any $Ca^{2+}$ vacancies in the M2 positions except in competition with $Mn^{2+}$ ions, which have a stronger preference than $Fe^{2+}$ for the pyroxene M2 positions [8]. The Mn hedenbergite, therefore, was expected to contain negligible $Fe^{2+}$ ions in its M2-sites.

**EXPERIMENTAL DETAILS.** Powdered pyroxenes (particle sizes <45 microns) were heated in air in the temperature range 400-800°C for different time periods. Mossbauer spectra at ambient temperatures and at 4.2K were used to identify the appearance of ferric iron in the oxidized pyroxenes. For most specimens, only ferric doublets (in addition to ferrous doublets) were present in the 295K Mossbauer spectra, but at 4.2K sextets attributable to ferric oxides (hematite, maghemite or magnesioferrite) were weakly developed indicating the formation of nanophase $Fe_2O_3$ phases in and on the surfaces of the pyroxene crystallites. The 4.2K spectra also indicated magnetic ordering of structural $Fe^{2+}$ and $Fe^{3+}$ ions in the two hedenbergites. Visible - near infrared reflectance spectra of selected samples were measured by Steve Pratt at Brown University using the RELAB facility there [9].

**RESULTS.** Examples of reflectance spectra of different pyroxenes oxidized in air are illustrated in Figures 1 to 4. Two extreme situations reflecting different $Fe^{2+}$ site occupancies are demonstrated by the spectra of orthopyroxene (Fig.1) and Mn-hedenbergite (Fig.4). In orthopyroxene, M2-site $Fe^{2+}$ ions are responsible for the absorption bands at 0.9 and 1.8 μm, the band depths of which are considerably reduced by oxidation of $Fe^{2+}$ to $Fe^{3+}$ ions. After heating in air, the increased absorption between 0.4 and 0.9 μm may be attributed to $Fe^{3+}$ CF transitions (which, for hematite, occur at 0.44, 0.51, 0.65 and 0.88 μm [10]) and to $Fe^{2+} \rightarrow Fe^{3+}$ intervalence charge transfer transitions (IVCT) occurring in orthopyroxene around 0.7 μm [6]. The Mn-hedenbergite spectra (Fig.4) originating from CF transitions in M1-site $Fe^{2+}$ at approx. 0.95 and 1.15 μm are severely modified after oxidation by spectral features attributable to nanophase $Fe_2O_3$ and structural $Fe^{3+}$, particularly the $Fe^{2+} \rightarrow Fe^{3+}$ IVCT occurring in calcic clinopyroxenes around 0.8 μm [5,6]. In the spectrum of the $Ca^{2+}$-deficient hedenbergite (Fig. 3), the M2-site $Fe^{2+}$ CF bands at 1.05 and 2.3 μm are obliterated by oxidation of $Fe^{2+}$ to $Fe^{3+}$, a similar trend also being observed in the spectra of the heated augite (Fig. 2).

**DISCUSSION.** The reduced band depths of the pyroxene 1 micron and 2 micron spectral features may be attributed to two related causes: first, loss of $Fe^{2+}$ ions in the pyroxene M2 sites after they become oxidized to $Fe^{3+}$ ions; and second, increased absorption by the ferric iron, either as structural $Fe^{3+}$ ions in the pyroxenes, or as nanophase $Fe_2O_3$ formed in and on the surfaces of the pyroxene grains. Similar contrasts of band depths may be seen between dark-region and bright-region spectra of Mars [11]. These and earlier results [1] suggest a mechanism for producing the nanophase hematite popularly considered to be responsible for the features observed around 0.65 and 0.87 μm in remote-sensed reflectance spectral profiles of Mars [12,13]: it results from aerial oxidation of structural $Fe^{2+}$ ions in olivines and pyroxenes to highly disseminated $Fe_2O_3$ [14].

**REFERENCES.** [1] K.S.Bartels & R.G.Burns, *Lunar Planet. Sci.*, XX, 44 (1989); [2] J.B.Adams, *JGR*, 79, 4829 (1974); [3] R.G.Burns, *Min. Mag.*, 53, 135 (1989); [4] M.D.Osborne *et al.*, *Proc. 9th LPSC*, 2949 (1978); [5] R.G.Burns & F.E.Huggins, *Am. Min.*, 58, 955 (19730; [6] G.R.Rossman, *Rev. Min.*, 7, 93 (1980); [7] G.Steffen *et al.*, *Phys. Chem. Min.*, 16, 120 (1988); [8] M.Cameron & J.J.Papike, *Rev. Min.*, 7, 5 (1980); [9] C.Pieters, *JGR*, 90, 12393 (1985); [10] D.M.Sherman & T.D.Waite, *Am. Min.*, 70, 1262 (1985); [11] R.B.Singer, *Adv. Space Sci.*, 5, 59 (1985); [12] R.V.Morris *et al.*, *JGR*, 94, 2760 (1960); [13] J.P.Bell *et al.*, *JGR*, in press; [14] Research supported by NASA grants NGR 7604 and NAGW 1078. We thank Steve Pratt for the reflectance spectral measurements.

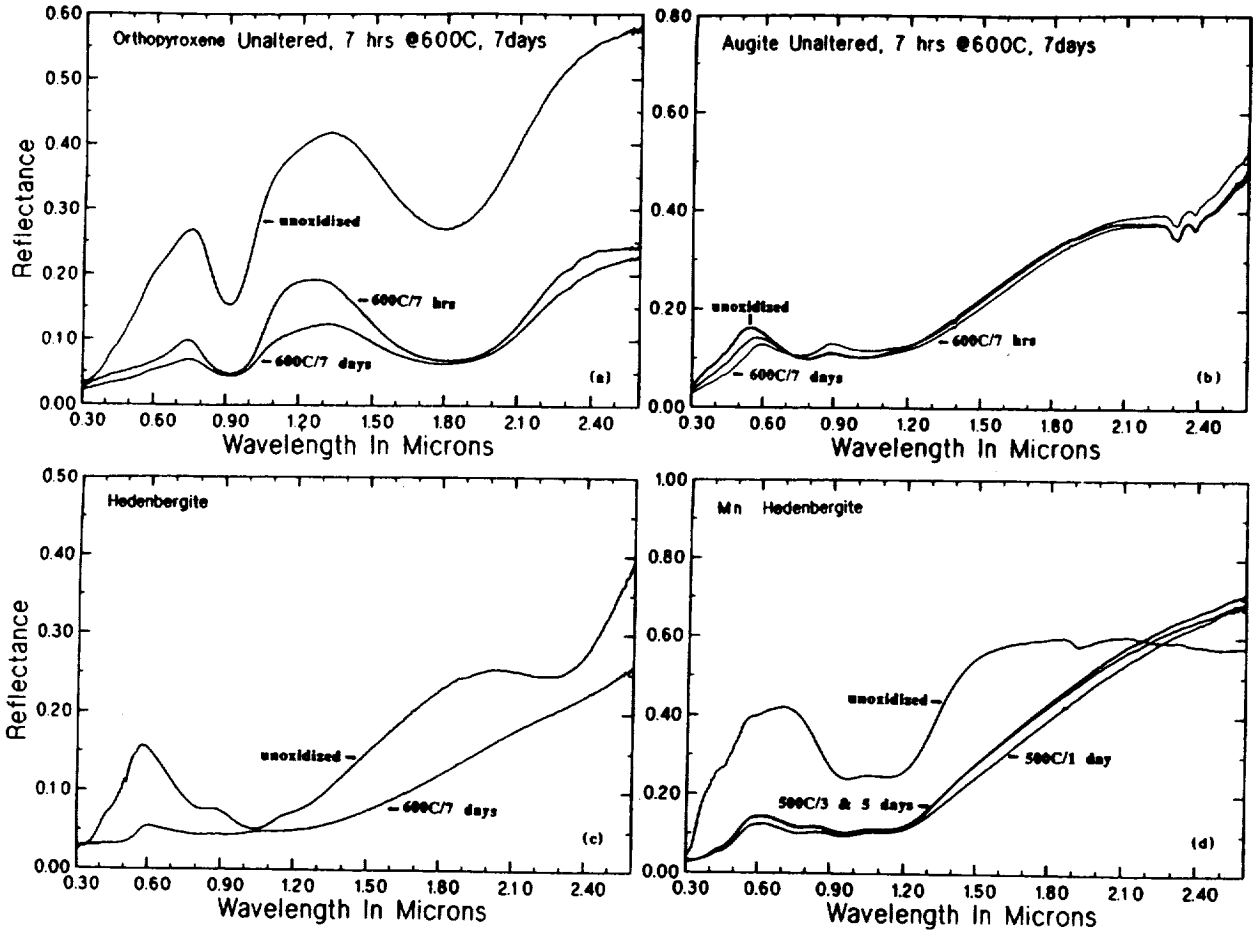


**FIGURE 1.** Reflectance spectra of pyroxenes before and after aerial oxidation. (a) orthopyroxene; (b) augite; (c) hedenbergite; and (d) Mn hedenbergite.

A RADAR-ECHO MODEL FOR MARS; T.W. Thompson, Calif. Inst. Tech., Jet Propulsion Laboratory, Pasadena, CA, 96011 and H.J. Moore, U.S. Geological Survey, Menlo Park, CA, 94025.

We have developed a radar-echo model for Mars based on 12.6-cm continuous-wave radio transmissions backscattered from the planet [1,2]. Our model (1) broadly matches the variations in depolarized and polarized total-radar cross sections with longitude observed by Goldstone in 1986 along 7° S. and (2) yields echo spectra that are generally similar to the observed spectra, with some departures.

In our model, Mars' surface is divided into radar map units that are based on generalized geologic map units [2]; the radar map units are further subdivided using thermal inertias [3]. Thermal inertias are used because the geologic map units are not sufficient to account for the quasi-specular echoes and normal reflectivities and thermal inertias are positively correlated along 7° S. and elsewhere [4,5]. For cratered uplands and plains units, model depolarized- echo strengths vary as A*cos[theta] (where [theta] is the incidence angle and A is a parameter assigned to the radar map unit on a degree by degree basis), and polarized diffuse-echo strengths vary as 3*A*cos[theta]. For most volcanic units, depolarized and polarized diffuse-echo strengths vary as $A*\cos^2[theta]$. Quasi-specular echoes were computed using Hagfors' scattering law [6] (integrated from -30° to +30° theta). Assignments of depolarized echo strengths, normal reflectivities, and root-mean-square (rms) slopes for the radar map units were guided by previous experience [2], thermal inertias [3], and the results from analyses of the quasi-specular echo spectra and then they were adjusted by trial and error methods to best fit the data. Coarse-scale topography is not included in the model.

Radar map units in our model include: (1) an extensive cratered uplands (background) unit with weak depolarized echo cross sections (0.01), average thermal inertias, moderate normal reflectivities (0.095), and moderate rms slopes (4.0°); (2) the volcanic units of the Tharsis, Elysium, and Amazonis regions with strong depolarized echo cross sections (0.04-0.133), low thermal inertias, low normal reflectivities (0.025-0.050), and large rms slopes (6-20°); and (3) the northern plains units with moderate to strong depolarized echo cross sections (0.017-0.045), moderate to very high thermal inertias, moderate to large normal reflectivities (0.075-0.15), and moderate rms slopes (3-5°). Arabia, an extensive unit of upland that is mantled by dust, has a low depolarized-echo cross section (0.007), low thermal inertia, small normal reflectivity (0.05), and small rms slope (3.0°). There are additional radar map units (there are about 140 radar map units). At this time, our model does not include an equatorial region extending from the vicinity of western Pavonis Mons to S.E. Elysium Planitia that has non-existent to very weak depolarized echoes or the very strong ones from the poles

observed at 3.6-cm wavelength [7].

Like the observations, model total-polarized echo cross sections vary with longitude as a two-cycle curve with maxima near 30° and 240° W. and minima near 130° and 330° W.; model total-depolarized-echo cross sections vary with longitude as a one-cycle curve with a maximum near 135° and a minimum near 330° W.; and, the ratio of total-depolarized and total-polarized cross sections (mu) vary with longitude as a one-cycle curve.

Model depolarized- and polarized-echo spectra, as well as ratios of the two, resemble those that are observed. For smooth regions with moderate thermal inertias and normal reflectivities, the central parts of polarized-echo spectra are dominated by the quasi-specular parts that form tall, narrow peaks that rest upon low, broad domes of the diffuse echoes. In rough regions with low thermal inertias and small normal reflectivities, the quasi-specular echoes form low broad peaks that rest upon and merge imperceptibly with the broad domes of the diffuse part of the echoes. Like the observed spectra, the forms of the polarized diffuse echoes tend to mimic the depolarized echoes except near the centers of the spectra where the quasi-specular parts of the polarized echoes totally dominate the spectra. For the model and observations, ratios of the spectra of depolarized and polarized echoes are similar.

Several aspects of our model are instructive and relevant to the interpretation of radar echoes from Mars. These aspects are related to the sizes of the heterogeneous radar map units areas sampled by the radar, and the way in which the radar samples the surface; for example: (1) quasi-specular echoes from horizontal surfaces may be asymmetrical with peaks displaced from zero-doppler frequency when the radar samples adjacent units with different roughnesses; (2) quasi-specular echoes from very smooth areas with embedded very rough areas may be so dominated by the smooth areas that the rough areas are not revealed in the spectra; and (3) the diffuse parts of the polarized echoes may contribute substantially to the polarized echoes. Careful examination of observed echoes show that the surface of Mars is, like our model, heterogeneous.

## REFERENCES

[1] Thompson, T.W., 1988, LPI Tech. Report 88-05, p. 107-108. [2] Thompson, T.W. and Moore, H.J., 1989, Proc. 19th Lunar and Planet. Sci. Conf., p. 409-422. [3] Palluconi, F.D. and Kieffer, H.H., 1981, Icarus, v. 45, p. 415-426. [4] Jakosky, B.M. and Christensen, P.R., 1986, Icarus, v. 66, p. 125-133. [5] Moore, H.J. and Jakosky, B.M., 1989, Icarus, v. 81, p. 164-184. [6] Hagfors, T., 1964, J. Geophys. Res., v. 69, p. 3779-3784. [7] Butler, B., Muhleman, D., Grossman, A., and Slade, M., 1989, Eos (Trans. Am. Geophys. Union), v. 70, #43, p. 1171.

# IMPLICATIONS OF CRUSTAL FORMATION ON MARS FROM PARAMETERIZED CONVECTION CALCULATIONS

D.L. Turcotte and J. Huang, Department of Geological Sciences, Cornell University, Ithaca, NY 14853

In order to better understand the evolution of Mars we have carried out a series of parameterized convection calculations (1). An important aspect of our analyses is the removal of the heat producing elements from the Martian mantle to the crust. The rate of crustal formation is calibrated using the present rate of crustal generation on the earth and the moon. The evolution of the mean mantle temperature, crustal thickness, lithosphere thickness, rate of volcanism, mantle heat flow, change of radius, and Urey number are obtained. Several studies (2-4) utilizing gravity anomalies and Airy compensation have suggested that the thickness of the Martian crust is 115-130 km. This is consistent with our results if the crustal fractionation parameter is in the range 0.0025-0.005. These are somewhat lower than the values inferred for the earth and moon which are near 0.001.

Accepting that the crustal fractionation factor for Mars is 0.003, we can determine rates of volcanism. The average amount of crust added in the last billion years (0-1 Gyr BP) is predicted to be 600 m, the average amount of crust added between 1-2 Gyr BP was 1.8 km, and the average amount of crust added between 2-3 Gyr BP was 2.9 km.

A detailed summary of the stratigraphy of Mars has been given by Tanaka (5). Relative ages are quite tightly constrained by crater counts, but absolute ages are uncertain due to uncertainties in the volcanic flux. The most recent volcanism is associated with the Upper Amazonian period. Volcanics of this period are associated with the Arcadra, Olympus Mons, Medusae Fossae, and Tharsis Montes Formations but the principal volcanics are flood basalts in the southern Elysium Planitia. These have an area of 100,000 $km^2$ but Tanaka (5) suggests that the thickness is only a few tens of meters. Taking a thickness of 50 m this is only 0.03 m when averaged over the surface of Mars.

Greeley (6) has estimated that 26 x $10^6$ $km^3$ of volcanics erupted during the Middle and Upper Amazonian. This corresponds to a mean thickness of 200 m when averaged over the entire surface

of Mars. Based on the meteorite flux intensity given by Hartmann et al (1981) the Upper Amazonian extends from 0 to 0.7 Gyr BP and the Middle Amazonian from 0.7 to 2.3 Gyr BP. Thus the Young volcanoes on Mars are consistent with our results. It should be emphasized, however, that there are considerable uncertainties in the absolute ages.

Other predictions of our calculations using $\chi = 0.003$ are that the lithosphere thickness $D_L = 400$ km, the Urey Number = 0.7, and a net contraction corresponding to $\delta r/r = -0.001$. We predict that a global expansion of $\delta r = 10$ km occurred in the first 200 Myr of the evolution of Mars. This expansion was caused by the density change associated with the generation of the early crust. For the remainder of the evolution of Mars a nearly steady contraction occurred associated with the cooling of the interior. The total contraction was $\delta r = -13$km.

The surface tectonic features of Mars include both extensional features and compressional features. Much of the evidence for lithospheric extension on Mars is provided by graben systems in and near the Tharsis region. These features are likely to be the result of the stresses generated by the Tharsis load. Wrinkle ridges occur commonly throughout ancient terrains. These can be attributed to thermal contraction.

References:

(1) Turcotte, D.L., et al., Proc. Lunar Planet. Sci. Conf. 10th, 2375-2392, 1979. (2) Sjogren, W.J. and R.N. Wimberly, Icarus 45, 331-338, 1981. (3) Sjogren, W.J. and S.J. Ritke, Geophys. Res. Let. 9, 739-742, 1982. (4) Janle, P., Moon Planets 28, 55-67, 1983. (5) Tanaka, K.L., J. Geophys. Res., 91, E139-E158, 1986. (6) Greeley, R., Science 236, 1653-1654, 1987. (7) Hartmann, W.K., et al., Basaltic Volcanism, 1049-1127, 1981.

**THE NATURE AND ORIGIN OF PERIODICALLY SPACED WRINKLE RIDGES ON MARS.** Thomas R. Watters, Center for Earth and Planetary Studies, National Air and Space Museum, Smithsonian Institution, Washington, D.C. 20560.

Over 3% of the surface of Mars is covered by smooth plains material characterized by landforms analogous to mare wrinkle ridges. Although the exact nature of these ridged plains materials has not been directly determined, indirect evidence suggests they are the result of flood volcanism (1,2,3). The origin of wrinkle ridges is also not agreed upon, and recent debates have focused on the role of buckling and reverse or thrust faulting (3,4,5). However, the general consensus is that wrinkle ridges are tectonic in origin resulting from horizontal compressive stresses.

The largest known occurrence of wrinkle ridges on the terrestrial planets, observed within a distinct physiographic province, is on the Tharsis Plateau of Mars (6). The average spacing, evaluated in six provinces of the Tharsis ridge system, is 30 km (2,934 measurements), equal to the average spacing of the crosscutting wrinkle ridges of Hesperia Planum (7). There have been a number of buckling models proposed to explain the periodic nature of the wrinkle ridges (8,9,10,11,12) and some recent debate as to whether the lithosphere is involved in the deformation (thick-skinned) or not (thin-skinned). One reason for considering models that do not require wrinkle ridges be rooted in the lithosphere is the unlikelihood that stresses penetrating both the crust and lithosphere were involved in the deformation of ridged plains units well distant from Tharsis, particularly the many relatively small, isolated areas of ridged plains material that occupy topographic lows within intercrater plains.

In the models evaluated in this study, it is assumed that the ridged plains material behaves as both a single member and a multilayer with frictionless contacts, resting on a mechanically weak megaregolith substrate of finite thickness that has buckled at a critical wavelength of folding. The basement does not directly participate in the deformation that results in the ridges, thus no assumption of whole or partial lithosphere deformation is necessary to explain the periodic spacing. Free slip between layers is assumed based on the possible existence of mechanically weak interbeds in the ridged plains sequence separating groups of flows. Interbeds separating groups or units of flows are not uncommon within mare basalts on the Moon or in terrestrial continental flood basalt sequences (13,14,15) and may contribute to the localization of buckling (16). The rheologic behavior of the ridged plains and megaregolith are approximated by a linear elastic and linear viscous material. The models are examined for a range in: 1) the strength contrast between the ridged plains material and the underlying megaregolith of 100, 1,000 and 5,000; 2) thickness of the ridged plains material of 250 to 3,500 m; 3) thickness of the megaregolith of 1,000 to 5,000 m; and 4) number of layers (n) of 1 to 12. For the elastic case, wavelengths consistent with many of the observed spacings are obtained at critical stresses below the yield-strength of a basalt-like material for $n > 5$. For $n = 8$, wavelengths range from 27 to 42 km for thicknesses of the ridged plains material ranging from 1,900 to 3,500 m over a range in thickness of the substrate of 1,000 to 5,000 m and ratio in Young's modulus of 1,000 to 5,000. The cases of $n = 1$ (i.e., a single member) through 5 do not yield admissible wavelengths. At the upper limit of the model parameters, the average thickness of the ridged plains necessary to account

for the minimum average spacing of the ridges (20 km) is roughly 1,700 m. If the ridge spacing is the result of elastic buckling, the relatively high contrast in Young's modulus required ($\geq$ 1,000) is only possible if there were high pore-fluid pressure within the megaregolith at the time of deformation that reduced the effect of the overburden.

Over the same range in values of the parameters, viscous buckling is much less restricted than the elastic case. The observed wavelengths can be accounted for over almost the entire range of viscosity contrast, ridged plains material thickness and substrate thickness for either a single layer or a multilayer. The minimum average spacing of the ridges can be explained with a single layer (n = 1) at the lower limit of the estimated thickness of the ridged plains material (250 m), at the upper limit of the substrate thickness and viscosity contrast. In addition, viscous buckling is viable if the megaregolith were dry, water-rich or ice-rich at the time of deformation.

***References Cited:***

(1) Greeley, R., E. Theilig, J.E. Guest, M.H. Carr, H. Masursky and J.A. Cutts, *JGR, 82,* 4039-4109, 1977. (2) Scott, D.H. and K.L. Tanaka, *USGS Map I-1802-A,* Denver, Colo., 1986. (3) Watters, T.R., *JGR, 93,* 10,236-10,254, 1988. (4) Plescia, J.B. and M.P. Golombek, *GSA Bull., 97,* 1289-1299, 1986. (5) Sharpton, V.L. and J.W. Head, *Proc. LPSC IX,* 307-317, 1987. (6) Watters, T.R. and T.A. Maxwell, *JGR, 91,* 8113-8125, 1986. (7) Watters T.R. and D.J. Chadwick, *LPI Tech. Rep. No. 89-06,* 68-70, 1989. (8) Saunders, R.S. and T.E. Gregory, *NASA Tech. Memo. TM82385,* 93-94, 1980. (9) Watters, T.R. and T.A. Maxwell, *LPSC XVI,* 897-898, 1985. (10) Watters, T.R., *Fourth International Conference on Mars,* 206-207, 1989. (11) Zuber, M.T. and L.L. Aist, *LPSC XX,* 1261-1262, 1989. (12) Zuber, M.T. and L.L. Aist, submitted to *JGR,* 1989. (13) Peeples, W.J., R.W. Sill, T.W. May, S.H. Ward, R.J. Phillips, R.L. Jordan, E.A. Abott, and T.J. Killpack, *JGR, 83,* 3459-3468, 1978. (14) Reidel, S.P., T.L. Tolan, P.R. Hooper, K.R. Fecht, M.H. Beeson, R.D. Bentley, and J.L. Anderson, *GSA Sp. Paper 239,* in press, 1989. (15) BVSP, 1286 pp., Pergamon Press, New York, 1981. (16) Watters, T.R., *GSA Sp. Paper 239,* in press, 1989.

**DOMAINS OF REGIONAL PURE SHEAR ON THE TERRESTRIAL PLANETS.**

Thomas R. Watters and Michael J. Tuttle, Center for Earth and Planetary Studies, National Air and Space Museum, Smithsonian Institution, Washington, D.C. 20560

Tectonic domains where major fold and thrust fault trends are transected by conjugate strike-slip faults have been documented within fold-thrust belts on the Earth (1,2). The geometric relationships between the structures is best explained by a pure shear mechanism because of the limited extent and lateral displacements of the strike-slip faults (see 2). Given a N-S directed compressive stress, the system of structures possible includes E-W trending first-order folds and first-order right-lateral and conjugate left-lateral strike-slip faults with an angle $\theta$ to the primary stress direction. The angle $\theta$ is constrained by the Coulomb-Navier criterion where $\theta$ is related to the coefficient of internal friction $\mu$. For typical values of $\mu$ between 0.58 and 1.0, $\theta$ is in the range of 22.5°-30°.

***Yakima Fold Belt, Columbia Plateau, Earth***

The anticlinal ridges in the continental flood basalts of the Columbia Plateau (or Columbia Basin) are long, narrow, periodically spaced structures with broad relatively undeformed synclines. The anticlinal ridges are believed to be the result of initial buckling in response to a horizontal compressive load followed by dominantly reverse to thrust faulting (3). Numerous strike-slip faults have been mapped in the southern portion of the fold belt (4). The lateral displacement along the most extensive faults is typically small (< 1 km). The strike-slip faults can be classified as either tear faults, faults of limited extent or regional faults (5). As part of this study, over 80 lineaments have been mapped, 73 of which are located in the southern portion of the fold belt. Many of these correspond to previously mapped right-lateral strike-slip faults. The mean direction of the known and suspected strike-slip faults in the southern portion of the fold belt is N37°W. Taking the normal to the mean direction of the anticlines to be the approximate direction of the principal compressive stress, the mean direction of the known and suspected right-lateral strike-slip faults is within the range for $\theta$. The anticlinal ridges of the Columbia Plateau are good analogs to first-order ridges in wrinkle ridge assemblages that occur in the ridged plains material on Mars (6).

***Wrinkle Ridge Assemblages, Mars***

Wrinkle ridges occur in smooth plains material that is inferred to be volcanic in origin. These ridges are also believed to form in response to horizontal compression with reverse or thrust faulting developed as a result of buckling (flexure-fracture) or buckling the result of reverse or thrust faulting (fracture-flexure) (6,7). If the ridged plains material has deformed in a similar style to the basalts of the Columbia Plateau, then strike-slip faults and their associated secondary structures may be common on Mars. Lineaments that transect wrinkle ridges have been found in medium and high resolution Viking Orbiter images. Some are comparable in scale to strike-slip faults associated with the anticlines on the Columbia Plateau. Lineaments of limited areal extent that sharply truncate both *en echelon* stepping and individual ridge segments are interpreted to be tear faults. Crosscutting lineaments of greater areal extent ($\leq$ 100 km) occur near or within the expected range for $\theta$ and are interpreted to be strike-slip

faults consistent with a domain of regional pure shear. Like their analogs on the Columbia Plateau, the strike-slip faults accommodate a portion of the relatively low bulk strain apparent in the ridged plains. Other evidence of strike-slip faulting on Mars has been recently reported by Forsythe and Zimbelman (8) and Schultz (9).

*Ridge Belts, Venus*

Parallel to subparallel ridges form the prominent ridge belts identified in Venera 15/16 images. Although the role of extension (10) and compression (11,12) in origin of the ridge belts is under debate, the similarity in morphology of the ridges to wrinkle ridges suggests that they are the result of horizontal compression. Frank and Head (11) describe some of the ridges as broad arches and compare them to arches associated with maria wrinkle ridges. Crosscutting lineaments are common in the ridge belts (11,12). These lineaments often occur in conjugate sets and evidence of strike-slip motion has been reported (11,12), however we observe little or no apparent displacement along the lineaments studied thus far. The areal extent, limited apparent displacement and the estimated values of $\theta$ determine for the lineaments are consistent with the development of strike-slip faults in a domain of regional pure shear. Based on the assumption that the morphology and fold geometry of the ridges is similar to that of wrinkle ridges, crude estimates of the bulk strain within the ridge belts in the Pandrosos and Ahsonnutli Dorsa regions are as high as 7% (see 6), as compared to a maximum of roughly 2% estimated bulk strain for ridged plains of Tharsis and 5% for the deformed basalts of the Columbia Plateau.

*References Cited:*

(1) Tirrul, R., I.R. Bell, R.J. Griffis and V.E. Camp, *GSA Bull., 94,* 134-150, 1983. (2) Sylvester, A.G., *GSA Bull., 100,* 1666-1703, 1988. (3) Watters, T.R., in *GSA Sp. Paper 239*, in press, 1989. (4) Anderson, J.L., Ph.D. dissertation, Univ. South. CA, 1987. (5) T.L. Tolan, J.L. Anderson and M.H. Beeson, this volume. (6) Watters, T.R., *JGR 93*, 10,236-10,254, 1988. (7) Plescia, J.B. and M.P. Golombek, *GSA Bull., 97,* 1289-1299, 1986. (8) Forsythe R.D. and J.R. Zimbelman, *Nature, 336*, 143-146, 1988. (9) Schultz, R.A., *Nature, 341*, 424-426, 1989. (10) Sukhanov, A.L. and Pronin, A.A., *Proc. LPSC XIX*, 335-348, 1989. (11) Frank, S.L. and J.W. Head, *Venus Geoscience Tutorial, LPI No. 708*, 13-14, 1989. (12) Kryuchkov, V.P., *LPSC XX*, 546-547, 1989.

**ORIGIN OF CURVILINEAR GRABEN IN SOUTHWEST LUNAE PLANUM, MARS.**

Thomas R. Watters and Michael J. Tuttle, Center for Earth and Planetary Studies, National Air and Space Museum, Smithsonian Institution, Washington, D.C. 20560

The southwest Lunae Planum region of the Tharsis Plateau is being mapped at the 1:500,000 scale as part of the Mars Geologic Mapping program. The western margin of the ridged plains and plateau plains units in this region is marked by a steep, 3 km high erosional scarp. The plateau units in this region are cut by sets of curvilinear graben that occur within a 150 km zone of the scarp. There are three sets of graben in the region, set A cuts Noachian cratered uplands, set B cuts Hesperian plateau material and set C cuts both Hesperian plateau and ridged plains material (see A, B and C, fig. 1). The graben in set A have a mean direction of N12°E and are partially covered by ridged plains material that embays the cratered uplands (fig. 1, see A). Graben set B cuts plains material that appears to be continuous with the ridged plains material but lacks wrinkle ridges (fig. 1, see B). The trend of many of these graben (mean direction N10°E) are parallel to those in the adjacent cratered uplands. This suggests that these graben are the result of reactivation of a preexisting extensional fabric.

The orientation of graben in set A and B is not consistent with any phase of Tharsis radial extension (1). Circumferential oriented extensional stresses are predicted in this region in isostatic adjustment models (2,3,4), however, the curvature of the graben suggests that they were part of a circular swarm with a radius of approximately 300 km. Circular graben swarms are not uncommon in the Tharsis region. The most likely origin of the extensional stresses is local uplift resulting from the emplacement of an intrusive body. If this is the case, the initial intrusion may have coincided with some of the earliest tectonic activity in the Tharsis region.

The third set of graben (C) cut ridges plains material forming non-orthogonal ridge-fault crosscutting angular relationships (fig. 1, see C). This clearly indicates that graben formation postdates the deformation that resulted in the wrinkle ridges (5). The orientation of the graben in set C (mean direction N49°E) is also not consistent with Tharsis radial extension. However, unlike the other graben sets, the C graben parallel the scarp (mean direction of scarp segments is N52°E). Although the graben in set C do not appear to be related to the other sets, the orientations of the graben in sets B and C become parallel where they cut the same unit (fig. 1, see arrow). This suggests that in this area, the graben in set C were influenced by the same preexisting extensional fabric. The parallel nature of the graben and scarp suggests that the two are related. Possible explanations are: 1) the graben influenced scarp retreat, or 2) graben formation was influenced by, or a result of, the scarp. Extensional stresses near the scarp will result from the release of confining pressure, however, the magnitude of the stress would be expected to decay rapidly with distance from the wall. Another possibility is that extensional stresses resulted from loss of support. If the ridged plains overlie a thick megaregolith that was exposed by erosion, material may have been removed by undercutting and/or sapping. A finite element analysis is planned to determine under what conditions, if any, graben could form at the observed distances from the scarp.

***References Cited:***
(1) Plescia, J.B. and R.S. Saunders, *JGR, 87*, 9775-9791, 1982. (2) Banerdt, W.B., R.J. Phillips, N.H. Sleep, and R.S. Saunders, *JGR, 87*, 9723-9733, 1982. (3) Banerdt, W.B., M.P. Golombek, and K.L. Tanaka, submitted to *Mars*, University of Arizona Press, Tucson, 1989. (4) Sleep, N.H. and R.J. Phillips, *JGR, 90*, 4469-4489, 1985. (5) Watters, T.R. and T.A. Maxwell, *Icarus, 56*, 278-298, 1983.

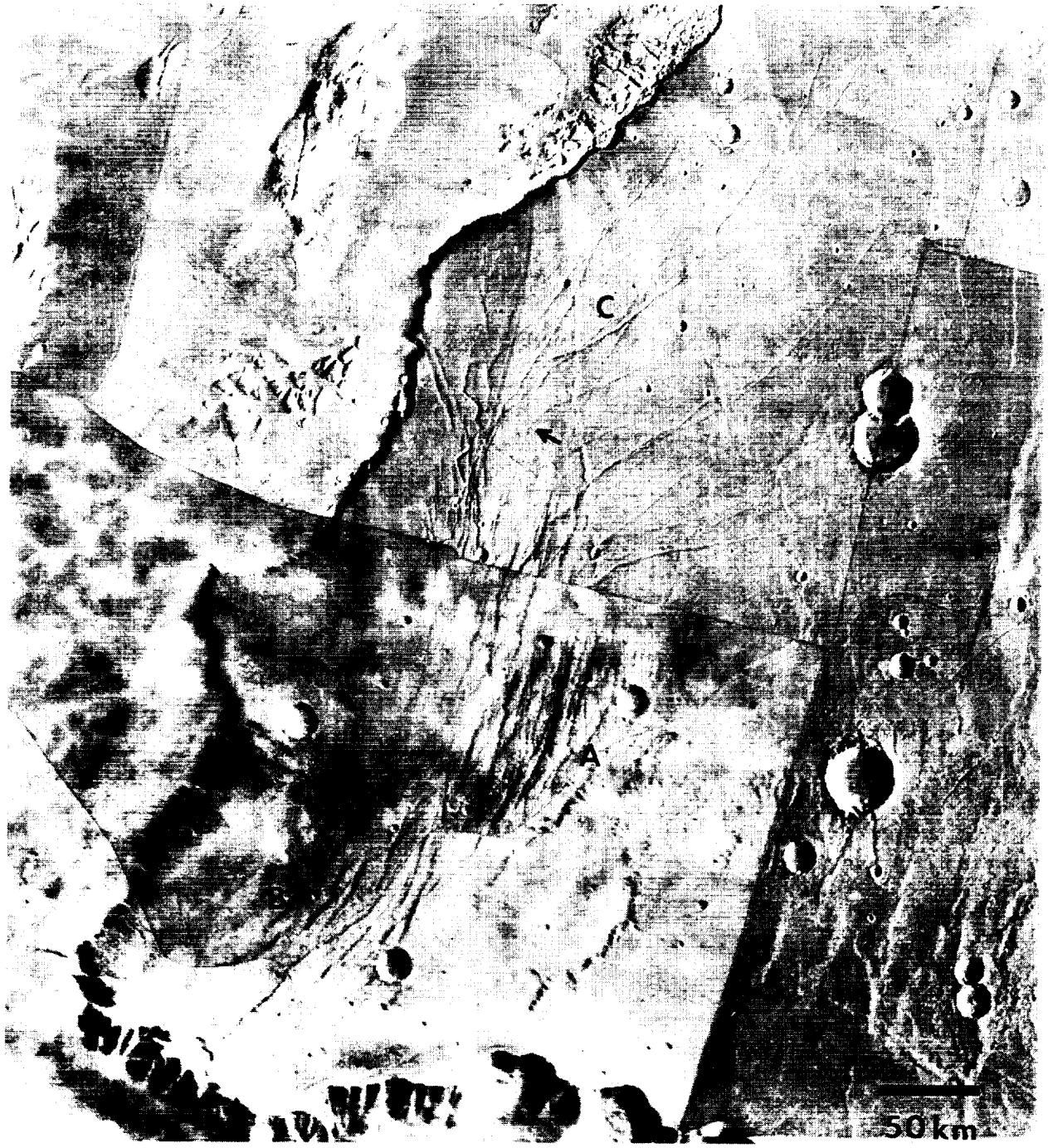


Fig. 1. Photomaps of southwest Lunae Planum. The three sets of graben in the region are marked A, B and C.

**DISTRIBUTION OF STRAIN IN THE FLOOR OF THE OLYMPUS MONS CALDERA.** Thomas R. Watters and D. John Chadwick, Center for Earth and Planetary Studies, National Air and Space Museum, Smithsonian Institution, Washington, D.C. 20560, and Michael C. Liu, Department of Astronomy, Cornell University, Ithaca, NY 14853

The Olympus Mons caldera is made up of six coalescing volcanic craters (fig. 1). Based on comparisons with terrestrial volcanoes, such as Mauna Loa, Hawaii (1, 2), the volcanic craters are interpreted to be the result of collapse of a solidified lava lake due to evacuation of the magma chamber during late-stage summit activity (3). The floors of several of the craters are characterized by a large number of deformational features in the form of graben and wrinkle ridges. The largest and oldest of the volcanic craters (crater 6, see 3), approximately 65 km in diameter, has a well developed circumferential graben system in the margins of the floor (fig. 1). Wrinkle ridges are present in the interior of the floor but have been sharply truncated by at least three successive collapse episodes.

The origin of the stresses that generated the observed structures is likely the result of subsidence of the central portion of crater floors (3). Using topography derived by Wu et al. (4), subsidence is evident across the floor of the large crater (fig. 2, 5X vertical exaggeration). The cause of the subsidence is presumed to be loss of support of the caldera floor by withdrawal of the underlying magma, probably the result of flank eruptions. In a finite element analysis, Zuber and Mouginis-Mark (5) have shown that compressive and extensional stresses compatible with the generalized location of the structures can be generated by subsidence. A detailed assessment of the location of the wrinkle ridges and graben relative to the topography is useful in refining such models.

The distribution of the circumferential graben on the floor of large crater is not uniform. Mouginis-Mark (3) notes that the widths of graben are greatest near the crater edge and narrow toward the center of the floor. The most extensive fracturing of the floor is on the southern edge, near the rim of the of crater 3 (fig. 1). The average slope of the floor in the area of these graben is roughly 4° (fig. 2), the largest slopes observed on the floor. On the northern edge, there are fewer graben and the average slope of the floor is less (roughly 3°). Thus, the areas of greatest slope and possibly greatest flexure of the floor correspond to areas with the greatest observed extension. This correlation supports the assumption that the structures are the result of downward displacement of the floor. As noted by Zuber and Mouginis-Mark (5), many of the wrinkle ridges occur in topographic lows. In contrast to the circumferential graben, the ridges are not strongly radially distributed, but are confined to a roughly E-W oriented trough (fig. 2). The most prominent wrinkle ridge on the crater floor is located close to the area of lowest elevation. The average slope of the floor in area of the ridges is $\leq 2°$. Preliminary estimates of the bulk horizontal shortening and extension in the crater floor, using average values of the shortening across the ridges (see 6) and the extension across the graben (see 7), are roughly compatible at 1.5-2.0 km. Based on the topography and the distribution of structures, the subsidence appears to have been asymmetric with greater downward displacement and deformation of the southern half of the floor.

***References Cited:***
(1) Carr, M.H., *JGR, 78,* 4049-4062,1973. (2) Greeley, R., *Geology, 1,* 175-180, 1973. (3) Mouginis-Mark, P.J., *Proc. LPSC XII,* 1981. (4) Wu, S.S.C., P.A. Garcia, R. Jordan, F.J. Schafer and B.A. Skiff, *Nature, 309,* 432-435, 1984. (5) Zuber, M.T. and P.J. Mouginis-Mark, *LPI Tech. Rep. No. 89-06,* 74-75, 1989. (6) Watters, T.R., *JGR, 93,* 10,236-10,254, 1988. (7) Golombek, M.P., *JGR, 84,* 4657-4666, 1979.

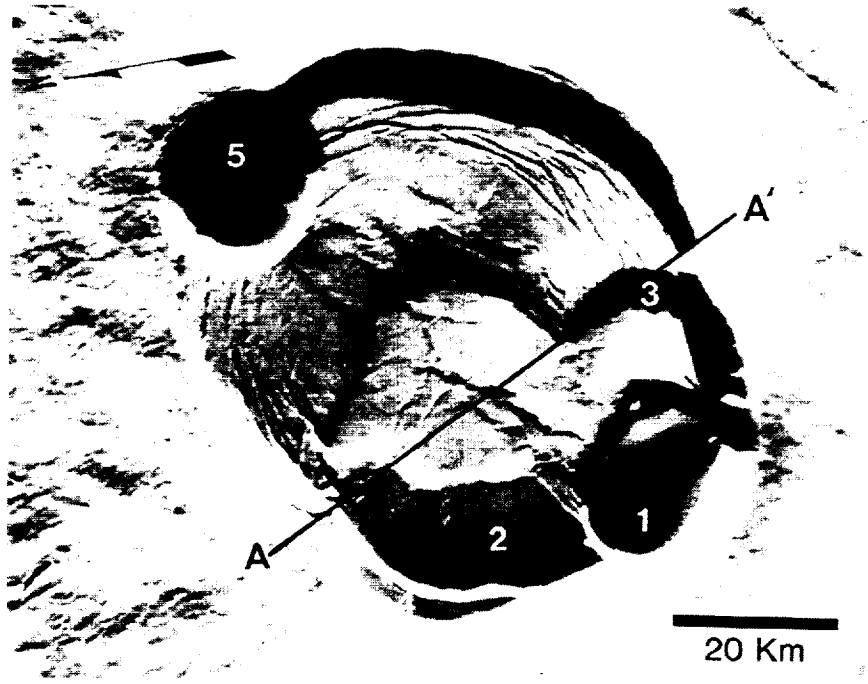


Fig. 1. Nested summit caldera of Olympus Mons.

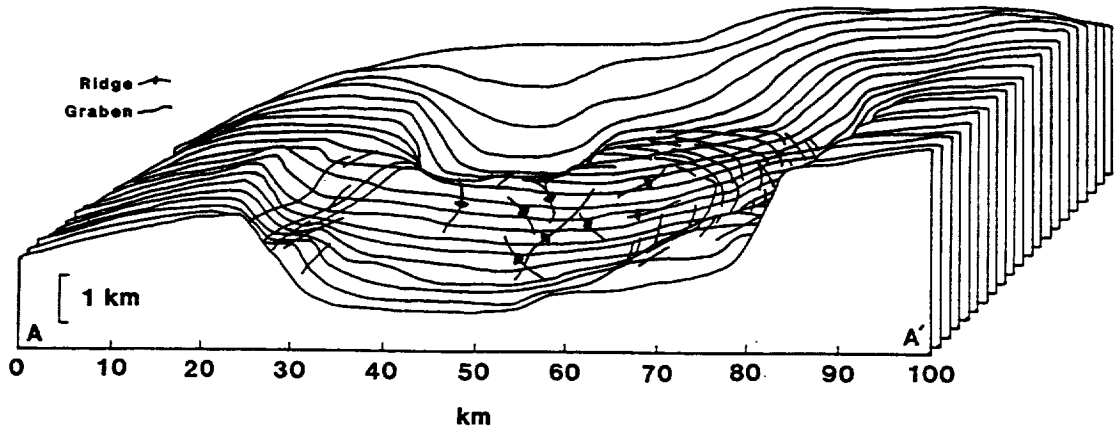


Fig. 2. Topographic profiles of a portion of the caldera with the location of prominent wrinkle ridges and graben.

**SYMMETRY OF INFERRED STRESS FIELDS IN THE THARSIS REGION OF MARS.** Thomas R. Watters and Michael J. Tuttle, Center for Earth and Planetary Studies, National Air and Space Museum, Smithsonian Institution, Washington, D.C. 20560, and Francis J. Kiger, Department of Geology and Astronomy, West Chester University, West Chester, Pennsylvania, 19383

Understanding the origin of the stresses that generated the radial fracture system and circumferential wrinkle ridge system on the Tharsis Plateau is key to unraveling the tectonic evolution of the region. Banerdt et al. (1,2) and Sleep and Phillips (3) have proposed models for the origin of the stresses and calculated stress trajectories that can be compared to the observed tectonic features. The stress fields predicted in these models are strongly radial to an area near Pavonis Mons. If these models are correct, the stress inferred from the structures should be strongly radial to this area.

The radial nature of the inferred stresses has been analyzed using a stereonet in a number of studies (4,5,6,7). In a recent study, Golombek (8), using graben data compiled by Plescia and Saunders (5) and ridge data subsampled into length-weighted vector means compiled by Watters and Maxwell (6), concluded that the graben and wrinkle ridges define a significantly radial system. With respect to the wrinkle ridges, this conclusion is in contrast to the findings of Watters and Maxwell (6) and is not the result of a net manipulation error as reported by Golombek (8). The method used by Golombek (8) involves fitting great circles with the correct angular relationship on the net to the vector normals. The resulting great circles are then geographically correct traces of the inferred principal stress on the surface. Watters and Maxwell (6) used the azimuth of the vector normals to fit the great circles. This method does not generate geographically correct traces of the inferred stresses, but can be used to test radial symmetry.

In an effort to address the question of the significance of the radial symmetry of the system of structures, a wrinkle ridge data set consisting of 1845 ridge segments and a graben data set consisting of 6841 fault segments is used in a beta analysis. Great circles that are geographically correct traces of the inferred principal stresses (8) are fit to each graben segment and the normals to each ridge segment. The 1.7 million intersections of the ridge data are distributed in a broad girdle with a maximum concentration of 5% per 1% area centered at approximately 5°S, 110°W (fig. 1). The 32 million intersections of the graben data are distributed in a symmetric pattern, elongated in a N-S direction with a maximum concentration of 12% per 1% area roughly centered at 3°S, 110°W (fig. 2).

The agreement between the locations of the maximum concentrations of intersections for the two systems of structures supports models where isostatic and flexural loading stresses result from the observed topography and gravity (1,2,3). However, in the isostatic case of Banerdt et al. (2), the predicted compressional stresses would result in a strongly radially symmetric ridge system (maximum concentration of 45% per 1% area located at roughly 5°N, 105°W). Even when the predicted stress trajectories are varied by as much as 10°, the maximum concentration does not approach 5%.

A possible explanation for the difference between the predicted stresses and those inferred from the observed structures is that some component of the total stress responsible for the wrinkle ridges is not accounted for in the models. Additional components of stress may have resulted from: 1) gravitationally induced down-surface slope stresses (9) generated when the

regional topographic slope was greater than at present, and 2) local and/or regional subsidence.

***References Cited:*** (1) Banerdt, W.B., R.J. Phillips, N.H. Sleep, and R.S. Saunders, *JGR, 87*, 9723-9733, 1982. (2) Banerdt, W.B., M.P. Golombek, and K.L. Tanaka, submitted to *Mars*, University of Arizona Press, Tucson, 1989. (3) Sleep, N.H. and R.J. Phillips, *JGR, 90*, 4469-4489, 1985. (4) Wise, D.U., M.P. Golombek and G.E. McGill, *Icarus, 38*, 456-472, 1979. (5) Plescia, J.B. and R.S. Saunders, *JGR, 87*, 9775-9791, 1982. (6) Watters, T.R. and T.A. Maxwell, *JGR, 91*, 8113-8125, 1986. (7) Schultz R.A., *JGR, 90*, 1985. (8) Golombek, M.P., *LPSC XX*, 345-346, 1989. (9) Elliott, D., *JGR, 81*, 949-963, 1976.

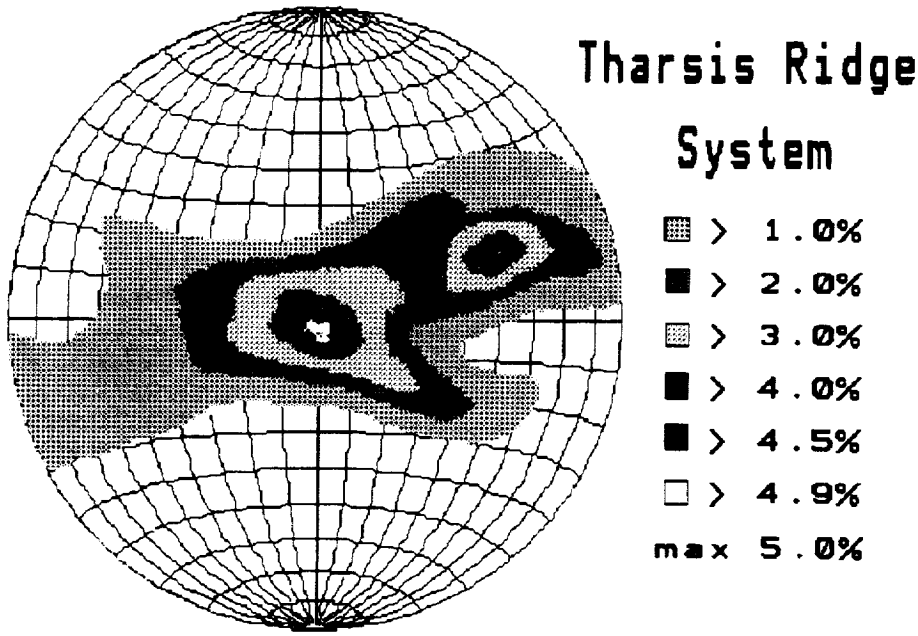


Fig. 1. Contours 1-2-3-4-4.5-4.9% per 1% area.

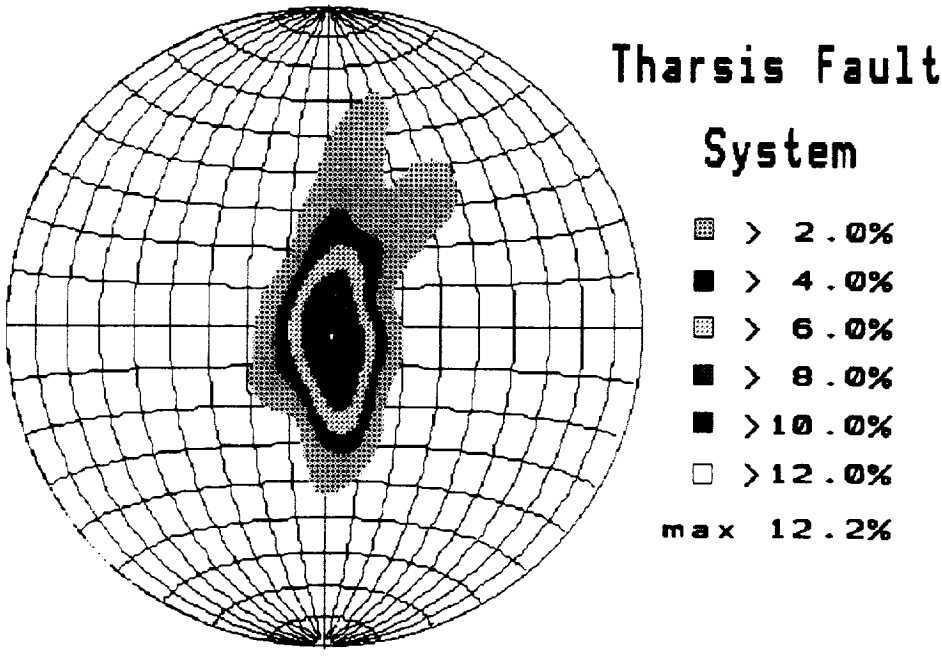


Fig. 2. Contours 2-4-6-8-10-12% per 1% area.

SIMULANTS FOR MARTIAN SURFACE MATERIALS; P. W. Weiblen, Space Science Center, U. of Minnesota, Minneapolis, MN 55455

Spectral-remote sensing observations and direct chemical and physical property measurements by the Viking Landers place constraints on the mineralogical and textural characteristics of the surface materials on Mars (1). Based on these data a number of terrestrial analogs for the fine dust components have been suggested, in particular, highly oxidized smectite clays with admixtures of iron oxyhydroxides and various sulfate minerals (2). Unfortunately, the available data on Martian materials is not sufficiently definitive to provide unambiguous guides to good choices for useful simulants which are already needed in the precursor research for future missions to Mars (Glaser, pers. comm., 1989).

Burns (3) noted that the chemistry and infrared spectra of hydrated, oxidized, iron-rich oikocrysts of olivine in Keweenawan (1.1 billion year old) olivine gabbros from the Midcontinent Rift (4) compare favorably with the Viking Lander and remote sensing data on Martian surface materials. The hydrated and oxidized iron-rich material has been referred to as "hisingerite" in the literature (5). It will be noted that compared to the Viking Lander data, the analyses of "hisingerite" are lower in alumina and lime. Addition of plagioclase would compensate for this difference. It is suggested that aeolian winnowing of hydrated and oxidized weathering products of basalt might produce such a mixture. It is interesting to note that in thin section the "hisingerite" is a bright red material. Analyses are in progress to characterize this material which appears to consist of a variety of ferric iron-rich clays associated with biotite, chlorite, and serpentine.

A simulant should be from a well-defined geologic site that is accessible and from which documented samples can be obtained. The occurrence of altered Keweenawan basalt on the North Shore of Lake Superior meets these criteria (4) and the necessary detailed characterization of collected material is now in progress to provide investigators with at least one possible simulant for Martian surface materials.

References: 1) Banin, A. (1988), LPI Technical Rpt. 88-07, 35,36. 2) Banin, A (1989) LPI Technical Rpt. 89-01, 15,17. 3) Burns, R.G. (1986) Nature, v. 320, #6, 55,56. 4) Weiblen, P.W., Saini-Eidukat, B., Miller, J.D. (1989) AGU Field Trip Guidebook T-345, 28th. Intl. Geol. Cong., pp. 43. 5) Whelan, J.A. & Goldich, S.S. (1961) Am. Min., v.46, 1412,1423.

N91-23007

# PRE-TERRESTRIAL ORIGIN OF "RUST" IN THE NAKHLA METEORITE.

Susan J. Wentworth[1] and James L. Gooding[2], [1]Lockheed/ESC, 2400 NASA Rd. 1, Houston TX 77058. [2]SN21/Planetary Science Branch, NASA/Johnson Space Center, Houston, TX 77058.

**INTRODUCTION.** As part of our campaign to identify and rigorously test evidence for aqueous geochemistry in shergottite, nakhlite, and chassignite (SNC) meteorites, we previously reported evidence for pre-terrestrial origin of calcium carbonate associated with silicate "rust" in Nakhla [1]. Here we present quantitative elemental compositions and summarize textural evidence for pre-terrestrial origin of the rust. We denote the material in question as "rust" because its phase composition remains unknown. The rust is probably the same as the iddingsite-like material reported by Bunch and Reid [2] and might be related to pockets of material called "brownies" by Papanastassiou and Wasserburg [3].

**SAMPLES AND METHODS.** Although our previous work on Nakhla [1,4,5] has also involved untreated interior and exterior chips obtained from the British Museum (Natural History), all data reported here were obtained from polished thin sections prepared from Nakhla specimen, USNM-426 (Smithsonian Institution). Scanning electron microscopy (SEM) and energy-dispersive X-ray spectrometry (EDS) followed our previously described procedures and included mineral-standardized, quantitative EDS analyses. Relative to conventional wavelength-dispersive microprobe analyses, our method permitted beam-spot sizes of 1-10 $\mu$m, as necessitated by the rust occurrences.

**RESULTS AND DISCUSSION.** *MICROSTRATIGRAPHY.* Compelling evidence for pre-terrestrial origin of the rust is found as rust veins truncated by fusion crust (Fig. 1) and preserved as faults in sutured igneous crystals (Fig. 2). Rust veins that approach the meteorite's fusion crust become discontinuous and exhibit vugs that suggest partial decrepitation; no rust veins that penetrate fusion crust have been found. Because the rust probably contains volatile compounds (see below), it is reasonable to expect that heating near the ablation surface (formed during atmospheric entry to Earth) would encourage devolatilization of the rust. Hence, absence of rust veins in fusion crust and vugs in rust veins near fusion crust (but not at distance from fusion crust) clearly imply that the rust existed in the meteorite before atmospheric entry. At least one unmistakable example of a vein post-dated by later endogenous events occurs as a faulted rust vein enclosed in an olivine crystal (Fig. 2). It is obvious that the rust vein has been broken by a fault but the two disjointed sections of the vein are separated by clear olivine rather than an open fracture. We infer that, after faulting, the fracture was at least partially healed by elevated pressure. It is difficult to conceive any reasonable natural processes that would break and suture an igneous mineral after the meteorite arrived on Earth. Accordingly, disturbance of the rust vein must have occurred before the meteorite arrived on Earth and, most likely, on the Nakhla parent planet. *COMPOSITION.* Our results for the average elemental composition of the rust (Table 1) generally agree with those of Bunch and Reid [2] except for Al and Na. Compared with the earlier data [2], we find much lower Al. Because our analyses of Al in Nakhla plagioclase and pyroxene agree with the respective data of Bunch and Reid [2], no systematic analytical error is suspected in our Al data. Our Na results for plagioclase agree with those of Bunch and Reid [2] but are systematically high relative to reference samples that contain very minor to trace Na. We conclude that the rust actually contains < 1% $Na_2O$. Low analytical totals, both in

Table 1. Elemental compositions (weight percent) of rust in Nakhla determined by electron probe microanalysis (all iron calculated as $Fe_2O_3$; EDS background problem makes our Na results systematically high; nr = not reported).

| | $SiO_2$ | $TiO_2$ | $Al_2O_3$ | $Cr_2O_3$ | $Fe_2O_3$ | NiO | MnO | MgO | CaO | $Na_2O$ | $K_2O$ | $P_2O_5$ | $SO_3$ | Cl | Total |
|---|---|---|---|---|---|---|---|---|---|---|---|---|---|---|---|
| Avg. of 78 spots | 40.21 | 0.02 | 0.74 | 0.03 | 37.93 | < 0.01 | 0.63 | 6.82 | 1.14 | (1.16) | 0.60 | 0.06 | 0.14 | 0.66 | 90.13 |
| Standard deviation (this work) | 3.66 | 0.03 | 0.31 | 0.03 | 4.68 | 0.01 | 0.26 | 0.71 | 1.51 | (0.37) | 0.17 | 0.09 | 0.12 | 0.33 | |
| Unknown "iddingsite" (Bunch and Reid [2]) | 43.6 | nr | 5.8 | nr | 30.56 | nr | 0.37 | 9.4 | 0.73 | 0.21 | 0.10 | nr | nr | nr | 90.77 |

our data and in those of Bunch and Reid [2], suggest that the rust contains water. Although admixed carbonate occurs in some places [1], carbon contents in carbonate-free areas are near background levels and do not contribute significantly to the deficit. Intrinsic sulfur is very low except in those places where admixed calcium sulfate is found. Chlorine, however, is a characteristic component that is not correlated with known occurrences of sodium chloride. The fluids that deposited the rust probably carried chloride that was not indigenous to the igneous-rock parent of Nakhla. Absence of significant interelemental correlations implies that the rust is a single phase with compositional heterogeneities at the scale of 1-10 $\mu$m. Poor crystallinity was previously inferred from a preliminary transmission electron microscopy (TEM) study [6]. In terms of a single-phase model, structural-formula calculations by the method of Gooding [7] show that our average rust composition gives nearly equal goodness-of-fit values for dioctahedral smectite and stilpnomelane. By definition, genuine iddingsite (a smectite-goethite mixture), would contain smectite as a major component. New high-resolution TEM analyses are needed to verify whether the rust is crystalline or mostly a colloidal gel.

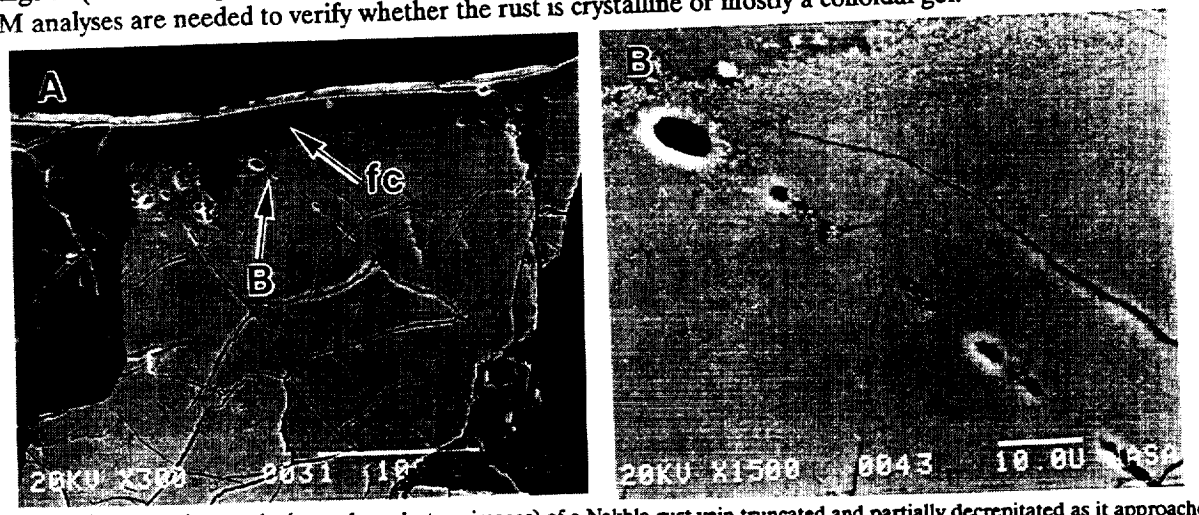


Figure 1. SEM photomicrographs (secondary-electron images) of a Nakhla rust vein truncated and partially decrepitated as it approaches fusion crust (fc). Scale bars are in micrometers.

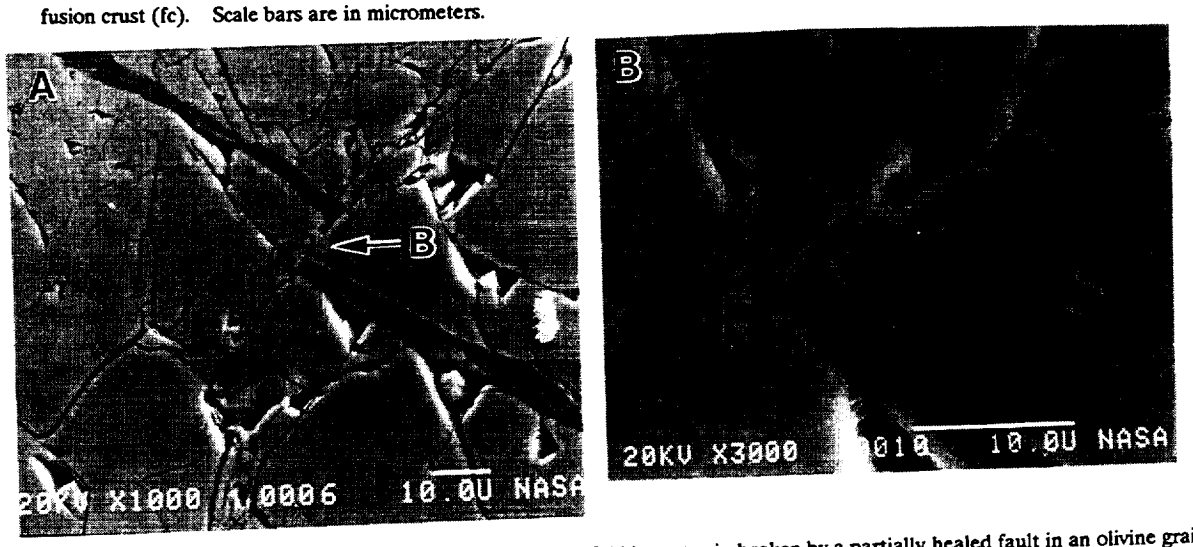


Figure 2. SEM photomicrographs (secondary-electron images) of a Nakhla rust vein broken by a partially healed fault in an olivine grain. Frame (B) is a detailed view of the area marked by an arrow in (A). Scale bars are in micrometers.

**References.** [1] Wentworth S. J. and Gooding J. L. (1989) *Lunar Planet. Sci XX*, LPI, Houston, p. 1193-1194. [2] Bunch T. E. and Reid A. M. (1975) *Meteoritics, 10*, p. 303-315. [3] Papanastassiou D. A. and Wasserburg G. J. (1974) *Geophys. Res. Lett., 1*, p. 23-26. [4] Wentworth S. J. and Gooding J. L. (1988) *Lunar Planet. Sci. XIX*, LPI, Houston, p. 1261-1262. [5] Wentworth S. J. and Gooding J. L. (1988) *Meteoritics, 23*, p. 310. [6] Ashworth J. R. and Hutchison R. (1975) *Nature, 256*, p. 714-715. [7] Gooding J. L. (1985) *Lunar Planet. Sci. XVI*, LPI, Houston, p. 278-279.

A MODEL FOR CRUSTAL SUBDUCTION BY LARGE IMPACTS; R. W. Wichman and P. H. Schultz, Dept of Geological Sciences, Brown University, Providence, R.I. 02912.

**Introduction:** In the standard model of crater excavation, ballistically ejected material represents only about half the volume of the transient cavity (1). The other half corresponds to downwardly displaced, shock-compressed material driven beneath the transient cavity (e.g., 1, 2, 3, 4, 5). In large craters, the final crater then forms by the collapse of this transient cavity with uplift and inward flow of the shocked, displaced material comprising the crater floor (6). Although this idealized model of crater formation fits most well-preserved planetary impact structures, it implicitly assumes an elastic halfspace beneath the target surface which may be inappropriate for modeling the largest early basin-forming impacts. For these very large impacts, the depth of the transient cavity may excede the lithospheric thickness and, at least on Mars, such cavities apparently can interact with underlying viscous mantle regimes during basin formation (7). The extreme size of these cratering events also challenges some of the assumptions concerning cavity growth and collapse extrapolated from smaller structures (8). In this abstract, we propose that viscous deformation beneath very large impacts can allow emplacement of vertically displaced crustal material in the mantle, and we speculate on the implications such "impact subduction" might have for subsequent mantle evolution.

**Subduction Model:** Although material flow fields result in ballistic trajectories for most near-surface regions of the transient cavity, a full target section is preserved under the center of the impact. In the case of an elastic half space, compression of this section against undeformed rocks at greater depth enhances lateral flow, disrupting the column and spreading it across the base of the transient cavity. If viscous flow occurs beneath the impact, however, downward displacement of this crustal section is partly accomodated by lateral flow in the mantle below. This process transfers impact deformation from the lithospheric section to the mantle and results in the emplacement of shocked crustal material into rocks of the upper mantle or asthenosphere. Although later dynamic rebound might limit the depths such material could reach, rebound uplifts the region beneath the crater as a whole (not the displaced elements of the transient cavity alone) and the sub-impact crustal section initially should stay in the mantle.

Viscous deformation of the mantle during impact is thus a necesary condition for the emplacement of crustal sections at depth. The probability of such deformation can be evaluated by comparing the duration of the impact event to the Maxwell time ($T_m$) of the mantle: $T_m = \tau/2\mu\,\dot{\epsilon}$ where $\tau$ is applied shear stress, $\mu$ is shear modulus (~ $10^6$ MPa) and $\dot{\epsilon}$ is strain rate of deformation. The Maxwell time is defined as the time required for viscous creep under stress to equal elastic strain (9); consequently, viscous behavior occurs when deformation times are greater than $T_m$. Deformation is essentially elastic for timescales less than $T_m$ (9). If an impact generates shear stresses of over 10 kilobars ($10^3$ MPa), strain rates in an olivine mantle range from $10^{-2}$ to $10^{-4}$ /s for mantle temperatures of 800–1000°C (10). These values translate to Maxwell times on the order of 1–100 seconds. Because mantle flow requires that the duration of impact exceed $T_m$, only large, low-velocity (5–6 km/s) impactors (which have impactor penetration times of several tens of seconds (8)) are likely to induce such a viscous mantle response.

The extent of viscous deformation beneath an impact depends on the impact angle and the duration of the impact relative to $T_m$. If we define $d$ as the depth of the transient cavity (roughly the penetration depth of the projectile into the target), for near-vertical (>60°) impacts, $d$ can be approximated by the projectile diameter ($D_p$) but $d$ decreases significantly as the impact angle is then reduced to 5° (11). While rare, near-vertical impacts are not improbable and are the most likely to emplace material at depth in the mantle. For a near-vertical impact with a duration equal to $T_m$, therefore, we expect viscous mantle deformation comparable to the size of the impact cavity extending to depths of ~$D_p$ beneath the base of the transient cavity. Since the thickness of the down-driven core is of the same scale as the mantle deformation, the crustal section remains near the base of the transient cavity and is likely to be embedded in the basin floor after dynamic rebound. If the duration of the impact is significantly greater than $T_m$, however, lithospheric material can penetrate the mantle to depths of several $D_p$. We propose that mantle flow will engulf this displaced crustal section outright with depths of crustal burial in the range of ~ $0.5D_p$ to $2D_p$. This burial of crustal material in the mantle is reminiscent of terrestrial plate subduction and, for a projectile 200 km in diameter, such "subduction" could bury crust to depths of between 100 and 400 km.

The requirement of large, low-velocity impacts for this subduction mechanism limits the extent of this process in planetary history. First, impacts of sufficient size are restricted to the period of basin-forming impacts before ~3.7 Ga. The low impact velocity, however, is a stronger constraint on the occurrence of impact subduction, since only a few planetary impactor populations permit impacts at 5–6 km/s. The planet most likely to have experienced such collisions is Mars, where impact velocities range down to ~5 km/s for co-orbiting, heliocentric objects (12). The coincidence in age of these basins with a time of predicted high mantle temperatures (13) also favors subduction by this mechanism. On the Earth and Venus, impact velocities range from 15–40 km/s and 17–44 km/s, respectively (8,14) and impact subduction is much less likely. Although viscous deformation beneath the impact is still possible at velocities of 15 km/s (for mantle temperatures on the order of

1300–1400°), the increased extent of of vaporization and melting beneath the impact may preclude preservation of a lithospheric section in the mantle during cavity collapse. Some contamination of the mantle by projectile or crustal components might still be expected, however. On Mercury, the predicted impact velocities for comets and earth-crossing asteroids (~34–44 km/s (8)) probably preclude impact subduction. Nevertheless, impactors from the postulated population of Vulcan asteroids (15) should have had much lower velocities, so impact subduction is also possible for Mercury. The probability of subduction on the Moon (impact velocities down to ~6 km/s (12)), depends more strongly on the state of the lunar interior. Thinner lithospheres associated with a magma ocean might permit early subduction events, but the growth of the lithosphere over time would inhibit mantle flow and prevent later subduction.

**Implications:** Unlike the more continuous subduction of oceanic plates observed on Earth, impact subduction is randomly located and episodic on a global scale. Hence only random and isolated regions of a planetary mantle can be modified by this process. Long-term effects of oceanic subduction such as repeated passage of melts into island arcs or convection beneath back arc basins are thus unlikely to occur for impact subduction. In further contrast, mantle cooling associated with subduction of cold lithospheric plates should not occur with impact subduction due to both shock heating and shear deformation in the subducted section. To first order, this section is presumed to be in thermal equilibrium with normal mantle temperatures at the time of emplacement. Although such a view is over simplistic, the mantle evolution sequence presented below can be regarded as indicative of the relative time scales required to achieve various mantle states.

Impact subduction can potentially influence mantle evolution in two ways. Injection of crustal radiogenic elements into the mantle could affect the long-term thermal history, whereas the introduction of crustal volatiles could affect the melting sequence. In the first case, a crustal block would begin to melt in ~4–6 Ma for subduction to 10 kb pressure with an initial post-impact temperature of 1000°C. Total equilibrium melting then would occur in 9–11 Ma. Significant mantle melting is unlikely to result in this time, since ~16 Ma are needed to achieve lherzolite melting temperatures outside a subducted crustal block. The melting of embedded crustal material, however, will influence the long term thermal evolution of the surrounding mantle. Since a fraction of melt is trapped along grain boundaries during porous flow, we can approximate the mantle composition after crustal melting by mixing a disseminated crustal component into the mantle. For mantle-crust ratios of 100:1, such mixing can double the abundance of heat producing elements in the mantle and these added heat sources eventually can induce mantle partial melts some 100–500 Ma after the subduction event.

The subduction of volatile concentrations could produce mantle melts on much shorter time scales. Although water is unlikely to be a major constituent of the crustal section as a whole, water or ice may be concentrated in near surface regions. For a volatile-rich regolith 500 m thick with 25% porosity, subduction under a 100-km radius projectile can subduct over 1000 $km^3$ of water. If the projectile caps the subducted section and drives it into the mantle, this volatile phase may not escape into the transient cavity and will be trapped instead near the top of the crustal section. Addition of such a vapor phase to surrounding mantle compositions significantly reduces the solidus temperatures and, at 1000°C and 10 kb, can initiate immediate mantle melting. If carbonates are present in the martian regolith, the associated fluid-rich and volatile phases could possibly acheive a kimberlitic character.

**Conclusions:** Large, low velocity impacts may inject significant crustal sections into a planetary mantle, but this process will be most efficient if the mantle yields viscously around impact-driven subsidence. Such behavior is most likely before 3.7 Ga on Mars, but also may have occurred on Mercury or the early Moon. The depth of subduction is dependent on the relative scale of impact and mantle flow regimes, but can achieve depths of over 100–200 km for projectiles over 100 km in radius. The effects of such subduction on mantle evolution are unlike those observed in terrestrial subduction zones and primarily reflect the effects of subducted volatile and radiogenic isotope concentrations. Escape of vapor into the mantle should produce kimberlite-like mantle melts soon after impact. Crustal melts develop some 5–10 Ma after impact and enrich higher mantle regions in radiogenic isotopes. Finally, isotopic heating of this enriched mantle may lead to renewed mantle melting several hundred million years after the original impact event. Such a mantle melt sequence may fit the general sequence of highland volcanism observed on Mars where explosive, patera volcanism evidently preceded formation of most of the basaltic shields and ridged plains (16).

REFERENCES: 1) Stoffler et al (1975) *J. Geophys. Res. 80*, p. 4062–4077. 2) Gault et al (1968) In *Shock Metamorphism of Natural Materials* (R.M. French and N.M. Short, eds.) p. 87–99. 3) Dence et al (1977) In *Impact and Explosion Cratering* (D.J. Roddy, R.O. Peppin and R.B. Merrill, eds.) p. 247–275. 4) Schultz et al (1981) *Proc. Lunar Planet. Sci. 12A*, p. 181–195. 5) Croft (1981) *Proc. Lunar Planet. Sci. 12A*, p. 207–225. 6) Grieve (1981) *Proc. Lunar Planet. Sci. 12A*, p. 37–57. 7) Wichman and Schultz (1989) *J. Geophys. Res. 94*, 17333–17357. 8) Schultz (1988) In *Mercury* (F. Villas, C.R. Chapman and M.S. Matthews, eds.) p. 274–335. 9) Melosh (1989) *Impact Cratering*, p. 156. 10) Stocker and Ashby (1973) *Rev. Geophys. Space Physics 11*, p. 391–426. 11) Gault and Wedekind (1978) *Proc. Lunar Planet. Sci. Conf. 9*, 3843–3875. 12) Hartmann (1977) *Icarus 31*, 260–276. 13) Schubert et al (1979) *Icarus 38*, 192–211. 14) Shoemaker (1977) *Impact and Explosion Cratering* (Roddy, D.J., Peppin, R.D., and Merrill, R.B., eds) pp. 617–628. 15) Leake et al (1987) *Icarus 71*, 350–375. 16) Greeley and Spudis (1981) *Rev. Geoph. Space Phys. 19*, 13–41.

LARGE SCALE COMPRESSION STRUCTURES IN THE ERIDANIA–PHAETHONTIS REGION: MORE EVIDENCE FOR POLAR WANDERING. R. W. Wichman and P. H. Schultz, Dept. of Geological Sciences, Brown University, Providence R.I.

**INTRODUCTION:** Although most tectonic structures on Mars can be associated with stresses due to either Tharsis formation (1,2,3,4) or basin modification (4,5,6), some structures in the martian highlands appear to be independent of both stress sources. Two major systems of ridges and scarps rival the lobate scarps of Mercury in size and indicate that a large, regional–scale compressional event occurred in the Terra Cimmeria/Terra Sirenum region (7). These structures cannot be explained by either Tharsis–centered or basin–centered regional stress models, but may reflect deformation due to polar wandering as predicted by Melosh (8). If the Tharsis Province was not so interesting tectonically, the size and isolation of these features would have attracted immediate attention and possibly stimulated discussions comparable to those of the mid–1970's for Mercury. In this abstract, we use crater deformation to estimate the amount of crustal shortening across these scarp/ridge systems and reconsider the possible sources the causative compressional stress field.

**FEATURE DESCRIPTION:** The ridge systems described here are Eridania Scopulus and a system of scarps and ridges located near the Copernicus impact basin. The two systems are of similar age with crater dates (derived from linear crater counts (6,9)) of ~381 ± 270 and ~341 ± 240 $N(>5)/10^6$ $km^2$, respectively. The Copernicus ridge system is at least 840 km in length, whereas Eridania Scopulus extends over 1000 km. Shadow measurements indicate typical scarp and ridge heights of 500–700 m with a maximum relief exceeding 1 km. The systems are thus comparable in size and scale of deformation to the mercurian lobate scarps, which are typically several hundreds of kilometers in length and range in relief from a few hundreds of meters to one or two kilometers (10,11). The martian systems differ, however, in detailed morphology from the mercurian lobate scarps. The mercurian scarps are typically more rounded and flatter in profile than the martian features; and while the mercurian scarps occur as long, individual features, the martian systems are continuous bands of deformation 100 to 200 km wide containing between 2 and 5 distinct, parallel to subparallel structures. In general, these structures are scarp–like with a backslope away from the scarp on the uplifted side. Where they cross the floors of large craters (>20 km diameter) or intercrater plains units, scarp expression is subdued and more rounded. In some plains regions the scarps then merge into wrinkle ridge systems of the same orientation. Finally, the martian scarp systems coincide with or form apparent linear topographic highs (figure 1). Such behavior is not characteristic of the mercurian lobate scarps and may reflect the combined effects of uplift across individual structures in the martian systems.

**CRUSTAL SHORTENING:** The nature and degree of deformation in the martian ridge/scarps are best revealed by the modification of craters. Deformation most commonly joins scarps of higher relief on each side of the crater with a linear, asymmetric ridge cutting directly across the crater floor. This pattern resembles crater deformation along the mercurian lobate scarps (11), but differs from the typical deformation associated with smaller wrinkle ridges, which tend to curve around a crater interior instead of cutting directly across it (4,12). A less common modification along the martian ridge/scarps preserves partial craters on the elevated side of a scarp but does not preserve the corresponding down–thrown rim sections (figure 1). Three craters appear foreshortened due to compressional deformation; one of these also shows an offset rim along the scarp resembling deformation of the Guido d'Arezzo crater by the Vostok scarp on Mercury (11). For initially circular craters with no extension perpendicular to compression, the difference between the long and short axes of a deformed crater provides a measure of the regional shortening across the structure. Such measurements for these three craters indicate on the order of 1.5–3 km of crustal shortening across individual scarp features. This is comparable to the values derived by Strom et al (10) for Mercury, where approximately 1–2 km of shortening is estimated for individual mercurian lobate scarps.

The linear nature of deformation in crater interiors and the preservation of uplifted partial craters are consistent with compression by deep–seated thrust or reverse faulting. Consequently, the observed scarp relief helps to constrain fault models for comparison with the observed crater shortening. For a reverse fault with a dip of 60° and a scarp 500 m in elevation, we would expect ~290 m of shortening, a value some 5 to 10 times smaller than that indicated by the deformed craters. Alternatively, a thrust fault with a dip of 25° and scarp relief of 500 m would indicate ~1000 m of shortening, consistent with the estimated crater deformation. Therefore, a thrust fault model for these scarps appears consistent with the observed deformation, and the parallel scarps in the Eridania and Copernicus–Newton systems might represent systems of associated thrust sheets. If the shortening over each thrust is on the order of 1–2 km, in keeping with the crater deformation, such systems could accomodate up to 5 to 10 km of regional shortening perpendicular to the scarp trends.

**DISCUSSION:** The timing of this compressional event can be derived from the crater ages of the two systems and is broadly correlated to the time of Tharsis formation (figure 2). Due to the large error bars, however, these age determinations encompass both the time of ancient Tharsis faulting and the later main phase of Tharsis radial fracturing. Although coincident in time with Tharsis–centered

deformation, the scarp/ridge systems occur over 70° from the center of Tharsis. Of the Tharsis load models developed by Banerdt et al (3), only the isostatic load model could provide compressive stresses at this distance from Tharsis. Based on the observed deformation east of Tharsis, however, Banerdt et al argue that this model only applies to regions less than 40° from the Tharsis center. Furthermore, the two scarp/ridge systems occur at a distinct angle to each other; neither trend is consistent with the Tharsis stress orientations. Because the systems are well removed from the nearest recognized large impact basins (Hellas, Isidis), basin-centered stresses also seems negligible. Even if a large buried basin did exist in the region, current models of basin-centered deformation (6) could not account for the observed pattern of regional compression.

Some significant regional stress field independent of both Tharsis and basin-controlled deformation thus appears responsible for the formation of these ridge/scarp systems. The global contraction mechanism proposed for Mercury (10,11) seems unlikely on Mars given the early timing and regional scale of the ridge/scarps as well as the widespread contemporary extension associated with Tharsis. Polar wandering, however, can simultaneously produce regions of compressive and tensile stress at the several kilobar level (8), thereby producing the scale of deformation indicated by the crater shortening data. The location and orientation of the scarp/ridge systems are consistent with polar wandering in response to Tharsis development (7), as is the correlation in age of ridge formation with initial Tharsis activity.

**CONCLUSIONS:** Large ridge/scarp systems in the Terra Cimeria/Terra Sirenum region appear to reflect a major regional event of compressional deformation with regional crustal shortening of up to 5–10 km. Although contemporary with Tharsis fracturing, ridge system formation appears to be independent of Tharsis stress fields and is more consistent with deformation expected in the polar wander scenario of Schultz and Lutz (7).

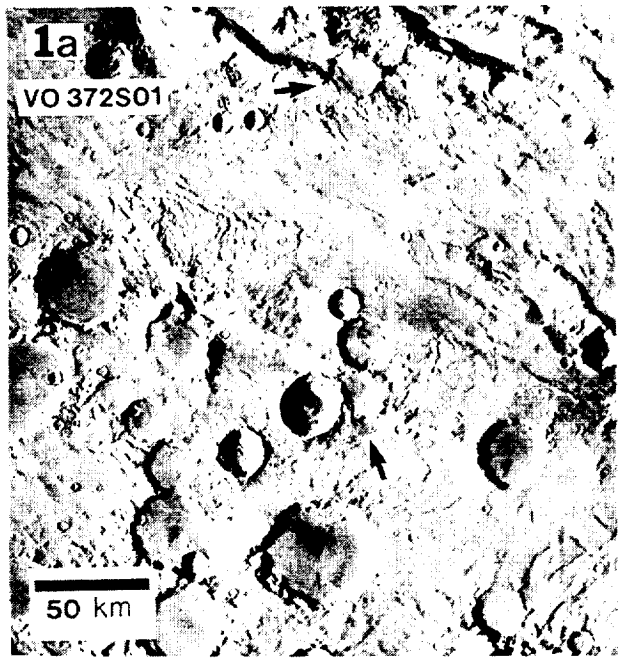


**Figure 1.** Parts of the Copernicus system (a) and Eridania Scopulus (b). Arrows indicate craters modified by scarp formation.

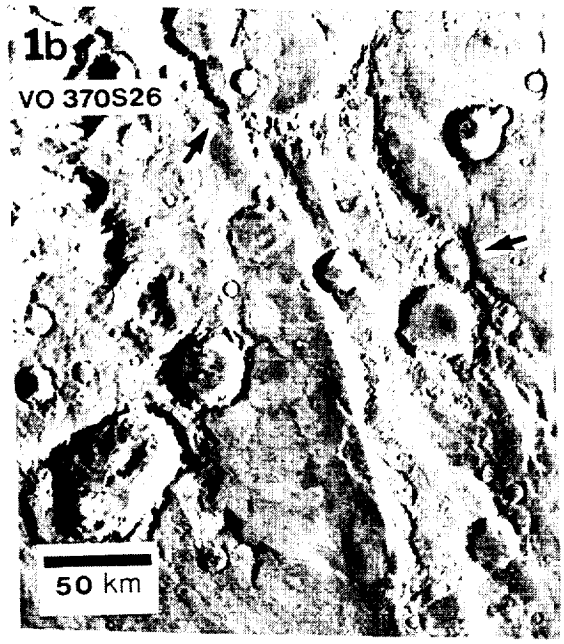


**REFERENCES:** 1)Wise et al (1979) *Icarus 38*, 456-472. 2)Plescia and Saunders (1982) *J. Geoph. Res. 87*, 9775-9791. 3) Banerdt et al (1982) *J. Geoph. Res. 87*, 9723-9734. 4) Chicarro et al (1985) *Icarus 63*, 153-174. 5) Wichman and Schultz (1987) *Lunar Planet. Sci. Conf. 18*, 1078-1079. 6) Wichman and Schultz (1989) *J. Geoph. Res. 94*, 17333-17357. 7) Schultz and Lutz (1988) *Icarus 73*, 91-141. 8) Melosh (1980) *Icarus 44*, 745-751. 9) Wichman and Schultz (1986) *Lunar Planet. Sci. Conf. 17*, 942-943. 10) Strom et al (1975) *J. Geoph. Res. 80*, 2478-2507. 11) Strom (1978) *Space Sci. Rev. 24*, 3-70. 12) Schultz (1976) *Moon Morphology.*

## 2. AGE OF RIDGE/SCARP SYSTEMS

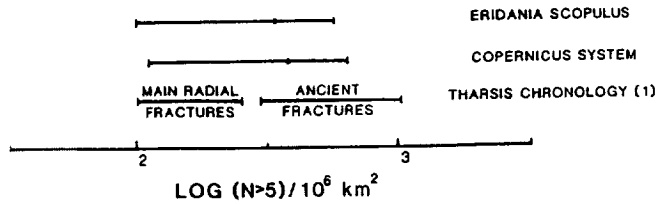


**Figure 2.** Crater ages derived from linear crater counts (6) for the scarp/ridge systems compared to the Tharsis tectonic history of Wise et al (1).

**POSSIBLE AEOLIAN MEGARIPPLES ON MARS;** S. H. Williams, Lunar and Planetary Institute, Houston, TX 77058

Images with sufficiently high spatial resolution are required for the accurate remote identification of surface units and landforms and the determination of the geologic history of a region. Less than 1% of the Viking orbiter image dataset has spatial resolutions less than 10 meters/pixel (1). The lower-resolution images contain much useful information; however, information that would otherwise be invisible is revealed in the higher-resolution images (1). The point is well illustrated in the Acheron Fossae region of Mars by one of the highest-resolution Viking image sequences (Figure 1). There, valleys are filled with what was interpreted as smooth layers of debris mass wasted from the valley walls, based on 57 m/pxl images from the Viking primary mission (2,3). Viking frames 442B01-10, at 8 m/pxl resolution, show that the valley floors are not smooth at all, but rather are covered with mounds of material interpreted as dunes (1). The morphology of the mounds closely resembles both the eroded remnants of a once more extensive covering layer (Figure 2) and the dunes associated with some terrestrial *draa* (4). Contrast enhancement and detailed analysis of the images in the sequence may lead to a slightly different conclusion: the mounds may be yardangs; erosional, not depositional, features. The mounds for the most part parallel the valleys, as would be expected from wind erosion.

Striations oriented perpendicular to the valley axis can be seen in several locations (Figure 1). The are spaced approximately 50 m apart and are most common at the valley wall/floor junction, although they are also found among the mounds in the middle of the valley. The striations are here interpreted to be aeolian megaripples formed from debris weathered from the yardangs. Terrestrial aeolian megaripples have wavelengths up to 25 m (5); it is not unreasonable that larger megaripples might form under favorable martian conditions, given the wind speeds available and the lower martian gravity. If the megaripple interpretation is correct, then by terrestrial analog the deposit in which they occur has a bimodal particle size distribution (5,6). One size will undergo saltation, the other, concentrated at the crests of the megaripples, is too large and/or too dense to be put into saltation (6). For Mars, the former is sand-sized (a few hundred microns), the latter, gravel-sized, provided the materials have typical densities. The presence of megaripples constrains models of surface erosion; particles of specific sizes and local wind speeds on the order of 100 m/s are required (5). The presence of megaripples among the mounds supports the notion that the latter are erosional features, as it is less likely that two different-sized bedforms in loose material would superimpose into the observed pattern. Further, megaripples indicate that the particles in the ripples are strong enough to withstand being transported at least short distances by the wind and being exposed to frequent saltation impact.

The megaripples of Acheron Fossae exist because of a favorable combination of conditions: regional wind pattern, topographic control of local winds and sediment transport, and overall sediment supply and mobility. Similar conditions must prevail in many places on Mars; we see only these few because of limited photographic coverage. Improved data from future missions raises the exciting prospect of assessing in more detail the degree of aeolian modification of the martian surface.

REFERENCES

1) Zimbelman, J. R. (1987), *Icarus, 71*, 257-267; 2) Squyres, S. W. (1978), *Icarus, 34*, 600-613; 3) Squyres, S. W. (1979) *Jour. Geophys. Res., 84*, 8087-8096; 4) Wilson, I. G. (1972) *Sedimentology, 19*, 173-210; 5) Greeley, R. and J. Iversen (1985), *Wind as a Geological Process on Earth, Mars, Venus, and Titan*, Cambridge; 6) Greeley, R. and A.R. Peterfreund (1981), *GSA Abs. w/ Prog., 13*, n. 7, 463.

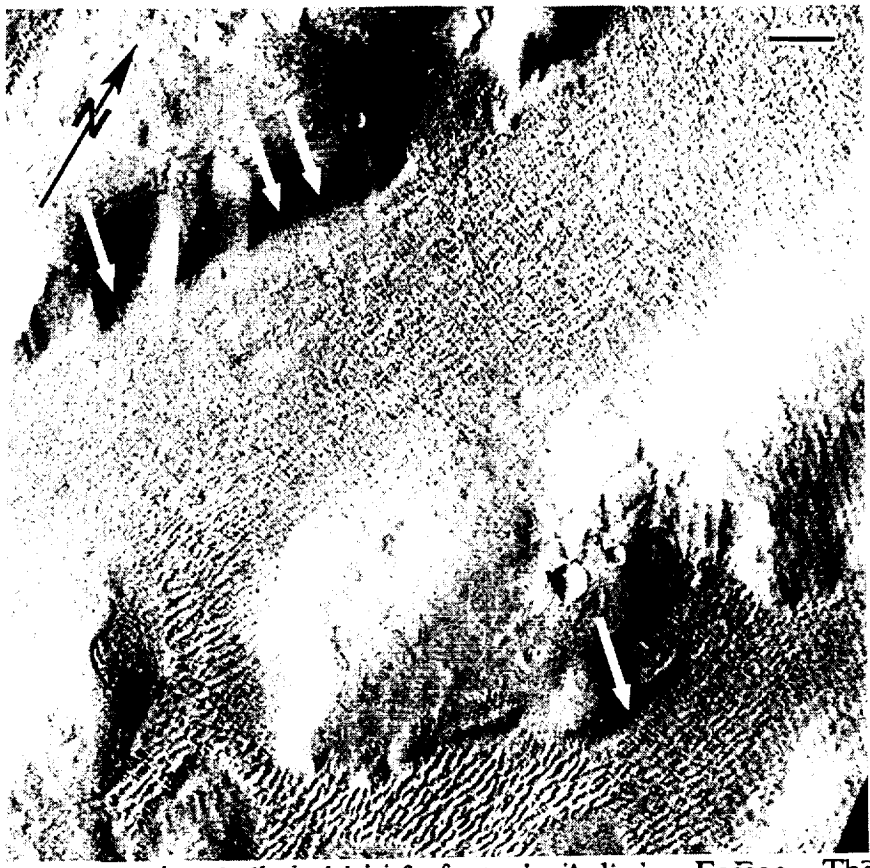

**Figure 1.** Wind erosion and deposition features in Acheron Fossae. The larger mounds in the valleys are probably erosional, the smaller striations (white arrows) are probably aeolian megaripples. Part of Viking orbiter frame 442B10, NGF orthographic version with maximum contrast enhancement by a simple linear stretch. The scale bar is 1 km long.

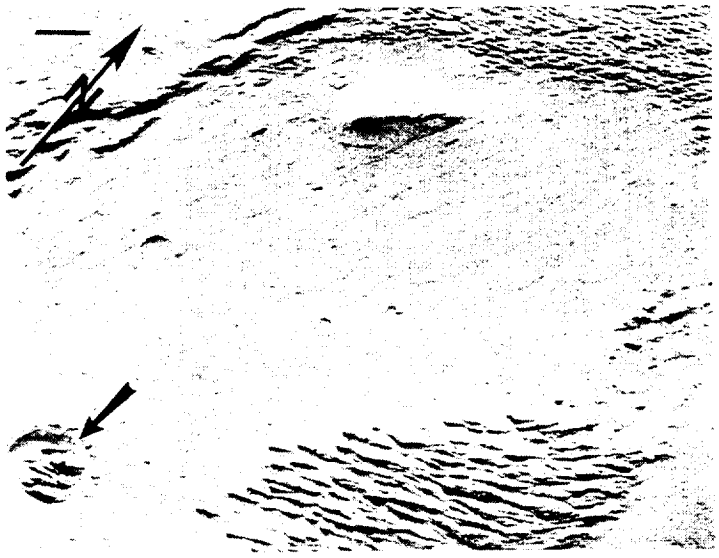

**Figure 2.** Erosional remnants of an older cover persist as yardangs in topographically-protected locations, here a crater undergoing erosional exhumation. Part of Viking orbiter frame 728A62, NGF rectilinear version. The scale bar is 1 km long.

**PRELIMINARY GEOLOGIC MAPPING NEAR THE NILOSYRTIS MENSAE, MARS;** Steven H. Williams, Lunar and Planetary Institute, 3303 NASA Road 1, Houston, TX 77058 and James R. Zimbelman, Center for Earth and Planetary Studies, National Air and Space Museum, Smithsonian Institution, Washington, DC, 20560.

Geologic mapping (1:500,000 scale) of the MTM 40292 and 40297 quadrangles in southwestern Utopia north of the Protonilus Mensae is being conducted as a part of the Mars Geologic Mapping program; this is a preliminary report. The study area is located in MC-6SW (37.5-42.5$^{o}$ latitude, 290-300$^{o}$ longitude) on the lowland side of the global dichotomy boundary. The area near the boundary is of considerable interest because the nature and timing of geologic events that have occurred there can be used to constrain models of the origin and evolution of the dichotomy. The mapping will address the sequence of geologic events that have formed and modified the lowland terrain near the boundary, specifically the origin, nature, and erosion of any mantling deposits.

Previous mapping on a global scale (1) identified the basic regional geologic units: Hesperian-age rolling plains to the north, Hesperian-age knobby materials, and Amazonian-age cratered plains. Later mapping grouped the older units together and identified the smoother materials in the study area as Amazonian-age smooth and etched plains (2). Outside of the study area, there are Hesperian-age plains to the north in Utopia Planitia and Noachian-age plateau units to the south whose surface morphology indicates they overlie heavily cratered terrain (2).

Virtually the entire map area is mantled by an irregular deposit of material that is apparently fine-grained and erodible (Figures 1 and 2). It is also extremely young, as there is not a single crater larger than 1 km in the map area that was emplaced atop the mantle. The volcanic plains unit beneath the mantle has an N(2) age of ~500 (Upper Hesperian) and an N(1) age of ~1200 (middle Lower Amazonian). The former is considered more reliable because no doubt some of the 1 km craters are completely mantled. An Upper Hesperian age for the plains is consistent with the presence on them of clusters of secondary craters whose orientation suggests they were formed by ejecta from the Lyot impact, which occurred in the Lower Amazonian (3).

Knobs abound in the study area; many are presumably caused by the mantling of pre-existing topography, and, in many cases, the older core of the knob is exposed. Many such knob cores are surrounded by small scarplets; it is not yet clear whether the scarplets are the eroded edges of mantle beds that at one time draped over the knob core and have been subsequently exposed by erosion or they are eroded versions of the lobate debris aprons described in (4). There appears to be a morphologic distinction between the knobs that are remnants of the Noachian-age plateau units to the south and those that are reflections of the topography of the heavily cratered basement, as indicated by their distribution. Many craters in the study area contain concentric crater fill, which may indicate downslope movement of volatile-rich material (5) or repeated cycles of aeolian gradation (6). The mantle is probably fine-grained and poorly consolidated, as indicated by its much greater susceptibility to erosion relative to other units. Occasional channels and terrain softening features are additional evidence that the mantle was at one time volatile-rich (Figures 1 and 2); perhaps the mantle is an air-fall deposit of some sort (7).

**REFERENCES**

1) Scott, D.H. and M.H. Carr (1978), *USGS Map I-1083*; 2) Greeley, R. and J.E. Guest (1987), *USGS Map I-1802-B*; 3) Tanaka, K.L. (1986), *J. Geophys. Res.*, *91*, E139-E158; 4) Squyres, S.W. (1979), *J. Geophys. Res.*, *84*, 8087-8096; 5) Squyres, S.W. (1989), *Icarus*, *79*, 229-288; 6) Zimbelman, J.R., S.M. Clifford, and S.H. Williams (1989), *Proceedings 19th LPSC*, 397-407; 7) Williams, S.H. and J.R. Zimbelman (1989), in *LPSC XX*, 1209-1210.


Figure 1. The structure of the mantling unit is complex. Some knobs protrude above the mantle, others do not; it is not yet clear whether the mantle used to drape over the knobs and has been eroded back or the knobs are surrounded by an eroded debris apron. The mantle appears to be draped over the rim of crater Renaudot at the top of the image and locally has undergone surface channeling (arrow). Viking frame 234S76, NGF orthographic version; the scale bar is 10 km long.


Figure 2. The study area has many craters with concentric crater fill (arrows). The mantle is not so thick that it completely buries the small craters on the unit beneath it. Naturally, the best-developed channels (right side) lie just outside the study area. Viking frame 235S03, NGF orthographic version; the scale bar is 10 km long.

WIDTHS OF DIKES ON EARTH AND MARS; Lionel Wilson and Elisabeth A. Parfitt, Environmental Science Division, Lancaster University, Lancaster LA1 4YQ, U.K.

The widths of basaltic bodies on Earth currently classified as dikes vary from ~ a few cm to ~5 m in the rift zones of Hawaiian volcanoes (1, 2), through ~25 m for tertiary dikes in the north of England (3), to ~6 km for macro-dikes such as the Great Dike of Zimbabwe (4, 5). All of these bodies are classified as dikes on the basis that they are planar, i.e., their extent in one horizontal direction (length) is very much greater than their extent in the other (width). Their vertical extent cannot generally be determined, but is commonly inferred also to be much greater than the width. The term 'dike' is currently used not only to describe the morphology of planar rock bodies but also to imply the mechanism of their emplacement: dikes are assumed to be the result of the forcible intrusion of magma into sub-surface fractures which are themselves produced by the magma migration (6). The great widths of macro-dikes on Earth then have profound implications for the pressure and stress conditions under which they were emplaced. The question of dike widths on Mars has been raised in connection with the high effusion rates inferred for some martian lavas (7). We investigate the maximum dike widths likely to occur on both planets.

The geometry of an intruded dike is a function of the pressure at the dike centre, the depth to the centre, the density contrast between the magma and country rocks, the regional tension gradient, the planetary gravity and the fracture toughness of the host rocks (8-13). Rubin and Pollard (13) give equations for the stability of dikes originating in central, relatively shallow magma reservoirs and emplaced laterally within the rift zones of oceanic hot-spot shield volcanoes like Kilauea, Hawaii. The main characteristic of such dikes is that they have greater lateral than vertical extent. Recent work shows that this lateral emplacement is common in extensional tectonic environments on Earth: the central rifting zone of Iceland (14) is clearly populated by similar systems of reservoirs and lateral dike swarms, and the spatial variations of composition of samples dredged from ocean floor spreading ridges are consistent with such a pattern (15). Continental rift systems are also characterised by chains of central volcanoes with lateral rift zones (16). On Mars, some volcanoes such as Arsia Mons and Pavonis Mons have rift zones morphologically similar to those of terrestrial oceanic shields. We conclude that the Rubin and Pollard (13) model is appropriate for the analysis of all these dike systems.

A dike will propagate laterally or vertically if the stress intensity at the dike tip ($k^b$) or at the upper ($k^{+a}$) or lower ($k^{-a}$) edge exceeds the fracture toughness of the country rock, $k_{crit}$. If the stress intensity falls below zero the dike will begin to close and for stress intensities between these two extremes the dike has a stable geometry. The stress intensities $k^{+a}$, $k^{-a}$ and $k^b$ are (13):

$$k^{+a} = x_1 P_0 a^{1/2} - \left(\frac{1}{\pi} + \frac{1}{4}\right) x_2 \nabla P_u a^{3/2} + \left(\frac{1}{\pi} - \frac{1}{4}\right) x_3 \nabla P_l a^{3/2} \quad \text{..... (1)}$$

$$k^{-a} = y_1 P_0 a^{1/2} - \left(\frac{1}{\pi} - \frac{1}{4}\right) y_2 \nabla P_u a^{3/2} + \left(\frac{1}{\pi} + \frac{1}{4}\right) y_3 \nabla P_l a^{3/2} \quad \text{..... (2)}$$

$$k^b = (2/\pi) P_0 a^{1/2} - (1/6\pi) \nabla P_u a^{3/2} + (1/6\pi) \nabla P_l a^{3/2} \quad \text{..... (3)}$$

where $P_0$ is the excess pressure at the dike centre; a is the dike half-height and $x_{1-3}$ and $y_{1-3}$ are correction factors (13) used to account for the proximity of the dike to the surface. $\nabla P_u$ and $\nabla P_l$ are vertical gradients of the regional stress given by:

$$\nabla P_u = (\rho_m - \rho_{ru}) g + \nabla T \quad \text{.... (4a);} \qquad \nabla P_l = (\rho_m - \rho_{rl}) g + \nabla T \quad \text{.... (4b),}$$

where $\rho_m$ is the magma density; $\rho_{ru}$ is the density of the country rock above the dike centre; $\rho_{rl}$ is the density of the country rock below the dike centre; $\nabla T$ is the vertical gradient of the regional tension; and g is the acceleration due to gravity. The average dike width is given by:

$$t = \{(1 - \upsilon) / \mu\} \{(\pi/2) z_1 P_0 a - 0.333 z_2 \nabla P_u a^2 + 0.333 z_3 \nabla P_l a^2\} \quad \text{..... (5)}$$

where $\upsilon$ is Poisson's ratio, $\mu$ is the shear modulus of the country rocks and $z_{1-3}$ are correction factors for proximity to the surface (13).

We have calculated mean thicknesses of stable dikes for the widest possible range of physically plausible conditions. The driving pressure, $P_0$, was varied from 0·3 to 30 MPa; the regional tension gradient, $\nabla T$, from $10^2$ to $10^4$ Pa/m; the fracture toughness, $k_{crit}$ from 70 to 130 MPa $m^{1/2}$ and the depth to the dike centre from 3 to 20 km. Only the upper end of the range of $P_0$ is found to be important in affecting our conclusions, and the value 30 MPa was chosen to represent the greatest likely tensile strength of country rocks (17). The range of the regional tension gradients reflect the values of $\nabla P_u$ and $\nabla P_l$ given in Rubin and Pollard (13). Their values of $\nabla P_u$ and $\nabla P_l$ in the range 3 to 11 x $10^3$ Pa/m imply values of $\nabla T$ of 0 to 8 x $10^3$ Pa/m; the upper value is

about one third of the gravitational weight of the country rocks, a likely upper limit (11). The range of fracture toughnesses is suggested by our current work on dikes in the East Rift Zone of Kilauea volcano (19), and is consistent with values quoted by Rubin and Pollard (13). The range of depth to dike centre represents dikes propagating from shallow magma reservoirs, at the lower end, to dikes occupying the entire vertical extent of the brittle lithosphere.

For each combination of parameters a dike was 'grown' from a starting half-height of 100m. The dependence of dike width on pressure and height ensures that the largest widths will result for dikes that grow to a large vertical extent with a high driving pressure; and the maximum driving pressures can be generated when a dike is grown from a small height. The dike is grown from its initial height by increasing the height in incremental steps and calculating $k^{+a}$ and $k^{-a}$ at each step; as long as both $k^{+a}$ and $k^{-a} > k_{crit}$ the height is further increased. In practice, solutions for $P_o \leq 5$ MPa never achieve a stable configuration in the sense of ceasing to grow at their upper and lower edges simultaneously but instead propagate downwards through the crust while closing at their upper ($k^{+a}$) edge. The dikes become unstable most rapidly when the tension gradient $\nabla T$ is large - such gradients give high tensions in the lower half of the dike which make the fracture of rocks at depth much easier than in the upper portion of the dike. Higher driving pressures stabilise the dike even when the tension gradient is also high. For pressures higher than the critical value of 5 MPa, the dike will continue to grow until its upper edge intersects the surface, i.e., large pressures and therefore wide dikes always feed eruptions.

Our results (see Table) show that the maximum dike width is only weakly dependent on the fracture toughness, gravity and regional tension gradient: the fracture toughness determines the pressure threshold for propagation to begin but does not alter the maximum width achieved; a doubling of the regional tension gradient alters the maximum dike width by < 1%. The maximum width is chiefly controlled by the driving pressure and the depth to the dike centre. The largest dikes are produced for large driving pressures at great depth within the crust; thus maximum dike widths are limited by crustal thickness and rock strength (which limits the amount of excess pressure that can be generated before dike propagation starts).

The *maximum* dike width likely to be achieved under physically plausible conditions on Earth is ~100 m and on Mars is ~200 m. Since these widths are achieved only by adopting the most favorable values of all the important parameters, it is clearly unlikely that they would be significantly exceeded in practice. Thus terrestrial structures like the Great Dike in southern Africa cannot be intrusive dikes. They must represent the operation of some quite different process: the intermittent, massive flooding of subsiding graben systems suggests itself as the most plausible mechanism given the continental extensional environments of these features and their tendancy to exhibit internal layering (4).

There is clearly scope for martian dikes in the shallow lithosphere to be systematically wider by a factor of about 2 than their terrestrial equivalents. However, it is not clear, given the functional dependance of effusion rate on fissure width (18), that this difference alone is great enough to account for the very high martian effusion rates deduced by many investigators.

***References*** (1) Macdonald, G.A., Abbott, A.T. & Peterson, F.L. (1987) Volcanoes in the Sea; The geology of Hawaii. (2) Walker, G.P.L. (1988) Ch. 41, U.S.G.S. Prof. Paper 1350. (3) Macdonald, R., Wilson, L., Thorpe, R.S., & Martin, A. (1988) *J. Petrol.* **29,** 559-583. (4) Bichan, R. ( 1970) pp 51-71 in *African magmatism and tectonics* (eds. T.N. Clifford & I.G. Gass). (5) Wilson, A.H. (1982) *J. Petrol.* **23,** 240-292. (6) Spence, D.A. & Turcotte, D.L. (1985) *J. G .R.* **90,** 575-580. (7) Cattermole, P. (1987) *J. G. R.* **92,** E553-E560. (8) Weertman, J. (1970) *J. G. R.* **76,** 1171-1183. (9) Secor, D.T. & Pollard, D.D. (1975) *G. R. L.* **2,** 510-513. (10) Pollard, D.D. (1976) *G. R. L.* **3,** 513-516. (11) Pollard, D.D. & Muller, O.H. (1976) *J. G. R.* **81,** 975-984. (12) Pollard, D.D. & Holzhausen, G. (1978) *Tectonophysics* **53,** 27-57. (13) Rubin, A.M. & Pollard, D.D. (1987) Ch. 53 , U.S.G.S. Prof. Paper 1350. (14) Foulger, G.R., Long, R.E., Einarsson, P. & Bjornsson, A. (1989) *Nature* **337,** 640-642. (15) Batiza, R., Melson,W.G. & O'Hearn, T.O. (1988) *Nature* **335,** 428-431. (16) Baker, B.H., Mohr, P.A. & Williams, L.A.J. (1972) *G. S. A. Special Paper* **136,** 67 pp. (17) Blake, S. (1981) *Nature* **289,** 783-785. (18) Wilson, L. & Head, J.W. (1983) *Nature* **302,** 663-669. (19) Parfitt, E.A. (in press) *J.G.R.*

Table. Dike widths (in metres) on Earth and Mars, given as a function of depth to dike centre, D, and driving pressure, $P_0$.

| | Earth | | | Mars | | |
|---|---|---|---|---|---|---|
| D/km | $P_0$/MPa = 5 | 10 | 30 | $P_0$/MPa = 5 | 10 | 30 |
| 3 | 2.24 | 9.1 | 37 | 5.03 | 12 | 40 |
| 5 | 2.03 | 9.9 | 56 | 6.31 | 18 | 64 |
| 10 | 1.97 | 7.9 | 87 | 5.15 | 24 | 119 |
| 20 | 1.97 | 8.0 | 76 | 4.92 | 21 | 190 |

A SEARCH FOR CARBONATE MINERALS IN CHASSIGNY; I.P.Wright, M.M.Grady and C.T.Pillinger, Planetary Sciences Unit, Department of Earth Sciences, Open University, Walton Hall, Milton Keynes MK7 6AA, England.

With the presence of carbonates firmly established in the nakhlite, Nakhla, [1,2] and the shergottite, EETA 79001, [3,4,5] it seemed appropriate to assess the likelihood that such minerals may be present in the only known chassignite (Chassigny). At the outset, it was anticipated that significant quantities of carbonates would probably not be detected in Chassigny, as a previously undertaken detailed petrographic study [6] had not produced a positive identification. However, carbonates in the other SNC meteorites were detected by gas release experiments (*i.e.* stepped heating, acid-dissolution *etc.*) prior to petrographic recognition. Stepped heating analyses on Chassigny have been made twice previously [7,8], but in neither case was there any evidence to suggest the presence of carbonates.

Notwithstanding these results, a large sample (130.383 mg) of Chassigny whole rock material was subjected to orthophosphoric acid-dissolution (30 minutes @ 25°C - a procedure known to convert carbon in the form of carbonate minerals, such as calcite, to $CO_2$ gas). Somewhat surprisingly, 327 ng of carbon as $CO_2$ was released during the dissolution, corresponding to 2.5 ppm C, with $\delta^{13}C_{PDB}$ of -4.7‰ and $\delta^{18}O_{SMOW}$ of +39.6‰. If it is assumed that the $CO_2$ arises from the dissolution of calcite then the $\delta^{18}O_{SMOW}$ of the mineral phase is +29.1‰. The oxygen isotope datum is similar, albeit slightly $^{18}O$-enriched, to values acquired from acid-dissolutions of the other SNC meteorites (+21 to +26‰). However, the carbon in the Chassigny carbonate is somewhat less $^{13}C$-enriched than the equivalent minerals in either Nakhla ($\delta^{13}C$ >+15‰) or EETA 79001 ($\delta^{13}C$ = +7 to +10‰). Nevertheless, the $\delta^{13}C$ value of -4.7‰ is distinctly different from that of the whole rock, known from previous studies to be -25.7 to -22.7‰.

In order to pursue further the possibility that carbonates are present in Chassigny, two whole rock samples were analysed by stepped combustion. The first sample was measured using the standard extraction procedure - the results are shown in the figure. The second sample was treated with dichloromethane, a technique shown to be effective in the removal of surficial terrestrial organic contamination from basaltic glass fragments [9]. The results from this second extraction ($\Sigma C$ = 450 ppm, $\Sigma\delta^{13}C$ = -24.9‰) are very similar to the first ( $\Sigma C$ = 442 ppm, $\Sigma\delta^{13}C$ = -26.2‰) indicating that, for Chassigny at least, dichloromethane has little effect on the carbon components present. In common with previous analyses the first step in both stepped combustions (*i.e.* room temperature to 200°C) yielded isotopically light $CO_2$ ($\delta^{13}C$ = -34, -36‰). From 200-400°C the isotopic composition was observed to rise to -20, -18‰, as in previous experiments [7]. Between 400 and 500°C the $\delta^{13}C$ values become slightly more negative by about 2‰. It seems that 50-60% of the carbon released below 500°C in Chassigny (corresponding to about 250 ppm of C) probably has a $\delta^{13}C$ of *ca.* -18‰. A carbon isotopic composition of this nature is unusual for terrestrial organic contamination and so it is considered that this might be an indigenous component. On the other hand, the isotopically light carbon released at the lowest temperature may be related to that component observed in other SNC meteorites, which again is not obviously a terrestrial contaminant [8]. It is noteworthy that dichloromethane was not effective in removing any

of the low-temperature carbon. Clearly the carbon must be different to that which is easily removed from basaltic glasses and assumed to be organic contamination acquired during laboratory handling of the samples or as a result of exposure in the environment [9].

Returning to the figure, it can be seen that from 500 to 700°C there is evidence for an isotopically heavy component. As this is the temperature range over which carbonates decrepitate it seems safe to conclude that Chassigny does indeed contain such minerals. 5 ppm carbon with $\delta^{13}C$ of -14.1‰ is released between 500 and 700°C; assuming two components of carbon contribute to the measured values then 1.5 – 2.0 ppm carbon with $\delta^{13}C$ of -4.7‰ are present in this sample (the range in carbon concentration corresponding to whether the second component is assumed to have $\delta^{13}C$ of -18 or -20‰). This agrees well with the result from the acid-dissolution experiment which gave a value for the carbon content of 2.5 ppm.

During a survey of carbon in HED samples, no evidence was found for carbonates in any sample other than Kapoeta, which is a regolith breccia containing clasts of carbonaceous chondrite materials. Furthermore, carbonates have never been found in any lunar rocks, or lunar meteorites. Thus, it seems that the presence of carbonates in SNC meteorites is a function of the geological complexity of the parent body (Mars). The carbonates found in Chassigny ($\delta^{13}C$ = -4.7‰) appear to have a different carbon isotopic composition to those in either Nakhla (>+15‰) or EETA 79001 (+7 to +10‰). The spread in $\delta^{13}C$ between carbonates of the three SNC meteorites may well document different formation conditions, or locations, on the parent body.

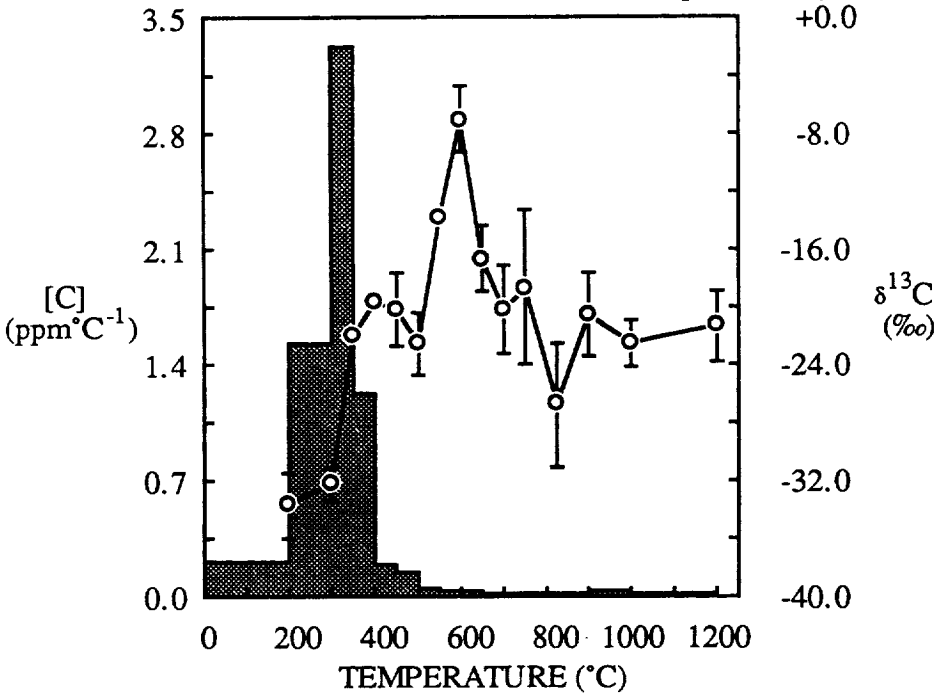


References: [1] Carr *et al.* (1985), *Nature*, **314**, 248-50; [2] Wentworth and Gooding (1989), *LPS*, **XX**, 1193-4; [3] Wright *et al.* (1988), *GCA*, **52**, 917-24; [4] Clayton and Mayeda (1988), *GCA*, **52**, 925-7; [5] Gooding *et al.* (1988), *GCA*, **52**, 909-15; [6] Floran *et al.* (1978), *GCA*, **42**, 1213-29; [7] Fallick *et al.* (1983), *LPS*, **XIV**, 183-4; [8] Wright *et al.* (in prep.); [9] Mattey *et al.* (1989), *GCA*, **53**, 2377-86.

# VOLUMETRIC DISTRIBUTIONS OF MARS TOPOGRAPHY

Sherman S. C. Wu, and Annie Howington-Kraus, U.S. Geological Survey, Flagstaff, AZ 86001

A new global topographic map of Mars has been published [1]. The map was compiled at a scale of 1:15 million with a contour interval of 1 km by the synthesis of data acquired from various scientific experiments of both the Mariner and Viking Missions [2]. Contour lines of the map are referred to the Mars topographic datum [3]. Those in the equatorial belt (between lat 30° N. and 30° S.) were extracted from 1:2 million-scale contour maps compiled on analytical stereoplotters by stereophotogrammetric methods using Viking Orbiter pictures. The planetwide control net was used for control [4].

A Mars Digital Terrain Model (DTM) has been derived [5] from the global topographic map. From the DTM, we calculated the distribution of Mars' volume above and below its datum. We first mosaicked data from the western and eastern hemispheres with data from the two polar regions and converted the result to a Sinusoidal Equal Area projection. We then calculated volumes in 36 separate blocks, each covering 30° of latitude and 60° of longitude (Fig. 1). The volumes were calculated by multiplying each 1 $km^2$ area by the surface height above or depth below the datum. In Table 1, the volumes of each of the six zones (based on longitudes) are listed in the bottom row, and the volumes of each of the six bands (based on latitudes) are listed in the last column. In volume, the western hemisphere is about 32 million $km^3$ greater than the eastern, and the southern hemisphere is about 166 million $km^3$ greater than the northern. Total global volumes are 259.4 $km^3$ above the datum and 68.3 $km^3$ below it. The mean elevation above the datum is about 1.5 km.

We have also generated maps in color of Mars' topography and its volumetric distributions.

References: [1] U.S. Geological Survey, 1989, Misc. Inv. Ser. Map I-2030, 3 sheets, scale 1:15,000,000. [2] Wu, S. S. C., Jordan, Raymond, and Schafer, F. J., 1985, NASA Tech. Memo. 88383, p. 614-617. [3] Wu, S. S. C., 1981, Annales de Geophysique, Centre National de la Recherche Scientifique, Numero 1, Tome 37, p. 147-160. [4] Wu. S. S. C., and Schafer, F. J., 1984, Tech. Papers of 50th Annual Meeting of Am. Soc. of Photogram. v. 2, p. 456-463. [5] Wu, S. S. C., and Howington-Kraus, A. E., 1987, LPS XVIII, p. 1108-1109.

Table 1. Volume Distributions of Mars Topography. (All values are $X10^4 km^3$.)

| Longitude(w) / Latitude | 180°-120° | 120°-60° | 60°-0° | 360°-300° | 300°-240° | 240°-180° | Total |
|---|---|---|---|---|---|---|---|
| N90°-30 | +0<br>-3.134 | +0.027<br>-2.390 | +0.017<br>-3.756 | +0.070<br>-2.431 | +0.064<br>-2.097 | +0.005<br>-4.180 | +0.183<br>-17.988 |
| N60°-30° | +1.230<br>-5.821 | +10.718<br>-0.383 | +0.042<br>-6.139 | +3.764<br>-1.066 | +0.933<br>-4.900 | +0.747<br>-5.307 | +17.434<br>-23.616 |
| N30°-0° | +9.659<br>-5.009 | +25.755<br>-0.029 | +1.860<br>-4.521 | +9.870<br>-0.004 | +6.766<br>-4.400 | +1.721<br>-5.069 | +55.631<br>-19.032 |
| S0°-30° | +22.969<br>-0.001 | +30.605<br>-0.044 | +10.630<br>-0.852 | +21.549<br>-0.024 | +14.062<br>-0.163 | +14.321<br>-0.577 | +113.536<br>-1.161 |
| S30°-60° | +10.827<br>-0 | +10.790<br>-0 | +9.781<br>-0 | +14.763<br>-1.423 | +6.650<br>-4.616 | +5.487<br>-0 | +48.304<br>-6.039 |
| S60°-90° | +1.991<br>-0 | +2.960<br>-0 | +4.359<br>-0 | +5.252<br>-0 | +5.803<br>-0 | +3.992<br>-0 | +24.359<br>-0 |
| | +36.676<br>-13.965 | +80.55<br>-2.846 | 26.089<br>-15.268 | +55.268<br>-4.948 | +34.284<br>-16.176 | 26.723<br>-15.133 | +259.445<br>-68.336 |

Remark: Positive volumes are solid mass above the topographic datum whereas negative volumes are empty space below the topographic datum.

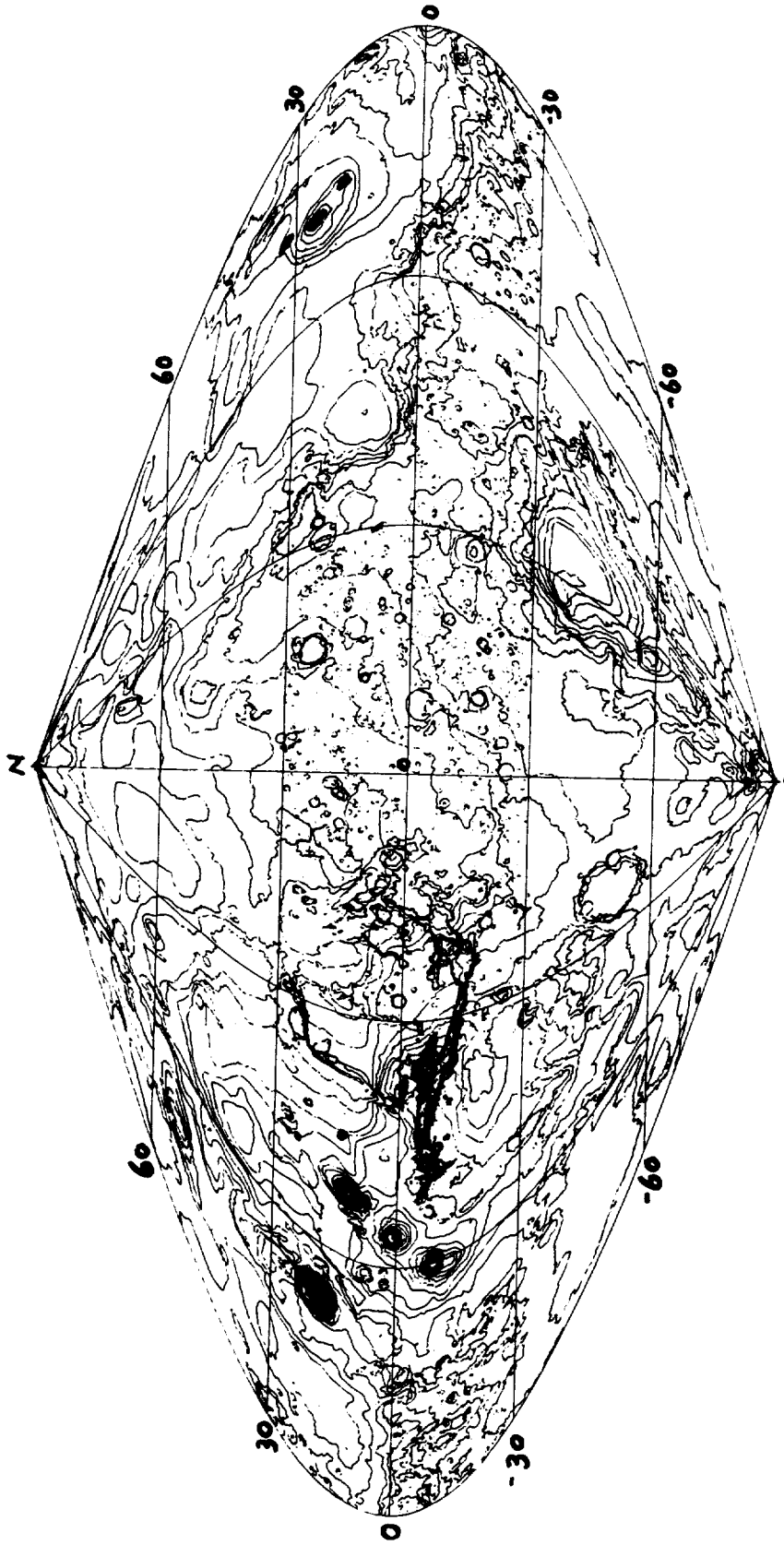


Figure 1. The global topographic map of Mars in sinusoidal equal area projection.

VOLUMETRIC DETERMINATIONS OF VALLES MARINERIS OF MARS, Sherman S. C. Wu, Patricia A. Garcia, and Annie Howington-Kraus, U.S. Geological Survey, Flagstaff, AZ 86001.

Valles Marineris, the canyonlands of Mars, extend for about 5,000 km from long 30° to 110°. The widest segment of the canyons is about 600 km across, and their maximum depth is about 9 km. By using a digital terrain model of seven 1:2,000,000-scale contour maps (MC17-NE, MC18-NW, -NE, -SE, MC19-NW, -SW, and MC11-SW) [1], we calculated volumes of the canyon system (Table 1) in two separate parts (Fig. 1a): a western segment, which includes Noctis Labyrinthus and the main body of Valles Marineris; and an eastern segment, which includes some of the troughs, chaotic terrain, and channels. We calculated the missing canyon volume within the boundaries shown in Fig. 1b by multiplying each 1 $km^2$ area by its depth. Assuming a density of 3.0 g $cm^{-3}$ [2], we estimate the missing mass of the canyons and the channels to be 14.706 X $10^{18}$ kg. The total volume of the western segment is 2.891 X $10^6 km^3$, and its mass is 8.673 X $10^{18}$kg. This volume is about equal to the volume of the Tharsis dome above 8-km elevation and to one-sixth the volume of the Tharsis dome above 3-km elevation [3].

Table 1. Volumes of Valles Marineris Canyons and Channels. (All volumes are X $10^6 km^3$.)

| Elevation (km) | Western Segment | | Eastern Segment | | Total |
|---|---|---|---|---|---|
| | Increment | Cumulative | Increment | Cumulative | Cumulative |
| -4 | | | 0 | 0 | 0 |
| -3 | | | 0.009 | 0.009 | 0.009 |
| -2 | 0 | 0 | 0.091 | 0.100 | 0.100 |
| -1 | 0.006 | 0.006 | 0.382 | 0.482 | 0.488 |
| 0 | 0.039 | 0.045 | 0.586 | 1.068 | 1.113 |
| 1 | 0.100 | 0.145 | 0.398 | 1.466 | 1.611 |
| 2 | 0.187 | 0.332 | 0.312 | 1.778 | 2.110 |
| 3 | 0.264 | 0.596 | 0.207 | 1.985 | 2.581 |
| 4 | 0.348 | 0.944 | 0.025 | 2.010 | 2.954 |
| 5 | 0.409 | 1.353 | | | 3.363 |
| 6 | 0.489 | 1.842 | | | 3.852 |
| 7 | 0.512 | 2.354 | | | 4.364 |
| 8 | 0.428 | 2.782 | | | 4.792 |
| 9 | 0.104 | 2.886 | | | 4.896 |
| 10 | 0.005 | 2.891 | | | 4.901 |

References: [1] Wu, S. S. C., Jordan, Raymond, and Schafer, F. J., 1985, NASA Tech. Memo. 87563, p. 612-613. [2] Hiller, K. H., Janle, P., Neukum, G. P. O., Guest, J. E., and Lopes, R. M., 1982, Jour. Geophys. Research, v. 87, p. 9905-9915. [3] Wu, S. S. C., Garcia, P. A., Howington-Kraus, A., and Kelly, C. T., 1988, Lunar and Planetary Science Conference XIX, p. 1300-1301. [4] U.S. Geological Survey, 1989, Misc. Inv. Ser. Map I-2030, 3 sheets, scale 1:15,000,000.

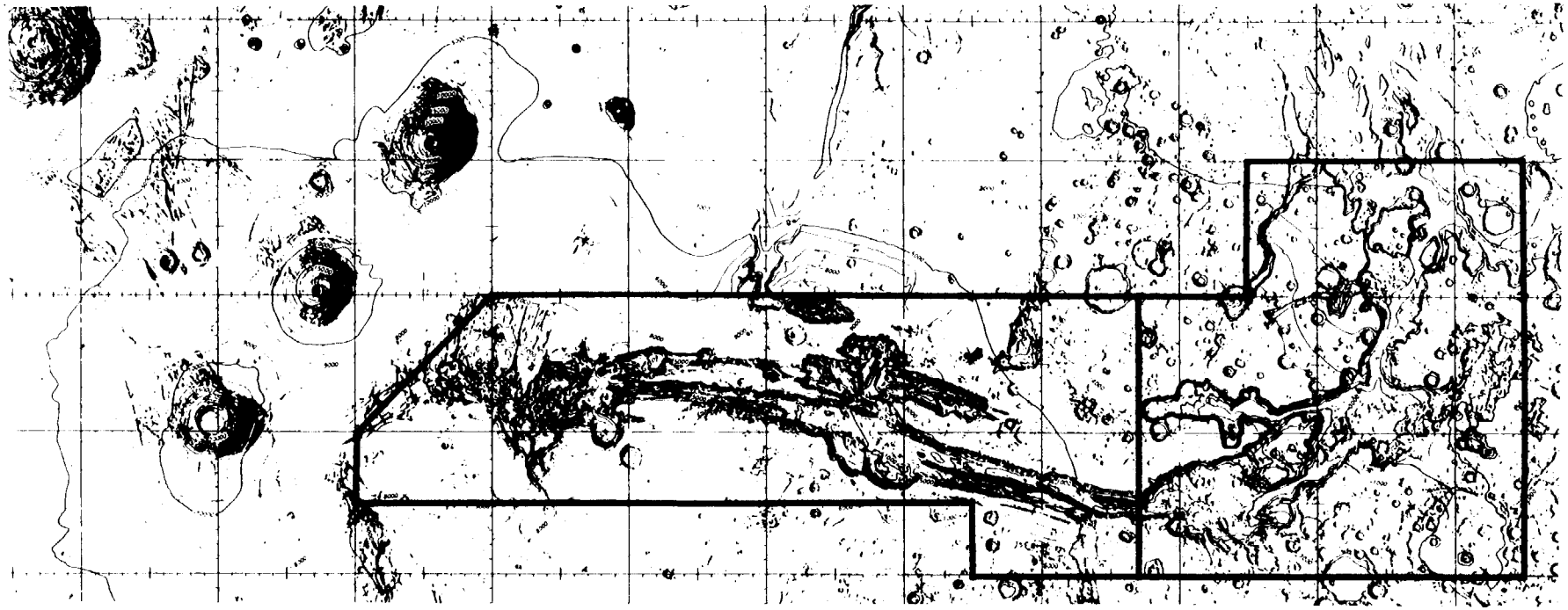

Figure 1a. Part of topographic map of Mars (U.S. Geological Survey, 1989) showing western and eastern segments of Valles Marineris.

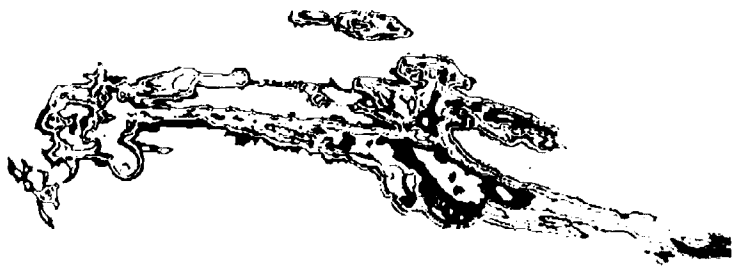

Figure 1b. Digital terrain model of western segment of Valles Marineris used in volumetric determinations.

GEOLOGIC MAPPING OF THE CENTRAL MANGALA VALLES REGION, MARS; James R. Zimbelman, Center for Earth and Planetary Studies, National Air and Space Museum, Smithsonian Institution, Washington, D.C. 20560.

Geologic mapping of the southern and central portions of Mangala Valles has been carried out as part of the Mars Geologic Mapping program. Three adjacent geologic maps have been prepared at a scale of 1:500,000 by researchers at NASM and at Arizona State University (1,2); the work presented here concerns the northernmost of the three maps (MTM sheet -10147). Physiography around the central reaches of Mangala Valles is dominated by exposures of ancient Noachian material severely disrupted by lobate scarps (Fig. 1). The scarps are interpreted to be faults within the oldest materials, similar to what is observed around southern Mangala Valles (1,2). The scarps in MTM -10147 lack the km-scale vertical relief of some scarps to the south (3,4) but they are still major topographic features. The orientation of the scarps in MTM -10147 changes from a north-south trend prominent to the south (1,2) to a northeast-southwest trend (Figs. 1,2). Both trends are likely due to an ancient impact basin in Daedalia Planum (5). Amazonian-Hesperian Mangala Valles materials embay the western margin of the Noachian materials (Fig. 2). Hesperian intercrater plains north of the Mangala Valles materials are scoured by overland flow likely associated with Mangala Valles flood events. Amazonain-Hesperian Tharsis plains embay the Noachian materials on the east (Fig. 2).

REFERENCES: 1) R. Greeley and R.A. Craddock, MTM -20147 geologic map (in press). 2) J.R. Zimbelman et al., MTM -15147 geologic map (in press). 3) J.R. Zimbelman, Trans. AGU 69(16), 390, 1988. 4) R.A. Craddock et al. (this volume). 5) R.A. Craddock et al., LPS XIX, 213-214, 1988 (JGR, in press).

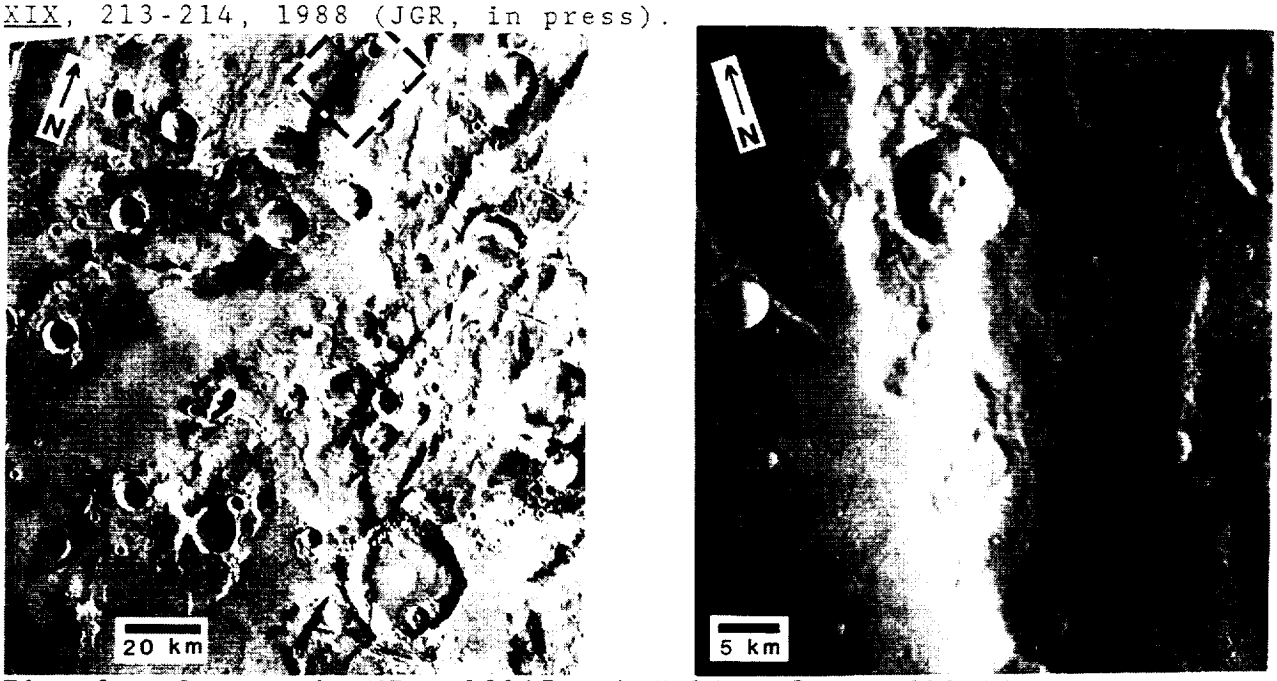


Fig. 1. Scarps in MTM -10147. a) Viking frame 639A10; box shows location of part b. b) Viking frame 454S01.

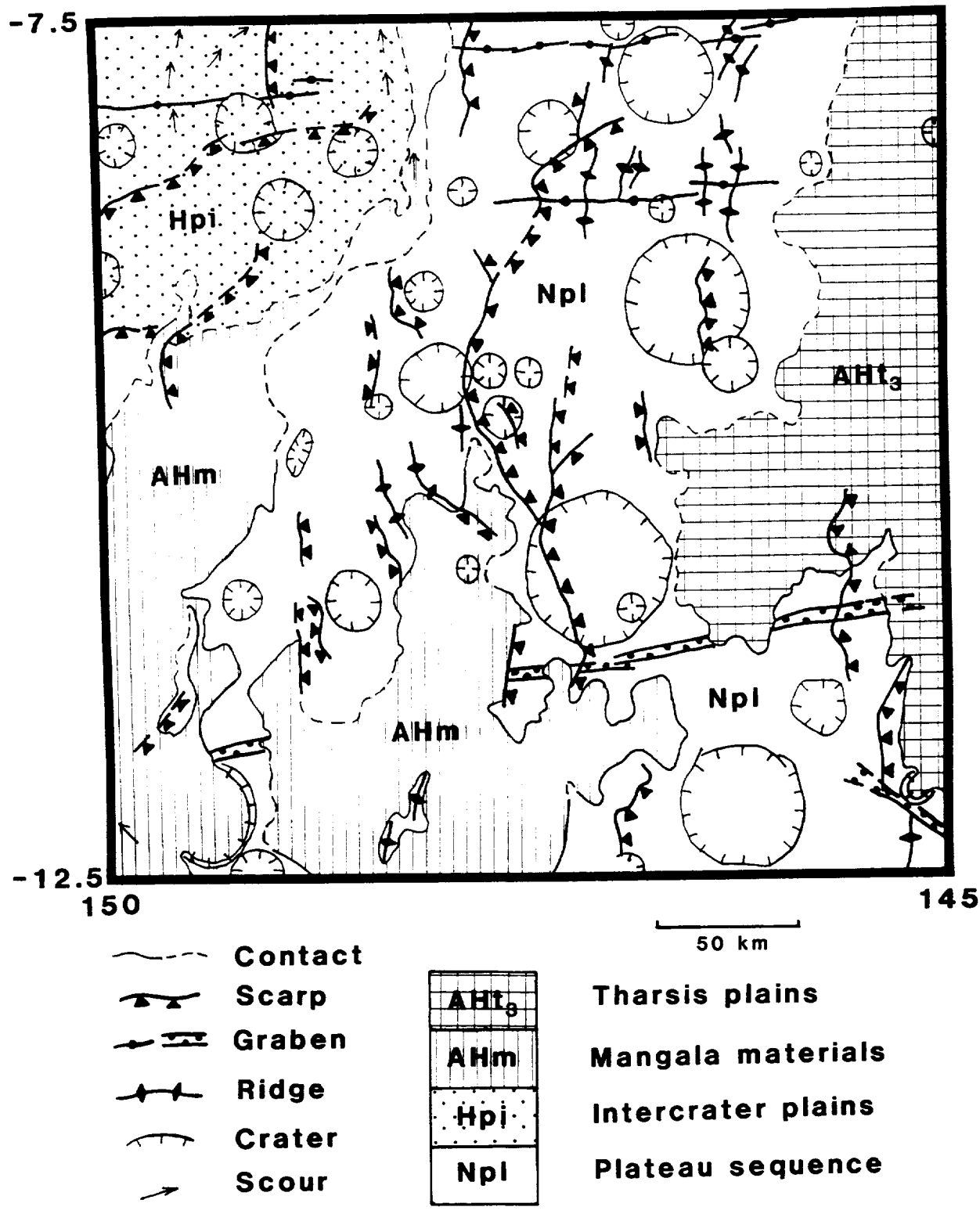


Fig. 2. Simplified geologic map of MTM -10147. Scarps are prominent in the Noachian and Hesperian materials, in places deflecting the flow of younger Amazonian-Hesperian materials from Mangala Valles and Tharsis. [Supported by NASA grant NAGW-1390]

HENRY CRATER, MARS: THICK, LAYERED DEPOSIT PRESERVED ON A CRATER FLOOR IN THE MARTIAN HIGHLANDS; James R. Zimbelman, Center for Earth and Planetary Studies, National Air and Space Museum, Smithsonian Institution, Washington, D.C. 20560

Henry crater (11.0° N, 336.6° W) is a 165-km-diameter impact crater located in a portion of the martian highlands that extends well into the northern hemisphere of Mars. Henry crater is distinctive from numerous craters in its immediate vicinity because of the presence of an irregular mound of material on the crater floor. The mound has a smooth texture (at the >200 m/pixel resolution of the available images; see Fig. 1) that is very different from the intricate texture of the surrounding highlands surface. Several layers (representing increased competence?) are exposed along the eroded southeastern margin of the mound (Fig. 1), leading to the interpretation that the deposit is a remnant of a previously extensive mantle laid down over the cratered highland surface (1). The mechanism of deposition at Henry crater is not immediately evident in the available images, but this deposit has been interpreted as a remnant of a polar deposit emplaced when this location was at one time close to the rotation axis of Mars (1). This work presents additional information on the characteristics of this deposit.

Images obtained on different orbits of the Viking spacecraft have been combined to produce a stereogram of Henry crater and its interior layered deposit (Fig. 1). The relief visible in the stereo model shows that 1) the layered deposit is smoother than the highlands surface on both the vertical as well as the horizontal scale, 2) the deposit stands well above the crater floor but definitely below the rim of the crater, and 3) structural control is very evident in the highlands surface and, to a lesser degree, in the deposit as well (see Fig. 2). Earth-based radar measurements (described in 2) collected during 1978 (3) quantify the relief of the layered deposit as between 500 m and 1000 m, depending on the true magnitude of an apparent westward dip to the crater floor (Fig. 3). If almost 1 km of material once covered the entire highlands surface, its preservation only within craters argues for extremely intensive erosion of very weak material, with no observable erosion of the original highlands material. Radar signals were reflected from the layered deposit, in contrast to material of similar appearance located west of Tharsis that shows no reflected or scattered radar signal (4). This suggests that the Henry crater deposit is more indurated or deeply eroded than the materials west of Tharsis. Four craters on the layered deposit imply an upper Hesperian age [$N(2)=500\pm250/10^6$ km$^2$], considerably older than the antipodal Amazonian deposits in Tharsis (5), raising a possible problem for the polar wandering mechanism.

REFERENCES: 1) P.H. Schultz and A.B. Lutz, Icarus 73, 91-141, 1988. 2) G.S. Downs et al., Icarus 26, 273-312, 1975. 3) G.S. Downs et al., J. Geophys. Res. 87, 9747-9754, 1982. [Digital version of topographic data provided by G. Downs, 1985]. 4) B. Butler et al., Trans. AGU 70(43), 1171, 1989. 5) D.H. Scott and K.L. Tanaka, USGS Map I-1802-A, 1986. [Supported by NAGW-1804]

AN EVALUATION OF THE POSSIBLE EXTENT OF BEDROCK EXPOSURE IN THE SINUS MERIDIANI REGION OF THE MARTIAN HIGHLANDS; James R. Zimbelman and Robert A. Craddock, Center for Earth and Planetary Studies, National Air and Space Museum, Smithsonian Institution, Washington, D.C. 20560

A major objective in remote sensing studies of Mars is to provide constraints on the properties and compostion of the bedrock in the area under observation. However, the active aeolian environment and the ubiquitous presence of dust on Mars make the realization of this objective difficult at best, and impossible at worst. Here we present results of work undertaken to relate the amount of (possible) bedrock exposures visible in the highest resolution Viking imaging data to results obtained from remote sensing studies of the Sinus Meridiani region.

The location chosen for this study (15°N to 15°S, 330° to 360°W) includes a significant portion of the classical low albedo region of Sinus Meridiani and is entirely within the cratered highland terrain of Mars. This region has been the subject of several studies of spectral reflectance at visual wavelengths (1-5), as well as being included in global studies at thermal infrared (6-10) and radar (11-13) wavelengths. This wealth of remote sensing data has important implications for the aeolian environment of Mars (e.g., 1, 4-6, 9, 14) but the degree to which these data can be related to bedrock that underlies the aeolian cover is more difficult to assess. Most studies of visual reflectance conclude that low albedo regions are "less" obscured by the dust that dominates the high albedo regions (e.g., 1-3). However, what fraction of the martian surface (having either low or high albedo) has a reasonable likelihood of providing information about rocks associated with the terrains present on various geologic units? Presley and Arvidson (4) used visual and thermal infrared data to infer that the surficial units exposed in western Arabia and Sinus Meridiani were mixed aeolian deposits, predominantly decoupled from the underlying bedrock. Thus, any bedrock exposures will likely be small compared to the scale of the data used in that study (hundreds of meters to kilometers, 4). Thermal infrared measurements at multiple wavelengths indicate that from 5% to 20% of the martian surface consists of material much more competent than dust or sand (15), with the low albedo regions generally having more exposed competent materials than the high albedo regions (10). Unfortunately, the competent materials observed in this manner may be either rocks (10, 15) or indurated sediments (16). We are using the highest resolution Viking images (all with <35 m/pixel) obtained within the study area to provide an independent assessment of the surface exposures that are most likely relevant to the local geology.

What do we look for in the images as representing possible exposures of bedrock? Bedrock is defined as "the solid rock underlying the soil and other unconsolidated materials, or appearing at the surface where these [unconsolidated materials] are absent" (17). Thus, we looked for locations that had the least likelihood of an overlying accumlation of unconsolidated materials, particularly sand or dust transported to the area by aeolian processes. The images examined in the study (Table 1) have resolutions of from 8 to 34 m/pixel, so we are unable to identify features smaller than a few tens of meters in dimension, so it is likely that there are areas within any given picture element that include some aeolian dust or sand. However, it seems likely that steep slopes will shed most unconsolidated materials downslope and thus provide the "cleanest" surface that might reasonably be expected to include bedrock. This assumption means that our results are best considered to be upper limits.

# EXTENT OF BEDROCK EXPOSURE IN THE MARTIAN HIGHLANDS

Zimbelman, J.R., and Craddock, R.A.

We examined almost 400 high resolution images that fell within the study area, estimating the percentage of the area of each frame that was a possible exposure of the underlying bedrock. Interior walls of impact craters (e.g., Viking orbiter frame 748A12) provided the most numerous occurrences of steep slopes of competent material. However, even the best images had smooth-textured surfaces covering the majority of crater interiors--areas that probably include some talus accumulations but which also might be mantled by dust--that were not considered to be good candidates for possible bedrock exposure. Walls of channels and other cliffs provided additional candidates sites. We also noted steep slopes on materials that are easily eroded and appear to be superposed on the surrounding terrain (e.g., Viking orbiter frame 708A25). these materials appear to be related to major depositional events within the region; this material is probably more competent that aeolian dust but it less likely that it will be related to the local geology. The entire image set provided the following results: 70% had <1% bedrock exposure, 25% have <5% bedrock exposure, and only 5% have <10% bedrock exposure (all of which are eroded layers like Viking orbiter frame 708A25). The high resolution images covered only about 10% of the total study area but we believe they are representative of the region as a whole. We found no significant difference in exposures between high albedo and low albedo regions, although the layered material is somewhat more common in the low albedo regions. These results will be compared to high resolution thermal infrared data to assess whether the competent depositional layers might be related to exposures of competent "duricrust" inferred from thermal infrared data (e.g., 16).

[This work was supported by NASA grant NAGW-1804.]

Table 1. High resolution Viking images in study region.

| | | |
|---|---|---|
| 392B01-20 | 436A52-74 | 749A07-30 |
| 409B17-40 | 709A01-48 | 826A21-44 |
| 410B01-40 | 746A48 | 826A51-74 |
| 411B01-32 | 746A51-68 | |
| 411B67-98 | 747A31-58 | |
| 416B34-35 | 748A01-16 | |
| 572B67-76 | 748A21-42 | |

REFERENCES: 1) L.A. Soderblom et al., Icarus 34, 446-464, 1978. 2) T.B. McCord et al., J. Geophys. Res. 87, 10129-10148, 1982. 3) R.E. Arvidson et al., J. Geophys. Res. 87, 10149-10157, 1982. 4) M.A. Presley and R.E. Arvidson, Icarus 75, 499-517, 1988. 5) E.L. Strickland, LPS XX, 1077-1078, 1989. 6) H.H. Kieffer et al., J. Geophys. Res. 82, 4249-4291, 1977. 7) J.R. Zimbelman and H.H. Kieffer, J. Geophys. Res. 84, 8239-8251, 1979. 8) F.D. Palluconi and H.H. Kieffer, Icarus 45, 415-426, 1981. 9) J.R. Zimbelman and R. Greeley, J. Geophys. Res. 87, 10181-10189, 1982. 10) P.R. Christensen, Icarus 68, 217-238, 1986. 11) G.S. Downs et al., Icarus 18, 8-21, 1973. 12) G.S. Downs et al., Icarus 26, 273-312, 1975. 13) G.S. Downs et al., J. Geophys. Res. 87, 9747-9754, 1982. 14) P.R. Christensen, J. Geophys. Res. 91, 3533-3545, 1986. 15) P.R. Christensen, J. Geophys. Res. 87, 9985-9998, 1982. 16) B.M Jakosky and P.R. Christensen, J. Geophys. Res. 91, 3547-3560, 1986. 17) Webster's Third New Int. Dictionary, G.&C. Merriam Co., Springfield, Mass., p. 196, 1971.

## CONSTRAINTS ON THE DEPTH AND GEOMETRY OF THE MAGMA CHAMBER OF THE OLYMPUS MONS VOLCANO, MARS;

*M.T. Zuber*, Geodynamics Branch, Code 621, NASA/Goddard Space Flight Center, Greenbelt, MD 20771, *and P.J. Mouginis-Mark*, Planetary Geosciences Division, Hawaii Institute of Geophysics, University of Hawaii, Honolulu, HI 96822.

The summit caldera of the Olympus Mons volcano exhibits one of the clearest examples of tectonic processes associated with shield volcanism on Mars [1,2]. Within the 80 km diameter structure are six nested craters that indicate that the volcano edifice has undergone multiple collapse episodes [1]. Also found within the caldera are numerous compressional (ridges) and extensional (graben) tectonic features. Analysis of the topography of the caldera as derived from stereophotogrammetry [3] shows that the central portion of the largest (and oldest) crater, which contains radial and concentric ridges, represents a topographic low, while the crater perimeter, which is characterized by concentric graben, forms a topographic high. The relationship of the summit topography to the tectonic features, in combination with photogeologic evidence for basalt-like resurfacing of the caldera floor [4,5], is believed to indicate that a large lava lake has cooled and subsided due to pressure reduction in the underlying magma chamber.

The radial distance from center of the transition from concentric ridges to concentric graben within the oldest crater provides a constraint on the geometry and depth of the subsurface magmatic reservoir at the time of subsidence. In this study we use this constraint to investigate the size, shape and depth of the reservoir. Our approach consists of calculating radial surface stresses ($\sigma_{rro}$) corresponding to a range of subsurface pressure distributions representing an evacuating magma chamber. We then compare the stress patterns to the observed radial positions of concentric ridges and graben. We solve the problem by employing a finite element approach using the program TECTON [6]. An axisymmetric geometry and linear elastic material properties are assumed. The magma chamber is modeled as an elliptically-shaped source; nodes within the ellipse are characterized by a stress condition that represents an instantaneous pressure drop. Parameters of interest include the horizontal ($a$) and vertical ($b$) dimensions of the magma chamber and the depth to the top of the chamber ($d$). The following boundary conditions are imposed: vanishing horizontal ($u$) displacements at the center of symmetry of the volcano; vanishing vertical ($w$) displacements at depths much greater than the crater radius; and vanishing horizontal and vertical displacements at radial distances far from the crater rim. Numerical analyses were performed to assure that solutions were not sensitive to the far field boundary conditions.

Examples of radial surface stress distributions for a series of magma chamber depths with $a=R_c$ (where $R_c$ is the crater radius) and $b/a=0.5$ are shown in Figure 1. The state of stress as inferred from the ridges and graben changes from compression (-) to extension (+) at a radial distance ($r$) of approximately $0.53R_c$ [5], where $R_c$ is the crater radius (32 km). For these assumed parameters, the corresponding pattern of stresses indicates that the top of the magma chamber at the time of subsidence was located at a depth of less than $0.5R_c$ (best-fit range $8 \le d \le 16$ km). The best-fit depth is not very sensitive to the aspect ratio of the chamber (Figure 2), the difference in Young's Modulus between the chamber and surroundings (for $E_{mc}/E_s < .1$), or details of the imposed pressure distribution. However, as shown in Figure 3, depth is highly sensitive to magma chamber width. The magma chamber is unlikely to be markedly narrower than the crater; if it is wider, then Figure 3 illustrates that a shallower maximum depth than determined from Figure 1 is implied. Superposition of near-summit stresses associated with self-compression of the volcano [7] would also shift the maximum to shallower depths. We thus conclude that if concentric ridges and graben within the largest and oldest crater in the Olympus Mons caldera complex formed as a consequence of subsidence related to magma chamber withdrawal, then the magma chamber was located within the volcanic edifice, at a depth less than half the crater radius. This result is in agreement with our previous analysis that assumed simpler chamber geometries [8,9]. With appropriate scaling for the difference in gravity between Mars and Earth, this depth is similar to that observed for the magma chamber beneath the Kilauea caldera [10], which would suggest a gross similarity of internal structure of the two shields.

**References:** [1]Mouginis-Mark, P.J., *Proc. Lunar Planet. Sci. Conf. XII*, 1431-1447, 1981. [2]Mouginis-Mark, P.J., et al., submitted to *Mars*, University of Arizona Press, Tucson, 1989. [3]Wu, S.S.C., et al., *Nature, 309*, 432-435, 1984. [4]Greeley, R., and P.D. Spudis, *Rev. Geophys., 19*, 13-41, 1981. [5]Mouginis-Mark, P.J. et al. this volume. [6]Melosh, H.J., and A. Raefsky, *Geophys. J. R. ast. Soc., 60*, 333, 1980. [7]Thomas, P.J., et al., *J. Geophys. Res.*, in press, 1989. [8]Zuber, M.T. and P.J. Mouginis-Mark, *Proc. MEVTV Confererence on Tectonic Features on Mars*, LPI, Houston, 1989.

[9]Zuber, M.T., and P.J. Mouginis-Mark, *MEVTV Conf. on Magma Bodies*, LPI, Houston, 1990.
[10]Ryan, M.P., et al., *J. Geophys. Res.*, *88*, 4147-4181, 1983.

*Figure 1.* Radial surface stress ($\sigma_{rro}$) vs. distance from the crater center ($r/R_c$, where $R_c$= crater radius) due to deflation of a subsurface magma chamber. Stress patterns are shown for a range of depths ($d$). Assumes an elliptical chamber with width $a=R_c$ and height $b=0.5a$. Negative stresses are compressional and positive stresses are extensional.

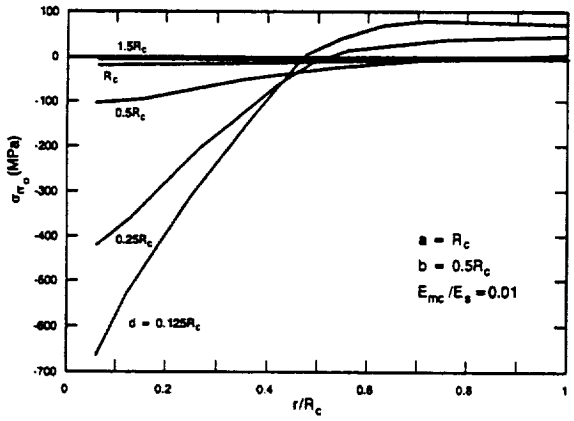


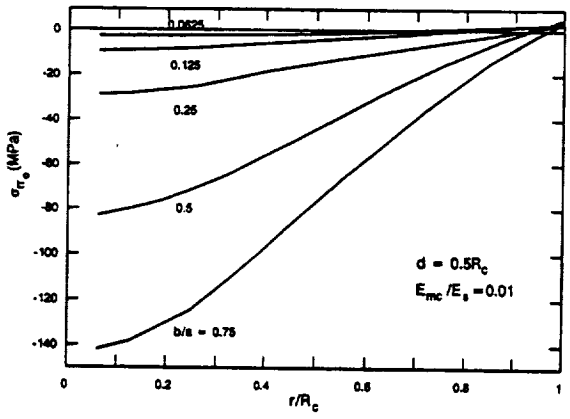


*Figure 2.* Plot of $\sigma_{rro}$ vs. $r/R_c$ for a range of magma chamber aspect ratios ($b/a$) assuming $a=R_c$ and $d=0.5R_c$. Note that the transition from compression (-) to extension (+) is not sensitive to this parameter except for very small $b/a$.

*Figure 3.* Plot of $\sigma_{rro}$ vs. $r/R_c$ for a range of magma chamber widths ($a$) assuming $b=d=0.25R_c$. Note that a wide magma chamber undergoes the transition from compression (-) to extension (+) at greater distances from the crater center than a narrow magma chamber. Therefore a chamber with $a>R_c$ must be shallower than a chamber with $a=R_c$ to explain the transition from concentric ridges to concentric graben at $r\sim0.5R_c$ in the Olympus Mons caldera.

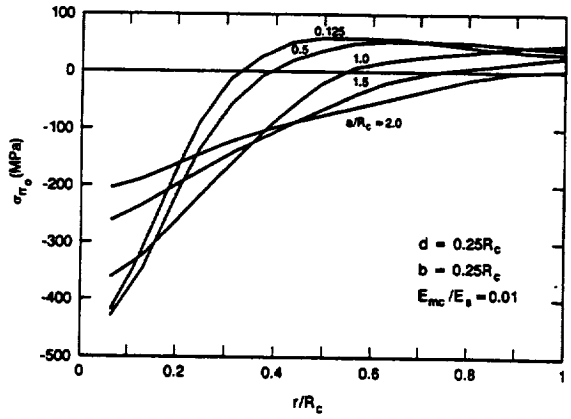


U.S.GOVERNMENT PRINTING OFFICE:1990-561-057/20079